A Proof-Of-Principle Cavity-Based X-Ray Free-Electron-Laser Demonstrator at the European XFEL

Dissertation
zur Erlangung des Doktorgrades
an der Fakultät für Mathematik, Informatik und Naturwissenschaften
Fachbereich Physik
der Universität Hamburg

vorgelegt von

Patrick Rauer

Hamburg

2022

Gutachter der Dissertation:	Prof. em. Dr. Jörg Roßbach Dr. Winfried Decking
Zusammensetzung der Prüfungskommission:	Prof. em. Dr. Jörg Roßbach Dr. Winfried Decking Prof. Dr. Daniela Pfannkuche Prof. Dr. Wolfgang Hillert Dr. Harald Sinn
Vorsitzende der Prüfungskommission:	Prof. Dr. Daniela Pfannkuche
Datum der Disputation:	02.03.2022
Vorsitzender Fach-Promotionsausschuss PHYSIK:	Prof. Dr. Michael Potthoff
Leiter des Fachbereichs Physik:	Prof. Dr. Wolfgang Hansen
Dekan der Fakultät MIN:	Prof. Dr. Heinrich Graener

Abstract

This thesis is centered on the foreseen realization and performance of a proof-of-principle cavity based (hard) X-ray FEL (CBXFEL) demonstrator experiment at the European XFEL facility. A CBXFEL promises to address the prominent issue of longitudinal coherence and (stable) high, narrow bandwidth spectral flux in the hard X-ray regime, in which the usually employed self amplified spontaneous emission (SASE) scheme is severely lacking.

In order to study the highly coupled system of FEL production, X-ray propagation and the crystals' thermal response, affecting the reflection characteristics, a computational framework was set up. It chains the popular *Genesis-1.3* FEL program with the self-written, highly optimized *parallel X-ray Cavity Propagator* (pXCP) wavefront propagation code and a *finite element* (FE) based modeling of the strongly non-linear thermal diffusion. In order to properly account for low-temperature thermal transport with an increased relevance of phonon boundary scattering, thermal conductivities obtained from first-principles simulation are used.

Thorough simulations are carried out, which account for realistic electron bunch distribution, inter RF-pulse bunch fluctuations and various possible errors of the X-ray optics. They reveal that with well inside state of the art optical tolerances, a simplistic two crystal backscattering setup would fulfill the main goal of the demonstrator, which is to proof that seeding and exponential radiation build with spectral narrowing occurs. However, due to the strong heating of the crystals and the following thermoelastic response, stable operation at high peak brilliance will not be feasible. Following the principle, experimental nature of the CBXFEL demonstrator setup, these effects will need to be properly measured. Using this data, counter measures can be developed towards the future realization of a permanent CBXFEL source at the European XFEL facility.

Kurzzusammenfassung

Diese Dissertation behandelt die Realisierung und erwartbaren Charakteristika eines geplanten Proof-of-Principle Cavity Based (hard) X-ray FEL (CBXFEL) Demonstrator Experimentes am European XFEL. Ein CBXFEL verspricht einen hohen Grad an longitudinaler Kohärenz, im Kontrast zu dem meist eingesetzten self amplified spontaneous emission (SASE) Prinzip. Darüber hinaus wird eine sowohl sehr hohe als auch stabile spektrale Photonenflussdichte bei niedriger Bandbreite erwartet.

Zur Untersuchung des stark gekoppelte Systems von FEL-Erzeugung, Röntgenpropagation und der thermischen Antwort der Kristalle wurde ein numerisches System entwickelt. Dieses verbindet das beliebte *Genesis-1.3*FEL Programm mit dem selbstgeschriebenen und stark optimierten *parallel X-ray Cavity Propagator* (pCXP) Programm zur Propagation von Wellenfronten und dem kommerziellen *Comsol Multiphysics*®. Letzteres wird eingesetzt zur *finite Elemente* (FE) basierten Modellierung der stark nicht-linearen thermischen Diffusion. Thermische Leitfähigkeiten aus *first-principles* Simulationen wurden verwendet zur Simulation des thermischen Transports bei tiefen Temperaturen, und der damit verbundenen erhöhten Relevanz von Grenzflächen-Streuung.

Mit diesem numerischen Ansatz sind sorgfältige Simulationen durchgeführt, die realistische Elektronenverteilungen, inter RF-Puls Elektronenpaket Fluktuationen sowie verschiedene Fehler der Röntgenoptiken mit einbeziehen. Diese Simulationen zeigen, dass innerhalb Toleranzen auf dem Stand der Technik eine simple Röntgenkavität mit zwei Kristallen in Rückstreugeometrie das Hauptziel des Demonstrators erfüllen würde. Dies ist, zu beweisen, dass sich FEL seeding und ein exponentielles Wachstum der Strahlung im Resonator ausbilden bei gleichzeitiger Verkleinerung der Bandbreite. Aufgrund der starken Erhitzung der Kristalle und der daraus folgenden thermoelastischen Antwort ist, allerdings, eine stabile Operation bei hoher Spitzenbrillanz nicht möglich. Im Bezug auf die experimentelle Natur des CBXFEL Demonstrators sollen diese Effekte sorgfältig gemessen werden. Auf Basis der gemessenen Daten lassen sich schließlich Gegenmaßnahmen entwickeln zur Realisierung einer permanenten CBXFEL Strahlungsquelle am European XFEL.

Contents

List of Figures

List of Tables

> *There are two ways of spreading light:*
> *to be the candle or the mirror that reflects it.*
> ***Edith Wharton***

1 Introduction

The interaction of light with our surroundings is the predominant way for most of us to perceive our environment. Scientists have used this interaction for a long time to study the physics of nature. The principle of *light amplification by stimulated emission of radiation* (laser) has proven to be one of the most important scientific tools of our days. Experiments and commercial applications, from ones needing very high intensities in a short amount of time (down to attoseconds) to ones needing very well defined energies of the participating quanta of light (the photons) with a high degree of three dimensional coherency, have benefited enormously.

Traditional lasers are based on the excitation of electrons in gases, liquids or solids into elevated states with well defined energies. There they mostly remain until a photon of corresponding energy leads to a stimulated drop of the electrons into their ground states emitting photons with equal phase. As a laser is most effective when the number of stimulative emitted photons is high, the electrons need to stay a sufficient time in their exited states. These lifetimes on the other hand correlate to the frequency linewidth and thereby to the wavelengths of the emitted photons making it increasingly difficult to operate laser at low wavelengths[1, Chapter 1]. This difficulty is amplified by the lack of high quality reflecting mirrors in the low-wavelength regime needed for forming a reflecting cavity on which most lasers are based. To-date no population inversion based laser for the Å to single nm regime exists yet. Though, recently it was proposed to use a high intensity high repetition rate *free-electron laser* (FEL) as pumping source in combination with a crystal mirror X-ray cavity to overcome this [2].

On the other side X-ray radiation [3] (reaching from 0.01 nm to 10 nm) has proven an important experimental means and has played a pivotal role in society - for example due to its important role in the understanding of the DNA. Originally located in the scientific field of physics, X-rays soon became a tool for research in almost all branches of science [4, ch.1]. This is due to its broad range of application reaching from crystallography - to study the structure of materials -, over spectrography to imaging techniques being used as well in medicine as in archeology [4, 5]. To-date electron accelerators have become - using the principle of synchrotron radiation - the most important facilities to produce intense and tunable low wavelength radiation from the UV to the X-ray regime. Originally perceived as a bothersome side-effect which limits the maximum energy in circular electron accelerators [6], it has become a desirable effect for which more than 70 dedicated large scale research facilities have been or are being built [4, ch.1].

A standard figure of merit for synchrotrons is the *brilliance* describing the spectral flux of radiation per unit source area and unit solid angle. Over the last six decades there has been an increase of the order of 10^{23} with the apex of peak brilliance being attributed to the construction of so called *X-Ray free-electron lasers* (XFELS) as can be seen in Figure (1.1). In chapter **2** there is a comprehensive overview over the physics of synchrotrons and of FELs.

Current hard XFEL facilities such as LCLS, euXFEL, SACLA, SwissFEL and PAL are based on the self-amplified spontaneous emission (SASE) scheme for operation. While these sources produce very brilliant femtosecond X-ray pulses with excellent transverse coherence, they suffer from two major disadvantages. For one, they need very long undulator sections to reach saturation due to being initially seeded by comparably weak spontaneous emission. More fundamental is its rather low degree of monochromaticity on the order of 1 ‰ and the lack of longitudinal coherence as one radiation pulse consists of 100 to 10000s of longitudinal modes [7][1]. This is making them inferior to classical optical lasers which may provide nearly full longitudinal coherence and outstanding monochromaticity smaller than 1×10^{-10}. In order to reach a lower frequency bandwidth on the order of 10^{-6} to 10^{-5} and to select only a single longitudinal mode, one needs to use crystal monochromators. These are selecting only a small portion of the SASE spectrum, different from shot to shot, cutting away the majority of incident flux with the resulting transmitted radiation fluctuating over roughly 100 %. Over the recent years multiple schemes have been proposed and partly realized to improve this. These schemes attribute to the seeding of the electron bunches by a monochromatic source. Seeded XFELs for example promise new frontiers in the investigation of non-linear X-ray optics [8, 9]. Schemes based on the seeding by an external source such as *high-harmonic generation*, *high-gain harmonic generation* and *echo-enabled harmonic generation* are more suited to the soft X-ray regime [10][2]. For the hard X-ray regime the principle of self-seeding [13] using crystal monochromators in between two undulator sections has first been demonstrated at LCLS in 2012 [14] and was later also shown at PAL [15] and SACLA [16]. Recently at the EuXFEL

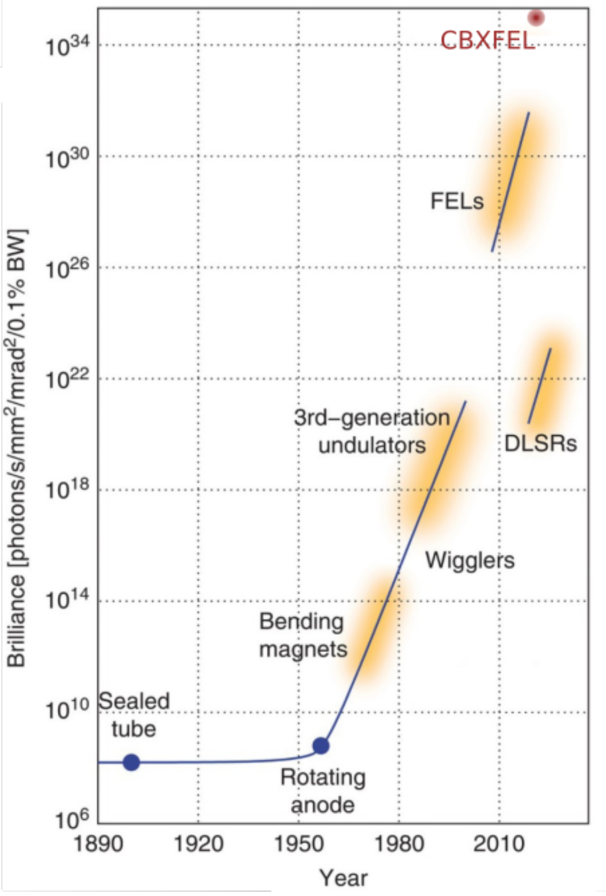

Figure 1.1: Historic perspective of the enormous increase in brilliance over the past decades. The red dot roughly denotes the peak brilliance of a CBXFEL at the euXFEL calculated in this work. Adapted from [4].

---

[1] The degree of longitudinal coherence scales inversely to the number of longitudinal modes.

[2] Recently, it has been proposed to combine a*high-gain harmonic generation* scheme with an oscillator scheme (see below) to enable high repetition rate seeding [11, 12].

preliminary commissioning results were obtained [17]. While the self-seeding process showed an increase in spectral brilliance [15, 16], it still lacks from three deficiencies. The first is the remaining need for long undulator sections. The second and more prominent is the rather high shot-to-shot spectral flux jitter [15]. This might be reduced by using a cascaded three-section self seeding scheme [18, 19] installed at the EuXFEL, which also promises to improve the signal-to-noise ratio. But the concept remains to be proven [17]. The third is the degradation of the electron bunches due to the first undulator section/s producing the seed, which can be overcome by using fresh electron slices for each section.

An approach promising to diminish these effects is the low-gain *X-ray free-electron-laser oscillator* (XFELO) proposed by *Kim et al.* in 2008 [20] or the high gain *X-ray regenerative amplifier FEL* (XRAFEL) proposed by *Huang and Ruth* in 2006 [21], which have received growing interest over the recent years [22–33]. These *cavity based X-ray FEL* (CBXFEL) schemes are based on using a short undulator section, compared to state of the art hard X-Ray SASE sources, and a highly reflective X-ray cavity based on very pure diamond or silicon crystals serving as Bragg reflectors. As these Bragg reflectors also act as spectral filters, an XFELO promises a spectral bandwidth on the order of the crystals bandwidth ($\Delta\lambda/\lambda_c \approx 10^{-5} - 10^{-7}$) and therefore orders of magnitude better than SASE FELs. For the XFELO, as the radiation field is built up over many cavity round trips, very low shot-to-shot fluctuations can be expected, even making it a promising candidate for X-ray quantum optics (XQO) [29]. In the following, these schemes will be summarized under the more general phrase *c̲avity b̲ased XFEL* (CBXFEL).

With the recently commissioned European XFEL the realization of an XFELO becomes in reach. This is due to the facility's excellent electron beam properties and especially due to its very high bunch repetition rate of up to $4.5\,\mathrm{MHz}$ in pulsed-mode [34] which enables resonator lengths of only $33\,\mathrm{m}$. As will be evident from section **5**, given the beam properties of the European XFEL the single pass gain is in between the original propositions by *Kim et al.* in 2008 and *Huang and Ruth* in 2006. This comes with some advantages such as lower demands on the mechanical tolerances, but also with some disadvantages as will be discussed later.

A major issue one needs to address when dealing with an CBXFEL is the effect of the light-matter interaction between the X-ray field and the Bragg reflectors. This is due to the high requirements for the angular and spatial stability [35, 36] as well as the necessity of very stable Bragg conditions.

1.1 Thesis Structure

This thesis centers around the question if the implementation of an CBXFEL is feasible at the EuXFEL facility also including the effect of heating of the monochromators. It emphasizes on the development, analysis and discussion of a proof-of-principle CBXFEL demonstrator experiment, which shall be realized in the near feature. The demonstrator will be a comparatively simplistic version of a CBXFEL mainly consisting of two diamond reflectors added by optical focussing elements.

The text is structured as followed: First an overview over synchrotron and FEL physics, with an emphasizes on the latter and including information about CBXFEL sources, is given in Chapter **2**. In Chapter **3** the physics of the radiation-crystal interaction relevant for a CBXFEL will be discussed. This includes the influence of the crystal on the radiation in the form of diffraction as well as the influence of the radiation on the crystal in the form of heating. In Chapter **4** the computational approach to simulate a multiple round trip cavity based XFEL is presented. This includes a self written wavefront propagation code, which interfaces both to the well-known FEL simulation program *Genesis-1.3* for the FEL part and to the calculation of the crystal thermal answer being realized by the commercial software *Comsol Multiphysics*®. It enables, for the first time, a fully coupled approach to study a CBXFEL including the influence of heat load. This program will be used in Chapter **5** to calculate the optimal parameters for the CBXFEL proof-of-principle experiment at the end of the SASE1 beamline at the EuXFEL. At last, in Chapter **6** a conclusion and a concise outlook will be given. In the appendix, important but not crucial information regarding the central points of the CBXFEL are given. These include a shallow description of electron beam related parameters in Appendix **A**, an overview over the European XFEL accelerator and FEL lines in Appendix **B**, a description of the crystal and total reflecting mirror assembly in **C** and, finally, in Appendix **D** some notes about the gaussian beam fundamental mode and what this dictates for an optical cavity.

2 The principles of free-electron lasers

In this chapter the physics of FEL- and synchrotron radiation – on which former is based on – shall be shortly highlighted. For a more profound overview on the topic the reader is referred to the big pool of well researched literature, like for example [4, 37–40].
The chapter will begin with the definition of some important properties which are general to photon beams and not specific to synchrotron based sources. It proceeds with an introduction to synchrotron radiation and will segue into the principles of FEL radiation discussing the different types of FELs – FEL Oscillators, FEL Amplifiers and SASE FELs – and important parameters for their description. Finally, cavity based XFELs (CBXFELs) shall be superficially described and classified into above types.

2.1 General Properties of Radiation Beams

Principally, alike electron beams electromagnetic radiation can be described on a six dimensional phase space. For laser beams with a defined axis of propagation, one can conveniently distinguish the phase space into longitudinal phase space coordinates (t, ω) parallel to the propagation axis and the transverse coordinates $\boldsymbol{x}_\perp, \boldsymbol{k}_\perp$. Regarding the longitudinal coordinates, the radiation field is usually expressed either in the time- t or the frequency ω domain, with both being the Fourier transformation of each other:

$$\begin{aligned} \boldsymbol{\mathcal{E}}(t) = {} & \tfrac{1}{2\pi} \int \tilde{\boldsymbol{\mathcal{E}}}_\omega \exp\left(-\mathrm{i}\omega t\right) \mathrm{d}\omega, \\ \tilde{\boldsymbol{\mathcal{E}}}_\omega = {} & \int \boldsymbol{\mathcal{E}}(t) \exp\left(\mathrm{i}\omega t\right) \mathrm{d}t. \end{aligned} \tag{2.1}$$

Assuming a quasi-monochromatic wave, meaning that the electromagnetic field amplitude can be expressed by $\boldsymbol{\mathcal{E}}(t) = \boldsymbol{E}(t)e^{\mathrm{i}\omega_0 t}$ with $\boldsymbol{E}(t)$ being slowly varying in time compared to $\mathrm{e}^{\mathrm{i}\omega_0 t}$ with the carrier frequency ω_0, the slowly varying $\boldsymbol{E}(t)$ can be considered a good representation of the electromagnetic field. For the frequency space this component becomes $\tilde{\boldsymbol{E}}_\omega = \tilde{\boldsymbol{\mathcal{E}}}_{\omega-\omega_0}$. In the following, $\boldsymbol{E}(t)$ and $\tilde{\boldsymbol{E}}_\omega$ will be used instead of $\boldsymbol{\mathcal{E}}(t)$ and $\tilde{\boldsymbol{\mathcal{E}}}_\omega$, respectively. Also, to stay consistent with later chapters, the spectral component will be expressed in form of the photon energy

$$\begin{aligned} E_{\mathrm{ph}} &= \hbar\omega \\ \rightarrow \boldsymbol{E}\left(E_{\mathrm{ph}}\right) &\mathrel{\widehat{=}} \boldsymbol{E}_\omega, \end{aligned}$$

with the reduced planck constant $\hbar = 6.582\,119\,569 \times 10^{-16}$ eV s.
As for the longitudinal coordinates, in the transverse domain the radiation field can either be expressed in the spatial $\boldsymbol{x}_\perp$ or in the angular $\boldsymbol{k}_\perp$ domain:

$$\begin{aligned} \boldsymbol{E}\left(\boldsymbol{x}_\perp\right) = {} & \tfrac{1}{(2\pi)^2} \iint \boldsymbol{A}\left(\boldsymbol{k}_\perp\right) \exp\left(-\mathrm{i}\boldsymbol{k}_\perp \boldsymbol{x}_\perp\right) \mathrm{d}\boldsymbol{k}_\perp, \\ \boldsymbol{A}\left(\boldsymbol{k}_\perp\right) = {} & \iint \boldsymbol{E}\left(\boldsymbol{x}_\perp\right) \exp\left(\mathrm{i}\boldsymbol{k}_\perp \boldsymbol{x}_\perp\right) \mathrm{d}\boldsymbol{x}_\perp, \end{aligned} \tag{2.2}$$

where the transformation is equally valid in time- as in the frequency representation.
As the longitudinal and transverse degrees of freedom often have very distinct characteristics, it is beneficial to divide these and treat them separately. Therefore, it is convenient to find a one dimensional representation for the longitudinal and a two dimensional representation for the tranverse coordinates. There are basically two choices for these representations. The first is to look at the longitudinal radiation distribution at a specific transverse position or the transverse radiation distribution at a frequency/time. The second is to look at the longitudinal radiation distribution integrated over the full transverse spatial/angular space or the transverse radiation distribution integrated over the full radiation pulse bandwidth/duration. In this work, usually the integrated representation is used as it is not dependent on a specific position and hence more stable against local deviations in the other, orthogonal phase space. This is especially useful when dealing with statistical, non-deterministic fluctuations. In this regard, the power profile of the radiation field, which is the Poynting vector $\boldsymbol{S} = (\boldsymbol{E} \times \boldsymbol{B})$ projected on the propagation axis $\hat{\boldsymbol{z}}$ and integrated over the transverse plane $\boldsymbol{x}_\perp$, is a suitable representation for the time domain [39, p.17]. For a quasi-monochromatic wave in vacuum, one obtains for the power [41, p.61]

$$P(t) = \iint \hat{\boldsymbol{z}} \cdot \langle \boldsymbol{S} \rangle_{T_0} \mathrm{d}\boldsymbol{x}_\perp = \frac{1}{\mu_0 c} \iint |\boldsymbol{E}(\boldsymbol{x}_\perp, t)|^2 \mathrm{d}\boldsymbol{x}_\perp = \iint I(\boldsymbol{x}_\perp) \mathrm{d}\boldsymbol{x}_\perp, \tag{2.3}$$

where the $\langle . \rangle$ denotes averaging over the period $T_0 = {}^{2\pi}/_{\omega_0}$ of the carrier frequency, $I(\boldsymbol{x}_\perp)$ is the spatially dependent intensity and c =299 792 458 m/s and μ_0 =1.256 637 062 12(19) × 10^{-6} N/A^2 are the speed of light and the vacuum permeability[42]. In a similar fashion the spectral energy density is defined as

$$\mathcal{S}(E_{\mathrm{ph}}) = \iint \frac{1}{\mu_0 c} |\tilde{\boldsymbol{E}}\left(\boldsymbol{x}_\perp, E_{\mathrm{ph}}\right)|^2 \mathrm{d}\boldsymbol{x}_\perp \tag{2.4}$$

The radiant energy Q_{pulse} can be obtained by either integrating over the power profile or the spectral energy density:

$$Q_{\mathrm{pulse}} = \int P(t) \mathrm{d}t = \int \mathcal{S}(E_{\mathrm{ph}}) \mathrm{d}E_{\mathrm{ph}}. \tag{2.5}$$

Likewise, for the transverse coordinates one may define for the spatial domain the *radiant fluence*

$$W = \frac{\partial Q_{\mathrm{pulse}}}{\partial \boldsymbol{x}_\perp} = \int \boldsymbol{E}\left(\boldsymbol{x}_\perp, t\right) \mathrm{d}t = \int \tilde{\boldsymbol{E}}\left(\boldsymbol{x}_\perp, E_{\mathrm{ph}}\right) \mathrm{d}E_{\mathrm{ph}} \tag{2.6}$$

and for the angular domain the *radiant angular fluence*

$$W_\phi = \frac{\partial Q_{\mathrm{pulse}}}{\partial \boldsymbol{k}_\perp} = \int \boldsymbol{A}\left(\boldsymbol{k}_\perp, t\right) \mathrm{d}t = \int \tilde{\boldsymbol{A}}\left(\boldsymbol{k}_\perp, E_{\mathrm{ph}}\right) \mathrm{d}E_{\mathrm{ph}}. \tag{2.7}$$

Many characteristic properties can be expressed as moments of the radiation distribution, where again a subdivision is made into longitudinal and transverse moments. For both, one has to distinguish between integrated moments and slice or axial moments. For former, the longitudinal moments are the weighted mean over the transverse phase space and vice versa. For latter, the longitudinal moments are taken at a specific position $(\boldsymbol{x}_{\perp,0})$ or $(\boldsymbol{k}_{\perp,0})$, respectively. In this work, as for the phase space representations, usually the integral convention is used being more stable against local deviations.

Specifically, for the integrated longitudinal moments $(t, E_{\mathrm{ph}})^i$, with $i \in \mathcal{N}$, we have

$$\begin{aligned} \langle t^i \rangle = & \frac{\iiint t^i |E\left(\boldsymbol{x}_\perp, t\right)|^2 \mathrm{d}\boldsymbol{x}_\perp \mathrm{d}t}{\iiint |E\left(\boldsymbol{x}_\perp, t\right)|^2 \mathrm{d}\boldsymbol{x}_\perp \mathrm{d}t} = \frac{\iiint t^i |A\left(\boldsymbol{k}_\perp, t\right)|^2 \mathrm{d}\boldsymbol{k}_\perp \mathrm{d}t}{\iiint |A\left(\boldsymbol{x}_\perp, t\right)|^2 \mathrm{d}\boldsymbol{k}_\perp \mathrm{d}t}, \\ \langle E_{\mathrm{ph}}^i \rangle = & \frac{\iiint E_{\mathrm{ph}}^i |\tilde{E}\left(\boldsymbol{x}_\perp, E_{\mathrm{ph}}\right)|^2 \mathrm{d}\boldsymbol{x}_\perp \mathrm{d}E_{\mathrm{ph}}}{\iiint |\tilde{E}\left(\boldsymbol{x}_\perp, E_{\mathrm{ph}}\right)|^2 \mathrm{d}\boldsymbol{x}_\perp \mathrm{d}E_{\mathrm{ph}}} = \frac{\iiint \omega^i |\tilde{A}\left(\boldsymbol{k}_\perp, E_{\mathrm{ph}}\right)|^2 \mathrm{d}\boldsymbol{k}_\perp \mathrm{d}E_{\mathrm{ph}}}{\iiint |\tilde{A}\left(\boldsymbol{x}_\perp, E_{\mathrm{ph}}\right)|^2 \mathrm{d}\boldsymbol{k}_\perp \mathrm{d}E_{\mathrm{ph}}}. \end{aligned} \tag{2.8}$$

Under the assumption of an approximately normal distributed beam, the bandwidth and the duration can be well described by the respective standard deviation, which can be expressed in terms of the longitudinal moments

$$\sigma_E^2 = \langle E_{\mathrm{ph}}^2 \rangle - \langle E_{\mathrm{ph}} \rangle^2 \tag{2.9}$$

$$\sigma_t^2 = \langle t^2 \rangle - \langle t \rangle^2 . \tag{2.10}$$

The same applies to the transverse degrees of freedom $\boldsymbol{x}_\perp = (x, y)$ and $\boldsymbol{k}_\perp = (k_x, k_y)$, with the addition that generally coupling terms $\langle xy \rangle \neq 0$ and $\langle k_x k_y \rangle \neq 0$ between the transverse degrees of freedom persist:

$$\begin{aligned} \langle x^i y^j \rangle = & \frac{\iiint x^i y^j |E\left(\boldsymbol{x}_\perp, t\right)|^2 \mathrm{d}t \mathrm{d}\boldsymbol{x}_\perp}{\iiint |E\left(\boldsymbol{x}_\perp, t\right)|^2 \mathrm{d}t \mathrm{d}\boldsymbol{x}_\perp} = \frac{\iiint x^i y^j |\tilde{E}\left(\boldsymbol{x}_\perp, E_{\mathrm{ph}}\right)|^2 \mathrm{d}E_{\mathrm{ph}} \boldsymbol{x}_\perp}{\iiint |\tilde{E}\left(\boldsymbol{x}_\perp, E_{\mathrm{ph}}\right)|^2 \mathrm{d}E_{\mathrm{ph}} \mathrm{d}\boldsymbol{x}_\perp}, \\ \langle k_x^i k_y^j \rangle = & \frac{\iiint k_x^i k_y^j |A\left(\boldsymbol{k}_\perp, t\right)|^2 \mathrm{d}t \mathrm{d}\boldsymbol{k}_\perp}{\iiint |A\left(\boldsymbol{k}_\perp, t\right)|^2 \mathrm{d}t \mathrm{d}\boldsymbol{k}_\perp} = \frac{\iiint k_x^i k_y^j |\tilde{A}\left(\boldsymbol{k}_\perp, E_{\mathrm{ph}}\right)|^2 \mathrm{d}E_{\mathrm{ph}} \mathrm{d}\boldsymbol{k}_\perp}{\iiint |\tilde{A}\left(\boldsymbol{x}_\perp, E_{\mathrm{ph}}\right)|^2 \mathrm{d}E_{\mathrm{ph}} \mathrm{d}\boldsymbol{k}_\perp}. \end{aligned} \tag{2.11}$$

As for the longitudinal moments, assuming a normal distributed beam, the width and divergence can be expressed by the respective standard deviations via [43]

$$\boldsymbol{\sigma}_{\boldsymbol{r}}^2 = \left[\begin{pmatrix} \langle x^2 \rangle & \langle xy \rangle \\ \langle xy \rangle & \langle y^2 \rangle \end{pmatrix} - \begin{pmatrix} \langle x \rangle^2 & \langle x \rangle \langle y \rangle \\ \langle x \rangle \langle y \rangle & \langle y \rangle^2 \end{pmatrix} \right] \tag{2.12}$$

$$\boldsymbol{\sigma}_{\boldsymbol{k}}^2 = \left[\begin{pmatrix} \langle k_x^2 \rangle & \langle k_x k_y \rangle \\ \langle k_x k_y \rangle & \langle k_y^2 \rangle \end{pmatrix} - \begin{pmatrix} \langle k_x \rangle^2 & \langle k_x \rangle \langle k_y \rangle \\ \langle k_x \rangle \langle k_y \rangle & \langle k_y \rangle^2 \end{pmatrix} \right] . \tag{2.13}$$

As was mentioned above, these standard deviations are a good measure for the width of the respective phase space coordinate if the phase space can generally be approximated by a normal distribution. This is often the case for radiation either averaged over many round trips or radiation driven by a gaussian distributed electron beam. As we will see in Chapter **5** it is not a good approximation for the CBXFEL radiation beam, at least not for the case studied here, which shows a rather wide tail besides the central peak in the longitudinal coordinates. As the standard deviation weights these outliers quadratically, in this work often also the *Mean Absolute Deviation* (MAD) is used as measure for bandwidth and duration, which is more robust with respect to deviations from the normal distribution [44, ch.13.7]. It is defined for a variable $u = (\omega, t)$ as

$$\mathcal{D}_{u,\mathrm{MAD}} = \frac{\iiint |u - \langle u\rangle| |E(\boldsymbol{x}_\perp, u)|^2 \mathrm{d}\boldsymbol{x}_\perp \mathrm{d}u}{\iiint |E(\boldsymbol{x}_\perp, u)|^2 \mathrm{d}\boldsymbol{x}_\perp \mathrm{d}u} = \frac{\iiint |u - \langle u\rangle| |A(\boldsymbol{k}_\perp, u)|^2 \mathrm{d}\boldsymbol{k}_\perp \mathrm{d}u}{\iiint |A(\boldsymbol{x}_\perp, u)|^2 \mathrm{d}\boldsymbol{k}_\perp \mathrm{d}u} \tag{2.14}$$

, where $\langle u\rangle$ is the coordinate's mean as defined by the first moment $i = 1$ in equation (2.8). For a normal distribution $\sigma_u = \sqrt{\frac{\pi}{2}}\mathcal{D}_{u,\mathrm{MAD}}$ [44, p.628].

For the special case of perfect linear transport – meaning only elements linearly dependent on the phase-space coordinates with 100 % transmittance are considered –, one may define a phase space measure which is constant over propagation. For the transverse phase space, assuming a transversely totally coherent beam, one may define the factor [43]

$$J = 0.5\mathrm{Tr}\left(\boldsymbol{M}^4\right) \tag{2.15}$$

$$\text{with} \quad \boldsymbol{M}^4 = 4\left(\boldsymbol{\sigma}_{\boldsymbol{r}}^2 \boldsymbol{\sigma}_{\boldsymbol{k}}^2 - S^2\right), \tag{2.16}$$

where Tr is the trace operator, $k_0 = {}^{\omega_0}/_{c} = {}^{E_{\mathrm{ph},0}}/_{\hbar c}$ and

$$S = -\frac{1}{Q_{\mathrm{pulse}}} \cdot \begin{pmatrix} \iint |E|^2 (x - \langle x\rangle) \frac{\partial\phi}{\partial x} \mathrm{d}\boldsymbol{x}_\perp \mathrm{d}t & \iint |E|^2 (x - \langle x\rangle) \frac{\partial\phi}{\partial y} \mathrm{d}\boldsymbol{x}_\perp \mathrm{d}t \\ \iint |E|^2 (y - \langle y\rangle) \frac{\partial\phi}{\partial x} \mathrm{d}\boldsymbol{x}_\perp \mathrm{d}t & \iint |E|^2 (y - \langle y\rangle) \frac{\partial\phi}{\partial y} \mathrm{d}\boldsymbol{x}_\perp \mathrm{d}t \end{pmatrix},$$

$$\text{with} \quad \Phi(\boldsymbol{x}_\perp, t) = \mathrm{phase}\left[\boldsymbol{E}(\boldsymbol{x}_\perp, t)\right]$$

is a measure for the wavefront. J obtains its minimal value of one for a gaussian beam. As such, the value J is also a measure for the deviation from a gaussian beam.

For pulsed FELs experiments, where often a monochromator is involved, the so called peak spectral brightness [45, 37, ch. 9.1]

$$\mathcal{B} = \frac{\hbar \mathrm{d}^2 \mathcal{N}_{\mathrm{ph}}}{4\pi^2 \Delta\mathcal{A} \Delta\Theta \mathrm{d}E_{\mathrm{ph}} \mathrm{d}t}, \tag{2.17}$$

which is the density of photons in the full six dimensional phase space, has evolved as a figure of merit. $\Delta\mathcal{A}$ is the spatial source size and $\Delta\Theta$ is the source divergence. Just as the gaussian quality factor, it is a conserved quantity through propagation in a perfect linear optical system. The spectral photon flux ${}^{\hbar\mathrm{d}^2\mathcal{N}_{\mathrm{ph}}}/_{\mathrm{d}t\mathrm{d}E_{\mathrm{ph}}}$ can be approximated as the total number of photons per unit time $\dot{N}_{\mathrm{Ph}} = {}^{P}/_{E_{\mathrm{ph},0}}$ divided by the relative bandwidth $\Delta E_{\mathrm{ph}}/E_{\mathrm{ph},0}$ [37, ch.9.1]. Assuming a coherent beam that can be approximated by a rectangular shape of width $\Delta E_{\mathrm{ph}} = \sqrt{2\pi}\sigma_E$ in the spectral domain and equally rectangular shape of duration $\Delta t = \sqrt{2\pi}\sigma_t$, one can write the spectral photon flux as

$$\frac{\hbar \mathrm{d}^2 \mathcal{N}_\mathrm{ph}}{\mathrm{d}E_\mathrm{ph}\mathrm{d}t} \approx \frac{Q_\mathrm{pulse}}{2\pi\sigma_E\sigma_t}. \tag{2.18}$$

The difficulty now arises, how to assess the diffraction limited source size ΔA and divergence $\Delta\Theta$. The simplest approach is to use the projected moments $\Delta A \approx \sigma_x\sigma_y$ (Eq. (2.12)) in the spatial domain and $\Delta\Theta \approx \lambda_0^2\sigma_{k_x}\sigma_{k_y} = \hbar\lambda_0\sigma_{k_x}\sigma_{k_y}/E_\mathrm{ph}$ (Eq. (2.13)) in the angular domain, independently. Then one can make use of the gaussian quality factor Eq. (2.16) and calculate the brilliance Eq. (2.17) as

$$\mathcal{B} = \frac{Q_\mathrm{pulse}}{\pi^2\hbar\lambda_0 c M_{xx}^2 M_{yy}^2}\frac{E_\mathrm{ph,0}}{\sigma_t\sigma_E}, \tag{2.19}$$

where $\lambda_0 = {}^{hc}/_{E_\mathrm{ph,0}}$ is the central wavelength and $M_{xx|yy}^2 = \sqrt{M_{xx|yy}^4}$.

However, being based on the simple product of projected size and projected divergence, the gaussian quality factor can principally strongly deviate from the real phase space volume, as it cannot model strong correlations between position and angle [45]. For a more general assessment of the phase space volume and, therefore, the brilliance Eq. (2.17), one should have a closer look at the coherence properties of the radiation. Actually, the properties derived up to now all were based on the assumption of a coherent distribution, where the different domains can be properly divided. This is generally not the case. The basic concept for the theory of optical coherence is the *mutual coherence function*(MCF) [46]

$$\Gamma\left(\boldsymbol{x}_{\perp,1}, \boldsymbol{x}_{\perp,2}, t_1, t_2\right) = \left\langle \mathcal{E}^*\left(\boldsymbol{x}_{\perp,1}, t_1\right)\mathcal{E}\left(\boldsymbol{x}_{\perp}, t_2\right)\right\rangle, \tag{2.20}$$

where $\langle . \rangle$ denotes an ensemble average to account for the statistical nature of coherence. Assuming the radiation field as quasi-stationary, meaning that the statistical properties of the radiation do not dependent on the actual time [41, p.608], then the mutual coherence function can be defined in terms of the time difference $t_1 - t_2$

$$\Gamma\left(\boldsymbol{x}_{\perp,1}, \boldsymbol{x}_{\perp,2}, t_1 - t_2\right) = \left\langle \mathcal{E}^*\left(\boldsymbol{x}_{\perp,1}, t_1\right)\mathcal{E}\left(\boldsymbol{x}_{\perp}, t_2\right)\right\rangle.$$

Based on the MCF, one may define a normalized version

$$g_1\left(\boldsymbol{x}_{\perp,1}, \boldsymbol{x}_{\perp,2}, t_1 - t_2\right) = \frac{\left\langle E^*\left(\boldsymbol{x}_{\perp,1}, t_1\right)E\left(\boldsymbol{x}_{\perp,2}, t_2\right)\right\rangle}{\left[\left\langle\left|E\left(\boldsymbol{x}_{\perp,1}, t_1\right)\right|^2\right\rangle\left\langle\left|E\left(\boldsymbol{x}_{\perp,2}, t_2\right)\right|^2\right\rangle\right]^{\frac{1}{2}}}, \tag{2.21}$$

where the electromagnetic field function $\mathcal{E}$ has been replaced by its slowly varying amplitude. The normalized MCF becomes unity for a fully coherent field and 0 for a fully incoherent one. The field hence is partially coherent for any value between.

The longitudinal domain coherence can be described by the first-order time correlation function

$\mathcal{C}(t_1, t_2)$, which is the normalized MCF (2.21) g_1 taken at position $\boldsymbol{x}_{\perp,1} = \boldsymbol{x}_{\perp,2}$. Under the assumption of the quasi-stationary process, following the Wiener-Khintchine theorem, one can then write this using the spectral domain representation as [46, 37, pp119 ff.]

$$\mathcal{C}(\tau) = \frac{\langle \int |\tilde{E}\left(E_{\text{ph}}\right)|^2 e^{\mathrm{i}E_{\text{ph}}\tau/\hbar} \mathrm{d}E_{\text{ph}} \rangle}{\langle \int |\tilde{E}\left(E_{\text{ph}}\right)|^2 \mathrm{d}E_{\text{ph}} \rangle} \tag{2.22}$$

. One can then define a coherence time via [47, 48]

$$\tau_{\text{coh}} = \int_{-\infty}^{\infty} |\mathcal{C}(\tau)|^2 \mathrm{d}\tau. \tag{2.23}$$

Under the quasi-stationary assumption the transverse coherence function γ is independent of time and becomes

$$\gamma\left(\boldsymbol{x}_{\perp,1}, \boldsymbol{x}_{\perp,2}\right) = \frac{\langle E^*\left(\boldsymbol{x}_{\perp,1}\right) E\left(\boldsymbol{x}_{\perp,2}\right) \rangle}{\left[\langle |E\left(\boldsymbol{x}_{\perp,1}\right)|^2 \rangle \langle |E\left(\boldsymbol{x}_{\perp,2}\right)|^2 \rangle\right]^{\frac{1}{2}}}.$$

Based on the transverse coherence function, one may define a single parameter ξ characterizing the degree of transverse coherence, which is [47]

$$\xi_{\text{coh}} = \frac{\iiiint |\gamma\left(\boldsymbol{x}_{\perp,1}, \boldsymbol{x}_{\perp,2}\right)|^2 |E\left(\boldsymbol{x}_{\perp,1}\right)|^2 |E\left(\boldsymbol{x}_{\perp,2}\right)|^2 \mathrm{d}\boldsymbol{x}_{\perp,1} \mathrm{d}\boldsymbol{x}_{\perp,2}}{\left[\iint |E\left(\boldsymbol{x}_{\perp}\right)|^2 \mathrm{d}\boldsymbol{x}_{\perp}\right]^2}. \tag{2.24}$$

Using the definition of the transverse coherence, one can adjust the general definition of peak brilliance (2.17) to the more general case of partial coherence via [47]

$$\mathcal{B} = \frac{4E_{\text{ph},0} \mathrm{d}\dot{N}_{\text{ph}}}{\mathrm{d}E_{\text{ph}}} \frac{\xi}{\lambda_0^2} \approx \frac{2Q_{\text{pulse}}}{\pi^2 \hbar \lambda_0 c} \frac{E_{\text{ph},0}}{\sigma_t \sigma_E} \xi_{\text{coh}}, \tag{2.25}$$

where for the last step the same simplifications as for Eq. (2.19) have been applied. Equation (2.25) is a more general expression for the brilliance, but much more time demanding to numerically calculate as well as more involved to assess experimentally.

For some cases, it is useful to characterize a radiation pulse in both spectral and temporal domain. There are many choices of time-frequency signal distributions which all have certain advantages and disadvantages. One of these representations is the Wigner distribution, which is defined as [49]

$$\mathcal{W}\left(\boldsymbol{x}_{\perp,1}, t, E_{\text{ph}}\right) = \frac{1}{2\pi} \int_{-\infty}^{\infty} \Gamma\left(\boldsymbol{x}_{\perp,1} = \boldsymbol{x}_{\perp,2}, t, t+\tau\right) e^{\mathrm{i}E_{\text{ph}}\tau/\hbar} \mathrm{d}\tau, \tag{2.26}$$

where $\Gamma(\boldsymbol{x}_{\perp,1} = \boldsymbol{x}_{\perp,2}, t, \tau)$ is the mutual coherence function (2.20) at the transverse position $\boldsymbol{x}_{\perp,1} = \boldsymbol{x}_{\perp,2}$. From all time-frequency representations the Wiener distribution has the highest (actually infinite) resolution in both domains. This comes with the downside that it also yields non-physical negative values and interference cross-terms, which are usually difficult to interpret. Nonetheless, it can be qualitatively interpreted equally to other time-frequency distribution[3] with the advantage of providing a high resolution. The intensity profile and spectral power at $\boldsymbol{x}_{\perp,1}$ can be expressed as projections of the Wigner distribution on the time- or spectral domain, respectively[49]:

$$\begin{aligned}\langle I\left(\boldsymbol{x}_{\perp}, t\right)\rangle &= \int_{-\infty}^{\infty} \mathcal{W}\left(\boldsymbol{x}_{\perp}, t, E_{\mathrm{ph}}\right) \mathrm{d}E_{\mathrm{ph}} \\ \langle \tilde{I}\left(\boldsymbol{x}_{\perp}, E_{\mathrm{ph}}\right)\rangle &= \int_{-\infty}^{\infty} \mathcal{W}\left(\boldsymbol{x}_{\perp}, t, E_{\mathrm{ph}}\right) \mathrm{d}t\end{aligned}$$

The first moments of the Wigner distribution are the group delay $\langle t_0\rangle\left(\boldsymbol{x}_{\perp}, E_{\mathrm{ph}}\right)$ and instantaneous photon energy $\langle E_{\mathrm{ph},0}\rangle\left(\boldsymbol{x}_{\perp}, t\right)$ in the temporal and spectral domain, respectively:

$$\langle t_0\rangle\left(\boldsymbol{x}_{\perp}, E_{\mathrm{ph}}\right) = \frac{1}{\langle \tilde{I}\left(\boldsymbol{x}_{\perp}, E_{\mathrm{ph}}\right)\rangle} \int_{-\infty}^{\infty} t\mathcal{W}\left(\boldsymbol{x}_{\perp}, t, E_{\mathrm{ph}}\right) \mathrm{d}t \tag{2.27}$$

$$\langle E_{\mathrm{ph},0}\rangle\left(\boldsymbol{x}_{\perp}, t\right) = \frac{1}{\langle I\left(\boldsymbol{x}_{\perp}, t\right)\rangle} \int_{-\infty}^{\infty} E_{\mathrm{ph}}\mathcal{W}\left(\boldsymbol{x}_{\perp}, t, E_{\mathrm{ph}}\right) \mathrm{d}E_{\mathrm{ph}} \tag{2.28}$$

Likewise, the group duration $\langle\sigma_t\rangle\left(\boldsymbol{x}_{\perp}, E_{\mathrm{ph}}\right)$ and instantaneous bandwidth $\langle\sigma_E\rangle\left(\boldsymbol{x}_{\perp}, t\right)$ are given by the second moments[49] via

$$\langle\sigma_t\rangle^2\left(\boldsymbol{x}_{\perp}, E_{\mathrm{ph}}\right) = \frac{1}{\langle \tilde{I}\left(\boldsymbol{x}_{\perp}, E_{\mathrm{ph}}\right)\rangle} \int_{-\infty}^{\infty} \left(\langle t_0\rangle - t\right)^2\mathcal{W}\left(\boldsymbol{x}_{\perp}, t, E_{\mathrm{ph}}\right) \mathrm{d}t \tag{2.29}$$

$$\langle\sigma_E\rangle^2\left(\boldsymbol{x}_{\perp}, t\right) = \frac{1}{\langle I\left(\boldsymbol{x}_{\perp}, t\right)\rangle} \int_{-\infty}^{\infty} \left(\langle E_{\mathrm{ph},0}\rangle - E_{\mathrm{ph}}\right)^2\mathcal{W}\left(\boldsymbol{x}_{\perp}, t, E_{\mathrm{ph}}\right) \mathrm{d}E_{\mathrm{ph}}. \tag{2.30}$$

2.2 Synchrotron and Undulator radiation

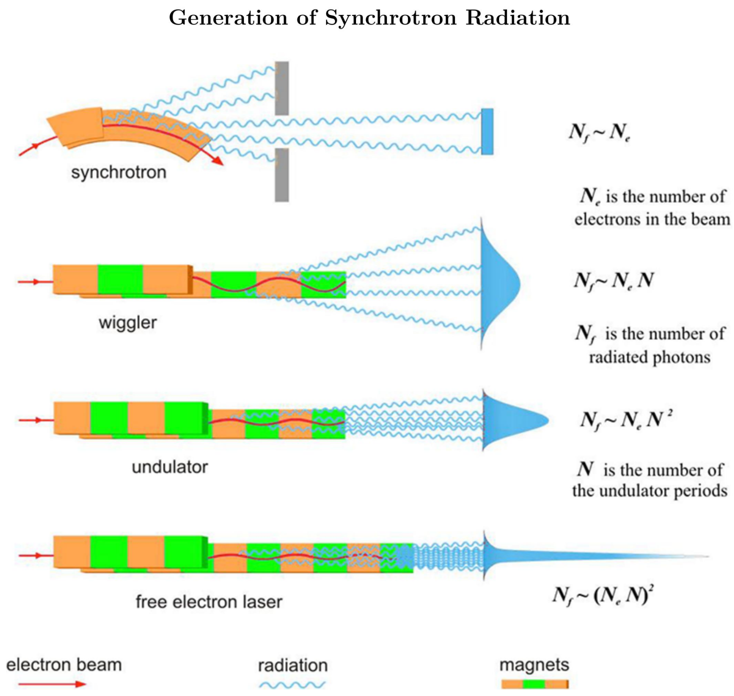

Figure 2.1: Schematics visualizing different types of electron accelerator based radiation sources: Bending magnet (Synchrotron), Wiggler, Undulator and FEL. For an undulator, the photon flux $N_f \propto N^2$ scaling with the square number of undulator periods N is noted. This is the case if radiation within a narrow cone $1/\gamma$ close to the forward direction is considered, which is an frequent application of undulators. From [50], under a Creative Commons licence (`https://creativecommons.org/licenses/by/3.0/`).

---

[3] Actually, any representation of the quite general *Cohen* class of time-frequency representations can be expressed in terms of the Wigner distribution[49].

Figure (2.1) highlights different types of electron accelerator generated radiation, starting with the most basic on top and ending with the most involved. The synchrotron radiation sketched in the top picture derives its name from the fact, that it was first observed 1945 at the 70 MeV synchrotron facility at General Electric Research Laboratory in Schenectady, New York [4, Ch. 1.2]. This radiation is based on the principle, that charged particles which undergo acceleration emit electromagnetic radiation transversely to the direction of acceleration. For non-relativistic particles this radiation follows a dipole-distribution with the nodal axis lying in the direction of acceleration. The emitted radiation is given by the Lamor-formula [37, p. 18]

$$\boldsymbol{P} = \frac{\mathrm{e}^2}{6\pi\epsilon_0 c^3}\dot{\boldsymbol{v}}^2, \tag{2.31}$$

where $\dot{\boldsymbol{v}}$ is the particles acceleration, $\mathrm{e} = 1.602\,176\,634 \times 10^{-19}$ C[42] is the elementary charge and $\epsilon = {}^{1}\!/_{\mu_0 c^2}$ is the vacuum permittivity. For a relativistic particle with a speed $v \approx c$ and therefore a high Lorentz-factor $\gamma = 1/\sqrt{1-({}^{v}\!/_{c})^2}$ (see Appendix **A**), equation (2.31) only holds in a coordinate system moving along with the particle. For an observer at rest, equation (2.31) needs to be transformed using a Lorentz transformation. This leads to a distribution which is highly suppressed in the direction opposite to the electron's motion and strongly enhanced in the forward direction. The radiation power emitted from a relativistic electron in a bending magnet is [40, pp. 24 ff.]

$$P_{syn} = \frac{\mathrm{e}^2 c}{6\pi\epsilon_0}\frac{\gamma^4}{r_{DM}^2}, \tag{2.32}$$

where r_{DM} is the radius of the trajectory of the deflection. The radiation emitted at every point of the bending trajectory has a rms opening angle of approximately $1/\gamma$, which is widened by the bending radius [4, ch. 3.5.1]. The frequency spectrum of the emitted radiation has a wide distribution for frequencies $\omega \ll \omega_c$ and exponentially decreases for frequencies $\omega \gg \omega_c$, where $\omega_c = {}^{3\gamma^3 c}\!/_{2r_{DM}}$ is a characteristic frequency of the synchrotron radiation [51, ch. 14.6]. As this synchrotron or bending magnetic radiation scales with the power of four with the kinetic energy, it was originally considered a severe nuisance in accelerator physics strongly limiting the maximum achievable energy in circular electron accelerators. With time, the outstanding properties of synchrotron radiation, especially the small angular divergence $1/\gamma$, gave rise to facilities especially dedicated to its production starting in 1981 with the *Synchrotron Radiation Source* (SRS) in Daresbury, England. The properties of the synchrotron radiation were further improved by the use of special insertion devices, the so called *Wigglers* and *Undulators* (see Figure (2.1,middle)).

2.2.1 Undulator and Wiggler radiation

Undulators and *wigglers* are a periodic sequence of magnets of alternating polarity, which are bending the electrons back and forth along a nominally straight trajectory. The magnetic field of a planar Undulator/Wiggler, which is without loss of generality assumed to be polarized in the $\hat{y}$-direction, can be described by

$$\boldsymbol{B} = -B_0 \cosh(k_U y) \sin(k_U z)\hat{y} - B_0 \sinh(k_U y) \cos(k_U z)\hat{x} \underbrace{\approx}_{k_U|y| \ll 1} -B_0 \sin(k_U z), \quad (2.33)$$

where $k_U = 2\pi/\lambda_U$ and λ_U is the period of the magnetic arrangement. For an electron initially moving along $\hat{z}$, very close to the symmetry axis $y = 0$ and under the specific initial conditions

$$x(z=0) = 0 \quad \text{and} \quad v_x(z=0) = \frac{eB_0}{\gamma m_e k_U}, \quad (2.34)$$

which can be fixed by appropriate beam steering, the electron velocity up to second order in ${}^{v_x}/_{v_z}$ and $1/\gamma$ becomes [37, Ch. 2.2]

$$\begin{aligned} v_x(t) = &\ \frac{Kc}{\gamma} \cos(\bar{v}_z k_U t), \quad v_y = 0, \quad v_z(t) = \bar{v}_z - \frac{cK}{4\gamma^2} \cos(2\bar{v}_z k_U t), \\ \text{with } \bar{v}_z = &\ c\left(1 - \frac{1}{2\gamma^2}\left(1 + \frac{K^2}{2}\right)\right). \end{aligned} \quad (2.35)$$

Under the initial conditions (2.34), the resulting particle trajectory is

$$x(t) \approx \frac{K}{\gamma k_U} \sin(k_U \bar{v}_z t), \quad z(t) \approx \bar{v}_z t - \frac{K^2}{8\gamma^2 k_U} \sin(2\bar{v}_z k_U t) \quad (2.36)$$

In above equations the *undulator parameter*

$$K = \frac{eB_0}{m_e c k_U} \quad (2.37)$$

has been introduced, which is also relevant for *free-electron lasers* later on. In above equation the electron mass m_e =0.510 998 950 00(15) MeV[42] was introduced.

The transition between an Undulator and a Wiggler is defined by the quantity of K, with undulators having $K \tilde{<} 1$ and wigglers $K \gg 1$. It is apparent from the velocities (2.35) that the maximum slope of the electron in the magnetic structure is $\frac{K}{\gamma}$. Hence, the slope of trajectory is exactly K times the emission angle of the synchrotron radiation.

For a wiggler with $K \gg 1$ the resulting radiation behaves like a 'search light' oscillating with c/λ_U. It is quite similar to the bending magnet radiation with the advantage of the actual on-axis intensity scaling with the number $2 * N_U$ of magnetic poles [39, pp.33 ff.].

In contrast, for undulators ($K \tilde{<} 1$) the movement of the 'search light' beam is on the same scale as its own emission angle. This leads to a partially coherent[4] overlap and interference of the

---

[4] For the case of one single electron the produced radiation is indeed fully transversely coherent. For an electron distribution with finite emittance ϵ the transverse coherence decreases with increasing emittance [39, pp. 61 ff.]. The emittance becomes dominant if $\epsilon_{x,y} > {}^{\lambda}/_{2\pi}$, which is usually the case for the $\hat{x}$-direction for hard X-ray beams and electron distributions in third generation electron storage-rings.

individual oscillations[5]. For the hypothetic case of complete coherence and an infinite number N_U of undulator periods, all contributions but a resonant one would interfere destructively and cancel in the spectral domain. This angular dependent resonant photon energy can be derived by Lorentz-transformation from the dipole frequency as [37, pp. 15 ff.]

$$\begin{aligned} E^{(n)}_{\mathrm{ph},r}(\Theta) =&\ n\hbar k_U 2\gamma^2 c\left(1+\frac{K^2}{2}+\gamma^2\Theta^2\right)^{-1}, \\ \leftrightarrow \lambda^{(n)}_r(\Theta) =&\ \frac{1}{n}\frac{\lambda_U}{2\gamma^2}\left(1+K^2/2+\gamma^2\Theta^2\right), \end{aligned} \qquad \text{for } n \in \mathbb{N} \tag{2.38}$$

where $n \geq 1$ is a harmonic number and Θ is the observation angle. The strength of the individual harmonics is dependent on the Undulator parameter K, with the first harmonic being more dominant the lower the K. The actual field strength $E_n(\boldsymbol{\Theta}, E_{\mathrm{ph}}, z)$ of the harmonic n scales with a complex function incorporating the Bessel function J_v in dependence of the undulator parameter K [39, pp.49 ff.]:

$$\frac{E_n\left(\boldsymbol{\Theta}=0, E_{\mathrm{ph}}=E^{(n)}_{\mathrm{ph},r}, z\right)}{E_1\left(\boldsymbol{\Theta}=0, E_{\mathrm{ph}}=E^{(1)}_{\mathrm{ph},r}, z\right)} = \frac{[JJ]_n}{[JJ]_1}$$

with

$$[JJ]_n = (-1)^{\frac{n-1}{2}}\left[J_{(n-1)/2}\left(\frac{nK^2}{4+2K^2}\right) - J_{(n+1)/2}\left(\frac{nK^2}{4+2K^2}\right)\right] \tag{2.39}$$

On-axis only the odd harmonics persist due to the antisymmetrie of the particle trajectory with respect to its half-period $\lambda_U/2$, which is canceling out the even contributions to the Fourier expansion.

Besides the difference in the spectrum, the radiation produced by an undulator is better collimated than that produced by a bending magnet as is also sketched in Figure (2.1). The root-mean-square angular width of undulator radiation near the resonant wavelength can be approximated by [37, ch. 2.4][6]

$$\sigma_\Theta \approx \frac{1}{\gamma}\sqrt{\frac{1+K^2/2}{2N_U}} \ll \frac{1}{\gamma}. \tag{2.40}$$

So far, an undulator with infinite length was considered. For a finite number of undulator periods and therefore a finite number of oscillation cycles the spectral shape of the field at the rear of

---

[5] The distinction between undulators and wigglers are somewhat artificial. Also for wigglers there is a narrowing of the spectral linewidth along the electron propagation axis, only that the fraction of light in that direction is smaller, dependent on the actual magnitude of K.

[6] It is important to note that relation (2.40) only holds if one is restricted to a narrow frequency range around the resonant frequency (2.38). Otherwise the angular width of the radiation cone becomes equal to the maximum slope of the electron trajectory $\Theta_{cone} \approx {}^{K}\!/_{\gamma}$.

the undulator ($z = L_U = N_U \cdot \lambda_U$) is smeared following a sinc function

$$|E|_n(\boldsymbol{\Theta}, E_{\text{ph}}, z = L_U) \propto \text{sinc}\left(\pi N_U \left(\frac{E_{\text{ph}} - E_{\text{ph},r}^{(n)}}{E_{\text{ph},r}^{(1)}} + \frac{n(\gamma\Theta)^2}{1 + K^2/2}\right)\right), \tag{2.41}$$

which yields roughly a relative spectral width of

$$\frac{E_{\text{ph}} - E_{\text{ph},r}^{(n)}}{E_{\text{ph},r}^{(n)}} \approx \frac{1}{nN_U}. \tag{2.42}$$

The frequency width widens with the electron momentum spread $\sigma_\eta = \sigma_\gamma/\gamma$ of the electron beam which becomes significant if $\sigma_\eta \tilde{>} {}^1\!/_{2\pi N_U}$.

While undulator radiation differs considerably in the spectral and angular characteristics compared to bending magnet radiation and therefore in brilliance (2.17), it does not differ in the total amount of power if integrated over all harmonics and angles[7]. Especially, the number of electrons in the electron distribution driving the radiative process only enters linearly in the total output power (neglecting space charge effects) how it is common for incoherent processes.

It is to be noted, that the first harmonic fundamental wavelength $\lambda_r^{(1)}$ from eq. (2.38) agrees with the distance the radiation slips ahead of the emitting electron during one undulator period λ_U. Therefore, taking into account the entire undulator length $L_U = N_U\lambda_U$, the correlation time over which electrons can 'communicate' with each others is

$$\sigma_\tau = \frac{N_U\lambda_r^{(1)}}{c} = \frac{2\pi\hbar N_U}{E_{\text{ph},r}^{(1)}} \approx \frac{2\pi\hbar}{\Delta E},$$

where for the last step the approximation (2.42) was used. For hard X-rays the coherence time is on the order of 100 as [39], which is much shorter than the typical picoseconds bunch length in an synchrotron light source. Hence, the synchrotron radiation is to be considered a chaotic source consisting of 10000s of longitudinal modes.

Generally, the statistically averaged spectral energy density of N_e electrons is equal to [39, ch. 1.2.6, 40, p. 42]

$$\begin{aligned}\langle S(E_{\text{ph}})\rangle \propto \langle\sum_{i,j}^{N_e} \tilde{E}_i(E_{\text{ph}})\tilde{E}_j^*(E_{\text{ph}})\rangle &\propto \langle\sum_{i,j}^{N_e} e^{iE_{\text{ph}}(t+t_i)/\hbar} e^{-iE_{\text{ph}}(t+t_j)/\hbar}\rangle \\ &= N_e + \langle\sum_{i\neq j}^{N_e} e^{iE_{\text{ph}}(t_j - t_j)/\hbar}\rangle\,,\end{aligned} \tag{2.43}$$

where the sum goes over the electrons in the bunch, $\tilde{E}_{i,j}$ denotes the spectral contribution at photon energy E_{ph} of the single electron i or j, $t_{i,j}$ denote the position in the electron bunch and the $\langle \ldots \rangle$ expresses the statistical average over many ensembles. The first term on the right

---

[7] Bending magnet and undulator radiation are equal if the bending magnet arc length $r_{DM} * \Delta\Theta$ is replaced by the undulator length L_U and its magnetic field strength by the undulator rms field strength $\bar{B}u = B_0/2$ [39, ch. 2.4.3].

side is the incoherent contribution to the total radiation power and the second term the coherent contribution, quadratic in the number of electrons. Assuming that the electrons are uncorrelated, one can express the statistical time $\langle t_i \rangle$ by a single particle distribution function $f(t)$, so that

$$\begin{aligned} \langle\sum_{i\neq j}^{N_e} e^{iE_{\mathrm{ph}}\,(t_i\,-\,t_j)/\hbar}\rangle =&N_e\,(N_e-1)\cdot\int \mathrm{d}t e^{iE_{\mathrm{ph}}t/\hbar} f(t) = N_e\,(N_e-1)\,\tilde{f}(E_{\mathrm{ph}}) \\ \to \langle S(E_{\mathrm{ph}})\rangle \propto&N_e\left(1+(N_e-1)\tilde{f}(\omega)\right) \end{aligned} \tag{2.44}$$

For an electron beam following a gaussian distribution of bunch length σ_{el}, the term $f(E_{\mathrm{ph}}) = \exp\left(-\left[{}^{E_{\mathrm{ph}}\sigma_{\mathrm{el}}}/_{c\hbar}\right]^2\right)$ becomes exceedingly small for all wavelengths $\lambda < \sigma_{\mathrm{el}}$ [39, ch. 1.2.6, 40, pp. 43 ff.]. For this reason the coherent contribution to the synchrotron or Undulator radiation is usually limited to the optical spectral regime $\lambda\tilde{>}300\,\mathrm{nm}$ even for highly compressed electrons beams of femtosecond duration [39, ch.1.2.6], which is a more formal explanation for the lack of coherent radiation in synchrotron sources than the heuristic argument made above.
The coherent contribution $N_e(N_e-1)f(E_{\mathrm{ph}})$ can be considered the most fundamental difference between bending magnet or undulator radiation sources and *free-electron lasers* (FELs). For latter, there exist considerable Fourier content or bunching of electrons at resonant frequencies, apparent as spike in the distribution $\tilde{f}(E_{\mathrm{ph}})$. This leads to an enhancement of the radiation power with the squared number of particles at these frequencies, or more precisely the squared number of particles N_c in one correlation length $N_U\lambda_r^{(}1)$. As will be shown below, these resonant frequencies agree with the fundamental frequencies of undulator radiation (2.38).

2.3 Free-Electron Lasers

In the previous section, it was assumed that the radiation has no influence on the electron itself. But under certain favorable conditions, at the FEL resonance, the emitted radiation can modulate the electron beam in such a way, that a considerable bunching $\tilde{f}(E_{\mathrm{ph}})$ is created. This on the other hand leads to an increase in radiation power following (2.44), so that an exponential gain in radiation power can be achieved. This process is analogous to the stimulated emission in optical lasers [52, ch. 7.3], with the advantage of FELs not being bound to specific electronic levels. This theoretically enables lasing at any desired wavelength.
Modelling the radiation field as a monochromatic wave with wave number $k_l = 2\pi/\lambda$ copropagating with the electron beam

$$\boldsymbol{E} = E_0\cos\left(k_l\left(z - {}^{t}/_{c}\right) + \Phi\right)\hat{\boldsymbol{x}}, \tag{2.45}$$

the rate of energy transfer $\dot{\gamma} = {}^{\mathrm{d}\gamma}/_{\mathrm{d}t}$ from the photon field to the electrons can be expressed via the momentary work of the electromagnetic field on the particles:

$$\dot{\gamma} = -e\boldsymbol{E}\boldsymbol{v} = -\frac{eE_0Kc}{\gamma}\cos\left(k_U z\right)\cos\left(k_l\left(z - {}^{t}/_{c}\right) + \Phi\right), \tag{2.46}$$

where the definition (2.35) for the electron velocity $\boldsymbol{v}$ has been used. A positive $\dot{\gamma}$ relates to a energy transfer of the radiation field to the electron and vice versa. For an FEL obviously $\dot{\gamma} < 0$ is desired.

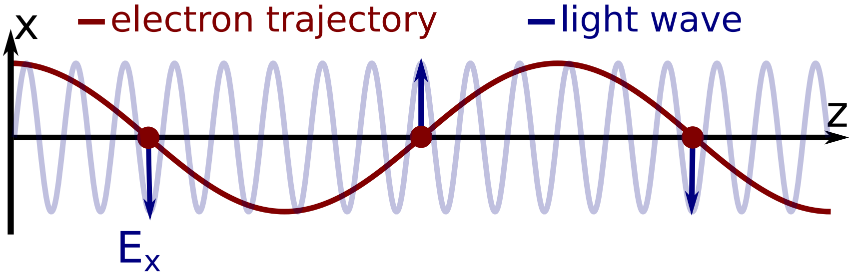

Figure 2.2: Sketch for the condition of sustained energy transfer of the electron to the radiation field. The transfer can only be sustained if the direction of the electron velocity and the electric field agree at each undulator half period.

As was already mentioned in the last section about undulator radiation, the radiation always slips ahead of the emitting electron by the fundamental resonance wavelength λ_r (eq. (2.38)) over one undulator period λ_u. Hence, assuming periodicity of the electron beam, a sustained energy transfer $\dot{\gamma} < 0$ is only possible if the phase of the electromagnetic field and the electron velocity agree such, that the direction of $\boldsymbol{E}$ and v_x agree at every undulator half period. This is sketched in Figure (2.2). In the following this shall be quantized in the form of the so-called *Pendulum equations*. It has to be noted that a planar Undulator is assumed. An helical Undulator would slightly change the formulae derived hereafter, while keeping the principal features the same.

2.3.1 Pendulum equations

Starting from equation (2.46) and identifying the electron position z as

$$z(t) = \bar{v}_z t - \frac{K^2}{8\gamma^2 k_U} \sin(2\bar{v}_z k_U t), \quad \text{with } \bar{v}_z = c\left(1 - \frac{1}{2\gamma^2}\left(1 + \frac{K^2}{2}\right)\right),$$

the energy transfer of the electrons becomes after some algebra [37, ch. 3.5]

$$\dot{\gamma} = -\frac{ecKE_0}{2\gamma} \sum_{n=0}^{\infty} \left[J_n\left(-\frac{K^2 k_l}{8\gamma^2 k_U}\right) + J_{n+1}\left(-\frac{K^2 k_l}{8\gamma^2 k_U}\right)\right] \cos(\Psi_n(t)), \tag{2.47}$$

$$\text{with} \quad \Psi_n(t) = (k_l + (2n+1)k_U)\bar{v}_z t - k_l c t + \Phi, \tag{2.48}$$

where $\Psi_n(t)$ is called the *ponderomotive phase*. Above derivation was made under the assumption that $k_U z(t) \approx k_U \bar{v}_z t$, which is well justified considerig that $k_U \ll k_l$ and ${}^{v_z(t)}/_{\bar{v}_z} - 1 \ll 1$. It is evident from equation (2.47) that the energy transfer $\dot{\gamma}$ can only be sustained in average over many undulator periods, if the ponderomotive phase remains constant. From this demand

$$\Psi_n(t) = \text{const} \quad \Leftrightarrow \quad \frac{\mathrm{d}\Psi_n(t)}{\mathrm{d}t} = (k_l + (2n+1)k_U)\bar{v}_z - k_l c = 0,$$

one can derive a resonant condition for the wavelength, which is in good approximation

$$\lambda_l^{(n)} = \frac{1}{n}\frac{\lambda_u}{2\gamma^2}\left(1 + \frac{K^2}{2}\right), \quad \text{with } n = 1, 3, 5, \dots \,. \tag{2.49}$$

The resonance wavelength agrees with the fundamental wavelength of undulator radiation in forward direction (2.38). This is important for the *Self Amplified Spontaneous Emission* scheme, where the spontaneous undulator emission acts as seeding field. This will be discussed later. From here on, only the fundamental harmonic $n = 1$ will be considered and the index n will be dropped.

In the following, the term γ_r will be used to define the energy which is in resonance with a monochromatic wave of wavelength λ_l. Further introducing the electronic energy deviation

$$\eta = \frac{\gamma - \gamma_r}{\gamma_r}, \tag{2.50}$$

one can derive under the assumption $\eta \ll 1$ for the advance of the ponderomotive phase and the electron energy the following form [37, pp.33 ff. 39, pp.92 ff.]:

$$\boxed{\Psi' = \frac{\mathrm{d}\Psi}{\mathrm{d}z} = 2k_U\eta \quad \text{and} \quad \eta' = \frac{\mathrm{d}\eta}{\mathrm{d}z} = -\frac{eE_0K[JJ]}{2m_ec^2\gamma_r^2}\cos\Psi}, \tag{2.51}$$

where the term $[JJ]$ is the longitudinal correction defined in equation (2.39). Upper equations are usually referred to as the *Pendulum equations* as they are equivalent to the second order differential equations defining the mathematic pendulum.

In an intuitive picture the ponderomotive phase can be related to the electrons longitudinal coordinate inside the bunch:

$$\zeta = \frac{\Psi + \pi/2}{2\pi}\lambda_l, \tag{2.52}$$

where the bunch center $\Psi = 0$ corresponds to $\Psi = -\pi/2$ at which the energy transfer $\dot{\eta}$ is maximal. In this picture it is evident that the equations (2.51) correspond to a modulation of the longitudinal components of the electron phase space.

In analogy to the mathematical pendulum one may define the pendulum Hamiltonian [37, ch. 3.3.1]

$$H(\Psi, \eta) = k_U\eta^2 + \frac{eE_0K[JJ]}{2m_ec^2\gamma_r^2}\left(1 + \sin\Psi\right). \tag{2.53}$$

The evolution of the longitudinal phase space (Ψ, η) follows the curves of $H(\Psi, \eta) = \mathrm{const}$. One may define a separatrix

$$\eta_{\mathrm{sep}}(\Psi) = \pm\sqrt{\frac{eE_0K[JJ]}{k_U m_e c^2 \gamma_r^2}} \cos\left(\frac{\Psi + \pi/2}{2}\right), \tag{2.54}$$

which is separating the regions of bounded motions from the region of unbounded motion. The area inside the separatrix is commonly referred to as the FEL-bucket. $\Psi = -\pi/2, \eta = 0$ represents a fixpoint where the electron does not show any phase space motion. Inside the FEL-bucket the electrons perform periodic oscillations for the case of a constant electromagnetic field amplitude E_0. The oscillation frequency Ω near the fixpoint is defined as[39, ch.3.2.2]

$$\Omega = \sqrt{\frac{eE_0K[JJ]k_U}{m_e c^2 \gamma_r^2}}. \tag{2.55}$$

The phase space trajectories for two initially monochromatic electron beams, one at resonance $\eta = 0$ and one slightly above resonance $\eta > 0$ are sketched in Figure (2.3).

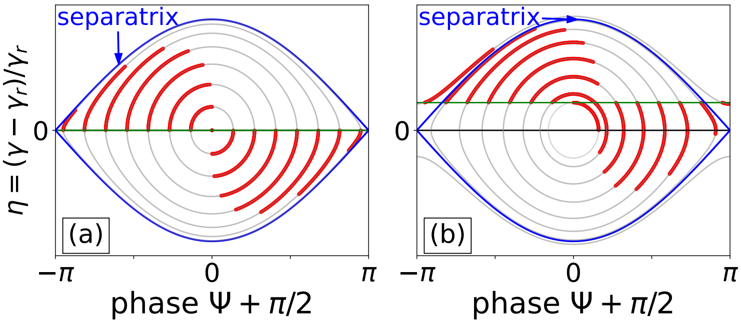

Figure 2.3: The phase space motion (red) of 15 electrons equally distributed over one period of the ponderomotive phase $\Psi \in (-3\pi/2, \pi/2]$. The light gray curves show the trajectories of the constant Hamiltonian (2.53). (a) shows the motion for electrons with an initial energy $\gamma = \gamma_r$. The same number of electrons lose energy as they gain energy, so the statistically averaged $\langle\dot{\eta}\rangle = 0$ and the radiation power stays constant. (b) shows the electron motion for an initial energy $0 < \eta < \eta_{\max}$. Here the change $\langle\dot{\eta}\rangle < 0$, so in average the radiation gains in power. Adapted from [37].

2.3.2 Low Gain

It is evident from Figure (2.3) that the radiation power remains invariant for an initial electron energy at resonance $\eta_0 = 0$, while it gains energy for $\eta_0 > 0$ and loses energy for $\eta_0 < 0$. The radiation gain, which is formally defined as relative gain of the radiation intensity $I(z) = c\epsilon_0|\boldsymbol{E}(\boldsymbol{z})|^2$ over one Undulator length L_U

$$\mathcal{G} = \frac{I(L_U) - I(z=0)}{I(z=0)} \tag{2.56}$$

shall be quantified in this section under the assumption that the electric field strength $E(z)$ remains almost constant ($\mathcal{G} \ll 1$). Under this assumption, which is commonly referred to as *low gain regime*, the pendulum equations are fully sufficient to describe the interaction of electrons and light wave[8].

Following a second order perturbation approach in the oscillation frequency times the squared undulator length squared $(\Omega L_U)^2$, one can derive for the gain the following formular [39, pp.83-88]:

$$\mathcal{G}(\eta_0) = -\frac{\pi n_e e^2 (K[JJ])^2 N_U^3 \lambda_U^2}{4\epsilon_0 m_e c^2 \gamma_r^3} \cdot \frac{\partial}{\partial \xi}\left(\frac{\sin^2 \xi(\eta_0)}{\xi^2(\eta_0)}\right) \quad \text{with} \quad \xi(\eta_0) = 2\pi N_U \eta_0, \qquad (2.57)$$

where n_e is the electron number density. In above formular it was assumed that the wavelength is fixed, for example by an external seed laser or the longitudinal eigenmode of an optical cavity.

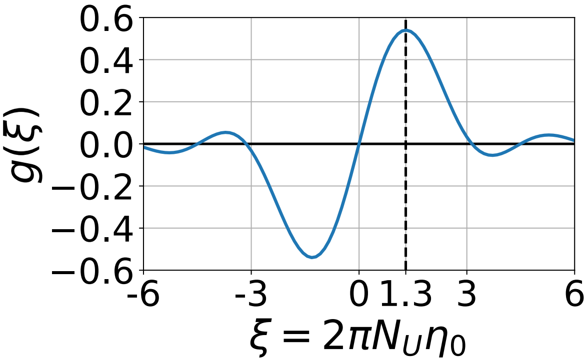

Figure 2.4: The general low gain function $g(\xi) = -{}^{\partial}/_{\partial\xi}\left({}^{\sin^2 \xi(\eta_0)}/_{\xi^2(\eta_0)}\right)$ showing the scaling of any low gain FEL with the initial energy offset η.

If one would define $\eta = -{}^{E_{\text{ph}}}/_{E_{\text{ph},r}} - 1$ in terms of the light wave photon energy, equation (2.57) becomes proportional to the negative derivative of the lineshape curve $|E|(\Theta = 0, E_{\text{ph}}, z = L_U, \gamma)$ of undulator radiation (2.41) in forward direction

$$\mathcal{G}(\eta_0) \propto -\frac{\partial |E|(\Theta = 0, E_{\text{ph}}, z = L_U, \gamma = \gamma_r (1 + \eta_0))}{\partial E_{\text{ph}}}.$$

This is referred to as *Madey's first theorem* [53] after *J.M.J.Madey* who was the first to actually realize a low gain free electron laser. In Figure (2.4) the gain function $g(\xi) = -{}^{\partial}/_{\partial\xi}\left({}^{\sin^2 \xi(\eta_0)}/_{\xi^2(\eta_0)}\right)$ is plotted against the normalized energy deviation $\xi = 2\pi N_U \eta_0$. It is evident that the light wave will gain energy for positive η_0 and will lose energy for negative η_0 with the maximum gain at $\eta_0^{\text{opt}} \approx {}^{1.3}/_{2\pi N_U}$.

The low gain FEL considered above is commonly realized in the form of an optical oscillator, where the FEL radiation is trapped in an optical cavity and passes a short undulator many times in close spatial and temporal overlap with an electron bunch. During each passage, the radiation power grows by only a few percent following equation (2.57). However, it has to be noted that the FEL gain in equation (2.57) was assumed independent of the actual field strength E_0. This

---

[8] One can also derive the low gain equation by a perturbative expansion of the more general high gain equations which will be shown later.

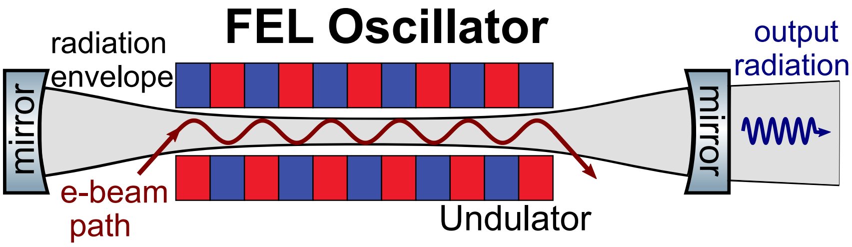

Figure 2.5: A sketch of the FEL Oscillator being based on an optical cavity..

would lead to an infinite growth in the field intensity in an FEL oscillator, which is obviously non-physical. As equation (2.57) was derived for low field strength, it becomes invalid for high values of E_0. At high field strength, the gain saturates and decreases until the gain and losses per roundtrip cancel each other.

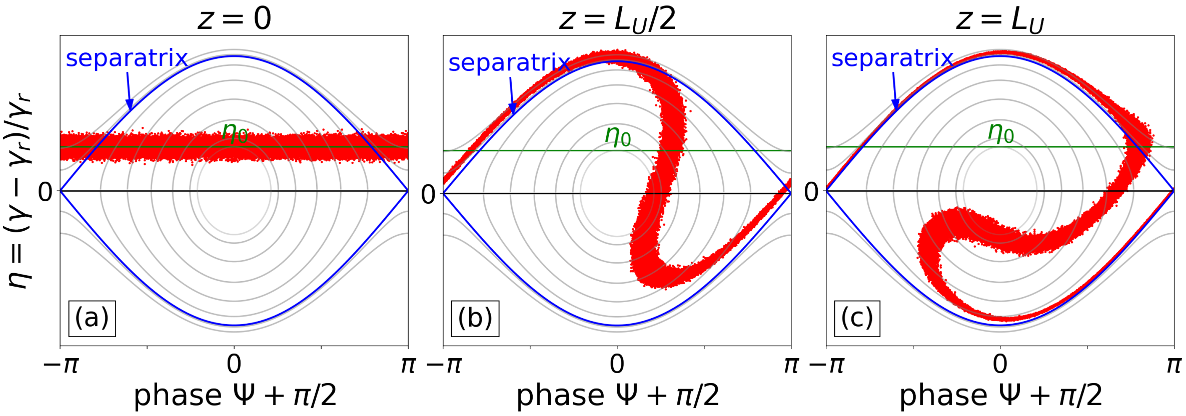

Figure 2.6: Phase space motion of electrons initially centered around the optimally scaled energy offset $\eta_0^{\text{opt}} = 1.3/(2\pi N_U)$(a) under the influence of a strong electromagnetic field. At half the (short) undulator length (b), the electrons have already considerably rotated in the FEL bucket. At the end of the Undulator (c) the statistical average of the electron bunch is rotating upwards in the phase space again, therefore reabsorbing energy $\dot{\eta} > 0$ from the radiation field.

This shall not be quantified here but is qualitatively visualized by Figure (2.6). For high field strengths the electron distribution gets trapped by the FEL bucket and the electrons begin to rotate in the phase space. For high enough E_0 the electrons reach a point already before leaving the Undulator where they begin to reabsorb energy from the radiation field therefore reducing the gain. In Figure (2.6(b)) one can additionally observe a considerable bunching of the electron distribution inside one FEL bucket of length λ_l what will become important for the high gain FEL discussed hereafter.

2.3.3 High Gain FEL

For the high gain FEL the radiation field gains considerable energy during one single pass through the undulator. This is particularly important for the extreme ultraviolet (EUV) to the X-ray regime where optical mirrors and therefore an oscillator scheme are not available[9]. Under

---

[9] It is precisely the topic of this thesis to study an intermediate gain FEL oscillator in the hard X-ray regime using Bragg reflectors inst+ead of optical mirrors.

these circumstances, the assumption that the electric field remains constant during one passage obviously does not hold and the pendulum equations (2.51) need to be solved in conjunction with the wave equation for the electromagnetic field. The field growth in an high gain FEL is directly related to the evolution of microbunching as it was discussed at the end of Section **2.2.1** and was hinted at in Figure (2.6(b)). This microbunching qualitatively develops as to the electrons, which loose energy to the radiation, field travel on a sinusoidal trajectory of larger amplitude than the electrons gaining energy, which is concentrating the electrons in the center of one FEL bucket. As the FEL buckets have a periodicity of one wavelength λ_l, in view of equation (2.44) this leads to an exponential increase in lasing power (also see [37, ch. 4.2]).

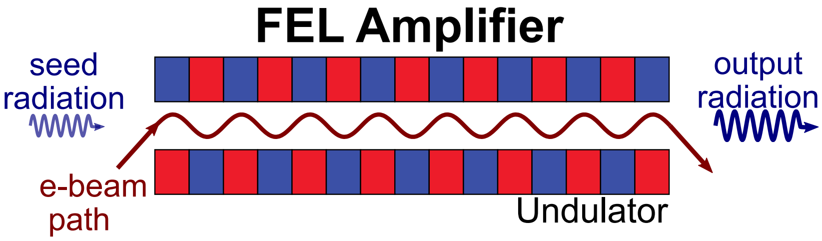

Figure 2.7: A sketch of the FEL Amplifier amplifying already existing external seed radiation in a long undulator section, where saturation is reached after one single pass.

In order to quantize the high gain FEL equation, as noted above, one additionally has to solve for the wave equation of the radiation field. In the following the case of a FEL amplifier sketched in Figure (2.7) will be discussed. In this case the FEL process is initiated by a monochromatic seed of wavelength λ_l, respectively photon energy $E_{\text{ph},l}$. For simplification the wave equation will be approximated as one dimensional, which is equivalent to assuming the electromagnetic field as a plane wave. Further using the *Slowly Varying Amplitude* (SVA) approximation[10] , one yields for the (paraxial) wave equation driven by a source current $\boldsymbol{J}$ in the frequency domain [39, pp.37 ff.]

$$\frac{\partial}{\partial z}\tilde{\boldsymbol{E}}_\perp(E_{\text{ph},l}, z) = \sum_{j=1}^{N_e} \frac{e\beta_{\perp,j}}{8\pi\epsilon_0 c\mathcal{A}_{\text{tr}}} e^{ik(ct_j(z)-z)}, \tag{2.58}$$

with N_e being the total number of electrons, $\mathcal{A}_{\text{tr}}$ being the transverse area of the charge density, $t_j(z)$ being the arrival time at position z and $\beta_{\perp,j} = v$ being the scaled transverse velocity of the j^{th} electron, which is assumed to be entirely in the $\hat{\boldsymbol{x}}$-direction ($\tilde{\boldsymbol{E}}_\perp = \tilde{E}_x\hat{\boldsymbol{x}}$). By identifying the transverse velocity $\beta_{\perp,j} = v_{\perp,j}/c$ by equation (2.35) and in consistency with the SVA only keeping the slowly varying phase of the current in equation (2.58), one arrives for the first harmonic at [39, pp. 91 ff.]:

$$\left[\frac{\partial}{\partial z} + i\frac{k-k_l}{k_l}k_U\right] E_\nu(z) \approx \frac{ek_l K[JJ]}{8\pi\epsilon_0\gamma_r\mathcal{A}_{\text{tr}}} \sum_{j=1}^{N_e} e^{-ik/k_l\left(\Psi_j(z)+\frac{\pi}{2}\right)}, \tag{2.59}$$

---

[10] This is a reasonable approximation for the envelope $\tilde{\boldsymbol{E}}(E_{\text{ph},l}, z)$ which is assumed to vary slowly over one undulator period λ_U and hence, very slowly over one wavelength $\lambda_l \ll \lambda_U$ [37, p. 46].

where the phase shifted electric field amplitude

$$\tilde{E}_\nu(z) = ck_l e^{-i\frac{k-k_l}{k_l}k_U z}\tilde{E}_x(E_{\mathrm{ph},l}, z)$$

has been introduced and the particle energy γ_j has been approximated by the resonant energy γ_r.

By Fourier transforming equation (2.59) into the time domain and averaging the transverse current over some periods in the ponderomotive phase Ψ in accordance with the SVA approximation, one arrives at [39, pp.93 ff.]

$$\begin{aligned} \left[\frac{\partial}{\partial z} + k_U\frac{\partial}{\partial \Psi}\right] E_x\left(z, \Psi_m\right) &= -\frac{K[JJ]}{2\epsilon_0 c\gamma_r} j_0(\Psi_m)\frac{1}{N_\lambda}\sum_{j\in\Delta\Psi} e^{-i\left(\Psi_j(z)+\frac{\pi}{2}\right)} \\ &= -\frac{K[JJ]}{4\epsilon_0 c\gamma_r}\tilde{j}_1\left(z, \Psi_m\right), \end{aligned} \tag{2.60}$$

where the slowly varying current density $j_0(\Psi_m)$ and the modulation current density$\tilde{j}_1(z, \Psi_m)$ were introduced with

$$j_0(\Psi_m) = -\frac{ecN_\lambda(\Psi_m)}{\lambda_l \mathcal{A}_{\mathrm{tr}}} \quad \text{and} \quad \tilde{j}_1(z, \Psi_m) = j_0(\Psi_m)\frac{2}{N_\Delta}\sum_{j\in\Delta\Psi} e^{-i\left(\Psi_j(z)+\frac{\pi}{2}\right)}. \tag{2.61}$$

N_λ refers to the local number of electrons in one resonant wavelength λ_l at the coordinate Ψ_m[11]. $N_\Delta = N_\lambda\left({}^{\Delta\Psi}/_{2\pi}\right)$ refers to the number of electrons in one longitudinal slice $\Delta\Psi$ that satisfy $|\Psi_j - \Psi_m| \leq \Delta\Psi/2$, where Ψ_m is the ponderomotive phase in the middle of the slice $\Delta\Psi$. $\Delta\Psi$ is chosen such that it is much less than the coherence length divided by the wavelength $\Delta\Psi \ll {}^{l_{\mathrm{coh}}}/_{\lambda_l} \approx {}^{1}/_{2\rho_{\mathrm{FEL}}}$ [39, pp. 93]. ρ_{FEL} is the so-called *FEL parameter* which will be introduced in equation (2.66).

Accounting for space charge effects $\boldsymbol{\nabla E} = \rho/\epsilon_0$, with ρ being the charge density, additionally yields a longitudinal component of the electric field [37, ch. 4.4.2]:

$$\tilde{E}(z) \approx -i\frac{\hbar}{\epsilon_0 E_{\mathrm{ph},l}}\tilde{j}_1(z) \tag{2.62}$$

---

[11] Remember that, following equation (2.52), the ponderomotive phase is equivalent to the longitudinal position in the reference frame of the electron bunch.

Inserting equations (2.60) and (2.62) into the Pendulum equations (2.51) yields the *coupled first order equations*

$$\frac{\mathrm{d}\Psi_j}{\mathrm{d}z} = 2k_U\eta_j, \quad j = 1, \dots, N \tag{2.63a}$$

$$\frac{\mathrm{d}\eta_j}{\mathrm{d}z} = -\frac{e}{m_e c^2\gamma_r}\Re\left[\left(\frac{K[JJ]\tilde{E}(z,\Psi_m)}{2\gamma_r} - i\frac{\hbar\tilde{j}_1(z,\Psi_m)}{\epsilon_0 E_{\mathrm{ph},l}}\right)e^{i\Psi_j}\right] \tag{2.63b}$$

$$\tilde{j}_1(z,\Psi_m) = j_0\frac{2}{N_\Delta}\sum_{j\in\Delta\Psi}\exp\left[-i\left(\Psi_j\right)\right] \tag{2.63c}$$

$$\left[\frac{\partial}{\partial z} + k_U\frac{\partial}{\partial\Psi}\right]\tilde{E}\left(z,\Psi_m\right) = -\frac{K[JJ]}{4\epsilon_0 c\gamma_r}\tilde{j}_1\left(z,\Psi_m\right), \tag{2.63d}$$

which are fully describing the one dimensional high gain FEL.

Assuming a monochromatic beam $\eta_j = \eta_0$, ignoring the dependence of the electromagnetic field on the ponderomotive phase Ψ – or the longitudinal bunch coordinate ζ – and only accounting for small density modulations $\tilde{j}_1 \ll j_0$, one can linearize the coupled first order equations and arrive at the *third-order differential equation of the high gain FEL* [37, ch. 4.7]:

$$iE_x''' - 4k_U\eta_0 E_x'' + i\left[k_p^2 - \left(2k_U\eta\right)^2\right]E_x' + 8k_U^3\rho_{\mathrm{FEL}}^3 E_x = 0, \tag{2.64}$$

where the dimensionless *space charge parameter*

$$k_p = \sqrt{\frac{2k_U e^2 n_e}{m_e\epsilon_0 c^2 k_l\gamma_r}} \tag{2.65}$$

and the *FEL-parameter* [54]

$$\rho_{\mathrm{FEL}} = \left[\frac{\left(K[JJ]\right)^2 e^2 n_e}{32\epsilon_0 m_e c^2 k_U^2\gamma_r^3}\right]^{\frac{1}{3}} \tag{2.66}$$

have been introduced. n_e is the electric charge density.

Taking into account a polychromatic electron beam which has an initial energy distribution $F_0(\eta)$, one can derive by using the Vlasov equations and the Ansatz

$$\tilde{E}_x(z) = A\exp(\alpha z)$$

the following eigenvalue problem [37, ch.10.4]

$$\alpha = \left[i\frac{\rho_{\mathrm{FEL}}^3}{8k_U^3} - k_p^2\alpha\right]\int_{-\delta}^{\delta}\frac{F_0(\eta)}{\left(\alpha + i2k_U\eta\right)^2}\mathrm{d}\eta \tag{2.67}$$

$$\text{with} \quad \int_{-\delta}^{\delta}F_0(\eta) = 1 \quad \text{and} \quad F_0(|\eta| > \delta) = 0,$$

where the amplitudes A are found from the initial value problem. $F_0(\eta)$ is usually assumed as a truncated gaussian distribution. Assuming an initial, monochromatic seed radiation field of amplitude E_{seed} with $\eta = 0$, a vanishing initial density modulation $\tilde{j}_1 \approx 0$ and neglecting the space charge term $k_p = 0$ for simplicity, the solution of the third order equation (2.64) becomes [37, ch. 4.8]

$$\tilde{E}_x(z) = \frac{E_{\text{seed}}}{3}\left[e^{\left(i+\sqrt{3}\right)\rho_{\text{FEL}}k_U z} + e^{\left(i-\sqrt{3}\right)\rho_{\text{FEL}}k_U z} + e^{-i2\rho_{\text{FEL}}k_U z}\right]. \tag{2.68}$$

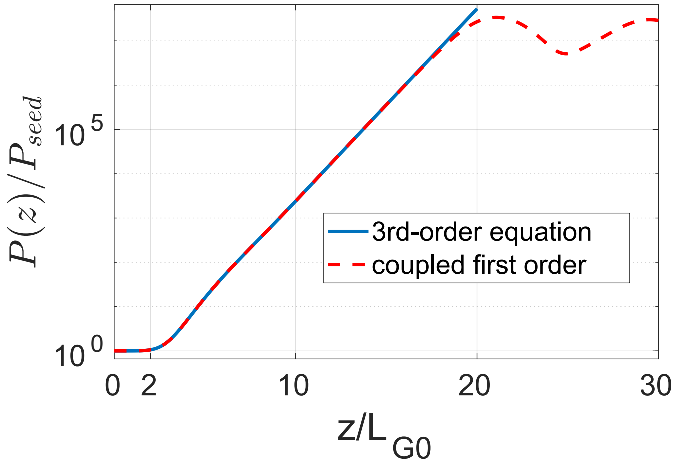

Figure 2.8: One dimensional solution to an exemplary, almost monochromatic $\sigma_\eta \ll \rho_{\text{FEL}}$, time-independent seeded high gain FEL following the simplified third-order equation (2.68) (blue) and the fully coupled first order equations (2.63) (red dashed) in the time independent case. Both solutions agree for small z, but while the third order equation predicts infinite growth the coupled first order solution saturates at around $z \approx 20L_{G0}$.

In Figure (2.8) the power evolution of an exemplary solution to the third order equation (2.68)[12] together with the coupled first order equations (2.63) is plotted. In Figure (2.9) the respective phase space together with the local longitudinal charge density normed such that $\int_\Delta \rho_n(\Psi)\mathrm{d}\Psi = N_\Delta$ is shown for different positions z in the undulator. In Figure (2.8) and Figure (2.9) one can make out three regimes. The first is the *lethargy regime* with the power $P(z) \propto |\tilde{E}_z|^2$ remaining almost constant due to the second, exponentially decreasing term and the third, oscillating term compensating the exponentially increasing first term. The phase space distribution as is exemplarily shown for $z = 2L_{G0}$ in Figure (2.9)(a) remains approximately unperturbed compared to the initial distribution. After a distance of $z \approx (2-3)L_{G0}$ the FEL enters the exponential growth regime

$$P(z) \approx P_{\text{seed}} \exp\left(2\sqrt{3}\rho_{\text{FEL}}k_U z\right) = P_{\text{seed}} \exp\left(\frac{z}{L_{G0}}\right),$$

where the FEL gain length

$$L_{G0} = \frac{1}{2\sqrt{3}\rho_{\text{FEL}}k_U} \tag{2.69}$$

---

[12] While the requisites of a monochromatic beam for equation (2.68) are not exactly met for the exemplary case shown in Figure (2.8), the small energy spread $\sigma_\eta \ll \rho_n$ leads to only small deviations as apparent from the good agreement between the simplified, analytic third order solution (2.68) and the coupled first order solution (2.63).

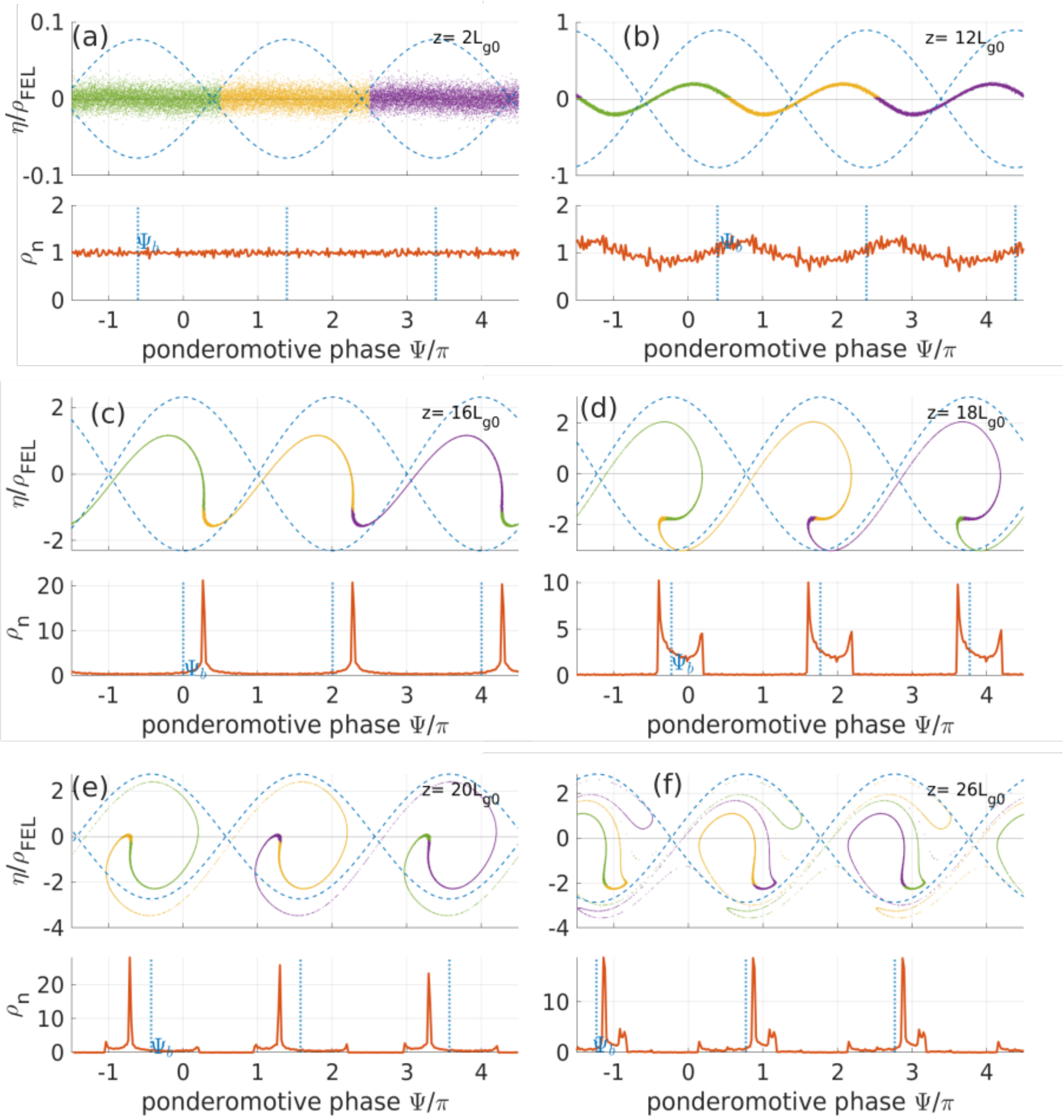

Figure 2.9: Distribution in the electron phase space (Ψ, η) and normalized longitudinal charge density ρ_n at different positions z. As a guide for the eye the seperatrix (2.54) is drawn as dashed blue line in the phase space plot. Also, the center Ψ_b of the FEL bucket is shown as vertical blue dotted line in the charge density subplot. The phase space evolution corresponds to the same solution as the exemplary seeded high gain FEL shown in Figure (2.8). While the electron phase space distribution is initially randomly distributed (see$z = 2L_{G0}$), up to $z \leq 16L_{G0}$ significant microbunching is developing, visible as single spikes in the longitudinal charge density. For $z \geq 18L_{G0}$ the electron phase space is rotating over more than half a period and additional spikes appear in the charge density. For $z = 26L_{G0}$ the electron phase space is strongly distorted.

has been introduced. In this regime as exemplarily shown for $z = 12L_{G0}$ in Figure (2.9)(b) significant microbunching is developing right to the bucket center, indicated as Ψ_b. Following (2.63) and (2.44) this leads to an increasing transfer of the electron energy to the radiation field and therefore to exponential growth. The associated energy $F(\eta)$ modulation can be considered roughly harmonic and therefore treatable by the linearized third order equations.

The last regime is the *saturation regime* not accounted for by the third order equations. In the saturation regime the modulation $\tilde{j}_1(z)$ of the current density becomes comparable or greater than

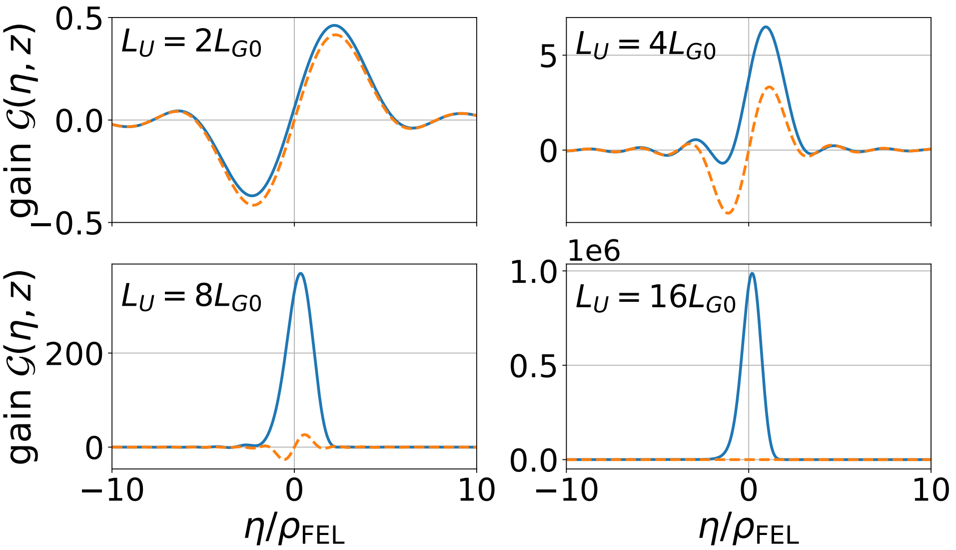

Figure 2.10: The FEL gain (2.56) obtained from the monochromatic third order equation (2.64) (blue curve) in dependence of the initial electron energy detune η_0 for different positions z in the undulator. With increasing z the η_{opt} of maximal gain shifts to $\eta_{\mathrm{opt}} = 0$ and the width of the gain curve shrinks to $\sigma_\eta \approx 0.5\rho_{\mathrm{FEL}}$. For comparison the low-gain function (2.57) is shown as orange dashed line. Adapted from [37, p. 66].

.

the base current density j_0 therefore contradicting the assumptions made for equation (2.64). At around $z = 16L_{G0}$ the microbunching is fully developed as evident from the narrow spike in the charge density in Figure (2.9)(c,bottom). The energy modulation on the other hand is clearly inharmonic and can therefore not be accounted for by linear theory. At $z = 18L_{G0}$ (see Figure (2.9)(d)) a significant number of electrons has rotated to the left of the FEL bucket. This is accordingly leading to spikes in the charge density located left of bucket center Ψ_b where the electrons reabsorb energy from the radiation field, which is decreasing the FEL power growth. At the peak power at $z \approx 20L_{G0}$ (see Figure (2.9)(e)) the majority of the electrons are located in the left bucket half. This is leading to the decrease in radiative power for $z \geq 20L_{G0}$ shown in Figure (2.8). Trapped in the FEL bucket the electrons continue to rotate in the longitudinal phase space, so that around $z \approx\approx 25L_{G0}$ the electrons are located in the right half of the FEL bucket again, so that the power is growing again. This leads to the oscillation of the power observed in Figure (2.8) [37, ch. 5.6] and to a degradation of the actual beam quality [55].

These oscillations are much less pronounced when taking into account the full three-dimensional electron phase space, due to the dependence of the phase space motion on the transverse position. This leads to electrons at different transverse positions reaching the saturation point at different z, ultimately smearing out the saturation regime.

Owing to the importance of the modulation current $\tilde{j}_1(z)$ in the exponential growth regime, the optimal energy detuning $\eta_{0,\mathrm{opt}}$ shifts with the length of the undulator. The gain curves in dependence of the initial energy detune η_0 for different position in the undulator is plotted in Figure (2.10). It shows two important results which can be derived from the third order equation (2.64). First, the optimal energy detune for a saturated high gain FEL is $\eta_{0,\mathrm{opt}} = 0$. Second, with increasing distance z the bandwidth of the gain curve shrinks. This can be approximated for the gain deep in the exponential regime as [37, p. 69]

$$\sigma_\eta(z) \approx 3\rho_{FEL}\sqrt{\frac{L_{G0}}{2z}}. \tag{2.70}$$

Hence, a saturated high gain FEL puts stronger demands on the energy spread of the initial electron distribution than a low (or intermediate) gain FEL. This is especially demanding for the hard X-ray regime where the FEL parameter is $\rho \tilde{<} 1 \times 10^{-4}$ and is one reason why X-ray FEL put a serious demand on the electron beam optics.

On the other hand, assuming a fixed electron beam energy, variable seeding photon energy E_{ph} and rewriting the energy detune in dependence of E_{ph}, one yields

$$\eta_{E_{\mathrm{ph}}} = -\frac{E_{\mathrm{ph}} - E_{\mathrm{ph},r}}{2E_{\mathrm{ph},r}} \Rightarrow \sigma_E(z) \approx 3\sqrt{2}\rho_{\mathrm{FEL}} E_{\mathrm{ph},r}\sqrt{\frac{L_G 0}{z}}. \tag{2.71}$$

This shows that the high gain FEL serves as narrow bandwidth amplifier with a bandwidth at saturation $\sigma_{E_{\mathrm{ph}}}(20L_{G0}) \approx \rho_{\mathrm{FEL}} E_{\mathrm{ph},r}$.

2.3.4 SASE FEL

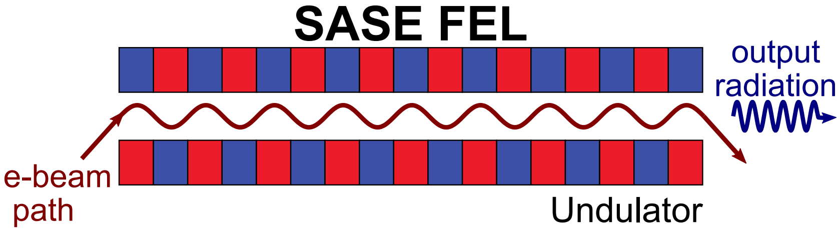

Figure 2.11: A sketch of the *Self Amplified Spontaneous Emission* (SASE) FEL neither relying on mirrors or seed radiation.

Up to now it was assumed that the FEL was initiated by a monochromatic seed laser. Actually, the FEL process can also be seeded by the incoherent spontaneous undulator radiation generated in the first section of a long undulator. This process is known as *Self Amplified Spontaneous Emission*(SASE). A SASE FEL is sketched in Figure (2.11). It strongly resembles the FEL amplifier in Figure (2.7) but does not require seed radiation and usually is slightly longer to reach saturation.

An equivalent formulation to the startup from spontaneous radiation, which is better compatible with the coupled first order equations (2.63), is that the FEL is started from an initial modulation current $\tilde{j}_1(0)$ given by the white noise spectrum of the randomly distributed electron bunch[13]. The respective modulation current of this *shot noise* can be modelled by the number of electrons inside one coherence length [39, ch. 3.4.5]. For SASE this coherence length can be estimated

---

[13] For the third order equation (2.64) this amounts to a change in the initial boundary conditions [37, ch. 5.3].

by the amplification bandwidth (2.71) in saturation, which is approximately $\sigma_{E,\mathrm{sat.}} \approx \rho_{\mathrm{FEL}} E_{\mathrm{ph}}$. This leads to $l_{\mathrm{coh}} \approx \lambda_l / \rho_{\mathrm{FEL}}$ [39, ch.3.4.5 & pp.115 ff.]. This leads to [37, pp.219 ff.]

$$\tilde{\jmath}_1(0) \approx 2\sqrt{\frac{eI_0 c\rho_{\mathrm{FEL}}}{\lambda_l}\frac{1}{\mathcal{A}_{\mathrm{tr}}}}. \tag{2.72}$$

For the linear FEL regime (lethargy and exponential growth), one can than solve for the electric field the following boundary value problem[37, ch.7.1.1]

$$E(z) = \frac{K[JJ]}{4\epsilon_0 c\gamma_r^2}\left(e^{\alpha_1 z}\; e^{\alpha_2 z}\; e^{\alpha_3 z}\right)\begin{pmatrix} 1 & 1 & 1 \\ \alpha_1 & \alpha_2 & \alpha_3 \\ \alpha_1^2 & \alpha_2^2 & \alpha_3^2 \end{pmatrix}\begin{pmatrix} 0 \\ 1 \\ i2k_U\eta \end{pmatrix}\tilde{\jmath}_1(0), \tag{2.73}$$

where the eigenvalues α_i are obtained by solving the eigensystem constituted by the third order equations (2.64) or (2.67).[14]

As a matter of fact, the FEL initiated by this shot noise is always present and competing with the seed laser initiation in the case of an FEL amplifier, which puts strong demands on the seed radiation field. This proves to be troublesome for the EUV and the X-ray regime due to the lack of appropriate stable seed lasers, which is why especially for X-ray wavelengths the FELs usually operate in the SASE scheme.

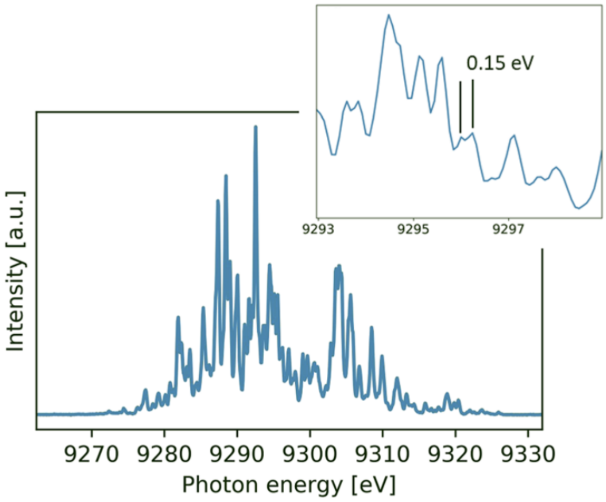

Figure 2.12: An experimental measurement of the SASE spectrum of a 250 pC electron beam at 9 keV photon energy using the HIREX transmissive spectrometer. From [56].

While already the first SASE FEL *Flash* in Hamburg has proven that it is possible to generate highly brilliant, transversely coherent radiation [57] in SASE mode, all SASE have in common that they lack longitudinal coherence. As SASE originates from spontaneous Undulator radiation it also inherits its longitudinally stochastic nature. Given the temporal coherence time $t_{\mathrm{coh}} \approx \lambda_l/c\rho_{\mathrm{FEL}}$, which is on the 1×10^{-16} s level for hard X-ray radiation [48], it is evident that for typical electron bunches of lengths $\sigma_{r,el} \approx$10 fs to 100 fs, the resulting radiation consists of

---

[14] The equation (2.73) actually is a rather crude approximation not taking into account the evolving FEL bandwidth (2.70). A better procedure solves for a range of frequencies ω and computes the resulting electric field as integral over these solutions [37, ch.7.1.2]. But for the examined case of the CBXFEL as described in Chapter **4**, this is of minor importance.

1×10^2 to 1×10^3 longitudinal modes. This is also evident from an experimental measurement shown in Figure (2.12).

As already discussed in the introduction, this lack of longitudinal coherence gave rise to serious effort to improve this. The most prominent schemes are self-seeding in the hard X-ray regime [13–17] or external seeding in the soft X-ray regime [10] as well as cavity based X-ray FELs being the topic of this thesis.

2.3.5 3D effects

The results presented so far were obtained by using a one dimensional approximation. Taking into account the full six-dimensional (electron) phase-space leads to some additions and modification to the theory thus far, with the principal results remaining qualitatively unchanged.

A quite obvious addition is the demand for transversal overlap of radiation field and electron beam. For a SASE this amounts to stringent demands on the alignment of the undulators in order not to introduce deviations in the particle trajectory. For FEL amplifiers or FEL oscillators it additionally demands for a matching of the radiation field focussing and the electron beam size in order to provide maximal transversal overlap and therefore maximum gain. In case of high gain FELs and therefore long undulator sections taking into account the optical diffraction of the light wave, it is difficult to maintain complete overlap over the entire undulator distance. But for high gain FELs there exists an effect counteracting the radiation widening called *gain guiding*. Due to the exponential growth of the radiation field after the lethargy regime, the radiation field is dominated by the newly generated radiation in two to three gain lengths. The width of this newly generated radiation is determined by the electron beam while the more distant field contribution subject to widening can be neglected in comparison [37, ch.6.1.3].

This gain guiding is also the reason why a SASE FEL being initiated on transversely only partially coherent spontaneous undulator radiation exhibits a high degree of transverse coherence in saturation[48, 55, 57]. Assuming the initial radiation field being composed of many gaussian modes, the fundamental TEM00 mode exhibits the smallest width and therefore the best overlap with the electron beam. Hence, this mode displays the highest FEL gain and effectively is the only one persisting at saturation [37, ch. 7.2.2].

Ming Xie [58] proposed a correction of the 1D FEL gain length

$$L_{G,3D} = L_{G0}(1 + \mathit{\Delta}) \tag{2.74}$$

to take into account finite energy spread σ_η of the electron beam, finite beam emittance ϵ – assuming $\epsilon_x = \epsilon_y$ – and diffraction of the radiation field under the assumption of an initially gaussian distributed electron beam. Introducing the three beam dependent parameters

$$X_\gamma = \frac{L_{G0} 4\pi\sigma_\eta}{\lambda_u}, \quad X_d = \frac{L_{G0}\lambda_l}{4\pi\sigma_{r,el}^2}, \quad X_\epsilon = \frac{L_{G0} 4\pi\epsilon}{\bar{\beta}\lambda_l}, \tag{2.75}$$

relating to energy spread, diffraction and emittance respectively, the correction $\varDelta$ is parametrized as

$$\begin{aligned}\varDelta = \quad & a_1 X_d^{a_2} + a_3 X_\epsilon^{a_4} + a_5 X_\gamma^{a_6} + a_7 X_\epsilon^{a_8} X_\gamma^{a_9} + a_{10} X_d^{a_{11}} X_\gamma^{a_{12}} \\ & + a_{13} X_d^{a_{14}} X_\epsilon^{a_{15}} + a_{16} X_d^{a_{17}} X_\epsilon^{a_{18}} X_\gamma^{a_{19}}\end{aligned} \tag{2.76}$$

with

$$\begin{aligned} a_1 &= 0.45, & a_2 &= 0.57, & a_3 &= 0.55, & a_4 &= 1.6, & a_5 &= 3.0, \\ a_6 &= 2.0, & a_7 &= 0.35, & a_8 &= 2.9, & a_9 &= 2.4, & a_{10} &= 51 \\ a_{11} &= 0.95, & a_{12} &= 3.0, & a_{13} &= 5.4, & a_{14} &= 0.7, & a_{15} &= 1.9, \\ a_{16} &= 1140, & a_{17} &= 2.2, & a_{18} &= 2.9, & a_{19} &= 3.2. \end{aligned}$$

K. Kim and *M. Xie* found from fitting accurate simulations that taking into account the three dimensional decrease of the gain length the radiation power in saturation scales as [59]

$$P_{\mathrm{sat}} \approx 1.6 \rho_{\mathrm{FEL}} \left(\frac{L_{G0}}{L_{G,3D}} \right)^2 P_{beam}. \tag{2.77}$$

$P_{beam} = \gamma_r m_e c^2 I_0 / e$ refers to the total power of the electron beam[15].

2.4 Cavity based X-ray FELs

Cavity based X-ray FELs are, as evident from the name, very similar to optical cavity based laser oscillators. As optical mirrors are not available for the X-ray region, *Z. Huang and R. D. Ruth* in 2006 [21] as well as *K.-J.Kim et al.* in 2008 [20] proposed to use crystal mirrors based on Bragg reflection instead (see Section **3.1**). These may reach peak reflectivities as high as 99 % and can compete with optical reflectors [61]. The concept by *K.-J.Kim et al.* is working in the low gain regime and is closely tied to the optical FELO depicted in Figure (2.5). An important difference in comparison to the classic FEL oscillator is that the crystal mirrors are only reflecting in a narrow spectral bandwidth, which is why they are widely used for X-ray monochromators in the X-ray regime. This is introducing additional band filtering to the FELO theory [39, ch. 7]. While this makes the theory more complicated, it enforces that the stored radiation has a bandwidth comparable to the crystal bandwidth, which is significantly improving the longitudinal coherence and the brilliance [20].

On the other side, the concept of *Z. Huang and R. D. Ruth* is based on high gain theory and is conceptually related to the seeded FEL amplifier depicted in Figure (2.7) with the seed being regenerated at every roundtrip, which gave rise to the name *X-ray Regenerative Amplifier FEL*

---

[15] *Kroll, Morton and Rosenbluth* showed in [60] that it is possible to increase the extracted power further by quadratically adjusting the undulator parameter K and therefore the resonant particle energy γ_r in saturation to account for the electrons losing energy. This is referred to as undulator *tapering* and is especially effective for seeded FEL having a clearly defined radiation phase [39, ch. 4.5].

(XRAFEL) [21]. At the first round trip the process is initiated by SASE which is then band filtered by the crystal mirrors and fed back to the undulator to seed the next, fresh electron bunch. As the seed at the second round trip is therefore based on shot noise, it is highly stochastic in nature and consequently strongly fluctuating. This however stabilizes with subsequent round trips due to the increasing strength of the seed signal [21, 31].

Compared to optical or infrared wavelength FELOs the FEL generation is much more demanding in the hard X-ray regime as the electron beam emittance needs to be on the same order of magnitude as the light wave emittance $\epsilon_{ph} \approx \lambda/4\pi$, which is in the angstrom range. Therefore, linacs – or *energy recovery linacs* – are commonly proposed for the realization of an XFELO or XRAFEL [20, 25, 28, 31, 32, 62, 63] as they provide significantly improved electron beam propetries compared to the periodic storage rings, which demand a stable and periodic electron phase space for a couple of hours[16].

A major difference between the XFELO and XRAFEL concept lays in what is ultimately determining the radiation pulse characteristics. For the high gain XRAFEL the characteristics are determined by the electron bunch characteristics and the FEL process, with the time-bandwidth and the spatial width-angular divergence product ideally given by Fourier's limit. In contrast, for the low gain XFELO the radiation pulse characteristics in saturation are determined by the stable modes of the X-ray optical cavity [23]. As these cavity modes are perfectly deterministic in nature (for a stable cavity), an XFELO promises perfectly stable, very narrow linewidth radiation pulses, which may be used to seed a high gain amplifier [30, 64, 65] or even to realize advanced concepts of optical lasers such as laser combs [29]. On the other hand, being determined by the optical cavity, an XFELO also requires very accurate optics and alignment on the nanoradian level [20, 23, 64, 66]. In comparison, an XRAFEL is more stable towards imperfect optics as the high gain can compensate for bad overlap between electron bunch and seeding radiation and the optical guiding in the FEL process can compensate for wavefront distortions [31, 32, 67]. As a downside, the longitudinal profile and stability are more dependent on the longitudinal phase space and stability of the electron bunches, respectively.

The central wavelength in an XFELO or XRAFEL is determined by the crystal's spectral reflection and therefore approximately by Bragg's law $\lambda_c \approx 2d_H \sin\Theta_H$ with Bragg's angle Θ_H and the crystal plane spacing d_H (for details see Section **3.1**). Therefore, in order to sustain the continuous spectral tunability of SASE FELs, one needs to make the Bragg angle continuously adjustable. This evidently is not possible in the very simple two-mirror or fixed distance three mirror setups originally proposed [20, 21]. By introducing more mirrors and allowing for movement of the crystal positions, the Bragg angle can be made adjustable allowing for frequency tunability [22, 31] with the cost of a more involved optical setup. In Figure (2.13) besides the non-tunable two mirror layout a four and a six mirror XFELO configuration are depicted, with the six mirror configuration allowing for tunability in a more confined transverse area.

As for both XRAFEL and XFELO the radiation is principally confined inside the optical cavity,

---

[16] There also exist a proposal to realize an XFELO in a future "ultimate" diffraction limited storage ring [24] where the emittance is significantly reduced compared to common third generation sources such as PetraIII.

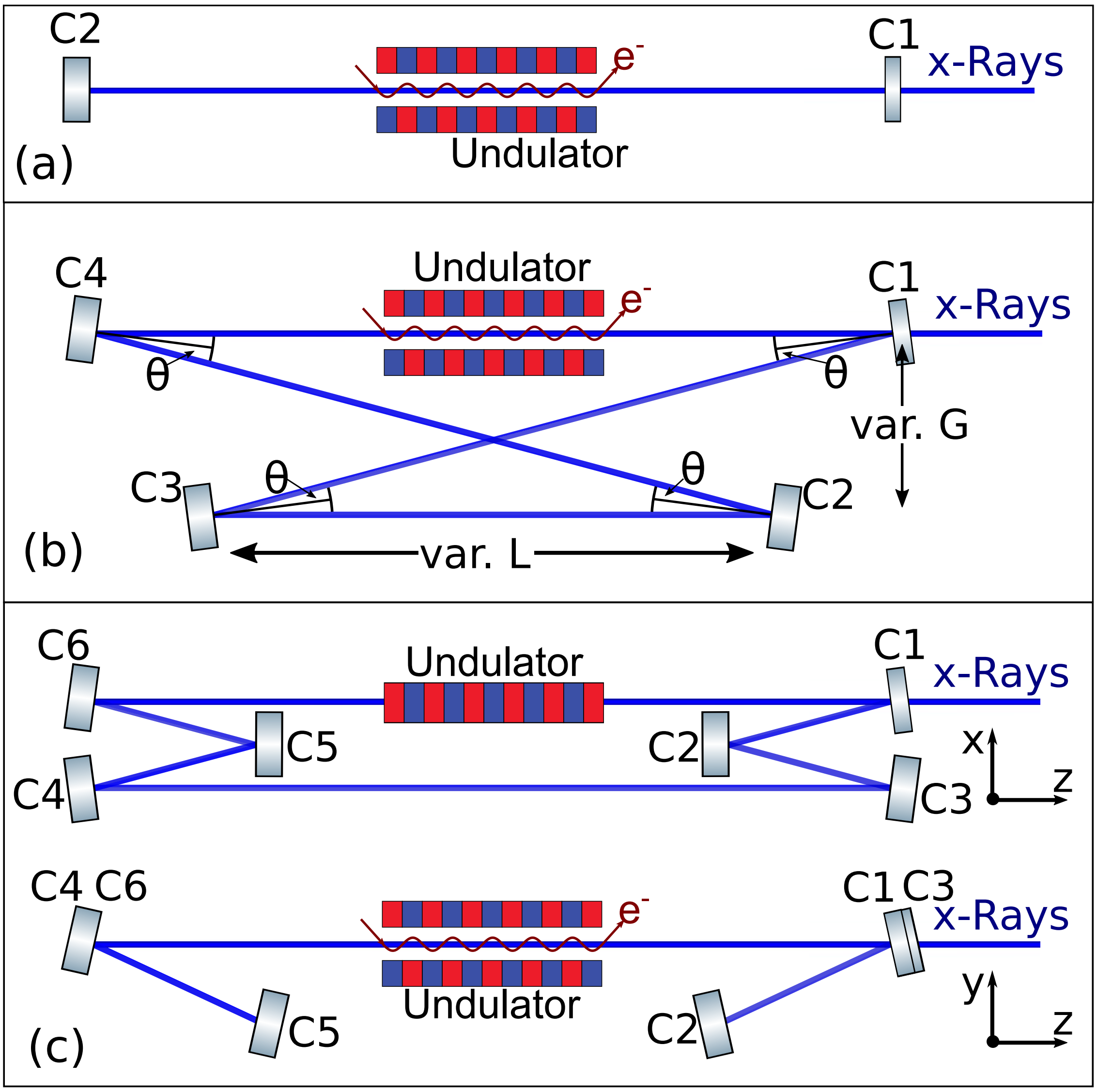

Figure 2.13: Schematics of different CBXFEL layouts without (a) and with (b+c) wavelength tunability. While for the most simple two crystal mirror layout (a) the angles of incidence Θ are fixed, so is the wavelength. In the four mirror layout (b) the angles Θ and therefore the principle wavelength are adjustable by tuning both the transverse distance G between mirrors C1 and C2 (and between C3 and C4) as well as the longitudinal distance L between mirrors C2 and C3. All tuning happens inside one plane. The range of tunability is given by the geometric constraints of the surroundings and the requirement of a constant photon round trip length L_{cav}. In the six mirror option (c) the geometric constraints are a little bit relaxed by applying a different tuning in the $x-z$ and $y-z$ plane.

one needs to introduce an outcoupling mechanism to actually make use of the radiation. Generally, this outcoupling needs to be on the few percentage level for the low gain XFELO owing to the requirement that the roundtrip loss $\mathcal{L}$ does not exceed the single pass FEL gain $\mathcal{G}-\mathcal{L}>1$. For the high gain (X)RAFEL the higher gain compensates for higher cavity losses allowing for much higher outcoupling rates up to >99 % [31, 32, 68–70].

The most obvious outcoupling scheme, proposed by *K.-J. Kim et al.* in 2008 [20], is to use a thin mirror with a tranmission of a few percent per roundtrip, depending on the actual photon energy. This schemes needs, especially at low photon energies, very thin mirrors, which might be troublesome regarding stability. A method to increase the stability of these mirrors is the use of so-called drumhead crystals, which are thick on the borders but milled to few micrometers in the center [71, 72]. Nonetheless, these thin crystals are problematic regarding the distribution of the heat load due to the much increased boundary scattering [26, 27] (see Section **3.2**). Anyhow, they are bad choices for the higher outcoupling rates of a XRAFEL as the required high transmission rates would demand unrealistically thin crystals.

Another, very simple outcoupling scheme, which was proposed by *Z. Huang and R. D. Ruth* for the XRAFEL [21], is to use the regular spectral transmission of the crystal. This transmission is nearly zero at the central reflection wavelength, but rises to the tenth of percent level, depending on the absorption rate, outside the reflection bandwidth (see Section **3.1**). This scheme is only applicable to intermediate and high gain FEL generation, as only the at every round trip newly generated fraction of radiation outside the reflection bandwidth is extracted, determined by the longitudinal electron phase space in conjunction with the FEL process. This fraction would be very low for a low gain FEL.

Another, potentially attractive mechanism for both high gain as low gain cavity based FELs is the use of intracavity beam splitters, for example using additional crystal mirrors [73] or diffraction gratings [56, 74, 75]. The gratings have the advantage over the crystal mirrors that they can be rather thick, whereas the crystals need to be comparably thin on the tens of micrometer scale, to allow for sufficient transmission [73], which might introduce problems in the stability. In case of the grating, one can then either use the first diffracted orders for outcoupling or, for the high gain case, even use the 0th order for outcoupling and use the diffracted orders as seed for the subsequent round trips. By varying thickness and angle of the grating, one can additionally vary the outcoupling efficiency [75].

A method, which has not yet been proposed in literature, would be to use the strong polarization dependence of the dynamic diffraction (see Section **3.1**). Principally, for crystal reflection any reflection is prohibited in direction of the initial radiation polarization axis, leading to high transmission roughly independent of the crystal thickness (aside the absorption). This would only work for the cavity layouts (b) and (c) presented in Figure (2.13), as the exact backscattering geometry in (a) has no polarization dependence. By appropriately choosing the direction of reflection one could therefore set the transmission rate without relying on thin crystals. By additionally using variable polarization undulators or quatre-wave plates one could even continuously tune the outcoupling rate.

A method working solely for the high gain case is the usage of pinhole crystal mirrors [31, 32] as originally applied at the infrared RAFEL [69]. By using an appropriately shaped pinhole it is possible to couple out a considerable fraction of the pulse energy. Due to the optical guiding of the radiation field in the undulator which is increasing with increasing seed strength [31, 32, 70], the radiation beam width is bigger at low signal and vice versa for the strong signal. Hence, the outcoupling rate increases with the FEL power, allowing for stronger optical feedback at the first round trips. Nonetheless, as the pinhole is introducing strong diffraction effects also at the first round trips, the gain must be strong enough to compensate for these.

A very different approach is, after having the radiation field built up over multiple round trips, to dump 100 % of the stored power in the cavity. This can be done in the sense of a Bragg switch by instantly detuning from the resonant Bragg condition, for example by heating [76, 77] or sudden variation of the angle of incidence. Even in the optimal case, where the cavity can return to the stable state directly after applying the “switch”, this method comes with the disadvantage of strongly reducing the radiation pulse repetition rate, as the radiation field needs to return to its saturated state.

The last outcoupling mechanism discussed here is to use the electron beam or more specifically the microbunching induced by the FEL process. By applying a micro-bunch rotation to the electron phase space [78] and using a short undulator afterburner behind the optical cavity, it should be principally possible to extract coherent X-ray radiation from the kicked electrons beam [33]. While prior outcoupling mechanisms are adapations from the field of optical lasers, this scheme is very specific to the field of synchrotron sources.

3 X-Ray Crystal Interaction

When X-ray photons (or photons in general) are impinging on a crystal, they are partially transmitted, partially reflected and partially absorbed. As the absorption changes the inner energy and therefore the thermodynamic state of the crystal, it ultimately influences the reflection and transmission, which on the other hand is influencing the absorption. This generally makes light-matter interaction a strongly coupled mechanism. In other words, it means that the light is influencing the crystal with which it is interacting, while the crystal on the other hand is influencing the incoming light. Fortunately, these two directions can be decoupled in the framework of this thesis as the relevant interactions are happening on two strongly differing timescales.

The process of absorption and thereby also the fraction of absorbed photons depends strongly on the photon wavelength. For X-rays the absorption is driven by excitation of inner shell electrons into high valence states [79, ch.5.2, 80]. These (photo-)electrons then relax back into their original states – under the precondition of comparably weak photon densities which do not change the overall material phase. The relaxation mainly takes place by the recombination of the inner hole states with the electrons of outer shells. These transitions are either accompanied by the emission of photons of appropriate wavelengths, called *fluorescence*, or by excitation of another valence electron of reduced kinetic energy, the *Auger-electrons*[79, ch.5.2]. In the case of fluorescence the energy leaves the crystal and therefore does not contribute to heating and, hence, does not disturb the X-ray matter interaction. In the second case of Auger-electrons, the energy stays inside the crystal system and, for insulators for which valence electrons are an unfavorable state, ultimately dissipate the energy into lattice excitation in the form of phonons[81][17].

For light elements with a low atomic number Z the relaxation via Auger-electrons (unfortunately) strongly dominates over the fluorescence. This also includes diamond as the crystal assumed for the actual realization of the CBXFEL at the European XFEL facility. While luminescence of diamond in the visible spectrum due to recombination of, already partially thermalized, valence electrons after X-ray irradiation is experimentally confirmed [82, 83], the actual luminescent yield is comparably low and mostly attributed to defects in the crystal.

In the following it is assumed that the entire absorbed photon energy will be converted into phonons and therefore in second order into temperature[18]. As discussed above, the process of lattice thermalization is a multiple step process and therefore requires a certain time. While the Auger-electron ionization cascade takes place on a femtosecond time-scale, the actual thermalization to the lattice is much slower on the picosecond scale [81, 84]. Therefore, even if the photon pulse is only 100 fs long, the (lattice) temperature rise will take place on the ps scale. For this work it is assumed to be on the order of 100 ps[19].

---

[17] This process already starts after the excitation of the first photo-electrons, but is typically much slower than the thermalization via Auger-electrons [81].

[18] While this certainly is incorrect in a strict sense, it can be seen as a rather accurate approximation. Furthermore, it is the worst case scenario for the influence on the X-ray scattering and therefore the CBXFEL stability.

[19] For the process of incoherent heat dissipation accounted for in this work, the precise number of the thermalization time is of reduced interest. This is due to the actual timescale of heat dissipation being on the multiple nanosecond level (see Sections **4.3.1** and **5.2.3**), so that both a femtosecond scale as a picosecond scale thermal-

This timescale is much longer than the actual duration of the (CB)XFEL pulse. As the X-ray diffraction (reflection) is primarily affected by the lattice configuration and not its electronic state, as was mentioned above, the X-ray pulse does not have impact on itself during the diffraction process. It does, however, influence the 'next' pulses impinging on the crystal after one or multiple round trips through the X-ray optical cavity. So, even if the initial temperature rise after absorption would have a strong effect on the reflection of the X-rays at the crystal mirror, the actual CBXFEL may not be disturbed if the crystal (mostly) returns to its original lattice configuration inside the photon-matter interaction volume during one round trip.

The actual answer of the crystal to dissipate the heat is manifold. The bulk of the heat will be carried away by thermal diffusion, meaning that the phonons carrying the heat will incoherently dissipate through the crystal. At the arrival of the subsequent X-ray pulse the excess heat remaining in the interaction volume is associated with an expanded lattice, which is shifting the X-ray diffraction resonance.

Beside this quasi-static lattice expansion, where the lattice only is dependent on the temperature at this exact moment, there also is a dynamic thermomechanical response of the crystal due to the abruptly changing lattice configuration after absorption (see for example [86]). While the associated lattice waves or mesoscopic vibrations, which are deeply connected to coherent phonon modes, only carry little heat, they are much more persistent than the incoherent phonon modes [85, 87].

Ultimately, the elastic response can cumulate to macroscopic vibration modes of the whole crystal [85, 87]. These are strongly dependent on the crystal shape and actual energy associated with the thermomechanical response and take place on a much longer time scale.

This thesis is focussed on the thermal conduction and the simplified quasi-static lattice expansion. As was discussed in previous publications [26, 27, 88–90], it is important to operate the crystal mirrors at cryogenic temperatures. The deviation from classic diffusive heat transport is also approximately accounted for in this work.

While the thermomechanical response definitely is important, it is very involved and its calculation very time demanding. However, they are both numerically as experimentally investigated in the thesis by *I. Bahns* [85], which also has a focus on the effect of the heat load on the CBXFEL performance. In the framework of this thesis, the dynamic lattice expansion is only superficially accounted for in Section **5.2.3**, but will be further investigated in the near future.

In the following, first an introduction to the (decoupled) diffraction of X-rays at crystals in the framework of *dynamic diffraction theory* is given. Then, in **3.2** the thermal response of the crystal with an emphasizes on the thermal conduction process is described. Both sections are held rather general, but have a small emphasize on the case of diamond as a face-centered isotropic cubic insulator.

---

ization appear as effectively instantaneous. On the other hand it might make a difference for the thermoelastic response, as this is highly dependent on the dynamics (time-derivative) of the temperature evolution (see Thesis by *I. Bahns* [85]).

3.1 X-ray diffraction

Crystals irradiated by X-ray light produce a characteristic pattern of the reflected rays. This was first found by *Laue, Friedrich and Kipping* in 1912 [91] and shortly after confirmed by *William Henry Bragg* and his son *William Lawrence Bragg* [92]. Bragg shaped the well-known *Bragg's law*

$$2d_H \sin(\Theta_B) = n\lambda, \quad \text{with } n \in \mathbb{Z}, \tag{3.1}$$

where λ is the X-ray wavelength, Θ_B is the glancing angle of incidence for which a reflection can be measured and d_H is the lattice spacing for net planes of the miller's indices $H = (h, k, l)$, with $h, k, l \in \mathbb{N}$. Miller's indices are used for denoting equivalent planes. They are defined as the inverse of the points of interception of the plane with the main crystal axis in wholes of the lattice constants (a_x, a_y, a_z) [93, Ch. 1.1.3]. For diamond, which has a face centered cubic lattice, the lattice spacing is isotrop ($a_x = a_y = a_z = a_0$) and therefore

$$d^C_{(h,k,l)} = \frac{a_0}{\sqrt{h^2 + k^2 + l^2}}. \tag{3.2}$$

It is obvious from equations Eqs. (3.1) to (3.2), that with a change of the lattice constant – for example due to heating and therewith thermal expansion – the reflection condition will also change.

While Bragg's simple formular proved to be very accurate, his derivation was heavily based on assumptions which are hard to justify and will not be explained here. *Laue et al.* used a more realistic derivation. They yielded a less clean result, but which can be shown to be equivalent to Bragg's law (3.1). For their derivation, the concept of the *Bravais*-lattice is of importance. The Bravais-lattice is an representation of the crystal lattice as infinite array described by a set of discrete translations $\boldsymbol{R} = \hat{n}_x a_x + \hat{n}_z a_z + \hat{n}_z a_z$ where $\hat{n}_x, \hat{n}_y, \hat{n}_z$ form an orthonormal basis. Fundamental for a Bravais-lattice is that the lattice will look exactly the same no matter from which lattice point it is observed [93, Ch. 1.1.1]. *Laue et al.* assumed, that a plane wave $E(r) = E_0 \mathrm{e}^{i\boldsymbol{kr}}$ with the wavenumber k is incident on the crystal's *Bravais*-lattice. At every point of it a new spherical wave originates. As the X-ray wavelength is on the same order of magnitude as the spacing between these spherical waves, they will exhibit significant interference.

This is show in Figure (3.1(a)), where only one plane wave component with wavevector $\boldsymbol{k}$ is displayed for convenience. Considering elastic scattering $|\boldsymbol{k}| = |\boldsymbol{k}'|$, one can straight forwardly show that the reflection will show constructive interference if the *von Laue* condition

$$\boldsymbol{k}' - \boldsymbol{k} = \boldsymbol{G} \quad \text{with } \boldsymbol{G} \cdot \boldsymbol{R} = 2\pi n \quad \text{and } n \in \mathbb{N} \tag{3.3}$$

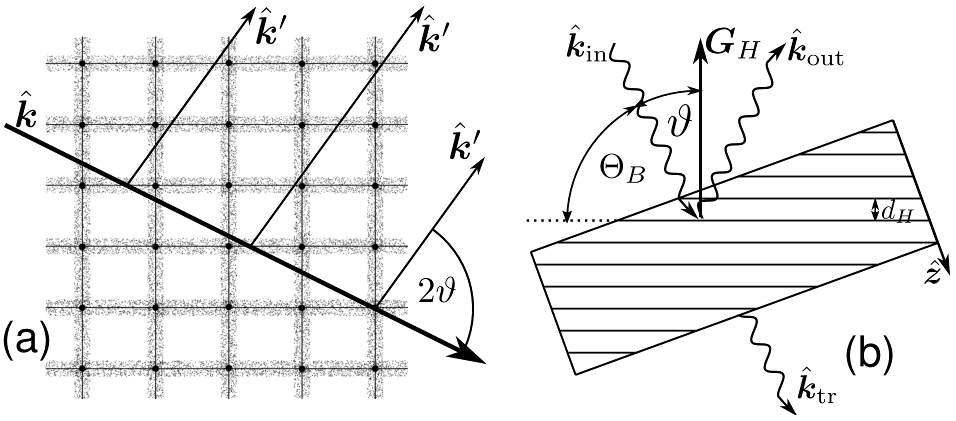

Figure 3.1: Sketch of the Bragg/von-Laue reflection in (a). New waves originate at the density variations of the lattice planes stimulated by an incident plane wave of wavevector $\boldsymbol{k}$. Only the plane wave components with wavevector $\boldsymbol{k}'$ of the sperical waves are displayed for convenience. The interference between the incident and reflected waves will be constructive if the von-Laue condition (3.3) is met. (b) illustrates the reflection geometry with Bragg angle Θ_B, grazing angle ϑ and reciprocal lattice vector $\boldsymbol{G}_H$ for the scattering plane H. In general, the plane H and the crystal surface do not need to be parallel. (Modified from [94, Fig. 2.8])

is met. $\boldsymbol{G}$ is called the reciprocal lattice vector which forms the Bravais-lattice of the reciprocal lattice. The basis vectors of the reciprocal lattice are defined by

$$\hat{b}_x = 2\pi\frac{\hat{n}_y \times \hat{n}_z}{\hat{n}_x\hat{n}_y\hat{n}_z} \quad \hat{b}_y = 2\pi\frac{\hat{n}_z \times \hat{n}_x}{\hat{n}_x\hat{n}_y\hat{n}_z} \quad \hat{b}_z = 2\pi\frac{\hat{n}_x \times \hat{n}_y}{\hat{n}_x\hat{n}_y\hat{n}_z} \qquad \text{and} \quad \boldsymbol{G}_{hkl} = h\hat{b}_x + k\hat{b}_y + l\hat{b}_z. \tag{3.4}$$

For elastic scattering and taking into account that $|\boldsymbol{k}| = k = 2\pi/\lambda$, equation (3.3) becomes $|\boldsymbol{G}| = 2|k|\sin\Theta_B$. As for the reciprocal lattice vector the condition $|G|_H = {}^{2\pi n}/_{d_H}$ with $n \in \mathbb{N}$ holds, one directly arrives at the Bragg condition.

3.1.1 Dynamical theory of X-ray diffraction

Up to now the reflection was considered in an idealized way, as it was assumed that the scattering was perfectly localized at the points of the Bravais-lattice. This originated in a reflection condition where one exact reflection angle Θ_B was found for the X-ray wavelength λ. Such a delta-distributed relation obviously is nonphysical. The dynamical theory of X-ray diffraction accounts for the density distribution of the atoms in the lattice, the refraction of the light inside the crystal and multiple scattering events of the radiation [94, ch. 1.1]. This theory is in good agreement with very accurate experiments and also correctly predicts finite reflection widths either in angle or in wavelength. In the following the derivation of the dynamic theory shall be sketched. While the derivation will be rather general, a focus will be on the special case of two-beam diffraction as this is of major importance for a CBXFEL . Two-beam diffraction means, that the reflection condition is met for exactly one set of net planes of order H resulting in one transmitted and one reflected beam. Generally, the reflection condition can be fulfilled for many different sets of miller's indices. This results in the more general but also, due to the interaction between the different reflection orders, more complicated n-beam diffraction. As n-beam diffraction is the reason why an CBXFEL shall not be operated at exact Θ_B =90°, this case shall be superficially sketched as well. The derivations presented hereafter will mostly be based on the book *"X-ray diffraction"* by *Y. Shvyd'ko* [94]. Finally, the diffraction in a strained crystal shall be outlined. A sketch of a simplified reflection geometry is shown in Figure (3.1(b)).

Like in the derivation of the von-Laue condition, the incident radiation is assumed as a linearly polarized plane, monochromatic wave $\boldsymbol{\mathcal{E}}(\boldsymbol{r},t) = \boldsymbol{\mathcal{E}}_i \exp\left[\mathrm{i}\left(\boldsymbol{k}_0\boldsymbol{r} - \omega t\right)\right]$ with the vacuum wave vector $\boldsymbol{k}_0$ and frequency $\omega = \frac{E_{ph}}{\hbar} = \frac{2\pi c}{\lambda} = kc$. This induces a radiation field $\boldsymbol{D}(\boldsymbol{r},t) = \exp\left(i\omega t\right)\boldsymbol{D}(\boldsymbol{r})$ inside the crystal. The spatial part is subject to the wave equation in dielectric solids[94]

$$\left[-\nabla^2 - k^2\right]\boldsymbol{D}(\boldsymbol{r}) = k^2\chi(\boldsymbol{r})\boldsymbol{D}(\boldsymbol{r}), \tag{3.5}$$

where $k = |\boldsymbol{k}_0|$ and K is the corresponding in-crystal wave-number. $\chi(\boldsymbol{r})$ is the electric susceptibility, which is a continuous periodic function with the symmetry of the crystal lattice. As such it can be expressed as a Fourier decomposition in reciprocal space:

$$\chi(\boldsymbol{r}) = \sum_H \chi_H \exp\left(\mathrm{i}\,\boldsymbol{G}_H\boldsymbol{r}\right) \qquad \text{with} \quad \chi_H = -\frac{r_e}{\pi}\frac{F_H}{V}\lambda^2 \tag{3.6}$$

with the reciprocal space vector $\boldsymbol{G}_H$ and the $\boldsymbol{G}_H$-specific structure factor F_H [94, ch. 2.2.1]. The structure factor is defined as

$$F_H = \sum_n f_n\left(\boldsymbol{G}_H\right)\exp\left(i\boldsymbol{G}_H\boldsymbol{r}_n - W_n\left(\boldsymbol{G}_H\right)\right), \tag{3.7}$$

where the sum is over the atoms in the unit cell. The quantity

$$\exp\left(-W_n(\boldsymbol{G}_H)\right) = \exp\left(-|\boldsymbol{G}_H|^2 < \boldsymbol{u}^2 > /2\right)$$

is the square of the temperature dependent *Debye-Waller*-factor, which expresses the kinetic motion of the atoms in form of the mean squared displacement $< \boldsymbol{u}^2 >$. The term $f_n\left(\boldsymbol{G}_H\right) = f^{(}_n0)\left(\boldsymbol{G}_H\right) + f'_n\left(E_{ph}\right) + if''_n\left(E_{ph}\right)$ is the atomic scattering amplitude. It is composed of the atomic form factor $f^{(}_n0)\left(\boldsymbol{G}_H\right)$ which is the Fourier-transform of the atomic charge density and the wavelength dependent anomalous scattering corrections $f'_n\left(E_{ph}\right)$ and $if''_n\left(E_{ph}\right)$. The value of these corrections can be found tabulated in various sources and are mainly determined by the photoelectric absorption and inelastic compton scattering [95, p. 41][20]. In this work the computational library *xraylib* [96] is used for the computation of the susceptibilities χ_H. The sum over $\exp\left(i\boldsymbol{G}_H\boldsymbol{r}_n\right)$ in equation (3.7) also has significant implication. Considering a lattice with multiple atoms of the same kind (meaning the same $f_n\left(\boldsymbol{G}_H\right)$), then this factor strongly

---

[20] The imaginary $f''(E_{ph})$ is determining the absorption of the X-rays in the crystal as described in the beginning of this Chapter and therefore ultimately leading to the temperature rise.

suppresses specific reflection orders $H = (h, k, l)$ which would be allowed with respect to the von-Laue relation (3.3). These reflection are termed *forbidden* reflexes. For a diamond fcc lattice, which has identical atoms at the positions (000), $(\frac{1}{2}\frac{1}{2}0)$, $(\frac{1}{2}0\frac{1}{2})$, $(0\frac{1}{2}\frac{1}{2})$, $(\frac{1}{4}\frac{1}{4}\frac{1}{4})$, $(\frac{3}{4}\frac{3}{4}\frac{1}{4})$, $(\frac{3}{4}\frac{1}{4}\frac{3}{4})$ and $(\frac{1}{4}\frac{3}{4}\frac{3}{4})$, the structure factor (neglecting the Debye-Waller factor) becomes

$$
\begin{aligned}
F_{hkl} = f\left(\boldsymbol{G}_{hkl}\right) \quad & \cdot \Big(1 + e^{\mathrm{i}\pi(h+k)} + \quad e^{\mathrm{i}\pi(h+l)} + e^{\mathrm{i}\pi(k+l)} \\
& \quad + e^{\mathrm{i}\frac{\pi}{2}(h+k+l)} + \quad e^{\mathrm{i}\frac{\pi}{2}(3h+3k+l)} + e^{\mathrm{i}\frac{\pi}{2}(3h+k+3l)} + e^{\mathrm{i}\frac{\pi}{2}(h+3k+3l)}\Big) \\
\Rightarrow \; F_{hkl} \neq 0 \;\text{ if} & \begin{cases} \operatorname{mod}(h+k+l, 4) = 0 \quad \text{and} \quad h, k, l \text{ are even numbers each} \\ h, k, l \text{ are odd numbers each} \end{cases}
\end{aligned}
\tag{3.8}
$$

From the periodicity of the susceptibility $\chi(\boldsymbol{r})$ it follows that the solution of eq. (3.5) is a Bloch-wave:

$$
\boldsymbol{D}(\boldsymbol{r}) = \sum_{H} \boldsymbol{D}_H e^{\mathrm{i}\boldsymbol{K}_H \boldsymbol{r}} \qquad\qquad \text{with} \quad \boldsymbol{K}_H = \boldsymbol{K}_0 + \boldsymbol{G}_H, \tag{3.9}
$$

with the in-crystal wave-vector $\boldsymbol{K}_0$ closely related to the vacuum wave-vector $\boldsymbol{k}_0$ (see eq. (3.12) below). Inserting above equation (3.9) as well as equation (3.6) into the differential equation (3.5) and doing a comparison of coefficients in $\exp\left(i\boldsymbol{G}_H \boldsymbol{r}\right)$ in conjunction with some simple algebra, one can derive

$$
\begin{aligned}
\frac{|\boldsymbol{K}_H^2| - k^2}{k^2} \boldsymbol{D}_H &= \sum_{H'} \chi_{H-H'} \boldsymbol{D}_{H'}. \\
\Leftrightarrow \boldsymbol{D}_H &= \frac{k^2}{|\boldsymbol{K}_H^2| - k^2(1+\chi_0)} \sum_{H' \neq H} \chi_{H-H'} \boldsymbol{D}_{H'}
\end{aligned}
\tag{3.10}
$$

As the factors $\chi_{H-H'}$ are very small, only those $\boldsymbol{D}_H$ are significant for which the *excitation condition*

$$
K_H \approx k|1 + \frac{\chi_0}{2}| \tag{3.11}
$$

holds, which is quite similar to the von-Laue condition (3.3).

According to eq. (3.9) the radiation field inside the crystal is a set of plane waves with wave vectors $\boldsymbol{K}_H$, which upon leaving the crystal become externally propagating plane waves with wave vector $\boldsymbol{k}_H$. The condition of continuity of the tangential component of the wavevectors imposes

$$
\boldsymbol{K}_0 = \boldsymbol{k}_0 + \xi \hat{\boldsymbol{z}}, \qquad\qquad \boldsymbol{K}_H = \boldsymbol{k}_H + \xi_H \hat{\boldsymbol{z}}, \tag{3.12}
$$

for the relation between the vacuum and in-crystal wavevectors. The unknown ξ as well as ξ_H must be very small, about $k|\chi_0|/2$ in the sense of the *excitation condition* (3.11)

In the following it is assumed that the light is linearly polarized

$$\boldsymbol{D}_H = D_H^{\sigma}\boldsymbol{\sigma}_H + D_H^{\pi}\boldsymbol{\pi}_H$$

with the mutually orthogonal unit polarization vectors $\boldsymbol{\sigma}_H$ and $\boldsymbol{\pi}_H$, which are both normal to $\boldsymbol{K}_H$.[21]. By demanding elastic scattering and thereby conservation of energy $|\boldsymbol{k}_H| = |\boldsymbol{k}_0| = K$ equation (3.10) becomes after some algebra [94, ch. 2.2.8]:

$$\sum_{H',s'=\sigma,\pi} G_{HH'}^{ss'} D_{H'}^{s'} - \left(2\gamma_H \frac{\xi}{k} + \frac{\xi^2}{k^2}\right) D_H^s = 0 \qquad \text{with} \quad s\,(s') = \pi, \sigma, \tag{3.13}$$

$$G_{HH'}^{ss'} = \chi_{H-H'} P_{HH'}^{ss'} - \alpha_H \delta_{HH'}^{ss'}, \qquad P_{HH'}^{ss'} = (\boldsymbol{s}_H \boldsymbol{s}'_H)\,, \tag{3.14}$$

$$\gamma_H = \frac{(\boldsymbol{k}_0 + \boldsymbol{G}_H)\hat{\boldsymbol{z}}}{k} \quad \text{and} \quad \alpha_H = \frac{2\boldsymbol{k}_0 \boldsymbol{G}_H + \boldsymbol{G}_H^2}{k^2}, \tag{3.15}$$

where $\delta_{HH'}^{ss'}$ is the Kronecker delta symbol and $P_{HH'}^{ss'}$ is the polarization matrix. This matrix describes the probability amplitude of scattering of a plane wave with wave vector $\boldsymbol{K}_H$ and polarization $\boldsymbol{s}$ into a plane wave with wave vector $\boldsymbol{K}_{H'}$ and polarization $\boldsymbol{s'}$. γ_H is the direction cosine of $\boldsymbol{k}_H$ with respect to the inward surface normal and α_H is the so-called deviation parameter. As will be shown below it is a fundamental parameter in the description of the reflectivity and transmissivity. The quantities of $G_{HH'}^{ss'}$ span the so-called scattering matrix of rank $2n$.
This forms a system of $2n$ homogeneous equations for the unknowns D_H^s with a non-trivial solution only if the system's determinant equals zero. This leads to a polynomial of degree $4n$ in the quantity ξ, giving rise to $4n$ characteristic values of ξ_ν and $\boldsymbol{K}_{0(\nu)} = \boldsymbol{k}_0 + \xi_\nu \hat{\boldsymbol{z}}$, respectively. For cases of non-grazing incidence, i.e.meaning $\boldsymbol{K}_0\hat{\boldsymbol{z}} \gg 0$, $|\xi| \approx |\chi|_0 k \ll k$ and the quadratic term in equation (3.13) can be neglected, so that the polynomial reduces to a degree of $2n$.
The actual solution is a superposition of each individual solutions ξ_v. The net radiation inside the crystal can than be expressed as [94, ch. 2.2.9]

$$\boldsymbol{\mathcal{D}}(\boldsymbol{r}) = \sum_H e^{\mathrm{i}(\boldsymbol{k}_0 + \boldsymbol{G}_H)\boldsymbol{r}} \boldsymbol{D}_H(z), \tag{3.16}$$

$$\boldsymbol{D}_H(z) = \sum_\nu \Lambda_\nu \boldsymbol{D}_{H(\nu)} e^{\mathrm{i}\xi_\nu z}. \tag{3.17}$$

The unknown coefficients Λ_ν can be derived from the boundary conditions for the component $\boldsymbol{D}_H$ at the front $z = 0$ or the rear $z = t_c$ of the crystal.
The boundary conditions can be written as

$$\begin{aligned} \boldsymbol{D}_0(0) = &\ \boldsymbol{\mathcal{E}}_i, \\ \boldsymbol{D}_H(0) = &\ 0 \qquad \text{Laue} - \text{case wave.}, \\ \boldsymbol{D}_H(t_c) = &\ 0 \qquad \text{Bragg} - \text{case wave.}, \end{aligned} \tag{3.18}$$

---

[21] There exists an infinite amount of choices for $\boldsymbol{\sigma}_H$ and $\boldsymbol{\pi}_H$. Normally, they are chosen such that the cross-coupling is very small $\boldsymbol{\sigma}_{H1} \cdot \boldsymbol{\pi}_{H2} \approx 0$, which eases computation.

where $\boldsymbol{\mathcal{E}}_i$ is the amplitude of the incoming wave. It differs between two different scattering geometries, the Laue and the Bragg case. In the Laue case the direction cosines $\gamma_{0/H}$ (3.15) of the diffracted and the incoming beams have the same sign meaning the diffracted wave propagates to the inside of the crystal. In the Bragg case the direction cosine of the diffracted and the transmitted beam have opposite sign. This means that the diffracted beam propagates towards the outside. With these boundary conditions, the problem (3.13) is fully specified.

3.1.2 2-Beam Diffraction

For the 2-beam case, one assumes that the excitation condition (3.11) is fulfilled only for two particular waves with the wave vectors $\boldsymbol{K}_0$ and $\boldsymbol{K}_H$.
Defining the polarization as [94, ch. 2.2.8]

$$\boldsymbol{\sigma}_0 = \frac{\boldsymbol{H} \times \boldsymbol{K}_0}{|\boldsymbol{H} \times \boldsymbol{K}_0|} \qquad \boldsymbol{\sigma}_H = \frac{\boldsymbol{K}_H \times \boldsymbol{K}_0}{|\boldsymbol{K}_H \times \boldsymbol{K}_0|} \qquad \boldsymbol{\pi}_{0,H} = \frac{\boldsymbol{K}_{0,H} \times \boldsymbol{\sigma}_{0,H}}{|\boldsymbol{K}_{0,,H}|}, \tag{3.19}$$

leads to a polarization matrix of $P_{0H}^{ss'} = 0$ for $s \neq s'$. Therewith, the constituting system of equations (3.13) reduces to two independent sets of equations for each polarization component:

$$\det \begin{pmatrix} \chi_0 - \epsilon & \chi_{\bar{H}} P_{0H}^{ss} \\ \chi_H b P_{H0}^{ss} & (\chi_0 - \alpha) b - \epsilon \end{pmatrix} = 0, \tag{3.20}$$

$$\text{with} \qquad \epsilon = 2\gamma_0 \frac{\xi}{k} + \frac{\xi^2}{k^2} \approx 2\gamma_0 \frac{\xi}{k} \quad \text{and} \quad b = \frac{\gamma_0}{\gamma_H}, \tag{3.21}$$

where $s = \sigma$ or $s = \pi$, $\bar{H} = -H$ and the index H is omitted for α defined by (3.15). b is called the asymmetry factor. If the reflecting plane is parallel to the crystal surface, i.e. $\boldsymbol{G_H} \parallel \hat{z}_{\text{surf}}$, then $b \approx \pm 1$. The negative sign refers to Bragg-case and the positive sign to Laue-case reflection. The coefficients of the polarization matrix are $P_{0H}^{\sigma\sigma} = P_{H0}^{\sigma\sigma} = 1$ and $P_{0H}^{\pi\pi} = P_{H0}^{\pi\pi} = \cos(2\Theta)$ where Θ is the glancing angle towards plane H, being equivalent to the Bragg angle[22]. In the following the indices are dropped and P refers to either π or σ polarized light. Solving (3.20) leads to following eigenvalues

$$\begin{aligned} \epsilon_\pm = {} & \chi_0 - \tilde{\alpha} \pm \sqrt{(\tilde{\alpha}^2 + P^2 b \chi_H \chi_{\bar{H}})} \quad \rightarrow \xi_\pm \approx k \frac{\epsilon_\pm}{2\gamma_0}, \\ \text{with} \quad \tilde{\alpha} = {} & \frac{1}{2} (\alpha b + \chi_0 (1 - b)). \end{aligned} \tag{3.22}$$

---

[22] As was noted in Subsection **2.4** about CBXFELs the angle dependency of the polarization coefficients of π polarized incoming light could be used to tune the reflection and transmission characteristics. This is particularly true for an angle of incidence of $\pi/4$, where $P^{\pi\pi} = 0$ and therefore $R^{\pi\pi} = 0$. By adjusting the fraction of the $\pi-$polarization on the incoming light, the reflection characteristics of the entire system can be adjusted.

Assuming Bragg-case boundary conditions (3.18), one arrives at the following values for the field amplitudes (3.17) [94, ch. 2.4.1][23]

$$\begin{aligned} D_0(z) = & \ \mathcal{E}_i \frac{R_+ e^{i\xi_-(z-t_c)} - R_- e^{i\xi_+(z-t_c)}}{R_+ e^{-i\xi_- t_c} - R_- e^{-i\xi_+ t_c}} \\ D_H(z) = & \ \mathcal{E}_i R_+ R_- \frac{e^{i\xi_-(z-t_c)} - e^{i\xi_+(z-t_c)}}{R_+ e^{-i\xi_- t_c} - R_- e^{-i\xi_+ t_c}} \end{aligned} \tag{3.23}$$

where t_c is the crystal depth and

$$R_\pm = \frac{\epsilon_\pm - \chi_0}{P\chi_{\bar{H}}}.$$

This yields for the complex reflectivity $r_{0H} = D_H(0)/\mathcal{E}_i$ and transmissivity $t_{00} = D_0(t_c)/\mathcal{E}_i$

$$r_{0H} = R_+ R_- \frac{1 - e^{i(\xi_+ - \xi_-)t_c}}{R_- - R_+ e^{i(\xi_+ - \xi_-)t_c}} \tag{3.24}$$

$$t_{00} = e^{i\xi_+ t_c} \frac{R_- - R_+}{R_- - R_+ e^{i(\xi_+ - \xi_-)t_c}}. \tag{3.25}$$

The absolute reflectivity R and transmissivity T can be easily calculated as the squared magnitude of r_{0H} and t_{00}, respectively. For asymmetric reflection $b \neq 0$ the reflectivity R is additionally normalized by the change of cross section between incoming and reflected beam, which is exactly $|b|^{-1}$ [94, ch. 2.2.11]:

$$R = |b|^{-1} |r_{0H}|^2 \tag{3.26}$$

$$T = |t_{00}|^2 \tag{3.27}$$

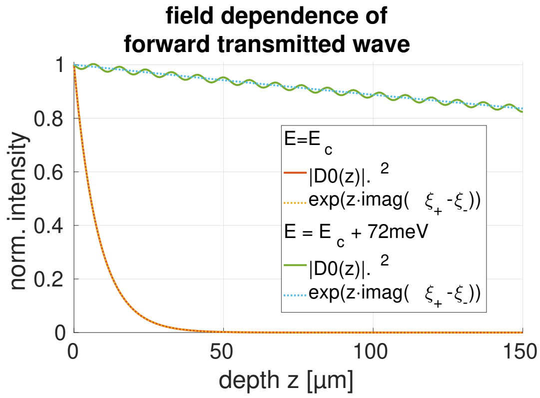

Figure 3.2: Field dependence of the forward transmitted wave in the crystal

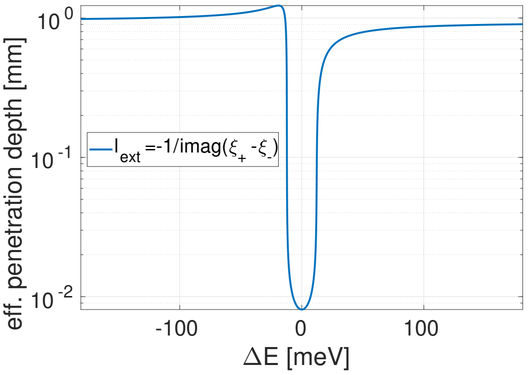

Figure 3.3: Effective penetration depth in dependence of the photon energy.

In Figure (3.2) the squared magnitude of the forward transmitted wave $D_0(z)$ is plotted against the crystal depth for two different photon energies for the exemplary case of a C (3 3 3) reflec-

---

[23] The polarization index and the direction of the field amplitudes are neglected for simplicity.

tion at $\Theta = 90°$. For the forward transmitted field at the energy $E_c = 9.03\,\mathrm{keV}$ of maximum reflectivity (see eq. (3.31) below), the amplitude rapidly declines against crystal depth, as the reflection is very effective. For the field some tens of meV away from E_c, the intensity drops much more slowly with crystal depth. As only a small fraction of the incident field is actually reflected at this energy, the decrease is dominated by the crystal absorption. One can also see some oscillations with depth in the field amplitude. These come from interference effects of the waves created at the surface of the crystal and its backside[24]. They do not appear at $E_{\mathrm{ph}} = E_c$ as close to no radiation actually reaches the crystal backside. In Figure (3.2) it is also shown that the field decline can be described by $\exp\left(z \cdot \mathrm{imag}(\xi_+ - \xi_-)\right)$. The quantity

$$l_{ext} = -\frac{1}{\mathrm{imag}(\xi_+ - \xi_-)} \tag{3.28}$$

is the effective penetration depth of the incoming wave into the crystal. As plotted in Figure (3.3) it is strongly dependent on the photon energy/wavelength. At the center of reflection $E_{\mathrm{ph}} = E_c$ it has its smallest value in the micrometer range and is dominated by the reflection. Away from E_c the reflection becomes less efficient and the penetration depth increases until far from the excitation condition (3.11) it is equal to the absorption depth.

To yield a more comprehensive picture of the two beam reflection, a few approximations will be made. First, a thick crystal $t_c \gg l_{ext}$ is assumed. Second, there is no absorption. Third, the crystal is centrosymmetric leading to $\chi_H = \chi_{\bar{H}}$. With these approximations one can define the reflectivity as a simple function [94, ch. 2.4.3]:

$$R(y) = |-y \pm \sqrt{y^2 - 1}|^2, \quad \text{with} \quad y = \frac{\alpha b + \chi_0(1-b)}{2|\chi_H P|\sqrt{|b|}}, \tag{3.29}$$

where the sign is chosen such that $|R| \leq 1$. In the region $-1 < y < 1$ total reflection $R(y) = 1$ is achieved. Using equations (3.6) and (3.15) this corresponds to a spectral width of

$$\epsilon_H = \frac{\Delta E}{E_c} = \frac{4 r_e d_H^2}{\sqrt{|b|}\pi V} |P F_H| \tag{3.30}$$

and a center of reflection ($y = 0$) of

$$\begin{aligned} E_c \sin\Theta_c &= \frac{hc}{2d_H}\left(1 + w_H\right) \\ \leftrightarrow \quad \lambda_c &= \frac{2d_H \sin\Theta_c}{1 + w_H} \\ \text{with} \quad w_H &= \frac{b-1}{2b}\frac{2r_e d_H^2}{\pi V}\,\mathrm{Re}\left(F_0(\lambda_c)\right) \end{aligned} \tag{3.31}$$

---

[24] One has to keep in mind that the solution (3.23) is based on a monochromatic and therefore infinitely long incoming wave. This leads to phenomena such as the ‘standing’ wave displayed for $E_{\mathrm{ph}} = E_c + 72\,\mathrm{meV}$.

Equation (3.31) can be referred to as the modified Bragg condition as it is similar to the Bragg condition (3.1) with the difference of a small correction w_H. This correction implements the effect of refraction neglected in the Laue theory.

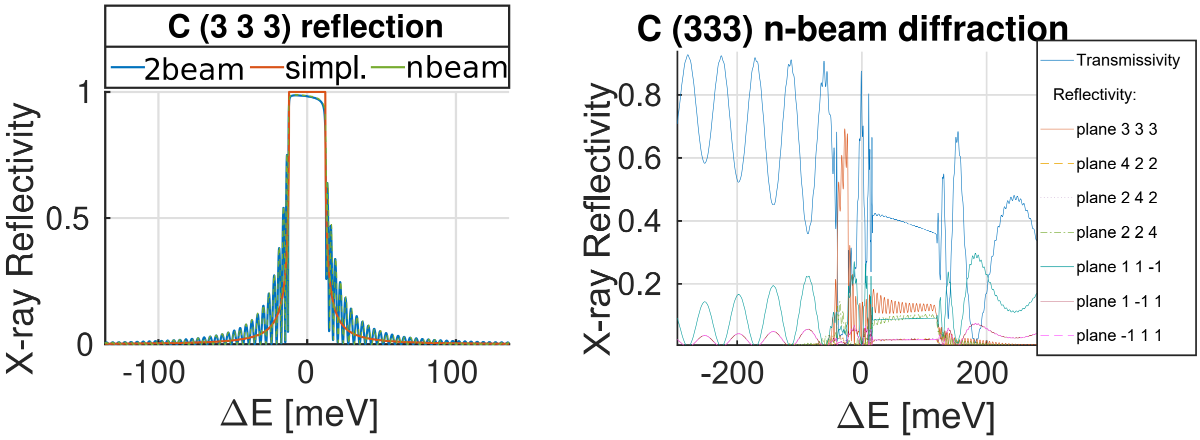

Figure 3.4: Spectral reflection of diamond in C(333) surface orientation close to normal incidence ($\Theta_{(333)} = \frac{\pi}{2} - 3.1\,\mathrm{mrad}$) (a) and exactly at normal incidence $\Theta_{(333)} = \frac{\pi}{2}$ (b). The solid blue curve in (a) displays the results for the *two-beam approximation* when only two beams are permitted. It is based on the 'full' calculation following Eqs. (3.20) to (3.25). The red curve is based on the simplification (3.29) for an infinitely thick crystal without absorption. Besides the difference in the peak reflectivity the full treatment exhibits oscillating side wings. The dashed green curve shows the general solution of (3.13) where any number of beam excitations are allowed. There is perfect agreement with the two-beam approximation, showing that latter is perfectly appropriate for slight detune from normal incidence. (b) shows the general solution of (3.13) for the case of exact normal incidence. The spectral reflectivity evidently is strongly disturbed with respect to the two beam case presented in (a).

In Figure (3.4(a)) the two beam case reflectivity for diamond close to backreflection ($\Theta_H = \pi/2 - 3.1\,\mathrm{mrad}$) and H =(3 3 3) has been plotted. The blue curve represents the full calculation based on equations Eqs. (3.22) to (3.25) for a $t_c = 150\,\mu\mathrm{m}$ thick crystal and the red curve the simplified formula (3.29). While the basic shape and the spectral width of the two curves roughly agree, there are some obvious abbreviations. For one, the maximum reflectivity in the full calculation is less then one due to the finit depth of the crystal and especially due to absorption. Second, the reflectivity curve is not symmetric due to the wavelength dependency of the susceptibility. And third, on the side wings the blue curve exhibits strong oscillations. These are created by the interference of the waves created at the entry and the exit surface. As in the region of maximum reflection only a small fraction of the wave actually reaches the exit surface (see Figure (3.3)), the effect cannot be seen there.
Finally, it has to be noted that following eq. (3.12) the refraction inside the crystal generally leads to small deviations from the reflective law stating the angle of reflection equals the angle of incidence for the wave outside the crystal. Instead the reflected wave vector in vacuum $\boldsymbol{k}_H = \boldsymbol{k} + \boldsymbol{G}_H + \Delta_H \boldsymbol{z}_{\mathrm{surf}}$ has to be corrected by a small factor $\Delta_H = k\left(\pm\sqrt{\gamma_H^2 - \alpha_H} - \gamma_H\right)$ [94, ch. 2.2.4]. Generally, $\boldsymbol{\Delta}_H$ is dependent on the photon energy, which leads to angular dispersion. For the specific case of symmetric reflection $\boldsymbol{G}_H \parallel \boldsymbol{z}_{\mathrm{surf}}$ used in this work, the factor Δ_H and therefore also the angular dispersion vanish.

3.1.3 n-beam diffraction

Principally, the excitation condition (3.11) can be fulfilled for multiple reciprocal lattice vectors at once. This case is especially frequent for cubic crystals such as diamond with a high degree of symmetry. Particularly, for cubic crystals multiple beam reflection always occurs at exact backscattering $\boldsymbol{k}_0 \parallel \boldsymbol{k}_H$ for reflection orders $H \neq (111)$. In these cases, the full set of equations (3.13) need to be solved for, commonly also incorporating polarization mixing and often also grazing emergence of some of the reflected beams. These beams are strongly correlated leading to a much more complicated picture.

In Figure (3.4(b)) the transmissivity and reflectivity has been plotted for all beams fulfilling the excitation condition at $E_c = 9.03\,\mathrm{keV}$, $\boldsymbol{z}_{\mathrm{surf}} \parallel (333)$ and normal incidence. Evidently, in comparison to Figure (3.4(a)), the participation of multiple beams in the diffraction process leads to a much more involved reflection pattern also for the individual reflections. Looking at the symmetric $H = (333)$ reflection, the peak reflectivity is reduced while the overall spectral width is increased. Also the point of maximum reflection has shifted. While it may principally be possible to operate an CBXFEL with these reflection patterns, it is unclear if this actually upholds under realistic non-idealized operation conditions. For one, such a reflection pattern actually has never been accurately measured. Second, in the n-beam case the reflection pattern is more strongly dependent on the actual strain in the crystal as will be shortly derived in the following section. Hence, it is advisable to operate the crystal mirrors slightly shifted by some millradiant from exact backscattering. Then, as visible in Figure (3.4(a)), the two-beam approximation is fully applicable. Generally, the amount of angular detune is dependent on the geometric setup, or rather how the crystal axis relate to the macroscopic angles. For the reflection geometry assumed for the CBXFEL demonstrator, this is discussed in Section **5.1** and the necessary angular detune to reach a case describable by the two-beam case is shown in Figure (5.3).

3.1.4 Diffraction in strained crystals

Up to now, idealized crystals were assumed. Generally, crystals will be subject to a strain field $\boldsymbol{\eta}(\boldsymbol{r})$ with the atomic spacing slightly varying with position. This strain might originate from temperature gradients in the crystal leading to position dependent thermal expansion, the elastic response (see [85]) or from mechanic tension.

One approach to solve the perturbed diffraction problem is based on solving the unstrained dynamic diffraction theory (3.13) for partitions of the crystal with approximately constant lattice spacing and amending the problem by continuous boundary conditions between the partitions. This approach is quite suitable for a crystal with only depth dependent strain, as then the partions can be made layer wise. This is analogous to diffraction in multilayer or superlattice crystal systems (see for example [97–101]). However, this approach becomes increasingly complicated when treating fully three dimensional strain fields and/or diffraction. A general theory, describing the propagation of X-rays in distorted crystals for an arbitrary incident wave was elaborated independently by Takagi [102] and Taupin [103]. According to the Takagi-Taupin theory in a crystal deformed by a displacement field $\boldsymbol{u}(\boldsymbol{r})$ the susceptibility becomes

$$\chi(\boldsymbol{r}) = \chi^{(p)}(\boldsymbol{r} - \boldsymbol{u}(\boldsymbol{r})), \tag{3.32}$$

where $\chi^{(p)}$ is the susceptibility of the perfect unstrained crystal. Then the solution to the fundamental differential equation (3.5) can be equally sought in the form of a Bloch-wave [104]:

$$\boldsymbol{D}(\boldsymbol{r}) = \sum_H \boldsymbol{D}_H(\boldsymbol{r}) \exp\left(i\boldsymbol{K}_H - \boldsymbol{G}_H\boldsymbol{u}(\boldsymbol{r})\right). \tag{3.33}$$

This includes two modifications compared to the expansion in the unstrained crystal. The first is that the amplitudes $\boldsymbol{D}_H(\boldsymbol{r})$ have becomes slowly varying functions of the position. The second is that the constituent waves are not plane but have a spatially varying wave vector $\boldsymbol{K}'_H = \boldsymbol{\nabla}\left[\boldsymbol{K}_H\boldsymbol{r} - \boldsymbol{G}_H\boldsymbol{u}(\boldsymbol{r})\right] = \boldsymbol{K}_H - \nabla\left[\boldsymbol{G}_H\boldsymbol{u}(\boldsymbol{r})\right]$. Inserting (3.32) and (3.33) into the constituting equation (3.5) and neglecting higher order derivatives of $\boldsymbol{D}_H(\boldsymbol{r})$ and $\boldsymbol{G}_H\boldsymbol{u}(\boldsymbol{r})$, as they are slowly varying compared to $\boldsymbol{K}_H\boldsymbol{r}$, one arrives at [104, 105]

$$2i(\nabla_H)\boldsymbol{D}_H + \left[\frac{\left(\boldsymbol{K_H} - \nabla\left[\boldsymbol{G}_H\boldsymbol{u}(\boldsymbol{r})\right]\right)^2}{k} - k\left(1+\chi_0\right)\right]\boldsymbol{D}_H = k\sum_{H'\neq H}\chi_{H'-H}\boldsymbol{D}_{H'}, \tag{3.34}$$

where ∇_H is the derivative along direction $\boldsymbol{s}_H = \frac{\boldsymbol{K}_H}{|K_H|}$. Unlike the unstrained case (3.13) the choice of the in-material wavevector $\boldsymbol{K}_H$ is quite abitrary, as its deviations can be incoorperated into the spatially varying amplitude $\boldsymbol{D}_H(\boldsymbol{r})$. Anyhow, the choice of $\boldsymbol{K}_H$ needs to be incorporated into appropriate boundary conditions.

One can see that only the components of the displacement field $\boldsymbol{u}(\boldsymbol{r})$ parallel to the reciprocal lattice vector $\boldsymbol{G}_H$ enter into the differential equation (3.34). Also, solely the derivative of the displacement field appears and,therefore, only the strain field is relevant for the (internal) reflection[25]. This is to be expected as the diffraction should not change with respect to a constant shift $\boldsymbol{u}(\boldsymbol{r}) = \mathrm{const}$ of the crystal position. For the two beam case, the displacement field therefore basically becomes a scalar field. Also, a solution of equation (3.34) can be obtained by using an appropriate differentiation scheme on a two dimensional mesh spanned by the two fundamental directions $\boldsymbol{s}_0$ and $\boldsymbol{s}_H$ [104–106]. For the general n-beam case on the other hand a lot of different components of $\boldsymbol{u}(\boldsymbol{r})$ need to be taken into account, making the solution much more complicated. Also, the differentiation in (3.34) needs to be done along all directions $\boldsymbol{s}_H$ making it much more inefficient and numerically unstable.

For the specific case of symmetric reflection in diamond close to normal incidence, as is relevant for this work, the solution simplifies further under the prerequisite that the two beam case is applicable. Basically, the problem can then be approached by solving the constituting system (3.5) in its one dimensional depth dependent form for each point on the crystal surface. The solution of the one-dimensional differential equation (3.5) can either be conducted by solving

---

[25] It has to be noted that the actual displacement of the crystal surface has some importance for the reflection, as it introduces an optical path difference compared to the non-displaced crystal.

the one-dimensional Takagi-Taupin equation or by using the multilayer approach discussed at the beginning of this paragraph.

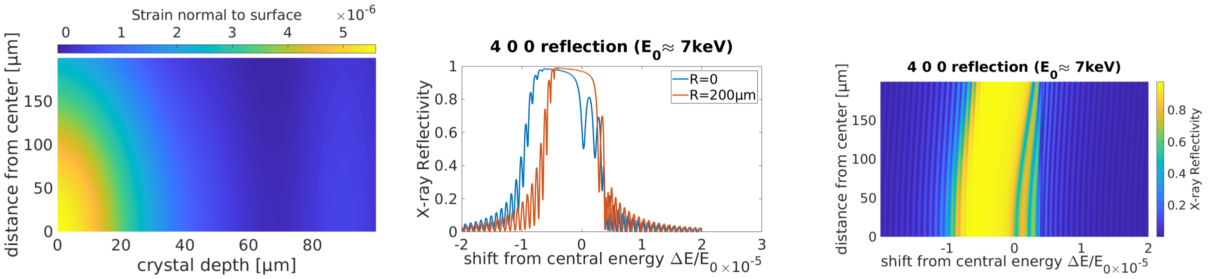

(a) Cylindrically symmetric scalar strain field for the strain component normal to the surface.

(b) Reflection curves of the strained crystal at the crystal center and at R =200μm away from the center.

(c) Scalar strain field for the strain component normal to the surface.

Figure 3.5: Example for symmetric dynamic diffraction close to normal incidence in a strained crystal. (a) shows an examplary strain field taken from [85]. (b) shows the spectral diffraction curves in the crystal center where the strain is maximum and at 200 μm off the center where the crystal is approximately undistorted. (c) shows the full spectral diffraction curves along the crystal surface. One can see both a shift of the center of reflection as well as a widening of the reflection with surface position.

Figure (3.5) displays the spectral dynamic diffraction for an exemplary displacement field shown in Figure (3.5(a)) computed by the multilayer matrix recursion approach derived by *Stepanov et al*[100]. Figure (3.5(b)) shows the spectral reflection curves for two points on the crystal surface. The red curves represents the reflection 200 μm away from the center of the crystal where the strain is comparably low. Here the reflection strongly resembles the one of an unstrained crystal as presented in Figure (3.4(a)). In the center of the crystal, the strain is maximal and the blue reflection curve is distorted with respect to the red one. The overall increased strain along the surface normal at this position is analogous to an increased lattice spacing. Following the modified Bragg condition (3.31), this leads to a shift of the entire reflection curve. Also, one can see a widening of the spectral reflection. This is due to the strain varying with depth in the crystal which leads to the reflection conditions varying with depth. Both effects can also be seen in Figure (3.5(c)) where the spectral reflection is plotted against the crystal surface position. It has to be noted that the presented case is assuming rather low values of strain, which only have a weak effect on the X-ray diffraction and particularly do not affect the maximum reflectivity.

3.2 Thermal Response of the Crystal

Regarding the millijoule scale X-ray pulses impinging on the diamond crystals at a megahertz repetition rate in the CBXFEL (see Chapter **5**), it is obvious that the thermal answer of the crystal is relevant for maintaining a stable operation. As was discussed in the beginning of this chapter, this thesis will focus on the thermal conduction subfraction of the crystal thermal answer. In this Section, first, the physics of cumulative lattice excitation – the phonons – will be scratched. Then their density of states, the connection to the speed of sound and following the lattice heat capacity will be reviewed. Finally, the process of thermal conduction will be examined. This includes the discussion of the very accurate but complicated *Peierls Phonon Boltzmann equation*[107] (PBE) describing both ballistic and diffusive processes. Finally, its relation to two diffusive approximations neglecting ballistic phonons will be highlighted: the *Cattaneo equation* and the well known and commonly applied *Fourier heat equation*.

3.2.1 Cumulative lattice excitations

In an insulator such as diamond the thermal properties and the thermal conduction is determined by the excitation of the crystal lattice, which are quantized in the form of so called *phonons*.
If one atom or molecule in the crystal lattice is removed from its equilibrium position, then the demand of minimizing the internal energy will exert a force on the neighboring atoms. This on the other hand will exert a force on their neighboring atoms, so that at last a shift of one atom will lead to an excitation of the entire lattice. This corresponds in a one dimensional picture to a chain of point masses each being connected by springs of different strengths.
The Hamiltionian of the system can be separated into

$$\mathcal{H} = \mathcal{H}_a + \mathcal{T}_{\text{nuc}},$$

where the latter is the kinetic energy of the nuclei and the prior can be identified as potential term. In the commonly used adiabatic approximation, $\mathcal{H}_a$ is considered as independent of $\mathcal{T}_{\text{nuc}}$, which makes it possible to compute it as function of the position of the nuclei [93, ch. 5.1]. The total energy of the system can, following above hamiltonian, be described as

$$E_{\text{tot}} = U_{\text{pot}} + \mathcal{T}_{\text{nuc}},$$

where U_{pot} is the cumulative potential energy of all atoms in the solid, which also initially incorporates the excess heat energy directly after absorption of a photon, as relevant for this work. In general U_{pot} is a function of the instantaneous position of all the atoms in the solid. One can approximate U_{pot} in a taylor expansion in the atoms' deflection $\boldsymbol{u}_i$ from the equilibrium position resulting in [108, 109]:

$$\begin{aligned}
U_{\text{pot}} &= U_0 + \sum_{\boldsymbol{R}}\sum_{i}\sum_{\alpha} \left.\frac{\partial U_{\text{pot}}}{\partial u^{\alpha}_{\boldsymbol{R}i}}\right|_0 u^{\alpha}_{\boldsymbol{R}i} + \sum_{\boldsymbol{R},\boldsymbol{R}'}\sum_{i,j}\sum_{\alpha,\beta} \left.\frac{\partial^2 U_{\text{pot}}}{\partial u^{\alpha}_{\boldsymbol{R}i}\partial u^{\beta}_{\boldsymbol{R}'j}}\right|_0 u^{\alpha}_{\boldsymbol{R}i}u^{\beta}_{\boldsymbol{R}'j} \\
&\quad + \sum_{\boldsymbol{R},\boldsymbol{R}',\boldsymbol{R}''}\sum_{i,j,k}\sum_{\alpha,\beta,\gamma} \left.\frac{\partial^3 U_{\text{pot}}}{\partial u^{\alpha}_{\boldsymbol{R}i}\partial u^{\beta}_{\boldsymbol{R}'j}\partial u^{\gamma}_{\boldsymbol{R}''k}}\right|_0 u^{\alpha}_{\boldsymbol{R}i}u^{\beta}_{\boldsymbol{R},j}u^{\gamma}_{\boldsymbol{R}'',k} + \dots, \\
&= U_0 + \sum_{\boldsymbol{R}}\sum_{i}\sum_{\alpha} \Pi^{\alpha}_{\boldsymbol{R}i}u^{\alpha}_{\boldsymbol{R}i} + \sum_{\boldsymbol{R},\boldsymbol{R}'}\sum_{i,j}\sum_{\alpha,\beta} \Phi^{\alpha\beta}_{\boldsymbol{R}i\boldsymbol{R}'j}u^{\alpha}_{\boldsymbol{R}i}u^{\beta}_{\boldsymbol{R}'j} \\
&\quad + \sum_{\boldsymbol{R},\boldsymbol{R}',\boldsymbol{R}''}\sum_{i,j,k}\sum_{\alpha,\beta,\gamma} \Psi^{\alpha\beta\gamma}_{\boldsymbol{R}i\boldsymbol{R}'j\boldsymbol{R}''k}u^{\alpha}_{\boldsymbol{R}i}u^{\beta}_{\boldsymbol{R}'j}u^{\gamma}_{\boldsymbol{R}''k} + \dots .
\end{aligned} \tag{3.35}$$

$\boldsymbol{R}$, $\boldsymbol{R}'$ and $\boldsymbol{R}''$ signify the position of the atoms, the indices i, j, k denote summation over atoms in the unit cell and α, β, γ over principal directions (for example $\hat{\boldsymbol{x}}, \hat{\boldsymbol{y}}, \hat{\boldsymbol{z}}$). $\Pi^{\alpha}_{\boldsymbol{R}i}$ is the negative of the net force acting on the atom i in direction α, being zero in equibilibrium, and $\Phi^{\alpha\beta}_{\boldsymbol{R}i\boldsymbol{R}'j}$ and $\Psi^{\alpha\beta\gamma}_{\boldsymbol{R}i\boldsymbol{R}'j\boldsymbol{R}''k}$ being the harmonic and cubic (anharmonic) force constants, respectively. These force constants can be computed starting from the lattice structure using either empirical potentials, *Density Functional Theory*(DFT) or *Density Functional Pertubation Theory*(DFPT) [108, 110]. In order to make computation feasible, a cutoff radius is used which defines the number of nearest neighbors which are taken into account in the computation. This cutoff radius is often found by numeric optimization. While empiric potentials have been successfully used for the harmonic force constants for a long time, DFT and DFPT have brought a great advance in computation of the anharmonic force constants in the recent years[108].

Commonly, the harmonic approximation is applied which takes into account only the harmonic force constants. In this approximation the force exerted on an atom i at position $\boldsymbol{R}$ after deflection $\boldsymbol{u}_{\boldsymbol{R}'j}$ of an atom j at position $\boldsymbol{R}'$ is

$$\boldsymbol{F}_{\boldsymbol{R}i} = -\boldsymbol{\Phi}_{\boldsymbol{R}i\boldsymbol{R}'j}\boldsymbol{u}_{\boldsymbol{R}'j}.$$

Here the directional harmonic force constant was cast into a second order tensor $\boldsymbol{\Phi}_{\boldsymbol{R}i\boldsymbol{R}'j}$. By making use of the translational symmetry of the crystal, which means that the force constants do only rely on the relational position of the atoms $\tilde{\boldsymbol{R}} = \boldsymbol{R} - \boldsymbol{R}'$ and not on the absolute position, the equation of motion can be written as [109]

$$M_i \ddot{\boldsymbol{u}}_{\boldsymbol{R}i} = -\sum_{\tilde{\boldsymbol{R}},j} \Phi_{ij}\left(\tilde{\boldsymbol{R}}\right)\boldsymbol{u}_{\boldsymbol{R}+\tilde{\boldsymbol{R}}'j} \tag{3.36}$$

By inserting the plane wave Ansatz

$$\boldsymbol{u}_{\boldsymbol{R}i}(t) = \boldsymbol{A}_i e^{-\imath[\omega t - \boldsymbol{q}\boldsymbol{R}]}$$

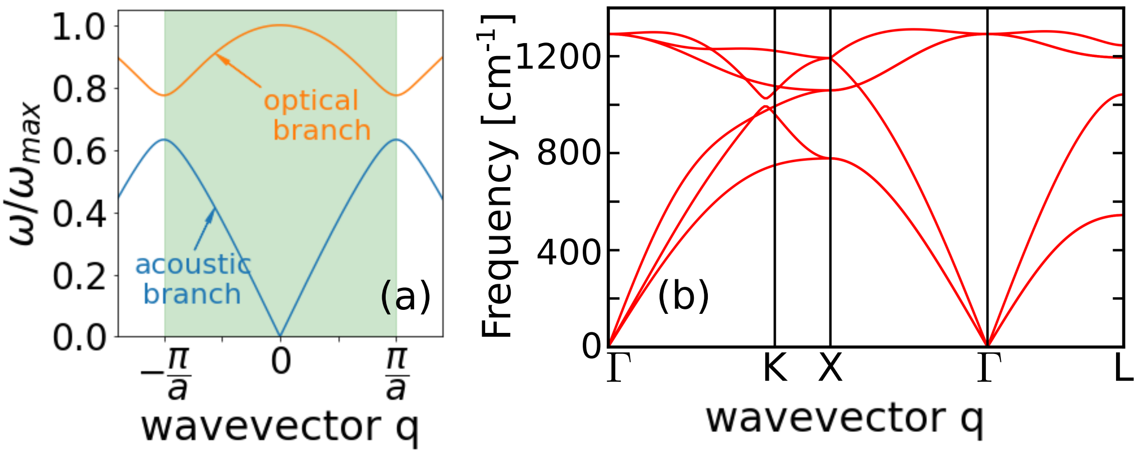

Figure 3.6: Dispersion relations in the simplified 1D, nearest neighbor approximation following (3.38) in (a) and realistic 3D dispersion relation of room temperature diamond calculated using the DFT-package *Exciting* [111] in (b). In (b) the paths $\overline{\Gamma K}$, $\overline{\Gamma X}$ and $\overline{\Gamma L}$ are the [1 0 0]-direction, the [1 1 0]-direction and the [1 1 1]-direction, respectively.

into the equation of motion (3.36) one arrives at the condition

$$\det\left[\sum_{\tilde{\boldsymbol{R}}} \boldsymbol{\Phi}\left(\tilde{\boldsymbol{R}}\right) e^{\imath \boldsymbol{q}\tilde{\boldsymbol{R}}} - \omega^2 \operatorname{diag}\left(\boldsymbol{M}\right) \otimes \mathbb{1}_d\right] = 0. \tag{3.37}$$

$\operatorname{diag}\left(\boldsymbol{M}\right)$ is a diagonal matrix with the size of the number of atoms in the unit cell, with every diagonal entry representing the mass of the specific atom. $\mathbb{1}_d$ is the unit matrix with the same dimension d as the deflection (usually three). $\otimes$ is the kronecker-product so that $\operatorname{diag}\left(\boldsymbol{M}\right) \otimes \mathbb{1}_d$ produces a matrix of the same dimensionality as $\boldsymbol{\Phi}$.

For getting a more comprehensive picture the specific case of a diamond fcc structure having a unit cell of two equal atoms of mass M will be examined. For simplification only one dimension[26] is considered and only nearest neighbor interaction is taken into account. This leads to

$$\omega^2 = \frac{C_1 + C_2}{M} \pm \frac{1}{M}\sqrt{(C_1^2 + C_2^2 + 2K_1K_2\cos\left(qa\right))}, \tag{3.38}$$

where a is the lattice constant. Upper equation is equal to a linear chain of atoms with two differing spring constants. $C_1 = \Phi_{12}(a - \tilde{R})$ describes the spring constant between the two atoms of the same unit cell and $C_2 = \Phi_{12}(\tilde{R})$ between the two atoms of the adjacent unit cells.

Both the general equation (3.37) and the simple equation (3.38) are dispersion relations connecting a frequency ω to a (quasi-)impulse $\boldsymbol{q}$. An exemplary dispersion relation following equation (3.38) is plotted in Figure (3.6(a)). One can clearly distinguish two branches, one with a steep slope labeled acoustic and one with higher higher frequencies but more shallow slope labeled optical. While the optical branch is important for the concept of the lattice density of states (see the following paragraph), it does contribute only little to the thermal conduction due to its

---

[26] The one dimensional approximation is surprisingly accurate due to the symmetries in the crystal [109].

generally small group velocity

$$v_{G,r}(\boldsymbol{q}) = \boldsymbol{\nabla}_{\boldsymbol{q}}\omega_r(\boldsymbol{q}), \tag{3.39}$$

where the subscript r refers to the dispersion branch.
In Figure (3.6(b)) a realistic three-dimensional dispersion relation of diamond at room temperature is plotted. It exhibits a dispersion relation with six individual branches. These correspond to two transversal and one longitudinal acoustic branches as well as two transversal and one longitudinal optical branches. It also shows a dependence on direction. This is not a contradiction to diamond being isotrop, as the displayed directions form a non-orthogonal basis.
Generally, each of the solutions $\omega(\boldsymbol{q})$ can be regarded as a quantum of vibration with impulse $\boldsymbol{q}$ and energy $\hbar\omega$, the so called phonons.

3.2.1.1 Phonons – the quanta of lattice vibration

When looking at the general dispersion relation (3.37), which is based on the harmonic approximation, one may note that it is similar to that of a harmonic oscillator. In analogy to the theory of electromagnetic fields, each of these decoupled harmonic oscillators is regarded as a quantum of the lattice vibration. These quanta are named *phonons* in analogy to *photons* and carry an energy $\omega_{\boldsymbol{q},r}$ and impulse $\boldsymbol{q}$, where r is the dispersion branch.
However, they have a peculiarity compared to classical particles which shaped the term quasiparticles. Due to the periodicity of the lattice with the lattice constant a, their impulse is only uniquely defined in the range $q^i \in \left(-\frac{\pi}{a^i}, \frac{\pi}{a^i}\right)$, that is inside the first *Brillouin-zone*. This is highlighted in Figure (3.6(a)) by the greenly shaded region. Outside this region, the dispersion relation repeats. This means that a phonon with momentum $\boldsymbol{q}$ is virtually identical to a phonon with impulse $\boldsymbol{q}+n\cdot\boldsymbol{G}$, where n is an arbitrary integer and $\boldsymbol{G}$ is the reziproke lattice vector. This is particularly important for scattering processes involving phonons. While these processes must fullfil the conservation of energy, the conservation of momentum is valid only up to a reciprocal lattice vector $\boldsymbol{G}$.
As phonons are bosons just like photons, their mean number in equilibrium at a temperature T is given by the *Bose-Einstein* distribution[93, 109]

$$n_{\mathrm{eq},(\boldsymbol{q},r)}(T) = \left[\exp\left(\frac{\hbar\omega_r(\boldsymbol{q})}{k_B T}\right) - 1\right]^{-1}. \tag{3.40}$$

The total (inner) energy of the lattice vibrations[27] is analogous to that of a sum over many independent quantum mechanical harmonic oscillators [93, ch. 6.1.3]:

$$U_{\mathrm{tot}} = U_0 + \sum_{r,\boldsymbol{q}} \left(n_{\mathrm{eq},(\boldsymbol{q},r)} + \frac{1}{2}\right)\hbar\omega_r(\boldsymbol{q}) \tag{3.41}$$

---

[27] In the case of an insulator, the total energy of lattice vibrations is approximately equal to the total energy of the system.

In the following, U_{tot} will be abreviated by U.

The number of modes $\boldsymbol{q}$ is dependent on the size of the crystal.The smallest spacing $\mathrm{d}q_i$ between to modes in direction i in momentum space is equal to $2\pi/N_i$, where N_i is the number of elementary cells in direction i. For a big crystal and $\lim\limits_{N\to\infty}$, a sum over the modes can be replaced by an integral over q:

$$\sum_\lambda f(\omega_r(\boldsymbol{q})) = \frac{V}{(2\pi)^3}\sum_r\int_{1.\text{BZ}} f(\omega_r(\boldsymbol{q}))\mathrm{d}^3q,$$

where $f(\omega_\lambda)$ is any integrable function dependent on the phonon frequency, r is the branch index, V is the crystal volume and $\frac{V}{(2\pi)^3}$ is the density of states in three dimensional momentum space. In frequency space this can be expressed as [93]

$$\sum_\lambda f(\omega_r(\boldsymbol{q})) = \int f(\omega)D(\omega)\mathrm{d}\omega \quad \text{with} \quad D(\omega) = \frac{V}{(2\pi)^3}\sum_r\int_{\omega=\text{const}}\frac{\mathrm{d}S_{\boldsymbol{q}}}{|\nabla_q\omega_r(\boldsymbol{q})|} \tag{3.42}$$

with $D(\omega_r(\boldsymbol{q}))$ being the density of states in frequency domain. The integrand $\mathrm{d}S_{(r,\boldsymbol{q})}$ is over the surface of constant frequency defined by the dispersion relation. It is apparent from equation (3.42) that the density is particularly high for regions of low group velocity.

3.2.2 heat capacity

The heat capacity of a solid is a measure for the rise of temperature ΔT caused by the inflow of heat. The volumetric heat capacity C_v (the heat capacity at constant volume[28]) is defined by

$$C_v = \left(\frac{\partial U}{\partial T}\right)_V = \sum_{r,\boldsymbol{q}}\left[\underbrace{\frac{\partial}{\partial T}\hbar\omega_r(\boldsymbol{q})n_{(r,\boldsymbol{q})}(T)}_{C_{V,\boldsymbol{q}r}}\right] = \frac{\partial}{\partial T}\left[\sum_r\int D(\omega)\frac{\hbar\omega}{\exp\left(^{\hbar\omega}/_{k_BT}\right)-1}\right] \tag{3.43}$$

with the mode resolved heat capacity $C_{V,\boldsymbol{q}r}$. Often the specific heat

$$c_V = \frac{C_V}{M} = \frac{C_V}{\rho V}, \tag{3.44}$$

is used instead, where M is the crystal mass, ρ is the crystal density and V is the crystal volume. The specific heat is independent of the crystal volume and therefore is a true material parameter. A common and rather accurate approximation to equation (3.43) is the so called *Debye-Model.* This model assumes for one that the dispersion relation is described by three branches of individual but constant group velocities $\omega_r = v_r|\boldsymbol{q}|$ with $r = (1,2,3)$. These velocities can be summed up to the mean speed of sound $\frac{3}{v_s} = \sum_r^3\frac{1}{v_r}$. The density of states then becomes $D(\omega) = \frac{3V}{2\pi^2}\frac{\omega^2}{v_S^3}$.

---

[28] Experimentally, often the heat capacity at constant pressure C_p is measured, which is $C_p = C_V + TV\alpha_V^2B$ with the heat expansion coefficient α_V and the Bulk modulus B[93].

Also, a maximum Debye-frequency $\omega_D = v_s \left(6\pi^2 \frac{N}{V}\right)^{\frac{1}{3}}$ is defined, which is just the frequency for which the linear dispersion relations after integration yields the phonon number N. One can express an equivalent Debye-temperature

$$\Theta_D = \frac{\hbar\omega_D}{k_B} = \frac{\hbar v_s}{k_B}\left(6\pi^2 \frac{N}{V}\right)^{\frac{1}{3}} \tag{3.45}$$

Then the volumetric heat capacity becomes[93]

$$\begin{aligned} C_V^D(T) =& 9Nk_B\left(\frac{T}{\Theta_D}\right)^3 \int_0^{\Theta_D/T} \frac{x^4 e^x}{(e^x-1)^2} \mathrm{d}x \\ C_V^D(\lim_{T\to\infty}) \approx& 3Nk_B \\ C_V^D(\lim_{T\to 0}) \approx& \frac{12\pi^4}{5} Nk_B \left(\frac{T}{\Theta_D}^3\right) \end{aligned} \tag{3.46}$$

The last two lines are analytic approximations in the high temperature and low temperature case. The high temperature approximation reproduces the limit of an ideal gas.

The Debye model is a good approximation for temperatures much smaller than the Debye temperature. This is due to the fact that at these comparably low temperatures predominantly low frequency states are populated, which roughly follow a linear dispersion relation as can be seen in Figure (3.6(a)).

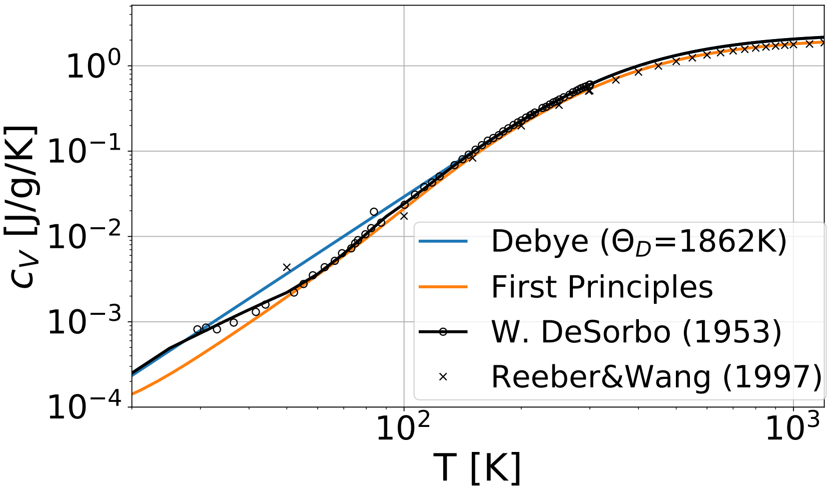

Figure 3.7: Log-log plot of the specific heat of diamond versus temperature calculated with the Debye-approximation (3.46) (blue curve), directly from first principles and the density of states referring to equation (3.43) using the program *almaBTE* [112] (orange curve). Also literature values are displayed from *W. DeSorbo* [113] (black circles + black line) and *Reeber and Wang* [114] (black crosses). The circles refer to actual low temperature caloric measurements by *W. DeSorbo* and the black line is a debye model fit with variable temperature dependent debye temperature $\Theta_D(T)$. The black crosses refer to interpolations by *Reeber and Wang* on various sets of measurements. For the later work the first principles data is used which fits the literature values quite accurately both for the low temperatures as well as the high temperatures.

For diamond, which has a very high Debye temperature of $\Theta_D = 1862\,\mathrm{K}$ [113], the Debye model is rather accurate as can be seen in comparison with literature values in Figure (3.7). In Figure (3.7) also values calculated using the more general equation (3.43) and the density of states from *first principles* are shown. The values were computed using the program *almaBTE* [112]. They match the literature values both in the low temperature as in the high temperature regime, except for a deviation at very low $T < 50\,\mathrm{K}$, for which the measurement by *W. DeSorbo* is debatable to begin with [115]. This data will later be used in the simulations for the heat capacity. Regarding both the Debye-approximation as well as the actual measurements by *DeSorbo et al* [113], it is evident that at low temperatures the heat capacity has a very steep gradient. For comparison, the specific heat at $T = 77\,\mathrm{K}$ is $c_V(77\,\mathrm{K}) = 0.0091\,\mathrm{J/(g\,K)}$ compared to $c_V(300\,\mathrm{K}) = 0.604\,\mathrm{J/(g\,K)}$ at room temperature, which are two orders of magnitude difference. Considering an instantaneous heat load Q_abs and integrating equation (3.43) yields

$$\begin{aligned} \int_0^{\Delta T} C_V\left(\delta T + T_0\right)\mathrm{d}(\delta T) &= Q_\mathrm{abs}, \qquad (3.47) \\ \rightarrow \Delta T \left(\lim_{Q_\mathrm{abs}\rightarrow 0}\right) &= {}^{Q_\mathrm{abs}}\!/_{C_V\,(T_0)}, \end{aligned}$$

where the last line is the linearized form which is only accurate for low heat loads or high temperatures with an almost constant C_V. Equation (3.47) shows in conjunction with above observation that for the same heat load the associated temperature jump will be much bigger at low temperatures than at high temperatures. Taking into account that the thermal conductivity (see below) is strongly non-linear in temperature, this obviously has a strong impact on the crystal thermal response.

3.2.3 Anharmonic Effects

Up to now, all the phonon related properties were entirely based on the harmonic term in the expansion of the inner energy (3.35). However, this harmonic expansion neglects some important effects such as the thermal expansion or the interaction between individual phonon modes. Latter is already apparent in the general dispersion relation (3.37) which describes fully decoupled harmonic oscillators. The disappearance of the thermal expansion follows from the point, that in an harmonic potential the excited vibration modes change with temperature – this means kinetic energy –, but the overall mean displacement, or lattice spacing, remains the same. In order to take into account these effects, the terms with order three and higher need to be integrated into the analysis. Adding the anharmonic force constants $\Psi^{\alpha\beta\gamma}_{\boldsymbol{R}i\boldsymbol{R}'j\boldsymbol{R}''k}$ to the analysis, one has to consider additionally quadratic terms in the equation of motion (3.36). These quadratic terms lead to a mixture of the individual solutions and therefore to an interaction between the phonon modes. The anharmonic force constants $\Psi^{\alpha\beta\gamma}_{\boldsymbol{R}i\boldsymbol{R}'j\boldsymbol{R}''k}$ therefore also induces the appearance of three phonon scattering processes, which are of high importance for the thermal conduction.

3.2.3.1 Thermal Expansion The linear expansion coefficient is a solid's change of length with change of temperature. It is defined as [93]

$$\alpha_L = \frac{1}{L}\frac{\partial L}{\partial T}\bigg|_{P=\mathrm{const}} = \frac{1}{3V}\frac{\partial V}{\partial T}\bigg|_{P=\mathrm{const}} = \frac{1}{3B}\frac{\partial P}{\partial T}\bigg|_{V=\mathrm{const}}, \tag{3.48}$$

where P is the pressure and $B = -V\dfrac{\partial P}{\partial V}$ is the bulk modulus. In above derivation it was assumed, that $\dfrac{\partial B}{\partial T} \approx 0$. The pressure P can be thermodynamically defined as derivation of the helmholtz free energy F against the volume at constant temperature

$$P = -\frac{\partial F}{\partial V}\bigg|_{T=\mathrm{const}}$$

Using $F = U - TS$ with the inner energy U, the entropy S and $T\dfrac{\partial S}{\partial V}\bigg|_{T=\mathrm{const}}$ this becomes

$$\begin{aligned} P &= -\frac{\partial}{\partial V}\left[U - T\int_0^T \frac{\partial U}{\partial T'}\frac{\mathrm{d}'T}{T'}\right] \\ &= -B\frac{\delta V}{V} - \frac{\partial}{\partial V}\sum_{\boldsymbol{q},r}\frac{1}{2}\hbar\omega_r(\boldsymbol{q}) - \sum_{\boldsymbol{q},r}\hbar\frac{\partial \omega_r(\boldsymbol{q})}{\partial V}\frac{1}{\exp\left(\dfrac{\hbar\omega_r(\boldsymbol{q})}{k_B T}\right) - 1}, \end{aligned}$$

where equation (3.41) was used for the right hand side. If upper equation is inserted into the definition of the linear expansion coefficient (3.48) and one additionally considers the mode resolved specific heat Eqs. (3.43) to (3.44), one arrives at [93]

$$\alpha_L = -\frac{1}{3B}\sum_{\boldsymbol{q}r}\underbrace{\left(-\frac{V}{\omega_r(\boldsymbol{q})}\frac{\partial \omega_r(\boldsymbol{q})}{\partial V}\right)}_{\gamma_{r,\boldsymbol{q}}} c_{V,\boldsymbol{q}r}, \tag{3.49}$$

where the mode dependent *Grüneisen*-parameter $\gamma_{\boldsymbol{q}r}$ was introduced. Additionally using the mean Grüneisen-parameter $\gamma = \dfrac{\sum_{\boldsymbol{q}r}\gamma_{\boldsymbol{q}r}c_{V,\boldsymbol{q}r}}{\sum_{\boldsymbol{q}r}c_{V,\boldsymbol{q}r}}$, the linear thermal expansion coefficient becomes

$$\alpha_L = \frac{\gamma c_V}{3B}. \tag{3.50}$$

In general non-isotropic systems, the linear expansion is direction dependent, so one has to append a direction dependent weighting factor – the projection of $\boldsymbol{q}$ on the direction of interest – to the mode summation.

At first sight of the definition (3.48) one might assume that the much increased temperature jump for the same heat load at low temperatures would also lead to an increased relative expansion

$$\eta_{\mathrm{th}}(\Delta T) = \frac{a(T_0 + \Delta T)}{a(T_0)} - 1 = \exp\left[\int_0^{\Delta T}\alpha_L(\delta T + T_0)\,\mathrm{d}(\delta T)\right] - 1. \tag{3.51}$$

However, assuming a constant Grüneisen-parameter γ as well as a constant bulk modulus B[29] and inserting both (3.50) and (3.47) into above equation yields

$$\eta_{\mathrm{th}}\left(Q_{\mathrm{abs}}\right) \approx \exp\left[\frac{\gamma}{3B}\int_0^{\Delta T} c_V\left(\delta T + T_0\right) \mathrm{d}(\delta T)\right] - 1 = \exp\left(\frac{\gamma}{3B} Q_{\mathrm{abs}}\right) - 1. \tag{3.52}$$

This shows that the actual quasi-static thermal expansion induced by X-ray absorption is mostly independent of the initial crystal temperature. Consequently, the increased thermal conduction at low temperatures (see below) is a strong argument for using cooled diamond crystals.

3.2.4 Thermal conduction

Thermal conductivity describes the dissipation of a systems internal energy to equilibrium due to random collisions and the diffusion of the heat carrying particles. The rate of this dissipation scales with the difference in internal energy – the pertubation of equibilibrium – and varies with temperature. *Jean Baptiste Joseph baron Fourier* established an empirical relationship between the heat flow $\boldsymbol{J}$ and the temperature gradient $\boldsymbol{\nabla} T$ in a material stating

> the heat flux resulting from thermal conduction is negatively proportional to the magnitude of the temperature gradient and opposite to it in sign
>
> **J. B. J. Fourier (1822)**

. This can be mathematically defined as *Fourier's law of heat conduction*

$$\boldsymbol{J} = -\,\boldsymbol{\kappa}\boldsymbol{\nabla} T. \tag{3.53}$$

$\boldsymbol{\kappa}$ is the material dependent thermal conductivity, which is a symmetric second order tensor in general, but reduces to a scalar value for isotropic systems such as diamond.
This can be combined with the equation of energy conservation

$$\begin{aligned} \frac{\partial U}{\partial t} &+ \boldsymbol{\nabla}\boldsymbol{J} = \dot{Q}_{gen} \\ \overset{V=\text{const}}{\Leftrightarrow} \quad C_v \frac{\partial T}{\partial t} &+ \boldsymbol{\nabla}\boldsymbol{J} = \dot{Q}_{gen}, \end{aligned} \tag{3.54}$$

where U is the internal energy, $\dot{Q}_{gen}$ is an additional heat generation source and C_v is the volumetric heat capacity of the material (3.43). For the second line, the approximation of constant crystal volume was used. Differentiating equation (3.53) in space and inserting it into equation (3.54) leads to the famous heat equation:

$$\rho c_V \frac{\partial T}{\partial t} = \boldsymbol{\nabla}\left(\boldsymbol{\kappa}\boldsymbol{\nabla} T\right) + \dot{Q}_{gen} \tag{3.55}$$

---

[29] While this is certainly not correct, both parameters are only very weakly dependent on the temperature.

As stated, the upper equation was found empirically. To understand thermal conduction on a microscopic level, Peierls extended Boltzmann's equation for the dynamics of gases to describe the transport of interacting phonons under assumption of anharmonic terms in the crystal potential (see equation (3.35)) [107]. This equation, the *Phonon* or *Peierls Boltzmann Equation* (PBE) shall be described in the following, being a very accurate model for thermal transport in insulating solids. Afterwards, it shall be derived how this relates to the classically used diffusion equations such as Fourier's heat law (3.53) and the related heat equation.

3.2.4.1 The Phonon Boltzmann Equation (PBE): In general, the Boltzmann Transport Equation describes the distribution density of (quasi-)particles in the interplay of driving external fields and relaxation by scattering processes. For the case of phonons in the presence of a time dependent heat source $\dot{Q}(\boldsymbol{x}, t)$ this can be written as [116]

$$\frac{\partial n_\lambda(t,\boldsymbol{x})}{\partial t} = \left.\frac{\partial n_\lambda(t,\boldsymbol{x})}{\partial t}\right|_{\text{coll.}} - \boldsymbol{v}_\lambda \cdot \boldsymbol{\nabla} n_\lambda(t,\boldsymbol{x}) + \dot{Q}_\lambda(\boldsymbol{x},t), \tag{3.56}$$

where n_λ is the phonon distribution of the phonon mode $\lambda = (\boldsymbol{q}, r)$ with r being the dispersion branch, $\boldsymbol{v}_\lambda$ is the modes group velocity and $\dot{Q}_\lambda$ is the generation rate of phonons of mode λ. The collision term $\left.{}^{\partial n_\lambda}\!/\!_{\partial t}\right|_{\text{coll.}}$ is driving the phonon distribution back into its equilibrium form $n_{\text{eq},\lambda}(T_{\text{eq}}) = \left[\exp\left({}^{\hbar\omega_\lambda}\!/\!_{k_B T_{\text{eq}}}\right) - 1\right]^{-1}$ with the equilibrium temperature T_{eq} (see equation (3.40)). As the temperature is an equilibrium concept, it is not defined for a system not in equilibrium as denoted in (3.56). However, due to the temperature being a common concept in thermal conduction processes, often a local quasi temperature T_{loc} is defined in terms of a hypothetic equilibrium distribution with the same local energy density[117, 118]

$$\begin{aligned} \sum_\lambda \hbar\omega_\lambda n_\lambda(t,\boldsymbol{x}) &= \sum_\lambda \hbar\omega_\lambda n_{\text{eq},\lambda}\left[T_{\text{loc}}(t,\boldsymbol{x})\right] \\ \leftrightarrow \int \hbar\omega n(t,\boldsymbol{x},\omega) D(\omega) \mathrm{d}\omega &= \int \hbar\omega n_{\text{eq}}\left[\omega, T_{\text{loc}}(t,\boldsymbol{x})\right] D(\omega)\mathrm{d}\omega, \end{aligned} \tag{3.57}$$

where the sum is over all possible phonon modes λ and for the last line equation (3.42) with the density of states $D(\omega)$ was used.

To solve equation (3.56), one needs to know the phonon dispersion relation, as can be for example measured by neutron scattering, by photon based Raman and Brillouin scattering for spectral points near the Brillouin-zone [93, 109, 119] or by inelastic X-ray scattering. It is known for most basic materials. Besides, it can be properly derived from well benchmarked first principle calculations [108, 112, 120] (For diamond see for example *Ward et al.* [121]). The group velocity (3.39) can then be calculated as derivative of the dispersion relation. The hardest part for solving (3.56) is to evaluate the collision term $\left.{}^{\partial n_\lambda}\!/\!_{\partial t}\right|_{\text{coll.}}$. The term is very peculiar for the actual collision mechanism. For insulators, the dominant ones are intrinsic phonon-phonon scattering, spontaneous decay important at very low temperatures $T \rightarrow 0$ and, dependent on the geometrical dimensions or material granularity, external boundary scattering [108, 119]. Usually, three-phonon and two-phonon-isotope scattering events are regarded as particularly important for bulk materials [108, 120, 122]. Then, the collision operator for the bulk of the system can be denoted as [117, 122][30]:

$$
\begin{aligned}
&\frac{4N}{\pi\hbar}\left.\frac{\partial n_\lambda}{\partial t}\right|_{\text{coll.}} = \qquad (3.58)\\
&\sum_{\lambda',\lambda''}^{+}\left[\left(n_\lambda+1\right)\left(n_{\lambda'}+1\right)n_{\lambda''}-n_\lambda n_{\lambda'}\left(n_{\lambda''}+1\right)\right]\frac{\left|\mathcal{V}^{3-\mathrm{ph},+}_{\lambda+\lambda'\leftrightarrow\lambda''}\right|^2}{\omega_\lambda\omega_{\lambda'}\omega_{\lambda''}}\delta(\omega_\lambda+\omega_{\lambda'}-\omega_{\lambda''})\\
&+\frac{1}{2}\sum_{\lambda',\lambda''}^{-}\left[\left(n_\lambda+1\right)n_{\lambda'}n_{\lambda''}-n_\lambda\left(n_{\lambda'}+1\right)\left(n_{\lambda''}+1\right)\right]\frac{\left|\mathcal{V}^{3-\mathrm{ph},-}_{\lambda\leftrightarrow\lambda'+\lambda''}\right|^2}{\omega_\lambda\omega_{\lambda'}\omega_{\lambda''}}\delta(\omega_\lambda-\omega_{\lambda'}-\omega_{\lambda''})\\
&+\frac{2}{\hbar}\sum_{\lambda'}\left[\left(n_\lambda+1\right)n_{\lambda'}-n_\lambda\left(n_{\lambda'}+1\right)\right]\omega_\lambda^2\mathcal{V}^{\mathrm{iso}}_{\lambda\leftrightarrow\lambda'}\delta(\omega_\lambda-\omega_{\lambda'})
\end{aligned}
$$

where N is the total number of phonon modes and $\delta(x)$ desribes the Dirac delta distribution assuring conservation of energy for the individual scattering events (see below). The first summand on the right hand side comprises three-phonon absorption events where two phonons with λ and λ' with quasi-impulses ($\boldsymbol{k}$,$\boldsymbol{k}'$) and frequencies ($\omega_{\boldsymbol{k}p}$,$\omega_{\boldsymbol{k}'p'}$), respectively, collide under production of a new phonon λ'' with quasi-impuls $\boldsymbol{k}'' = \boldsymbol{k} + \boldsymbol{k}' \pm \boldsymbol{G}$ and frequency $\omega_{\boldsymbol{k}''p''} = \omega_{\boldsymbol{k}p} + \omega_{\boldsymbol{k}'p'}$. $\boldsymbol{G}$ is either 0 or a reciprocal lattice vector. In case of the former, the process is called *Normal* process which leads to a redistribution of phonon modes but does not limit the thermal conductivity. In case of the latter, one speaks about a *Umklapp* process which limits the thermal conductivity due to a change in overall direction [109, 119]. The second summand in (3.58) expresses the inverse process where one phonon λ decays into two phonons λ' and λ''. The transition probability matrices $\mathcal{V}^{3-\mathrm{ph},+}_{\lambda+\lambda'\leftrightarrow+\lambda''}$ and $\mathcal{V}^{3-\mathrm{ph},-}_{\lambda\leftrightarrow\lambda'+\lambda''}$ are complex functions which depend on the anharmonic force constants $\Psi^{\alpha\beta\gamma}_{ijk}$ (see equation (3.35)) as denoted in [108, 119, 120, 122, 123]. The third summand in equation (3.58) refers to isotope scattering with $\mathcal{V}^{\mathrm{iso}}_{\lambda\leftrightarrow\lambda'}$ being dependent on the actual isotope concentration and their mass deviation [119, 120, 122]. This term is the reason why the low temperature conductivity of high κ materials such as Diamond span a very wide range [121, 124, 125].

Assuming a small and stationary temperature gradient $\boldsymbol{\nabla}T$, one can expand the non-equilibrium phonon distribution n_λ to first order yielding $n_\lambda = n_{\mathrm{eq},\lambda} + g_\lambda$ with g_λ being a small linear deviation as may be expressed by $g_\lambda = -\boldsymbol{F}_\lambda\boldsymbol{\nabla}T\frac{\mathrm{d}n_{\mathrm{eq},\lambda}}{\mathrm{d}T}$. Assuming that ${\partial n_\lambda}/{\partial T} \approx {\partial n_{\mathrm{eq},\lambda}}/{\partial T}$ and $\mathcal{O}(\boldsymbol{F}_\lambda\boldsymbol{\nabla}T)^2 \approx 0$, equation (3.56) can be rewritten in the form [120, 122]:

$$
\boldsymbol{F}_\lambda = \tau^0_\lambda\left(\boldsymbol{v}_\lambda + \boldsymbol{\Delta}_\lambda\right). \tag{3.59}
$$

$\boldsymbol{F}_\lambda$ can be interpreted as the distance a phonon in mode λ in average travels until it scatters and thereby equilibrates the system. It consists of a part $\tau^0_\lambda\boldsymbol{v}_\lambda$, which only accounts for phonons

---

[30] At temperatures comparable to the Debye temperature also higher order scattering terms relating to higher order terms in the taylor expansion of the free energy (3.41) become important. Due to the high numerical demand for computing these scattering terms, they are rarely incorporated [108, 110]

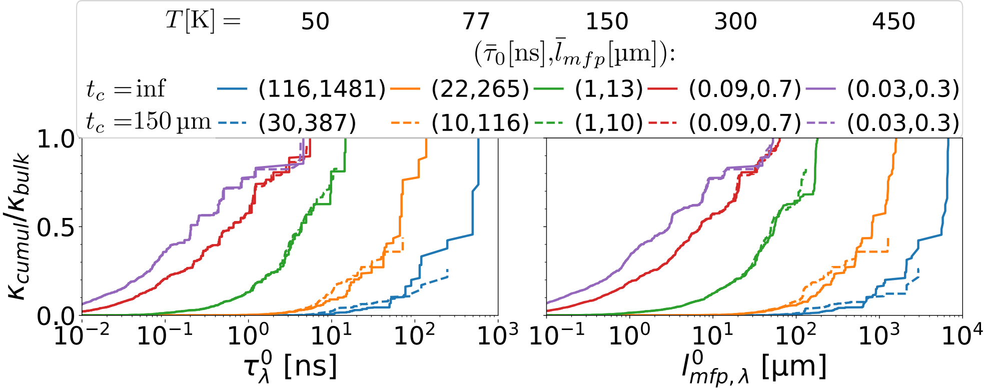

Figure 3.8: Temperature dependent, normed cumulative thermal conductivity of the different phonon modes in diamond in the [0,0,1]-direction ordered by their single mode relaxation time (left) and their single mode mean free path (right). The cases of a bulk diamond (solid curves) and a thin film of $t_c = 150\,\mu\text{m}$ thickness (dashed curves) are shown (see following paragraph and Section **4.3**).

staying in their respective mode λ, and a correction term $\tau^0_\lambda \boldsymbol{\Delta}_\lambda$ enumerating the redistribution of the phonons, which thereby changes the scattering probabilities. The term τ^0_λ denotes the single mode relaxation time (SMRT), which can be obtained from pertubation theory assuming that all modes other than λ are in thermal equilibrium ($\boldsymbol{F}_{\lambda'} = \boldsymbol{F}_{\lambda''} = 0$) [119, 122]:

$$\frac{1}{\tau^0_\lambda} = \frac{1}{N}\left(\sum_{\lambda'\lambda''}^{+}\Gamma^{3-\text{ph},+}_{\lambda+\lambda'\leftrightarrow\lambda''} + \frac{1}{2}\sum_{\lambda'\lambda''}^{-}\Gamma^{3-\text{ph},-}_{\lambda\leftrightarrow\lambda'+\lambda''} + \sum_{\lambda'}\Gamma^{\text{iso}}_{\lambda\leftrightarrow\lambda'}\right), \tag{3.60}$$

where the quantities $\Gamma^{3-\text{ph},\pm}_{\lambda\lambda'\lambda''}$ and $\Gamma^{\text{iso}}_{\lambda\leftrightarrow\lambda'}$ are the three-phonon absorption, emission and the two-phonon isotope scattering rates respectively [120]:

$$\begin{aligned}
\Gamma^{3-\text{ph},+}_{\lambda+\lambda'\leftrightarrow\lambda''} &= \frac{\hbar\pi}{4}\frac{n_{\text{eq},\lambda} - n_{\text{eq},\lambda'}}{\omega_\lambda\omega_{\lambda'}\omega_{\lambda''}}\left|\mathcal{V}^{3-\text{ph},+}_{\lambda+\lambda'\leftrightarrow\lambda'}\right|^2 \delta(\omega_\lambda + \omega_{\lambda'} - \omega_{\lambda''}) \\
\Gamma^{3-\text{ph},-}_{\lambda\leftrightarrow\lambda'+\lambda''} &= \frac{\hbar\pi}{4}\frac{n_{\text{eq},\lambda} + n_{\text{eq},\lambda'} + 1}{\omega_\lambda\omega_{\lambda'}\omega_{\lambda''}}\left|\mathcal{V}^{3-\text{ph},-}_{\lambda\leftrightarrow\lambda'+\lambda''}\right|^2 \delta(\omega_\lambda - \omega_{\lambda'} - \omega_{\lambda''}) \\
\Gamma^{\text{iso}}_{\lambda\leftrightarrow\lambda'} &= \frac{\pi}{2}\omega_{\lambda^2}\mathcal{V}^{\text{iso}}_{\lambda\leftrightarrow\lambda'}\delta(\omega_\lambda - \omega_{\lambda'})
\end{aligned} \tag{3.61}$$

A term strongly related to the relaxation time is the single mode mean free path $l^0_{\text{mfp},\lambda}$, which is the space a phonon of mode λ traverses until it scatters the first time:

$$l^{(0)}_{\text{mfp},\lambda} = |\boldsymbol{v}_\lambda|\,\tau^0_\lambda \tag{3.62}$$

Both the single mode relaxation time τ^0_λ and the single mode mean free path $l^0_{\text{mfp},\lambda}$ are strongly varying by orders of magnitude with the actual mode λ and with the temperature T, due to the change in phonon mode density n_λ. For example, for diamond the single mode relaxation time ranges from single picoseconds to hundreds of nanoseconds as presented in Figure (3.8). The relaxation time and mean free path spectrum at low temperatures are, however, heavily impeded by the finite size of the crystals, as used for diamond monochromators.

The second term $\boldsymbol{\Delta}_\lambda$ in equation (3.59) evaluates to

$$\begin{aligned}\boldsymbol{\Delta}_\lambda = \frac{1}{N}\Bigg[&\sum_{\lambda'\lambda''}^{+}\Gamma^{3-\text{ph},+}_{\lambda+\lambda'\leftrightarrow\lambda''}\left(\frac{\omega_{\lambda'}}{\omega_\lambda}\boldsymbol{F}_{\lambda'}-\frac{\omega_{\lambda''}}{\omega_\lambda}\boldsymbol{F}_{\lambda''}\right)\\ &+\frac{1}{2}\sum^{-}_{\lambda'\lambda''}\Gamma^{3-\text{ph},-}_{\lambda\leftrightarrow\lambda'+\lambda''}\left(\frac{\omega_{\lambda'}}{\omega_\lambda}\boldsymbol{F}_{\lambda'}+\frac{\omega_{\lambda''}}{\omega_\lambda}\boldsymbol{F}_{\lambda''}\right)+\sum_{\lambda'}\Gamma^{\text{iso}}_{\lambda\leftrightarrow\lambda'}\boldsymbol{F}_{\lambda'}\Bigg]\,.\end{aligned} \tag{3.63}$$

It describes the deviation from the SMRT due to the correlation between the off-equilibrium phonon mode deviations $\text{corr}(\boldsymbol{F}_\lambda, \boldsymbol{F}_{\lambda'}) \neq 0$. Regarding three-phonon processes, the SMRT τ^0_λ basically regards both Normal and Umklapp scattering processes as resistive, as both eliminate a specific phonon of mode λ and therefore limit its lifetime. This is nonphysical, as in case of a Normal process only the energy gets redistributed while the momentum remains unchanged, which is not limiting the heat transfer [108, 119, 120]. On the other hand the term $\boldsymbol{\Delta}_\lambda$ treats this difference as both elimination, recreation and redistribution are accounted for. In this sense the SMRT approximation becomes quite accurate when the fraction of Umklapp processes is strong like it is the case for Si and Ge for example [126]. On the other hand for stiff materials like diamond with a high relevance of normal processes, the SMRT becomes quite erroneous already at intermediate temperatures and the full non-equilibrium equation (3.59) needs to be solved[31] [121].

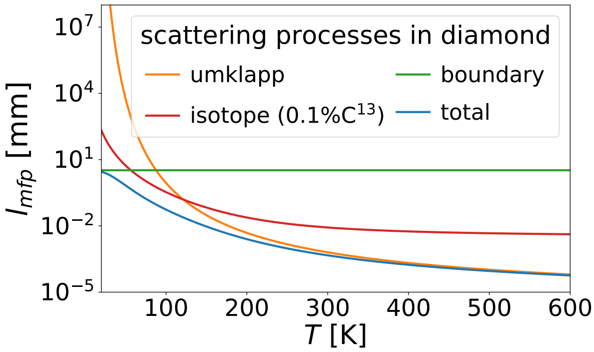

Figure 3.9: The graph displays the temperature evolution of the three scattering contributions of *Umklapp*-scattering, *isotope*-scattering and *boundary*-scattering as well as the combined mean free path. The data was derived from experimental measurements of *Wei et al.* [124] on pure, isotopically enriched diamond and their fit based on the *Callaway-model* [127]. The Callaway-model is an approximation based on the Debye-model, which takes into account the redistribution of the phonon modes by normal processes.

Figure (3.9) shows an exemplary temperature evolution of the mean free path of the three scattering contributions of *Umklapp*-scattering, *isotope*-scattering and *boundary*-scattering as well as the combined mean free path in pure, isotopically enriched diamond. The data, derived from measurements by *Wei et al.* and their fit based on the *Callaway-model* [127] approximately takes into account the redistribution of the phonon models by normal processes. One can nicely see the temperature dependence of the individual scattering channels. At high temperatures the Umklapp scattering events dominate, which are roughly proportional to the phonon density $n_{\text{eq}(T,\omega)}$ and therefore strongly increase with temperature. Correspondingly, the mean free path approximately decreases inversely to T at high temperatures [128, ch. 6.4.3]. At intermediate

---

[31] Stiffness usually relates to a very steep slope of the density of states – also relating to a high speed of sound. This also means that the population of phonon modes close to the Brillouin edge, which are driving the Umklapp processes, rises rather slowly with temperature. This on the other hand means a high fraction of Normal processes.

temperatures in a pure sample with low defect concentration and comparably low probability of Umklapp scattering events[32], isotope scattering becomes increasingly important, as it only involves two phonons, which additionally do not need to be close to the Brillouin edge. At even lower temperatures the temperature independent boundary scattering becomes dominating, which signifies the onset of the *Casimir regime* [119]. This will be discussed a little bit below.

As the thermal conductivity κ apparent in Fourier's law (3.53) classically is a common parameter to assess the thermal conduction in materials, it is meaningful how the Phonon Boltzmann equation (see Eqs. (3.56) to (3.63)) relates to this quantity. First, the heat flux $\boldsymbol{J}$ can be noted as the directional flux of phonons of mode λ with the probability distribution n_λ and energy $\hbar\omega_\lambda$ summed over λs [120]:

$$\boldsymbol{J} = \frac{1}{V}\sum_\lambda \hbar\omega_\lambda \boldsymbol{v}_\lambda n_\lambda, \tag{3.64}$$

Furthermore, by using $n_\lambda \approx n_{\text{eq},\lambda} - \frac{\hbar\omega_\lambda}{k_B T^2}\boldsymbol{F}_\lambda n_{\text{eq},\lambda}\left(n_{\text{eq},\lambda}+1\right)\boldsymbol{\nabla} T$ and noting that the equilibrium distribution $n_{\text{eq},\lambda}$ does not contribute to any energy flow $\boldsymbol{J}$, one can derive by comparison with Eq. (3.53) for the thermal conductivity tensor [120]:

$$\boldsymbol{\kappa} = \frac{1}{V k_B T^2}\sum_\lambda n_{\text{eq},\lambda}\left(n_{\text{eq},\lambda}+1\right)\left(\hbar\omega_\lambda\right)^2 \boldsymbol{v}_\lambda \boldsymbol{F}_\lambda^{\mathrm{T}}. \tag{3.65}$$

Evidently, the equations Eqs. (3.56) to (3.65) compose a lot unknown parameters. Generally, in order to solve equations (3.58), (3.63) or the simple *Single Mode Relaxation Time* (3.60) one needs to know the full phonon mode spectrum as well as the mode resolved transition probability matrices $\mathcal{V}^{3-\mathrm{ph},\pm}$ and $\mathcal{V}^{\mathrm{iso}}$. Nonetheless, over the last decade there has been a tremendous advance in so called first principle calculations. Starting from the lattice structure they derive the harmonic and anharmonic force constants by using either empiric potentials or *Density Functional Theory* and *Density Functional Perturbation Theory*. With these one can evaluate the non-equilibrium phonon densities and at last the (mode-resolved) thermal conductivity (3.65). The predicted $\kappa^{\mathrm{sim.}}$ ofen agree with the experimentally derived $\kappa^{\mathrm{exp.}}$ within the range of measurement uncertainty over a wide temperature range [108, 110][33]. There exist a multitude of available programs to do these first principle calculation such as *ShenBTE*[120], *AlmaBTE*[112] and *Phono3Py*[129] to name some. These programs may be especially useful for the study of exotic materials which are difficult to examine experimentally. But also for well researched materials such as silicon [122, 123, 130] or diamond[121] they have the big advantage to provide the full phonon mode resolved parameters which are nearly impossible to measure completely. In this

---

[32] Umklapp scattering is most probable for phonons close to the Brillouin edge. For stiff materials such as diamond with a high phonon group velocity these states correspond to high ω and are therefore only little populated at low temperatures.

[33] This accuracy decreases for very low temperatures as well as for high temperatures close to the Debye temperature. The first is due to the increasing importance of defect and isotope scattering which is very dependent on the individual sample quality. The second is due to the increasing importance of higher order force constants.

work the first-principle program *almaBTE* is used for the thermal conductivity of diamond (see Section **4.3**).

3.2.4.2 The relation of the PBE to the diffusive laws: The heat equation (3.55) in the stationary and the transient case are still the common model to study thermal transport in experiment and simulation. This is due to multiple reasons. First is the high amount of experience treating these models. Second is that a full solution of the PBE can evidently be very demanding or even infeasible for many 'real' problems. Third is that for experimental measurements the multitude of free parameters in the PBE make a concise physical interpretation of the experiment very difficult. Consequently it is important to understand how the PBE (3.56) and the classic Fourier's heat equation (3.53) are interconnected and when the Fourier's heat law might become erroneous.

For bulk systems and in stationary transport (meaning $\left.\frac{\partial n_\lambda(t,\boldsymbol{x})}{\partial t}\right|_{\text{coll.}} = \boldsymbol{v}_\lambda \cdot \boldsymbol{\nabla} n_\lambda(t,\boldsymbol{x})$) it can be readily seen from equations Eqs. (3.64) to (3.65) that Fourier's law and the BTE are perfectly compatible[34]. The applicability of Fourier's law is basically limited by three factors. The first two relate to the quotient of the mean free paths (3.62) to a characteristic length L_{ch} of the system, which may be expressed by the *Knudsen number*

$$\mathrm{Kn}_\lambda = {}^{l_{\text{mfp},\lambda}}/_{L_{ch}}. \tag{3.66}$$

The third relates to the quotient of the relaxation time (3.60) to a characteristic time τ_c in transient problems, which may be expressed by a characteristic nonedimensional time

$$\eta_C = {}^{\tau_\lambda}/_{\tau_C}. \tag{3.67}$$

In the following these different factors shall be discussed. The phonon mode parameter λ will be dropped for convenience.

Finite size of the crystal: The first limitation is related to the finite size of the system under consideration. Generally by doing a hilbert type expansion of the linearized BTE in the Knudsen number, one can show that Fourier's law can be applied unconditionally at zeroth order in the Knudsen number. This agrees well with the applicability of diffusive equation in the bulk limit $Kn \ll 1$. For higher orders of Kn, the solution needs to be corrected by appropriate kinetic boundary layers and conditions to account for ballistic thermal transport[131]. This becomes increasingly difficult with increasing order of Kn and is therefore only applicable for Knudsen numbers scaling up to $Kn < 0.1$[131].

For Knudsen numbers $Kn \tilde{>} 0.1$ there are basically two possibilities. The first is to solve the (reduced) BTE (3.56) or (3.59) by amending the suitable boundary conditions. As this is nu-

---

[34] One has to see that this primarily refers to the heat flow $\boldsymbol{J}$. As the PBE does not request (quasi-)thermal equilibrium, it cannot easily be cast into the *heat equation* (3.55), which relies on the definition of a temperature.

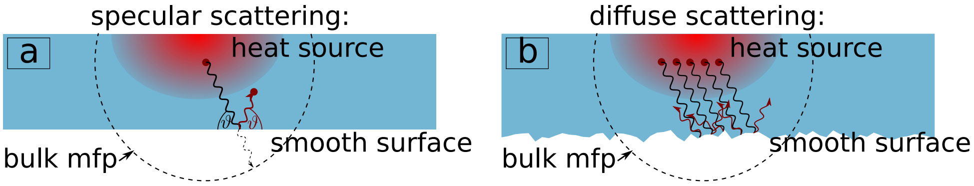

Figure 3.10: A sketch of specular (a) and diffuse (b) phonon boundary scattering in thin crystals, where the mean free path of the phonons is on the same order as the crystal thickness. The black splines represent phonons originating at the red spots in the bulk of the crystal, and the red splines the reflected phonons. In case of specular reflection (a) at a smooth surface the well known relation of photon reflection holds that the angle of incidence equals the angle of reflection. As this does not change the net lateral momentum of the phonon, it does not impede on the in-plane heat conduction. For the case of diffuse scattering (b) where the surface is apparently rough for the phonon of the specific wavevector q, the phonons get 'approximately' reflected isotropically into the entire semi-sphere. As this is changing the net lateral momentum, it does lower the in-plane heat conduction. The actual rate of the diffusional and specular reflection is both dependent on the surface roughness and the specific phonon mode wavevector.

merically very difficult [131–133], analytic derivations are often conducted which rely on heavy simplifications like one-dimensional transport [134–139].

The other often applied method for implementing the influence of boundaries is denoting them as sources of scattering and, thereby, implementing them into the scattering operator by [120, 122]

$$\left.\frac{\partial n_\lambda}{\partial t}\right|_{\text{coll.}}^{\text{(eff.)}} = \left.\frac{\partial n_\lambda}{\partial t}\right|_{\text{coll.}}^{\text{(bulk)}} + \left.\frac{\partial n_\lambda}{\partial t}\right|_{\text{coll.}}^{\text{(boundary)}} , \tag{3.68}$$

where $\left.\frac{\partial n_\lambda}{\partial t}\right|_{\text{coll.}}^{\text{(bulk)}}$ has the form as shown in Eq. (3.58) or the simplified Eq. (3.63). Using this approach the boundary scattering can be directly implemented into the common thermal conductivity tensor $\boldsymbol{\kappa}_{\text{eff.}}$ by Eq. (3.65). There are many different ways to calculate or estimate the $\left.\frac{\partial n_\lambda}{\partial t}\right|_{\text{coll.}}^{\text{(boundaries)}}$ [135, 140–148] which are normally implemented using the *Single Mode Relaxation Time* (SPRT) approximation. Both approaches rely on the assumption that the boundaries do not influence the intrinsic force constants or phonon density of states which are therefore assumed to be equal to the bulk values. This can break down when the system size becomes comparable to the wavelength of the participating phonons. For silicon this assumption is certified for sample dimensions spanning more than sixteen unit cells [149]. Principally, there are many different kinds of boundary conditions from fully thermalizing – assuming perfect heat resevoirs – to adiabatic boundary conditions where the heat and the phonons are confined in the sample. For the CBXFEL case, the latter is especially important, as the crystals, which reflect the X-rays, mostly have only contact to vacuum. Also, on the short pulse-to-pulse period, radiative emission from the boundaries can be considered negligible. When considering adiabatic boundaries on the BTE level, one has to differ between two important boundary phonon scattering mechanisms. These processes are sketched in Figure (3.10) and strongly relate to the reflection of photons. The first is (elastic) specular reflection. In this case, the transverse mo-

mentum of the phonons is preserved. Therefore, the mean free path of the phonons projected to in-plane coordinates and the corresponding fraction of thermal transport do not change. The other process is (elastic) diffuse scattering. In this case, the phonon is scattered isotropically into the full semi-sphere. As this obviously changes the direction of heat flow it poses a finite thermal resistance. As in radiation transport, the fraction p of specular reflection is dependent on the roughness of the boundary and generally wavelength dependent[149].
It has to be noted that while the treatment of boundaries via a reduced thermal conductivity yields the correct heat flux, it does not provide full insight into the actual phonon density and the related temperature distribution[136].

Size of heat source: The second factor is the finite size L_Q of the heat source or the curvature of the gradient $\boldsymbol{\nabla} T$. Fourier's law is based on the diffusive assumption. That means that collisions happen everywhere at every moment from which concludes that heat carriers react to the perturbation of the equilibrium in their direct vicinity. This is apparent in the heat flux at position $\boldsymbol{x}'$ being proportional to the local temperature gradient at position x. On the other hand in the BTE the heat carriers statistically scatter after traversing a distance $l_{\mathrm{mfp},\lambda}$. They therefore see the perturbation of equilibrium at the position $\boldsymbol{x}' + l_{\mathrm{mfp},\lambda}\hat{\boldsymbol{v}}_\lambda$. This averages out for heat sources of size $L_Q \gg l_{\mathrm{mfp}}$ or temperature gradients $\|(\boldsymbol{\nabla} T)_{\boldsymbol{x}'}\| \approx \|(\boldsymbol{\nabla} T)_{\boldsymbol{x}'+l_{\mathrm{mfp}}\hat{\boldsymbol{v}}}\|$, which makes Fourier's law fully applicable. For $L_Q \tilde{>} 0.1 * l_{\mathrm{mfp}}$ or heat gradients varying on a scale $\|(\boldsymbol{\nabla} T)_{\boldsymbol{x}'}\| \neq \|(\boldsymbol{\nabla} T)_{\boldsymbol{x}'+10 l_{\mathrm{mfp}}\hat{\boldsymbol{v}}}\|$ modification become apparent due to non-local heat transfer. An analytic derivation of the linear BTE shows that both the heat source term and the temperature gradient need to be convoluted by exponential decay functions with a decay length on the order of the mean free path [116]. Recently it has been analytically shown, that for multidimensional $D \geq 2$ thermal conduction this difference is not only apparent in the actual temperature distribution but also in the effective heat flux [150]. This leads to a heat source size dependent effective thermal conduction if evaluated by Fourier's law, which has also been proofed in experiment [116, 151–153]. This is actually used in thermal grating experiments, where the characteristic size of the source is systematically varied, to evaluate the mean free path spectrum of the phonon modes in a sample [142, 154–156].

Characteristic time duration: For a bulk system, one can derive a diffusive law from the Phonon Boltzmann equation (3.56) also in the transient case using some (partially strong) assumptions. The first two are to use the linearized Phonon Boltzmann equation in the *Single*

Mode Relaxation Time approximation, which means

$$\begin{aligned}
\left.\frac{\partial n_\lambda}{\delta t}\right|_{\text{scatter}} &= -\frac{n_\lambda - n_{\text{eq.},\lambda}}{\tau_\lambda^0}, \\
\boldsymbol{v}_\lambda \boldsymbol{\nabla} n_\lambda &= \boldsymbol{v}_\lambda \frac{\partial n_{\text{eq},\lambda}}{\partial T} \boldsymbol{\nabla} T \\
\boldsymbol{F}_\lambda &= \tau_\lambda^0 \boldsymbol{v}_\lambda \\
\text{and} \qquad \boldsymbol{\kappa} &= \frac{1}{k_B T} \sum_\lambda n_{\text{eq},\lambda} \left(n_{\text{eq},\lambda} + 1\right) \left(\hbar\omega_\lambda\right)^2 \boldsymbol{v}_\lambda \boldsymbol{v}_\lambda^T \tau_\lambda^0
\end{aligned}$$

Inserted into the transient PBE and multiplied by $\hbar\omega_\lambda \boldsymbol{v}_\lambda$, this leads to

$$\tau_\lambda^0 \frac{\partial\left(\hbar\omega_\lambda n_\lambda\right)}{\partial t} + \hbar\omega_\lambda \boldsymbol{v}_\lambda \left(n_\lambda - n_{\text{eq.},\lambda}\right) - \frac{1}{k_B T} n_{\text{eq.},\lambda}\left(n_{\text{eq.},\lambda} + 1\right)\left(\hbar\omega_\lambda\right)^2 \boldsymbol{v}_\lambda \boldsymbol{v}_\lambda^T \tau_\lambda^0 \boldsymbol{\nabla} T = 0$$

Summing this equation over all phonon modes λ and making the strong assumption of the *gray approximation*, which is that all phonon modes have the same mean relaxation time $\tau_\lambda^0 = \bar{\tau}$, one can derive under comparison with (3.64):

$$\bar{\tau} \frac{\partial \boldsymbol{J}}{\partial t} + \boldsymbol{J} - \boldsymbol{\kappa} \boldsymbol{\nabla} T = 0 \tag{3.69}$$

Here again the fact was used, that the equilibrium distribution $n_{\text{eq.},\lambda}$ does not contribute to any heat flux. The value of $\bar{\tau}$ is strongly decreasing with the temperature due to the increasing phonon density and, therefore, increased rate of 3-phonon scattering events. As presented in Figure (3.8), in diamond $\bar{\tau}$ ranges from picoseconds to more than 100 nanoseconds. However, the mean relaxation time is heavily decreased when accounting for the finite size of the diamond crystal, as also displayed in Figure (3.8). Equation (3.69) interestingly matches the *Maxwell-Cattaneo-Vernotte*-equation[157–159]. The additional time derivative in (3.69) compared to Fourier's law (3.53) was introduced in order to compensate for the infinite speed of propagation of information in Fourier type conduction [160]. Latter can be seen from the fact that in the heat equation (3.55) a sudden change of temperature would instantly give rise to a thermal answer everywhere in the crystal. Combined with the energy conservation relation (3.54) and assuming linear conduction equation (3.69) leads to the *hyperbolic heat equation*(HHE) [160]

$$\frac{\partial^2 T}{\partial t^2} + \frac{1}{\bar{\tau}} \frac{\partial T}{\partial t} = \frac{1}{\left(\bar{\tau} C_v\right)} \boldsymbol{\nabla}\left(\boldsymbol{\kappa} \boldsymbol{\nabla} T\right). \tag{3.70}$$

Equation (3.70) is a hyperbolic wave equation, where waves of temperature are transmitted with the finite speed $\frac{\kappa}{\bar{\tau} C_v}$.

While it is generally agreed upon that such a finite propagation speed is physically correct and therefore lacking in the traditional heat equation (3.55), the HHE is rarely used in real applications [160]. This is for one for its specific form being not entirely undisputed, as can also be seen from the partially strong assumptions in above derivation. Another point is that effects following from the HHE, such as the phenomena of *second sound*, have only been measured in few materials at very low temperatures $T < 15\,\mathrm{K}$[160, 161]. This is due to the fact that for most cases the mean relaxation time $\bar{\tau}$ is very small. For most practical situations the characteristic time of interest τ_C is much bigger than $\bar{\tau}$. In these cases the second derivative in the HHE (3.70) goes to zero and the HHE reduces to the traditional heat equation (3.55). This is also the case for the thin diamond crystals and multiple of hundreds nanoseconds time spans between two subsequent X-ray pulses as relevant for the CBXFEL at the European XFEL.

To summarize, one can expect deviations from the diffusional *Fourier heat equation* both for the case of finite size geometry as for a finite size heat source. The actual treatment of these can become very difficult and they are usually handled assuming strong assumption or specially shaped sample geometries which provide simplified solutions. How these effects are treated in the scope of the CBXFEL demonstrator will be further discussed in the next Chapter about the computational framework in Subsection **5.2.3**.

While deviations also appear in the time-domain, they can be concluded to be of minor importance for the hundred nanoseconds characteristic time scale relevant for this work and will, consequentially, be neglected in the following.

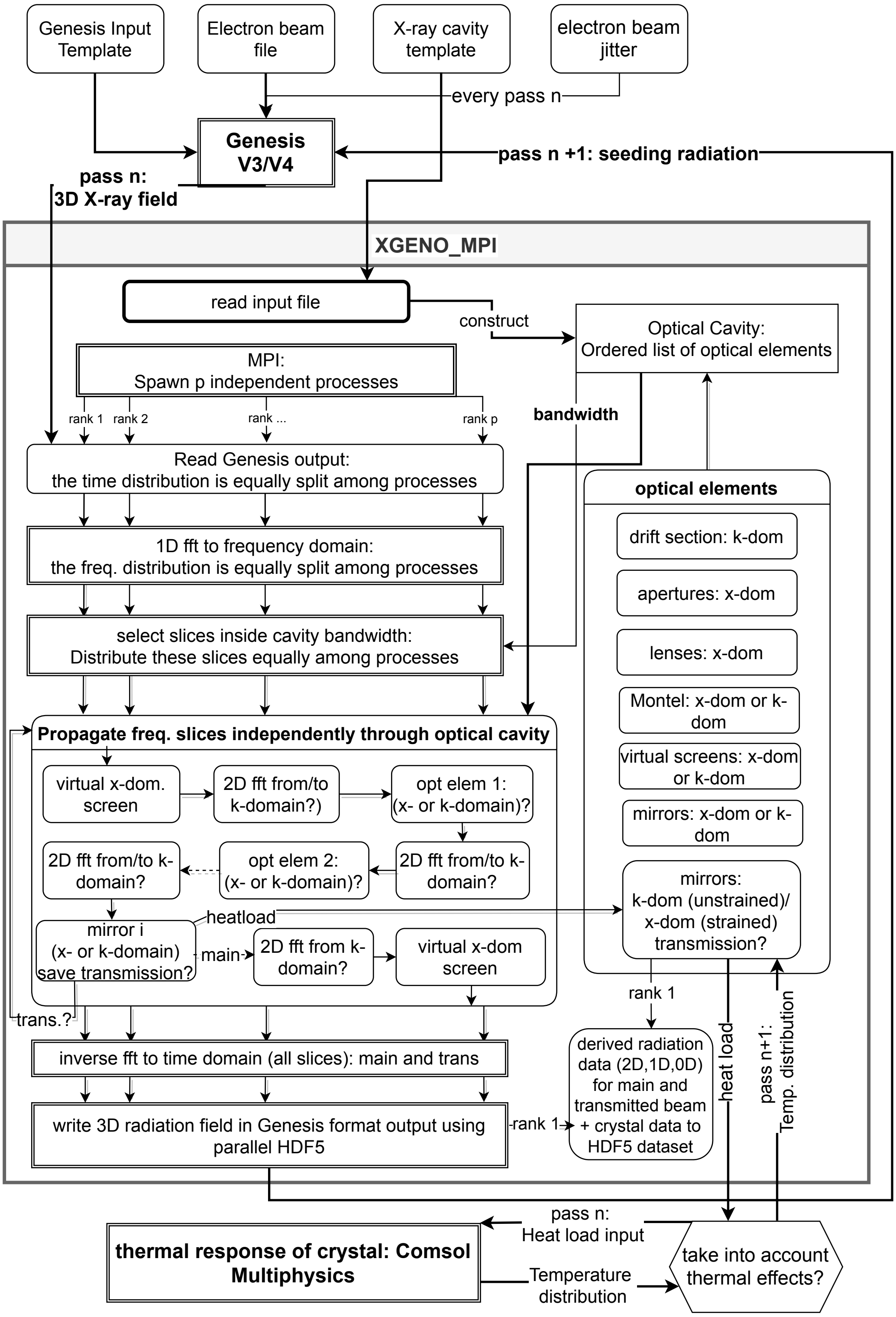

Figure 4.1: Sketch of the full program flow. The big central box sketches the *parallel X-ray Cavity Propagator* (pXCP) program. The double bordered rectangular boxes correspond to the parts using MPI collective communication and the rounded boxes to the *embarrassingly parallel* parts.

4 The Computational Framework

The program of simulation as it is being used in this work for simulating a CBXFEL is basically a mixture of three different subprograms which are intertwined to model a multi pass Cavity Based X-ray Free-Electron Laser. These subprograms - each devoted a subsection in the following - take care of

1. The X-Ray amplfification/FEL simulation subpart (see **4.1**)
2. The propagation of the X-Ray radiation including dynamic diffraction (see **4.2**)
3. The thermal response of the crystal (see **4.3**)

A sketch of the program structure is displayed in Figure (4.1). The fully coupled approach of FEL generation, FEL seeding, wavefront propagation and thermal response to the dynamic diffraction on a multipass basis is very unique to this thesis.

4.1 FEL Simulation

For the generation of the FEL radiation in a planar undulator the fourth version[35] of the well known and well benchmarked program *Genesis-1.3* [162–164] is used. The full radiation data is written out after each round trip and is then read in by the propagation routine (see next section). Afterwards the propagated radiation is reread by *Genesis-1.3* and used as seeding radiation.

A major difference in this work compared to the former, resembling thesis by *J. Zemella*[165] is that for the first passes before the circulating radiation is dominated by the seeded fraction - called the *startup*-regime in the following - a much finer lattice in the time domain is used (besides a much intensified treatment of the actual wavefront propagation and dynamic diffraction). This higher resolution is capable of accurately displaying the strongly fluctuating SASE fraction and the considerable synchrotron radiation background being of major importance in the startup-regime. This finer time resolution comes with a higher computational demand and especially a high data load on the order of ones to tens of GB which needs to be written out and read in at every round trip[36]. The time resolution is adaptively eased with increasing seeding depending on the change of the bandwidth as a smaller frequency bandwidth allows a coarser time resolution. For cases which proof to reach stable seeding, also an initially coarser resolution leads to the same results in saturation. Hence, for sufficiently checked cases the computation can be considerably sped up by coarsening the initial time resolution.

As has been sketched in Figure (2.10), for an intermediate gain FEL the optimum energy detune $\eta_{0,\mathrm{opt}}$ for maximum single pass gain is neither obtained from the simple relation $\eta_{0,\mathrm{opt}} \approx 0$ for saturated high gain FEL nor the weak gain relation $\eta_{0,\mathrm{opt}} \approx {}^{1.3}/_{2\pi N_U}$. Therefore, the optimal

---

[35] The 4th version never left the beta-phase and comes with some slight bugs. But for the cases of interest - meaning a short undulator section - both 2nd, 3rd and 4th version were compared and their output matched.

[36] A major advantage of the third to the second version of *Genesis-1.3* is the use of HDF5 [166] as base file format in the former. This eases and speeds up parallel in- and output tremendously, which is of major importance for this particular use case.

values need to be obtained numerically and case specifically.
For the case of the CBXFEL demonstrator experiment discussed in the follow-up Chapter **5** both the electron energy γ and the seeding wavelength λ_l are predefined by the euXFEL operation conditions and the Bragg reflection conditions, respectively. Therefore the detune η needs to be set by adjusting the (in the euXFEL case tunable) undulator parameter K. As a full multipass simulation is numerically quite expensive, the (in the euXFEL case) tunable undulator parameter K is set beforehand by an approximative pre step. This is done such that the gain is maximized for the first shot which originates from shot noise to ease the startup[37]. For this, the modified gain length $L_{G,3D} = L_{G0}(1 + \mathit{\Delta})$ is computed following the parametrization of *M. Xie* in equations Eqs. (2.74) to (2.76) in dependence of K. Based on the modified $L_{G,3D}$ the SASE initial value problem (2.73) is solved with the shot noise $\tilde{\jmath}_1(0) = \sqrt{\frac{eI_0\Delta\omega_{\text{Bragg}}}{\pi}\frac{1}{\mathcal{A}_{\text{tr}}}}$ being computed for the narrow spectral bandwidth $\Delta\omega = \Delta\omega_{Bragg}$ of the crystal reflection (3.30). The results are then optimized for maximum power by adjusting K.
Having obtained this K, a fine tuning step is done by doing a single *Genesis-1.3* run and shifting K such that the resulting (smoothed) radiation spectrum has a maximum at the reflection resonant frequency (3.31).

4.2 Propagation Using the Fourier-Optics Approach

In the *parallel X-ray Cavity Propagator*(pXCP) subprogram the X-ray radiation produced in the upstream undulator section and simulated by *Genesis-1.3* is read in and then propagated through an (X-ray) optical cavity.
The basic approach is to split the propagation through the optical cavity into free space propagation using the *angular spectrum method* and the action of a set of optical elements on the optical field. While it is possible to combine some optical elements into a single transfer function compatible with the angular spectrum method in the paraxial approximation using geometric optics [41, ch.4.2.7], which is even extendible to the longitudinal phase space [167], this will not be applied in this work. For one, such an approach is only available for objects describable by the ABCD matrixes of geometric optics [41, ch.2]. Second, the present code enables analysis of the propagated field along the cavity in order to allow for better understanding of the influence of the distinct optical elements and for later optimization of those.
It should be noted that the present code is, in principle, quite similar to the *Optical Propagation Code* (OPC) by *J.G. Karssenberg et al.*[168, 169], but optimized for the numerically very expensive CBXFEL case. As such it is written entirely in *C++* and makes heavy use of the *Message Passing Interface*(MPI) [170] for parallelization between distinct computing nodes in a *High Performance Computing*(HPC) cluster. The program layout is sketched in Figure (4.1).

---

[37] Actually, this does not provide the maximum pass to pass gain in the exponential growth regime, as then the problem shifts from the shot noise dominated SASE to a seeded FEL amplifier case. For specific cases in **5.2**, for example including electron energy jitter, the undulator parameter was (coarsely) optimized by doing simulations runs over a finite set of K values close to the approximative ideal K.

The basics shall be described later in this section. First the physical principles of the propagation approach, especially the angular spectrum method, shall be summarized. This will be followed by a short description of the optical elements implemented in the code.

4.2.1 Polychromatic propagation using the angular spectrum method

This subsection shall illuminate the physical requisites for the angular spectrum wave propagation approach. The interested reader is referred to the extensive literature on the topic (see for example [41, 171–174]).

Initially, the propagation of the principally polychromatic optical wave is divided into the propagation of many monochromatic wavelets by the means of Fourier transformation[171, ch.3.8, 172][38]

$$\begin{aligned} \tilde{\boldsymbol{E}}(\boldsymbol{r}, E_{\mathrm{ph}}) = & \int \boldsymbol{E}(\boldsymbol{r}, t) \exp\left(i^{E_{\mathrm{ph}}t}/_{\hbar}\right) \mathrm{d}t \\ \boldsymbol{E}(\boldsymbol{r}, t) = & \tfrac{1}{2\pi} \int \tilde{\boldsymbol{E}}(\boldsymbol{r}, E_{\mathrm{ph}}) \exp\left(-i^{E_{\mathrm{ph}}t}/_{\hbar}\right) \mathrm{d}E_{\mathrm{ph}}. \end{aligned} \tag{4.1}$$

A condition for this is that the optical cavity can be described as a time invariant linear system. Linearity means the property that a system response to an arbitrary input can be divided into the response to the decomposition of the input into elementary functions [171, ch.2.1]. A simple decomposition is to divide the input $g(t)$ into a linear combination of weighted and shifted delta-functions

$$g(t) = \int g(\tau)\delta(t-\tau)\mathrm{d}\tau,$$

where $g(\tau)$ can be considered the weight. If the linear response of the optical system now acts on this decomposition, which is described here by a mathematical operator $\mathcal{S}$, it can be brought into the integral yielding

$$\mathcal{S}\left[g(t)\right] = g_2(t) = \int g(\tau)h(t,\tau)\mathrm{d}\tau \quad \text{with} \quad h(t,\tau) = \mathcal{S}\left[\delta(t,\tau)\right]. \tag{4.2}$$

h is called the impulse response or in linear optics point-spreadfunction [171, ch.2.1].

This can be further simplified if the response is considered to be time invariant, which means that the response at time t to a unit input at time τ only depends on the time difference $t - \tau$. From this follows that the functional characteristics of the system do not change with time. Then equation (4.2) becomes a convolution of the input $g(\tau)$ with the impulse response $h(t-\tau)$, which can be expressed as the product of the respective fourier components in fourier space:

$$\begin{aligned} g_2(t) = & \int g(\tau)h(t-\tau)\mathrm{d}\tau \\ \leftrightarrow G_2(\omega) = & \; G(\omega)H(\omega) \end{aligned} \tag{4.3}$$

---

[38] To put it numerically more precise the *discrete Fourier transformation*(DFT)[175, ch.12] is used. For convenience this detail will be neglected here, but will be touched in Subsection **4.2.3**.

The latter is very convenient for the propagation through the X-ray optical cavity, as both free space propagation as well as reflection at the crystal mirrors are very natural to describe in frequency domain.

The question if the system at hand can be considered time invariant can be easily answered as yes for most considered optical elements, at least for the simplified description used here. Only the description of the crystal mirrors can in principal not be considered so, as (see Chapter **3**) the X-ray pulse influences the crystal response, so latter changes with time. Luckily, as was also eluded in the beginning of Chapter **3**, this functional change happens on a time scale larger than the pulse duration, so the time variance can be included in a discrete pulse-to-pulse manner.

The angular spectrum method used for free space propagation is based on the same foundation with the requisite to treat the propagation as space invariant linear system [171, ch.2.3.2]. This is valid for propagation through spatially homogenous media as is the case for free space propagation. Also it relies on the *scalar wave equation*, therefore neglecting the vectorial nature of the *Maxwell equations* [171, ch.3.2]. This scalar theory is accurate if two important assumptions are met. First, that the participating media is homogenous and isotropic leading to the response function being independent of the light wave's polarization. Second, that there are no transverse boundaries included which lead to a coupling of the different polarization components of the light field. The second is obviously not the case for apertures for example. Nonetheless, the introduced errors are negligibly small if the area affected by the boundaries is small compared to the extent of the area the wave is passing through. For apertures that results in the requisite that the extent of the aperture $\mathcal{A}_{\text{ap}}$ is big compared to the radiation wavelength $\mathcal{A}_{\text{ap}} \gg \lambda_l$[171, ch.3.2] Also, the error introduced by the scalar theory become big in the close vicinity of the boundaries, so the results become accurate a distance $z \gg \lambda_l$ away from the aperture [171, ch.3.10.2]. These requisits are easily met for X-ray pulses with wavelengths in the angstrom range.

The first requisite of independence of the polarization component also is met for most optical media integrated in the program. Again, the crystal mirrors are an exception, as they are generally polarization dependent (see equations (3.13) and (3.20)). For the special case treated here the angle of incidence on the mirrors is close to 90° where the reflection becomes polarization independent. For all other cases it would be possible to split the electromagnetic wave into two separate waves of individual polarization and treat them in the framework of scalar theory everywhere except at the mirrors. This would obviously double the computational cost and is therefore not done here. Also, as the FEL radiation of a planar undulator is linear polarized and also only couples to this specific polarization, it is principally sufficient to only propagate this one component and "throw" away the other. For the transmitted radiation on the other hand it would be necessary to use both components[39].

In the framework of the (monochromatic) scalar wave theory, the wave propagation can be de-

---

[39] The use of the polarization dependence of the transmission was proposed as an outcoupling mechanism in Section **2.4**

scribed by the *Helmholtz equation*

$$\left(\nabla^2 + k^2\right) \tilde{E}\left(\boldsymbol{x}_\perp, z, E_{\text{ph}}\right) = 0, \tag{4.4}$$

where $k = {}^{E_{\text{ph}}}/_{\hbar c}$ is the wave number and $\boldsymbol{x}_\perp = (x, y)$.
Inserting the angular decomposition expressed by the two dimensional fourier transformation

$$\tilde{E}\left(\boldsymbol{x}_\perp, z, E_{\text{ph}}\right) = \frac{1}{4\pi^2}\int\!\!\int A\left(\boldsymbol{k}_\perp, z, E_{\text{ph}}\right)\exp\left(-\mathrm{i}\boldsymbol{k}_\perp\boldsymbol{x}_\perp\right)\mathrm{d}\boldsymbol{k}_\perp \quad = \mathcal{F}_{\text{2D}}\left[\tilde{E}\right]\left(\boldsymbol{k}_\perp\right), \tag{4.5a}$$

$$\text{with} \quad A\left(\boldsymbol{k}_\perp, z, E_{\text{ph}}\right) = \int\!\!\int \tilde{E}\left(\boldsymbol{x}_\perp, z, E_{\text{ph}}\right)\exp(\mathrm{i}\boldsymbol{k}_\perp\boldsymbol{x}_\perp)\mathrm{d}\boldsymbol{x}_\perp \quad = \tilde{\mathcal{F}}_{\text{2D}}^{-1}\left[A\right]\left(\boldsymbol{x}_\perp\right), \tag{4.5b}$$

with $\boldsymbol{k}_\perp = (k_x, k_y)$, into the Helmholtz equation (4.4) leads to the solution [171, ch.3.10.2]

$$A\left(\boldsymbol{k}_\perp, z, E_{\text{ph}}\right) = A\left(\boldsymbol{k}_\perp, 0, E_{\text{ph}}\right)\exp\left(\mathrm{i}\sqrt{k^2 - \boldsymbol{k}_\perp^2}z\right) \tag{4.6}$$

to the free space propagation by a distance z for the individual angular components.
The free space propagation of the monochromatic field component $\tilde{E}$ by a distance z is therefore equivalent to propagating the individual angular components of the Fourier transformation $\mathcal{F}_{\text{2D}}$ and then applying the inverse Fourier transformation $\tilde{\mathcal{F}}_{\text{2D}}^{-1}$ [173, ch.6.2, 171, ch.3.10.2][40]:

$$\tilde{E}\left(\boldsymbol{x}_\perp, z, E_{\text{ph}}\right) = \tilde{\mathcal{F}}_{\text{2D}}^{-1}\left[\mathcal{F}_{\text{2D}}\left[\tilde{E}\left(\boldsymbol{x}_\perp^{'}, 0, E_{\text{ph}}\right)\right]\exp\left(\mathrm{i}\sqrt{k^2 - \boldsymbol{k}_\perp^2}z\right)\right]. \tag{4.7}$$

A physical analogue to above description is that the initial field is initially decomposed into an infinite number of plane wave components with continuously varying directions and differing amplitudes. These are propagating along perfectly straight paths given by their wave vector. This is evident from their free space propagation being completely described by the multiplication of a phase factor in equation (4.6). At each point z the full radiation field is given by the interference of these plane wave components, described by the inverse Fourier transformation [171, ch.3.10.1].
This angular spectrum method in conjunction with the high numerical efficiency of computational Fourier transformation (see Subsection **4.2.3**) is especially useful for the propagation of radiation fields of finite angular extent σ_Θ as it is the case for FEL (and undulator) radiation.

4.2.2 List of optical elements

While the free space propagation is most efficient in the angular (k-)domain, the response of some other optical elements is better treated in the spatial (x-)domain. In the following a short list of optical elements treated in the program to date[41] is given, which also specifies in which

---

[40] In ref. [171] an additional factor $\circ\left({}^{|\boldsymbol{k}_\perp|}/_{k}\right)$ is introduced, which accounts for the cutoff of plane wave components with wavevectors of higher magnitude than the original, which can occur in the vicinity of boundaries. These are rapidly attenuated with regard to equation (4.6) and can therefore be neglected for propagation distances $z \gg \lambda_l$. This actually is the mathematical formulation to the argument made in the discussion of the scalar theory.

[41] The code is written such that other elements can easily be added.

domain the element is treated.

4.2.2.1 Free Space Propagation (k-domain): As eluded above, the free space propagation by a distance $z \gg \lambda_l$ can be computed in k-domain by multiplication with a phase factor

$$A\left(\boldsymbol{k}_\perp, z, E_{\text{ph}}\right) = A\left(\boldsymbol{k}_\perp, 0, E_{\text{ph}}\right) \exp\left(\mathrm{i}\left(\sqrt{k^2 - \boldsymbol{k}_\perp^2} - k\right) z\right). \tag{4.8}$$

In above equation the rapidly oscillating term $\mathrm{i}kz$ has been subtracted. In the program the design optical path is generally treated such that the cavity length perfectly matches the repetition rate of the electrons (see Paragraph **4.2.2.8**). As in the full polychromatic propagation the wavelength/frequency dependent term $\mathrm{i}kz$ translates into a translation in time domain following the Fourier transformation's shift theorem, this term would violate the above convention.

4.2.2.2 Aperture(s) (x-domain): The integration of apertures of different form are very straight forward in x-domain. It amounts to setting the radiation field 0 to all the elements outside an area defined by an aperture function $f_{ap}(x, y, p)$:

$$\tilde{E}\left(\boldsymbol{x}_\perp, z_+, E_{\text{ph}}\right) = \tilde{E}\left(\boldsymbol{x}_\perp, z_-, E_{\text{ph}}\right) f_{ap}(x, y, p) \tag{4.9}$$

where p refers to a set of parameters necessary to describe the aperture.
The most relevant apertures are the rectangular aperture

$$f_{rect}(x, y, x_0, y_0, w_x, w_y) = \text{rect}\left(\frac{x - x_0}{w_x}\right) \text{rect}\left(\frac{y - y_0}{w_y}\right) \tag{4.10}$$

$$\text{with} \quad \text{rect}(x) = \begin{cases} 1 & |x| < 1 \\ 0.5 & |x| = 1 \\ 0 & \text{otherwise} \end{cases}, \tag{4.11}$$

the circular aperture

$$f_{circ}(x, y, x_0, y_0, w_c) = \begin{cases} 1 & \sqrt{(x - x_0)^2 + (y - y_0)^2}/w_c \leq 1 \\ 0 & \text{otherwise} \end{cases}, \tag{4.12}$$

and the stripe

$$f_{stripe}(x, y, c, \Theta, l) = \text{rect}\left(\frac{-x \sin\Theta + y \cos\Theta - c}{l}\right), \tag{4.13}$$

where Θ refers to the orientation of the stripe with respect to the x-axis.
These aperture functions also exist as inverse routines defined as

$$f_{ap}^{(\text{inv})} = 1 - f_{ap}. \tag{4.14}$$

4.2.2.3 (Thin) Lense (x-domain): Lenses are currently only implemented in the simplified thin lense approximation in the framework of paraxial optics. Latter means that only portions of the lense close to the optical axis are considered, which is equivalent to expressing [171, ch.4.2.3]

$$\frac{|k_x|}{k} \ll 1 \quad \text{and} \quad \frac{|k_y|}{k} \ll 1, \tag{4.15}$$

which is easily fulfilled for the well collimated FEL radiation. In this approximation the focussing/defocussing is computed by multiplication of the light field in the x-domain by a quadratic phase factor [171, ch.5.1]

$$\tilde{E}\left(\boldsymbol{x}_\perp, z_+, E_{\text{ph}}\right) = \tilde{E}\left(\boldsymbol{x}_\perp, z_-, E_{\text{ph}}\right) \exp\left(-i\frac{k}{2f}\boldsymbol{x}_\perp^2\right), \tag{4.16}$$

where $z_\pm$ refer to the position before (-) and behind (+) the lense. f is the focal length of the lense which has a positive value for a concave focussing and a negative value for a convex defocussing lense.

The quadratic phase factor introduced by the thin lense can be numerically quite bothersome, as will be shortly discussed in Subsection **4.2.3**.

4.2.2.4 (Curved) Mirror (x-domain): As the propagation framework relies on the definition of a design optical path, a perfect planar mirror does not introduce any change on the radiation field. This changes if the mirror is assumed to have a curvature and/or to be subject to shape or alignment errors.

In the prior case the curvature is simply taken into account by an equivalent thin lense [52, ch.1.8], which limits the treatment to parabolic curvatures. Then the focal length is equal to half the mirror curvature R.

There currently are two types of mirror errors included. First, a **tilt** error which shifts the propagation axis with respect to the design axis by a two dimensional angle $\Delta\boldsymbol{\Theta} = (\Delta\Theta_x, \Delta\Theta_y)$ (see below).

The second error implemented for the X-ray mirror is the figure or slope error with respect to the design shape[42]. This is implemented in the sense that an height error $\Delta h(x_p, y_p)$ at a position $\boldsymbol{x}_p = (x_p, y_p)$ introduces an optical path difference and therefore a longitudinal phase shift $\Delta\Phi(x_,p, y_p)$ to the radiation field via [176, 177]

$$\begin{aligned} \tilde{E}_\omega\left(\boldsymbol{x}_\perp, z_+\right) = &\ \tilde{E}_\omega\left(\boldsymbol{x}_\perp, z_-\right) \exp\left(\mathrm{i}\Delta\Phi(\boldsymbol{x}_\perp)\right). \\ \text{with} \quad \Delta\Phi(\boldsymbol{x}_\perp) = &\ 2k\Delta h(\boldsymbol{x}_\perp)\sin\Theta, \end{aligned} \tag{4.17}$$

where k is the wave number and Θ is the angle of incidence. The surface error $\Delta h(\boldsymbol{x}_\perp)$ needs to be passed as a table to the subroutine. It can either be derived from actual measurement or

---

[42] It has to be noted that the atomic scale roughness is not accounted for, which is estimated to be small enough to have a negligible influence.

by numerically generated maps, for example using power spectral density distributions with estimated rms height errors [176] (also see **5.2.2.6**).

4.2.2.5 Montel Mirror (x-domain): The Montel mirrors are specific X-ray optical elements under consideration for the CBXFEL Demonstrator discussed in Chapter **5** and are further specified in the Appendix **C.3**.
Program wise they can be implemented as a stack of two (curved) mirrors with optional errors, an rotated rectangular aperature due to the mirrors finite size and an optional gap at the center between the mirrors included as inverse stripe $f^{(\mathrm{inv})}_{stripe}$.

4.2.2.6 (Virtual, Transmissive) 2D Screen (k/x-domain): This elements does not have any influence on the propagating radiation field at all. Its purpose is to tell the program to measure the X-ray pulse properties as defined in Section **2.1** during propagation inside the cavity. These are, the transverse projections integrated over the full frequency space, the respective transverse moments $\langle \boldsymbol{x}_\perp^n/\boldsymbol{k}_\perp^n \rangle$ of order $n = 1, 2$ and the phase front $\mathcal{S}$, the spectral power density by integrating over the full transverse space for each spectral slice individually and the pulse energy by additionally integrating over both transverse and spectral coordinates. The projections and moments can be calculated either in spatial or in angular domain, where the default is to calculate them in the domain of the prior optical element. From these moments and the spectral contribution also the gaussian quality factor J and the temporal coherence τ_{coh} are computed using equations (2.15) and (3.60), respectively. For latter only the beam entering the cavity and the one exiting (as well the transmitted beams) are taken into account as it requires two virtual screens in x- and k-domain to be set at the same position, which is usually not the case (if yes, J can be computed in a post-processing step).

4.2.2.7 Crystal Mirror (k/x-domain): The crystal mirror is the most involved element of those implement in the program to date. The specific computational implementation and setup including the definition of the crystal orientation are further specified in Paragraph **4.2.3.2**. Here, only the effect of the mirrors on the photon pulse shall be sketched.
For the crystal mirror, the program basically divides the treatment into two cases, an unstrained and a strained one. In the usual unstrained case, the simple two beam case is considered following Subsection **3.1.2**. Then the complex reflectivity $r_{0H}(E_{\mathrm{ph}}, \boldsymbol{x}_\perp, \boldsymbol{k}_\perp) = r_{0H}(E_{\mathrm{ph}}, \boldsymbol{k}_\perp)$ and the complex transmissivity $t_{00}(E_{\mathrm{ph}}, \boldsymbol{x}_\perp, \boldsymbol{k}_\perp) = t_{00}(E_{\mathrm{ph}}, \boldsymbol{k}_\perp)$ are independent of the position $\boldsymbol{x}_\perp$ on the crystal surface. Hence, the computation can be fully performed in the k-domain without loss of information using equations Eqs. (3.24) to (3.25). For each different wave vector $\boldsymbol{k}_i$, the angle of incidence slightly changes and consequently does the reflectivity. This effect is usually quite small, considering the small divergence of (the relevant part of) the photon pulse and an incidence close to 90°. For other angles of incidence the effect can however have a relevant influence on CBXFEL performance [28].
As was mentioned above, if not told otherwise the program expects a cavity length matched

to the electron bunch repetition rate. However, the finite penetration into the crystal and the crystal's index of refraction being different from unity introduce a wave vector dependent phase shift. In time domain this frequency dependent phase shift relates to a mix of a time shift, originating from the fraction linear in frequency, as well as a stretching of the pulse originating from the higher order terms. Latter is to be expected considering the finite bandwidth of the reflection and the fourier time-bandwidth product [41, ch.5.1.4]

$$\sigma_t \sigma_E \geq {}^{\hbar}/_{4\pi}. \tag{4.18}$$

Following [94, p.113, 23] the time delay can be compensated by decreasing the cavity length by an amount $\Delta z = l_{\text{ext}(E_{\text{ph}}=E_c)} \sin\Theta$ or numerically by multiplying a phase factor $\Delta\Phi(k) = 2kl_{\text{ext}(E_{\text{ph}}=E_c)} \sin\Theta$. Θ refers to the angle of incidence and $l_{\text{ext}(E=E_c)}$ is the extinction length (3.28) at the crystal's resonant energy $E_{\text{ph}} = E_c$. Phenomenally, this formular corresponds to the photons traveling in average one extinction length until reflection. So the time delay is equal to the time required to transverse twice the penetration depth, once to the point of reflection and once back to the surface.

Summarized, the effect of the crystal on the photon pulse relates to

$$A\left(\boldsymbol{k}_\perp, z_+, E_{\text{ph}}\right) = A\left(\boldsymbol{k}_\perp, z_-, E_{\text{ph}}\right) r_{0H}(\boldsymbol{k}_\perp, E_{\text{ph}}) \exp\left(-2\mathrm{i}kl_{\text{ext}}\left(E_{\text{ph}} = E_c\right)\sin\Theta\right). \tag{4.19}$$

If required, the transmitted pulse can be computed via

$$A^{\text{trans}}\left(\boldsymbol{k}_\perp, z_+, E_{\text{ph}}\right) = A\left(\boldsymbol{k}_\perp, z_-, E_{\text{ph}}\right) t_{00}(\boldsymbol{k}_\perp, E_{\text{ph}}). \tag{4.20}$$

The second case treated in the program is the strained crystal in symmetric reflection geometry close to normal incidence. Then, as discussed in Subsection **3.1.4**, the reflectivity is dependent on the strain progression $\eta\left(\boldsymbol{x}_{\text{Surf}}, z\right)$ normal to the surface. As this strain is dependent on the surface position the same holds for the reflectivity. Consequently $r_{0H}\left(\boldsymbol{x}_\perp, \boldsymbol{k}_\perp, E_{\text{ph}}\right)$ and $t_{00}\left(\boldsymbol{x}_\perp, \boldsymbol{k}_\perp, E_{\text{ph}}\right)$ principally dependent on the full four dimensional transverse phase space of the radiation field. While it is principally possible to (also numerically) resolve localized spatial frequencies $\boldsymbol{k}_\perp\left(\boldsymbol{x}_\perp\right)$, it is in the general non-analytic case much more demanding than just applying a Fourier transformation where the spatial frequencies components are equally distributed over the entire space $\boldsymbol{x}$. [171, ch.2.2]. Considering that in view of Eqs. (3.30) to (3.31) a small angular shift predominantly results in a shift of the spectral reflection curve via

$$\frac{\partial E_c}{\partial\Theta} = -\frac{\hbar c}{4\pi d_H}\left(1 + \omega_H\right)\frac{\cos\Theta}{\sin^2\Theta}$$

and as the divergence of the radiation field of interest is rather small in the µrad regime, one can estimate for the relative shift

$$\frac{E_c(\Theta + \Delta\Theta)}{E_c(\Theta)} - 1 = \frac{\Delta E_c}{E_c} \underbrace{\approx}_{\Theta\approx\pi/2} \frac{1}{2}\Big(2(\Theta - \pi/2)\Delta\Theta + \Delta\Theta^2\Big)\,. \tag{4.21}$$

For above equation a taylor expansion for Θ near normal incidence was used, which was cut off for any term of order two or higher. Equation (4.21) amounts to a shift on the order of ${}^{\Delta E_c}\!/_{E_c} \approx 1 \times 10^{-9}$ for $\Delta\Theta$ ≈1 µrad and $\Theta \approx \pi/2 - 1\,\mathrm{mrad}$. This is orders of magnitude smaller than the reflection width and the localized spatial frequencies can therefore safely be omitted for the crystal mirror close to normal incidence.

Hence, in case of a strained crystal the response on the radiation field is performed in x-domain. The actual reflectivity $r_{0H}\left(\boldsymbol{x}_\perp, E_{\text{ph}}\right)$ and transmissivity $t_{00}\left(\boldsymbol{x}_\perp, E_{\text{ph}}\right)$ are computed using the patch layered approach discussed in Subsection **3.1.4**, where for each transversal surface position $\boldsymbol{x}_{Surf}(\boldsymbol{x}_\perp)$ mapped to the photon pulse positions $\boldsymbol{x}_\perp$ the reflectivity is computed with a one dimensional layer-by-layer method. The response on the photon pulse is analogous to the unstrained crystal but in the x-domain:

$$\begin{aligned}
\tilde{E}\left(\boldsymbol{x}_\perp, z_+, E_{\text{ph}}\right) =& \tilde{E}\left(\boldsymbol{x}_\perp, z_-, E_{\text{ph}}\right) r_{0H}(\boldsymbol{x}_\perp, E_{\text{ph}}) e^{-2ikl_{\text{ext}}(E_c,\eta=0)\sin\Theta} e^{-2iku_z(\boldsymbol{x}_\perp,s=0)}. & (4.22)\\
\tilde{E}^{\text{trans}}\left(\boldsymbol{x}_\perp, z_+, E_{\text{ph}}\right) =& \tilde{E}\left(\boldsymbol{x}_\perp, z_-, E_{\text{ph}}\right) t_{00}(\boldsymbol{x}_\perp, E_{\text{ph}}). & (4.23)
\end{aligned}$$

Again, the reflectivity has been appended a phase. The first phase factor is analogous to the unstrained crystal (4.19) to adjust for the time shift. It is computed for the unstrained case $(\eta = 0)$ as it is assumed infeasible to physically adjust for the dynamically varying strain and, as in the discussion regarding the optimized undulator parameter K_{opt}, it is chosen that the shift is per default optimized for the startup of the resonator where the crystal is still unstrained. This can however be altered by adding a constant, specific time shift (see below). The second phase shift is to account for the figure error of the crystal surface in analogy to the grazing incidence mirrors (2.48), where the normal displacement $u_z\left(\boldsymbol{x}_\perp, z = 0\right)$ at the surface $(z = 0)$ is analogous to the height error $\Delta h(\boldsymbol{x}_\perp)$ in equation (2.48). This also enables the computation of the influence of thermal response related bendings of the crystal, such as the ‘heat bubble’ caused by the potentially non-uniform thermal expansion.

A a benchmark for the (strained) crystal diffraction calculation, the subprogram used for evaluation was compared to the analytic results by *V.A. Bushuev* in 2013 [178], which were confirmed by *Z. Qu et al.* in 2020 [179]. Bushuev assumed a transversely varying temperature field, which is, however, homogenous in depth. Also, the thermal expansion coefficient was, for simplification, assumed to be temperature independent, which is a very coarse and inaccurate approximation (also see [88]). The results are presented in Figure (4.2) and show excellent agreement.

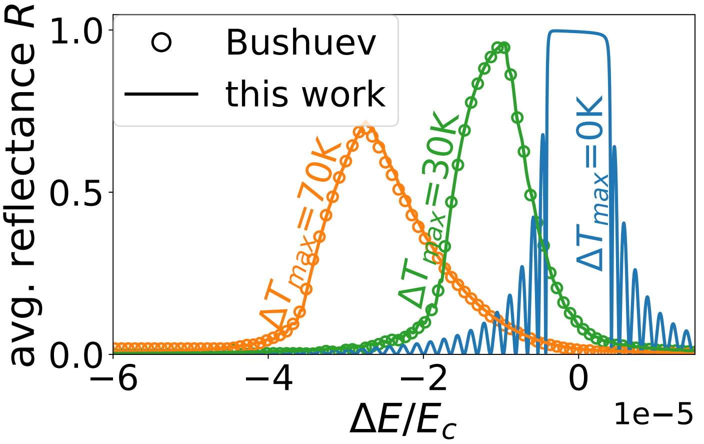

Figure 4.2: Comparison of the averaged crystal reflectivity $\bar{R}(E_{\text{ph}}) = \iint I_0(x,y)\,R(x,y,E_{\text{ph}})\,\mathrm{d}x\mathrm{d}y / \iint I_0(x,y)\,\mathrm{d}x\mathrm{d}y$, weighted by an incidence X-ray pulse of intensity $I_0(x,y) \propto \exp\left(-{x^2}/{r_x^2} - {y^2}/{r_y^2}\right)$, with the analytic results by *V.A. Bushuev* [178] and *Z. Qu et al.* [179]. (The results by *V.A. Bushuev* and *Z. Qu et al.* coincide.) The t_c=50 µm thick diamond (4 0 0) crystal is subject to a transversely non-uniform temperature distribution $T(x,y) = \Delta T_{\text{max}} \exp\left(-{x^2}/{\beta_x r_x^2} - {y^2}/{\beta_y r_y^2}\right)$. The parameters are r_y =720 µm, $r_x = {r_y}/{\sin(\Theta)}$ with $\Theta = 34.19°$, $\beta_x = 2.6$, $\beta_y = {\beta_x - 1}/{\cos^2(\Theta)} + 1$ and ΔT_{max} =0 K (blue), 30 K (green) and 70 K (orange). For the thermal expansion a constant expansion coefficient $\alpha(T) = \alpha$ =0.45 × 10^{-6} K^{-1} is assumed (which is a very coarse approximation). The agreement is excellent between this work and that by *V.A. Bushuev*.

4.2.2.8 Time Shift (both): As was shortly touched above in the reference to equation (4.8), the program generally expects a perfectly matched cavity length[43]. This perfect matching might be disturbed due to different reasons. For one, errors in the optical path length compared to the design optical path, for example due to longitudinal position errors of the mirror, are converted into shifts in the time domain. Second, one might want to request a certain longitudinal misalignment for tolerance studies. Third, a statistical distribution $F_{el,arrival}(t)$ of finite width $\sigma_{t,arrival}$ of the electron bunch's arrival time, called arrival time jitter hereafter, can as well be implemented as an arrival time jitter of the photon pulse. Due to time invariance of the optical system, all these time shifts can be summed up through the cavity and implemented into the radiation field as a last step. This is done using the shifting property of the Fourier transformation by multiplying a phase factor linearly varying with the photon energy in the spectral domain

$$E_{\text{shift}}(t, z = L_{cav}) = E(t - \Delta t, z = L_{cav}) \begin{aligned} &= \tilde{\mathcal{F}}_{1D}^{-1}\left[\tilde{E}(L_{cav}, E_{\text{ph}}) \exp(-\mathrm{i}k\Delta s)\right](t) \\ &= \tilde{\mathcal{F}}_{1D}^{-1}\left[\tilde{E}(L_{cav}, E_{\text{ph}}) \exp\left(-\mathrm{i}\frac{E_{\text{ph}}\Delta t}{\hbar}\right)\right](t), \end{aligned} \tag{4.24}$$

where $\Delta t = \Delta s / c$ is the total time shift accumulated over the different contributions.

4.2.2.9 Tilt (x-domain): If tilt is applied, the axis of propagation is shifted with respect to the design axis by an angle $\Delta\boldsymbol{\Theta} = (\Delta\Theta_x, \Delta\Theta_y, 0)$. It is implemented, using the shifting property of

---

[43] Actually, the monochromatizing mirrors might introduce an time shift of the arithmetic mean time $\bar{t}$ which is different to the compensation in (4.19) and (4.22) depending on the actual longitudinal distribution of the radiation field entering the cavity.

the Fourier transformation, as multiplication with a phase factor linearly varying with position in the x-domain [174, ch.6.1]

$$E_{\text{tilt}}\left(\boldsymbol{x}_{\perp}, z_{+}, E_{\text{ph}}\right) = E\left(\boldsymbol{x}_{\perp}, z_{-}, E_{\text{ph}}\right) e^{\mathrm{i}k\boldsymbol{x}_{\perp}\Delta\Theta} \tag{4.25}$$

where $z_{\pm}$ again refers to the position before (-) and behind (+) the tilted element. Comparison with equation (4.17) for the figure error shows that both tilt and figure errors are based on the same principle, that a position dependent shift in the height profile (a tilt can analogously be represented by a local wedge in the mirror surface) relates to a distortion of the wavefront.

4.2.3 The computational implementation

This paragraph shall give an overview over the basic computational layout, the design principles as well as some computational detail referring to the numerical implementation of the angular spectrum method. Details about the computational implementation of the Fourier transformation and the integration of the crystal mirrors will be specified in Subsection **4.2.3.1** and **4.2.3.2**, respectively.

As was mentioned before, the program is optimized for the use at HPC clusters using MPI, or more specifically MPI 3.0 with the implementation *Open MPI v4.1*[180]. Using MPI, the program is principally divided into many processes, which run independent of each other and only communicate if explicitly told so (the *message passing* fractions). The main part of the program, namely the propagation of the monochromatic Fourier components of the polychromatic wave, can be parallelized very efficiently in an *embarrassingly parallel manner*. This means, that during the propagation there is no communication at all between the single processes, which is due to the optical system being time invariant so that the monochromatic wave components do not influence each other. Most of the communication between the processes happens in the one dimensional fourier transformations to and back from the frequency domain, as one single component of the fourier spectrum is dependent on all components in the time profile. Also, when collecting the derived data, such as the transverse projections from the virtual screen, the spectra and the total photon energy, the processes need to communicate. However, as this data is much smaller than the full radiation field, the communication is very fast in comparison. The final communication occurs when saving the data back to file using *parallel HDF5*(PHDF5) [181], as all processes need to know the full layout of the hdf5 file.

As depicted in Figure (4.1), the program starts by reading in a simple namelist which defines the elements of the optical system discussed in **4.2.2**. At the beginning and the end of the list an x-domain virtual screen is appended (if not already there). For the crystal mirrors one can also specify if the transmitted radiation shall be saved. Additionally, one may define an additional optical system for the transmitted radiation to be propagated through without the additional overhead cost of writing out the data and reading it in again. If crystal mirrors are contained in the list, a cumulative bandwidth is computed based on the analytic two beam thick non-absorbing crystal approximation (3.30). In order to account for the wings of the reflection curve as well as for the transmitted energy, the system bandwidth is set four times the cumulative crystal bandwidth. For the unstrained crystal this is

$$E \in [E_{\min}, E_{\max}] = [\min\{E_{c,i}(1-2\epsilon_{H,i})\}, \max\{E_{c,i}(1+2\epsilon_{H,i})\}], \tag{4.26}$$

where $E_{c,i}$ and $\epsilon_{H,i}$ are the resonant photon energy and the relative spectral width of crystal i respectively. For the case of the strained crystal, using $d_H(\eta) = d_H(0)\cdot(1+\eta)$ the single mirror bandwidth is approximated as

$$\epsilon_{H,\text{strain}} \approx \epsilon_{H,\eta=0} + \max\{\eta(\boldsymbol{x}_\perp, s)\} - \min\{\eta(\boldsymbol{x}_\perp, s)\} + \mathcal{O}\left(\eta^2\right) + \mathcal{O}(\epsilon_H \eta), \tag{4.27}$$

where the higher order terms can be neglected for the usually small strain η. The formula is based on the simplification that all spatial positions $\boldsymbol{r} = (\boldsymbol{x}_\perp, s)$ are equally entering into the reflectivity and therefore into the bandwidth.

After setting up the optical system, the *Genesis-1.3* output is read using PHDF5, where the individual processes read in a finite, continuous subset[44] of the time slices written out by *Genesis-1.3* as well some additional information such as the central wavelength, the temporal spacing of the slices and the transverse grid spacing. While reading in the data the first informations about the radiation field is already gathered, specifically the transverse projection, the transverse spatial moments, the transversely integrated intensity profile and the pulse energy when entering the crystal. This data is communicated to the master process to later save it in a separate hdf5 file. Afterwards, the three dimensional radiation field is transformed into the frequency domain, where the transversely integrated frequency spectrum is additionally recorded. More details on the transformation procedure can be found in the next subsection.

From the full radiation field in the frequency domain those portions are selected which lie inside the optical system bandwidth defined by equation (4.26). While this can strongly reduce the overall computational cost, especially when the bandwidth of the *Genesis-1.3* output is much larger than the optical system bandwidth, it introduces quite some complication referring to the MPI implementation. Obviously, it is desired to have all processes contribute in the propagation. However, the subfraction of frequency components participating in the propagation normally is not evenly distributed over the individual processes. So, first a redistribution of the frequency components needs to be done which introduces communication overhead. Also, after the propagation, the frequency components again need to be redistributed to fit with the scheme of the Fourier transformation (see below.). This process is sketched in Figure (4.3). Some effort was made to speed up this redistribution as much as possible so that an effective speed up ≥ 1 compared to the no bandwidth selection case is always achieved.

Afterwards the finite subfraction of frequencies is propagated through the optical system. At the beginning of the optical system, the frequency components of the radiation field are in the spatial domain. For the following optical elements, the individual frequency components are, if

---

[44] Continuos in the sense, that the individual slices of the subsets are laying next to each other in physical space.

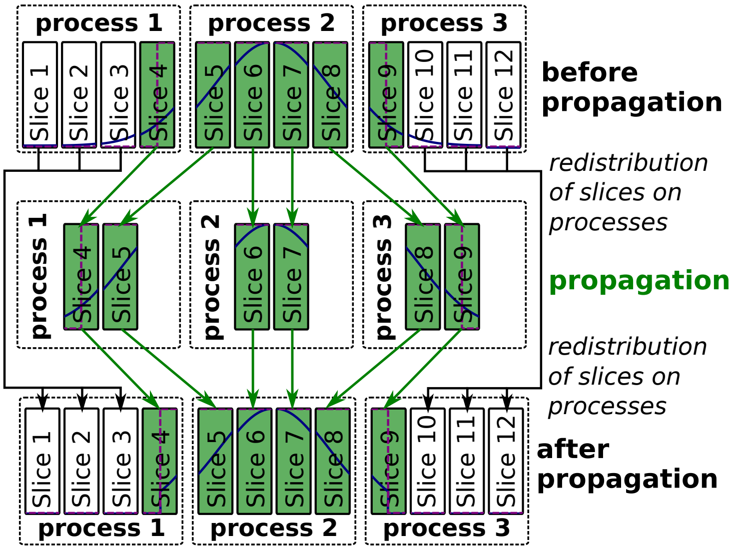

Figure 4.3: Sketch of the redistribution of radiation slices on different processes for the propagation. Exemplarily, a gaussian distributed frequency distribution of radiation field (blue curve) is sampled on 12 individual slices. Of these twelve slices the central six (marked green) are inside the reflection bandwidth, with the reflection curve being unrealistically approximated by a rectangular function (purple dashed curve). The slices outside the reflection width are directly set to zero. Initially, the (green) slices inside the reflection width participating in the propagation are distributed very unevenly. To maximize the efficiency of the propagation step, the green slices are then redistributed evenly on the participating processes. After propagation they are put back to their original position. Usually, many more radiation slices are present and many more processes are participating, so that the gain in efficiency is much more drastic than in this simplified example.

necessary, transformed into the domain specified in **4.2.2** by means of a two dimensional (inverse) fourier transformation. At the end of the optical system, the radiation components are required to be in the x-domain, so an inverse transformation is performed if needed. If defined, a transmitted field is (or transmitted fields are) created based on equations (4.20) or (4.23). After the propagation, the frequency components of the circulating as well as the transmitted field(s) are joined with the non propagated fraction which was set to zero[45]. Also the data recorded at the screen elements is gathered on the master process, from which some additional information is then derived. These include the gaussian quality factor J and the temporal coherence τ_{coh} using equations (2.15) and (3.60), respectively.

Afterwards, the circulating as well as the optional transmitted fields are transformed back to the time domain while computing the intensity profile. Finally, the gathered and derived data and the full three dimensional distribution of the circulating and the transmitted fields in the (x, t) domain are written out to HDF5 files, with latter being compatible to the input format required by *Genesis-1.3*.

To summarize, the *pXCB* program for the X-ray wavefront propagation through an X-ray op-

---

[45] This introduces considerable inaccuracy for the *transmitted* pulse at the first round trips, where only a tiny fraction of the transmitted total pulse energy is contained in the frequency components inside the reflection bandwidth. It therefore considerably underestimates the energy contained in the transmitted pulse at these round trips. However, it does not have any influence on the seeding power and, hence, on the seeding process. Additionally, for the CBXFEL the transmitted radiation at the first round trips is very small compared to the radiation in saturation. Therefore, the error can be considered tolerable, but should be kept in mind when analyzing the results.

tical cavity is highly optimized for parallel computation and has an additional speed up if the cavity has an inherent spectral bandwidth. The data format is based on the *HDF5* protocol, as this is both very efficient (data size and computation time wise) and also employed by *Genesis-1.3*. The cavity configuration can be easily configured by altering a simple namelist. Also, the program is able to take a lot of data during the propagation of the radiation through the cavity without significant loss in computational speed.

The reliability of the program was benchmarked both by comparison with analytic functions, such as the free space propagation of a square beam (a plane wave cut off at an aperture) [174, ch.5.3] and the propagation of a gaussian beam [41, ch.6.2]. Also the program was compared to the quite similar wave propagation submodule of the popular program *OCELOT* [182]. For the longitudinal domain the fourier transformation was tested by comparison with simple analytic test functions (for example a normal distribution), which were run through stand alone matlab treating the dynamic diffraction (which were additionally benchmarked with the programs available on *Sergey Stepanov X-ray Server* `https://x-server.gmca.aps.anl.gov/`).

4.2.3.1 Numerical Fourier transformation using the FFT As was discussed above, the physical approach is heavily based on Fourier transformations in one and two dimensions. Computationally a perfect continuos Fourier transform evidently does not exist. Instead the *discrete Fourier transformation*(DFT) or rather its variant *fast Fourier transformation*(FFT) is employed, which works on a grid of discretely sampled data [175, ch.12]. The very efficient external library *fftw3* [183] is used in this program. *fftw3* also has an MPI-parallelized implementation which is used for the one dimensional transform to and back from the frequency domain.

For a correct description of the data the sampling rate in one as well as two dimensions needs to be appropriately chosen. In this program as well as *Genesis-1.3* an even sampling of the continuous radiation field $E(x, y, t, z) = E_z(x, y, t)$ at position z

$$\tilde{E}_z(x, y, t) = \mathrm{comb}\left(\frac{x}{\Delta_x}\right)\mathrm{comb}\left(\frac{y}{\Delta_y}\right)\mathrm{comb}\left(\frac{t}{\Delta_t}\right)E_z(x, y, t),$$
$$\text{with} \quad \mathrm{comb}(x) = \sum_{n=0}^{\infty}\delta(x-n)$$

with sampling rates Δ_i is applied. If the non-sampled radiation field is band limited, which means that its Fourier transform is confined to a cube of size $2L_{x'}, 2L_{y'}, 2L_f$, where x', y' and f denote the transverse and longitudinal frequency variables, respectively, then complete reconstruction of the data can be achieved by choosing the sampling rates [171, ch.2.4]

$$\Delta_{x,N} = \frac{1}{2L_{x'}}, \quad \Delta_{y,N} = \frac{1}{2L_{y'}}, \quad \Delta_{t,N} = \frac{1}{2L_f}, \tag{4.28}$$

where $\Delta_{i,N}$ is called the *Nyquist critical sampling rate* [175, ch.2.1][46]. Actually, it is possible to perfectly reconstruct the original radiation field $E_z(x,y,t)$ by interpolation from the sampled data via

$$E_z(x,y,t) = \sum_{n,m,j=0}^{\infty} E_z\left(\frac{n}{2L_{x'}}, \frac{m}{2L_{y'}}, \frac{j}{2L_f}\right) \operatorname{sinc}\left(2L_{x'}x - n\right) \cdot \operatorname{sinc}\left(2L_{y'}y - m\right) \operatorname{sinc}\left(2L_f t - j\right),$$

which is know as the *Whittaker-Shannon sampling theorem*.

If the sampling rate $\Delta_i \leq \Delta_{i,N}$, then the sampled spectrum is a perfect representation of the original. On the other hand, if the sampling rate is chosen too low $\Delta_i > \Delta_{i,N}$, then an effect called *aliasing* will occur. Aliasing means that the power spectral density for frequencies $f_i > \frac{1}{\Delta_i}$ will be spuriously moved into the range $f \in \left(-\frac{1}{2\Delta_i}, \frac{1}{2\Delta_i}\right)$ [175, ch.2.1]. Hence, it is of high importance to appropriately chose the sampling rates to not overestimate the power spectral densities in the limited regions of interest.

Besides the sampling rate, the overall sampled volume and therefore the number of samples must be chosen such that it confines the entire data of interest in $(\boldsymbol{x}_\perp, t)$ space. Assuming the radiation is significant over a spatial region of size $(2L_x, 2L_y, 2L_t)$, at least

$$N_x = 4L_x L_{x'}, \quad N_y = 4L_y L_{y'}, \quad N_t = 4L_t L_f \tag{4.29}$$

samples are needed to properly describe it.

Especially for the propagation routines special care must be given with respect to the sampling rates and the number of samples, as both the spatial width as the band width of the radiation change throughout the propagation. This is particularly so as the number of samples or the sampling rate can not freely be changed in the optical system due to the requirement that the grid after one roundtrip through the cavity agrees with the grid defined by *Genesis-1.3*. As was already discussed in Section **4.1**, the time spacing of the *Genesis-1.3*-grid may be changed with subsequent round trips according to the output bandwidth. Nonetheless, especially for the transverse grid one must take into account the quadratically rising numeric demands with increasing number of samples. Anyways, the optical systems needs to be chosen such, that the radiation after one pass through the optical cavity agrees rather well with the electron bunch distribution and therefore with the *Genesis-1.3*-grid. In order to properly represent the radiation during the propagation through the cavity, where latter requirement is not necessarily met, the transverse grid as well as the time grid is strongly expanded by

$$N_{i,\mathrm{prop}} = 2^{\lceil \log_2(N_{i,\mathrm{gen}}) \rceil + 1} \tag{4.30}$$

---

[46] For functions $g(x)$ band limited around a central frequency f_c, upper theory can be applied as well using the shifting property of the Fourier transform by replacing $g(x)$ by $g'(x) = g(x)\exp(-i2\pi f_c x)$.

, where $N_{i,\mathrm{gen}}$ refers to the genesis grid and $\lceil x \rceil$ is the rounding up operator. The data for points $N_{i,\mathrm{gen}} < j \leq N_{i,\mathrm{prop}}$ is appended with zeros. Upper number of samples is convenient as the fft works fastest with powers of two [175, ch.12.2]. Writing out the data to *Genesis-1.3* then is equivalent to applying a rectangular aperture. This introduces some error in the respective frequency spectrum due to the artificial diffraction introduced. Anyhow, if the *Genesis-1.3*-grid is chosen much bigger than the actual electron beam size, the influence of this error remains negligibly small[47].

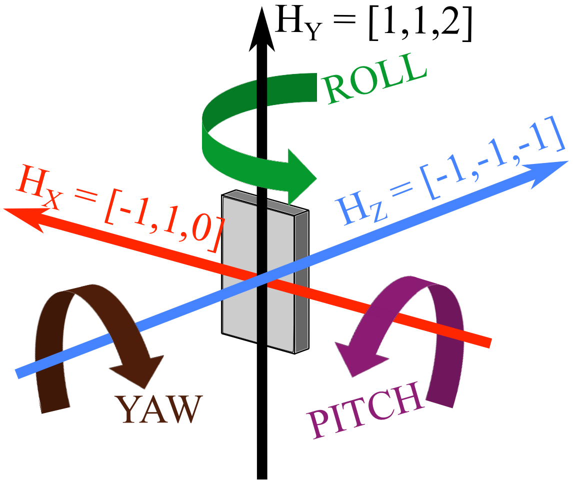

Figure 4.4: The pitch-roll-yaw convention used for setting up the crystal with respect to the photon pulse. The coordinate system at zero rotation coincides with the photon pulse' internal coordinate system. The orientation of the crystal planes in correspondence to the optical axis (x, y, z) as used for the $E_{\mathrm{ph}} = 9.05\,\mathrm{keV}$ C(333) CBXFEL demonstrator in Chapter **5** is also shown.

4.2.3.2 The crystal mirrors While for most optical elements defined in **4.2.2** it is sufficient to define a simple set of parameters, the crystal mirrors are more complicated and shall be described here in a bit more detail.

The mirrors are defined using a separate namelist containing necessary properties such as the crystal material, the crystal temperature, the crystal thickness and the orientation of the crystal. Latter must be based on some convention. In the program the *pitch-roll-yaw* convention is used as sketched in figure Figure (4.4)[48]. According to figure Figure (4.4) the pitch angle refers to a rotation around the (unrotated) $\hat{x}$-axis, the roll angle to a rotation around the (potentially rotated) $\hat{y}$-axis and yaw to a rotation around the (potentially rotated) $\hat{z}$-axis. The definition of these angles is amended by the optional definition of different mechanical errors. These are pointing errors of the different axis of rotation as well as angular errors. These errors enter as well in the dynamic diffraction calculations as in an additional **tilt** applied on the radiation field.

---

[47] It has to be noted that there exist adaptive routines to adjust for the change of spatial and angular width throughout an optical system, for example using multiple partial propagations in conjunction with absorbing boundaries [173, ch.8], where the number of steps are chosen in dependence of the beam moments. These algorithms are, however, quite error prone. For the present work the grid spacing and total grid size was chosen and checked by hand such that no aliasing influences the actual results. For the results presented in Section **5.2** a spacing of $\Delta x = \Delta y = 2.632\,\mu\mathrm{m}$ with $N_{x,\mathrm{gen}} = N_{y,\mathrm{gen}} = 229$ grid points for each dimension has usually been used. During propagation, the number of grid points was increased by zero padding to $N_{x,\mathrm{prop}} = N_{y,\mathrm{prop}} = 512$. For the Montel gap simulations in Paragraph **5.2.2.5** an increased sampling of $\Delta x = \Delta y = 1.068\,\mu\mathrm{m}$ and $N_{x,\mathrm{gen}} = N_{y,\mathrm{gen}} = 532$ was used. For the future, anyhow, an interface exists for the multi-step approach to be integrated without severe complications.

[48] The convention can easily be changed by replacing a single header file specifying the rotation matrix.

The orientation then needs to be further specified by relating the crystal axis to the internal orientation. This means that each axis $(\hat{x}, \hat{y}, \hat{z})$ refers to a plane of specific *Miller's indices*. In Figure (4.4) the crystal orientation is displayed which is also used for the $E_{\mathrm{ph}} = 9.05\,\mathrm{keV}$ C(333) CBXFEL demonstrator in Chapter **5**. Principally, any right handed set of basis vectors can be chosen, where one should keep in mind that the surface orientations differ in their ease of actual manufacturing/growing.

For the implemented two beam case one also needs to define the principal plane H for which the reflection is calculated. In the default case, this is equal to the surface plane.

For the case of a strained crystal one can also import two (cylinder symmetric) or three-dimensional (cartesian) data files containing the different directions of the vectorial displacement field $\boldsymbol{u}(x, y, s)$. If such a file is important, the routine directly employs the strained crystal calculation (4.22) and (4.23).

As was discussed in Section **3.1**, the Fourier components χ_H of the material susceptibility (3.6) are important parameters for the computation of the dynamic diffraction. As their derivation can become very complicated and is based on many external parameters and experimental measurements, as discussed in **3.1**, the susceptibilities are computed using the well benchmarked external library *xraylib*[96][49]. As the *xraylib* does not include the Debye-Waller factor, it is computed using a 4th order polynomial parametrization

$$W_n = \frac{B}{4d_H^2} \quad \text{with} \quad B = p_0 + p_1 T + p_2 T^2 + p_3 T^3 + p_4 T^4, \tag{4.31}$$

where the parameters p_i are obtained from fits to various experimental data done by *Gao and Peng*[185] for different materials. In Table 1 the parameters for diamond are listed.

T	p_0	p_1	p_2	p_3	p_4
$\leq$80 K	0.11918	-0.6360E-07	0.1962E-06	0.3167E-09	-0.1858E-11
$>$80 K	0.12034	-0.2231E-04	0.3348E-06	-0.2108E-09	0.5320E-13

Table 1: Debye-Waller parameters obtained by *Gao and Peng*[185] for fitting equation (4.31).

Also, thermal expansion neither is included in the *xraylib*. It is implemented in the diffraction calculations using the formula

$$a(T) = a_{300} \left(1 + \sum_{i=1}^{4(3)} \mathcal{T}_i X_i \cdot \left[\frac{1}{\exp\left(\mathcal{T}_i/T\right) + 1} - \frac{1}{\exp\left(\mathcal{T}_i/300\right) - 1}\right]\right) \tag{4.32}$$

adapted from *Reeber and Wang* [114] and *Jacobson and Stoupin* [186]. The associated parameters for diamond are listed in Table 2.

It is also important to collect the amount of energy absorbed in the crystal as well as its spatial distribution, as this is needed for the calculation of the crystal's thermal response. In the

---

[49] There actually also exists a self written code only defined for diamond based on the algorithm proposed by *VG Kohn* [184]. But it was dropped in favor of the much better benchmarked *xraylib*.

a_{300} [Å]	$\mathcal{T}_1$[K]	$\mathcal{T}_2$[K]	$\mathcal{T}_3$[K]	$\mathcal{T}_4$[K]	X_1 [10^{-7}/K]	X_2 [10^{-7}/K]	X_3 [10^{-7}/K]	X_4 [10^{-7}/K]
3.559	220	880	2137.5	/	0.4369	15.7867	42.5598	/
3.5671	159.3	548.5	1237.9	2117.8	0.096	2.656	26.799	23.303

Table 2: The upper line shows thermal expansion parameters obtained by *Reeber and Wang*[114] by fitting equation (4.32) to various experimental datasets in the temperature range $0\,\mathrm{K} < T \leq 3000\,\mathrm{K}$. The bottom line shows similar parameters obtained by *Jacobson and Stoupin* [186], but including the very accurate low temperature thermal expansion data from *Stoupin and Shvyd'ko* [187]. The more accurate data from the bottom line was used for the simulations including heat load effects in Section **5.2.3**, whereas the less accurate upper line was used for the static temperature simulations due to historic reasons. For the static temperature cases, a small change in lattice parameter a amounts to a roughly proportional shift in central photon energy, whereas the performance remains the same. Hence, for the simulations ignoring heat load effects, the exact thermal expansion is negligible.

unstrained crystal it is computed using

$$\begin{aligned}Q_{\text{abs}}\left(\boldsymbol{x}_\perp, s\right) = & \frac{W\left(\boldsymbol{x}_\perp, z\right)}{Q_{\text{pulse}}} \iiint A^2\left(\boldsymbol{k}_\perp, z-, E_{\text{ph}}\right) \\ & \frac{\left[1 - \left|r_{0H}\left(\boldsymbol{k}_\perp, E_{\text{ph}}\right)\right|^2 - \left|t_{00}\left(\boldsymbol{k}_\perp, E_{\text{ph}}\right)\right|^2\right] e^{-\frac{s}{l_{\text{ext}}(E_{\text{ph}})}}}{t_c\left(1 - e^{-\frac{t_c}{l_{\text{ext}}(E_{\text{ph}})}}\right)} \mathrm{d}\boldsymbol{k}_\perp \mathrm{d}E_{\text{ph}},\end{aligned} \tag{4.33}$$

where s is the in-depth position in the crystal, t_c is the crystal thickness, $W\left(\boldsymbol{x}_\perp, z\right)$ is the radiant fluence (2.6) and $Q_{\text{pulse}} = \iiint A\left(\boldsymbol{k}_\perp, E_{\text{ph}}\right) \mathrm{d}\boldsymbol{k}\mathrm{d}E_{\text{ph}}$. In above relation it is assumed that the crystal absorption is independent of the surface position so that the absorbed heat has the same transverse distribution as the radiant energy density. The totally absorbed energy if integrated over the entire crystal is equal the incoming energy times the integrated absolute reflectivity $R = |r_{0H}|^2$ minus the absolute Transmission $T = |t_{00}|^2$, which is precisely the fraction of energy remaining in the crystal.

For the case of the strained crystal, above relation is altered, as the extinction length is dependent on the strain at position $\boldsymbol{r} = (\boldsymbol{x}_\perp, z)$ and therefore also on the crystal depth. As described in Subsection **3.1.4**, the crystal is divided into n_{lay} layers of strain $\eta_n(\boldsymbol{x}_\perp) = \eta(\boldsymbol{x}_\perp, \bar{s}_i)$. $\bar{s}_i = {}^{s_i + s_{i+1}}/_2$ is the mid of layer $i \leq n_{lay}$ and s_i and s_{i+1} are the layer boundaries to the top and the bottom respectively with $s_0 = 0$ and $s_{n_{Lay}+1} = t_c$. With this convention, the depth dependence $\mathcal{Q}_{D,E_{\text{ph}}}\left(\boldsymbol{x}_\perp, s, E_{\text{ph}}\right)$ of the fraction of total absorbed energy $Q_{\text{abs}}\left(\boldsymbol{x}_\perp, s, E_{\text{ph}}\right) = Q_{\text{S}}\left(\boldsymbol{x}_\perp, E_{\text{ph}}\right) \mathcal{Q}_D\left(\boldsymbol{x}_\perp, s, E_{\text{ph}}\right)$ at photon energy E_{ph} approximately becomes

$$\begin{aligned}\mathcal{Q}_{D,E_{\text{ph}}}\left(\boldsymbol{x}_\perp, s\right) = & \exp\left[-\int_0^s \frac{1}{l_{\text{ext}}\left(\boldsymbol{x}_\perp, s', E_{\text{ph}}\right)} \mathrm{d}s'\right] \\ \approx & \prod_{s_i < s}\left(\exp\left[-\frac{s_i - s_{i-1}}{l_{\text{ext}}\left(\boldsymbol{x}_\perp, \bar{s}_{i-1}, E_{\text{ph}}\right)}\right]\right) \exp\left[-\frac{s - s_j}{l_{\text{ext}}\left(\boldsymbol{x}_\perp, \bar{s}_j, E_{\text{ph}}\right)}\right] \\ \text{with} \quad & s \in [s_j, s_j + 1) \,\text{and} \quad s_{i<0} = 0\end{aligned} \tag{4.34}$$

Using above equation (4.34) and noting that in the strained case the dependence on the angular distribution gets neglected, the spatially varying absorbed energy integrated over all frequencies is

$$Q_{\mathrm{abs}}\left(\boldsymbol{x}_\perp, s\right) = \int \frac{\left|\tilde{E}\left(\boldsymbol{x}_\perp, z_-, E_{\mathrm{ph}}\right)\right|\left[1 - \left|r_{0H}\left(\boldsymbol{x}_\perp, E_{\mathrm{ph}}\right)\right|^2 - \left|t_{00}\left(\boldsymbol{x}_\perp, E_{\mathrm{ph}}\right)\right|^2\right]}{\int_0^{t_c} \mathcal{Q}_D\left(\boldsymbol{x}_\perp, s', E_{\mathrm{ph}}\right) \mathrm{d}s'} \times \mathcal{Q}_D\left(\boldsymbol{x}_\perp, s, E_{\mathrm{ph}}\right) \mathrm{d}E_{\mathrm{ph}}. \tag{4.35}$$

As the thermal response is computed using a cylinder symmetric coordinate system to decrease the numerical cost (see below), above three dimensional distributions of absorbed pulse energy need to be converted into cylinder symmetric distributions. To do this, the two transverse dimensions (x, y) are interpolated to an evenly spaced one dimensional grid for the transverse radius $r = \sqrt{(x - x_0)^2 + (y - y_0)^2}$. The central point x_0, y_0 is chosen as the arithmetic mean of the radiation distribution at that point. Assuming cylinder symmetry, the overall absorbed energy at each point r gets normalized by the number of contributions to that point.

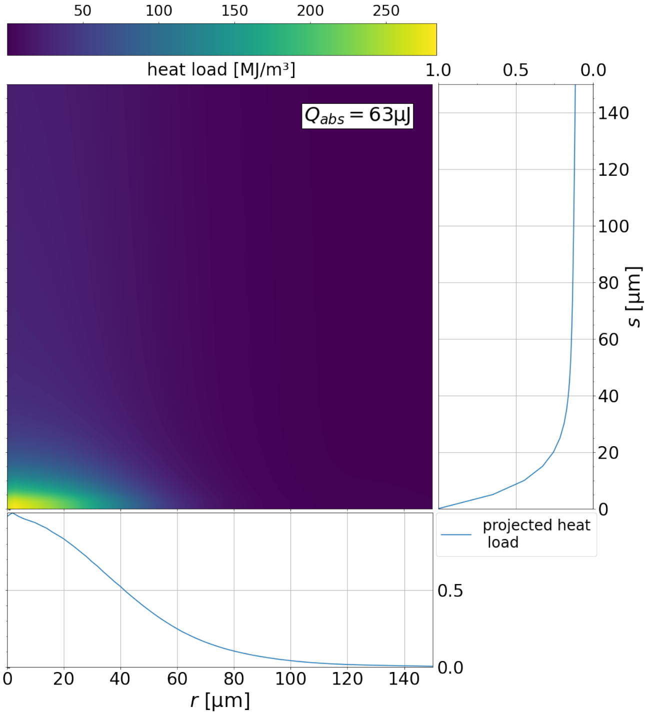

Figure 4.5: Heat load absorbed by a diamond crystal as derived from a saturated XFELO pulse at E_c =9.05 keV (from a full CBXFEL run including the thermal diffusion from Paragraph **5.2.3.5**) using equation (4.33).

In Figure (4.5) an exemplary heat load distribution at E_c =9.05 is plotted. It was calculated, using equation (4.33), from a stable, saturated CBXFEL pulse after a full simulation run, including the thermal diffusion problem, carried out for the CBXFEL demonstrator as presented in Paragraph **5.2.3.5**. The total absorbed energy amounts to $Q_{\mathrm{abs}}^{\mathrm{tot}} = 63\,\mu\mathrm{J}$. The absorbed heat load is rather gaussian distributed in radial direction as it completely inherits its transverse form from the transversely gaussian distributed CBXFEL pulse. In depth direction, however, the curve can be approximated by the sum of an exponentially decaying contribution and a constant background. Former can be traced back to the spectral fraction of incident X-ray radiation inside the crystal bandwidth and latter to the fraction outside the bandwidth, the decay of which

is described by the much larger absorption length (see Figure (3.3)).
To summarize, the implementation of the crystal can be precisely tuned by defining both the crystal orientation and the rotation convention. By default the *pitch-roll-yaw* orientation is employed. The orientation of the crystal can be further tuned by assuming errors such as angular misalignment, miscut or tilt of the rotation axis. The susceptibilities are computed using the external library *xraylib* [96], which is amended by temperature dependent definitions of the lattice spacing and the *Debye-Waller factor*. Furthermore the full spatial heat load on the crystal including the in-depth variation is computed for each frequency contribution separately and later integrated. Especially for the strained crystal case the in-depth variation is quite complex due to the varying reflection conditions with spatial position. In total this yields a very accurate spatial representation of the heat distribution. It should be noted that such a fully spatially and spectrally resolved representation is (to my knowledge) nowhere reported in literature. Commonly, a simplified gaussian or pencil transverse distributed heat load is assumed which is exponentially decaying with a mean extinction depth $\bar{l}_{ext}$. This usually is (for the unstrained case) a good estimation for the SASE case, where the extinction length can be well approximated by the absorption length. For the CBXFEL case, as can be also seen in Figure (4.5), it would evidently yield strong deviations to the actual case.
Such an treatment of the heat load is especially important for the fully coupled CBXFEL simulations, as the distribution of the heat load can influence the reflected pulse by the crystal thermal answer (see below), which is ultimately influencing the heat load distribution of the subsequent pulse. A static representation of the heat load with a non varying radial and in-depth distribution could not account for such effects.

4.3 The Crystals' Thermal Answer

As was discussed in Chapter **3**, the crystal-radiation interaction can be divided into a dynamic diffraction part, taken care of by the propagation code, and a thermal response part. The computational handling of latter shall be described in this section. As was pointed out in Section **3.2**, this thesis concentrates on the thermal conduction and quasi static thermal expansion at the arrival of the next X-ray pulse. For effects of the dynamic thermal expansion and the accompanying elastic response the interested reader is referred to the PhD thesis by *I. Bahns* [85]. First, the thermal transport model will be examined. Then, in a dedicated subsection, the numerical implementation using the *Finite Element Method* will be presented.
The thermal response is solved on the basis of the transient Fourier heat equation (3.55)

$$\rho c_V \frac{\partial T}{\partial t} = \boldsymbol{\nabla} \left(\boldsymbol{\kappa} \boldsymbol{\nabla} T \right) + \dot{Q}_{gen}, \tag{4.36}$$

where $\dot{Q}_{gen}(r, s, t)$ is the heat generation rate introduced by the absorption of the X-ray pulse. While the pulse integrated heat load is written by the X-ray propagation code in the framework of the crystal module, see equations (4.33) and (4.35), a properly normed time distribution $F_Q(t)$

needs to be imposed, so that

$$\dot{Q}_{gen}(\boldsymbol{x}_\perp, s, t) = Q_{abs}(\boldsymbol{x}_\perp, s)F_Q(t) \quad \text{with} \quad \int F_Q(t)\mathrm{d}t = 1. \tag{4.37}$$

After the duration t_{rep} of one round trip, which is assumed to be equal to the electron bunch repetition time $t_{\mathrm{rep}} = 1/f_{\mathrm{rep}}$, the crystal temperature $T_c\,(\boldsymbol{x}_\perp, s, t_{\mathrm{rep}})$ calculated by solving equation (4.36) and, if required, the displacement field $\boldsymbol{u}(\boldsymbol{x}_\perp, s, t_{\mathrm{rep}})$ caused by the quasi-static lattice expansion are written out to be read in by the crystal module of the propagation code. For the low temperature case the temperature $T_c\,(\boldsymbol{x}_\perp, s, t_{\mathrm{rep}})$ usually is approximately constant over the X-ray-crystal interaction volume. Then the computationally much less expensive unstrained crystal case can be applied with a crystal of elevated temperature $\bar{T}_c$. This condition must however be thoroughly checked.

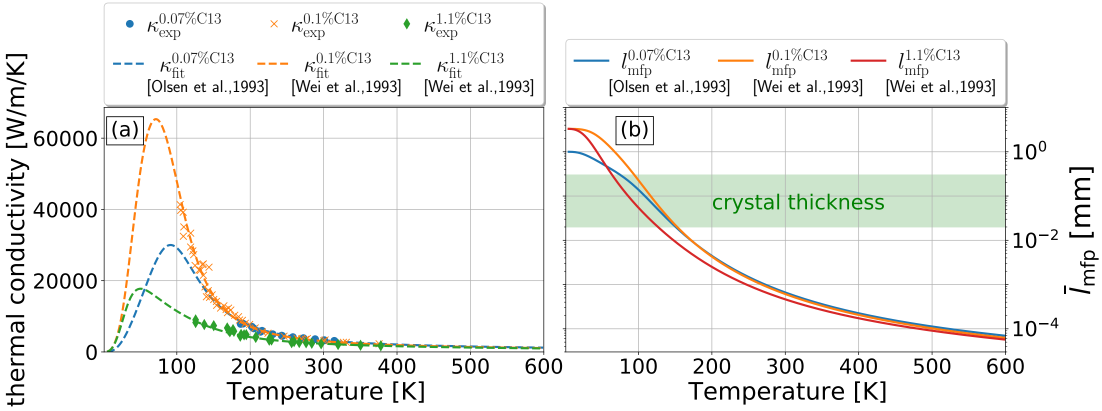

Figure 4.6: Figure (a) plots thermal conductivity data measured by *Olson et al.* [125] for isotopically enriched (99.93 %C_{12},0.07 %C_{13}), high qualitiy single crystalline diamond as well as data measured by *Wei et al.* [124] for both isotopically enriched (99.9 %C_{12},0.1 %C_{13}) and single crystalline natural type-IIa diamond (98.9 %C_{12},1.1 %C_{13}) The markers refer to experimentally measured data and the dashed lines to fits by the authors using a Debye-type model [125] neglecting normal scattering processes and a Callaway model [124, 127] additionally accounting for the redistribution of the phonon density due to N-processes. Figure (b) plots the weighted mean free path obtained by using the fitting parameters for the individual scattering processes obtained by the authors, inverting their fitting algorithms and doing a weighted average over the debye-model density of states. The shaded green area displays the range of typical thicknesses for bragg reflectors.

As was thoroughly discussed in Subsection **3.2.4**, deviations to Fourier's heat law are strongly to be expected when treating heat transport problems on dimensions on the order of the phonon's mean free path l_{mfp} or time scales on the order of the mean scattering time τ. While the latter is of minor interest for the CBXFEL, considering that $t_{\mathrm{rep}} \gg \tau$, the former will definitely have an effect on the thermal conduction at low temperatures. In Figure (4.6(b)) estimates for a gray model phonon mean free path $\bar{l}_{\mathrm{mfp}}$ are plotted for the data obtained by *Olsen et al.* [125] and *Wei et al.* [124] for isotopically enriched, synthetic and high quality, single crystalline type-IIa natural diamond. The respective thermal conductivities are displayed in Figure (4.6(a)).

One can readily see from Figure (4.6(b)) that at temperatures $T\tilde{<}150\,\mathrm{K}$ the mean free path becomes comparable or greater than the typical thickness of diamond Bragg reflectors in the micro meter range. As discussed in Subsection **3.2.4.2**, this can be effectively simulated by using a reduced, anisotropic thickness dependent thermal conductivity due to the additional boundary scattering. Actually, already in the mean free paths displayed in Figure (4.6(b)) a boundary scattering term is heuristically included limiting the mean free path in the $\lim\limits_{T\to 0}$ limit[50]. There also exist some argumentations that the effective thermal conductivities in conjunction with diffusive laws may well be able to capture the heat flow but not the actual temperature distribution. These argumentations are based, however, on isothermal boundaries [135, 136, 188], where the heat can leave the system and therefore leads to quite distinct temperature regions at and away from the boundaries. For the CBXFEL case considered here, the majority of the crystal surface is free standing, which can be approximated as adiabatic boundary conditions on the time-scale of one RF-pulse (also see the next Subsection **4.3.1**). The remaining surface fractions can also be considered adiabatic on this time-scale, as the diamond to (cupper) holder heat transfer can be considered significantly lower than the internal thermal conduction inside the crystal[51]. In this case, the total heat is confined to the crystal and also, after some while, will naturally be homogenized over the crystal.

The second factor leading to deviations from Fourier's law is the relation between the characteristic size of the heat source, which is the pulse diameter and penetration depth in case of X-ray absorption, and the mean free path l_{mfp}. Recently it was argued that the applicability of the diffusive equations would also persist into the (quasi-)ballistic regime Kn$\tilde{>}0.1$ [136–139] if one takes into account modified boundary conditions. But it was recently shown that this argumentation breaks down when considering multidimensional ($D \geq 2$) thermal transport [150, 189] with regard to the influence of the spatial extent of the heat source.

To fully treat the (quasi-)ballistic regime Kn$\tilde{>}0.1$, one would need to solve the full *Phonon Boltzmann equation* (3.56) in conjunction with the full scattering operator (3.58). Evidently, this is both analytically and numerically a very demanding task considering the high amount of degrees of freedom. As heat transport in microscale devices, for example in microchips, is a topic also of commercial interest, there is a lot of literature treating the highly ballistic $Kn \gg 1$ and quasi-ballistic $Kn \sim 1$ regimes. Usually, analytic derivations either treat only one regime or are based on heavy assumptions such as full linearity of the problem, time independence or no boundaries [116, 150, 189, 190]. Numerically, one can use for example the *discrete ordinate method* to treat the PBE in the gray approximation by discretizing the phase space both in spatial as in the angular domain. Anyhow, the problem will become computationally very demanding when treating problems bigger than the single micrometer scale [191] while not providing very accurate results due to the gray approximation which ignores the range of phonon mean free paths spanning multiple orders of magnitudes. The probably most promising approach is to use statistical, Monte Carlo based simulations to treat the PBE [131], an approach which was considerably improved over the last decade. Particularly, the usage of a deviational model could

---

[50] Besides the boundary scattering, at zero kelvin the phonon lifetimes are also limited by spontaneous anharmonic decay [119], which is not implemented in the models by *Olson et al* [125] and *Wei et al.* [124].

[51] The heat transfer from the crystal to the holder, induced by the active cooling, mainly becomes important for the time $t_{\mathrm{rep,RF}} = 100\,\mathrm{ms}$ between two RF-pulses.

also be applied to more complex problems. In this model only the phonons which deviate from some equilibrium distribution at the base temperature or a transient distribution calculated by a simplified model are generated [192]. This severely lifts the computational demands on the MC simulations.

Unfortunately, none of these approaches can be directly used for the intermediate gain CBXFEL problem which is a strongly multiscale one. Due to the high amount of absorbed pulse energy at every round trip, the temperature jumps after absorption can be much higher than $\Delta T > 100\,\mathrm{K}$ as will be shown in Chapter **5**. So for one, this certainly can only very locally be described by a linearized BTE and all of the analytic models presuming homogenous linearity fail. Also, while some fractions of the crystal are at these elevated temperatures with local knudsen numbers $Kn^{(\mathrm{loc})} \ll 1$, others fractions initially remain at a low base temperature with $Kn^{(\mathrm{loc})} \sim / \gg 1$. This makes approaches developed for only one distinct regime unfeasible. It also introduces severely different scales for a Monte Carlo simulation, which additionally vary rapidly in time due to the fast thermal diffusion introduced by the high temperature gradient. Moreover, for a simple deviational MC with the reference distribution defined for the base temperature $n_\lambda^{ref}(T_{\mathrm{base}})$, the number of created phonons would be exceedingly high taking into account the $\sim T^3$ scaling of the specific heat (3.43) and therefore the phonon density after a rise of $\Delta T > 100\,\mathrm{K}$. While it should be principally possible to model this problem by using a sophisticated multiscale model[131, 193] in conjunction with an appropriate reference distribution, something alike was never done before to the extent necessary here. Introducing such a program would therefore be a research project on his own and is out of scope for this work.

While there is no proper alternative to using the Fourier's heat law to begin with, there are some strong arguments for its applicability to the current case, even though it unfortunately cannot be benchmarked. For the strong temperature jumps introduced by the X-ray pulse, the thermal transport in this region can be considered diffusional. At the same time, the thermal transport in the low T regions is ballistic to quasi-ballistic and, hence, diffusional approaches will be inaccurate following above argumentation. On the other hand, following the deviational approach with only the excess phonons created in the heated regions contributing to the thermal transport and considering the phonon density scaling with $\sim \Delta T^3$, these regions initially carry rather little thermal energy and therefore do not contribute much to the full thermal conduction. Hence, the error introduced by the usage of a diffusional model is rather small in the time shortly after absorption of the pulses when the temperature remains high. While cooling down, the lateral dimensions of the heated region also grow[88, 178]. At the time the temperature reaches a value for which a proper consideration of the BTE is necessary, the lateral extent of the heat source is bigger than the mean free path of the phonons if latter is reduced by diffusive boundary scattering. Consequently the influence of the lateral extent [150] on the deviation from a diffusional model can be considered small. Also, over many experiments for the reduction of thermal conduction due to the finite depth of a sample, the usage of reduced effective conductivities seems to capture the relevant physics [153].

Additionally, fully diffuse boundary scattering as applied in this work is a very conservative assumption. On one hand, this preserves the usage of diffusional laws into the high Knudsen number regime $Kn \gg 1$ in the in-plane direction (which is the most relevant for the thin diamond plate). In contrast, a higher fraction p of specular reflection at the boundaries would make the diffusional laws less applicable, as specular reflection does not limit the free path of phonons. For the same reason, though, a high p would lead to a higher overall thermal conduction [194]. So if the CBXFEL works with $p = 0$, it definitely also works for $p > 0$ even if the actual temperature distribution cannot be properly described by Fourier's law.

To summarize, the thermal answer to an CBXFEL pulse at low crystal base temperatures is properly describable by using the diffusive Fourier's heat law (4.36) in conjunction with a reduced thermal conductivity due to diffusive scattering. In this work this is implemented by using the software suite *almaBTE* [112] which calculates the thermal conductivity from first principles as described in Section **3.2.4**. Calculating the contribution of boundary scattering from first principles has the big advantage that its influence on each phonon mode λ can be individually assessed, taking into account the mode dependent three dimensional group velocity $\boldsymbol{v}_\lambda$, specific heat contribution C_λ and bulk mean free path $l_{\mathrm{mfp},\lambda}$. This promises to yield much more accurate results than using single gray model mean free paths [143, 146, 147] such as those displayed in Figure (4.6(b)). In *almaBTE* the reduced thin film thermal conductivity is calculated as [112]

$$\kappa_{eff}(t_c) = \sum_\lambda S_\lambda(t_c) C_\lambda \|\boldsymbol{v}_\lambda\| l_{\mathrm{mfp},\lambda} \cos^2 \vartheta_\lambda, \tag{4.38}$$

where S_λ is a mode and film thickness t_c dependent suppression function and ϑ_λ is the angle between the specific transport axis and the group velocity. The suppression function S_λ is modelled using a mode and angle resolved Fuchs-Sondheimer approach [142] averaged over the film thickness [112]:

$$\begin{aligned} S_\lambda\left(t_c\right) = & \frac{1 - p \exp\left(-{}^{t_c}/_{\tilde{K}_\lambda}\right) - (1-p)\left[1 - \exp\left(-{}^{t_c}/_{K_\lambda}\right)\right]}{1 - p \exp\left(-{}^{t_c}/_{\tilde{K}_\lambda}\right)}, \\ \text{with} \quad \tilde{K}_\lambda = & \left({}^{v_{\hat{\boldsymbol{n}},\lambda}}/_{\|\boldsymbol{v}_\lambda\|}\right) l_{\mathrm{mfp},\lambda}, \end{aligned} \tag{4.39}$$

where p is the fraction of specular reflection and $v_{\hat{\boldsymbol{n}},\lambda}$ is the projection of the group velocity on the axis normal to the film surface.

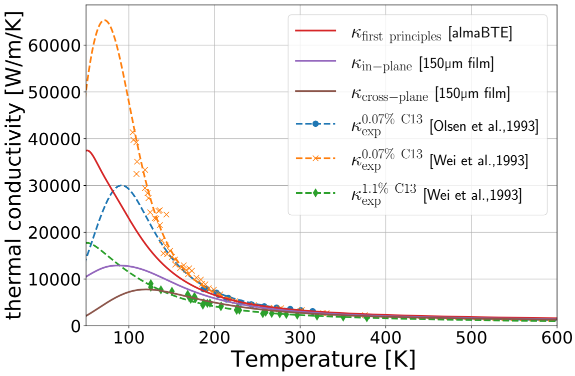

Figure 4.7: Thermal conductivities obtained from the first principles program *almaBTE* [112] for bulk diamond (red curve) as well as for diamond thin films of exemplary 150 µm thickness in in-plane (purple curve) as in cross-plane (brown curve) direction. Completely diffuse scattering is assumed. For comparison also experimental data and the respective fits are shown (see Figure (4.6(a))).

In Figure (4.7) the calculated thermal conductivity both for a bulk crystal as for the in- and cross-plane effective thermal conductivity in a t_c =150 µm thick diamond crystal is plotted. While the bulk curve cannot perfectly reproduce the thermal conductivity of the experimental measurements, it is well within the range of thermal conductivity variation with crystal quality. As the diamond used for the XFELO will be a high grade, X-ray optics quality one, a thermal conductivity better than a single crystalline natural type-IIa diamond is to be expected. As expected the effective thin film thermal conductivities are significantly reduced compared to the bulk values at low temperatures, while they match rather accurately at room temperature. Interestingly, the temperature of maximal thermal conductivity is also shifted due to the boundary scattering, making the T_{base}=50 K working point discussed in prior publications [26, 27] less attractive.

4.3.1 Simulating diffusive thermal transport: an External FEM Approach

For the computation of the thermal conduction problem, the *finite element method*(FEM) [195] based *heat transfer in solids* module of the commercial software *Comsol Multiphysics®* is used. Using the numeric approach of the FEM is advantageous to (quasi-)analytic solutions of the thermal transport problem [88, 178, 179, 196] as it can simulate both arbitrary heat load and initial temperature distributions and is able to calculate the nonlinear thermal answer both in spatial as in time domain. Using Comsol Multiphysics® has the additional benefit that it is very versatile and being actively developed providing very fast spatial and time domain solvers. Furthermore, it is very well benchmarked being an industry standard.

By assuming both an axial symmetric heat load as the cylinder symmetric thin disk geometry sketched in Figure (4.8(a)), the inherently three dimensional heat load problem is reduced to a two dimensional axial symmetric one. As the computational cost scales exponentially with the number of dimensions considered in the FEM, a two dimensional problem signifies an order(s) of magnitude speed up of the calculations compared to the three dimensional case. This is especially important as the thermal response is calculated for every crystal after each roundtrip through the cavity, so that for one single CBXFEL simulation run some hundred calculations are done. On the other hand, one has to keep in mind that the 2D axial symmetric assumption is a severe simplification and may introduce deviations compared to an actual setup.

For one, as mentioned above, it implies that the crystal sample has a disk shape with the X-ray pulse impinging on the center. Assuming a wide lateral extent of the crystal, the disk shape assumption might not introduce too much of an error. However, referring to a proposed three dimensional reflection geometry also used for the self-seeding setup at the European XFEL, sketched in Figure (4.8(b)), where the X-ray pulse impinges close to one of the outer boundaries, the assumption of a central interaction point clearly underestimates the influence of this particular outer boundary. The importance of an accurate three dimensional design of the crystal geometry, and the resulting differences in boundary conditions, is affirmed by *Z. Qu* in his PhD thesis [161, ch. 4.2].

Additionally, a positional jitter of the X-ray pulse on the crystal cannot be accounted for by the

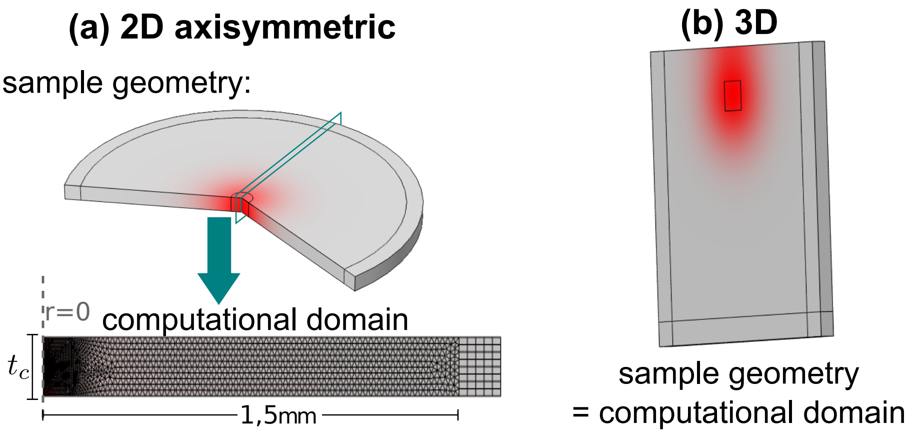

Figure 4.8: In (a,top) the axial symmetric thin disk sample geometry used for the Comsol Multiphysics® heat transport simulations is displayed. The red region marks the area where the X-ray pulse is incident. In (a,bottom) the two dimensional domain actually used for simulation is shown together with the FEM mesh. It is a slice at constant azimuthal angle through the origin. In (b) an actual three dimensional sample geometry is sketched, which might be actually employed in the CBXFEL demonstrator. Unlike (a) the interaction area is not in the crystal center but close by to one of the outer edges.

axial symmetric model. This, anyhow, can be considered of minor importance, as this positional jitter will be on the single to tens of micrometer scale while the heat conduction problem is on the millimeter scale.

The second strong simplification is the assumption of a axial symmetric heat load distribution. Also, this can be recognized as a small source of error, as, first, the same argument applies as for the positional jitter, and second, the resulting CBXFEL radiation actually is close to a axial symmetric one (see Chapter **5**).

Summarized, while the axial symmetric assumption is computationally necessary for studying the CBXFEL in a fully coupled fashion, especially the potentially wrong transverse position of the X-ray crystal interaction with respect to the outer boundaries may introduce errors. This has to be taken into account when making design decisions based on the simulative results presented here.

In Figure (4.8(a,bottom)) the computational domain, which basically is a slice through the center of the axial symmetric disk, is presented along with the FEM mesh of quadratic *Lagrange Elements* [197, ch.3.3.1] used for computation. In this geometry, all boundaries but the one at $r = R_{\max}$ were set as adiabatic/isolating. The boundary at $r = R_{\max}$ was set to isothermal with a prescribed temperature of $T_{\text{bndr}} = T_{\text{base}}$ to allow for outflow of the heat.

In Figure (4.8(a,bottom)) there are some features worth noting. For one, evidently the meshing is much finer at the origin $r = 0$ and becomes coarser with increasing r. This is due to $\dot{Q}$ being centered closely to $r = 0$ so that the temperature variation $\boldsymbol{\nabla} T$ is also highest there. As in the FEM the mesh must be able to resolve the variation of $\boldsymbol{\nabla} T$, this area naturally requires a denser meshing. The actual meshing was set by sweeping over mesh resolutions in the different regions in a multiple pass thermal transport simulation and setting the minimum resolution $\mathcal{R}$ after which the variations fell below a tolerance of $T_R - T_{R'} = 1E - 4$, where R' is the next finer resolution. In these simulations actual heat load profiles (4.33), similar to the one displayed in Figure (4.5), as obtained from a full CBXFEL run neglecting thermal transport, were used. Also, one may see that the mesh becomes equidistant and very coarse at the outer edge beginning at r =1.5 mm. This is to facilitate the usage of a so-called *infinite elements*(IE) domain integrated in Comsol Multiphysics®. Conceptually, an IE node applies a scaling to the internal radial coordinate such that the actual boundary conditions on the outside of the IE domain are effectively applied at a very large distance from the region of interest. This is of major computational advantage if one wants to simulate a crystal much bigger than the region of interest, which is the X-ray crystal interaction area in the CBXFEL case. Obviously, by integrating this feature, it is infeasible to study the actual long-time thermalization of the crystal to the crystal holder. Also, it is based on the strong assumption, that the boundaries will not have an effect on the thermal dynamics during one bunch train. Considering that the actual size of the crystal will be on the order of a couple of millimeters, above approximation is not perfectly accurate, but the introduced error is tolerable in view of the high computational gain. This is supported by Figure (4.9), which is displaying the homogenized crystal temperature for a plate shaped diamond crystal of size $V_c = 10\,\mathrm{mm} \times 5\,\mathrm{mm} \times 0.15\,\mathrm{mm}$ with (blue curve) and without (orange curve) thermal contact to a cupper holder for 300 round trips with $t_{\mathrm{rep}} = 4.44\,\mathrm{ns}$ spacing and individual absorbed heat energy of $Q_{\mathrm{abs}}^{\mathrm{tot}} = 63\,\mu\mathrm{J}$ at every pulse, corresponding to the heat load distribution in Figure (4.5). The calculation is based on the very artificial assumption of infinite thermal conductivity inside the diamond, which leads to a homogenous temperature at every time. This is strongly overestimating the thermalizing effect of the interface to the copper holder, as in the realistic case it takes some time for the heat to actually reach the interface. Then the temperature evolution in between the ith and $i+1$th X-ray pulse is fully determined by the interface conductance and can be calculated via

$$T_i\left(t_i\right) = \left(T_i(0) - T_{\mathrm{ext}}\right) e^{-G_{\mathrm{bnd}} A_{\mathrm{th}}.t}, \quad \text{with} \quad V_c \int_{T_{i-1}(t_{\mathrm{rep}})}^{T_i(0)} c_V(T')\mathrm{d}T' = Q_{\mathrm{abs},i},$$

where T_{ext} is the temperature of the holder, with $T_0 = T_{\mathrm{ext}}$ and set to $T_{\mathrm{ext}} = 77\,\mathrm{K}$, and for the right side an equality discussed a little bit below was used. A_{th} refers to the area which interfaces to the holder, which was assumed to be $A_{th} = 2 \times 4\,\mathrm{mm} \times 5\,\mathrm{mm}$ for this case, and G_{bnd} is the thermal interface conductance. Here, a value of $G_{\mathrm{bnd}} = 50\,\mathrm{MW}/(\mathrm{m\,K}^2)$ was assumed, which is very high compared to the literature value $G_{\mathrm{C-Cu}}^{\mathrm{lit.}} \approx 10\,\mathrm{MW}/(\mathrm{m\,K}^2)$ [198] for the interface between diamond and copper. Even under these strong assumptions, overestimating the thermalizing effect of the interface to the cupper holder, Figure (4.9) shows only little difference between the case with and without thermal conductance. Generally, it is quite clear that the temperature rise during one pulse train can be quite severe, reaching up to $\Delta T = 37\,\mathrm{K}$ after 300 pulses. This can only be mitigated by using a larger crystal.

The actual settings of the IE domain, specifically its distance to the origin $r = 0$ and the number of mesh layers, was set using the same approach as for the mesh resolution with the difference of using 20 heat pulses. The same approach was also applied for setting other numerically relevant

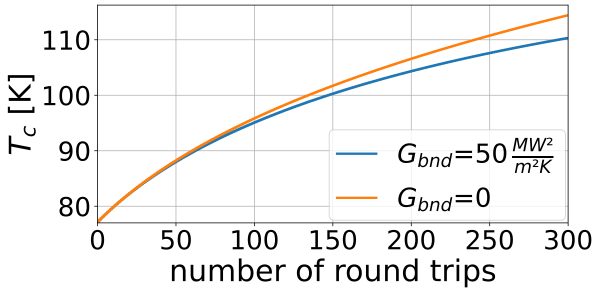

Figure 4.9: Temperature $T_c(t)$ of a plate shaped diamond crystal of size $V_c = 10\,\mathrm{mm} \times 5\,\mathrm{mm} \times 0.15\,\mathrm{mm}$ with (blue curve) and without (orange curve) thermal contact to a cupper holder at $T_{\mathrm{Cu}} = 77\,\mathrm{K}$ for 300 round trips with $t_{\mathrm{rep}} = 4.44\,\mathrm{ns}$ spacing and individual absorbed heat energy of $Q_{\mathrm{abs}} = 63\,\mu\mathrm{J}$ at every pulse. The area with thermal contact is assumed to be $A_{th} = 2 \times 4\,\mathrm{mm} \times 5\,\mathrm{mm}$. For the thermal interface conductance a value of $G_{\mathrm{bnd}} = 50\,\mathrm{MW}/(\mathrm{m\,K}^2)$ was assumed, which is very high compared to the literature value $G^{\mathrm{lit.}}_{\mathrm{C-Cu}} \approx 10\,\mathrm{MW}/(\mathrm{m\,K}^2)$ [198] for the interface between diamond and copper, which will probably be used for the experiment. The thermal conductivity of diamond was set to infinity, causing a homogenous temperature at all times, which is leading to a strong overestimation of the thermal conductance. Still, the difference between no thermal and with thermal interface is rather little.

parameters such as the error tolerance governing the time and the spatial solver.

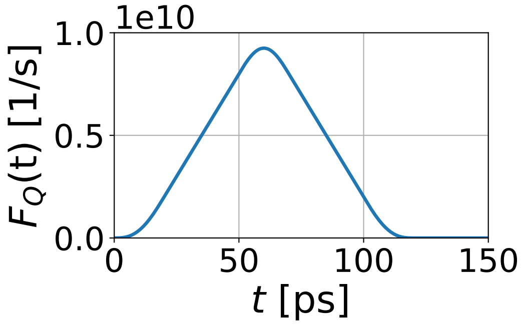

Figure 4.10: Temporal distribution of the absorbed heat used for the FEM simulations.

As was mentioned above and described in equation (4.37), the absorbed heat also has a temporal distribution besides the spatial one. As was discussed in **3**, this temporal distribution is not the same as the one of the incident X-ray pulse due to the duration τ_{therm} of the thermalization process. As this duration is unknown, a very rough estimate of τ_{therm} =100 ps is made. As the inertia of the thermal response after absorption is much larger, on the several nanosecond scale, fortunately, the actual value τ_{therm} is irrelevant in the context of this work. A smoothed triangle distribution as displayed in Figure (4.10) is chosen for modelling $F_Q(t)$, as it has proven to be numerically very stable. Analytically, under the assumption that $\boldsymbol{\nabla}(\boldsymbol{\kappa}\boldsymbol{\nabla}T) \ll \dot{Q}_{\mathrm{gen}}$ for $t \tilde{<} \tau_{\mathrm{therm}}$, equation (4.36) becomes (in equality to equation (3.47))

$$\rho \int_0^{\Delta T(\boldsymbol{x}_\perp, s)} c_V \left(\delta T + T_0\left(\boldsymbol{x}_\perp, s\right)\right) \mathrm{d}(\delta T) = Q_{\mathrm{abs}}(\boldsymbol{x}_\perp, s), \tag{4.40}$$

where $\Delta T(\boldsymbol{x}_\perp, s)$ is the temperature jump on top of the crystal temperature $T_0(\boldsymbol{x}_\perp, s)$ caused by the absorbed radiation energy. As such a delta-function like temperature jump can cause numerical difficulties, it is not applied here, but can be used as quasi-analytical benchmark for the temperature distribution after absorption.

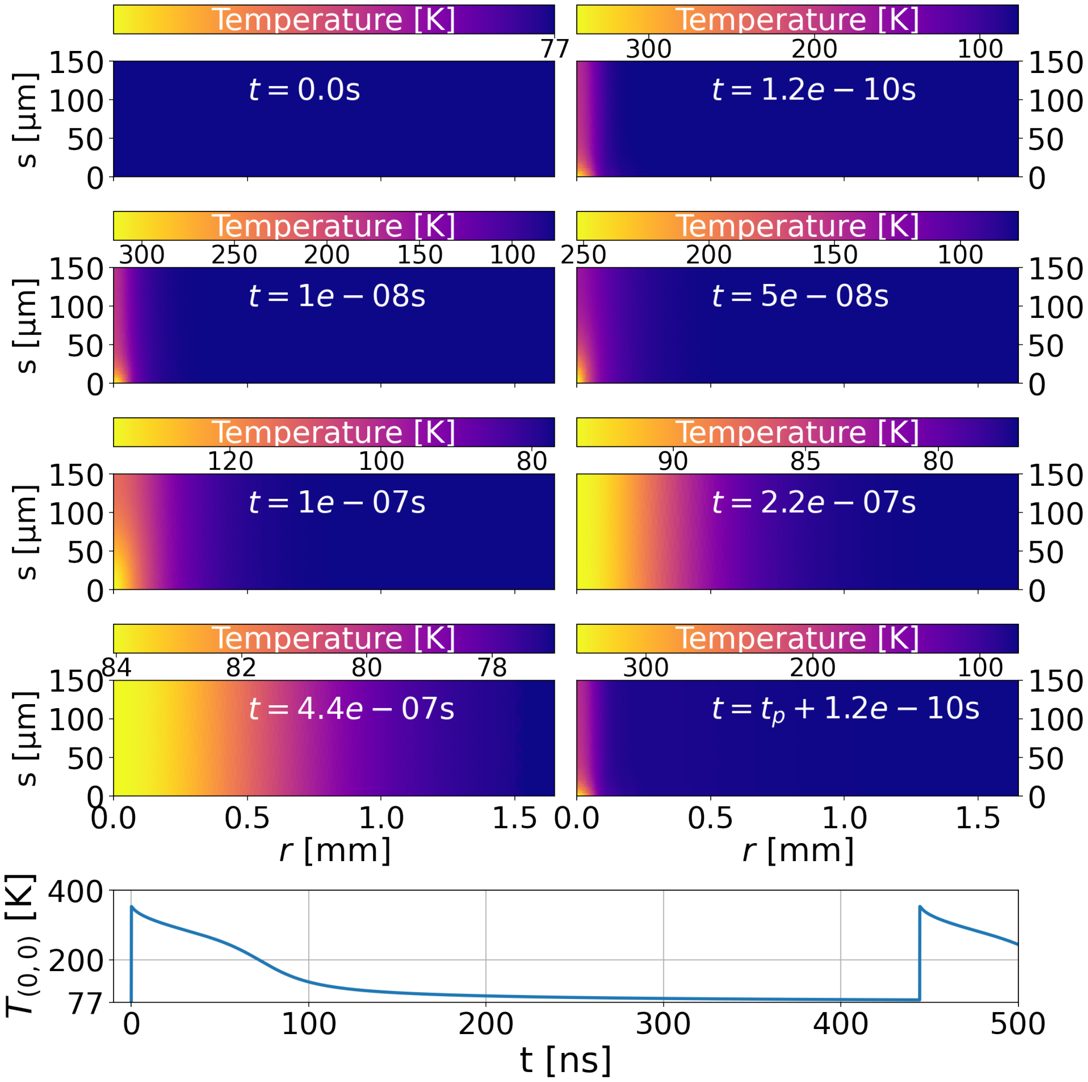

Figure 4.11: An exemplary temperature evolution after XFELO pulse. The image plots show the temperature distribution for different distinct times. The line plot in the bottom shows the temperature evolution vs time at the origin $(r, z) = (0, 0)$.

In Figure (4.11) a thermal transport simulation is shown starting at a base temperature of $T_{\text{base}} =$ 77 K with the input heat load distribution as displayed in Figure (4.5). Both in the bottom line plot showing the temperature evolution vs time at the origin $(r, z) = (0, 0)$ as well as in the top right plot one can see that the absorption of the CBXFEL pulse leads to a drastic temperature jump $\Delta T >$250 K. As the thermal conductivity of diamond is strongly reduced at these temperatures, it takes several nanoseconds for the heat to diffuse into the bulk of the crystal and also to homogenize along the z direction. This is especially visible in the bottom line plot, where the thermal evolution is almost linear in the first roughly 60 ns to 70 ns. This is due to the decrease in the thermal gradient ∇T compensating for the increase in thermal conductivity and vice versa. After this time, the increase in thermal conductivity becomes stronger than the decrease in gradient, leading the thermal diffusion to speed up. After another $\sim$ 50 ns the temperature homogenized over the region of interaction which is therefore slowing down the diffusion process at the origin. There are two important observations for the full CBXFEL simulations in the upcoming chapter. First, with the heat load profile used, it makes a big difference if the repetition time is $t_{\mathrm{rep}} = 444\,\mathrm{ns}$, like it was used here, or $t_{\mathrm{rep}} = 222\,\mathrm{ns}$ as it was originally planned. Second, also after $t_{\mathrm{rep}} = 444\,\mathrm{ns}$ the X-ray pulse crystal interaction region did not cool down back to the base temperature T_{base} =77 K. The influence of this remnant heating will be discussed in the next chapter.

5 A Cavity Based XFEL Demonstrator Experiment

This chapter shall describe a cavity based XFEL demonstrator experimental setup currently being developed at euXFEL and DESY.The basic idea of this setup is, as the name says, to demonstrate the working principle of a CBXFEL at the European XFEL accelerator. The major goal will be to prove that seeding occurs. This means that a radiation field builds up in the cavity which increases exponentially with subsequent round trips due to overlap with and seeding of the fresh electron bunches in the undulator. The second goal is to prove that stable operation of an CBXFEL is feasible. If this is not the case, for example due to heat load related issues, then the experiment shall give insights into these problems in order to develop strategies to overcome them.

This chapter is structured as follows. First, the design principles of the experimental setup will be highlighted. Then, thorough simulations based on the framework discussed in Chapter **4** will be presented. These serve to fix the base parameters of the setup, such as the photon energy, focussing strength and error tolerances. They also give an accurate estimate of the final output characteristics of the demonstrator. The simulations will be divided into three subparts, one for idealized simulations neglecting the impact of various sources of error and of heat load, one including error sources but neglecting heat load and the final one including error sources and the impact of heat load.

5.1 Design Principles

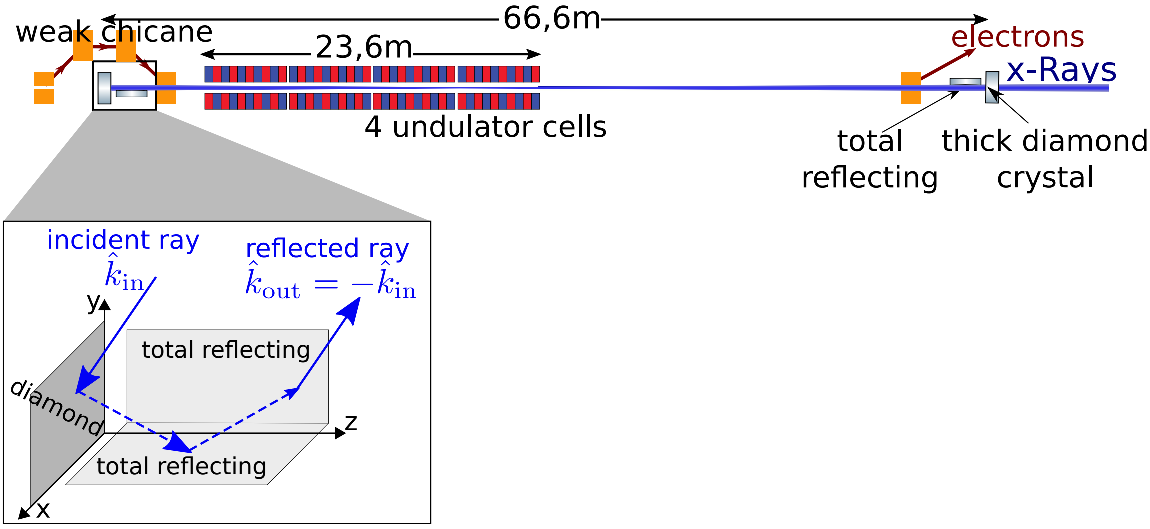

Figure 5.1: Conceptual design of the proof-of-principle CBXFEL demonstrator setup. It makes use of a retroreflecting mirror assembly, as will be shortly explained below and in more detail in Appendix **C**.

As was already touched above, the *Cavity Based X-FEL Demonstrator Experiment* is meant to prove the working principle of an (high-gain) CBXFEL source. It is not meant to leverage all the theoretically possible and advanced prospects such a source principally has to offer. In this regard, the basic design decisions towards the demonstrator are to keep the setup simple, taking

Figure 5.2: Picture of the exemplary undulator cell 32 of the SASE1 beamline during the construction phase. Credit: European XFEL GmbH

into account the electron parameters, the electron optics and the undulator lattice present at the European XFEL facility. This can be summarized by:

> As simple as possible, as complicated as necessary.

The conceptual design of the demonstrator, following these considerations, is depicted in Figure (5.1). It is planned as a two Bragg mirror back reflection cavity, dropping the potentially important feature of wavelength tunability (see Section **2.4**). This is due to two reasons. The first is to avoid the additional complexity and alignment steps introduced by the additional X-ray optical components necessary for a multiple Bragg-mirror cavity. This point is mitigated by the necessity to detune the crystal mirrors in the presented setup from exact normal incidence, which also requires the introduction of additional X-ray optical elements. This will be explained a little bit below. The second, more fundamental issue for the usage of a backscattering cavity geometry is the incompatibility of a multiple mirror scheme with the current EuXFEL undulator configuration. As clearly visible from Figure (5.2), in a multiple Bragg mirror configuration, where the incoming and the reflected radiation travel on clearly distinct path, the reflection angle needs to be along the horizontal tunnel axes as the vertical one is blocked by the support systems (see orange box above the undulator rack). The horizontal axis unfortunately is the same as the polarization axis of the synchrotron/FEL radiation produced by the planar undulators of the hard X-ray beamlines SASE1 and SASE2 of the European XFEL facility. Following equations Eqs. (3.19) to (3.24), this leads to a reduction of the polarization factor P and hence, to a reduction of the overall reflection R. At the extreme case of a reflection completely along the horizontal undulator axes, it would amount to a reflection of $R = 0$.

As mentioned above, a cavity configuration with the crystals in exact backscattering geometry is problematic. This is due to the multiple beam excitation discussed in Subsection **3.1.3**, which is always present for cubic crystals at 90° incidence due to the high symmetry and which reduces the reflection efficiency. There are two ways to get rid of these additional reflections. One is to use crystals with lower symmetry such as sapphire (α-Al_2O_3) [94, ch.2.5]. The other, trivial method which will be applied here to enable the use of cubic diamond, is to shift the angle of incidence by some milliradian using additional optical elements. More specifically, two grazing incidence mirrors, which will be aligned in nested Montel geometry (see **C.3**), will be used as sketched in Figure (5.1). The alignment needs to adapted such that only one beam is excited. The angular detune from exact backscattering necessary to achieve that is plotted in Figure (5.3) for the pitch-roll-yaw convention and the crystal plane orientation of Figure (4.4).

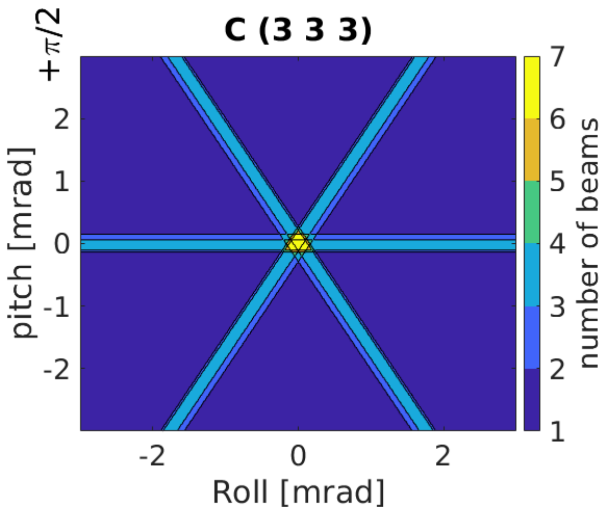

Figure 5.3: The number of orders participating in the reflection vs pitch and roll angle adapting the pitch-roll-yaw convention and the crystal plane orientation of Figure (4.4). The photon energy is matched to the exemplary, in this case symmetric C (3 3 3) reflection for all angles. It is worth noting that the area of multiple beam excitation would be widened by strain in the crystal.

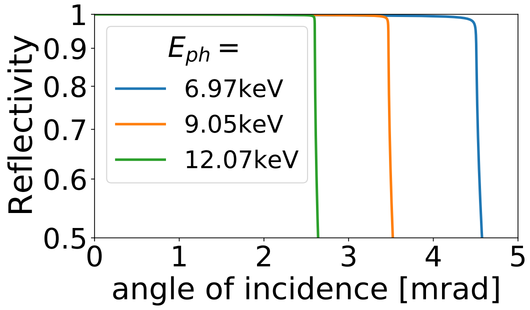

Figure 5.4: The reflectivity of B_4C against angle of incidence for different photon energies. The data is taken from `https://x-server.gmca.aps.anl.gov/TER_sl.html`.

The reflection efficiency of a common B_4C-coating is plotted in Figure (5.4) against the angle of incidence for three photon energies corresponding to the C(400), C(333) and C(444) reflection at normal incidence. Noting the mirror size as l, then the effective, approximately rectangular aperture introduced by the mirrors is $w^{\mathrm{ap}}_{x/y} = l \sin \Theta_{\mathrm{in},x/y}$ (see **C.1**). From Figure (5.4) and the observation that the maximum critical angle at which total reflection occurs scales inversely with photon energy, it is evident that lower photon energies allow for shorter mirrors. This is an important property, as the mirrors shall be as close as possible to the crystal mirror for reasons of stability and ease of alignment. Hence, they need to fit into the same mirror chamber. Requiring a reflection loss smaller than 5 ‰, the angles of incidence are $\Theta^{6.97\,\mathrm{keV}}_{\mathrm{in},x/y} \leq 3.86\,\mathrm{mrad}$, $\Theta^{9.05\,\mathrm{keV}}_{\mathrm{in},x/y} \leq 3.34\,\mathrm{mrad}$ and $\Theta^{12.07\,\mathrm{keV}}_{\mathrm{in},x/y} \leq 2.59\,\mathrm{mrad}$ for the C(400), C(333) and C(444) reflections, respectively. Assuming a lower limit of the aperture of $w^{\mathrm{ap}}_{x/y} \geq 300\,\mu\mathrm{m}$, as will be further highlighted in the simulation section, these correspond to $l_{6.97\,\mathrm{keV}} \tilde{>} 7.7\,\mathrm{cm}$, $l_{9.05\,\mathrm{keV}} \tilde{>} 9\,\mathrm{cm}$ and

$l_{12.07\,\mathrm{keV}} \gtrsim 11.7\,\mathrm{cm}$. If both mirrors are placed behind each other, these lengths need to be doubled. This is one of the reason why the 12 keV C(444) reflection case will be omitted in the following, even though it can be used with the same crystal orientation as the C(333) case. The second reason is that, under the precedence of a *proof of principle* experiment, the EuXFEL is running much more time at the $E_{\mathrm{ph}} \approx 9\,\mathrm{keV}$ photon energies than at $E_{\mathrm{ph}} \approx 12\,\mathrm{keV}$. Consequently, it should be much more straight forward to commission the FEL section at the lower photon energies.

While it would also be possible to only use one grazing incidence mirror to shift the crystal reflection from normal incidence, which would ease the size and or complexity of the setup, the use of two grazing incidence mirrors has a couple of advantages. For one, it will be necessary to apply focussing to the radiation beam to reduce the requirements on the optics alignment and beam stability. Adding two grazing incidence mirrors to each crystal, one can archive focussing in both transverse planes by applying meridional bendings to each mirror individually. The focussing length f is on the same scale as the crystal to crystal distance $L \approx 66.6\,\mathrm{m}$, as can be derived from the cavity stability criterion $0 \leq g \leq 1$ with $g = (1 - {}^{L}\!/_{2f_1})(1 - {}^{L}\!/_{2f_2})$ (see Appendix **D**). For the meridional focussing $R_m = {}^{2f_m}\!/_{\sin\Theta_{\mathrm{in}}}$ [4, p.136], one arrives at very slight bendings on the tens of kilometer scale, while for the sagittal bending, which would be needed for a single grazing incidence mirror, one arrives with $R_m = 2f_m \sin\Theta_{\mathrm{in}}$ [4, p.136] at bothersome bending radii on the centimeter scale.

A second advantage of the two grazing incidence plus one crystal mirror setup is, that by aligning them each with a 90° angle to each other, they form a so called *retroreflector* (for more details see **C.2**). A perfect retroreflector has the property that the reflected beam will always be perfectly antiparallel to the incoming one $\boldsymbol{k}_{\mathrm{out}} = -\boldsymbol{k}_{\mathrm{in}}$, no matter its direction $\hat{\boldsymbol{k}}_{in}$. For a setup where the individual elements have finite angular acceptance (limiting the angular acceptance of the full retroreflector accordingly) and which are not perfectly perpendicular to each other, this is obviously not the case. However, these angular acceptances are well above the hundred microradian level and, therefore, much more relaxed than the hundred nanoradian level that would be demanded otherwise. Also, as shown in the Appendix **C.2**, assuming a feasible dyadic error $\Delta\alpha = 2\,\mathrm{mrad}$ with respect to the 90° alignment of the grazing incidence mirrors, a compensation of the outer angular shift by more than two orders of magnitude can be achieved. By mounting the retroreflecting setup on the same stage, one can therefore effectively decouple the cavity from outer angular vibrations. On the other hand, angular movement or shift of the individual components with respect to each other, for example due to thermal load, will not be compensated.

As was mentioned above, using two grazing incidence mirrors behind each other would double the length of the setup, which might be problematic considering the finite size of the vacuum chamber. One can levitate this problem by using a nested, *Montel* geometry as described in the Appendix **C.3** and sketched in Figure (5.5). This has the advantage, besides the reduced overall length, that the mirrors' positions are fixed with respect to each other, reducing the overall individual degrees of freedom during alignment. The downside of this setup is, that at the edge

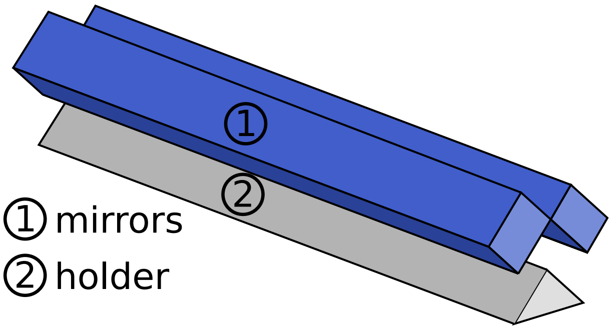

Figure 5.5: Sketch of a nested *Montel* geometry, where two mirrors are mounted perpendicular to each other on a common holder.

where both mirrors meet, a higher roughness or a physical gap can be observed, depending on the method of assembly [199]. The X-rays impinging on this gap, which can be assumed to have a size of w_{gap} =5 µm to 10 µm, can be conservatively assumed to not contribute to the seeding in the undulator section. In this sense, this area acts as a slit on the X-ray radiation field. The effect of this slit will be highlighted in the simulation section in **5.2.2.5**.

Another fundamental choice is the use of diamond as crystal reflector. This choice is due to the outstanding properties of diamond such as peak reflectivity [61, 200, 201], radiation hardness [202], low thermal expansion and absorption [61] and outstanding thermal conductivity at low temperatures [121, 124, 125]. Regarding the high thermal load on the crystals, these points are of high relevance towards the realization of a cavity based X-ray FEL [62, 90]. For this reason, the diamonds also need to be cooled to 'cryogenic'[52] temperature [26, 27, 62, 90]. The effect of heat load will be highlighted in Section **5.2.3**.

As discussed in Section **2.4**, there exist many different methods to couple out the radiation from the cavity. In agreement with the principle to keep the setup as simple as possible, with the use of the regular transmission through 'thick' diamond crystals [21] a very straightforward approach is applied. For an intermediate gain system, this approach has, as will be shown, the advantage of providing relatively high brilliance and spectral flux while being less affected by boundary scattering and elastic excitations compared to thin diamonds(see Sections **3.2.4** and Refs. [26, 27]).

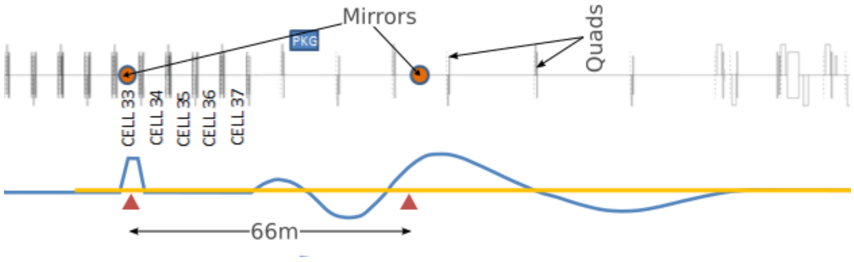

Figure 5.6: Schematics of the electron optics of the CBXFEL demonstrator experiment. The red dot and triangles represent the mirror positions in the upper and lower sketch, respectively. In the lower sketch the electron beam trajectory (blue) and nominal photon axis (yellow) are shown. Adapted from *W. Decking* (internal document). A more detailed sketch for the upstream mirror position is displayed in Figure (5.7).

The entire setup will be located at the end of the SASE1 beamline of the European XFEL facility.

---

[52] The term 'cryogenic' is a bit ambivalent. Here it refers to temperatures in the T_c =40 K to 100 K range, where as in other scientific areas 'cryogenic' refers to the at most single kelvin range.

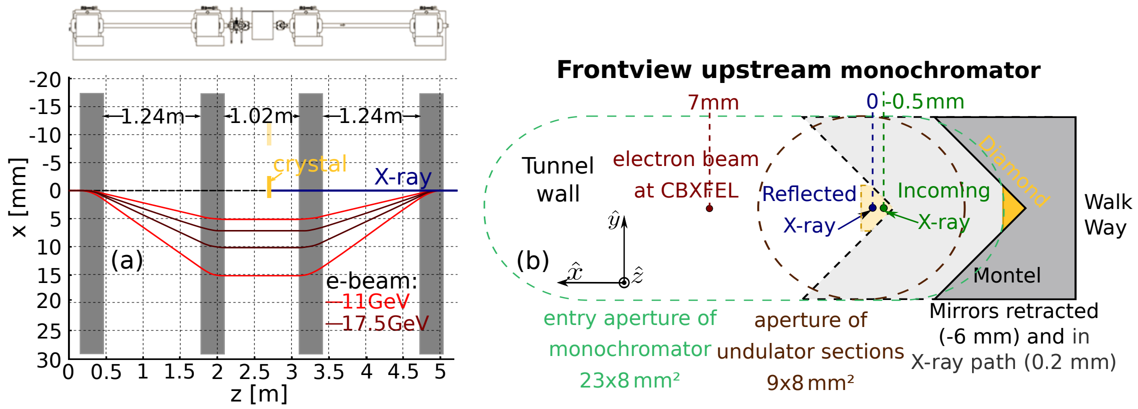

Figure 5.7: (a, bottom) shows a sketch of the four dipole chicane as used for the Hard X-ray Self-Seeding setup at SASE2 with possible transverse deflections for E_b =11 GeV and E_b =17.5 GeV. The $x = 0$ position refers to the nominal path of the electron beam with the chicane turned off, which coincides with the undulator axis. Then the crystal is retracted to the position x =−6 mm, which is shown as semi-transparent yellow patch. If the chicane is turned on, it can be inserted to x =0.2 mm to be on the nominal X-ray path. (a, upper) shows a top view drawing of the chicane layout. (Modified from [203] under a Creative Commons licence (`https://creativecommons.org/licenses/by/3.0/`).) (b) shows a frontview sketch of the inside of the upstream monochromator chamber in between the inner chicane dipols with the Montel (grey) and diamond mirror (yellow) positions. The opaque Montel and diamond patch show the retracted position for better visualization, whereas the semi-transparent patches show the position of the mirror and diamond inserted into the X-ray path. Also the projected aperture inside the undulator section is shown as brown dashed line and as light green dashed line the preliminary entry aperture into the monochromator chamber is displayed, which also needs to accommodate the deflected electron beam (red), which is shown for an exemplary deflection of x =7 mm for E_B =17.5 GeV. The green dot shows the X-ray path of the incoming X-ray pulse after reflection at the downstream mirrors and the blue dot the path after reflection at the upstream mirrors, which coincides with the undulator axis. The green dot has an offset of at least x =0.5 mm, which can be achieved by setting the position of the grazing incidence mirrors with respect to the diamond crystal. For the downstream mirror the position of the blue and green dot are switched. (Adapted from *H. Sinn*.)

As sketched in Figure (5.6), the fifth last undulator in cell #33 will be replaced by a four dipole chicane, which is the same as used for the Hard X-ray Self Seeding (HXRSS) setup at the SASE2 beamline [203] and which is sketched in Figure (5.7(a))[53]. A conceptual frontview of the inside of the vacuum chamber with the retroreflecting setup, which will will be placed in the center of the chicane, is displayed in Figure (5.7(b)). The actual three dimensional vacuum chamber geometry is in the process of being designed. It will be related to the chamber of the HXRSS setup presented in [204]. However, major modifications are necessary. For one, the chamber needs to additionally accommodate the multiple centimeters long grazing incidence mirrors. Second, the viewports will be set at different positions. For the HXRSS monochromator chamber a viewport with a scintillator screen was set at 90° above the crystal to use the corresponding bragg reflex at Θ_B =45° for calibration. However, the reflex at Θ_B=45° is far off the $\Theta_B \approx$90° as necessary for the CBXFEL demonstrator and, hence, the viewport has little purpose. Instead, viewports will be designed which correspond to the additional reflexes at perfect backscattering. And third, the actual rotational and translational stages will be quite different due to the

---

[53] The undulator cell will be shifted to the beginning of the beamline.

changed requirements of the CBXFEL monochromator compared to the HXRSS monochromator. The CBXFEL monochromator requires a much reduced range of angular motion, but with much more demanding tolerances on the nano radian level. Also, besides having the necessity of being moveable in the $\hat{\boldsymbol{x}}$ and $\hat{\boldsymbol{y}}$ direction, either the downstream or the upstream monochromator need to be tunable in the $\hat{\boldsymbol{z}}$ direction, to achieve almost exact synchronization of the X-ray circumference rate with the electron repetition rate. This additional $\hat{\boldsymbol{z}}$ tunability will be placed at the downstream mirror, which is placed outside the undulator area (see Figure (5.6) and text below) and, therefore, less constrained. The rotational and translational motion will be realized such that for all necessary degrees of freedom, which are all except the *yaw*-rotation (see Figure (4.4)) and the $\hat{\boldsymbol{z}}$ direction for the upstream monochromator, the mirror assembly including the diamond crystal will be moved. For the roll and pitch angle additional fine tuning stages will be added, which solely move the diamond crystal. The preliminary requirements for the individual stages, in accordance with the simulation results from Section **5.2.2** later on, are shown in Table 3.

Table 3: Preliminary requirements for rotational and translational stages at the CBXFEL monochromator. In the following M+C refers to the mirror assembly including the diamond crystal and C refers to the diamond crystal only.

Motion	Range	Repeatability	Nominal Resolution	Accuracy over Full Range
$\hat{\boldsymbol{x}}$-translation of M+C	−8 mm to 2 mm	5 µm	1 µm	5 %
$\hat{\boldsymbol{y}}$-translation of M+C	±2 mm	5 µm	1 µm	5 %
pitch-rotation of M+C	−0.5° to 1.5°	5 µrad	1 µrad	5 %
roll-rotation of M+C	±1°	5 µrad	1 µrad	5 %
pitch-rotation of C	±0.5°	100 nrad	30 nrad	10 %
roll-rotation of C	±0.5°	100 nrad	30 nrad	10 %

The vacuum chamber with the downstream mirror setup will be placed $L = 66.62\,\mathrm{m}$ downstream of the upstream one, outside of the undulator area. This distance matches the $f_{\mathrm{rep}} = 2.25\,\mathrm{MHz}$ repetition rate most commonly used at the EuXFEL. As the second chamber is outside the undulator area, the bounds on the electron trajectory are much less severe so that the already existing quadrupoles can be used to guide the electrons around the crystals as sketched in Figure (5.6). By properly adjusting the quadrupole strength, the electron beam can be returned to its nominal path and be distributed to the SASE3 beamline afterwards (see Appendix **B**). This quadrupole scheme also gives some space to place additional electron sensitive components. A disadvantage of this configuration is that the undulators are placed asymmetric with respect to the crystal mirrors, which will, hence, necessitate the use of assymetric focussing. This is, anyhow, rather straight forward. Additionally, as will be seen in the simulation section, this nominally produces a wider X-ray pulse on the upstream than the downstream mirror, which is helpful regarding the thermal management[54]. Also, the placement of the second mirror setup outside the undulator lattice has the severe advantage of not being bound to the undulator lattice period, which is not matching the electron repetition rate, and giving maximum freedom to the placement of components without disturbing the electron beam.

In order to maximize commissioning time, the experiment shall be compliant with the regular operation mode of the European XFEL SASE1 beamline, which is also why the mirror-mirror distance is matched to the commonly applied $f_{\mathrm{rep}} = 2.25\,\mathrm{MHz}$ electron bunch repetition rate. As such, it shall work with the regular electron optic parameters such as the quadrupole strengths in the undulator section, which yield an average beta of $\bar{\beta} = 32\,\mathrm{m}$ in the undulator region. Also, the demonstrator shall yield saturation with the 250 pC electron bunches which are usually used and therefore require the least tuning time. As the electron bunch phase space is of high importance for the FEL process, this 250 pC shall be shortly described in the following subsection.

5.1.1 250 pC electron bunch

In Figure (5.8) the electron beam distribution in the six dimensional phase space of the 250 pC bunch charge case is depicted. This beam distribution is what will be used for the simulations in the following Section. The data comes from thorough start to end simulations carried out by *I. Zagarodnov et al.* [205], which include the effects of incoherent and coherent synchrotron radiation, wakefields and space charge and were benchmarked to other programs and measurements at the actual accelerator. The electron energy is set to $E_{\mathrm{bunch}} = 16\,\mathrm{GeV}$, which is a little bit below the $E_{\mathrm{bunch}} = 17.5\,\mathrm{GeV}$ energy the European XFEL is designed for to run at in the future. However, the electron energy only enters approximately linear as well into the FEL gain (2.66) as into the saturated power (2.77), so small changes do not affect the overall results of the CBXFEL.

As can be seen from Figure (5.8), the electron bunch does not have a perfectly longitudinally flat distribution but has both transverse as well as longitudinal moments changing with the internal longitudinal position in the bunch. Especially the head of the bunch, which carries the highest charge density, is strongly distorted due to an interplay of space charge forces and wakefield effects. Following the 3D-gain estimation by *M.Xie* (2.74), this limits the contribution of the head to the FEL gain to less than one would expect from the high current.

Also, the bunch has a pronounced energy chirp, which was introduced to yield the peak current of 5.2 kA. For a seeded FEL, where the central wavelength is fixed by the seeding wavelength and the resonant condition is fixed to a certain electron energy, such an energy chirp leads to a decrease of the overall FEL gain. This as well as the non-flat current and transverse distribution lead to a differential gain, where the FEL gain changes with the longitudinal position in the bunch.

---

[54] As the downstream mirror is always the first to be irradiated by the freshly produced photons from the undulator section, it will see a higher heat load than the upstream which will see only the reflected pulse with reduced pulse energy. By adjusting the pulse width one could still reach the same peak radiant fluence. However, the range of beam width adjustment is rather limited due to the requirement for a stable cavity configuration.

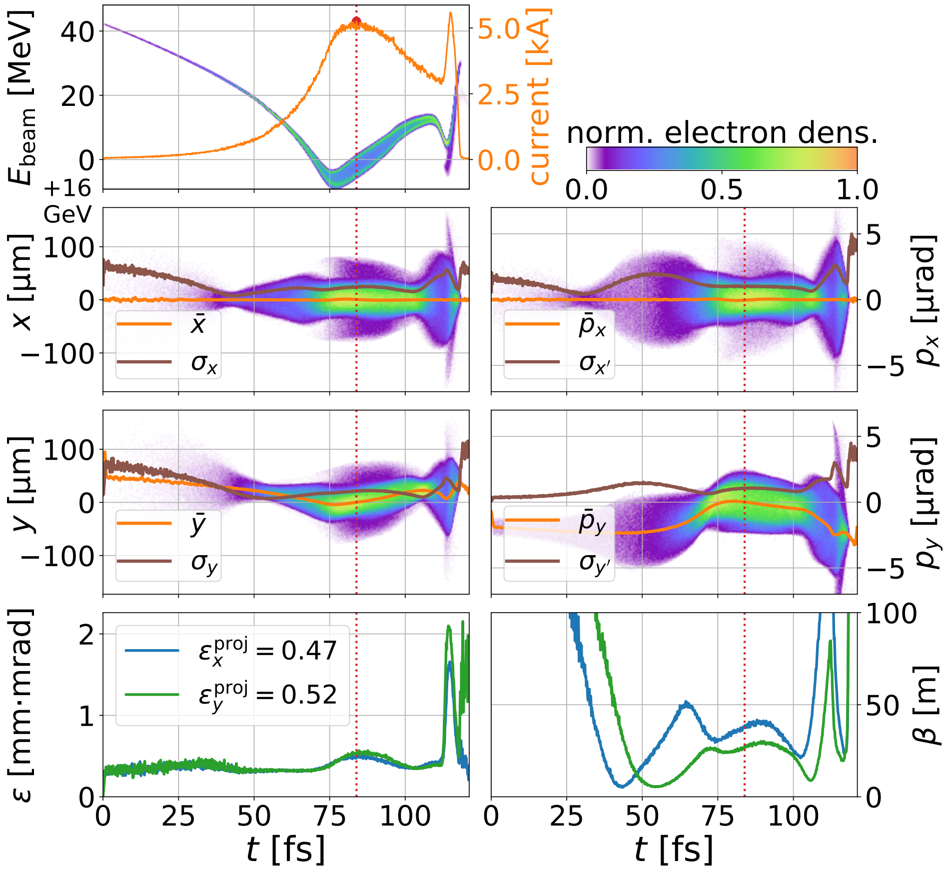

Figure 5.8: Phase space of the 250 pC electron bunch as simulated by *I. Zagarodnov et al.* [205]. The vertical, dotted red line denotes the transverse slice of the electron bunch which is matched to the electron optics. The data in the bottom left plot refers to the normalized emittance $\epsilon^n = \epsilon^{\mathrm{geom}} v\gamma_B/c$, where ϵ^{geom} is the beam energy γ_B dependent geometric emittance, v is the electron velocity and c is the speed of light.

This is sketched in Figure (5.9(a)) for the simplified case of a single frequency, constant seed focussed to the mid of the third undulator and matched to the reference slice displayed in Figure (5.8). Due to the effects discussed above, for both relevant seeding photon energies $E_{\mathrm{ph}} = 6.97\,\mathrm{keV}$ (blue) and $E_{\mathrm{ph}} = 9.05\,\mathrm{keV}$ (red) discussed in this work, the gain strongly deviates from the form of the current profile. This also results in a much reduced temporal duration of the newly produced FEL radiation. Also, it has to be noted that the points of maximum gain with $L_{G,\mathrm{min}} \approx 4\,\mathrm{m}$ for $E_{\mathrm{ph}} = 6.97\,\mathrm{keV}$ and $L_{G,\mathrm{min}} \approx 4.7\,\mathrm{m}$ for $E_{\mathrm{ph}} = 9.05\,\mathrm{keV}$ are not at the reference slice, but slightly shifted to the position of minimal rms width σ_x and σ_y.
The corresponding spectra are displayed in Figure (5.9(b)). As the frequency width of a distribution corresponds to its temporal duration, following Fourier's limit, the bandwidth of the spectrum becomes rather wide even when seeded by a perfectly monochromatic beam. The widths of the resulting spectra are also much wider than the corresponding spectral reflection widths of the diamond C(400) and C(333) reflection. This will lead to strong spectral sidewings. While these are only reflected very little, they can be nearly completly transmitted. This serves as the main outcoupling mechanism of the demonstrator, as will be shown in more detail in the

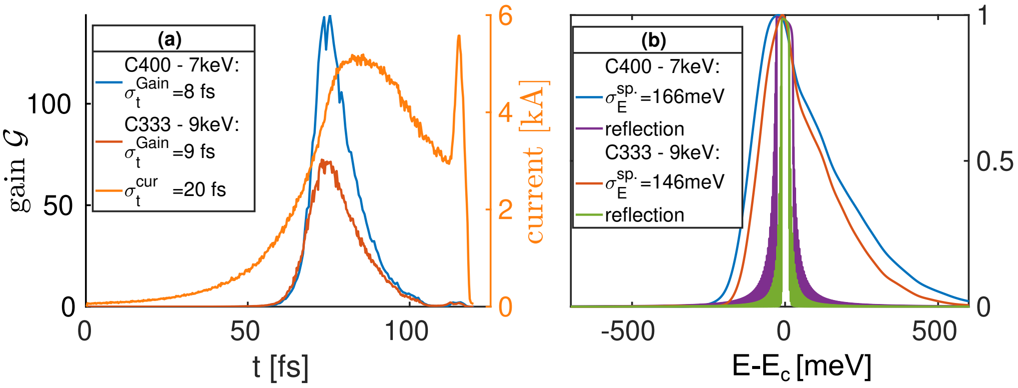

Figure 5.9: Results of *Genesis-1.3* runs without shot noise and single frequency seeds focussed to the mid of the second undulator of four undulators. (a) shows the resulting longitudinal gain profile for a $E_{\mathrm{ph}} = 6.97\,\mathrm{keV}$ (blue) and a $E_{\mathrm{ph}} = 9.05\,\mathrm{keV}$ seed (red) in comparison with the bunch current profile (orange). The widths of the gain curves are much shorter compared to the current for either photon energy. (b) displays the spectrum of the $E_{\mathrm{ph}} = 6.97\,\mathrm{keV}$ (blue) and the $E_{\mathrm{ph}} = 9.05\,\mathrm{keV}$ seeded FEL (red) at the end of the undulator. Both spectra are much wider than the spectral bandwidths of the respective C(400), $E_c = 6.97\,\mathrm{keV}$ (purple) and C(333), $E_c = 9.05\,\mathrm{keV}$ (green) reflections.

next section.

5.2 Performance of the CBXFEL demonstrator

In this section, based on thorough simulations, the performance of the CBXFEL demonstrator experiment shall be discussed for varying sets of parameters such as photon energy, focal length and numerous sources of errors. First, the situation without any errors will be presented for an exemplary photon energy of E_{ph} =9.05 keV to discuss the basic characteristics of the CBXFEL experiment. This will then be compared to the E_{ph} =6.97 keV case. These photon energies, corresponding to the C(400) and the C(333) reflection, respectively, have the additional advantage that they are in the range commonly used for user experiments and therefore do not request excessive tuning time. Afterwards, different sources of error will be introduced, including statistical shot to shot variations of the electron bunch arrival time, pointing and positions. This will be referred to as jitter in the following. Also, different effects introduced by the optical mirrors setup will be studied.

These include the angular and longitudinal misalignment of the mirrors, introducing a tilt and a time shift, respectively. Also the influence of the finite size of the grazing incidence mirrors, effectively introducing apertures into the optical system, the surface shape of the errors introducing wavefront distortions and, for the case of the Montel mirrors, the effect of the central ‘gap’, will be highlighted. Furthermore, the impact of (mounting) strain in the diamond crystal will be sketched. These mirrors will then be combined to study the feasibility of a demonstrator. This will be repeated with a reduced number of three actual undulator segments to make sure that the experiment can surely yield sufficient single pass gain to compensate for the cavity losses. Finally, the influence of the heat load on the system will be studied, primarily with the simplification of the thermal response being sufficiently described by the thermal diffusion, therefore neglecting the dynamic elastic response. However, latter will be included in a last study step to give an estimate of the impact of this process.

For the comparison of the CBXFEL performances, the radiation characteristics presented in Section **2.1** are frequently used. Especially the pulse energy, the bandwidth, temporal duration, temporal coherence and the brilliance are values which will be presented at the end of many paragraphs for saturation, meaning the state when the FEL gain and the per round trip losses cancel out. Also, different measures of gain will sometimes be used. These will be called the round trip (rt) gain and the FEL gain. The round trip gain is calculated using

$$\mathcal{G}_{\mathrm{rt}}^{\mathrm{pos}}(\#\mathrm{rn}) = \frac{Q_{\mathrm{pulse}}^{\mathrm{pos}}(\#\mathrm{rn})}{Q_{\mathrm{pulse}}^{\mathrm{pos}}(\#\mathrm{rn}-1)} - 1, \quad \mathrm{with} \quad \mathrm{pos} = \text{und or seed}, \tag{5.1}$$

where #rn is the round trip number. $Q_{\mathrm{pulse}}^{\mathrm{und}}$ is the pulse energy of the radiation directly after the undulator, entering the cavity and before reflection, and $Q_{\mathrm{pulse}}^{\mathrm{seed}}$ is the energy of the radiation reentering the undulators, after the reflection and seeding the upcoming electron bunch. The FEL gain is estimated as the integration over the time domain gain profile (2.56) and can be calculated as

$$\mathcal{G}_{\mathrm{FEL}}(\#rn) = \frac{Q_{\mathrm{pulse}}^{\mathrm{und}}(\#\mathrm{rn})}{Q_{\mathrm{pulse}}^{\mathrm{seed}}(\#\mathrm{rn}-1)} - 1. \tag{5.2}$$

While the round trip gain of the seeding pulse is a quite accurate measure of the actual seeding efficiency over the entire range of round trip numbers, the round trip gain of the undulator pulse and the FEL gain are unsuitable in this regard during the startup. As they incorporate the initially dominating synchrotron and SASE radiation background, they yield nonphysically high values during the first round trips.

5.2.1 The CBXFEL without error sources

5.2.1.1 C (3 3 3) reflection at 9.05 keV: As discussed above, the CBXFEL for the exemplary photon energy of E_{ph} =9.05 keV and neglecting the different error sources will be highlighted here.

For the idealized resonator without any additional losses but the outcoupling loss and the mirror absorptions, one can make a good estimate for the ideal focal lengths from gaussian resonator theory (see Appendix **D**) . Letting the radiation pulse waist be at the mid of the last undulator and matching the Rayleigh length to the reference particle as indicated in Figure (5.8), one arrives at an almost symmetric, confocal resonator with focal lengths $f_1 = 46\,\mathrm{m}$ for the downstream and $f_2 = 67.2\,\mathrm{m}$ for the upstream mirror assembly. The evolution of the gaussian beam waist for a stable resonator is displayed in figure Figure (5.10). It shows good matching with the electron beam and a wider radiation pulse width at the downstream than on the upstream mirror, which promises to be advantageous towards treating the impact of heat load.

The whole process from the shot noise dominated start up regime to the saturation regime shall

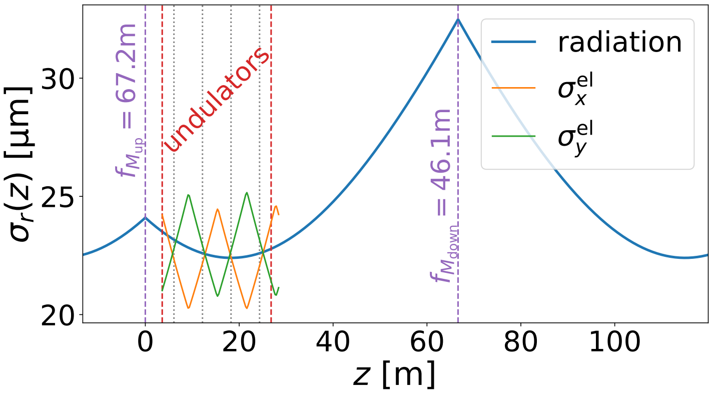

Figure 5.10: The radiation intensity rms width σ_r (2.12) (blue curve) in the X-ray cavity from optical resonator theory (see Appending **D**) for an asymmetric focussing of $f_{M_{\mathrm{down}}} = 46\,\mathrm{m}$ for the downstream mirror assembly and $f_{M_{\mathrm{up}}} = 67.2\,\mathrm{m}$ for the upstream one. These are matched to obtain a Rayleigh length of $z_R = \frac{4\pi\bar{\sigma}^2_{\mathrm{el},r}}{\lambda} = 46\,\mathrm{m}$ in accordance with equation (2.76), where $\bar{\sigma}_{\mathrm{el},r}$ =22.5 μm is the average electron beam size. Also the electron beam width $\sigma_{x,y}$ for the x and y coordinate are displayed as orange and green curves, respectively, showing a good transverse matching of radiation field and electron beam. The purple dashed, the red dashed and the grey dotted vertical lines highlight the position of the mirrors, the start and end of the undulators and the centers of the four undulator cells, respectively. The plot is periodic in z as it assumes the infinite extension of the optical cavity by the mirrors.

be discussed including the properties of the actually outcoupled photon pulses. This will serve as a reference for the following simulation results which will be reviewed in less detail.

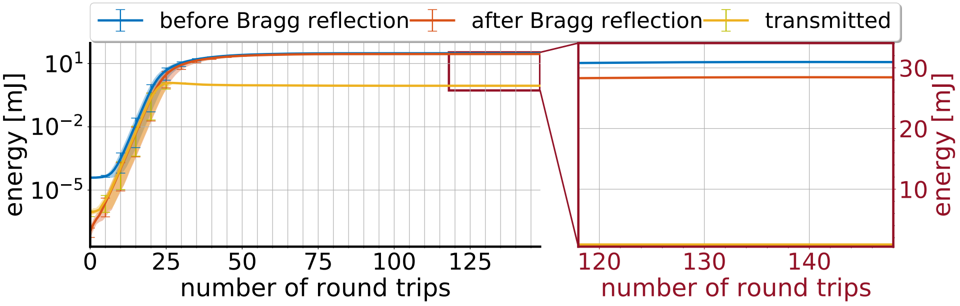

Figure 5.11: The left plot in logarithmic scale shows the full evolution of the pulse energy versus number of round trips. The right plot in linear scale displays a stable photon beam after saturation at very high pulse energies. The data was averaged over 15 individual runs/bunch trains with the shaded area showing the minimum/maximum values from these runs.

Figure (5.11) shows the photon pulse energy Q_{pulse} in mJ versus the number of round trips since startup for the radiation pulse directly after the undulator (before spectral filtering at the crystal mirrors, blue curve), for the radiation pulse after transversing the cavity (after reflection and before reentering the undulator to seed the upcoming electron bunch, red curve) and the transmitted pulse (orange curve). One has to note that at the startup the pulse energy of the blue and the orange curve are too low, as only a lower bandwidth fraction of the entire synchrotron radiation background is actually simulated to keep computational expenses at a minimum.

In Figure (5.11) one can basically distinguish between three regions. The first is the startup region, where the blue curve before reflection is largely independent of the seeding power (red curve) and there are strong differences in the seeding strength between the individual runs/bunch trains, as will be discussed in more detail a little bit below and is visible in Figure (5.16). The second is the exponential growth region, where the slope of both blue and red curve is constant and mostly the same for the individual bunch trains. The third region is the saturation regime, where the roundtrip gain first decreases and then becomes zero, leading to nearly completely stable shot to shot statistics. These three regions shall be discusses in the following.

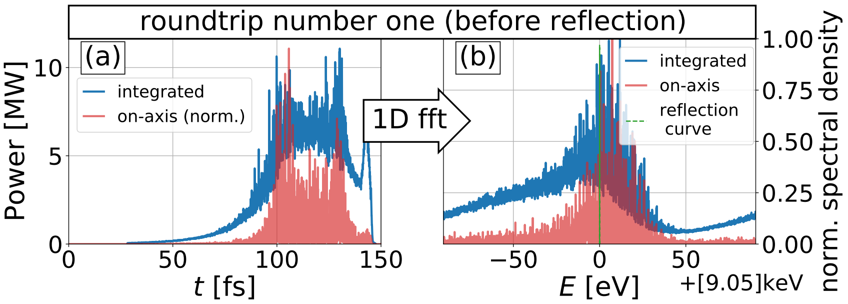

Figure 5.12: (a) and (b) display the longitudinal time domain and frequency domain radiation distributions of the radiation pulse directly after the undulator at the first pass of an exemplary bunch train. The blue curves represent the data integrated over the transverse space, following equations (2.3) and (2.4), having strong contributions of synchrotron radiation, and the light red curves the on-axis data being dominated by the SASE process. All curves are very noisy and the integrated frequency spectrum has a strong synchrotron radiation background, leading to a very wide bandwidth. This large bandwidth also leads to numerical *aliasing* in the spectral domain, apparent as a rising spectral energy density of the blue curve at the right site of (b). However, this does not affect the spectral energy density at the reflection energy and therefore the reflected spectrum. As a guide for the eye, in (b) also the cumulative reflection curve of the crystal mirrors is shown in green, appearing as a vertical line due to the much smaller bandwidth.

In the startup regime, the radiation is dominated by SASE with a strong synchrotron radiation background as visible in Figure (5.12), which displays (a) the time-domain intensity profile and (b) the corresponding frequency distribution. Both distributions consist, as expected from SASE, of thousands of longitudinal spikes, each representing an independent longitudinal mode. The integrated power profile in Figure (5.12(a)) interestingly reflects the electron bunch current distribution much more closely than the seeded gain profile presented in Figure (5.9(a)). This is due to the SASE process being much less sensitive to the electron bunch energy chirp and the synchrotron background being more accepting towards high emittance transverse distributions. Latter point becomes obvious when comparing the on-axis power (light red) with the integrated intensity. As the spontaneous synchrotron radiation has a much wider transverse distribution compared to SASE (see Section **2**), its relative contribution to the on-axis power becomes very small. Analyzing the difference between the blue and light red curve, evidently the contribution of current spike at the head of the electron bunch is strongly suppressed in the SASE process due to its large emittance (see Figure (5.8)). Generally, the SASE contribution has a shorter temporal duration than the synchrotron one, for the same reason that it is sensitive to distortions of the transverse phase space which are also quite strong in the tail of the bunch.

The spectrum displayed in Figure (5.12(b)) is, as expected, orders of magnitude wider than the spectral reflection width of the C(333) reflection. The synchrotron background apparent in the integrated spectrum (blue curve) additionally exhibits a very long spectral tail. This is due to the resonant energy scaling with the angle of radiation $\boldsymbol{\Theta}$ (as indicated in equation (2.38)), which becomes rather large for synchrotron radiation. Because of this large bandwidth, one can also observe a numeric artefact introduced by the finite sampling rate in time domain, which is the *aliasing*. As one can directly see for the blue curve in Figure (5.12(b)) the spectrum is cut on the left side before declining to zero. The fraction being cut is then reentering the spectral representation on the right side, which leads to the impression that the spectrum rises again after reaching the critical photon energy (2.38) at $E_{ph} = 9059\,\mathrm{eV}$. Luckily, this does not affect the XFELO process for two reasons. First, as qualitatively apparent from Figure (5.12(b)), this aliased fraction becomes very small at $E = E_c = 9.05\,\mathrm{keV}$. Second, even if no band filter would be present, these contributions correspond to large Θ, which would not contribute to the seeding process due to the finite angular acceptance of the optical cavity.

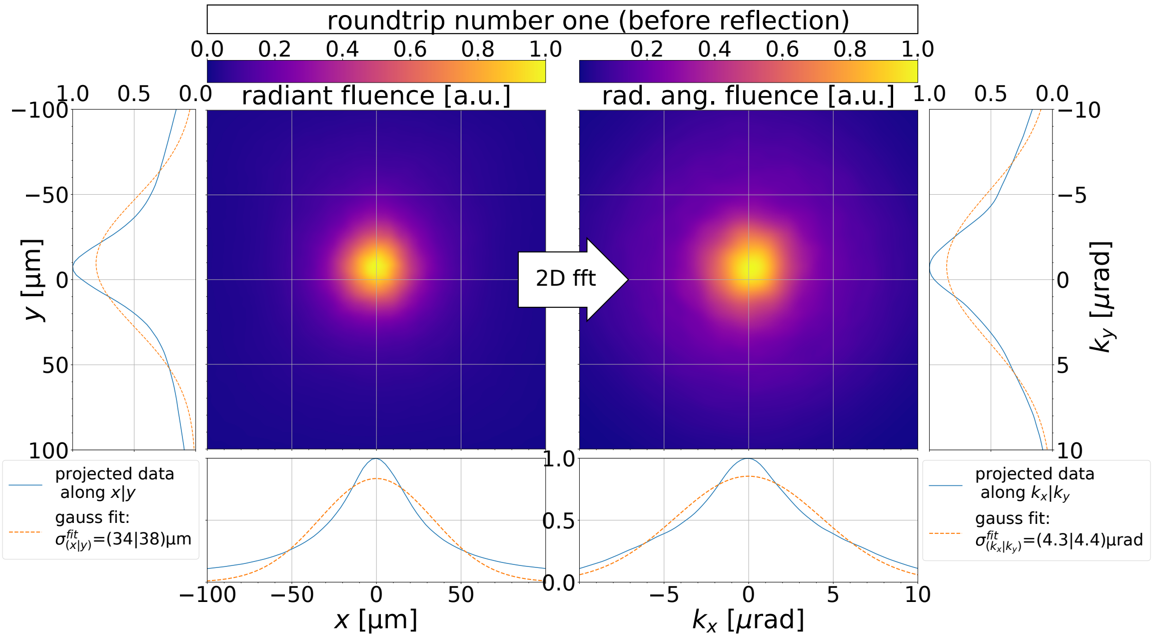

Figure 5.13: The left side of the figure represents the transverse distribution of the radiation pulse leaving the undulator in the spatial domain and the right side the corresponding distribution in angular domain, both integrated over the frequency domain. The one dimensional graphs on the bottoms and the sides of the two dimensional ones represent the projections of the fluence on the x- and y-axis, respectively. While the full two dimensional representations appear rather normal distributed, it is evident from the 1D projection in comparison with the respective gaussian fits (in red) that the distribution rather follows a lorentzian than a gaussian shape. This is due to the strong synchrotron background which has a much wider spatial and angular extent than the SASE fraction. All graphs only show a subset of the full simulation window.

Corresponding to the longitudinal representation in Figure (5.12), Figure (5.13) displays the radiant fluence (2.5) and radiant angular fluence (2.7). These are representing the spatial and angular distribution, respectively. While both do not follow a normal but rather a lorentzian distribution, due to the overlapping contributions of synchrotron background and SASE, they clearly are smoothly distributed. As will be shown below, this is primarily due to the averaging over the thousands of longitudinal modes, whereas each longitudinal mode rather is chaotically transverse distributed.

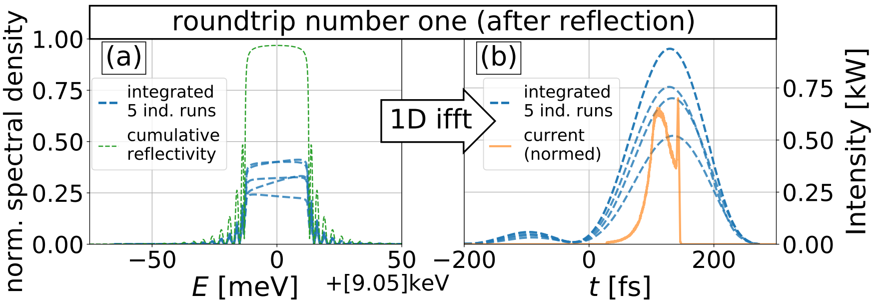

Figure 5.14: The blue curves in (a) and (b) display the integrated longitudinal frequency domain and time domain radiation distributions of the radiation pulse after spectral filtering at both diamond C (3 3 3) mirrors. The first pass of five individual bunch trains is displayed. The green curve in (a) represents the spectral reflection curve following the dynamic diffraction theory. It is evident in (b) that the reflected curve is much wider than the actual current distribution (orange) due to its much reduced bandwidth.

After reflection at the two diamond C (3 3 3) mirrors, as presented in Figure (5.14(a)) for five different bunch trains, only a tiny fraction of the full spectrum Figure (5.12(b)) is cut out, with the spectral peak fluctuating from bunch train to bunch train. One would normally expect from SASE radiation that the spectral peak should be fluctuating over nearly 100 %. This is not the case here, as the different angular components of the synchrotron radiation lead to a smoothing of the spiky on-axis radiation spectrum with $E_c(\Theta) \propto (\gamma^2\Theta^2)^{-1}$ (see equation (2.38)), which results in an almost constant base level of the spectral value. In the time domain, as displayed in Figure (5.12) the corresponding intensities profile fluctuate over the same magnitude. Also, the duraton of the reflected radiation pulse is much longer than the incoming pulse displayed in Figure (5.12(a))[55]. This poor matching in the time domain will obviously lead to a decrease in the integrated (energy) gain.

In Figure (5.15) the radiant fluence and radiant angular fluence after reflection at both diamond mirrors are displayed. Clearly, both the spatial as the angular distributions are distorted and strongly deviate from the ones before reflection, displayed in Figure (5.13). This is due to the lack of the averaging over the multitude of longitudinal modes. Among others, *Pelligrini et al.* discussed in [206] that each longitudinal mode of a (SASE) FEL initially exhibits a pronounced speckle pattern, which As in the short four undulator sections FEL gain guiding is not yet very effective, each longitudinal mode still comprises many different transverse modes, with the transverse mode strength statistically varying for every longitudinal mode. When averaging over thousands of these longitudinal modes, the in average nonetheless strongest TEM00 mode becomes dominant and the averaged distribution becomes approximately gaussian[56]. This is in accordance to, amongst others, the argumentation by *Pelligrini et al.* in [206] that each lon-

---

[55] Mathematically, this is due to the small frequency bandwidth $\sigma_f = 2.2\,\mathrm{THz}$ and the time-bandwidth product $\sigma_f\sigma_t \geq {}^1\!/_{4\pi}$, leading to $\sigma_t \geq 35\,\mathrm{fs}$, which is further widened due to the longitudinal distribution deviating from a transform limited gaussian. Physically, the widening is caused by the statistical distribution of the photon scattering events in the crystal, with the photons penetrating further being retarded with respect to the photons being scattered at the very surface.

[56] As explained above, the deviation of the gaussian form in Figure (5.13) is due to the different spatial extent of the synchrotron and the SASE contributions.

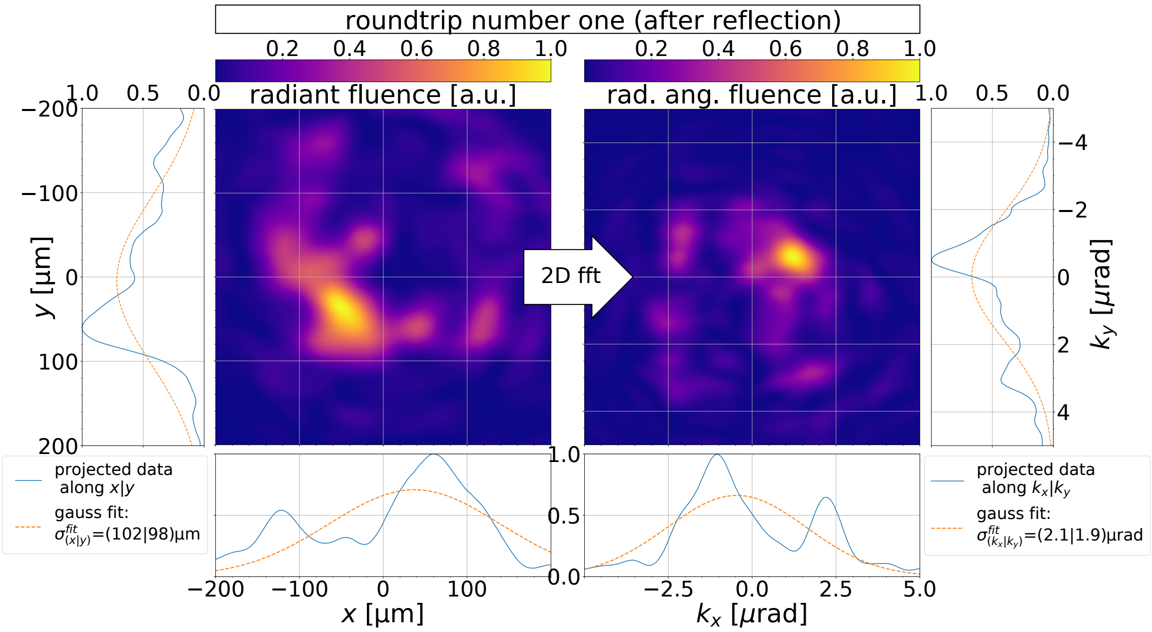

Figure 5.15: The radiant fluence (2.5) (left) and radiant angular fluence (2.7) (right) after spectral filtering at the C (3 3 3), representing the transverse distribution of a single longitudinal mode. Both angular and spatial distributions are disturbed with respect to the radiation before reflection in Figure (5.13). All graphs only show a subset of the full simulation window.

gitudinal mode of a (SASE) FEL initially exhibits a pronounced speckle pattern, which grows increasingly coherent with undulator length due to gain guiding. As above, *Pelligrini et al.* also discussed that due to averaging over many longitudinal modes, this speckle pattern is hardly visible when imaging the transverse distribution of the entire SASE spectrum.

Apart from the different functional form of the distribution curves, also the spatial rms width σ_r and the rms divergence σ_k are very distinct from the ones directly behind the undulators. The much reduced rms divergence σ_k is due to to two points. First is the focussing effect of the lenses, which should anyhow for ideal matching yield the same divergence as the newly produced radiation. The second, stronger influence is that the high Θ synchrotron contributions have critical frequencies $E_{c,\text{und}}(\Theta) < E_{\text{reflection}}$ and are therefore not existent in the longitudinal mode selected by the diamond's spectral filtering. Also, the rms spatial width σ_r is almost trice as big as anticipated from resonator theory (see Figure (5.10)). This is due to the transverse field evolution in Figure (5.10) being based on a pure TEM00 mode, which is not the case here, leading to a bad matching of transverse radiation and cavity modes. As the actual transverse radiation modes are, for the case of no seeding, differing from shot to shot, this bad transverse matching is the dominant reason for the high fluctuation of the seeding efficiency in the startup regime, as apparent from the energy evolution Figure (5.11) and the variation of the seeding round trip gain (equation (5.1)) for the second round trip displayed in Figure (5.16). Especially under the influence of errors or in the presence of (effective) apertures, as will be presented later, this bad transverse matching can severely limit the initial seeding efficiency.

With every roundtrip the seed becomes a bit stronger until, after a few round trips, the corresponding amplifying process is dominating over both SASE and synchrotron background inside

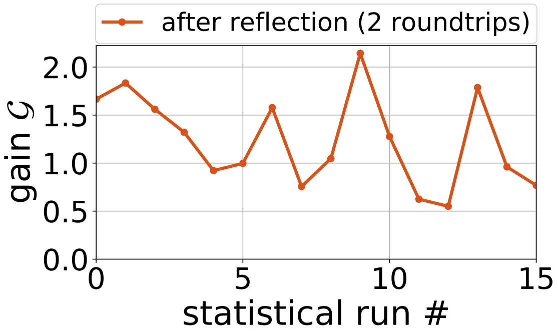

Figure 5.16: The seeding roundtrip gain (equation (5.1)) in the startup region for individual bunch trains. There is a strong fluctuation in gain.

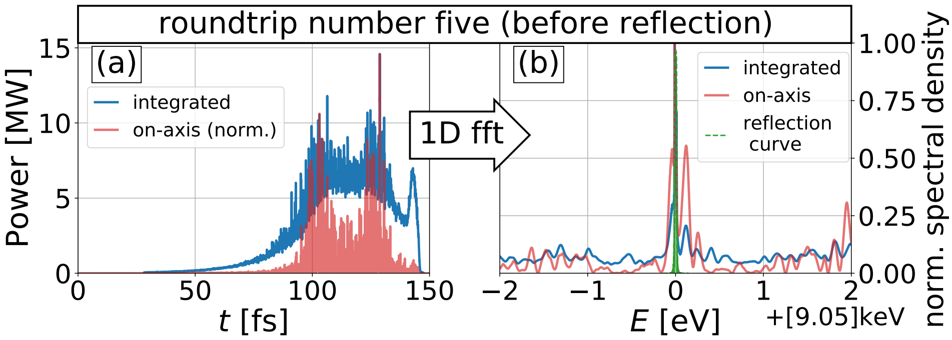

Figure 5.17: (a) and (b) display the longitudinal time domain and frequency domain radiation distributions of the radiation pulse directly after the undulator at the fifth pass of an exemplary bunch train. While (a) shows only minor differences with respect to the first roundtrip, one can clearly see a pronounced spectral peak in (b) at the reflection energy E_c. It has to be noted that only a small subset of the full spectrum is shown in (b) for better emphasizes of the spectral peak.

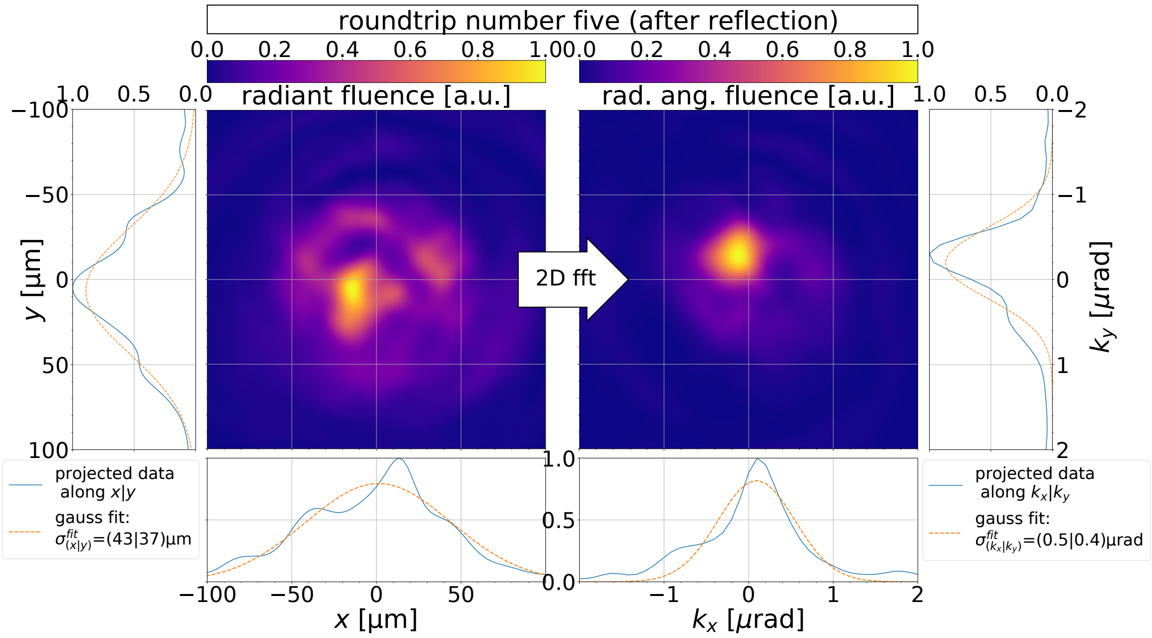

Figure 5.18: The radiant fluence (2.5)(left) and radiant angular fluence (2.7) after spectral filtering at the C(333), representing the transverse distribution of a single longitudinal mode. Both angular and spatial distributions are stabilized compared to the radiation at the first round trip in Figure (5.15). All graphs only show a subset of the full simulation window.

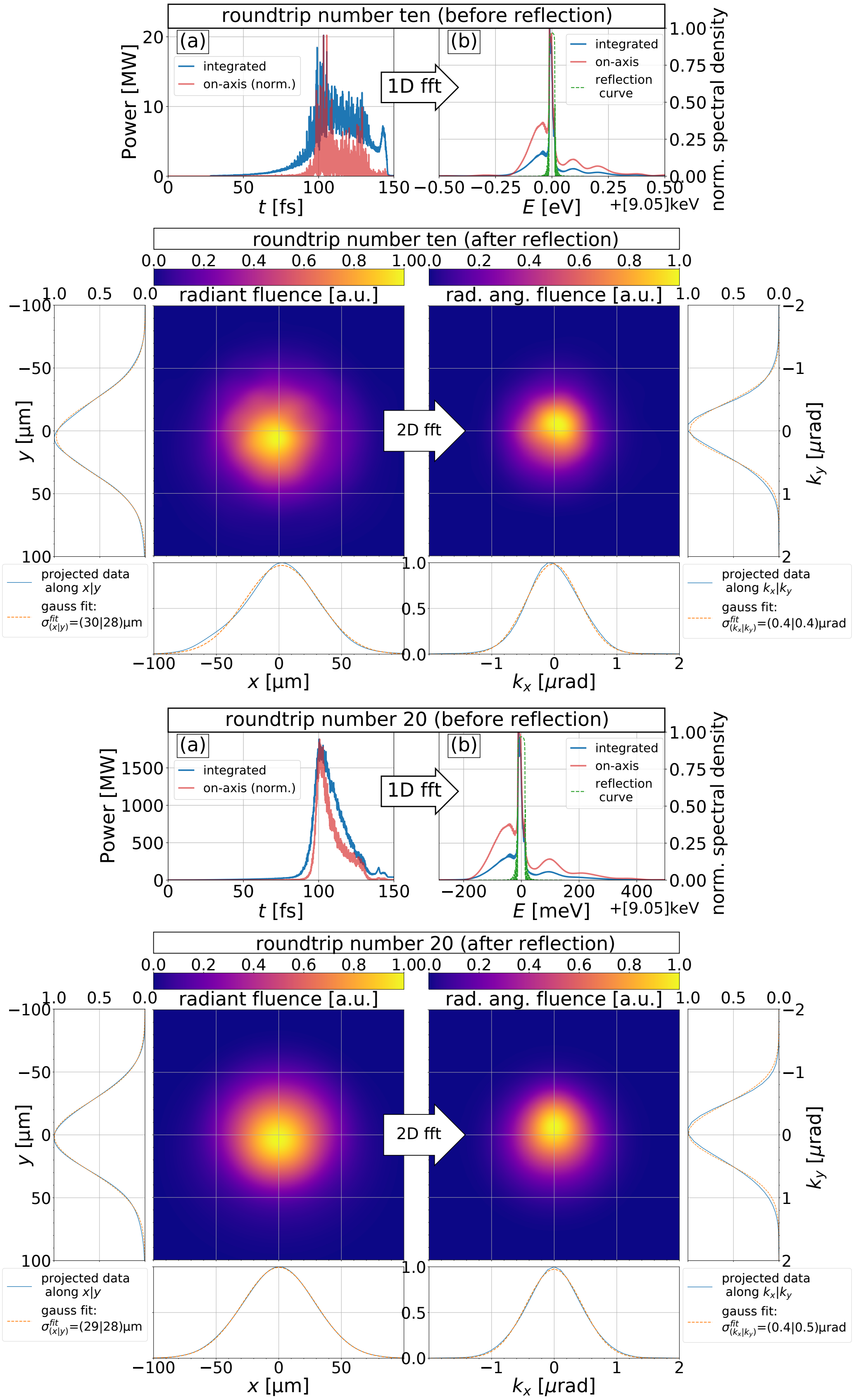

Figure 5.19: Longitudinal and tranverse representations for the round trips 10 and 20. One can see a strong influence of seeding both on the time-domain distribution as on the transverse distribution, which become almost fully gaussian with increasing round trips.

the narrow spectral window of the crystal reflection. This is shown in Figure (5.17(b)) exemplarily for the fifth round trip, where a pronounced peak is present at the photon energy of the reflection. This peak is accompanied by some side peaks which are more pronounced for the on-axis spectrum. They correspond to the elevated areas at $t \approx 105\,\mathrm{fs}$ and $t \approx 130\,\mathrm{fs}$ in the on-axis intensity displayed in Figure (5.17(a)).

With the domination of the amplified FEL fraction over the synchrotron and SASE background, also the transverse phase space stabilizes as shown in Figure (5.18). Especially, both spatial as well as angular width become smaller and match better to the gaussian cavity modes displayed in Figure (5.10).

With subsequent round trips the seed begins to dominate over the entire SASE and synchrotron radiation background, signifying the onset of the *exponential gain regime*. This also comes with an increasing stabilization of the transverse phase space, which is clearly visible in Figure (5.19). Interestingly, the increasing dominance of the seed also has a very pronounced influence on the temporal distribution of the undulator pulse, with the power profile before reflection for the 20th round trip strongly resembling the rough estimate shown in Figure (5.9(a)).

A characteristic feature of the exponential regime is the strong stabilization of the gain as visible from the variation range in Figure (5.20(a)) around roundtrip number 20. Also, the round trip gain before and after reflection as well as of the transmitted pulse become the same and yield, in this specific case, a value of $\mathcal{G}_{\mathrm{rt}} = 1.1$, roughly signifying a doubling of the pulse energy at every round trip. The round trip gain is about a factor of five smaller than the FEL gain, which amounts to $\mathcal{G}_{\mathrm{FEL}} \approx 5$ in the exponential growth regime. This discrepancy can easily be explained by taking into account that the reflection bandwidth is much smaller than the bandwidth of the newly generated radiation, as presented in Figure (5.9(b)) and also apparent in Figure (5.19). Actually, exactly this energy outside the reflection bandwidth is what will be transmitted and the reason why such an intermediate gain oscillator does not require a specific outcoupling scheme. The transmitted pulse will be further discussed below when highlighting the saturation regime. It should be noted that throughout the entire startup and most of the exponential gain regime the transmitted pulse carries more pulse energy than the reflected pulse, even though lower peak spectral flux.

The deviation of the calculated integrated FEL gain with the peak gain presented in Figure (5.9(a)) can be, analogously, explained by the bad matching of the duration of the seeding pulse and the electron bunch current. As the seeding pulse is much longer than the electron bunch, a high fraction of it is not contributing to the seeding at all. Due to the rather high slice gain, these fractions do only appear very little in the power profiles displayed in Figure (5.19), which are dominated by the newly generated radiation.

In Figure (5.20(a)) one can see the gain rapidly decreasing after roughly twenty round trips and the newly generated energy $Q^{\mathrm{new}}_{\mathrm{pulse}} = Q^{\mathrm{und}}_{\mathrm{pulse}}(\#\mathrm{rn}) - Q^{\mathrm{seed}}_{\mathrm{pulse}}(\#\mathrm{rn}-1)$, shown in Figure (5.20(b)), reaching a maximum around round trip 30. This is a clear sign for the *saturation regime*. As was thoroughly discussed in Chapter **2.3** and displayed in figures Figure (2.6) and Figure (2.9) for the cases of a low gain oscillator and an high gain FEL amplifier, with the studied case

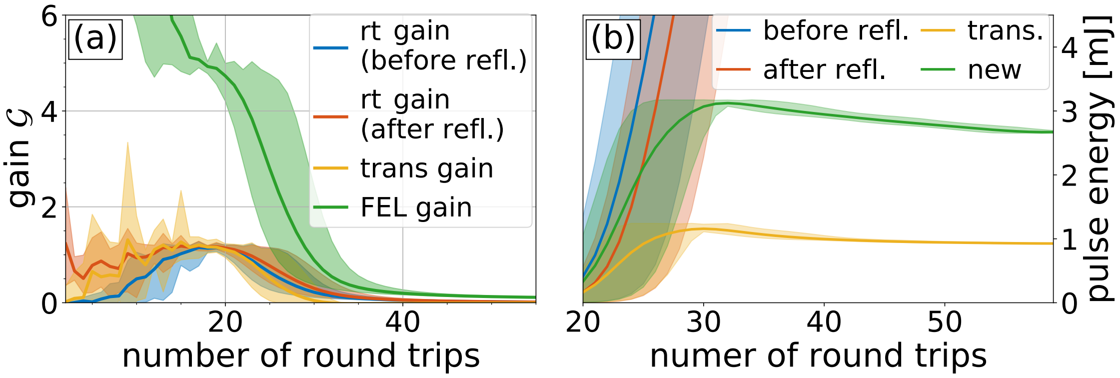

Figure 5.20: (a) shows the evolution of the round trip gain (labeled 'rt gain') before reflection (blue), after reflection (red) and of the transmitted pulse as well as the FEL gain. As mentioned before, the FEL gain is very inaccurate for the first round trips. (b) displays the corresponding evolution of the pulse energy of the pulses before and after reflection, the transmitted pulse as well as the energy newly generated in the undulators around the maximum of latter two. The shaded areas show the minimum-maximum range of the corresponding values from the 15 individual runs.

effectively being a mixture of both, the increasing seeding strength leads to a fully developed microbunching structure. Therefore one can observe a reduction in gain already for the short undulator length of $L_U = 20\,\mathrm{m} \approx 4.3 L_{G,\mathrm{min}}$ where $L_{G,\mathrm{min}} \approx 4.7\,\mathrm{m}$.

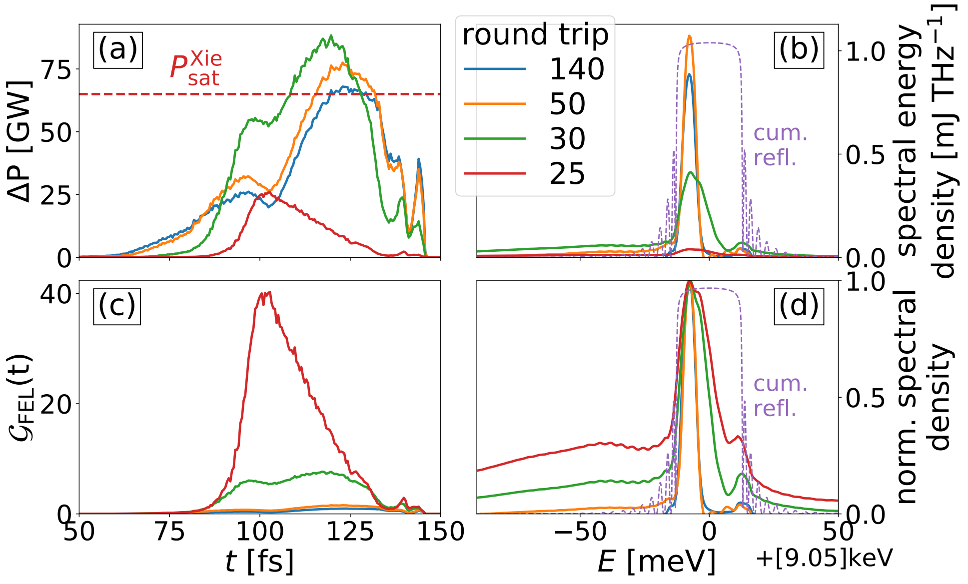

Figure 5.21: (a) displays the power profile of the radiation newly generated in the undulator section for exemplary round trips, which show an increasing time duration. As a rough estimate the saturation power from Eq. (2.77) following *Xie and Kim* of the beam slice with highest gain is also shown as a red dashed line. In (c) the corresponding gain is plotted, which quickly drops with increasing number of round trips in saturation. (b) and (d) display the spectra of the newly generated radiation in absolute and relative magnitude, respectively. These exhibit, in opposition to the power profile, a narrowing with increasing number of round trips. As a guide for the eye the cumulative reflection curve is shown as purple dashed line.

In Figure (5.21(a) and (c)) the evolution of the actual power and gain profiles is depicted for exemplary round trips in the saturation regime. Consistent with Figure (5.20(a)), one can observe the highest gain at round trip 20, while the highest intensity can be observed at round trip 30 in agreement with Figure (5.20(b)). In Figure (5.21(a)) also an estimation of the peak power in saturation $P_{\text{sat}}^{\text{Xie}} \approx 65\,\text{GW}$ is shown, which is based on the estimation by *Kim and Xie*[59] in equation (2.77). The value was calculated from the maximal FEL parameter ρ_{FEL} consistently estimated from equations (2.66) and (2.74) using the electron beam parameters from Figure (5.8). The actual simulated intensities are agreeing, taking into account this rough estimation[57], quite accurately.

A very interesting observation to note is that the intensity and therefore also the gain profile changes with the degree of saturation. While at round trip 20 the intensity and gain profile agree well with the estimation shown in Figure (5.9), one can already see for round trip 25 a decrease in the gain peak while the sides remain the same. This is due to the fraction of the beam with lower gain reaching saturation later than the peak slice. At round trip 30, where the newly generated energy and intensity reach their maximum, many more parts of the beam were able to reach saturation. This leads to a more flattop type of shape of the intensity and gain profiles, which are considerably differing from the one at round trip 20. At round trip 50 and 140, deep in (over)saturation, the parts of the beam of the lowest gain length are losing energy to the electron beam again, whereas the fractions with a considerably higher gain length, such as the distorted head with $L_G \approx 18\,\text{m}$, are still growing.

These effects lead, besides keeping the overall newly generated pulse energy high, to a temporal widening of the intensity and gain profiles. This on the other hand leads to a considerable narrowing of the (newly generated) spectral curve, as displayed in Figure (5.21(b) and (d)). This results in a very narrow bandwidth of only $\sigma_{E_{\text{ph}}} = 5.68(4)\,\text{meV}$ or ${}^{\sigma_{E_{\text{ph}}}}/_{E_c} = 6.27(5)E-7$, an increasing reflection efficiency and leads to a persistent round trip gain greater zero of the circulating radiation pulse.

From Figure (5.11) and Figure (5.20(b)) one can observe that the transmitted and newly generated energy, which is a good measure for the newly generated radiation inside the undulators, saturates much earlier than the energy of the pulse trapped in the cavity. Comparing Figure (5.20(b)) with Figure (5.11), it is also evident that the trapped pulse energy is almost one order of magnitude higher than what is newly generated at each round trip. This is an effect of the, artificially, high cavity quality, which has, aside the transmission and the absorption inside the crystals, no losses $(1-R)$, where R is the cumulative crystal reflectivity. The oscillator reaches a stable state, when

$$\begin{aligned} \Delta\mathcal{S}\left(E_{\text{ph}}\right) &= \left[1 - R\left(E_{\text{ph}}\right)\right]\mathcal{S}_{\text{sat}}\left(E_{\text{ph}}\right) \\ \Leftrightarrow \Delta Q_{\text{pulse}} &= \int \left[1 - R\left(E_{\text{ph}}\right)\right]\mathcal{S}_{\text{sat}}\left(E_{\text{ph}}\right)\mathrm{d}E_{\text{ph}}, \end{aligned}$$

where $\Delta\mathcal{S}\left(E_{\text{ph}}\right)$ is the newly generated spectral energy density, ΔQ_{pulse} is the newly generated pulse energy, $\mathcal{S}_{\text{sat}}\left(E_{\text{ph}}\right)$ is the spectral energy density in saturation and $R\left(E_{\text{ph}}\right)$ is the spectral

---

[57] Many assumptions made by *M. Xie*, such as a constant beta function and a homogeneous phase space distribution to which the photon beam can be matched, do not hold.

reflectivity.

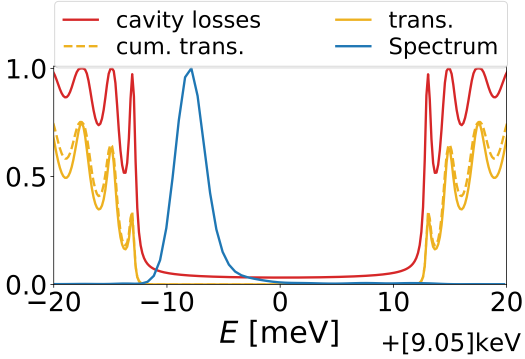

Figure 5.22: The cavity losses of the idealized cavity (red) together with the spectral distribution of the saturated radiation before reflection (blue),the transmission of the downstream crystal (solid orange) and the cumulative transmission of both mirrors (dotted orange). The difference between the red and the dotted orange curve amount to absorption.

In Figure (5.22) the spectral losses $1-R\left(E_{\text{ph}}\right)$ are plotted together with the saturated spectrum after the undulator. From the combination of the very low losses of only 3 % at the spectral peak together with the very narrow spectrum of the (also newly generated radiation), the total energy can reach the tremendously high peak pulse energies of $Q_{\text{pulse}}^{\text{und.}}=31.2(2)\,\text{mJ}$. This is somewhat analogous to classic high-Q laser oscillators, with the difference that the case discussed is a high gain system, therefore reaching much higher peak pulse energies. It has to be stressed, that this is an highly artificial case, as obviously other losses will be present inside the cavity[58]. Anyhow, for the study at hand, it has the advantage that unlike the 'real' cases discussed later, the radiation inside the cavity is strongly dominated by the circulating radiation, which will assume the transverse cavity modes dictated by the error free optical cavity. This can serve as a benchmark for the *pXCP* code.

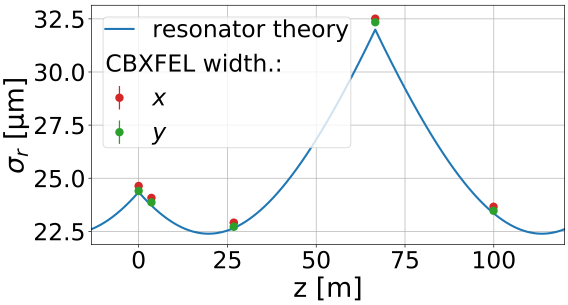

Figure 5.23: The figure shows the radiation pulse rms width from gaussian resonator theory (blue line) as well as the transverse rms moments σ_x and σ_y derived from the simulative radiation distribution in saturation for various positions in the cavity. The agreement is excellent.

In Figure (5.23) the derived rms widths (2.12) of the CBXFEL radiation pulse in saturation is plotted for exemplary positions in the X-ray optical cavity together with the nominal width as dictated from gaussian resonator theory. The agreement is excellent, with the small deviation amounting to the very good, but not perfect gaussian quality factor (2.16) of the radiation pulse of $J=1.121(3)$[59].

---

[58] Besides, it is not desirable to begin with, at least if no Q switching capability is foreseen, as these pulse energies put a very high load on the optics while actually degrading the quality of the transmitted beam due to oversaturation. Latter point will be discussed below. This is also the reason, why modern high gain lasers usually are 'low Q' cavities with very high outcoupling factors (see for example [31, 32]).

[59] The reason for this non-perfect gaussian quality is the variation of the transverse phase space of the electron beam distribution and therefore the newly generated radiation with the longitudinal position, which leads to a non-perfect matching of the cavity modes with the radiation. Still, a gaussian quality factor of $J=1.121(3)$ would be better than most commercial systems.

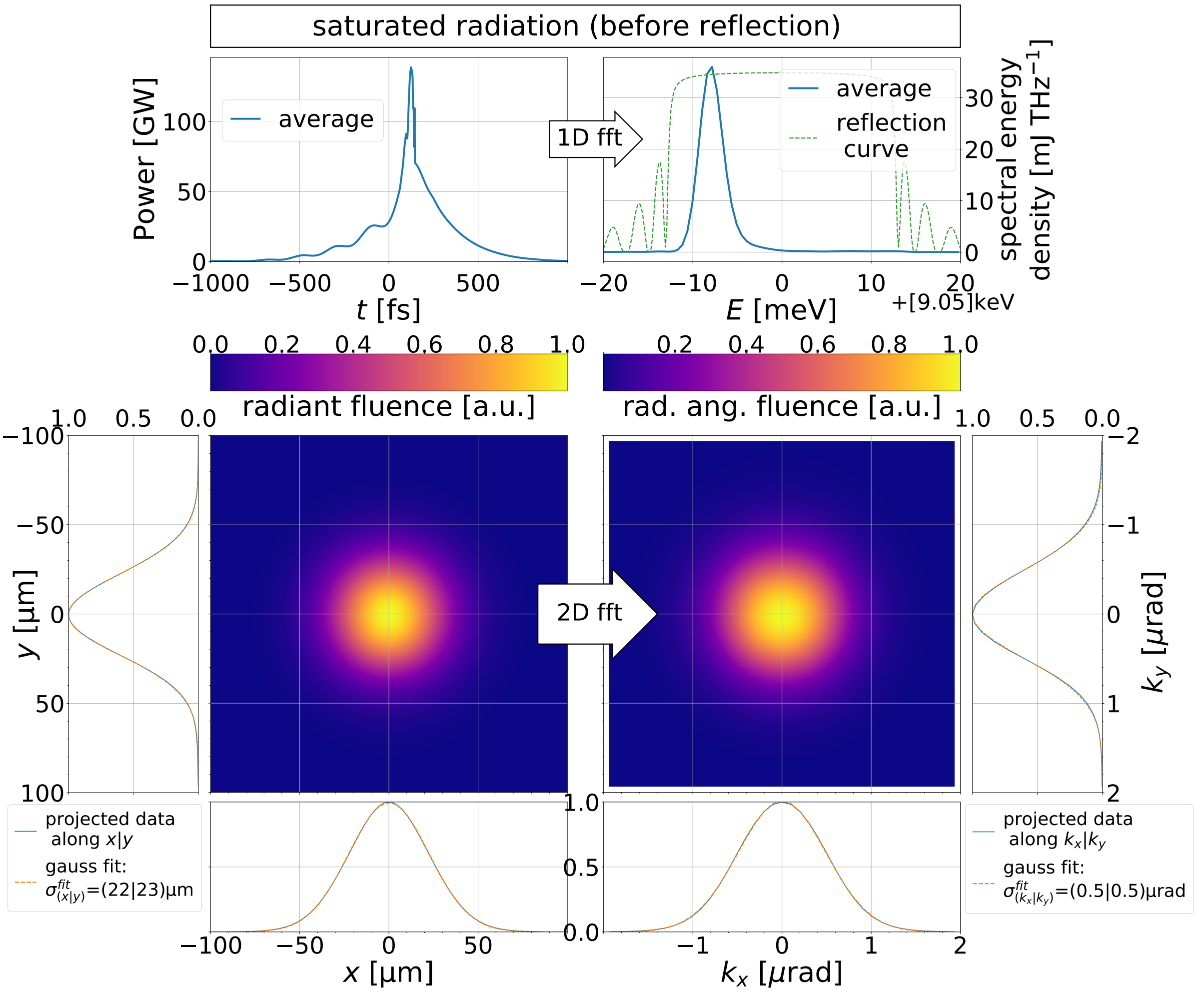

Figure 5.24: Longitudinal and tranverse representations of the radiation pulse before reflection in saturation. The distributions were averaged over fifty round trips in saturation for a single bunch train.

In Figure (5.24) the saturated longitudinal and transverse distributions of the radiation pulse before reflection are shown. As was already mentioned, the pulse has a spectrally very narrow distribution of only $\sigma_{E_{\mathrm{ph}}} = \sqrt{\frac{\pi}{2}}\mathcal{D}_{E_{\mathrm{ph}},\mathrm{MAD}} = 5.69(2)\,\mathrm{meV}$ or ${}^{\sigma_{E_{\mathrm{ph}}}}/_{E_c} = 6.28(3) \times 10^{-7}$ in the spectral domain[60]. Correspondingly, the temporal distribution has a long duration of $\sigma_t = 217(1)\,\mathrm{fs}$, which is roughly ten times longer than the actual electron bunch. This is due to the rather wide temporal response of the crystals (see Figure (5.14(b))) in conjunction with the low round trip gain in saturation, which leads to a domination of the pulse characteristics by the seeding radiation. Also, the beating in the crystal response is able to stack up over many round trips due to the low losses in the cavity, as can be seen in the step like curve progression in the tail of the temporal distribution in Figure (5.24). The time bandwidth product of the radiation pulse is $\sigma_t\sigma_f = 0.296$, which is about trice the minimal value of 0.08. This discrepancy is partly due to the energy and gain chirp in the electron bunch, but mainly due to the frequency-time correlation in the crystal response, induced by the strongly frequency dependent penetration depth. Still, the

---

[60] The bandwidth is computed using the mean absolut deviation(2.14), which is less sensitive to the wide tails in the spectral distribution. It is then transformed into the more common standard deviation.

temporal coherence calculated using equation (2.23) amounts to formidable $\tau_{\mathrm{coh}} = 724(7)\,\mathrm{fs}$. While this value can not directly be compared with the rms duration, it is certain in comparison with Figure (5.24) that the temporal coherence spans almost the entire photon pulse, signifying nearly complete temporal coherence.

The spatial and angular tranverse distributions presented in Figure (5.24) can be quite accurately described as gaussian, which is also expressed in the formidable gaussian quality factor of $J = 1.13(1)$, already mentioned above. Likewise, the degree of tranverse coherence based on equation (2.24) amounts to full $\xi \approx 99\,\%$[61].

In combination with the high degree of longitudinal coherence, the radiation pulse circulating in an ideal X-ray optical cavity at 9.05 keV would fulfill one of the main promises of the CBXFEL to deliver nearly fully three dimensionally coherent X-ray laser pulses. Also, using the pulse energy in saturation of $Q^{\mathrm{und}}_{\mathrm{pulse}} = 31.53(7)\,\mathrm{mJ}$ and putting it into equation (2.19) yields an unprecedented peak brilliance of $\mathcal{B}_p = 4.84(3) \times 10^{36}\,\#\mathrm{Phot/s/mm^2/mrad^2/0\,1\%BW}$, which is about three orders of magnitude higher than $\mathcal{B}_p^{\mathrm{SASE}} \approx 5 \times 10^{33}\,\#\mathrm{Phot/s/mm^2/mrad^2/0\,1\%BW}$ of a nominal SASE at the European XFEL[48], with an amazing, permil percentage shot to shot stability.

Unfortunately, besides being based on idealized assumptions, the presented pulse is not what is coupled out [62]. The transmitted radiation, which may be available in the experimental hutches (or for the purpose of the experiment for the photon diagnostics behind the Undulator section), is, as was already mentioned, the radiation outside the reflection bandwidth. As is depicted in Figure (5.22), the transmission becomes close to zero at the position of the main spectral peak of the circulating radiation. Instead, only the spectral side wings of the radiation are transmitted. As depicted in Figure (5.20(b)), while they carry a substantial fraction of the total pulse energy during startup and in the exponential regime, they saturate (and oversaturate) at a much lower pulse energy of $E^{\mathrm{tr}}_{\mathrm{pulse}} = 0.903(1)\,\mathrm{mJ}$.

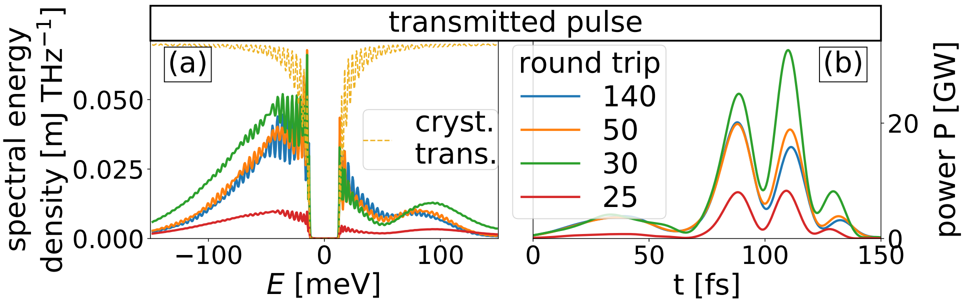

Figure 5.25: Spectra (a) and power profiles (b) of the transmitted pulse for exemplary round trips. In the spectral plot also the crystal transmission function (3.25) is displayed in orange.

In Figure (5.25) the spectral power densities and power profiles of the transmitted radiation

---

[61] The computation of the transverse coherence is very time demanding. Therefore it is only carried out for single distributions and is not averaged. Hence, unfortunately no error can be estimated.

[62] A cavity dumping mechanism (see Section **2.4**), where the entire radiation is coupled out at once, is imaginable and would, taking a saturation time of roughly 100 round trips, still yield a factor of roughly 100 better average brilliance than currently achievable. However, as was already mentioned and is further discussed in Section **5.2.3**, the thermal strain on the cavity would certainly be too high to work in the way as presented here.

pulse for exemplary round trips are shown. In accordance with the pulse energy evolution displayed in Figure (5.20(b)), the highest intensity and spectral energy densities can be observed at round trip 30. As expected from the crystal transmission function, the resulting spectra in Figure (5.25(a)) are zero at the center and have their maximum at (or close to) the edges of the total reflection region. As in the case for the newly generated energy, one can see a slight widening of the power profiles and a narrowing of the spectrum with increasing number of round trips, but the effect is much less pronounced than for the circulating pulse. The bandwidth of the transmitted pulse in saturation amounts to $\sigma_{E_{\mathrm{ph}}} = 60.05(1)\,\mathrm{meV}$ or $\sigma_{E_{\mathrm{ph}}}/E_c = 6.634(2)E-6$, which is much higher than the bandwidth of the circulating pulse after the undulator. the transmitted curve lacks the strong and narrow peak at the center of the reflection curve, which weight is significantly reducing the bandwidth of the circulating pulse before reflection. The coherence time $\tau_{\mathrm{coh}}^{\mathrm{tr}} = 25.76(1)\,\mathrm{fs}$ of the pulse in saturation equivalently is much lower than that of the circulating pulse. Also, and this is more important than the absolute value, it is much lower than the temporal duration $\sigma_t = 122.4(2)\,\mathrm{fs}$ of the transmitted power profile. Hence, the transmitted pulse is not fully coherent. It has nonetheless about a factor 100 better coherence properties than SASE radiation. While the statistical SASE background has a stronger influence on the transmitted than on the circulating pulse due to the lack of averaging, the main reason for this reduction is the frequency-time correlation introduced by the crystal transmission. This is also the reason why the temporal distribution is strongly differing from the electron bunch profile from which it was generated.

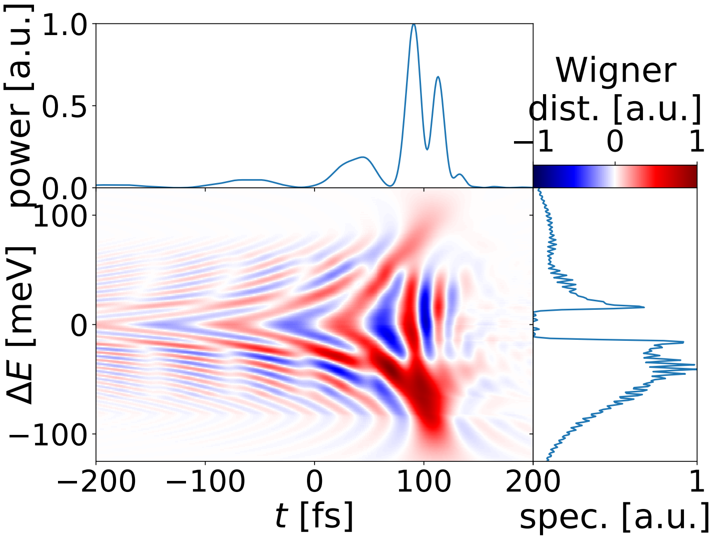

Figure 5.26: The wigner distribution [49] of saturated transmitted pulse together with the respective power profile (top) and the spectrum (right). The fluctuating negative (blue) and positive (red) regions are interference patterns characteristic to the Wigner distribution and are difficult to interpret. Nonetheless, one can see that the long tail in the time domain is due to the spectral region close to the gap induced by the crystal reflection. On the other hand the central peaks in the power profile equally extend over the full spectral range.

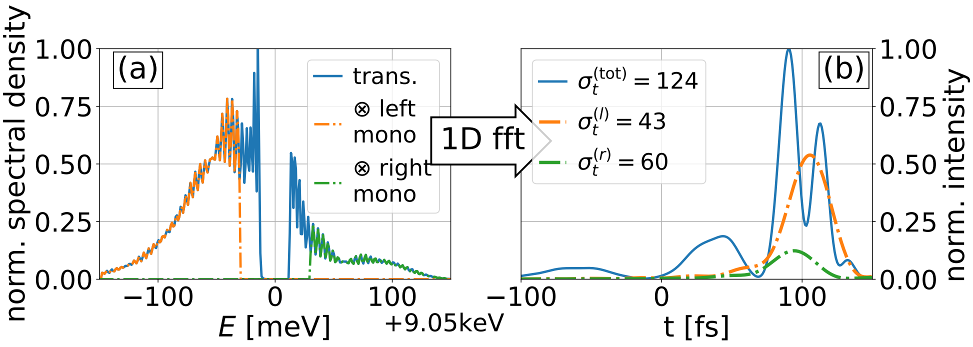

Figure 5.27: On-axis, single shot spectra and power profile of the full transmitted pulse in saturation (blue) and the same pulse additionally monochromatized by a simplified rectangle function, one left (orange) and one right (green) of the spectral gap. The monochromatized pulses have a shorter, single peak power profiles, even though having smaller bandwidth.

In Figure (5.26) the single-shot Wigner distribution (see equation (2.26)) of the transmitted pulse in saturation is displayed. While it is difficult to quantitatively interpret the distribution due to its complicated interference cross-terms, it is evident that the long tails of the temporal profile are governed by the central part of the spectral distribution. In this region reflections are still frequently occurring and the temporal profile is stretched by multiple (back and forth) reflections throughout the crystal. Also, the different lobes of the power profile are generated by interference patterns of these reflections. This argumentation agrees with the observation in Figure (5.26) that the spectral side wings further away from the 'spectral' gap are evidently contributing rather smoothly to the temporal distribution, as visible from the homogenously red patches without any blue mixed in. Hence, the double peak is caused by interference in the central spectral region, which is also evident from the fact that inside the multiple reflection bandwidth the Wigner distribution has strong negative values exactly at the positions of the minima.

Realizing that this multi peak time profile is produced by the time-frequency correlation of the crystal response close to the spectral gap, one can think about 'cleaning' the longitudinal distribution by appropriate, additional monochromatization of the transmitted pulse. This is displayed in Figure (5.27), where for simplification the monochromators were approximated by simple, very wide rectangle functions (mathematically, they are represented by the Heaviside step function, assuming the width of the monochromator is much wider than the bandwidth of the transmitted pulse.). The resulting time profiles of the monochromatized pulses indeed have a much shorter, single peak time distribution, which provides a higher degree of longitudinal coherence while only sacrificing about half of the total pulse energy.

In Figure (5.28) the spatial and angular transverse distribution of the transmitted pulse in saturation is displayed. While the distributions look perfectly gaussian at first sight, looking at the projections, one can see a small deviation from the gaussian fit in both the spatial as well as the angular y-axis. This agrees well with the slightly irregular distribution of the electron bunch in the z-y-plane. The deviation leads to a reduced gaussian quality factor of $J = 1.888(1)$. Also, the degree of transverse coherence amounts to, comparably low, $\xi^{\mathrm{tr}} = 0.73$.

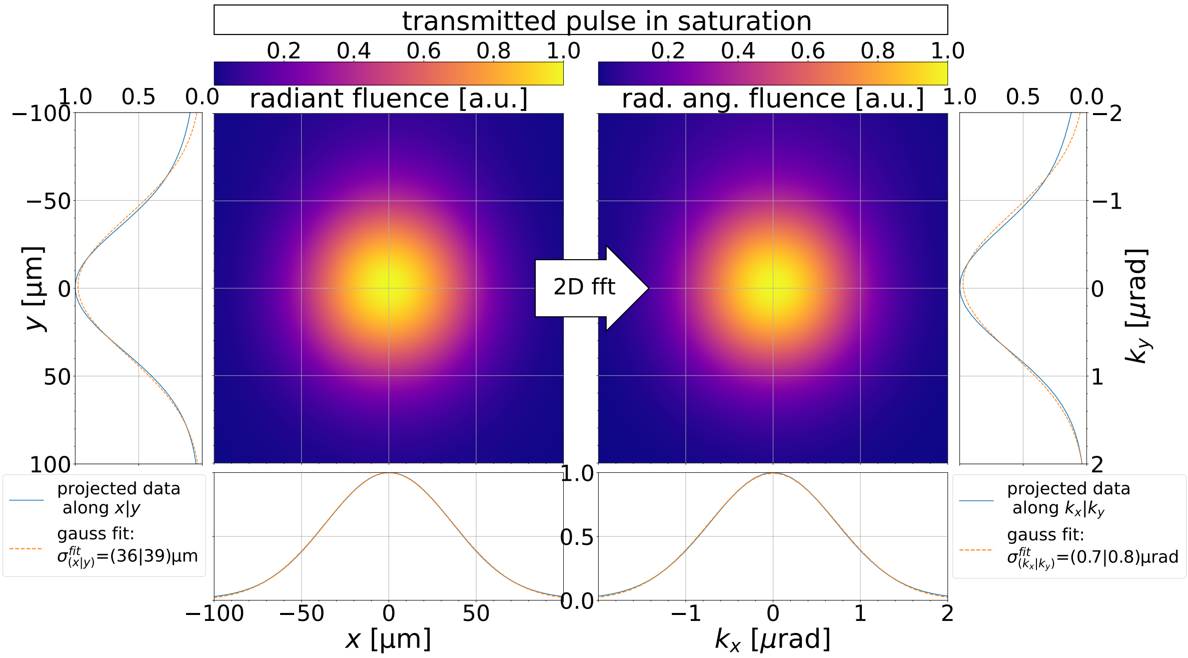

Figure 5.28: The spatial and angular transverse distribution of the transmitted pulse in saturation. Looking closely, one can see a slight deviation of a perfect gaussian profile in the spatial and angular y-axes.

This reduced transverse coherence is a characteristic signature of oversaturation, which is likewise occurring for SASE pulses [47, 48]. Putting these values together with the pulse energy and the longitudinal moments, one yields, using equation (2.25), a peak brilliance of $\mathcal{B} = 1.375(4) \times 10^{34}\,\#\mathrm{Phot/s/mm^2/mrad^2/0\,1\%BW}$. While this is a significantly lower brilliance than the circulating pulse, it is still considerably better than that of a SASE pulse.

However, the above noted brilliance of the transmitted pulse in saturation is not the best principally possible with this specific outcoupling scheme. As was already mentioned multiple times, the intense seed provided by the trapped pulse leads to oversaturation of the newly generated radiation. This is reducing the pulse energies, as displayed in Figure (5.20(b)), and more importantly the transverse quality of the transmitted radiation. This can be seen in Figure (5.29), where besides the gaussian quality J (purple curve) the peak brilliance computed by the approximative equation (2.19) (orange curve) is displayed. There is a strong correlation between J and $\mathcal{B}_p$ caused by the brilliance' square dependence on J. Evidently, the brilliance peaks at more

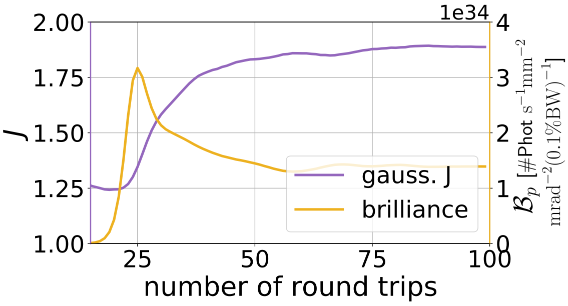

Figure 5.29: The evolution of the brilliance (orange) and gaussian quality factor (purple) of the transmitted pulse with number of round trips. There is a strong correlation between J and the brilliance, with both degrading strongly after their peak after roughly 25 round trips.

than twice the value of what is achieved in saturation[63]. For higher round trips the fraction of the beam with the highest transverse quality are going into oversaturation and therefore decrease in their transverse coherence [47, 48]. In terms of the pulse energy this is mostly compensated by other fractions of the beam with poorer transverse quality (emittance) and therefore higher gain lengths, which are not yet in oversaturation. However, the worse transverse quality of these fractions is transferred to the radiation pulse, which results in a worse J and tranverse coherence.

Table 4: Main parameters of the X-ray pulses in saturation for the idealized cavity at $E_c = 9.05\,\mathrm{keV}$. The errors denote the standard deviation of the shot-to-shot fluctuation in saturation as well as by averaging over 15 individual runs with equal base parameters. For comparison also SASE parameters for the 9.05 keV photon energy and the same electron distribution are appended. These are obtained by simulation (no taper) and scaling to measured energies.

Photon Energy E_{ph} [keV]	9.05		
	before reflection	transmitted	SASE
Pulse Energy E_{pulse} [mJ]	31.55(12)	0.915(23)	$\sim$3[207]
Bandwidth $\sigma_{E_{\mathrm{ph}}}{}^{a}$ [meV]	5.70(5)	60.3(4)	$\sim$37000
Pulse Length $\sigma_t{}^{a}$ [fs]	214(4)	123(4)	$\sim$11
Peak Brilliance $\mathcal{B}$ [^{b}]	$4.84(3) \times 10^{36}$	$1.375(4) \times 10^{34}$	5×10^{33} [48]
coherence time τ [fs]	717(15)	25.8(1)	$\sim$0.2 [48]

[a] The bandwidth/duration is computed using the mean absolut deviation $\mathcal{D}_{u,\mathrm{MAD}}$ (2.14), which is less sensitive to the wide tails in the spectral distribution. It is then transformed into the more common standard deviation $\sigma_u \approx \sqrt{\frac{\pi}{2}}\mathcal{D}_{E_{\mathrm{ph}},\mathrm{MAD}}$.

[b] #Phot/s/mm^2/mrad^2/0 1%BW

In table 4 the performance parameters of the CBXFEL in saturation for the circulating pulse before reflection and for the transmitted pulse are noted. For comparison also the parameters of a SASE pulse at the European XFEL at the same photon energy are put. It is obvious that the circulating pulse is by far superior to both transmitted and SASE pulse with the only downside of an increased pulse length. But one has to keep in mind that these are highly unrealistic values, which are based on an idealized cavity and, especially, neglect heat load effects, which would obviously be very severe at these pulse energies.

While the transmitted pulse cannot compare to the circulating one, set side to side to the SASE pulse, it is two to three orders of magnitude better in terms of bandwidth, two orders of magnitude better in peak spectral flux and temporal coherence and at least a factor two better in peak brilliance. Especially considering the scope of the project, which is to study the feasibility of a CBXFEL and not to deliver pulses to the users, these values are absolutely sufficient. For

---

[63] The small offset between the minimum gaussian quality factor and the maximum brilliance is due to the significant increase in pulse energy occurring between these round trips.

the feasibility study, the principal requirement is that the transmitted pulse is well detectable, which definitely is the case for the value presented here, and that the growth in energy from the startup to the saturation regime is outside the uncertainty range of the detectors. Also latter point is surely granted, considering the orders of magnitude difference in pulse energy from the first round trip to saturation, especially in conjunction with a monochromator. Additionally, it will be important to measure a bandwidth narrowing with subsequent round trips. As the bandwidth of the transmitted pulse, too, varies by orders of magnitude, the same point applies as for the pulse energy.

It should be noted, that the SASE pulses are superior in peak power compared to the transmitted pulse owing to their much shorter time duration, which can even be decreased by using shorter electron bunches. On the other side the CBXFEL is limited in the minimal achievable duration due to its low bandwidth[64]. In that sense it is obvious that for the study of ultrafast phenomena SASE is the natural choice, while the CBXFEL is far superior in the study of phenomena which require a fine spectral resolution.

While the simulations presented in this paragraph were based on the unrealistic situation of a perfect cavity without any influence of heat load, there are still many important points to be remembered for the following, more realistic cases. First, the simulations agree well to analytical estimates considering the peak power and the transverse distribution in saturation, which are particularly easy to make for this high Q cavity. These are good benchmarks considering the credibility of the code presented in Chapter **4**.

Second, during the *start up regime* the seeding efficiency is strongly fluctuating, which is both governed by fluctuations in the spectral content of the pulse after the undulator, as well as, and this is the dominating effect, in its transverse distribution. Owing to the rather short undulator section, the principal TEM00 mode has not yet dominated over other transverse modes which leads to a bad matching to the X-ray optical cavity.

The third point to learn is that while four EuXFEL undulator sections provide a lot of peak FEL gain in the *exponential gain regime*, the actual round trip gain is significantly lowered by the fact that the narrow spectral bandwidth of the reflectors is badly matched to the short time duration of the electron pulse. The gain is furthermore decreased by the pronounced energy chirp and the longitudinally varying transverse distribution of the electron bunch, as this decreases its spectral and transverse matching with the seeding radiation. On the other hand, the correspondingly much wider spectral distribution of the newly generated radiation is precisely what enables the proposed outcoupling scheme, where only the spectral side wings are transmitted, to function.

Fourth, in the *saturation regime* the fractions of the electron beam matching best to the photon pulse saturate much earlier than the other fractions. This leads to a widening of the gain curve with increasing seed power, which is, conversely, narrowing the spectral distribution of the newly generated radiation. As this reduces the spectral cavity losses, it allows the circulating radiation pulse to reach the astonishingly high pulse energies in saturation. On the other

---

[64] The time duration of the transmitted pulse can be significantly decreased by additional monochromatization, as proposed above. Nonetheless, it is limited on the lower end by the pulse' low bandwidth and Fourier's limit.

hand, the oversaturation of the well matched parts of the beam and increasing weight of the badly matched parts lead to a worsening of the transverse properties of the newly generated and therefore also transmitted radiation.

The last point to remember is the complex spectral-temporal distribution of the transmitted pulse which is caused by the time-frequency correlation of the crystal reflection and which leads to a decreased degree of temporal coherence. This could be improved by additional monochromatization for the cost of pulse energy. For the proof-of-principal demonstrator experiment, however, the non-monochromatized pulse can be considered absolutely sufficient.

Finally, it should be emphasized such a detailed analysis including the relevance of the stochastic fluctuations of the *startup regime*, the stabilization in the *exponential gain regime* and the gain curve evolution in the *saturation regime* has not been conducted before.

5.2.1.2 C (4 0 0) reflection at 6.97 keV: In this paragraph, the idealized CBXFEL for a photon energy of E_{ph} =6.97 keV, corresponding to the C(400) reflection shall shortly be highlighted. As the observations of the E_{ph} =9.05 keV qualitatively hold, only the quantitative differences shall be presented here.

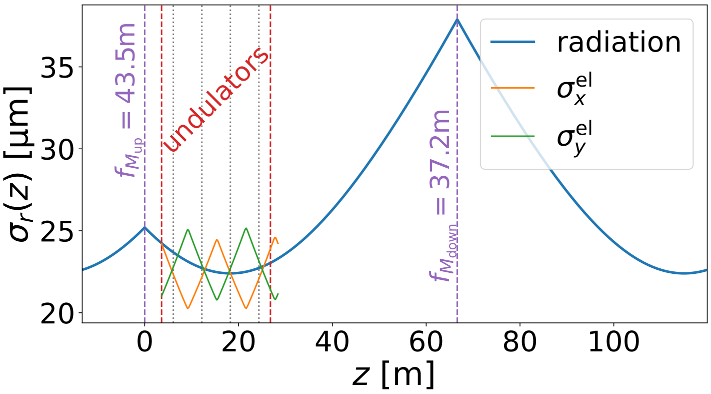

Figure 5.30: The radiation intensity rms width σ_r (2.12) (blue curve) in the X-ray cavity from optical resonator theory (see Appending **D**) for a 6.97 keV beam for an asymmetric focussing of $f_{M_{\mathrm{down}}} = 37.2\,\mathrm{m}$ for the downstream mirror assembly and $f_{M_{\mathrm{up}}} = 43.6\,\mathrm{m}$ for the upstream one. These are matched to obtain a rayleigh length of $z_R = \frac{4\pi\bar{\sigma}^2_{\mathrm{el},r}}{\lambda} = 35.6\,\mathrm{m}$ in accordance with equation (2.76), where $\bar{\sigma}_{\mathrm{el},r}$ =22.5 µm is the average electron beam size. Also the electron beam width $\sigma_{x,y}$ for the x and y coordinate are displayed as orange and green curves, respectively, showing a good transverse matching of radiation field and electron beam. The purple dashed, the red dashed and the grey dotted vertical lines highlight the position of the mirrors, the start and end of the undulators and the centers of the four undulator cells, respectively. The plot is periodic in z as it assumes the infinite extension of the optical cavity by the mirrors.

In Figure (5.30) the evolution of the gaussian beam size for a stable resonator is displayed, showing good matching to the electron beam. The focal lengths' $f_{M_{\mathrm{down}}} = 37.2\,\mathrm{m}$ for the downstream mirror assembly and $f_{M_{\mathrm{up}}} = 43.6\,\mathrm{m}$ of the mirror assembly are shorter (meaning stronger focussing) compared to the E_{ph} =9.05 keV case in order to compensate for the stronger divergence at higher wavelengths .

In Figure (5.31) the evolution of photon pulse energy for the idealized E_{ph} =6.97 keV photon

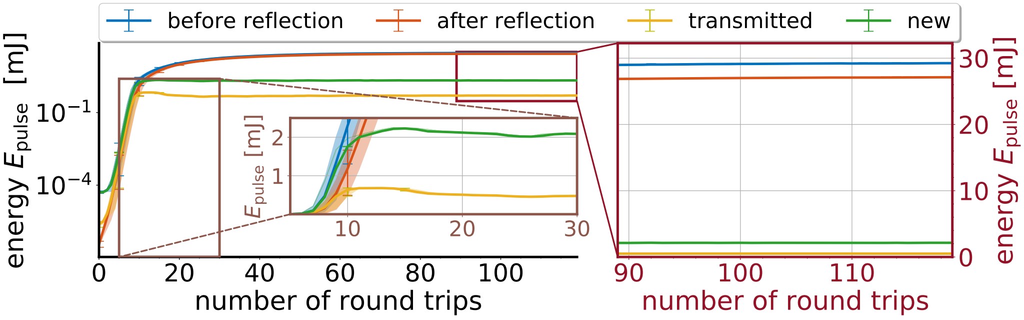

Figure 5.31: Photon pulse energy vs number of round trips for E_{ph} =6.97 keV (C400) photon energy neglecting error sources. The green curve is the pulse energy newly generated at each round trip, which is partially being entering into the circulating pulse, partially transmitted and partially absorbed. The left plot in logarithmic scale shows the full evolution of the pulse energy versus number of round trips and the right plot in linear scale displays a stable photon beam after saturation. The inset is a zoom on the energy evolution near the point of the maximum transmitted and newly generated radiation. The data was averaged over 15 individual runs/bunch trains with the shaded area showing the minimum/maximum values from these runs.

energy is displayed. The basic form of the evolution and the pulse energy $Q^{\mathrm{trans}}_{\mathrm{pulse}} = 29.20(5)\,\mathrm{mJ}$ of the circulating pulse in saturation is very similar to the E_{ph} =9.05 keV case. However, there are some differences to note. One is the much stronger slope of the curves, leading to a saturation of the transmitted and the newly generated energy at approximately round trip number 15, which is half the amount necessary for the E_{ph} =9.05 keV CBXFEL to saturate. The second is the weaker transmitted pulse in saturation, which saturates with $Q_{\mathrm{pulse}^{\mathrm{trans}}} = 0.506(4)\,\mathrm{mJ}$ at only around half the pulse energy of the E_{ph} =9.05 keV beam, and, as will be shown below, at a lower quality.

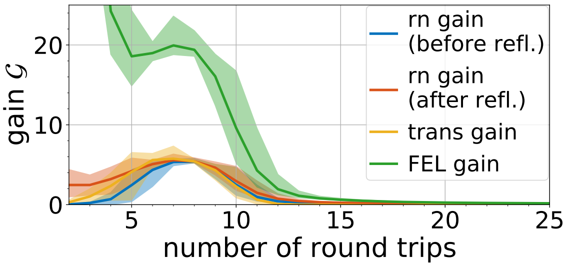

Figure 5.32: The evolution of the round trip gain before reflection (blue), after reflection (red) and of the transmitted pulse as well as the FEL gain. As mentioned before, the FEL gain is very inaccurate for the first round trips.

Both points are related to the more than twice as high FEL gain at 6.97 keV photon energy, as displayed in Figure (5.9(a)), Figure (5.32) and Figure (5.33(c)). This increased gain is by part due to the increased FEL parameter ρ_{FEL} (2.66), taking into account the higher resonant undulator parameter $^{\mathrm{d}K}/_{\mathrm{d}E_{\mathrm{ph}}} < 0$ at lower photon energies ((2.49)) and the smaller reduction by 3D effects due the more relaxed diffraction and emittance conditions (2.75) at E_{ph} =6.95 keV. Also, as visible in Figure (5.9(b)) and Figure (5.9(b) and (d)), the wider spectral width of the C(400) reflection leads to a better matching between the monochromatized seeding pulse and the electron bunch. These relaxed conditions also lead to, and this is the dominant influence on the round trip and integrated FEL gain, a wider gain profile, which leads to a better matching between the monochromatized seeding pulse and the electron bunch.

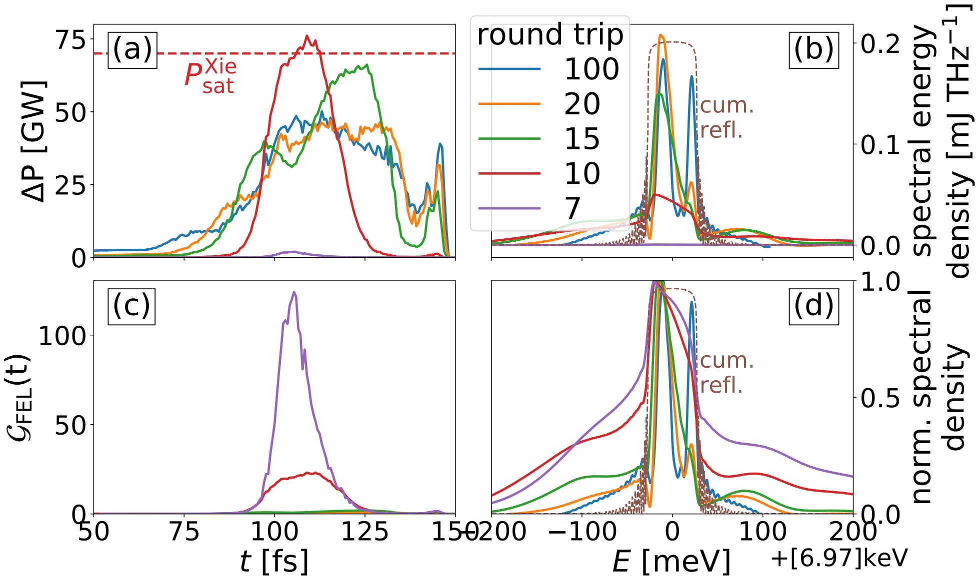

Figure 5.33: (a) displays the power profile of the radiation newly generated in the undulator section for exemplary round trips, which show an increasing time duration. As a rough estimate the saturation power (2.77) following *Kim and Xie* of the beam slice with highest gain is also shown as a red dashed line. In (c) the corresponding gain is plotted, which quickly drops with increasing number of round trips in saturation. (b) and (d) display the spectra of the newly generated radiation in absolute and relative magnitude, respectively. As a guide for the eye the cumulative reflection curve is shown as brown dashed line. Inside the reflection bandwidth the spectra have a double peak structure. As in the $E_c = 9.05\,\mathrm{keV}$ case they exhibit a narrowing with increasing number of round trips.

In analogy to the C(333) case, Figure (5.33(a)) exhibits a rather good matching with the *Kim and Xie* estimate of the saturation power (2.77). This saturation power is reached much earlier, due to the smaller gain length of $L_{G,\min} \approx 4\,\mathrm{m}$ and the above mentioned better match of the temporal profile of seeding pulse and electron bunch. Afterwards, one can again observe a reshaping of the power and the gain profiles, with the low gain length fractions of the bunch being in oversaturation and the high gain length fractions gaining energy. Due to the higher tolerance towards emittance effects, this gain is also quite pronounced in the transversely poor, high emittance parts of the beam. Besides, due to the lower initial gain length, more fractions of the electron bunch are in the state of oversaturation when the CBXFEL reaches full saturation. As in the C(333) reflection case, the widening of the gain profile leads to a narrowing of the spectral curve. But for the C(400) one can additionally observe the formation of a pronounced double peak structure in the reflection bandwidth. This is by part due to the wider spectral reflection width of the 6.97 keV C(400) reflection and by part due to the stronger influence of the head of the electron bunch. As the electron bunch has a pronounced energy chirp, the corresponding FEL spectrum of this head is slightly shifted with respect to the central part of the bunch.

In Figure (5.34) the longitudinal and transverse distributions of the saturated $E_{\text{ph}} = 6.97\,\mathrm{keV}$ radiation pulse after the undulator is displayed. Evidently, the transverse distribution is very well defined, which expresses itself in a very good gaussian quality factor (2.16) of $J = 1.143(6)$ and a good transverse coherence (2.24) of $\xi = 0.97$. This is due to the averaging of the circulating

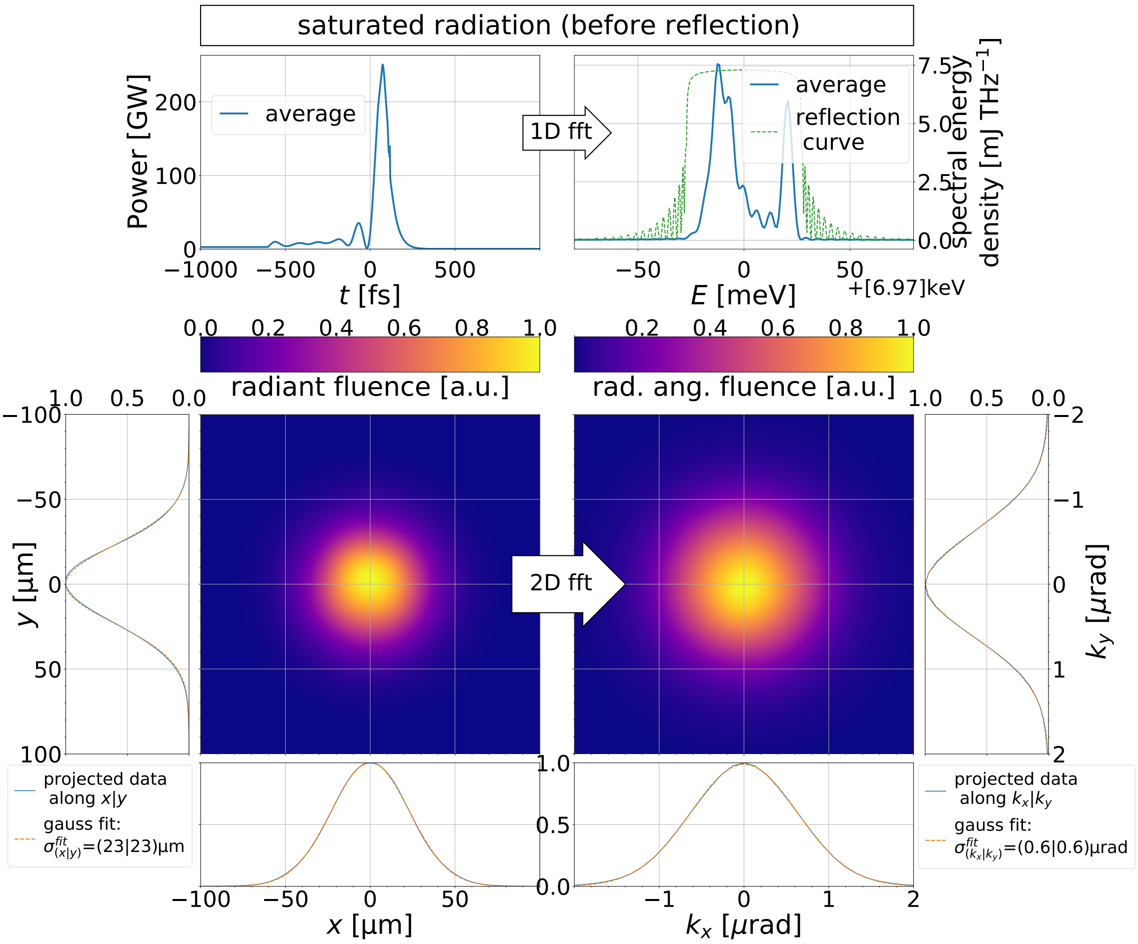

Figure 5.34: Longitudinal and transverse representations of the radiation pulse before reflection in saturation. The distributions were averaged over fifty round trips in saturation.

pulse over many round trips.

As was mentioned above, the frequency domain and, likewise, also the time domain distributions exhibit double peak structures, which are less smooth than for the $E_{\mathrm{ph}} = 9.05\,\mathrm{keV}$ case. In the frequency domain this results in an increased bandwidth of $\sigma_{E_{\mathrm{ph}}} = 18.8(9)\,\mathrm{meV}$. While this is more than twice the bandwidth as for the C (3 3 3) reflection, it is still a very small relative bandwidth of only $^{\sigma_{E_{\mathrm{ph}}}}/_{E_c} = 2.1(1)E-6$. In the time domain the temporal duration is $\sigma_t = 134.1(2)\,\mathrm{fs}$, which compares to the temporal coherence time of $\tau_{\mathrm{coh}} = 124.1(7)\,\mathrm{fs}$. This is a nearly complete longitudinal coherence, but is worse than for the $E_{\mathrm{ph}} = 9.05\,\mathrm{keV}$ case (see Table 4). This is only to be expected, taking into account the double peak structure of the longitudinal distribution. Combining these values with the high peak pulse energy of $E_{\mathrm{pulse}} = 29.20(5)\,\mathrm{mJ}$ also the 6.97 keV CBXFEL yields a tremendously high peak brilliance of $\mathcal{B}_p = 1.28(6) \times 10^{36}\,\#\mathrm{Phot/s/mm^2/mrad^2/0\,1\%BW}$.

In Figure (5.35) the longitudinal and transverse distributions of the transmitted radiation pulse in saturation are plotted. As for the C (3 3 3) reflection, the transverse distributions also display slight deviations from an ideal gaussian distributions, which result in a reduced gaussian qual-

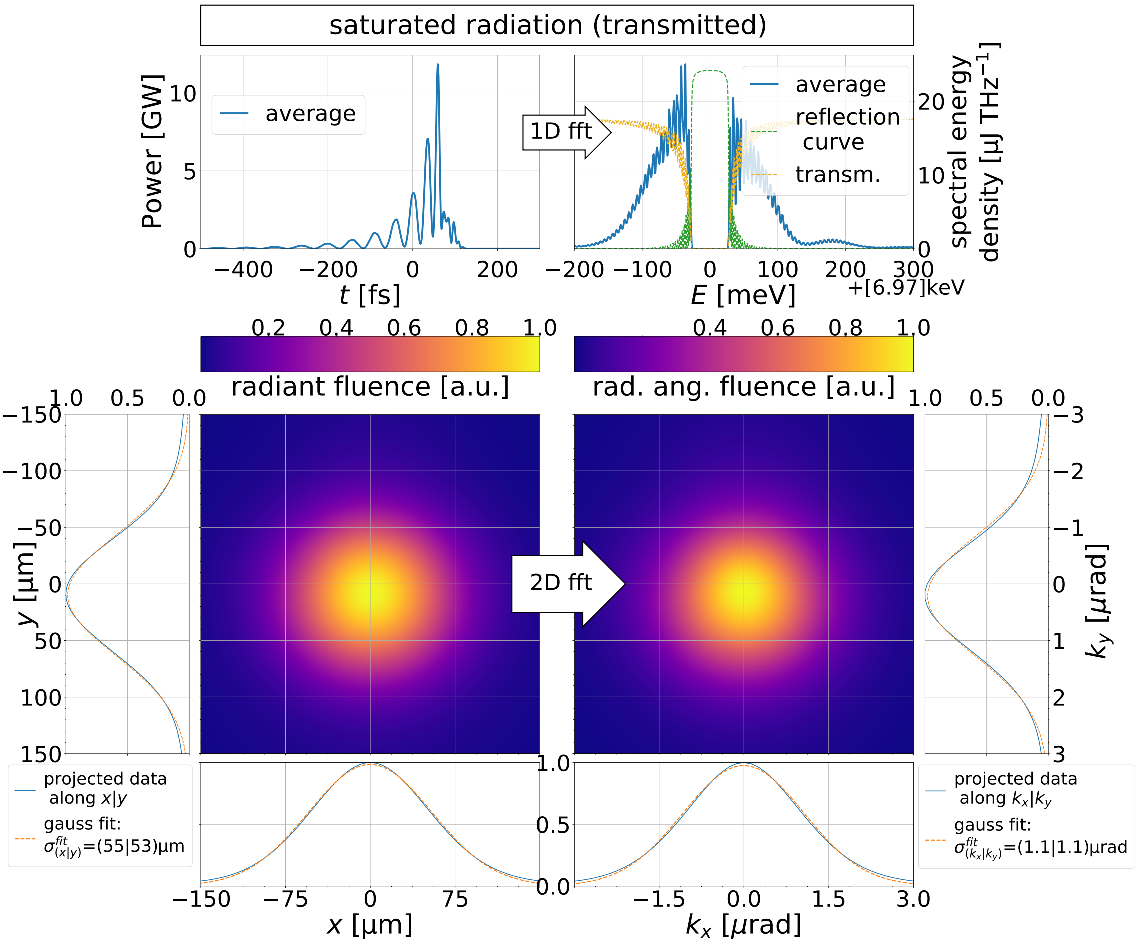

Figure 5.35: Longitudinal and tranverse representations of the transmitted radiation pulse. The distributions were averaged over fifty round trips in saturation. In the spectral plot the reflection (green) and transmission (orange) curve of the C(400) are additionally shown.

ity factor of $J = 2.40(23)$. These, with respect to the $E_{\mathrm{ph}} = 9.05\,\mathrm{keV}$ case, reduced values are caused by the stronger oversaturation of the electron bunch due to the shorter gain length, as was already mentioned above. The transverse coherence has anyhow the same value of $\xi = 0.73$. The bandwidth of the newly produced radiation is rather wide, as visible in Figure (5.33(d)), and therefore also the transmitted radiation has an increased bandwidth of $\sigma_{E_{\mathrm{ph}}} = 95.7(3)\,\mathrm{meV}$. The longitudinal distribution of the transmitted pulse is evidently strongly affected by the oscillations of the crystal transmissivity at the sides of the total reflection regions. Due to the wider bandwidth of the C(400) reflection, these oscillations have a stronger impact than for the $E_{\mathrm{ph}} = 9.05\,\mathrm{keV}$ transmission. This is especially visible in the time-domain profile, which exhibits many beats after the leading peak of only slowly decreasing strength. This stretches the duration of the transmission pulse to $\sigma_t = 162.7(6)\,\mathrm{fs}$ whereas the temporal coherence is slightly reduced to $\tau_{\mathrm{coh}} = 21.8(1)\,\mathrm{fs}$. The ratio of both therefore evidently corresponds to a decreased degree of coherence compared to the C(333) reflection case. The resulting peak brilliance logically also is reduced with $\mathcal{B}_p = 1.7(2) \times 10^{33}\,\#\mathrm{Phot/s/mm^2/mrad^2/0\,1\%BW}$, below the value of SASE radiation. The data of both transmitted and trapped radiation pulse is summarized in Table 5.

Table 5: Main parameters of the X-ray pulses in saturation for the idealized cavity at $E_c = 6.97\,\mathrm{keV}$. The errors denote the standard deviation of the shot-to-shot fluctuation in saturation as well as by averaging over 15 individual runs with equal base parameters.

Photon Energy E_{ph} [keV]		6.97	
	before reflection	transmitted	SASE
Pulse Energy Q_{pulse} [mJ]	29.20(5)	0.506(4)	~3[207]
Bandwidth $\sigma_{E_{\mathrm{ph}}}{}^{a}$ [meV]	18.8(9)	60.3(4)	~37000
Pulse Length $\sigma_t{}^{a}$ [fs]	134.1(2)	162.8(6)	~11
Peak Brilliance $\mathcal{B}$ [^{b}]	$1.28(6) \times 10^{36}$	$1.7(2) \times 10^{33}$	5×10^{33} [48]
coherence time τ [fs]	124.1(7)	21.8(1)	~0.2 [48]

[a] The bandwidth/duration is computed using the mean absolut deviation $\mathcal{D}_{u,\mathrm{MAD}}$ (2.14), which is less sensitive to the wide tails in the spectral distribution. It is then transformed into the more common standard deviation $\sigma_u \approx \sqrt{\frac{\pi}{2}}\mathcal{D}_{E_{\mathrm{ph}},\mathrm{MAD}}$.

[b] #Phot/s/mm^2/mrad^2/0 1%BW

To recapitulate, the CBXFEL based on the C(400) reflection at $E_{\mathrm{ph}} = 6.97\,\mathrm{keV}$ provides nearly twice as much round trip and FEL gain in the exponential gain regime compared to the C(333) reflection at $E_{\mathrm{ph}} = 9.05\,\mathrm{keV}$. In saturation, both crystal orientations provide closely resembling, very high pulse energies and very gaussian transverse distributions with nearly 100 % of transverse coherence. On the other hand, the C(400) reflection case shows slightly worse longitudinal properties due to the wider reflection bandwidth, which also result in a lower peak brilliance. Comparing the, for the experiment more relevant, transmitted pulses, the C(400) CBXFEL displays only about half the pulse energy and worse transverse as well as longitudinal properties. These degradations are caused by the stronger oversaturation of the electron bunch due to the lower gain length at $E_{\mathrm{ph}} = 6.97\,\mathrm{keV}$ and the higher bandwidth of the respective reflection. Also, and this was not mentioned earlier and is of high importance towards the stable realization of the CBXFEL, the absorption coefficient outside the reflection bandwidth is with $\mathcal{A} \approx 30\,\%$ for a t_c =150 µm crystal nearly trice as high for the $E_{\mathrm{ph}} = 6.97\,\mathrm{keV}$ as for $E_{\mathrm{ph}} = 9.05\,\mathrm{keV}$ photon energy. This not only results in a reduction of the pulse energy, as observed already in the idealized cavity case studied here, but also in an increased heat load on the crystals.

In short, taking into accounts the results of both the C(400) and the C(333) cases and realizing that already for the C(333) CBXFEL there is more than enough round trip gain, from the idealized treatment the CBXFEL using the C(333) reflection at $E_{\mathrm{ph}} = 9.05\,\mathrm{keV}$ seems highly advantageous. Therefore, in the following the discussion will focus solely on the C(333) CBXFEL case.

5.2.2 CBXFEL with errors

Unlike the idealized case discussed above, in this section the influence of different errors on the performance of the CBXFEL demonstrator shall be highlighted. Three different types of ‘errors’ will be discussed. The first are electron beam errors. The second are errors of the X-ray optics. And the third is the influence of the heat load, which will be devoted an own section (see **4.3**).

The electron beam related errors deemed relevant are, besides the non ideal phase space already discussed in Subsection **5.1.1**, the statistical shot to shot fluctuations of the electron beam position, pointing, its energy and its arrival time. In the following these will be respectively called position, pointing, energy and arrival time *jitter*.

The errors or non-idealized influence of the X-ray optics components principally comprise a whole zoo of effects. In this work the ones deemed most influential on the performance of the CBXFEL demonstrator shall be studied. These errors are the angular error of the radiation pulse trajectory introduced by the tilting of an individual component of the mirror assembly (which component principally does not matter), the aperture introduced by the finite size of the mirrors, the potential ‘Montel gap’ (see **C.3**), the surface roughness of the mirrors as well as static strain in the crystal, which would introduce distortions into the spectral reflection curves.

In order to highlight the individual influence of these errors, they will each be studied separately. Then, in a final step they will be combined with the tolerances deemed necessary.

5.2.2.1 Electron beam jitter To study the influence of the shot to shot fluctuations of the electron beam properties, a longitudinally constant offset in position (Δx and Δy), pointing ($\Delta x'$ and $\Delta y'$) and energy $\Delta\gamma$ is added to the electron bunch. The value of these offsets is randomly drawn at every round trip from a normal distribution. The same happens for the arrival time of the electron bunch, with the difference that the negative offset is assumed as a time shift of the radiation pulse via equation (4.24). This is equivalent to a time delay on the electron bunch, as the seeding only depends on the relative longitudinal position of electrons with respect to the radiation.

The widths of the normal distributions, from which the offsets are randomly drawn, are taken from experimental measurements carried out at the active accelerator. Based on these measurements, the mean position and the mean pointing of the electron bunch fluctuate over a rms width of roughly one tenth of the spatial and angular width of the bunch[208], which amounts to $\sigma_{x,y}^{\text{jit.}}$ =3 µm and $\sigma_{x',y'}^{\text{jit.}} = 100\,\text{nrad}$. The energy jitter was measured to fluctuate over one permille from shot to shot[208], which is for the 16 GeV electron beam studied here a total value of $\sigma_{\gamma}^{\text{jit.}} = 3.1$. The arrival time stability of the European XFEL was, based on the very precise timing system, quantified as very small $\sigma_{t,\text{arr.}}^{jit} = 20\,\text{fs}$[209].

In Figure (5.36) the evolution of the pulse energies versus number of round trips from fifteen bunch trains is plotted for a CBXFEL at $E_{\text{ph}} = 9.05\,\text{keV}$. In Table 6 the associated figures of merit of the CBXFEL performance are noted along with the values for the idealized cased.

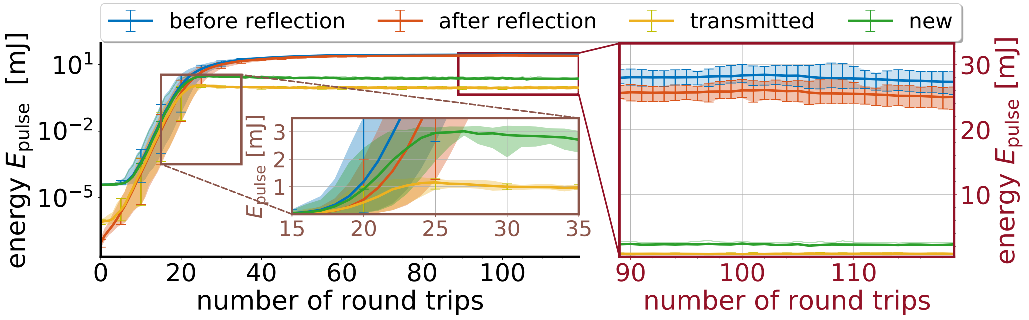

Figure 5.36: Photon pulse energy vs number of round trips for E_{ph} =9.05 keV (C333) photon energy including shot to shot jitter of the electron beam. The green curve is the pulse energy newly generated at each round trip, which is partially being entering into the circulating pulse, partially transmitted and partially absorbed. The left plot in logarithmic scale shows the full evolution of the pulse energy versus number of round trips and the right plot in linear scale displays a stable photon beam after saturation. The inset is a zoom on the energy evolution near the point of the maximum of the transmitted and newly generated radiation. The data was averaged over 15 individual runs/bunch trains with the shaded area showing the minimum/maximum values from these runs.

Table 6: Main parameters of the X-ray pulses in saturation for a CBXFEL at $E_c = 9.05\,\mathrm{keV}$ including statistical electron jitter. The errors denote the standard deviation of the shot-to-shot fluctuation in saturation as well as by averaging over 15 individual runs with equal base parameters.

Photon Energy E_{ph} [keV]	9.05			
	with el. jitter		idealized	
	before refl.	transmitted	before refl.	transmitted
Pulse Energy Q_{pulse} [mJ]	27.6(6)	0.904(65)	31.55(12)	0.915(23)
Bandwidth $\sigma_{E_{\text{ph}}}{}^{a}$ [meV]	7.5(2)	60(2)	5.70(5)	60.3(4)
Pulse Length $\sigma_t{}^{a}$ [fs]	166(2)	159(4)	214(4)	123(4)
Peak Brilliance $\mathcal{B}$ [^{b}]	$4.2(2) \times 10^{36}$	$1.1(2) \times 10^{34}$	$4.84(3) \times 10^{36}$	$1.375(4) \times 10^{34}$
coherence time τ [fs]	468(11)	27(2)	717(15)	25.8(1)
gaussian quality J	1.13(1)	1.90(8)	1.13(1)	1.888(1)

[a] The bandwidth/duration is computed using the mean absolut deviation $\mathcal{D}_{u,\mathrm{MAD}}$ (2.14), which is less sensitive to the wide tails in the spectral distribution. It is then transformed into the more common standard deviation $\sigma_u \approx \sqrt{\frac{\pi}{2}}\mathcal{D}_{E_{\mathrm{ph}},\mathrm{MAD}}$.

[b] #Phot/s/mm^2/mrad^2/0 1%BW

In comparison to Figure (5.11) and Table 4, one can see that for the circulating pulse the pulse energy decreases by roughly 4 mJ and the bandwidth increases by about one quarter, which also comes with an decrease in the temporal coherence time. As also the time duration significantly decreases, this has anyhow little influence on the peak brilliance or the degree of temporal coherence. For the transmitted pulse only a change in the temporal duration can be observed, which signifies a small decrease in the degree of temporal coherence. Anyhow, both for transmitted pulse as for the circulating pulse the change in overall performance is relatively small and the electron jitter is far from being a ‘show stopper’. This also holds when, as a test case, increasing

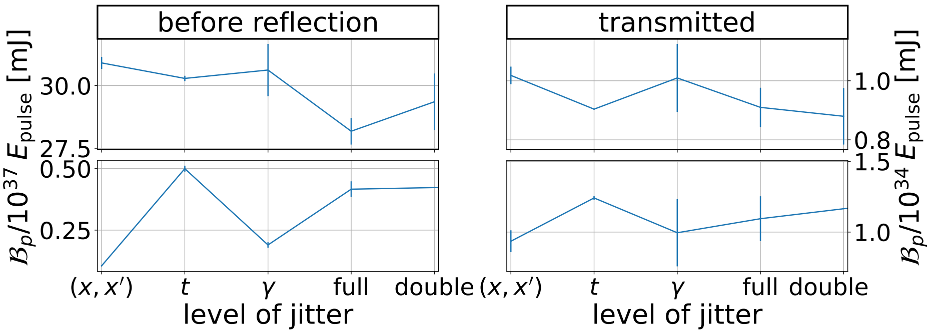

Figure 5.37: The pulse energies and brilliance of the circulating pulse before reflection and the transmitted pulse for different cases of electron jitter. The studied cases are only including positional and angular electron jitter with $\sigma^{\text{jit.}}_{x,y}$ =6 µm and $\sigma^{\text{jit.}}_{x',y'} = 200\,\text{nrad}$, only including arrival time jitter with $\sigma^{jit}_{t,\text{arr.}} = 30\,\text{fs}$, only beam energy jitter $\sigma^{\text{jit.}}_{\gamma} = 6.2$ and including all these sources of jitter with $\sigma^{\text{jit.}}_{x,y}$ =3 µm, $\sigma^{\text{jit.}}_{x,y} = 100\,\text{nrad}$, $\sigma^{jit}_{t,\text{arr.}} = 20\,\text{fs}$ and $\sigma^{\text{jit.}}_{\gamma} = 3.1$ as well as including all with stronger fluctuations $\sigma^{\text{jit.}}_{x,y}$ =6 µm, $\sigma^{\text{jit.}}_{x',y'}$ =200 nrad, $\sigma^{\text{jit.}}_{\gamma} = 6.2$ and $\sigma^{jit}_{t,\text{arr.}} = 30\,\text{fs}$. It is evident that the beam energy γ jitter has from the individual jitter sources the strongest influence on the radiation pulse stability.

the standard deviations of the jitter distributions to $\sigma^{\text{jit.}}_{x,y}$ =6 µm, $\sigma^{\text{jit.}}_{x',y'} = 200\,\text{nrad}$, $\sigma^{\text{jit.}}_{\gamma} = 6.2$ and $\sigma^{jit}_{t,\text{arr.}} = 30\,\text{fs}$. This is presented in Figure (5.37) with the label 'double'.

However, while the mean performance parameters only change little, the shot to shot fluctuations of the resulting radiation pulses increase strongly from the permille to the multiple percent level. Especially for the transmitted pulse the fluctuations are strong, as the pulse is, unlike the circulating pulse, fully dependent on the newly generated electromagnetic field inside the undulators. This newly generated energy is strongly dependent on the jittering properties of the electron bunch.

In Figure (5.37) the pulse energy and the brilliance of the circulating pulse before reflection and the transmitted pulse are displayed for different simulations runs with the different sources of jitter isolated. From the results, it is quite obvious that the dominant source of radiation pulse instability is the electron beam energy jitter.

The position and pointing jitter of the electron beam only have limited influence, even when taking double the standard deviations $\sigma^{\text{jit.}}_{x,y}$ =6 µm and $\sigma^{\text{jit.}}_{x,y} = 200\,\text{nrad}$, as done for the presented simulation. As these offsets are small with respect to the total radiation pulse width (both spatial and angular), the impact on the single pass gain is rather little. Besides, as was thoroughly discussed for the idealized cavity, in saturation the fractions of the beam which are reabsorbing energy from the radiation pulse due to oversaturation are compensated by other fractions of the beam which have not yet reached saturation and still provide FEL gain. This stabilizes the pulse energy against the initial level of gain to some degree.

One would estimate an arrival time jitter which is fluctuating over a level wider than the electron bunch length, as was studied here with $\sigma^{jit}_{t,\text{arr.}} = 30\,\text{fs}$, to have a severe influence on the CBXFEL demonstrator. As visible in Figure (5.37), this is not the case. The reason for this is the time domain stretching of the seeding pulse to the $\sigma_t > 100\,\text{fs}$ level due to the crystal reflection. So even having a $\Delta t = 50\,\text{fs}$ mismatch for an individual shot, photon beam and electron bunch will still have considerable overlap. The slight fluctuation in the seeding strength additionally gets compensated by the roughness of the newly generated energy versus gain in saturation, as was mentioned above. It has to be noted, that for the case including timing jitter the cavity had a constant longitudinal detune introduced, which provided better stability than optimal matching without the timing jitter.

Regarding the influence of the beam energy jitter, is has to be noted that the standard deviations of $\sigma_\gamma^{\text{jit.}}/\gamma_R = 1 \times 10^{-4}$ or even $\sigma_\gamma^{\text{jit.}}/\gamma_R = 2 \times 10^{-4}$ as assumed for Figure (5.37) are on the same scale as the actual gain parameter $\rho_{\text{FEL}} \approx 4 \times 10^{-4}$. This is of minor importance for SASE operation, as the central photon energy just shifts with the jitter of the beam energy. This, however, is obviously not possible for the case of the CBXFEL, as the photon energy E_{ph} is fixed by the reflection resonance $E_c = 9.05\,\text{keV}$. Besides, depending on the direction of the offset, there are shots were especially the parts of the beam which already have an initially low gain due to the strong chirp get an even worse gain. This becomes important for the saturation case and is the dominant effect for the shot to shot fluctuations visible.

To conclude, the inter-train fluctuations of the position, pointing, arrival time and energy of the electron beam only have little influence on the mean performance of the CBXFEL demonstrator. However, while the demonstrator is very robust even towards double the position, angular and arrival time jitter measured for the European XFEL[208, 209], the electron beam energy jitter introduces strong fluctuations especially in the transmitted power. This does not prohibit the main goal of the experiment to prove the working principle of a CBXFEL at the European XFEL. Yet, it does weaken one of the main selling points of the demonstrator, which is the extraordinary shot to shot stability. For the long run, it would therefore be important to invest in reduction of the beam energy jitter.

5.2.2.2 Mirror Tilt: The influence of the angular misalignment of the mirror assembly shall be highlighted here. Studying the influence of the angular misalignment on each angular degree of freedom of each of the six mirrors would lead to an exceedingly high numeric demand. Therefore only the impact of varying angular tilt of the downstream crystal mirror will be discussed, which is further simplified by assuming that the tilt in the roll- and in the pitch-axis is equal. This can, however, still serve as a meaningful measure to study the CBXFEL's general angular tolerance. This is due to three reasons.

For one, taking the electron bunch transverse distribution as approximately circular, the impact of the pitch- and roll-tilt should be quite comparable. Therefore studying a radial angular offset can be considered sufficient.

The second reason is that in the Montel setup the two grazing incidence mirrors are fixed with respect to each other and only the crystal mirror is free to be tuned in angle. As is shown in **C.2**, there is always an roll- and pitch configuration of the crystal to nearly perfectly recover the retroreflecting properties given a sufficiently small dyadic error $\Delta\alpha < 2\,\text{mrad}$ between the retroreflecting mirrors[65]. Hence, to study the impact of the angular misalignment of the three mirror setup, it is sufficient to look at the offset $\Delta\Theta$ from this ideal roll-pitch configuration of the crystal[66].

The third reason is that the downstream mirror assembly can be assumed to have a stronger impact on the CBXFEL saturation. This is due to the longer distance L the radiation has to travel before reentering the undulator, which yields a greater positional offset of $\Delta x = L\Delta x'$ assuming a drift section. As in the intermediate gain CBXFEL there is considerable gain guiding in the exponential gain regime, the angular offset introduced by both mirror assemblies gets averaged out and only the positional offset remains relevant. This, however, changes when the CBXFEL reaches the saturation regime and the circulating radiation is dominated by the cavity modes. Anyways, for the saturation regime the impact of both mirror assemblies on the stability should be approximately equal. Therefore it is sufficient to only study the downstream mirror assembly but keeping in mind that the angular tolerance is about two times tighter to accommodate for the worst case scenario when the tilt of both assemblies stack.

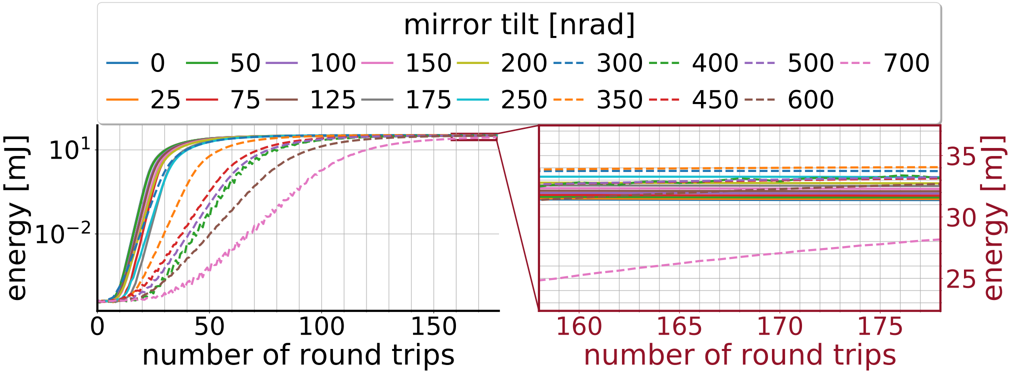

Figure 5.38: The pulse energy evolution $E_{\text{pulse}}^{(\text{und.})}$ of the radiation pulse before reflection for different magnitudes of (radial) angular tilt of the downstream crystal.

In Figure (5.38) the evolution of the pulse energy before reflection is displayed for various magnitudes of the angular tilt. It is evident, that for levels of tilt up to the two hundred nanoradian level there is hardly any change in the CBXFEL performance compared to the untilted case.

For levels of tilt at least up to $\Delta\Theta \leq 600\,\text{nrad}$ the main difference for the evolution of the pulse energy is the round trip gain, whereas the saturated pulse energy stays the same[67].

This can also be seen in Figure (5.39(a)), where the round trip gain $\mathcal{G}_{\mathcal{RT}}^{\text{seed}}$ of the seeding pulse is plotted for exemplary levels of tilt. In this figure, one can see that the gain is successively decreasing with increasing angular tilt for $\Delta\Theta > 100\,\text{nrad}$. This is to be expected given the decreasing transverse overlap between electron bunch and photon pulse with increasing tilt. As the gain of the four undulator section CBXFEL demonstrator at $E_{\text{ph}} = 9.05\,\text{keV}$ is very high, the reduction in gain has, however, small influence on the CBXFEL performance in saturation.

---

[65] As discussed in **C.2**, the variation of the incoming radiation with respect to the mirror assembly can be compensated by approximately a factor $2\Delta\alpha$.

[66] The dyadic error $\Delta\alpha$ adds an additional angular offset, but this contribution scales with $O(\Delta\alpha\Delta\Theta)$ and becomes negligibly small for small $\Delta\alpha$.

[67] It has to be noted that the $\Delta\Theta = 700\,\text{nrad}$ case has not yet reached saturation, so it might also show the same pulse energies in saturation.

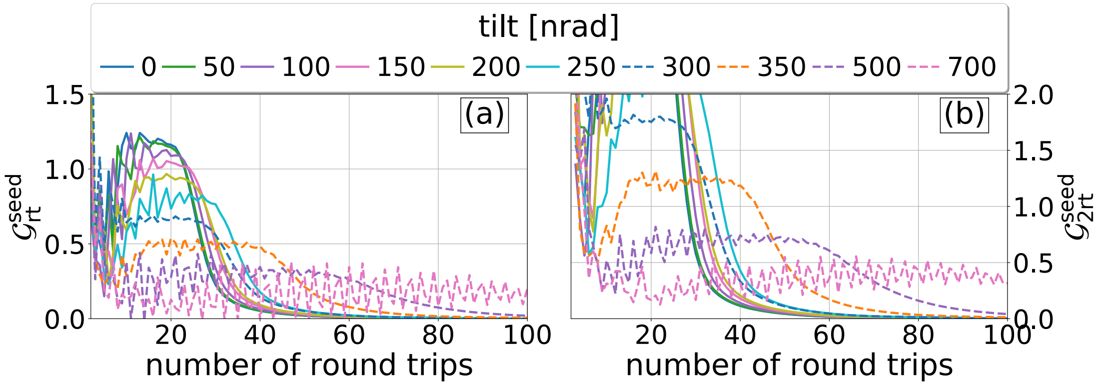

Figure 5.39: Evolution of the round trip gain of the seeding pulse for exemplary magnitudes of (radial) angular tilt of the downstream crystal. In (a) the regular round trip gain $\mathcal{G}_{\mathrm{rt}}^{seed}(\#\mathrm{rn}) = Q^{\mathrm{seed}}_{\mathrm{pulse}}(\#\mathrm{rn})/Q^{\mathrm{seed}}_{\mathrm{pulse}}(\#\mathrm{rn}-1) - 1$ is plotted and in (b) the round trip gain $\mathcal{G}_{\mathrm{2rt}}^{seed}(\#\mathrm{rn}) = Q^{\mathrm{seed}}_{\mathrm{pulse}}(\#\mathrm{rn})/Q^{\mathrm{seed}}_{\mathrm{pulse}}(\#\mathrm{rn}-2) - 1$ for every second round trip. One can see a clear decrease in gain for increasing level of tilt.

For tilts $\Delta\Theta \geq 350\,\mathrm{nrad}$, the round trip gain, besides decreasing in magnitude, becomes unstable and begins to fluctuate from shot to shot with the amplitude of the fluctuations increasing with tilt. For one, this is due to the CBXFEL entering the gain stabilizing exponential gain regime at later round trips. The second reason is that the radiation path loses its periodicity over the cavity length with the introduction of the tilt. This can be seen in Figure (5.40), where the x-axis radiant energy density computed from a simple ray tracing run is displayed for various level of tilt for a no-loss cavity without any internal generation.

For tilts higher than $200\,\mathrm{nrad}$ one can see a significant difference in the transverse distribution from the first to the second round trip. This is obviously influencing the seeding strength, with the seed having a better overlap and therefore increased gain for every second round trip. Especially for the $\Delta\Theta = 300\,\mathrm{nrad}$ and $\Delta\Theta = 400\,\mathrm{nrad}$ tilts there is very little overlap between the electron beam and the radiation seed after one round trip whereas the overlap becomes significantly better after the second. This is supported by the ‘two round trips gain’ $\mathcal{G}_{\mathrm{2rt}}^{seed}(\#\mathrm{rn}) = Q^{\mathrm{seed}}_{\mathrm{pulse}}(\#\mathrm{rn})/Q^{\mathrm{seed}}_{\mathrm{pulse}}(\#\mathrm{rn}-2) - 1$ displayed in Figure (5.39(b)). While for lower levels of tilt, the curve principally is just double the single round trip gain from Figure (5.39(a)), for higher tilts the afore mentioned oscillations strongly decrease in relative magnitude.

In Figure (5.41(left)) the pulse energy as well as the brilliance and the J of the radiation pulse in saturation is displayed. It affirms the above discussed features with the performance of both circulating radiation as transmitted radiation remaining on a high level for mirror tilts $\Delta\sigma \leq 400\,\mathrm{nrad}$[68]. For higher tilts, while the pulse energy stays on a very high level, one can see a strong degradation of the transverse quality of the radiation pulse.

The slight increase in pulse energy with increasing tilt for $\Delta\Theta \leq 350\,\mathrm{nrad}$ is due to the increas-

---

[68] It should be noted that the $\Delta\Theta = 400\,\mathrm{nrad}$ case is somewhat special, as it shows the strongest oscillations in gain which result in the most unstable transmitted beam. This fluctuating can can be traced to the strongly varying overlap between electrons and seed for the same reason as discussed above. That this variation is particularly strong can be considered somewhat like a resonance coincidence with the focussing lattice of the cavity. The same can be considered for the $\Delta\Theta = 700\,\mathrm{nrad}$ case, with the additional feature of the worse tranverse overlap of electron beam and photon pulse for latter.

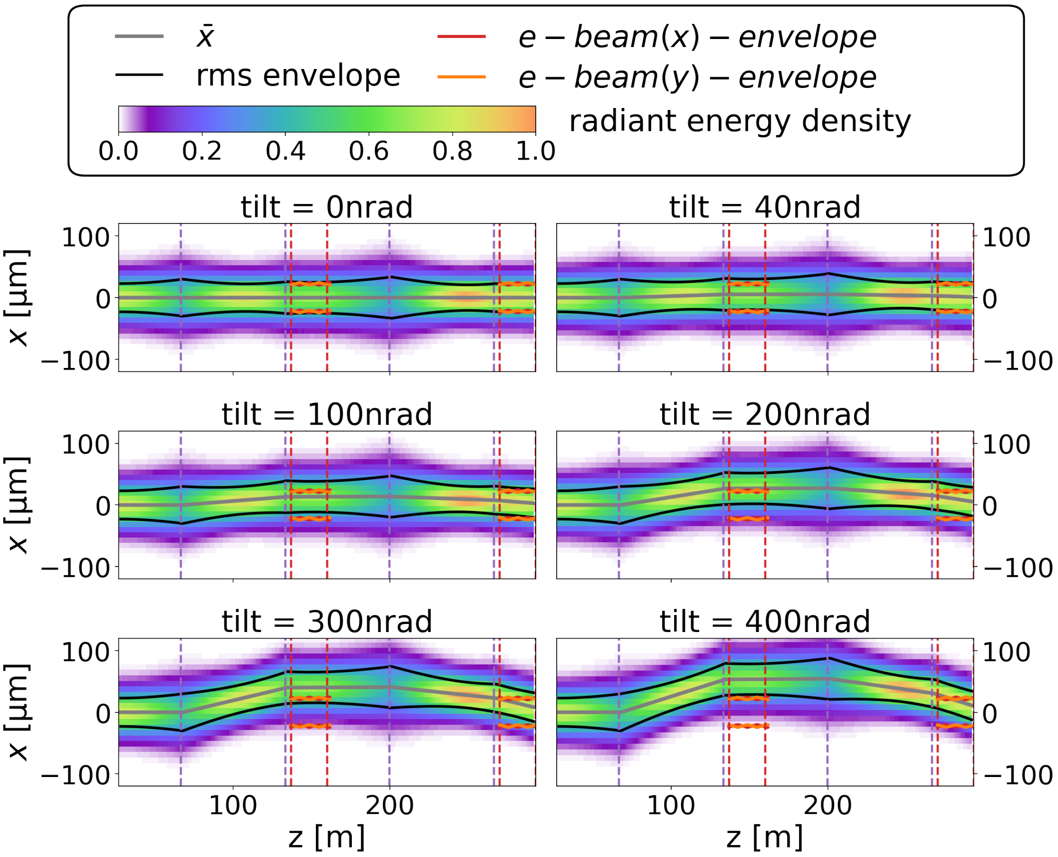

Figure 5.40: Evolution of the (normed) x-axis radiant energy density for various levels of tilt of the downstream crystal from simple (2×2) matrix formalism ray tracing without internal generation or losses. For the initial distribution 5×10^5 rays with $s_{0,i} = (x_{0,i}, k_{0,i})$ were drawn from a normal distribution with σ_x =22.84 µm and σ_k =0.485 µrad, which are derived from the gaussian stable mode. As guide for the eye the (focussing) mirrors are shown as vertical purple lines and the start and end of the undulator section as dashed red vertical line. As a reference also the rms envelope of the electron beam reference slice is displayed.

ing overlap of the radiation pulse with the 'badly matched' fractions of the electron beam, which become important at high seeding strengths as discussed for the idealized cavity **5.2.1**. This also results in a small narrowing of the spectral curve and therefore in a decrease in transmitted pulse energy.

Generally, it is important to note that the influence of the angular tilt of the crystal mirrors is much smaller than anticipated in original works [20, 165], which proposed tolerance on the tens of nrad scale. For one, this is due to the higher compensation of the decreased overlap with the much higher FEL gain considered for the demonstrator. Second, the original estimates were based on an overly simplified picture which looked only at one round trip of the central ray $s_0 = (x_0 = 0, k_0 = 0)$ and therefore the mean position of the radiation pulse. Tracing the full spatial and angular distribution of the rays as in Figure (5.40) also takes into account the actual width and its overlap with the electron bunch. Also, under the prerequisite that the gain in the system is high enough, it is also important to trace more than only one round trip, as both the centroid as well as the beam width change with the number of round trips. These effects lead to

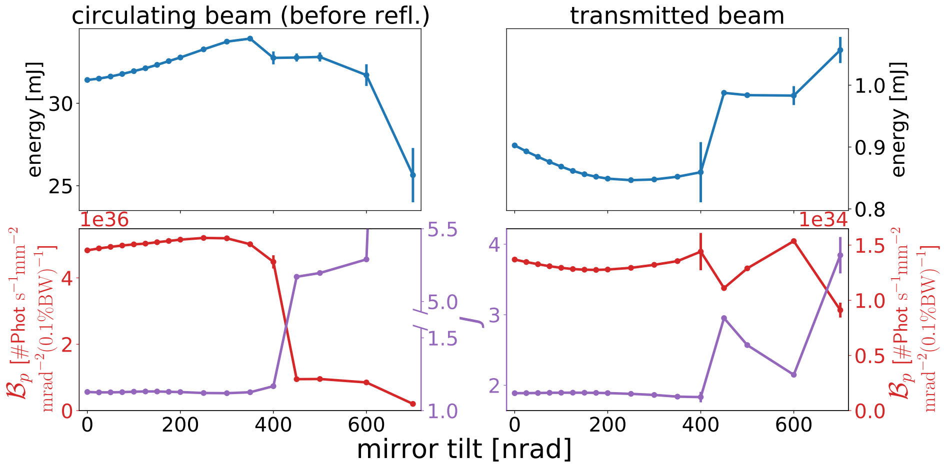

Figure 5.41: Pulse energy (top), brilliance and gaussian quality factor (bottom) of the circulating pulse before reflection (left) and the transmitted pulse (right) in saturation for different angular tilts of the downstream crystal mirror. Please note the discontinuous vertical-axis for the J plot of the circulating beam. The performance of the CBXFEL demonstrator remains very stable for tilts on the level $\Delta\Theta \leq 350\,\mathrm{nrad}$.

a better overlap of the electron beam with the radiation pulse.

To summarize, angular tilt on the level $\Delta\Theta \leq 400\,\mathrm{nrad}$ primarily effects the gain and therefore the number of round trips to reach saturation. As the initial gain of the CBXFEL demonstrator is rather high, it is very tolerable towards these reductions. In order to have safety measures towards other errors reducing the gain, one should however keep the mirror tilt at a level $\Delta\Theta \leq 200\,\mathrm{nrad}$ where the reduction in gain is very small. Keeping in mind that the second mirror assembly also introduces errors into the system, the tolerance against tilt can be concluded to be around $\Delta\Theta_{\mathrm{Tol.}} \approx 100\,\mathrm{nrad}$.

5.2.2.3 Longitudinal detune: Besides the influence of angular misalignment, the CBXFEL also is dependent on longitudinal mismatch, be it due to a static mismatch of the cavity length to the electron bunch repetition rate or due to dynamic vibrations. For these simulations the static case will be considered, as the dynamic, macroscopic vibrations will be on the single kilohertz level[69] and therefore appear as quasi-static on the time-scale of one bunch train. Also, the EuXFEL intra-train arrival time jitter of $\sigma_{t,\mathrm{arr.}}^{jit} = 20\,\mathrm{fs}$ will be considered, as it is naturally influencing the dependence of the longitudinal detune.

In the following the convention will be applied that a positive Δs corresponds to an increase in cavity length by Δs. As analogue representation the arrival time difference $\Delta t = -{}^{\Delta s}/_{c}$ will also often be shown, where a positive $\Delta t > 0$ corresponds to the seeding pulse (nominally) slipping ahead of the electron bunch.

In Figure (5.42) the pulse energy evolution of the circulating radiation pulse before reflection is displayed for various values of longitudinal mistune Δs. Aside from very big mistunes $\Delta s \tilde{<} {-20}\,\mu\mathrm{m}$ and $\Delta s \tilde{>} 15\,\mu\mathrm{m}$ the CBXFEL still saturates at very high pulse energies on the

---

[69] Unlike the microscopic internal 'vibrations' or strain waves, which can be induced by the heat load.

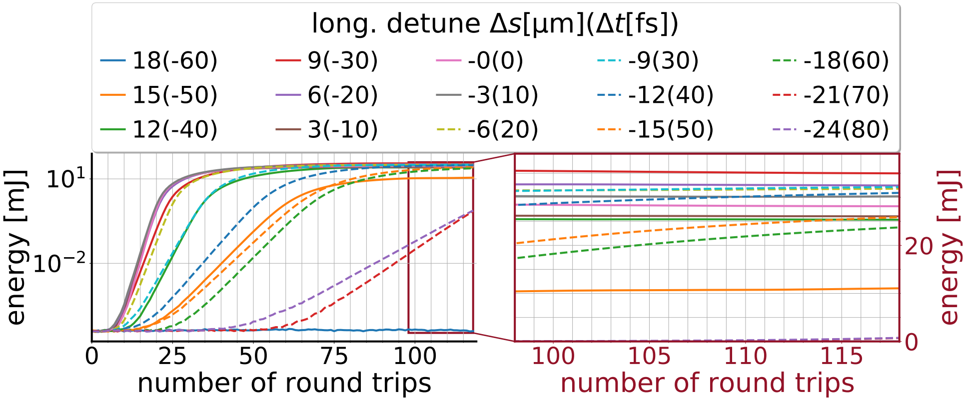

Figure 5.42: The pulse energy evolution $Q^{(\text{und.})}_{\text{pulse}}$ of the radiation pulse before reflection for different mismatches Δs of the cavity length, with $\Delta s > 0$ meaning a longer cavity and vice versa. These mismatches correspond to a time difference between electron bunch and photon pulse $\Delta t = -{}^{\Delta s}/_{c}$ with $\Delta t > 0$ signifying the radiation pulse arrives ahead of the electrons.

$Q^{(\text{und.})}_{\text{pulse,sat.}} > 20\,\text{mJ}$ level. However, unlike the influence of the angular tilt in Figure (5.38), there is a distinct variation of the pulse energy with smaller mistunes Δs. In Figure (5.43(a)) the

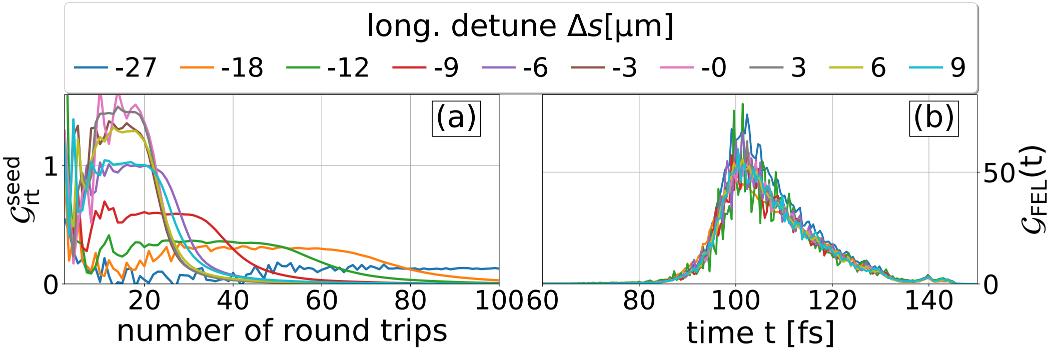

Figure 5.43: (a) shows the round trip gain (5.1) of the seeding radiation against number of round trips for varying mistunes Δs of the cavity length. (b) displays the actual gain profile of the FEL process for a single shot in the exponential gain regime for different longitudinal mistunes (with the actual round trip number varying dependent on Δs due to the varying onset of the exponential gain regime). The gain profile is approximately independent of the mistune.

round trip gain of the seeding radiation is displayed for different mistunes Δs. It shows that the longitudinal mistune already has an effect for mistunes on the $|\Delta s| \approx 3\,\mu\text{m}$ to $6\,\mu\text{m}$ range. This corresponds to a time difference of $|\Delta t| \approx 9\,\text{fs}$ to $18\,\text{fs}$, which is on the order of the electron bunch length. For increasing mistunes the gain continuously drops, which can anyhow be compensated due to the initially large gain of the idealized cavity, as was already discussed for the angular tilt.

The high stability against the longitudinal mistune follows the same argumentation as for the arrival time jitter, which is the stretched seeding signal with $\sigma_t > 100\,\text{fs}$. As the longitudinal mistune leads to an overlap of the electron bunch with weaker fractions of the pulse the round trip gain is reduced. The actual FEL gain is not affected as can be seen in Figure (5.43(b)).

In Figure (5.44(left)) the pulse energy as well as the brilliance and the time bandwidth product

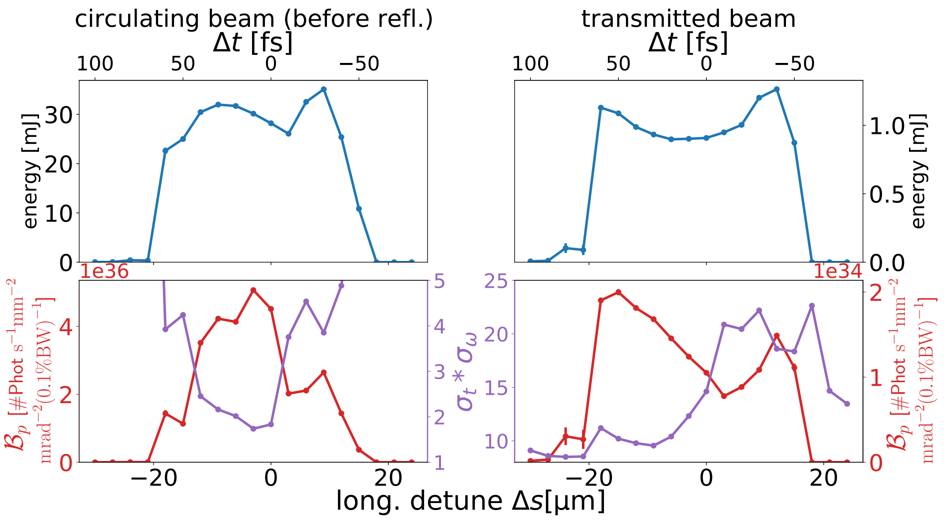

Figure 5.44: Pulse energy (top), brilliance (red, bottom) and time-bandwidth product (purple, bottom) of the circulating pulse before reflection (left) and the transmitted pulse (right) in saturation or different longitudinal mismatches of the cavity length.

of the radiation pulse in saturation is displayed. It affirms the stability of the CBXFEL demonstrator performance over a wide range of cavity length mismatches Δs. The same holds for the transmitted radiation shown in Figure (5.44(right)). As in the case of the tilt the transmitted pulse shows a somewhat inverse behavior to the circulating pulse, as a weaker pulse energy of the seeding pulse leads to a weaker oversaturation of the FEL process.

For $0 < \Delta s \tilde{<} 9$ μm, meaning a longer cavity length, one can observe an inverse trend of the brilliance and the pulse energy of the circulating radiation pulse. This is due to the pronounced increase in the time-bandwidth product with increasing Δs for $\Delta s > 0$, which is inverse proportionally affecting the peak brilliance. Such a pronounced increase in the time-bandwidth product can also be observed for negative $\Delta s \leq -13$ μm.

The reason for this increase can be traced back to the spectral-temporal coupling of the reflection. As was already described for the transmitted pulse in the idealized cavity **5.2.1**, different wavelengths or photon energies correspond to different reflection efficiencies in the diamond crystal. This again influences the penetration depth into the crystal and therewith the longitudinal offset introduced by the reflection. The oscillator is naturally adapting to the wavelength that has the best seeding efficiency. This also involves the wavelength with the best time domain matching to the electron bunch. Hence, the longitudinal mismatch has a direct influence on the radiation spectrum, as can be seen in Figure (5.45(a)). The effect is slightly more pronounced for positive $\Delta s > 0$, as this corresponds to the photon pulse slipping behind the electron bunch. This also means that the long tail of the seed cannot compensate for it and the compensation of the bad matching by the wavelength selection becomes particularly strong. However, the seeding pulse is also significantly stretched to positive t (see Figure (5.14) and Figure (5.24(upper))), so the difference between positive and negative mistune is rather small.

In Figure (5.45(b)) one can also see an influence of Δs on the spectrum of the transmitted pulse,

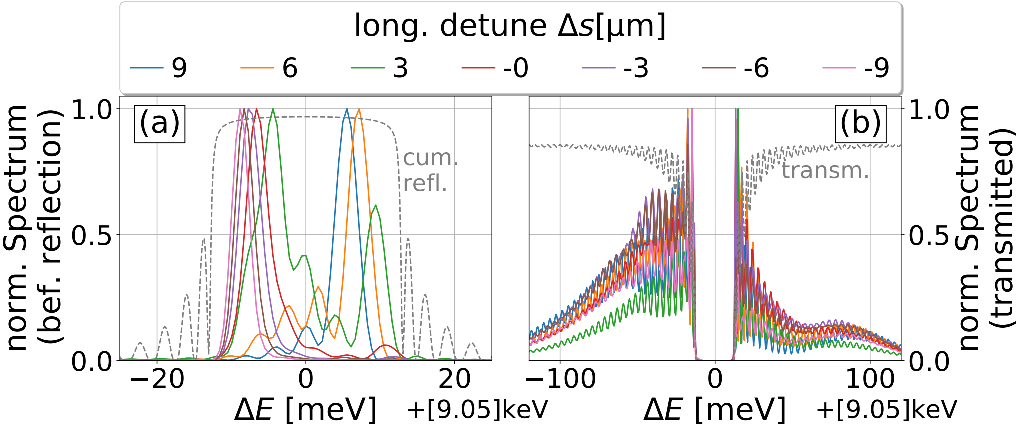

Figure 5.45: Normed spectra of the saturated circulating radiation pulse before reflection(a) and the saturated transmitted pulse(b) for different cavity length mismatches Δs.

with dominantly the bandwidth changing. A higher bandwidth results in a smaller effect of the strong temporal-spectral correlation close to the reflection bandwidth, as was discussed for the idealized cavity **5.2.1**. This leads to a better time-bandwidth product as shown in Figure (5.44(lower right)) and therefore in an increased brilliance.

To summarize, the CBXFEL is quite tolerant against longitudinal mistunes on the multiple μm level. This tolerance is slightly higher for a shortening $\Delta s < 0$ of the cavity than for an extension $\Delta s > 0$ due to the very long tail of the seeding pulse. It has also been shown that the radiation spectrum can be strongly affected by the cavity length, which can result in an enhanced quality of the transmitted pulse.

Principally, a tolerance towards the longitudinal mismatch of $\Delta s_{\text{tol.}} \approx 6\,\mu\text{m}$ can be considered sufficient. However, it is to note that the mechanical tolerance of the mirror positioning is half this value, as a mirror offset enters twice in the cavity length. Furthermore, there are two mirror assemblies. So following the same argumentation as for the angular misalignment, the demands should be twice as high, leading to a demand of the mechanical position tolerance of $\Delta s_{\text{tol.(mirr.)}} =$1 μm to 2 μm[70].

5.2.2.4 Finite size of the grazing incidence mirrors

As was already mentioned in Section **5.1**, the finite size of the grazing incidence mirrors is introducing a approximately rectangular aperture of size $w^{\text{ap}} = l \sin \Theta_{\text{in}}$ with l being the mirror length and Θ_{in} the grazing incidence angle. To enable the operation at $E_{\text{ph}} = 9.05\,\text{keV}$ and have some angular safety margins, referring to Figure (5.4) a grazing angle of $\Theta_{\text{in}} = 3.1\,\text{mrad}$ is assumed in the following. This corresponds to a scaling of physical length to projected aperture size of 3.1×10^{-3}, meaning that a length of $l \approx 3.2\,\text{cm}$ corresponds to $w^{\text{ap}} =$100 μm.

---

[70] How to properly align to these values is a point which remains under discussion. Having achieved proper transverse alignment, the most straight forward way would be to use the seeding of the X-rays itself. However, if this does not succeed, it would remain unclear if it is due to false longitudinal overlap or due to other issues. Another possibility under discussion is to use photon arrival time monitors with resolutions up to 10 fs, as planned for the European XFEL [210].

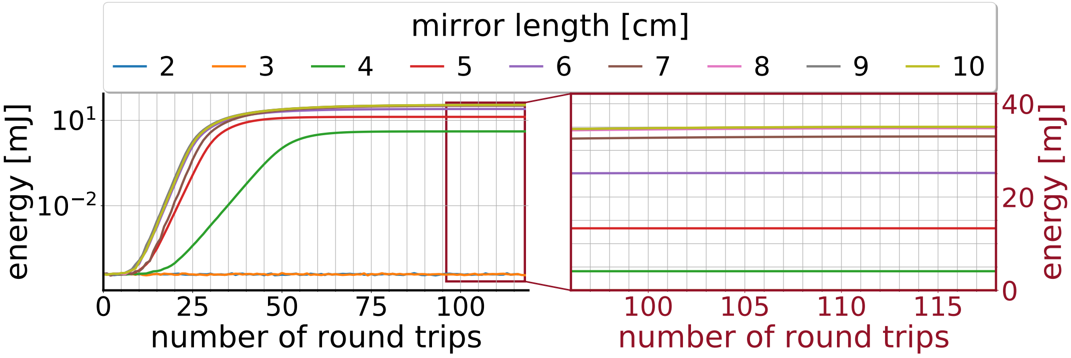

Figure 5.46: The pulse energy evolution $Q_{\text{pulse}}^{(\text{und.})}$ of the radiation pulse before reflection for different lengths of individual grazing incidence mirrors.

In Figure (5.46) the energy evolution of the circulating pulse before reflection for a CBXFEL with different mirror lengths is displayed. The simulations also include a downstream mirror tilt of $\Delta\Theta = 200\,\text{nrad}$, which was determined as angular tolerance of the CBXFEL demonstrator. This is done as the mirror tilt is changing the radiation pulse position on the mirrors and is therefore obviously affecting the influence of the mirror size. Evidently, there is hardly any influence of the mirror length for $l \geq 7\,\text{cm}$.

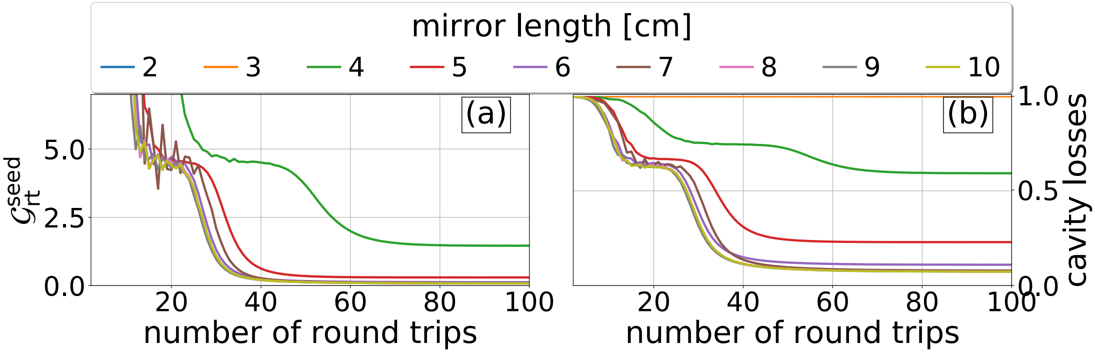

Figure 5.47: Round trip gain (5.1) of the seeding radiation (a) and cavity losses $\mathcal{L}_{\text{cav}}(\#\text{rn}) = 1 - E_{\text{pulse}}^{\text{seed}}(\#\text{rn})/E_{\text{pulse}}^{\text{Und}}(\#\text{rn})$ (b) against number of round trips for varying length of the individual grazing incidence mirrors. The cavity losses also incorporate the spectral losses due to the band filtering at the diamond mirrors. The cases $l = 2\,\text{cm}$ and $l = 3\,\text{cm}$ are not visible in (a), as they never enter the stable seeding regime and the synchrotron radiation remains dominant. This leads to a strongly overestimated seeding gain $\mathcal{G}_{\text{rt}}^{\text{seed}} \gg 5$. In (b) both cases are overlapping with $\mathcal{L}_{\text{cav}} \approx 1$.

This is also supported by Figure (5.47), where the round trip gain and the cavity losses for varying length of the individual grazing incidence mirrors are displayed. In analogy to the evolution of the pulse energy, for $l \geq 7\,\text{cm}$ there is neither a difference in the cavity losses nor in the round trip gain. For $l = 6\,\text{cm}$ the cavity losses in saturation are slightly higher, as a tiny fraction of the radiation is transversely cut off. For the lengths $l = 4\,\text{cm}$ and $l = 5\,\text{cm}$ a considerable fraction of radiation energy is cut off at the aperture. This leads to increased cavity losses which limit the pulse energy in saturation and also reduce the round trip gain, which naturally include the cavity losses.

A length of $l = 4\,\text{cm}$ corresponds to an aperture of size w^{ap} =124 µm. Assuming the validity of the simple ray tracing simulations Figure (5.40) for a tilt of 200 nrad, the beam has a standard deviation of σ_x ≈30 µm and a centroid $\bar{x}$ =0 µm at the position of the downstream mirror assembly and σ_x ≈26 µm and a centroid $\bar{x}$ =26 µm at the position of the upstream mirror assembly. Using a normally distributed beam, the aperture would then cut off about 7 % of the total power at the downstream and about 15 % at the upstream mirror. So this cannot fully account for the cavity losses shown in Figure (5.47(b)).

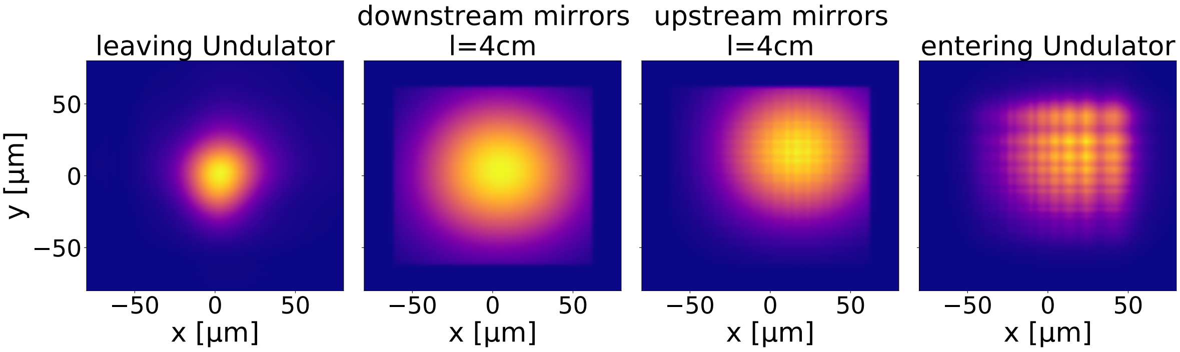

Figure 5.48: Spatial distributions of the circulating radiation pulse in saturation for 4cm mirror length directly after the undulator, after the downstream mirror assembly, after the upstream mirror assembly and before reentering the undulator section. One can clearly see the diffraction at the aperture introducing strong distortions into the transverse distribution.

There is an additional effect affecting the losses, which is the diffraction introduced by the apertures. This diffraction alters and widens the transverse distribution of the radiation pulse, which leads to slightly higher losses at both mirror assemblies. This is displayed in Figure (5.48) for the transverse distribution of the circulating radiation pulse in saturation for a individual mirror length of $l = 4\,\mathrm{cm}$. One can clearly observe distortions successively building up due to the diffraction introduced at the mirror assemblies, which finally leads to a quite distorted profile of the seeding pulse with an gaussian quality factor of $J = 9.28$[71]. This reduces the (non-saturation) gain length.

As was thoroughly discussed in **5.2.1**, this does not reduce the newly generated energy[72], as the undisturbed CBXFEL has far reached oversaturation. But, as shown in Figure (5.49), it affects the width of the gain profile in saturation and therefore the spectrum of the newly generated radiation. For the non disturbed CBXFEL, which is approximately the case at $l = 6\,\mathrm{cm}$, the cavity losses significantly drop in saturation due to the narrowing of the newly generated radiation. This is less the case for the CBXFEL at $l = 4\,\mathrm{cm}$ mirror length, which decreases the reduction in (spectral) cavity losses with increasing number of round trips as visible in Figure (5.47b).

For lengths $l \leq 3\,\mathrm{cm}$ the CBXFEL finally does not enter the exponential gain regime at all. A length of $l = 3\,\mathrm{cm}$ corresponds to an aperture of size w^{ap} =93 µm. Assuming the validity of the ray tracing simulations Figure (5.40) as above, this aperture would lead to a cut off of about

---

[71] One has to keep in mind, that the undulators start very close to the upstream mirror. So the apparently much stronger diffraction effects introduced by the upstream mirror compared to the downstream mirror, as visible in Figure (5.48), are mostly due to the much shorter drift length (3.6 m compared to 66.42 m), over which these distortions may smooth out.

[72] It even is beneficial as will be shown below.

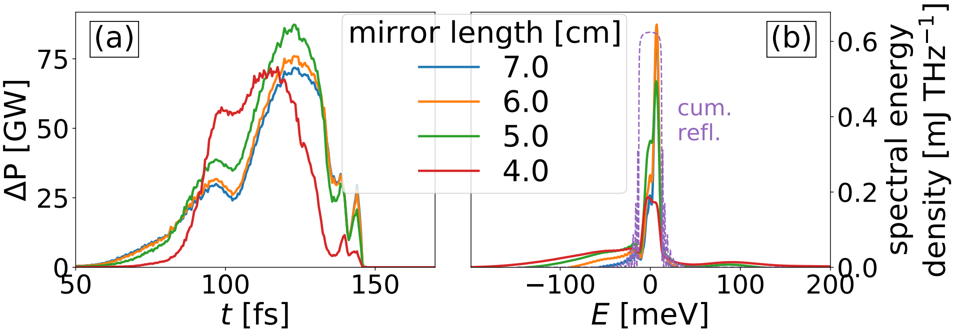

Figure 5.49: (a) displays the power profile of the radiation newly generated in the undulator section for exemplary mirror lengths, which show an increasing time duration with increasing length. (b) display the spectra of the newly generated radiation. These exhibit, in opposition to the power profile, a narrowing with increasing mirror length. As a guide for the eye the cumulative reflection curve is shown as purple dashed line.

22 % of the total power at the downstream and of about 38 % at the upstream mirror. While these losses are already very high, they cannot fully explain the failing onset of seeding. This is due to two additional effects. One is the additional distortions introduced by the diffraction effects, which are stronger than for $l = 4\,\mathrm{cm}$ due to the stronger cut off. The second effect is that, as discussed for the idealized cavity in **5.2.1**, the tranverse radiation distribution is very unstable and much wider during the start up. This increases the cut off losses and diffraction effects and lead to the observed case that the CBXFEL never reaches the stabilized exponential gain regime.

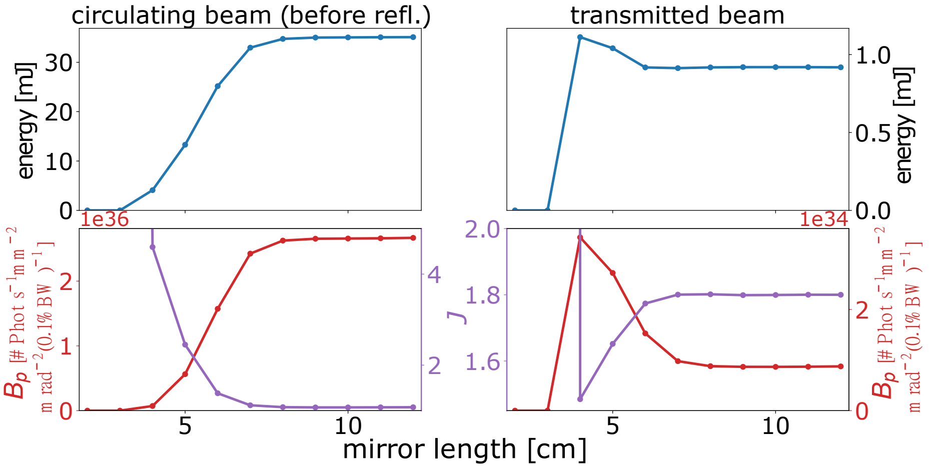

Figure 5.50: Pulse energy (top), brilliance and gaussian quality factor (bottom) of the circulating pulse before reflection (left) and the transmitted pulse (right) in saturation for different lengths of the grazing incidence mirrors. One can observe an inverse trend of the performance of the circulating and the transmitted pulse.

In Figure (5.50(left)) the pulse energy as well as the brilliance and the J of the radiation pulse in saturation is displayed. One can observe, as was discussed above, an increase of the saturated pulse energy with increasing mirror length, which becomes constant for $l \geq 8\,\mathrm{cm}$. The brilliance follows the same trend, but has a steeper gradient as it is additionally affected by the distortions of the transverse beam distribution which are introduced at low mirror lengths and are expressed in an increase in J.

Interestingly, Figure (5.50(right)) shows, with the exception of the lengths $l \leq 3\,\mathrm{cm}$, the inverse trend for the transmitted pulse. This is due to the oversaturation of the FEL process, which increases with increasing seeding strength, as already discussed for the idealized cavity. As the gain guiding cleans the transverse distributions of the newly generated radiation, even from a disturbed seeding pulse only the advantageous effects of the reduced gain remain.

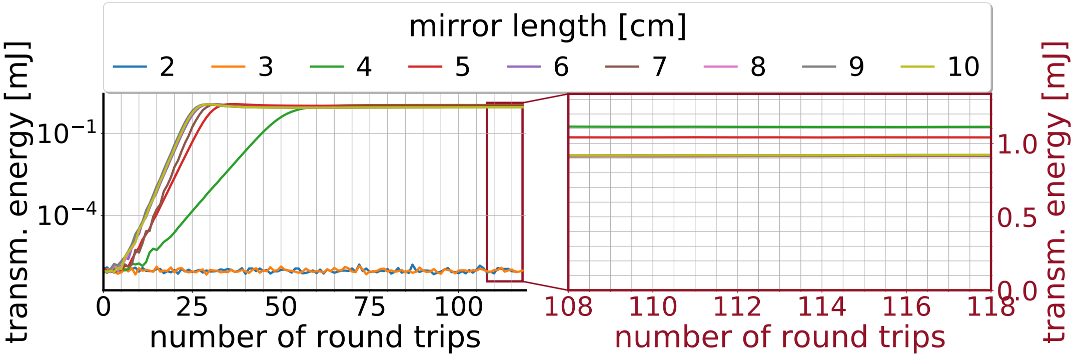

Figure 5.51: The pulse energy evolution $Q^{(\mathrm{und.})}_{\mathrm{pulse}}$ of the transmitted radiation pulse for different lengths of individual grazing incidence mirrors.

In Figure (5.51) the evolution of the transmitted pulse energy versus the number of round trips is shown. As Figure (5.50(right)) it displays the highest saturated pulse energy for the $l = 4\,\mathrm{cm}$ mirror length case. On the other hand, for $l = 4\,\mathrm{cm}$ the CBXFEL requires more than double the amount of round trips to reach the saturation regime, which is consistent with the reduced round trip gain.

To summarize, for mirror lengths $l \geq 7\,\mathrm{cm}$, corresponding to w^{ap} ≥217 µm aperture size, the CBXFEL demonstrator is not affected by the aperture effect. For lower mirror lengths the effective aperture not only leads to an increase in cavity losses, but also to a decrease of the quality of the transverse distribution due to diffraction effects, which result in a strong reduction of the brilliance of the circulating pulse.

For the transmitted pulse the opposite occurs, as the non disturbed CBXFEL demonstrator leads to a strong oversaturation during the FEL process degrading the quality of the transmitted pulse. In this sense one could assume a mirror length of $l = 4\,\mathrm{cm}$ as most beneficial, as it increases the quality of the transmitted pulse while also reducing the heat load on the crystal mirrors. But there are a couple of drawbacks to this approach.

For one, considering the superb quality of the circulating pulse, it might be advisable for the future to also out couple the full beam, for example by a cavity dumping approach or a grating (see Section **2.4**). This speaks against the degradation of the transverse quality of the circulating pulse, which would additionally not be possible to take back, as the mirror lengths are fixed once installed.

Another argument against the use of short mirrors is that already at a mirror length of $l = 3\,\mathrm{cm}$ the demonstrator would cease to work. So taking into account safety measures to also account for other effects decreasing the transverse quality and the round trip gain, a mirror length of $l = 4\,\mathrm{cm}$ is too close to the edge. Actually, as will be seen in the respective paragraph **5.2.2.6**, the figure errors of the mirror assembly lead to a widening of the X-ray pulse. In order to accommodate these widened pulses, the mirror length needs to be increased with respect to the result of this paragraph.

The last argument is that the same effect of a reduced circulating pulse energy with increased quality of the transmitted pulse can as well be achieved by detuning the undulator parameters. This has the additional advantage that it is a non fixed approach and can be adjusted during operation.

To conclude, a mirror length of $l = 7\,\mathrm{cm}$ is an optimal compromise between not disturbing the demonstrator performance and keeping the mirror short. As was already mentioned above, this requirement will be increased to $l = 9\,\mathrm{cm}$ based on the impact of the mirror figure error studied in Paragraph **5.2.2.6**.

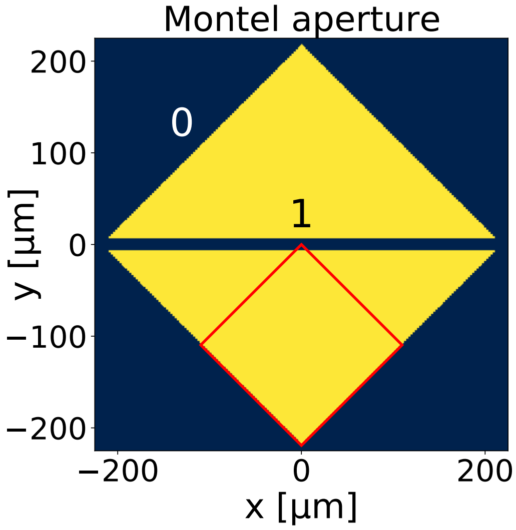

Figure 5.52: The projected aperture introduced by a l_M =10 cm long Montel assembly with a finite sized intersection gap of w_{gap} =10 µm. The yellow area corresponds to zero losses and the blue area to 100 % losses. The red rectangle shows an exemplary reduced aperture area to which the beam can be displaced to not interact with the gap. It has half the length of the total mirror. The orientation of the mirrors was rotated by 45° with respect to Paragraph **5.2.2.4** regarding the aperture effects in order to improve computational accuracy.

5.2.2.5 Montel gap: As was discussed in Section **5.1** about the principle design, in order to ease alignment the mirror assembly will most probably be based on a nested ‘Montel’ configuration. In this nested configuration there is a gap of at least w_g =5 µm to 10 µm size, where the individual grazing incidence mirrors intersect. This gap can numerically be considered as an absorbing slit or inverse aperture. When requiring the shortest possible realization of these mirrors, the radiation pulse must be centered just at this gap. The corresponding aperture function is sketched in Figure (5.52). The cutoff of a central line in the beam center will obviously influence the circulating radiation pulse. By shifting the position of the radiation pulse on the mirrors away from this central gap, one can mitigate its influence. As one needs to shift the beam towards the mirror edges, this comes for the cost of increased cut of losses at the effective aperture, resulting in the requirement of longer mirrors.

In this paragraph, the influence of the ‘Montel gap’ shall be estimated and if it is tolerable in order to reduce the overall mirror size. It has to be noted that these are indeed estimations, as the size of the gap is of the same order as the resolution of the computational mesh which reduces the accuracy. Compared to the prior simulations, the mesh resolution has been increased to account for at least three grid points per column inside the horizontal gap. This enables a rather exact representation of the gap's response function in angular space with some aliasing effects[73]. These effects decrease for higher gap widths.

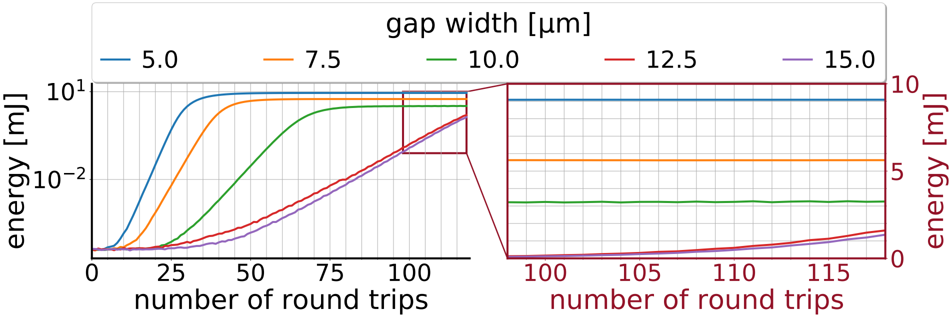

Figure 5.53: The pulse energy evolution $E_{\mathrm{pulse}}^{(\mathrm{und.})}$ of the radiation pulse before reflection for different widths of the Montel intersection gap.

In Figure (5.53) the pulse energy evolution of the radiation pulse before reflection is displayed for different widths w_{Gap} of the Montel intersection gap. In comparison with the idealized cavity, it is evident that already the smallest achievable Montel gap of w_{Gap}=5 µm results in a threefold reduction in pulse energy. The pulse energy is further decreased when increasing the gap width, which is to be expected. Anyhow, it has to be noted that the decrease in pulse energy does not correlate to the amount of pulse energy cut out at the gap, which would be on the order of roughly 5 percent per mirror assembly for w_{Gap}=5 µm. The main reason is, as for the case of the finite mirror size, the introduced diffraction. It should also be noted that the effective slit width is reduced by a factor of $\sqrt{2}$ compared to the physical gap width. This is an effect of the radiation pulse projection on the mirrors (in the small angle approximation).

In Figure (5.54) the spatial energy densities directly after the undulators, at the downstream mirror assembly, at the upstream mirror assembly and at the entry of the undulator section (seed) are presented for the exemplary Montel intersection gap widths w_{Gap} =5 µm, 10 µm and 15 µm. At the entry point into the undulators one can clearly observe strong diffraction effects, with the size of the features corresponding to the widths w_{Gap}. While for w_{Gap} =5 µm and 10 µm the distorted profile is partially 'washed' away by both the FEL gain and the beam divergence, for w_{Gap}=15 µm the spatial distribution is strongly resembling a TEM01 Gaussian-Hermite mode also after the undulators. Usually this mode is suppressed by the stronger gain of the TEM00 mode in the FEL process. But as the spatial distribution of the seed is much better matching to the TEM01, it receives stronger gain and is therefore dominating over the TEM00.

In Figure (5.55(left)) the pulse energy as well as the brilliance and the J of the radiation pulse in saturation is displayed for the different widths of the Montel gap. First, it affirms the strong

---

[73] Unfortunately, increasing the resolution of mesh while keeping the same computational area, as necessary to account for the size of the radiation beam, comes with a square in numerical cost. So in order to accurately map the gap, which would request about ten mesh points, an additional factor of ten increase in computational cost would be required. This unfortunately is not feasible.

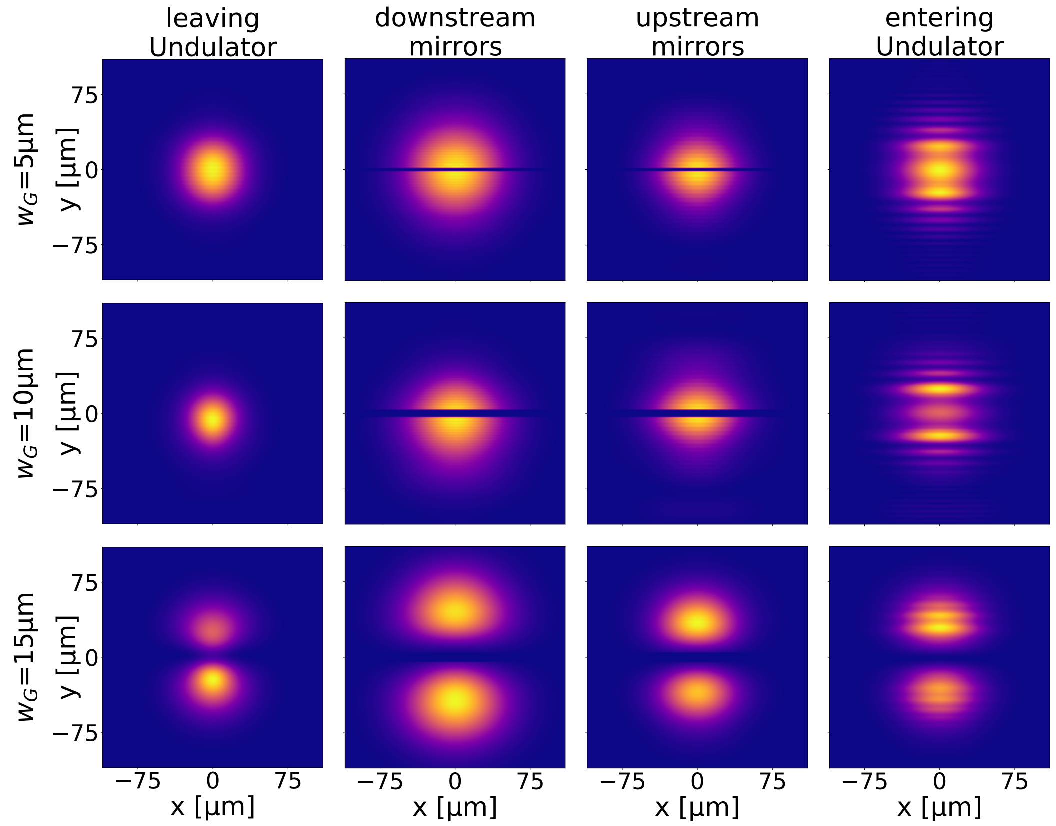

Figure 5.54: Spatial distributions of the circulating radiation pulse in saturation for three exemplary Montel intersection widths directly after the undulator, after the downstream mirror assembly, after the upstream mirror assembly and before reentering the undulator section. One can clearly see strong diffraction effects at the seeding beam. At w_{Gap}=15 µm the radiation profile is clearly following a TEM01 Gaussian-Hermite mode.

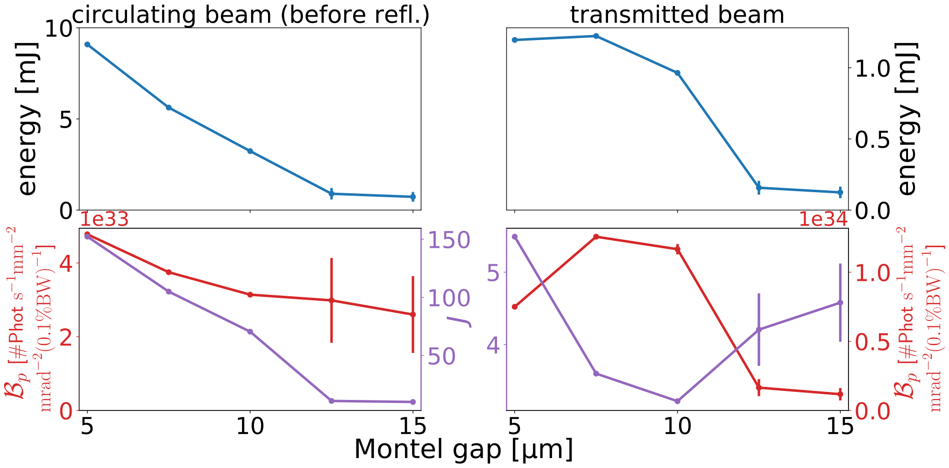

Figure 5.55: Pulse energy (top), brilliance and gaussian quality factor (bottom) of the circulating pulse before reflection (left) and the transmitted pulse (right) in saturation for different widths of the Montel intersection gap.

impact of the gap on the CBXFEL performance, resulting in a brilliance reduction by about three orders of magnitude. This strong reduction is mainly driven by the strong rise in the gaussian J, which is, at first sight surprisingly, decreasing with increasing w_{Gap}. This can be explained by the fact that at higher w_{Gap} the saturated circulating pulse energy is lower, which causes a relatively stronger contribution of the newly generated radiation. As the newly generated radiation has a better transverse quality due to the gain guiding, this reflects back on the circulating beam. The improved J at w_{Gap}=12.5 µm and 15 µm is due to the transverse distribution quite cleanly following a TEM01 profile. Such a profile is, regarding the size-divergence product, inferior to the single mode TEM00, but it is much better than a very noisy distribution as apparent for w_{Gap}=5 µm. Besides, as for the 10 µm the pulse after the undulators is strongly influenced by the newly generated radiation with a purified transverse distribution.

From Figure (5.55(right)) is is also apparent, that the transmitted radiation is affected by the distortions of the seeding pulse. The pulse energy stays at roughly the same level with exception of the TEM01 w_{Gap}=12.5 µm and 15 µm cases, which did not reach saturation in the simulation window. On the other hand the tranverse quality is affected by the distorted seed, which appears in an increased J. This is unlike the prior discussed cases, where the distortions of the seed were removed by the strong gain guiding in the FEL process. In Figure (5.56) the spatial profiles of the transmitted pulses are displayed, clearly exhibiting a TEM01 Gaussian-Hermite mode for the w_{Gap}=12.5 µm and 15 µm cases as discussed above. This also explains the particularly high J for this case as shown in Figure (5.55(right, bottom)). Interestingly, the w_{Gap}=15 µm case shows a clearer TEM01 transverse profile than the 12.5 µm case. This can probably be explained by the wider gap causing a transverse profile which is better coupling to the TEM01, whereas for the w_{Gap}=12.5 µm there is still some competition with the TEM00 mode, weakening the significance of the TEM01.

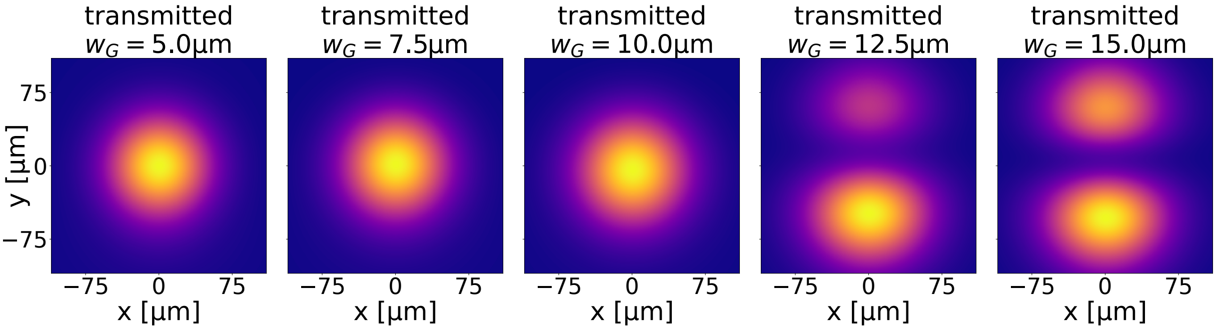

Figure 5.56: Spatial distributions of the transmitted radiation pulse in saturation for three different Montel intersection widths. While for w_{Gap}=5 µm to 10 µm the radiation profile can be described by a TEM00 mode, at w_{Gap}=12.5 µm and 15 µm the radiation profile is following a TEM01 Gaussian-Hermite mode, with the significance being higher for w_{Gap}=15 µm.

To conclude, the Montel intersection gap has a very strong impact on the CBXFEL performance even when considering the smallest achievable gap size of w_{Gap} ≈5 µm. Hence, it should be avoided if possible. If physical space is strongly constrained and the maximum mirror length is set, in reference to Paragraph **5.2.2.4**, it appears recommendable to rather allow for higher aperture losses by using only half of the mirror lengths. It should be noted that it is also possible to compromise between these two possibilities by shifting the relative position of the gap to a portion of the beam where it has less influence. The impact of this, however, needs further studies.

5.2.2.6 Figure error of the mirror surfaces: Up to now, the surfaces of the optical elements in the X-ray cavity were assumed to be either perfectly flat (crystals) or perfectly following the elliptical bending to achieve the required focussing (graz. incidence mirrors). This obviously is an idealized case. Regarding the low single angstrom level wavelength of the radiation and the high number of a total of six mirrors, an analysis of the introduced wavefront distortions are obligatory. It will, however, be assumed that the grazing incidence mirrors and diamond crystals are state of the art.

For the grazing incidence mirrors this means a peak-to-valley figure error $\Delta h(\boldsymbol{x})$ on the single nanometer scale and a surface roughness on the atomic level for few micrometers spatial wavelengths [177]. Due to the mirror assembly not being manufactured yet, the surface profiles need either to be used from already existing mirror pieces or computationally generated. Here, the second approach will be applied. It is based on the method of *Hua et al.*[176], which generates a height profile

$$h(x) = \frac{N_p}{l_{\text{mir}}} \tilde{\mathcal{F}}_{\text{1D}}^{-1} \left[\sqrt{l_{\text{mir}} \cdot \text{PSD(k)}} e^{i\phi(k)} \right] (x)$$

from the power spectral density $\text{PSD}(k)$. l_{mir} is the mirror length, N_p is the number of computational sample points, k is the spatial frequency. $\Phi(k)$ is a random phase value which is for each discrete k drawn from a uniform distribution with $\Phi \in (-\pi, \pi)$. It is used to generate varying surface profiles from a fixed power spectral density. The power spectral density is approximated as[176]

$$\text{PSD}(k) = a \cdot k^b$$

, where a can be matched to the desired rms value σ_h and b is in the range $b \in (-3, -1)$. Here b is fixed to a value of minus two.

These height errors enter twice as optical path difference into the wavefront propagation, as was described in the description of the *pCXP* program about curved mirrors in equation (4.17). For the wavefront this corresponds to a position (local mirror height) dependent phase shift

$$\Delta\Phi(\boldsymbol{x}_\perp) = 2k\Delta h(\boldsymbol{x}_\perp) \sin(\Theta_{in}),$$

where Θ_{in} =3.1 mrad is the grazing angle and k is the radiation wavevector. The individual mirror profiles are assumed to be one-dimensional as the projection of the X-ray pulse on the mirrors has a very large aspect ratio of $\sim \sin\Theta_{\text{in}}^{-1}$ and therefore the variation along the long dimension is much stronger than along the short. Combining both mirrors then yields a two dimensional map.

Figure (5.57) displays the surface profiles of an actual short mirror measured in the XRO group

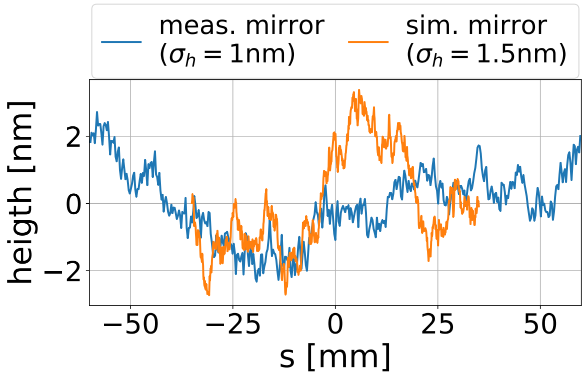

Figure 5.57: Comparison of the surface profiles of an actually manufactured short ($l_M = 12\,\mathrm{mm}$) mirror with σ_h =1 nm rms[211] and of a computationally generated mirror with σ_h =1.5 nm rms.

at the EuXFEL[211] and an exemplary dataset computed via above method. The basic features of the curves match rather well supporting the use of the computational method, with a slightly stronger high spatial frequency variations in the computed profile. The surface rms value σ_h =1.5 nm of the computed profile was chosen to be slightly higher than the measured one. This is due to two reasons. For one, the measured sample was a high quality one, so a higher error is introduced as a 'safety measure'. Second, it is set slightly higher to also accommodate for 'Bragg plane slope errors' in the diamond crystals.

Unlike for grazing incidence reflection, the dynamic diffraction in crystals is a process taking place over multiple micro meters in depth and therefore is much less sensitive to the actual surface profile[74]. Anyhow, also the individual atomic layers are not perfectly flat in reality. These 'Bragg plane slope errors' also introduce wavefront curvature to the reflected radiation pulse[212]. Recently, the average slope error in very high quality diamond were measured to be as low as ~0.1 µrad/mm^2[212]. Also, the slope $\Delta\Theta_B$ is almost constant over the size of the radiation beam σ_r <100 µm. Such a constant slope can be adjusted by proper alignment. Additionally, due to the rather small beam size considering an a-priori mapped crystal, it would be possible to select the best area for reflection.

Nonetheless, in order to account for a worst case scenario, a malicious influence of the bragg plane bending on the wavefront shall be accounted for. As a proper computation of a depth dependent variation of the bending is numerically very demanding, beside it being difficult to actually estimate, it is approximated by using an increased rms error σ_h =1.5 nm of the grazing incidence height profile.

Figure (5.58) displays the pulse energy evolution of the radiation pulse before reflection for ten different runs, each with a set of four randomly generated surface profiles of σ_h =1.5 nm as presented in Figure (5.59). A mirror length of $l_M = 7\,\mathrm{cm}$ was assumed in consistence with Paragraph **5.2.2.4**. Comparing Figure (5.58) to the pulse energy evolution in the idealized cavity (Figure (5.11)), the surface figure error evidently has a very strong impact with about a factor of three reduction in saturated pulse energy. Also, there is a strong variation of the pulse energy evolution and saturated energies with the actual set of surface profiles. This is due to, first, the

---

[74] The angular deviation of the surface shape only enters as a directional correction to the wave refraction when entering the crystal. As the refraction index (χ_0) in diamond for the X-ray wavelength is very small on the order of 1×10^{-4}, the corrections are pretty much negligible.

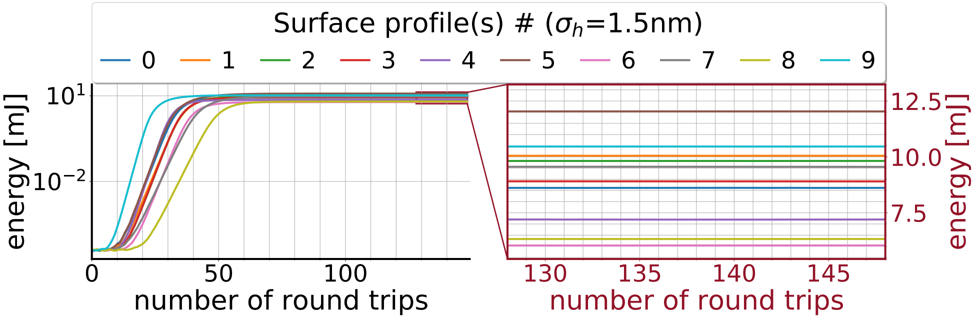

Figure 5.58: The pulse energy evolution of the circulating radiation before reflection for ten runs each with four randomly generated surface profiles of the same σ_h =1.5 nm as presented in Figure (5.59).

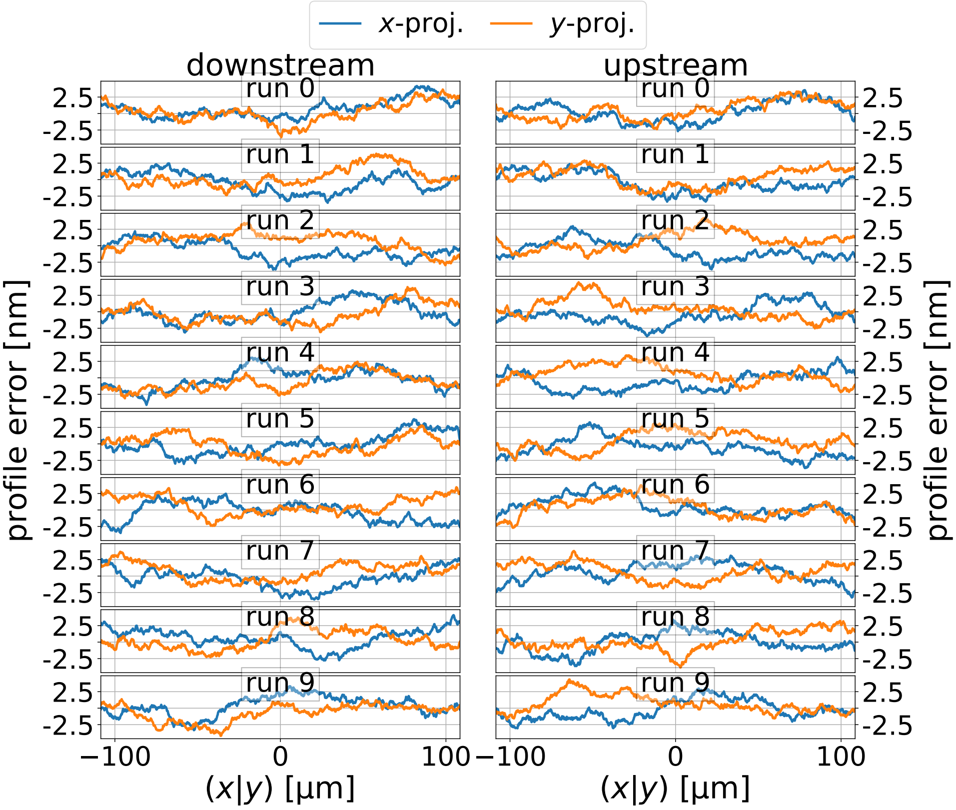

Figure 5.59: Computationally generated surface profile errors as used for ten different CBXFEL demonstrator simulations. Each row corresponds to an individual simulation run. The left and right column correspond to the downstream and upstream mirror assemblies, respectively. Each tile shows two profiles, corresponding to an individual mirror in the assembly, which project on the radiation pulse x- (blue) and y-axis (orange). One has to keep in mind that these two axis are perpendicular, so the associated profiles in average do not constructively or destructively interfere. Each profile has an rms value of σ_h =1.5 nm. The profiles are shown without the deliberately introduced curvature required for focussing.

from run to run differing spatial frequency of the h-variation, which strongly affects the actual wavefront propagation [46]. Second, for some sets the upstream and downstream profiles negate each other to a certain degree while for others they stack up, leading to an increased impact on the radiation wavefront. It is, anyhow, very hard to directly deduce the differing impact directly from the surface profiles presented in Figure (5.59).

In Figure (5.60(left)) the pulse energy as well as the brilliance and the J of the radiation pulse

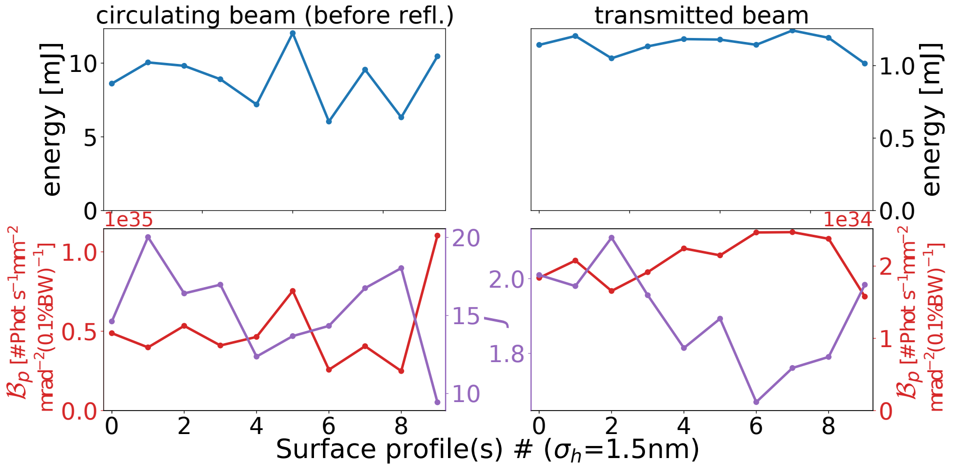

Figure 5.60: Pulse energy (top), brilliance and gaussian quality factor (bottom) of the circulating pulse before reflection (left) and the transmitted pulse (right) in saturation for different sets of mirror surface profiles as presented in Figure (5.59).

in saturation is displayed for the different runs. Besides showing the variation in pulse energy by nearly a factor of two, it also reveals a strong fluctuation in the quality of the transverse distribution and in the brilliance. Compared to the idealized CBXFEL demonstrator the brilliance exhibits a strong reduction by two orders of magnitude, which correlates to the factor ten increase in J and the square dependence of the approximated brilliance (2.19) on J.

In Figure (5.61) the spatial energy density directly after the undulators, at the downstream mirror assembly, at the upstream mirror assembly and at the entry of the undulator section (seed) are presented for three exemplary runs. These correspond, referring to Figure (5.60), to a somewhat average (run 3), a particularly bad (run 8) and a particularly good run (run 9). All runs exhibit strong distortions and a widening of the spatial profile at the entry point of the undulator section. The extent of these distortions directly correlates directly to the performance of the demonstrator. This makes sense, as a more distorted and more extended wavefront corresponds to a worse transverse matching to the electron bunch and therefore an decreased seeding (integrated) efficiency.

The spatial distribution at the position of the upstream mirror assembly appears much smoother than at the entry of the FEL section, even though one would expect a comparable impact by the figure error of the downstream mirror assembly. This is indeed the case, but the contributions are averaged out by the much longer propagation distance of $L_D \approx 66.42\,\mathrm{m}$ between the two mirrors assemblies compared to the distance of $L_D \approx 3.6\,\mathrm{m}$ from the upstream mirror to the undulator entrance.

It has to be noted, that referring to Figure (5.60(right)) the transmitted beam is, as was already observed for the other error sources, mostly unaffected by the profile error with even an inverse trend owing to the weaker oversaturation.

In Figure (5.62(left)) the pulse energy as well as the brilliance and the gaussian J of the radiation pulse in saturation is displayed for runs with randomly generated surface profiles of an increased

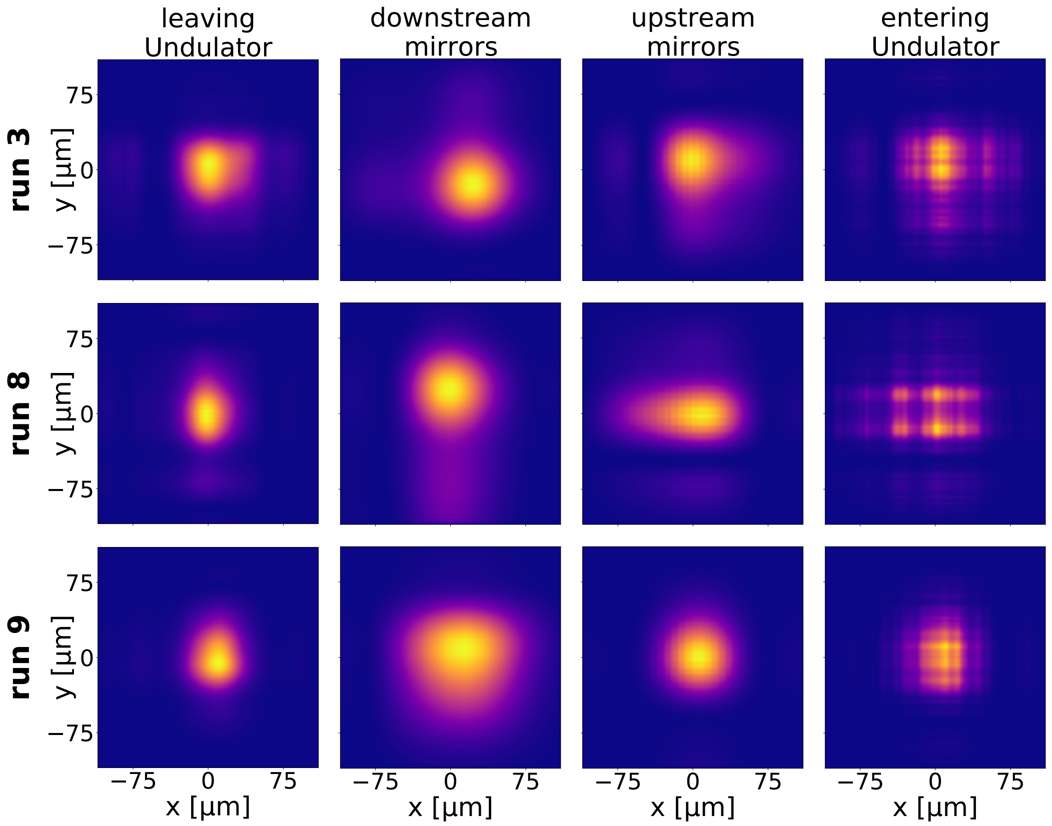

Figure 5.61: Spatial distributions of the circulating radiation pulse in saturation for the exemplary sets 3,8 and 9 of the mirror surface profiles Figure (5.59) directly after the undulator, after the downstream mirror assembly, after the upstream mirror assembly and before reentering the undulator section. One can clearly see strong diffraction effects at the seeding beam. The strength of these distortions correlate to the performance of the demonstrator as presented in Figure (5.60).

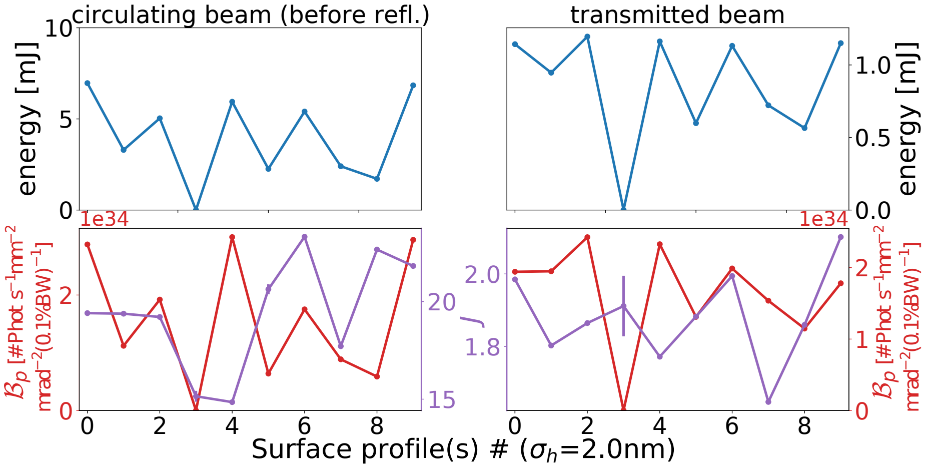

Figure 5.62: Pulse energy (top), brilliance and gaussian quality factor (bottom) of the circulating pulse before reflection (left) and the transmitted pulse (right) in saturation for ten randomly generated sets of mirror surface profiles of $\sigma_h = 2\,\mathrm{nm}$ rms figure error. One can clearly see a decrease in performance compared to $\sigma_h = 1.5\,\mathrm{nm}$ as presented in Figure (5.60).

figure error of $\sigma_h = 2\,\mathrm{nm}$ each. There is a strong impact of the slightly increased error on the demonstrator performance, even featuring a run which does not reach the stabilized gain regime at all. Also, unlike for the $\sigma_h = 1.5\,\mathrm{nm}$ case the transmitted beam is affected depending on the individual run.

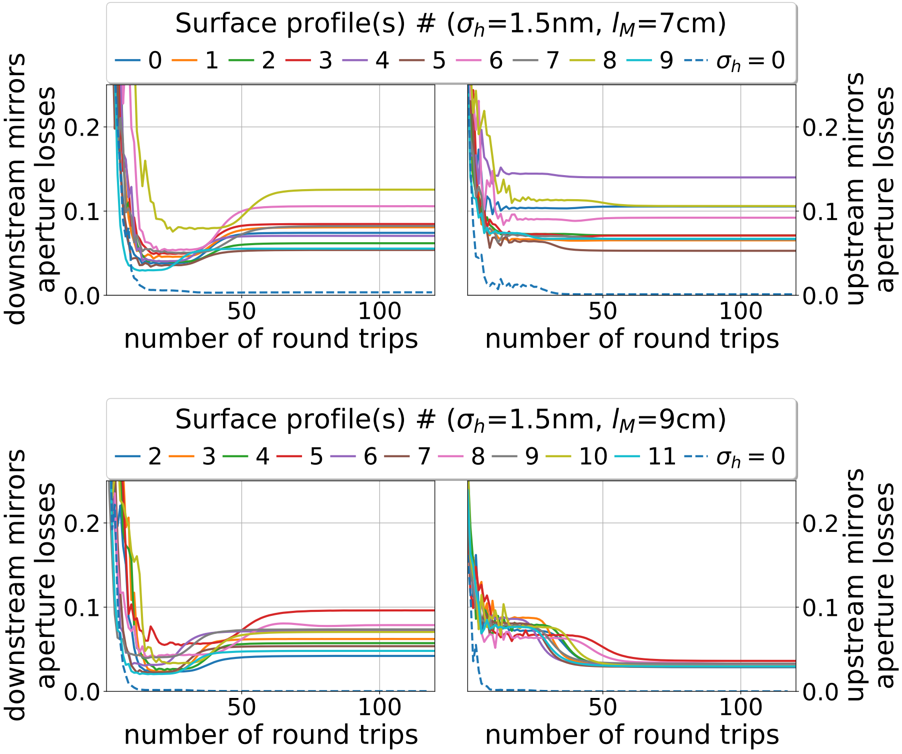

Figure 5.63: Fractional radiation beam losses at the downstream (left) and upstream mirror (right) apertures for l_M =7 cm (upper) and $l_M = 9\,\mathrm{cm}$ (lower) (no spectral losses) for different sets of surface profiles. For comparison the losses for the case of an ideal surface of $l_M = 7\,\mathrm{cm}$ and $l_M = 9\,\mathrm{cm}$ as discussed in Paragraph **5.2.2.4** are shown as blue dashed line. The losses are much less, proofing the increase of the aperture losses due to the wavefront distortions. On the other hand, increasing the mirror length from $l_M = 7\,\mathrm{cm}$ and $l_M = 9\,\mathrm{cm}$ strongly reduces the losses. The dip in the losses for the downstream mirrors at intermediate round trips is a signature of the *exponential gain regime*, where the radiation profile is dominated by the newly generated radiation which is not impacted by the wavefront distortions induced by the upstream mirrors. It should be noted that the surface profiles for the $l_M = 9\,\mathrm{cm}$ case are newly generated and different from those shown in Figure (5.59).

As presented in Figure (5.63(upper)) for the $\sigma_h = 1.5\,\mathrm{nm}$ case, the wavefront distortions introduced by the figure errors lead to a widening of the spatial pulse profile and therefore to a strong increase in aperture related cut of losses compared to the ideal mirror profile. This gives the hint that reducing the impact of the figure errors can partially be mitigated by increasing the mirror size, which is supported by Figure (5.63(lower)) showing that the aperture related cut off losses are indeed significantly reduced by using an increased mirror size of $l = 9\,\mathrm{cm}$.
However, referring to Figure (5.64(left)), the actual gain in CBXFEL performance is comparably small and within the statistical fluctuation induced by the randomly generated surface profiles[75]. This is due to the fractions of the pulse that are cut off at the edges of the mirrors are the ones,

---

[75] Unfortunately, it is not possible to use the same sets as presented in Figure (5.59), as this would result in a stretching of the spatial frequency, which has an positive, but nonphysical impact on the CBXFEL performance.

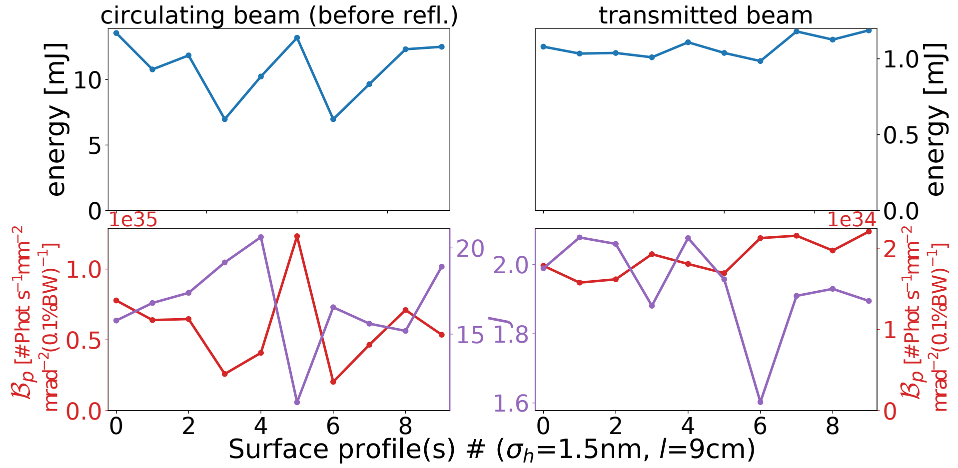

Figure 5.64: Pulse energy (top), brilliance and gaussian quality factor (bottom) of the circulating pulse before reflection (left) and the transmitted pulse (right) in saturation for ten randomly generated sets of mirror surface profiles of $\sigma_h = 1.5\,\mathrm{nm}$ rms figure error and $l_M = 9\,\mathrm{cm}$ mirror length.

which were already heavily spoiled and did not contribute to the seeding to begin with. Also, they were mostly corresponding to components in angular space of heavily misaligned $\boldsymbol{k}_\perp$, so removing them also does not create many interference patterns and diffraction effects in the actual radiation profile.

To conclude, the grazing incidence mirrors' figure errors have of all sources of error studied so far, excluding the avoidable Montel intersection gap, the strongest impact on the CBXFEL demonstrator performance. While the impact can be slightly reduced using larger mirrors, it shows that very high quality mirrors of $\sigma_h \leq 1.5\,\mathrm{nm}$ rms figure error are of major importance for the project. It also should be noted that a quantized analysis of the mirror surface errors on a cavity based X-ray FEL scheme was not carried out in prior works. On the other hand the present study quantitatively emphasizes the requirement of 'high-quality' mirrors and also clarifies to a certain extent, what 'high-quality' actually refers to.

5.2.2.7 Strained Crystal: As was shown in Section **3.1.4**, strain in a crystal has a definite effect on the crystal reflection. The effect of static strain, which may be caused by the mounting of the crystal or due to impurities in the crystal itself, shall be highlighted here. As it is quasi impossible to define the three dimensional strain states a priori, only the simple case of one dimensional in-depth strain, linearly varying over the crystal thickness and being constant over the radial position, will be discussed here.

While this surely is overly simplified, it highlights the basic influence of the strain. Additionally, it can be considered a worst case scenario. As will be seen below, what is important is the local strain gradient over local portions of the crystal. For gradients of higher order, while the maximum local gradient will be higher for the same total magnitude of strain, the minimum gradient will be lower. The crystal has a total thickness of t_c =150 µm, which is far larger than the electron bunch length. So reflection at different depths of the crystal corresponds to clearly distinct internal longitudinal positions of the seeding pulse. Hence, one can select the minimal strained portion of the crystal by longitudinally tuning the cavity length such that the corresponding internal longitudinal position in the seed matches to the electron bunch. For a linearly strained crystal with a constant gradient, this has no benefits other than selecting the reflection at the surface of the crystal to minimize absorption.

It should be noted, that from the experience from the different *Hard X-ray Self-Seeding* (HXRSS) experiments, which also use thin crystals as monochromators, there is no sign of static strain disturbing the operation. This was also recently confirmed by *Rocking curve imaging* on clamped diamond crystals, which did not show any difference to free standing diamond[212]. However, these experiences are based on preparing the crystals with strain relief cuts, which might disturb the thermomechanical stability of the crystals and are therefore not foreseen for the present experiments. This section is devoted to understand what levels of strain are tolerable. If these requirements are not met by the clamped crystals without the strain relief cuts, it would still be possible to add them afterwards.

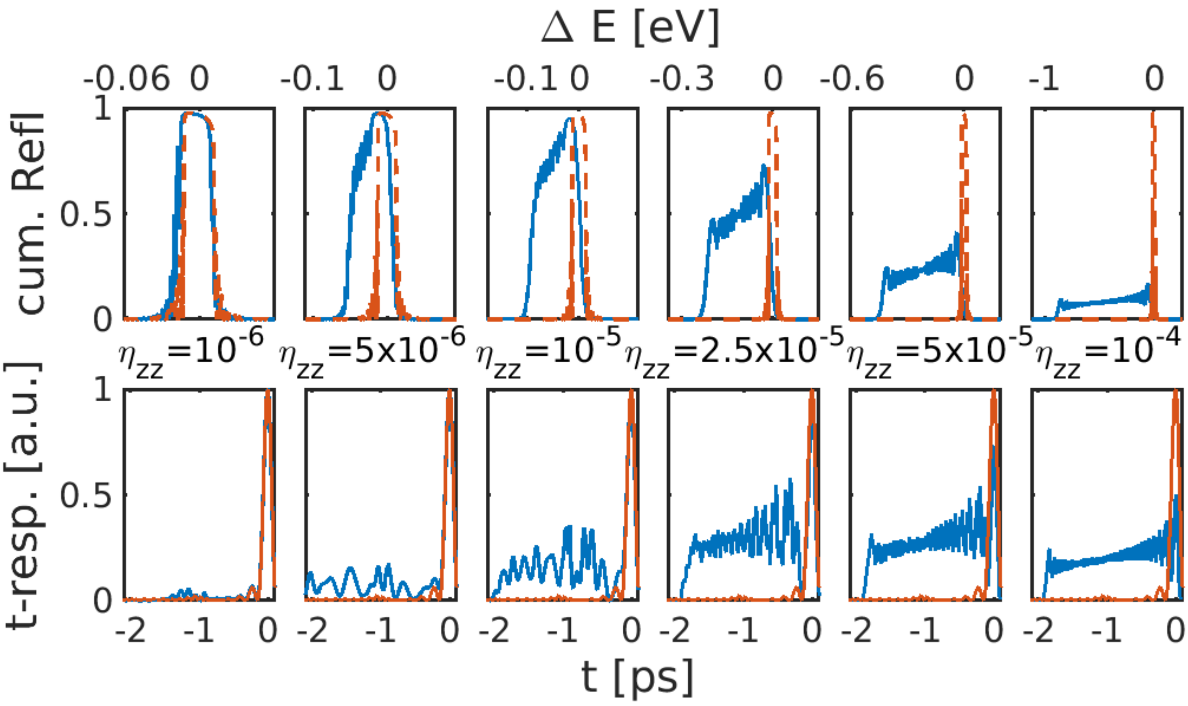

Figure 5.65: The spectral reflection curves (upper) against $\Delta E = E_{\mathrm{ph}} - 9.05\,\mathrm{keV}$ and associated time-domain response functions (lower) for the cumulative reflection of two t_c =150 µm thick, linearly strained C(333) crystals of varying maximum strain $\eta_{zz}^{\max}$. For reference also the curves of the unstrained crystal are shown as red dashed line.

In Figure (5.65) the reflection curves (upper) and the associated time-domain response (lower) for linearly strained C(333) diamond crystals are plotted for different levels of maximum strain $\eta_{zz}^{\max}$. For $\eta_{zz}^{\max} = 1 \times 10^{-6}$ there is only little impact compared to the unstrained crystal. For $5 \times 10^{-6} \leq \eta_{zz}^{\max} \leq 1 \times 10^{-5}$, one can see a widening in both spectral reflection width as duration of the temporal response, whereas the peak values remain roughly unchanged. For $\eta_{zz}^{\max} \geq 2.5 \times 10^{-5}$ besides the widening one can also observe an increasing drop of the peak reflectivity and peak time-domain response function. The widening of the crystal reflection has, as expected, a one to one correspondence to $\eta_{zz}^{\max}$. The total duration of the crystal response gets extended to about $\Delta t_R = 2\,\mathrm{ps}$. This is just the time duration for traveling through $4 \cdot t_c$ =600 µm of diamond crystal.

The strain in the crystal is effectively limiting the crystal depth for each spectral reflection channel to the depth over which the strain remains inside the reflection bandwidth of the undisturbed crystal. For $\eta_{zz}^{\max} \leq 1 \times 10^{-5}$ this depth is considerably smaller than the extinction length $l_{\text{ext}}^{\min}$ ≈8 µm, so there is only minor influence on the peak reflectivity. However, as different depths of the crystal scatter different wavelengths due to the varying atomic spacing, the reflection width varies accordingly. The reflection efficiency drops with the penetration depth into the crystal due to the increasing absorption, which accounts for the asymmetry around $E_{\text{ph}} = E_c = 9.05\,\mathrm{keV}$ of the reflection curves for $\eta_{zz}^{\max} \geq 5 \times 10^{-6}$. In between the maximum and minimum reflection energies the interference phenomena also apparent in the unstrained crystal are active, which lead to the oscillations shown in Figure (5.65(upper)). For $\eta_{zz}^{\max} \geq 1 \times 10^{-5}$, on the other hand, the spectral reflection depth becomes of the same order or smaller than the penetration depth, so there is a clear impact on the peak reflectivity.

Anyhow, due the widening of the bandwidth the spectrally integrated reflection efficiency $\int R\left(E_{\text{ph}}\right) \mathrm{d}E_{\text{ph}}$ stays the same or even increases for intermediate values of strain. Hence, one would trivially expect that the only impact of the normal strain on the CBXFEL demonstrator would be the increase of the bandwidth of the circulating radiation and a decrease in transmitted energy. However, as was discussed above and is clearly shown in Figure (5.65(lower)), the different reflected photon energies correspond to different layers of the crystal and therefore to different temporal delays with respect to the electron bunch. As the total duration $\Delta t_R = 2\,\mathrm{ps}$ is two orders of magnitude higher than the temporal duration of the electron bunch, a major fraction of the reflected pulse does not contribute at all to the seeding process. Instead, only a window of about $\Delta t_{\text{seed}} \approx 4\sigma_t^{\text{el.}} \approx 40\,\mathrm{fs}$ does contribute. In relation to the seeding efficiency $Q_{\text{seed},0}$ of the unstrained crystal, this ranges from $Q_{\text{seed},\eta}/Q_{\text{seed},0} \approx 1$ for $\eta_{zz}^{\max} = 1 \times 10^{-6}$ to $Q_{\text{seed},\eta}/Q_{\text{seed},0} \approx 0.45$ for $\eta_{zz}^{\max} = 1 \times 10^{-4}$.

Figure (5.66) affirms that the level of strain indeed has a strong impact on the CBXFEL performance. While for intermediate levels of strain, $\eta_{zz}^{\max} \leq 5 \times 10^{-6}$, the impact on both transmitted as well as circulating beam is small, for $\eta_{zz}^{\max} \geq 1 \times 10^{-5}$ the saturated pulse energy of the circulating beam is dropping, until at $\eta_{zz}^{\max} = 1 \times 10^{-4}$ the CBXFEL does not enter the exponential growth regime at all. Also, the time-bandwidth product is increasing due to the long time-domain tail of the reflected radiation. For the transmitted radiation this tail obviously does not appear and, as was frequently discussed above, the decrease in seeding strength is actually favorable, so there is an increase in pulse energy and brilliance, which peaks at $\eta_{zz}^{\max} = 2.5 \times 10^{-5}$. It has to be taken into account, however, that in combination with the afore discussed errors, this magnitude of strain could reduce the gain below a value, at which the demonstrator can reach the exponential growth regime.

To conclude, normal crystal strain does not only pertube the bandwidth of the CBXFEL demon-

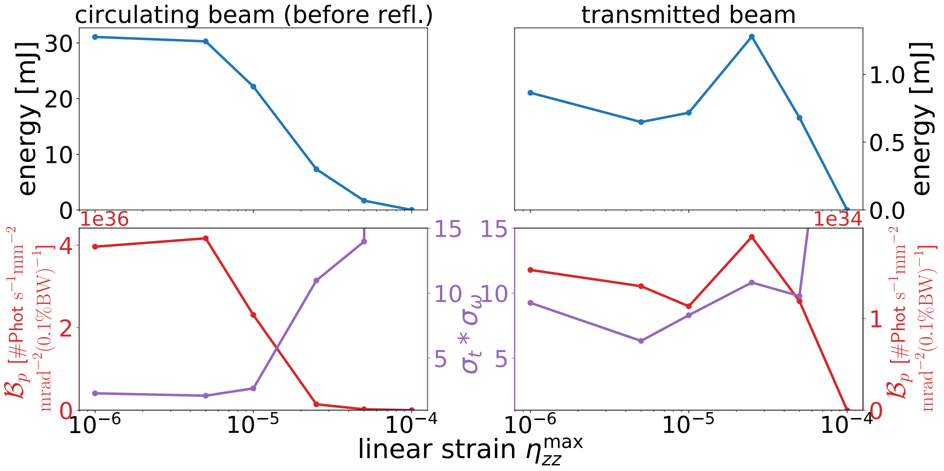

Figure 5.66: Pulse energy (top), brilliance and time-bandwidth product (bottom) of the circulating pulse before reflection (left) and the transmitted pulse (right) in saturation for different levels of linear normal strain.

strator, but also affects the gain and the performance in saturation. For a final realization of the demonstrator, it should be measured[76] if the strain in the clamped crystal is below a value of $\eta_{zz}^{\max} < 1 \times 10^{-5}$. If this is not the case, additional, possibly otherwise unfavorable, measures such as introducing strain relief cuts should be taken.

5.2.2.8 Combined errors: In this paragraph, it shall be studied how the accumulation of the afore discussed isolated errors influences the CBXFEL demonstrator. It will, however, be assumed, that the radiation pulse is shifted away from the Montel gap in a Montel assembly of $l_M^{\text{tot}} = 18\,\text{cm}$ total length, meaning $l_M^{\text{ap.}} = 9\,\text{cm}$ effective aperture length. Also, possible strain in the mirror will be neglected. This for three reasons. First, the model of a purely linear strain is highly heuristic. Second, regarding the discussion of the last paragraph, the strain should be in a range where it has only minor effects on the demonstrator. And third, the implemented numerical treatment of a strained crystal is computationally more expensive than that of an unstrained one.

So, the errors implemented for the following simulations are an angular tilt of 200 nrad, a finite (effective) mirror size of $l_M^{\text{ap.}} = 9\,\text{cm}$, a surface profile error of the grazing incidence mirrors of $\sigma_h = 1.5\,\text{nm}$ and jitter of the electron bunch distribution. For the surface profile the profile number 7 of the $l_M^{\text{ap.}} = 9\,\text{cm}$ long mirrors will be used. The electron jitter includes a positional jitter of $\sigma_{x,y}^{\text{jit.}}$ =3 µm, a pointing jitter of $\sigma_{x',y'}^{\text{jit.}} = 100\,\text{nrad}$, an energy jitter of $\sigma_\gamma^{\text{jit.}} = 3.1$ and an arrival time jitter of $\sigma_{t,\text{arr.}}^{jit} = 20\,\text{fs}$. Also, to account for additional losses, for example due to (the small, but existing) absorption in the grazing incidence mirrors, a cavity loss factor of $\mathcal{L}_{\text{cav}} = 0.03$ will be assumed, which is subtracted from the seeding pulse intensity and half of it from the transmitted pulse intensity.

---

[76] Assessment of the crystal strain can be carried out by X-ray rocking curve imaging, see for example [212].

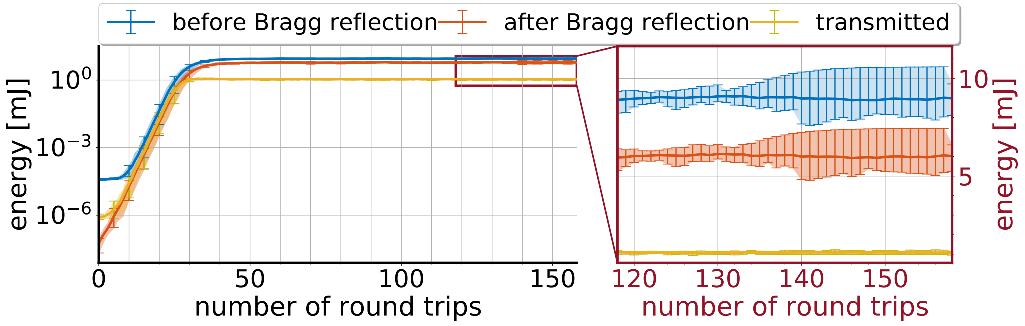

Figure 5.67: The left plot in logarithmic scale shows the full evolution of the pulse energy versus number of round trips for the non idealized cavity and the right plot in linear scale displays the photon beam after saturation. The data was averaged over 15 individual runs/bunch trains with the shaded area showing the minimum/maximum values from these runs.

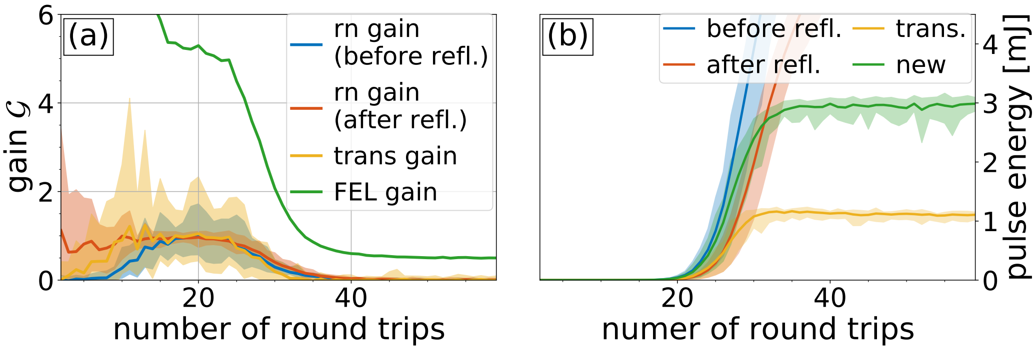

Figure 5.68: (a) shows the evolution of the round trip gain before reflection (blue), after reflection (red) and of the transmitted pulse as well as the FEL gain. As mentioned before, the FEL gain is very inaccurate for the first round trips. (b) displays the corresponding evolution of the pulse energy of the pulses before and after reflection, the transmitted pulse as well as the energy newly generated in the undulators. For better visualization only a subset of round trips is shown, which are centered around the maximum of the transmitted and newly generated pulse energy.

Figure (5.67) shows the photon pulse energy in mJ versus the number of round trips since startup for the radiation pulse directly after the undulator (before spectral filtering at the crystal mirrors, blue curve), for the radiation pulse after transversing the cavity (after reflection and before reentering the undulator to seed the upcoming electron bunch, red curve) and the transmitted pulse (orange curve). In comparison to the idealized cavity as shown in Figure (5.11), there are pronounced differences.

For one the shot to shot fluctuations are significantly increased. This is, as was analyzed in Paragraph **5.2.2.1**, primarily due to the electron energy jitter. Second, the pulse energy in saturation for the circulating pulse is reduced. And third, the number of round trips required to reach saturation is increased.

This is consistent with the evolution of the round trip and FEL gain shown in Figure (5.68(a)). The different gains all show a small (average) reduction with respect to the idealized cavity presented in Figure (5.20(a)). Furthermore, the gains for the ‘realistic’ demonstrator exhibit very pronounced shot to shot fluctuations. On the other hand, the newly generated energy as well as the transmitted radiation in saturation reach the same peak values and, unlike for the idealized cavity, remain at this level. Latter point is due to the lower seeding radiation power, which leads to lower oversaturation. The reason for the saturated pulse energy not reaching the same values as for the idealized case, even though the newly generated energy is the same, is due to the increased losses induced by the non-idealized X-ray optical cavity. Of the different error sources, as was discussed in the prior paragraphs, the influence of the profile error is by far the most prominent.

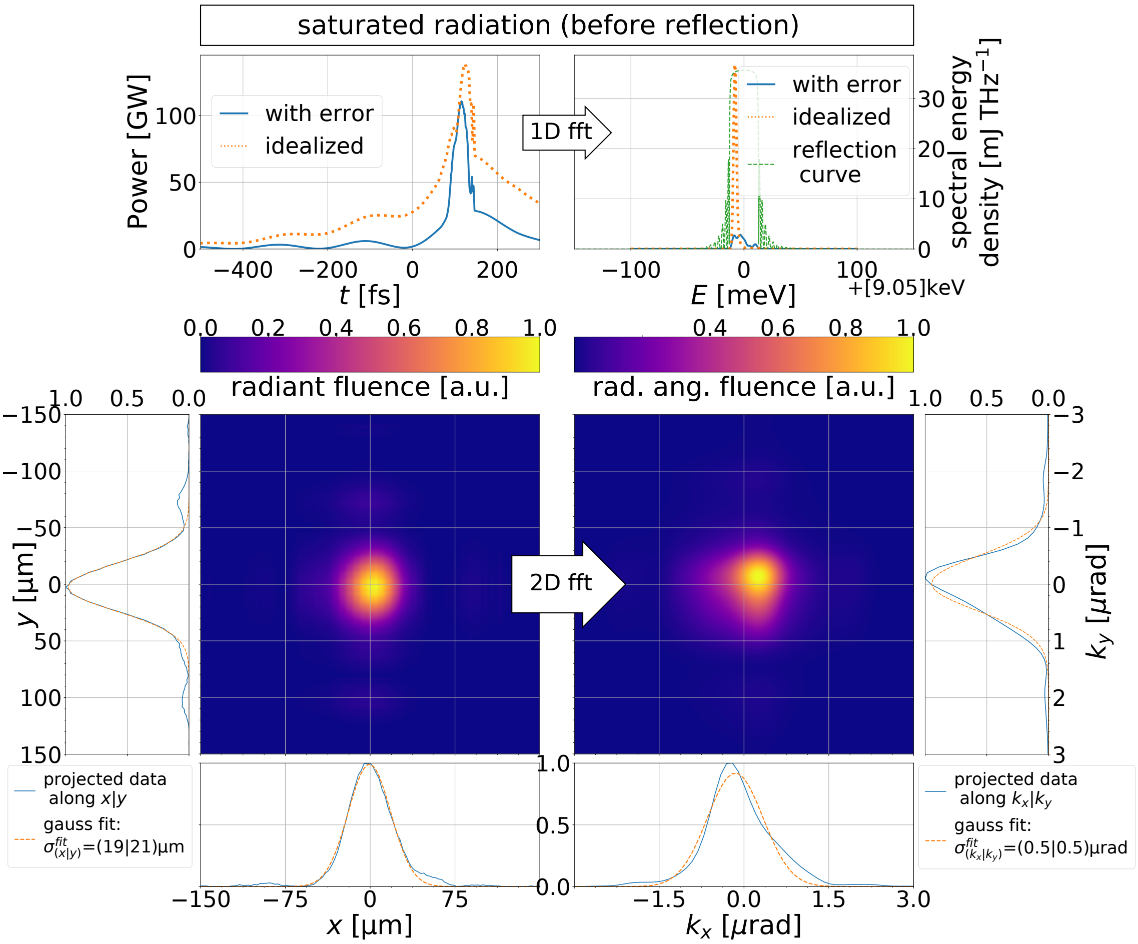

Figure 5.69: Longitudinal and transverse representations of the circulating radiation pulse before reflection in saturation. For the longitudinal distributions also the results of the idealized cavity are shown as orange dotted line for reference. The distributions were averaged over forty round trips in saturation.

In Figure (5.69) the longitudinal and transverse distribution of the saturated circulating pulse before reflection are displayed. Both spatial and angular distribution show deviations from a perfect gaussian, apparent as satellites in the spatial domain (see projections) and considerable blurring in the angular domain, which are induced by the mirror figure errors. This results in a reduced gaussian quality factor of $J = 15.3(2)$. One has to note, however, that this value might become better when travelling the kilometer distance from the CBXFEL demonstrator to the experiment, as the distorted components of the distributions would naturally spatially separate from the undistorted components over this wide distance and can be ‘cleaned’ by physical apertures. This is also expressed by a comparably good value of the transverse coherence of

$\xi_{\mathrm{coh}} = 0.89$[77], which is less affected by local deviations from a gaussian profile.

Also, for the longitudinal distribution significant differences to the idealized case can be observed. In particular, the CBXFEL demonstrator bandwidth $\sigma_E = 20.4(5)\,\mathrm{meV}$ has become much wider compared to the idealized case with $\sigma_E = 5.70(5)\,\mathrm{meV}$, even though staying at a very low level. This is due to multiple reasons. For one, the arrival time and energy jitter slightly shift the optimal position of the spectral peak on a shot to shot basis, which leads to a widening. But the dominant reason is the loss in both seeding power and seeding efficiency, latter due to the introduced transversal distortions. In consistency with the discussion for the idealized case in **5.2.1**, this leads to a shorter duration of the gain profile.

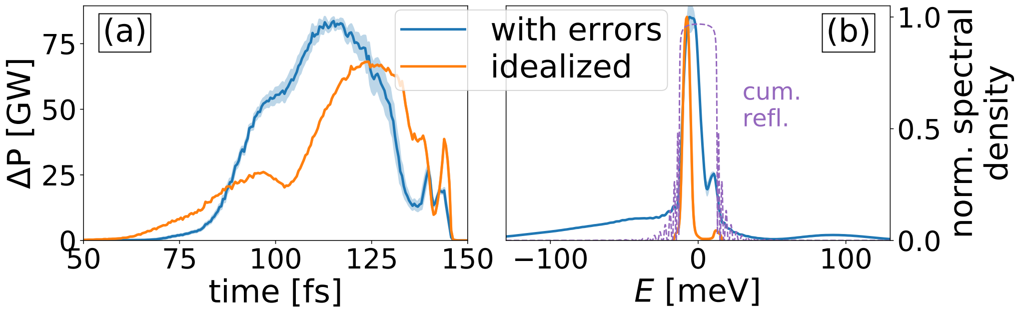

Figure 5.70: The intensity (a) and normed spectrum (b) of the newly generated radiation in the *saturation regime* for the case of the non-idealized CBXFEL demonstrator (blue curve) and the idealized one (orange). The rms duration of the newly generated intensity for the non-idealized case is shorter than for the idealized one, leading to a wider bandwidth in the spectral domain.

This is affirmed by Figure (5.70(a)), which shows the time-domain representation of the newly generated radiation for both idealized and not-idealized case, and reveals a shorter duration for the non-idealized one. This on the other hand results in a wider bandwidth of the newly generated radiation as presented in Figure (5.70(b)) and ultimately results in a wider bandwidth of the circulating radiation.

The time domain profile of the saturated circulating radiation pulse of the non-idealized demonstrator in Figure (5.69) reveals the principally same features as the idealized one, but shows a shorter time-duration of $\sigma_t^{(\mathrm{err.})}$=132(2) fs compared to $\sigma_t^{(\mathrm{ideal.})}$=214(4) fs. For one, this is due to the same reasons as discussed above for the spectral domain. But the dominant reason is, that for the idealized case with its very low losses the long time-domain tails induced by the crystal reflection stack up over many round trips and become quite important in saturation. For the non-idealized case having a higher relative contribution of the shorter newly generated radiation and higher cavity losses, these tails are less prominent.

Owing to the higher bandwidth the coherence time $\tau_{\mathrm{coh}^{\mathrm{err.}}}$=166(4) fs of the circulating pulse before reflection is much reduced in comparison to the idealized demonstrator with $\tau_{\mathrm{coh}^{\mathrm{ideal.}}}$= 717(15) fs, also in relation to the total duration. It is, anyhow, a very high degree of longitudinal coherence, far superior from SASE radiation. Putting together these values yields an approxi-

---

[77] The transverse coherence ξ_{coh} is based on the full 4D transverse phase space, whereas the gaussian quality factor J approximates the phase space area via integration in the separated 2D spatial and 2D angular domains. Hence, ξ is the more accurate value, however, numerically much more expensive to calculate.

mate peak brilliance (2.19) of $\mathcal{B}_p^{\text{err.}}$ =5.2(3) × 10^{34} #Phot/s/mm^2/mrad^2/0 1% BW, which is two orders lower than $\mathcal{B}_p^{\text{ideal.}}$ =4.84(3) × 10^{36} #Phot/s/mm^2/mrad^2/0 1% BW of the idealized cavity, which is dominantly due to the decreased transverse quality. On the other hand, basing the brilliance on the more accurate Eq. (2.25) and using the comparably high transverse coherence of $\xi_{\text{coh}} = 0.89$, yields a better peak brilliance of $\mathcal{B}_p^{\text{err.,coh}}$ =7.4 × 10^{35} #Phot/s/mm^2/mrad^2/0 1% BW, as it is less sensible to the distorted components of the transverse distribution, which can be partially removed (see above).

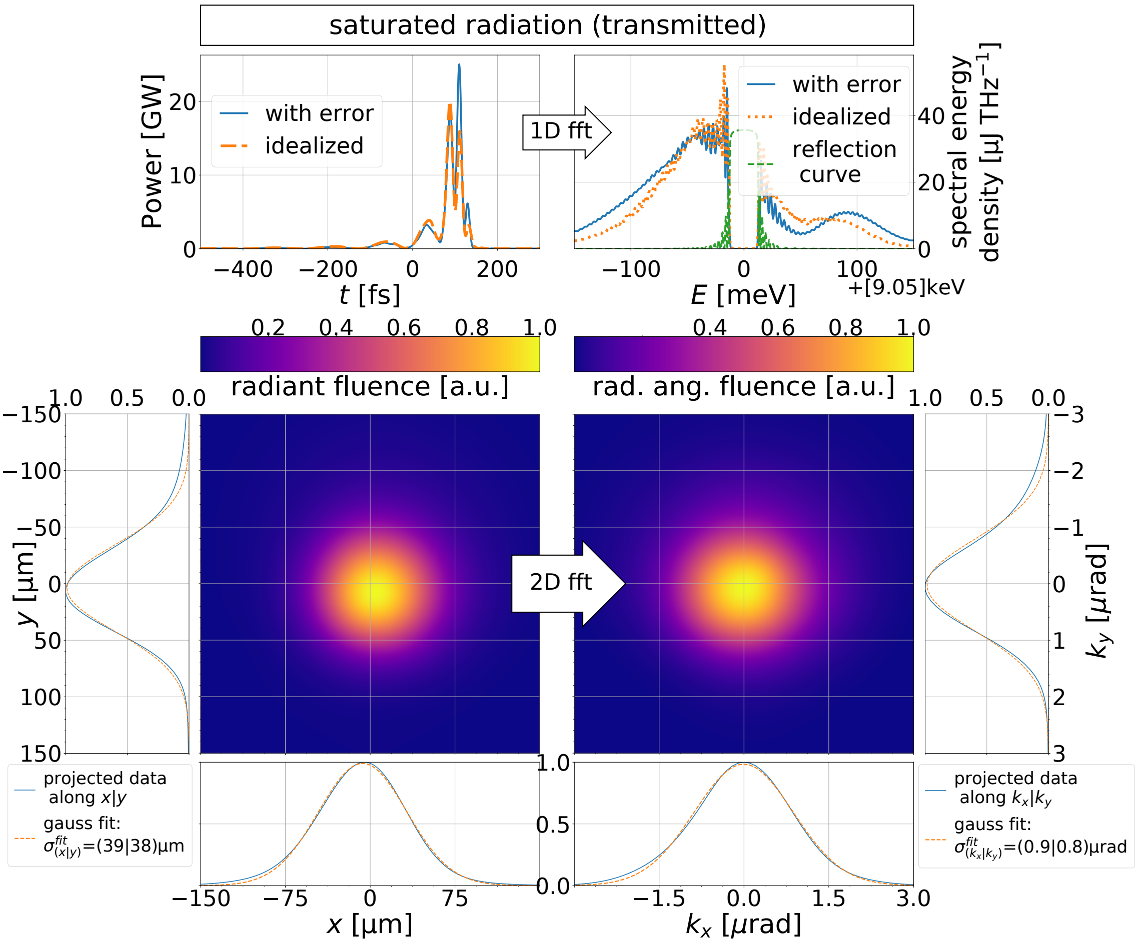

Figure 5.71: Longitudinal and tranverse representations of the transmitted radiation pulse in saturation for the CBXFEL demonstrator with combined error sources. For the longitudinal distributions also the results of the idealized cavity are shown as orange dotted line for reference. The distributions were averaged over forty round trips in saturation.

In Figure (5.69) the longitudinal and transverse distribution of the transmitted radiation pulse in saturation are displayed. The transverse distribution shows deviations from an ideal gaussian, apparent in the projections, which are however very small compared to the circulating pulse. This is also evident in the gaussian quality factor, which is with $J_{\text{tr}} = 2.18(6)$ much better than $J_{\text{circ.}} = 15.2(3)$ of the circulating pulse. This is due to the gain guiding in the FEL ‘washing’ out most of the transverse deviations introduced by the non perfect optics. Still, the distorted seed does result in a reduction of the transverse quality in comparison to the idealized cavity with $J_{\mathrm{tr,ideal.}} = 1.888(1)$, even though the pulse is less subject to oversaturation. The transverse coherence is with $\xi_{\mathrm{coh}}^{\mathrm{tr.}} = 0.84$ still smaller than $\xi_{\mathrm{coh}}^{\mathrm{circ.}} = 0.89$ of the circulating pulse. This is due to the stronger dependence on the electron phase space and correspondingly also the distorted fractions (such as the bunch head).

In the longitudinal domain the transmitted pulse of the non-idealized CBXFEL demonstrator strongly resembles that of the idealized demonstrator. The main difference is that the bandwidth $\sigma_E^{\mathrm{tr.,err.}} = 69(2)\,\mathrm{meV}$ in the non-idealized case is increased compared to $\sigma_E^{\mathrm{tr.,ideal.}} = 60.3(4)\,\mathrm{meV}$ in the idealized case. This is consistent with the higher bandwidth of the newly generated radiation discussed above and shown in Figure (5.70(b)). Though, the degree of temporal coherence is with $\tau_{\mathrm{coh}^{\mathrm{tr,err.}}}$=22.7(7) fs in $\sigma_t^{\mathrm{tr,err.}}$ =97(2) fs duration slightly enhanced compared to $\tau_{\mathrm{coh}^{\mathrm{tr,ideal.}}}$=25.8(1) fs in $\sigma_t^{\mathrm{tr,ideal.}}$ =123(4) fs. This is due to the decreased importance of the 'reflection edge' components of the wider bandwidth transmitted pulse. The peak brilliance is with $\mathcal{B}_p^{\mathrm{tr,err.}}$ =1.4(2) × 10^{34} #Phot/s/mm^2/mrad^2/0 1% BW nearly perfectly agreeing with $\mathcal{B}_p^{\mathrm{tr,ideal}} =$ 1.375(4) × 10^{34} #Phot/s/mm^2/mrad^2/0 1% BW of the idealized cavity.

Table 7: Main parameters of the X-ray pulses in saturation for a CBXFEL at $E_c = 9.05$ keV including combined error sources. The errors denote the standard deviation of the shot-to-shot fluctuation in saturation as well as by averaging over 15 individual runs with equal base parameters.

Photon Energy E_{ph} [keV]	9.05			
	with errors		idealized	
	before refl.	transmitted	before refl.	transmitted
Pulse Energy Q_{pulse} [mJ]	10.00(13)	0.95(5)	31.55(12)	0.915(23)
Bandwidth $\sigma_{E_{\mathrm{ph}}}{}^{a}$ [meV]	20.4(5)	68.6(1.3)	5.70(5)	60.3(4)
Pulse Length $\sigma_t{}^{a}$ [fs]	132(2)	97(2)	214(4)	123(4)
Peak Brilliance $\mathcal{B}$ [b]	5.2(3) × 10^{34}	1.4(2) × 10^{34}	4.84(3) × 10^{36}	1.375(4) × 10^{34}
coherence time τ [fs]	166(4)	22.7(7)	717(15)	25.8(1)
gaussian quality J	15.2(3)	2.18(6)	1.13(1)	1.888(1)

[a] The bandwidth/duration is computed using the mean absolut deviation $\mathcal{D}_{u,\mathrm{MAD}}$ (2.14), which is less sensitive to the wide tails in the spectral distribution. It is then transformed into the more common standard deviation $\sigma_u \approx \sqrt{\frac{\pi}{2}}\mathcal{D}_{E_{\mathrm{ph}},\mathrm{MAD}}$.

[b] #Phot/s/mm^2/mrad^2/0 1%BW

To conclude, the combined influence of electron shot to shot jitter and non-idealized X-ray optical components leads to a decrease in stability and significant reduction in the performance of the trapped radiation in the CBXFEL demonstrator, which is also summarized in Table 7. The performance still remains far superior from SASE and most advantages of the CBXFEL, which are the very high peak spectral flux and the high degree of three dimensional coherence, remain unchanged. Only the very high pulse to pulse stability is reduced, but remains on a high level and especially is fundamentally better than a monochromatized SASE FEL. Regarding the transmitted radiation, which is the more important to begin with if no cavity dumping is foreseen, the errors have only minor impact and mainly reduce the pulse energy shot to shot stability.

5.2.2.9 Three undulators: Up to now it was assumed that the four undulator sections would be perfectly aligned and calibrated. In order to account for the possible reduction in gain when these idealized conditions are not met, in this paragraph the CBXFEL demonstrator at $E_{\mathrm{ph}} = 9.05\,\mathrm{keV}$ including the combined error sources shall be studied with a reduced number of only three instead of four undulator sections of five meter length and 125 undulator periods each.

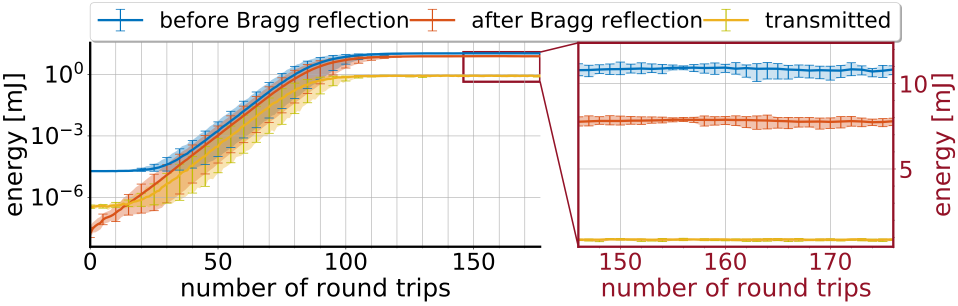

Figure 5.72: The left plot in logarithmic scale shows the full evolution of the pulse energy versus number of round trips for the non idealized cavity and using three undulator sections and the right plot in linear scale highlights the same photon beam after saturation. The data was averaged over 15 individual runs/bunch trains with the shaded area showing the minimum/maximum values from these runs.

In Figure (5.72) the photon pulse energy evolution is displayed for the case of an non-idealized CBXFEL using three instead of four undulator sections. The main difference in comparison to Figure (5.67), showing the case of four undulator sections, is that it takes about three times the amount of round trips to reach saturation. Anyhow, the pulse energy in saturation agrees very well between these two cases.

In Figure (5.73(a)) the evolution of the round trip (eq. (5.1)) and integrated FEL gain (eq. (5.2)) is plotted for the case of the three undulator sections CBXFEL demonstrator. In consistence with the energy evolution, the gains are strongly reduced by roughly a factor of three compared to the four undulators CBXFEL, leading to a later saturation. The per round trip newly generated energy in saturation, however, is as shown in Figure (5.73(b)) on exactly the same level as for the four undulator sections demonstrator Figure (5.68).

In Figure (5.74) the newly generated intensity (a) and spectrum (b) of both the three undulator sections (blue curve) as the four undulator sections (orange curve) are presented. They evidently agree quite well, with the three undulator sections case exhibiting a slightly wider time profile and, hence, a narrower spectral profile. As the seeding strength is mostly agreeing in both cases, the shorter length leads to a slightly less oversaturated electron bunch and a smoother distribution.

In Table 8 the derived performance parameters of the CBXFEL demonstrator with three undulator sections is presented in comparison to the four undulator sections case. In agreement with above discussion, both cases agree quite well with the three undulator sections case showing a

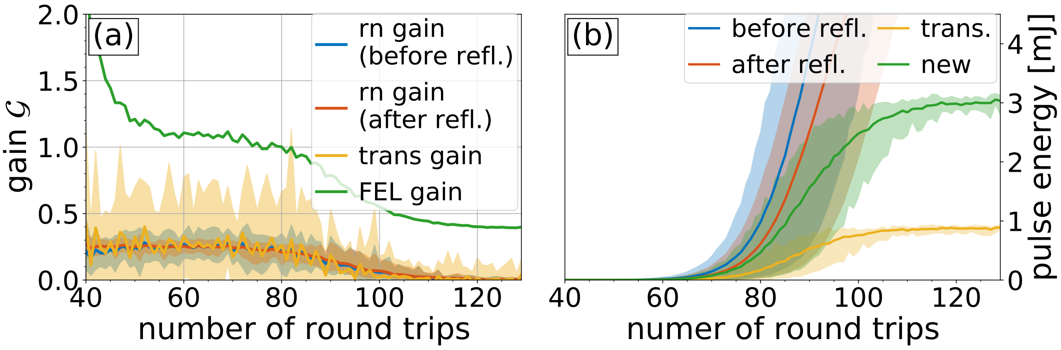

Figure 5.73: (a) shows the evolution of the round trip gain before reflection (blue), after reflection (red) and of the transmitted pulse as well as the FEL gain for the CBXFEL with three undulator sections. As mentioned before, the FEL gain is very inaccurate for the first round trips. (b) displays the corresponding evolution of the pulse energy of the pulses before and after reflection, the transmitted pulse as well as the energy newly generated in the undulators around the maximum of latter two. While the gain in the exponential gain regime is strongly reduced compared to the four undulator sections case, the FEL gain in saturation and, therefore, the amount of newly generated energy in saturation is roughly the same.

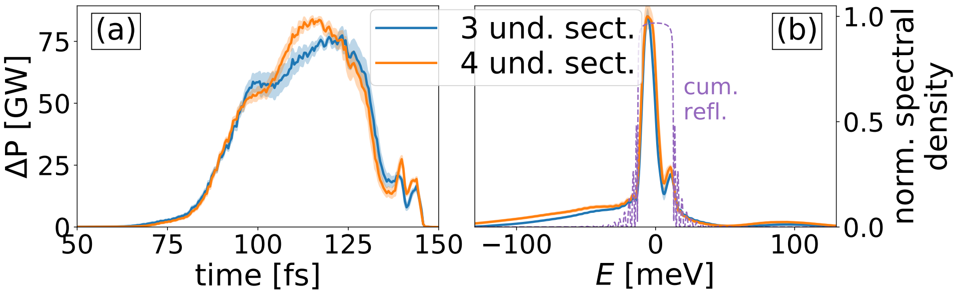

Figure 5.74: The intensity (a) and normed spectrum (b) of the newly generated radiation in the *saturation regime* for the case of the non-idealized CBXFEL demonstrator with three (blue curve) and four undulator sections (orange). The newly generated intensity and spectral profiles of both cases mostly agree, with the three undulator demonstrator exhibiting a slightly longer rms duration and therefore smaller bandwidth.

slightly better peak brilliance for the circulating pulse but a little worse peak brilliance for the transmitted one. The higher brilliance of the circulating pulse is due to the higher pulse energy and the smaller bandwidth. On the other hand the reduced brilliance of the transmitted radiation is due to the reduced pulse energy of the transmitted pulse, in agreement with the reduced bandwidth, and the worse time-bandwidth product which is caused by the crystal response time-frequency correlation near the reflection edge.

Generally, it is evident that also with a reduced FEL gain the CBXFEL demonstrator is still working and providing comparable performance as in 'the full gain' four undulator sections case. The major difference is the roughly doubled number of $\sim$ 130 round trips to reach (full) saturation. Considering the total number of 2700 round trips theoretically possible at the Eu-XFEL inside one pulse train, this obviously is no major problem. Actually, for the heat load problem the three undulator case will be primarily considered (see below).

5.2.2.10 Summary of the non-idealized CBXFEL demonstrator: In the prior section, it was shown that the CBXFEL demonstrator with an idealized cavity, but using a realistic 250 pC

Table 8: Main parameters of the X-ray pulses in saturation for a CBXFEL at $E_c = 9.05\,\mathrm{keV}$ including combined error sources and using a reduced number of three instead of four undulator sections. The errors denote the standard deviation of the shot-to-shot fluctuation in saturation as well as by averaging over 15 individual runs with equal base parameters.

Photon Energy E_{ph} [keV]	9.05			
	3 und. sect.		4 und. sect.	
	before refl.	transmitted	before refl.	transmitted
Pulse Energy Q_{pulse} [mJ]	10.9(2)	0.862(34)	10.00(13)	0.95(5)
Bandwidth $\sigma_{E_{\mathrm{ph}}}{}^{a}$ [meV]	15.2(3)	63.6(1.4)	20.4(5)	68.6(1.3)
Pulse Length $\sigma_t{}^{a}$ [fs]	128(2)	115(2)	131(2)	97(2)
Peak Brilliance $\mathcal{B}$ [^{b}]	$5.3(2) \times 10^{35}$	$6.8(6) \times 10^{34}$	$3.3(2) \times 10^{35}$	$8.8(9) \times 10^{34}$
coherence time τ [fs]	190(4)	26(1)	166(4)	22.7(7)
gaussian quality J	14.3(4)	2.33(7)	15.2(3)	2.18(6)

[a] The bandwidth/duration is computed using the mean absolut deviation $\mathcal{D}_{u,\mathrm{MAD}}$ (2.14), which is less sensitive to the wide tails in the spectral distribution. It is then transformed into the more common standard deviation $\sigma_u \approx \sqrt{\frac{\pi}{2}}\mathcal{D}_{E_{\mathrm{ph}},\mathrm{MAD}}$.

[b] #Phot/s/mm^2/mrad^2/0 1%BW

electron bunch phase space, both for an E_c =6.97 keV C(400) and E_c =9.05 keV C(333) diamond mirror configuration, would produce radiation pulses with outstanding characteristics, circulating through the cavity. Besides tremendously high pulse energies on the order of Q_{pulse} ≈30 mJ in saturation, they would have very low bandwidth on the order of $\sigma_E/E_c \approx 6 \times 10^{-7}$ to 2×10^{-6}, nearly complete three dimensional coherence, peak brilliance three orders of magnitude higher than SASE and very high pulse to pulse stability. On the other hand, only little of that is actually transferred to the transmitted radiation, which is, in the scheme used, solely extracted from the newly generated radiation. Still, also the transmitted radiation in this proof of principle scheme yields very good values compared to SASE, showing pulse energies in the range $Q_{\mathrm{pulse}^{\mathrm{tr}}}$ ≈0.6 mJ to 1 mJ, very low bandwidth $\sigma_E^{\mathrm{tr}}/E_c \approx 7 \times 10^{-6}$ to 1.4×10^{-5}, good coherence, about double the peak brilliance compared to SASE as well as very high pulse to pulse stability. As the E_c =9.05 keV case showed superior characteristics of the transmitted radiation and, furthermore, has a lower absorption coefficient, this C(333) reflection case was decided preferential over the E_c =6.97 keV C(400) case.

In this section it was compared, how statistical jitter of the electron bunch as well as non-idealized X-ray optical components would influence the above results. It was shown in, at least, **one of the most detailed analysis of CBXFEL error sources to-date**[78], that the CBXFEL demonstrator is quite robust towards most of these errors, especially with respect to the transmitted pulse. Regarding the electron jitter, it was deduced that, given the experimentally measured values at the EuXFEL, only the beam energy jitter on the order of $\sigma_\gamma/\gamma_0 = 1 \times 10^{-4}$ is actually

---

[78] This is to the best knowledge of the author in reference to the available literature on the topic, see for example [20–23, 25, 28, 31, 32, 36, 65–67, 165, 213–216].

having noteworthy influence. While it has only very little effect on the average performance, it increases the pulse to pulse fluctuations from the permille to the single percent level. These fluctuations are stronger for the transmitted pulse, as it does not experience any averaging over multiple electron bunches.

Regarding the tolerances, it was decided that each diamond mirror requires a $\Delta\Theta\leq$**100 nrad** angular accuracy as well as a Δs $\leq$**1 µm to 2 µm** longitudinal positioning accuracy[79].

It was further concluded that for the use of the nested Montel grazing incidence assembly, the radiation spot should preferably be shifted **away from the intersection 'gap'** between the two mirrors (see Appending **C.3**). While this would increase the minimum required lengths of the individual grazing incidence mirrors, it was also shown that the CBXFEL demonstrator is much more accepting towards aperture losses than towards the Montel 'gap'. Regarding the actual mirror length, taking into account mirror tilt, and especially, the mirror figure error, a length of l_M =**9 cm**[80] was decided as a good compromise between compactness and minimum impact on the demonstrator performance. This length would, however, need to be doubled for realization in a Montel assembly avoiding the intersection area. If the spatial constrains in the mirror vacuum chamber turn out to be very tight, also a reduced length of l_M $\approx$6 cm to 7 cm would be tolerable.

The most prominent error turned out to be the figure error of the individual mirror surfaces. As there are four grazing incidence mirrors (six mirrors in total including the diamond crystals), the individual errors stack and introduce strong wavefront distortions of the X-ray pulse. These distortions not only lower the transverse 'quality' of the circulating pulse (apparent in a reduced gaussian quality factor), increase the effective cavity losses and lower the total amount of pulse energy in saturation, but also influence the newly generated radiation and lower its transverse distribution quality. It was concluded that the maximum tolerable rms figure error is σ_h $\leq$**1.5 nm**, which even needs to be adjusted to slightly lower values, as in the analysis the plane bendings of the diamond mirrors were neglected.

Furthermore, as the crystal mirrors should ideally not be processed with 'strain relief cuts' in order not to decrease the crystals' thermoelastic stability, the influence of static (clamping) strain was (superficially) studied. One can deduce from the simulations that a maximum (normal) strain magnitude of η_{zz} $\leq$ $\mathbf{1\times10^{-5}}$ has very little impact on the CBXFEL demonstrator. If this is not the case, additional, possibly otherwise unfavorable, measures such as introducing the above mentioned strain relief cuts should be taken. In Table 9 above tolerances are summarized.

Finally, these errors, except the mirror strain and the Montel 'gap', were included with the above mentioned tolerances into one simulation run at E_c =9.05 keV. Even under the combined influence of these distinct error sources, the **CBXFEL demonstrator reaches saturation**. It does, however, show a decrease in stability due to the electron beam jitter and a significant reduction

---

[79] For the three mirrors retroreflecting setup, it is sufficient to tune one mirror with respect to the others, given sufficient pre-alignment on the milliradian level.

[80] Only regarding the tilt and neglecting figure errors, a length of l_M =7 cm would be sufficient.

Table 9: Tolerances required for a functional CBXFEL demonstrator setup as derived from the simulations of the previous paragraphs.

angular tilt $\Delta\Theta$	longitudinal position Δs	mirror length	mirror rms profile error σ_h	normal strain η_{zz}
100 nrad	1 µm to 2 µm	9 cm	1.5 nm	1×10^{-5}

in the performance of the trapped radiation compared to the idealized case, which is dominantly caused by the mirror figure error. Especially, a decrease in transverse quality to $J \approx 15$, a widening of the bandwidth to σ_E/E_c =2.24(5) $\times$ 10^{-6} and a threefold reduction of the pulse energy in saturation Q_{pulse} =10.00(13) mJ can be observed. However, the performance of this trapped, circulating radiation remains far superior to SASE with a much better pulse to pulse stability, nearly complete three dimensional coherence, two to three orders of magnitude better peak spectral flux and one order of magnitude better brilliance $\mathcal{B}_p^{\text{err.}}$ =5.2(3) $\times$ 10^{34} #Phot/s/mm^2/mrad^2/0 1% BW [81]. On the other hand, the transmitted radiation remains mostly unfazed by the different error sources, which is an feature of the comparably large gain in the FEL section.

These results also uphold when reducing the number of used undulator sections from four to three, to mimic the effect of non-idealized undulators. The only significant difference is the threefold reduction in round trip gain and, hence, the likewise increased number of round trips necessary to reach saturation from $n_{\text{sat}}^{4Und.}$ ≈50 to $n_{\text{sat}}^{3Und.}$ ≈120.

Finally, as will be seen in the next section, it should be emphasized that both the tremendous pulse energies of the idealized, but also the threefold reduced pulse energies of the non-idealized CBXFEL demonstrator, would be too high for the crystal mirrors to remain in stable seeding condition. In this sense, the presented performance can be regarded as an outlook for the future, when (and if) the thermal issues are sufficiently met.

Given the present 'simple' backscattering geometry and thermal management, ideally the demonstrator would be able to reach a stable intermediate state, where the additional losses induced by the thermal response would just compensate with the FEL gain. In this sense a less steep round trip gain appears advantageous, as it gives the CBXFEL system time to adapt from round trip to round trip and, hence, reach such a stable intermediate state. Therefore, the three undulator case will be primarily considered for the next section.

---

[81] It should be noted that using the transverse coherence ξ instead of the gaussian quality J, with former giving a more precise measure on the actually occupied phase space area, to estimate the brilliance with Eqs. (2.19) and (2.25), respectively, yields a roughly one magnitude better brilliance of $\mathcal{B}_p^{\text{err.,coh}}$ =7.4 $\times$ 10^{35} #Phot/s/mm^2/mrad^2/0 1% BW. While the high fraction of transverse coherence does not mean that the corresponding small volume of occupied phase space can actually be propagated to the experiments [45], it hints at the gaussian quality J being a bad measure for the transverse quality for this particular phase space distribution.

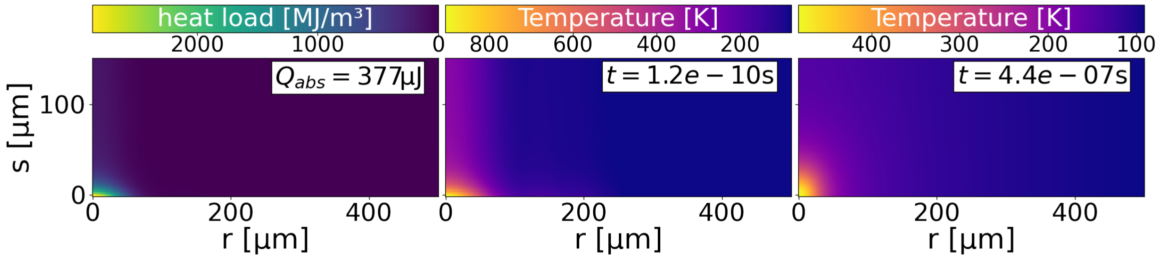

Figure 5.75: Heat load (left) of the saturated three undulator sections CBXFEL demonstrator and corresponding temperature distribution directly after absorption (middle) and at arrival of the subsequent X-ray pulse (right). The temperature evidently is far from returning to the initial conditions of $T_{c,\text{base}} = 77\,\text{K}$ after $t_{\text{rep}} = 444\,\text{ns}$.

5.2.3 Influence of heat load

The above discussed cases were all based on simulations neglecting the potentially important influence of the crystals' thermal answer to the impinging heat load (see Chapter **3**). Assuming the idealized CBXFEL demonstrator at $E_{\text{ph}} = 9.05\,\text{keV}$ C(333) with a saturated circulating pulse energy of $Q_{\text{pulse}} = 31.55(12)\,\text{mJ}$, the absorbed heat at the downstream mirror amounts to a total of Q_{abs} =925 µJ per round trip[82]. Using the full spatial profile of the absorbed heat load, calculated via equation (4.33), and determining the temperature profile directly after absorption via equation (3.47), yields a peak temperature jump of $\Delta T_{\text{max}} \approx 1770\,\text{K}$, starting from $T_0 = 77\,\text{K}$. Even neglecting secondary effects introduced by the abrupt thermal strain, this temperature jump is obviously much too high for the CBXFEL demonstrator to remain in a stable seeding condition. Actually, the peak absorbed dose is with 0.32 eV/atom rather close to the damage threshold of ~0.7 eV/atom [84] and degrading effects such as partial graphitization would be expected to occur. The infeasibility of the idealized demonstrator from thermal considerations was already repeatedly touched in the respective section.

However, as well for the demonstrator including the different error sources and assuming three undulator sections, which has a peak pulse energy of $Q_{\text{pulse}} = 10.9(2)\,\text{mJ}$, the total absorbed heat load is very high with Q_{abs} =377 µJ per round trip. Using the same approach as above, yields a temperature jump of $\Delta T \approx 834\,\text{K}$ after absorption. While this is considerably lower than for the idealized case, it is still too high for the crystal to return to the initial condition after one round trip. In Figure (5.75(middle)) shows the temperature distribution directly after absorption of the incident X-ray pulse and Figure (5.75(right)) the temperature distribution after $t_{\text{rep}} = 444\,\text{ns}$ at arrival of the subsequent pulse. These figures are based on the numerical modeling of the heat equation

$$\rho c_V \frac{\partial T}{\partial t} = \boldsymbol{\nabla}\left(\boldsymbol{\kappa}\boldsymbol{\nabla} T\right) + \dot{Q}_{gen},$$

as discussed in Section **3.2**.

This actually is a bit surprising at first sight, as the amount of absorbed heat is not unusually

---

[82] This value, without the spatial distribution, can easily be obtained by calculating the difference between totally reflected and transmitted energy at the specific mirror.

high, especially when compared to the soft X-ray SASE3 beamline, which has both higher peak energies [207] and a higher absorption coefficient[83]. Yet, first, also at the cryogenically cooled silicon monochromator at the MID instrument at the European XFEL facility [89] rocking curve shifts due to the heating were experimentally observed [217], even though much less strong than reported above. Second, due to the transverse demands of the X-ray optical cavity, the X-ray pulse is much stronger collimated on the crystals than for the usual EuXFEL beamline monochromators. There, the projection of the radiation pulse on the monochromator is much wider, both due to the natural divergence of the radiation as well as due to the typically strongly increased grazing angle of the monochromator with respect to the propagation axis.

Anyhow, it is to be expected that the effects of the heat load would influence the demonstrator way before reaching the high heat loads noted above. Hence, ideally, a stable condition can be be reached at a reduced pulse energy. This can obviously only be studied in a fully coupled treatment and justifies the amount of effort put into the computational program to enable such. In the following these coupled runs will be discussed for different initial conditions, which are different base temperature, crystal thickness, FEL gain and deliberately introduced cavity losses. These studies are all based on the thermal diffusion subfraction of the thermal response, treating the elastic response as quasi-static and the crystal strain fully determined by the temperature distribution at each specific time (see the discussion in Chapter **3**). To have an estimate on the impact of the full dynamic thermoelastic response of the crystal, thoroughly studied in the thesis of *I. Bahns* [85], additionally a single round trip simulation including this very involved physical process will be highlighted.

5.2.3.1 $T_{c,\mathrm{base}} = \mathbf{300\,K}$

In the past, it was often emphasized that a CBXFEL will most probably not work if not cooled to low temperatures [26, 27, 90]. However, these statements were based on less sophisticated, less coupled simulations and/or different cavity configurations yielding reduced heat loads. For the heat loads as presented above, which produce temperature jumps $\Delta T > 300\,\mathrm{K}$, it is questionable if cooling to a reduced base temperature actually makes a difference to begin with. In this paragraph, first the impact of the thermal response at room temperature, or rather $T_{c,\mathrm{base}} = 300\,\mathrm{K}$, shall be studied.

In Figure (5.76) the pulse energy evolution including the evolution of the integrated absorbed heat load on the crystal mirrors is displayed for one exemplary, fully coupled run of the three undulator sections CBXFEL demonstrator **5.2.2.9** at a crystal base temperature of $T_{c,\mathrm{base}} = 300\,\mathrm{K}$, including the influence of heat load[84]. Evidently, there are strong differences compared to the case ignoring heat load shown in Figure (5.72). These are both a nearly three orders of magnitudes strong reduction in peak pulse energy from $Q_{\mathrm{pulse}}^{\mathrm{max,no\ heat}} \approx 11\,\mathrm{mJ}$ to $Q_{\mathrm{pulse}}^{\mathrm{max,heat}} = 20.5\,\mu\mathrm{J}$ as well as strongly increased fluctuations $\sigma_Q/\bar{Q}_{\mathrm{pulse}} \approx 25\,\%$ in the ‘saturated’ pulse energy.

---

[83] `https://physics.nist.gov/PhysRefData/XrayMassCoef/ElemTab/z06.html`

[84] Multiple independent runs were actually carried out. But as they all showed the same characteristics, it was decided to only display one of them to clarify the results.

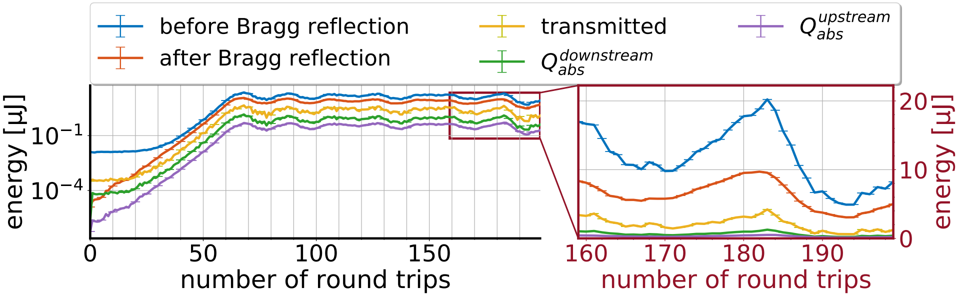

Figure 5.76: The evolution of the pulse energy and the integrated absorbed heat load at the downstream and upstream mirror of the three undulator sections CBXFEL demonstrator including the influence of heat load at a crystal base temperature of $T_{c,\mathrm{base}} = 300\,\mathrm{K}$. Compared to the case ignoring the influence of heat load in Figure (5.72) the curves show both a considerably lower peak pulse energy as well as strong fluctuations.

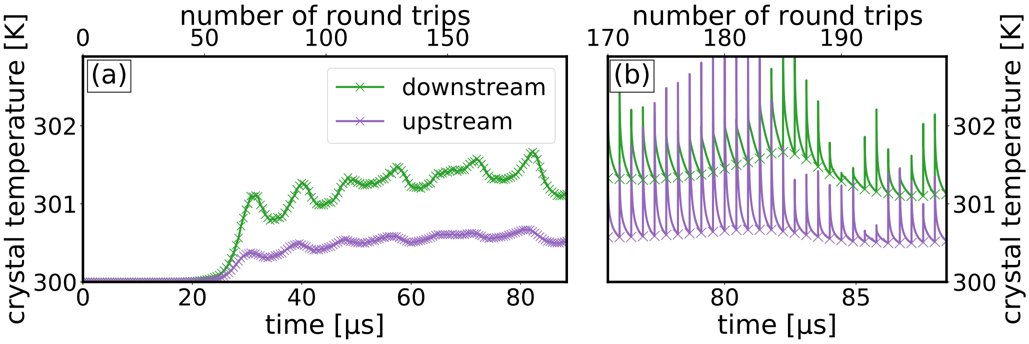

Figure 5.77: Central temperature $T(r = 0, s = 0, t)$ evolution of the downstream (red) and upstream (green) crystal in the fully coupled CBXFEL demonstrator run with $T_{c,\mathrm{base}} = 300\,\mathrm{K}$, corresponding to the pulse energy evolution in Figure (5.76). For visual reasons, (a) only shows the crystal temperatures at the arrival time of the subsequent X-ray pulse. (b) also shows the temperature evolution in between the X-ray round trips exemplarily for the last 24 round trips. The fluctuations in pulse energy in Figure (5.76) and in temperature correlate, with the temperature evolution in (a) clearly exhibiting remanent heating. (b) also shows the temperature spikes directly after absorption, which exponentially decrease, but do not return to the crystal base temperature.

In Figure (5.77) the temperature evolution of the downstream and upstream crystal mirror is plotted for the same run as for Figure (5.76). One can deduce a couple of facts from this picture. First, the temperature at the arrival of the subsequent X-ray pulse, as plotted in Figure (5.77(a)), clearly has a strong correlation to the pulse energy evolution in Figure (5.76), with the temperature peaking at the same number of round trips as the pulse energy and showing the same kind of fluctuations. This is due to the elevated temperature increasing the cavity losses $\mathcal{L}_{\mathrm{cav}}$, as will be discussed in more detail below, up to a point where the round trip gain $\mathcal{G}_{\mathrm{rt}} = (\mathcal{G}_{\mathrm{FEL}} + 1)\,(1 - \mathcal{L}_{\mathrm{cav}}) - 1$ becomes smaller than zero, which leads to a drop in pulse energy. As this drop in pulse energy is accompanied by a drop in heat load, the crystal temperature decreases down to a point, where the losses become smaller than the gain and the pulse energy is rising again. This is also visible in Figure (5.78).

Second, the downstream crystal heats up more significantly than the upstream one due to the difference in absorbed heat load, as plotted in Figure (5.76). This is due to the part of the spectrum

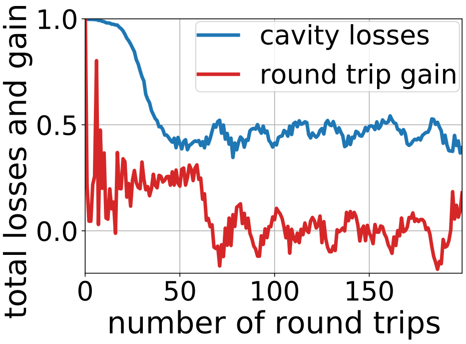

Figure 5.78: The evolution of the total cavity losses $\mathcal{L}_{\mathrm{cav}} = 1 - Q^{\mathrm{seed}}_{\mathrm{pulse}}/Q^{\mathrm{Und}}_{\mathrm{pulse}}$ as well as the round trip gain (after reflection) $\mathcal{G}_{\mathrm{rt}} \approx (\mathcal{G}_{\mathrm{FEL}} + 1)(1 - \mathcal{L}_{\mathrm{cav}})$ is plotted. The cavity losses and, consequently, the round trip gain are showing strong fluctuations in correspondence to the crystal temperature. As the round trip gain fluctuates around zero, these fluctuations are directly imprinted on the pulse energy evolution.

outside the reflection bandwidth being nearly completely transmitted through the downstream mirror and, hence, not being incident on the upstream one. As the radiation outside the reflection bandwidth is additionally more strongly absorbed, this has considerable influence on the amount of absorbed heat load. This problem, which is creating a temperature difference between the upstream and the downstream mirror, is not only apparent for the $T_{c,\mathrm{base}} = 300\,\mathrm{K}$, but for all crystal temperatures in general.
Third, as visible in Figure (5.77(b)), the temperature jumps directly after absorption of the X-ray pulse often are higher at the upstream mirror. On the other hand, as already noted above, the temperature at arrival of the next pulse consistently is lower at the upstream mirror than at the downstream one. This discrepancy is due to the difference in transverse extent of the X-ray pulses at the upstream and the downstream crystals[85]. As the pulses nominally are more strongly focussed on the upstream mirrors (see Figure (5.10)), the associated peak heat load is higher, leading to a higher temperature jump. This is accompanied by a stronger curvature $\nabla^2 T$ and, hence, an increased thermalization rate ${}^{\partial T}\!/\!_{\partial t}$. This is also apparent in an analytic solution (5.4) of the linear heat equation (3.55) derived below. As the total amount of absorbed energy $Q^{\mathrm{tot}}_{\mathrm{abs},i}$ is smaller at the upstream mirror, the remnant temperature rise becomes smaller after sufficient thermalization time.

One would naturally guess that the reason for the increased cavity losses with rising temperature, which are ultimately leading to the significantly decreased peak pulse energies and fluctuations, is the shift of the spectral reflection curve with temperature. As displayed in Figure (5.79) the reflection curves are indeed moved with respect to the resonant photon energy at $T_{c,\mathrm{base}} = 300\,\mathrm{K}$, which is denoted with the coordinate 0 in the graphs. More importantly, the spectral overlap between the downstream and upstream diamond reflection curve is decreased at the peak temperature, which is, consequently, leading to an increase in spectral cavity losses. However, the difference between the spectral overlap at the exemplary round trip 173, which marks a local maximum in the round trip gain $\mathcal{G}_{\mathrm{rt}}$, and round trip 185, marking a local minimum, is very little.

---

[85] Additionally, the radiation at the upstream mirror is nearly completely reflected and only a very little fraction is transmitted. Due to its short penetration depth, this reflected fraction is much more strongly collimated in-depth than the transmitted fraction. Besides, this fraction was only very little absorbed at the downstream mirror and therefore has roughly the same heat load, leading to almost the same peak values if projected on the longitudinal direction. In combination with the lower transverse extent, this leads to a higher local heat density than at the downstream mirror.

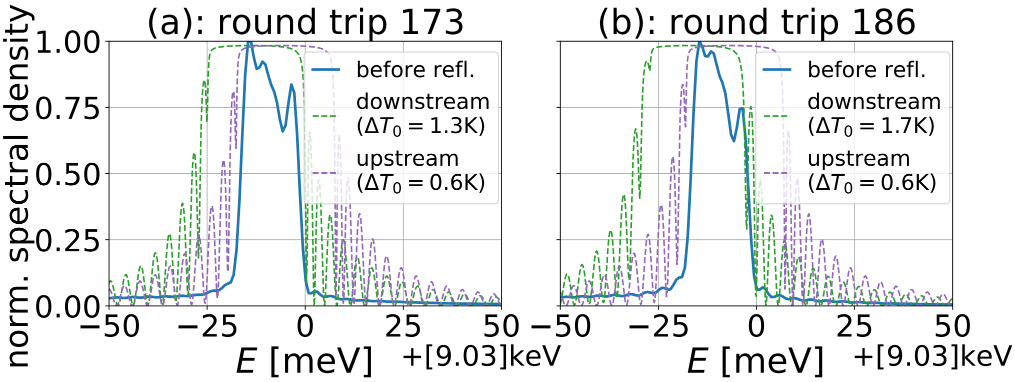

Figure 5.79: Spectral energy density and C (3 3 3) reflection curves for the upstream and downstream crystal (evaluated at $\boldsymbol{x}_\perp = 0$) for two exemplary round trips. Round trip 173 (a) denotes a local maximum in the round trip gain $\mathcal{G}_{\mathrm{rt}}$ and round trip 186 a local minimum. All reflection curves show a shift with respect to the nominal photon energy $\Delta E = 0$ at $T_{c,\mathrm{base}} = 300\,\mathrm{K}$, which is different between the downstream and upstream mirror due to their distinctive temperatures. This leads to a non perfect spectral overlap between the respective reflection curves and, hence, to spectral losses. These losses are higher for (b) at round trip 186.

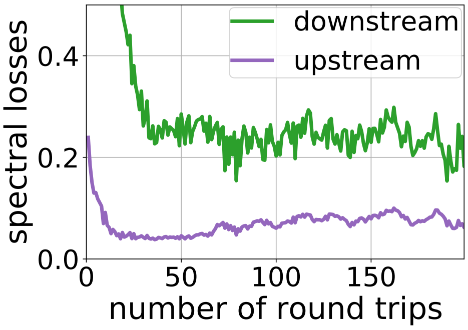

Figure 5.80: The cavity losses introduced by the spectral filtering of the upstream and downstream crystal. While the losses show an increase with number of round trips, fluctuations are only very weakly apparent.

Therefore, this cannot serve as sole explanation for the strong fluctuations observed. This is confirmed by Figure (5.80), which displays the evolution of the losses caused by the spectral cut off at the respective mirrors. While these losses do show an increase due to the risen crystal temperatures, they hardly show fluctuations.

Another contribution to the heat load induced cavity losses is the non-homogeneity of the temperature distribution in the X-ray crystal interaction volume at arrival of the subsequent X-ray pulse. This is displayed in Figure (5.81(a)) for the exemplary round trip number 186, at which the round trip gain has a local minimum. This non-homogeneity of the temperature distribution causes a position dependent displacement $u_z(x_\perp, s)$, which is displayed in Figure (5.81(b)). This locally varying displacement comes with a curvature of the crystal surface, shown in Figure (5.81(c)), which is adding a position dependent phase $-2ku_z(x_\perp, s = 0)$ to the electromagnetic field and therefore imprinting an additional, defocussing, phase front curvature. To approximately assess the influence of this effect, in Figure (5.81(c)) a locally varying 'mock' focal length is plotted in red. This mock focal length is calculated as the distance in z between the crystal surface and the intersection of the surface normal with the optical axis $f_{\mathrm{mock}} = -\frac{x_\perp}{2\partial u_z(x_\perp,0)/\partial x_\perp}$, basically approximating every point of the surface as a local parabola. This mock length is strongly decreasing with transverse position. But close to the optical axis, it is of compara-

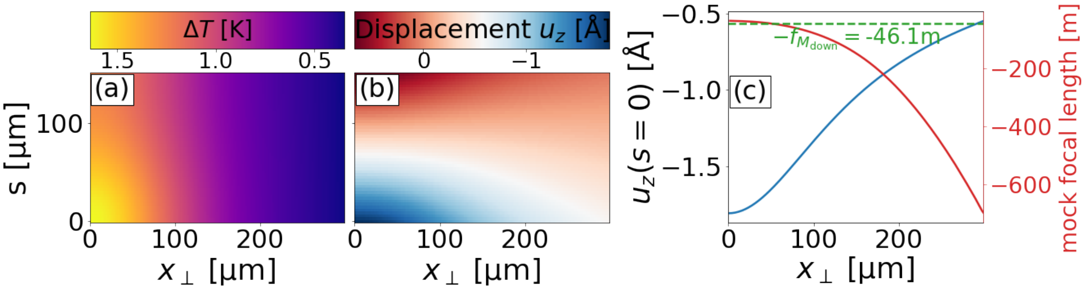

Figure 5.81: Temperature (a) and displacement (b) profiles at arrival of of the 186th round trip X-ray pulse. The non-homogenous distribution of the temperature $T_c(x_\perp, s)$ leads to a non-homogenous distribution of the displacement field $u_z(x_\perp, s)$. This on the other hand cumulates in a curvature of the crystal surface displayed as a blue line (in Å) in (c). (c) also shows a localized 'mock' focal length in red, which is calculated as the distance in z between the crystal surface and the intersection of the surface normal with the optical axis $f_{\text{mock}} = -\frac{x_\perp}{2^{\partial u_z(x_\perp,0)}/\partial x_\perp}$. It is strongly position dependent, but in the vicinity of the optical axis of the same magnitude as the deliberately introduced focussing $f_{\text{downstream}} = 46.1\,\text{m}$, which is shown (negated) as dashed green line. This emphasizes the impact of the surface curvature.

ble magnitude as the actual deliberately introduced focussing strength of the grazing incidence mirrors sketched as green line Figure (5.81(c)). This emphasizes the impact of the thermally induced surface curvature.

However, two points should be noted in this discussion. First, the introduction of the mock focal length is highly artificial, as the concept of a focal length is based on a polynomial tayloring of the surface up to second order [41, ch.2.4.4] (or see equation (4.16)). Then two focal lengths can be assigned, which are commonly valid for the entire surface. This is evidently not the case in Figure (5.81(c)). More importantly, the wavefront is not only affected by the curvature of the crystal surface, but also by the actual penetration depth l_{ext} into the crystal (see equations (4.19) and (4.22)). As this penetration depth is dependent on both the temperature as well as on the photon energy $\Delta E = E_{\text{ph}} - E_c$ with respect to the resonant energy E_c, which is shifting with temperature, l_{ext} is likewise varying with transverse position $x_\perp$. This contribution is superimposed on the surface curvature.

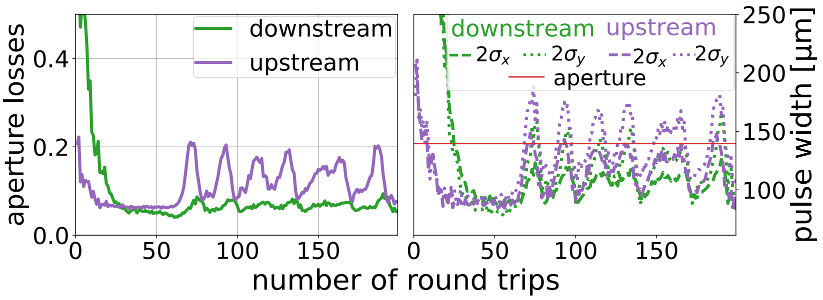

Figure 5.82: Evolution of the aperture cut-off losses (a) as well as of the pulse widths $2\sigma_{x|y}$ (b) at the downstream and upstream mirror assemblies. One can clearly see strong fluctuations in both aperture losses as pulse widths, with the fluctuations being stronger for the upstream as for the downstream mirrors. As a guide for the eye, half the effective aperture width $w^{\text{ap}}/2$ for the $l = 9\,\text{cm}$ individual mirror length is shown as red line in (b)..

Anyhow, Figure (5.82) shows that the non-homogeneity of the temperature distribution does have a strong impact on the pulse width and, hence, on the aperture losses. These show strong correlations to the total losses and the pulse energy evolution and can, therefore, be recognized as dominating reason for the low peak pulse energy and observed fluctuations.

While, referring to above results, operating the CBXFEL demonstrator at $T_{c,\text{base}} = 300\,\text{K}$ certainly is not favorable, from the point of view of this thesis, it has the 'advantage' that the temperature differences remain comparably small. Hence, the heat equation (3.55) can be approximated as a *linear* partial differential equation:

$$\frac{\partial T}{\partial t} = \frac{1}{\rho c_V} \boldsymbol{\nabla} \left(\boldsymbol{\kappa} \boldsymbol{\nabla} T \right) \approx \underbrace{\frac{\boldsymbol{\kappa}}{\rho c_V}}_{\mathcal{D}_{th}} \boldsymbol{\nabla}^2 T,$$

with the thermal diffusivity $\mathcal{D}_{th}$, which is approximated as a constant value. The analytic solution of above equation is strongly simplified. Comparing the analytic results with the numeric ones can serve as a good benchmark for the reliability of the numeric procedure described in Section **4.3.1**.

Evidently, the numerically evaluated full heat load profile Eq. (4.35) does not serve as a basis for an analytic derivation. Consequently, it will be approximated by

$$Q_{\text{abs,i}} \left(\boldsymbol{x}_\perp, s \right) \propto e^{-\boldsymbol{x}_\perp^2 / 2\sigma_r^2} \left[p_{in} e^{-s/l_{in}} + p_{out} e^{-s/l_{out}} \right], \tag{5.3}$$

where the heat load profile is described by a perfect gaussian in transverse direction and a superposition of two exponential decays with extinction lengths l_{in} and l_{out} in depth. These correspond to the radiation inside the mirrors reflection bandwidth, dominated by the comparably short reflection depth, and outside the reflection width, dominated by the much longer absorption length (see Figure (3.3)). t_c is the thickness of the crystal. The unknown parameters $\sigma_r, p_{in}, p_{out}, l_{in}$ and l_{out} are obtained by fitting equation (5.3) to the numerically obtained heat load profile $Q_{\text{abs},i} \left(\boldsymbol{x}_\perp, s \right)$ for every round trip i.

Linearly approximating the initial temperature jump caused by the absorbed heat as $\Delta T_i(t = 0) = Q_{\text{abs,i}}/\rho c_V$ and combining the solutions of *H. Sinn* [196] for the transverse dependence and *Carslaw and Jaeger* [218] for the in-depth dependence, one yields for the temperature evolution at the crystal center $\boldsymbol{x}_\perp = 0, s = 0$ after absorption of a single X-ray pulse i:

$$\begin{aligned}
\Delta T_{0,i}(t) =& \frac{\Delta T_{0,i} \left(t = 0 \right)}{1 + t 2\mathcal{D}_{th}/\sigma_r^2} \left[p_{in} \cdot \mathcal{Z} \left(t, l_{in} \right) + p_{out} \cdot \mathcal{Z} \left(t, l_{out} \right) \right], \qquad (5.4)\\
\text{with} \quad \mathcal{Z} \left(t, l \right) =& \frac{1}{t_c} \left[l \left(1 - e^{-t_c/l} \right) + 2 t_c^2 l \sum_{n=1}^{\infty} \exp \left(\frac{-n^2 \pi^2 \mathcal{D}_{th} t}{t_c^2} \right) \frac{\left(1 - e^{-t_c/l} \right) (-1)^n}{t_c^2 + l^2 n^2 \pi^2} \right]\\
\text{and} \quad \Delta T_{0,i} \left(t = 0 \right) =& \frac{Q_{\text{abs},i}^{\text{tot}}}{c_v \rho} \frac{1}{2\pi \sigma_r^2 \left[p_{in} l_{in} \left(1 - e^{-t_c/l_{in}} \right) + p_{out} l_{out} \left(1 - e^{-t_c/l_{out}} \right) \right]},
\end{aligned}$$

where $\Delta T_{0,i}(t)$ is the time-dependent temperature difference at the position $\boldsymbol{x}_\perp = 0, s = 0$, $Q^{\text{tot}}_{\text{abs},i}$ is the integrated absorbed heat load of the ith X-ray pulse and $\mathcal{D}_{th} = {}^{\kappa}/_{\rho c_v}$ is the thermal diffusivity, approximated as $\mathcal{D}_{th} \approx \mathcal{D}_{th}(T = 300\,\mathrm{K}) = 16.68\,\mathrm{cm}^2/\mathrm{s}$. For the temperature evolution of the crystal, subjected to many subsequent x-ray pulse, one obtains in the linear approximation, where the crystal's thermal response to each individual X-ray pulse is independent of the prior ones [196]:

$$\Delta T_{\text{tot}}\left(\boldsymbol{x}_\perp = 0, s = 0, t\right) = \sum_{t_i \leq t} \Delta T_i \left(\boldsymbol{x}_\perp = 0, s = 0, t - t_i\right), \tag{5.5}$$

where t_i is the arrival time of the ith X-ray pulse and the sum is over all pulses that fullfil $t_i \leq t$ with $t = 0$ starting at the arrival of the first X-ray pulse on the crystal.

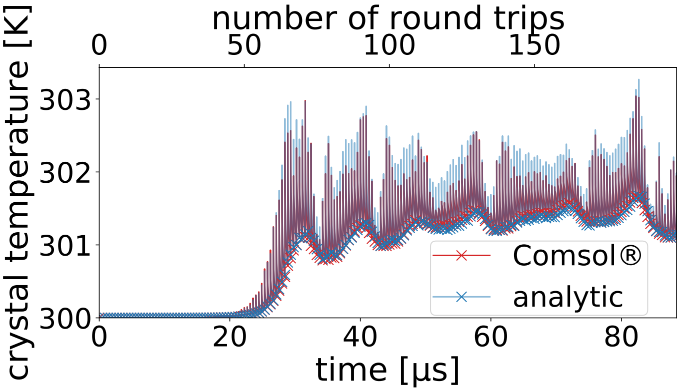

Figure 5.83: Temperature evolution of the downstream mirror obtained by numerical evaluation using *Comsol Multiphysics®* and by analytic estimation via Eqs. (5.4) to (5.5). The crosses denote the temperature at the arrival time of the subsequent X-ray pulse. The agreement, especially regarding the crosses, is very well.

In Figure (5.83) the central temperature evolution calculated using *Comsol Multiphysics®* is compared to the analytic approximation Eqs. (5.4) to (5.5) for the downstream crystal and the heat loads shown in Figure (5.76). While the individual temperature jumps after absorption of the X-ray pulses show deviations, the agreement between the temperatures at the arrival of the subsequent X-ray pulse is excellent, especially considering the multitude of approximations leading to Eqs. (5.4) to (5.5). The deviation in the temperature jump is caused by the approximation (5.3) for the heat load profile and especially the implied gaussian profile. As the numerically obtained heat load profile often is more spread out than presumed by the gaussian fit, the latter overestimates the peak heat load in the crystal center and, hence, the peak temperature jump after absorption. As the total amount of absorbed heat is not affected, the increased temperature jump is accompanied by an increased curvature $\nabla^2 T$, which leads to a faster relative diffusion rate away from the crystal center. These two opposing effects mostly compensate for each other, leading to the temperature agreeing with the more accurate numeric results after a time duration of $t_{\text{rep}} \approx 4.44\,\mathrm{ns}$ for which $2\mathcal{D}_{th} t \approx \sigma_r^2$. The presented results emphasize the reliability of the applied numerical procedure.

To summarize, at a crystal base temperature of $T_{c,\text{base}} = 300\,\mathrm{K}$, inclusion of the crystals' thermal response leads to significant differences to the prior cases, which neglected the crystals' thermal response. The most prominent differences are a nearly three orders of magnitude reduction of

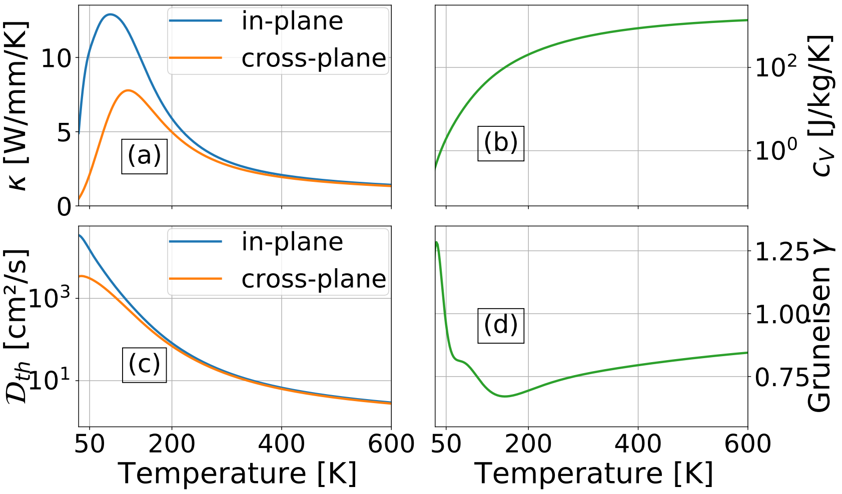

Figure 5.84: Temperature dependent parameters relevant for the thermal diffusion. The thermal conductivity (a) and the heat capacity (b) have been computed using *AlmaBTE* [112]. The thermal conductivity is based on the thin film approximation (4.38) with a film thickness of t_c =150 µm and is strongly reduced compared to the bulk values. The thermal diffusivity $\mathcal{D}_{th} = {}^{\kappa}/_{\rho c_V}$ (c) has been calculated from these values. (d) is the mean Grueneisen-parameter $\gamma = 3B\alpha_{th}/C_V$ relating the thermal expansion to the free energy. It is calculated by using the heat capacity as plotted and the thermal expansion α_{th} and bulk modulus B ≈444 GPa from *Jacobson and Stoupin* [186].

the peak pulse energy from $Q_{\text{pulse}}^{\text{max,no heat}} \approx 11\,\text{mJ}$ to $Q_{\text{pulse}}^{\text{max,heat}} = 20.5\,\mu\text{J}$ and strong fluctuations ${}^{\sigma_Q}/_{\bar{Q}_{\text{pulse}}} \approx 25\,\%$ in the 'saturated' pulse energy. The are two major reasons for these.

The first is a different heating of the downstream reflection curve with respect to the upstream one. This different heating leads to higher temperatures in the downstream mirror at arrival time of the subsequent X-ray pulse, which induces a shift of the downstream mirror's spectral reflection curve with respect to the upstream one. This then causes a decrease in spectral overlap and, hence, an increase in spectral cut off losses.

The second, and dominant, reason is a non-homogenous heat distribution at arrival of the subsequent X-ray pulse. This creates a transverse position dependent optical path length and therefore a change in the pulses' wavefront. This perturbed wavefront brings about an increase in pulse width at the upstream mirror, which ultimately leads to an increase in cut-off losses. The strength of this effect is correlating to the amount of heat load and therefore causes the beat in the pulse energy and round trip gain evolution.

Finally, the linear nature of the thermal load problem at $T_{c,\text{base}} = 300\,\text{K}$ was utilized to benchmark the numerical approach described in Section **4.3.1** with the analytic estimates Eqs. (5.4) to (5.5). The agreement is excellent, emphasizing the reliability of the numeric, *Comsol Multiphysics®* based, routine.

5.2.3.2 Low Temperatures at t_c=150 µm crystal thickness It has been repeatedly argued in literature [26, 27, 88, 90, 178, 219] that the head load problem is significantly eased by cooling the crystal to low base temperatures $T_{c,\text{base}}$. This is supported by the argumentation at the beginning of the prior Paragraph and by Figure (5.84), showing temperatures dependent parameters relevant for the thermal answer of the crystal. It is clearly evident from a highly elevated thermal diffusivity $\mathcal{D}_{th}(T)$ at low T, as shown in (c), that the thermal diffusion is much faster at low temperatures. This is slightly mitigated by the temperature dependence of the *Grueneisen* parameter, which is particularly high for low temperatures $T\tilde{<}50\,\mathrm{K}$ and has a minimum at $T \approx 155\,\mathrm{K}$ as displayed in Figure (5.84(d)). As, in reference to Paragraph **3.2.3.1**, the *Grueneisen* parameter γ_G relates the excess free energy in the crystal to its expansion, an elevated γ_G signifies a higher sensibility to excess heat. This should, however, principally be compensated by the strongly enhanced thermal diffusivity.

Nonetheless, owing to the strong non-linearity of the heat equation (3.55) at large temperature jumps ΔT_i, as they are apparent at low temperatures, it is difficult to determine an ideal crystal base temperature directly from analytic estimates. Therefore, a sweep over different crystal base temperatures $T_{c,\text{base}}$ =40 K, 50 K, 60 K, 70 K, 77 K, 90 K, 100 K and 120 K is carried out. A minimum temperature of $T_{c,\text{base}}$ =40 K was chosen as this corresponds to the minimum temperature, which is achievable with the pulse tube cooler system used for the cryogenically cooled channel cut silicon monochromators at the European XFEL [89], and which will probably also be used for the CBXFEL demonstrator monochromators.

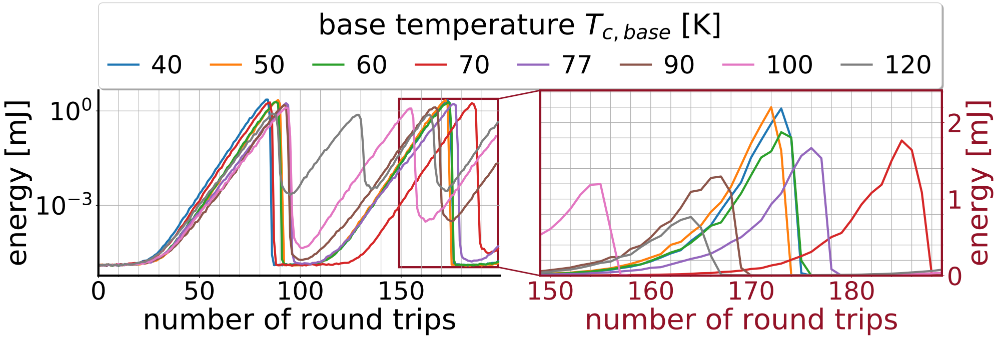

Figure 5.85: Pulse energy evolution under the influence of the crystals' thermal response for different crystal base temperatures $T_{c,\text{base}}$ =40 K, 50 K, 60 K, 70 K, 77 K, 90 K, 100 K and 120 K at t_c =150 µm. The CBXFEL demonstrator clearly is not stable, with the peak pulse energy varying with crystal temperature.

It is evident from the energy evolution displayed in Figure (5.85) that also cooling the diamond crystals does, unfortunately, not lead to a stable operational state of the CBXFEL demonstrator. While the demonstrator reaches much higher peak pulse energies compared to the $T_{c,\text{base}} = 300\,\mathrm{K}$ case, the cavity losses reach nearly 100 % directly after the peak and the entire seeding process basically starts anew[86]. The actual peak pulse energy scales inversely with the crystal base temperature, with lower $T_{c,\text{base}}$ reaching higher $Q^{\text{max}}_{\text{pulse}}$. This is due to the lower base temperatures corresponding to higher intrinsic cooling power, with the non-irradiated parts of the crystal serving as cooling bath for the interaction region, which allows the system to remain stable against higher amount of heat loads. In the following, the reason for the sudden increase of cavity losses, which is different to the fluctuations observed at room temperature, shall be

---

[86] As such, the system behaves comparable to a cavity dumped pulsed laser source (see Paragraph **5.2.3.6**).

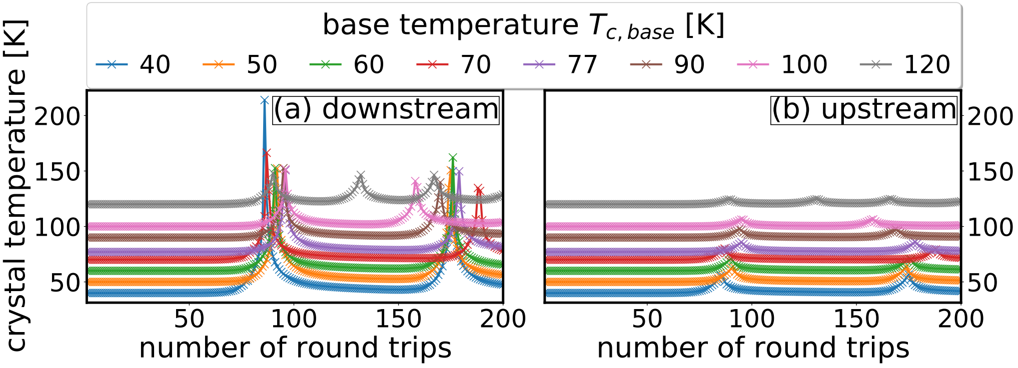

Figure 5.86: Evolution of the temperature at the arrival of the subsequent X-ray pulse for different initial temperatures for a crystal thickness of t_c=150 µm. (a) displays the temperature of the downstream crystal, which exhibits a much more pronounced heating than the upstream crystal displayed in (b). The strong spikes apparent in (a) correlate to the maxima of the photon pulse energy.

analyzed.

In Figure (5.86) the evolution of the temperature at arrival of the subsequent X-ray pulse is plotted at the downstream (a) and upstream (b) crystal for the different base temperatures $T_{c,\text{base}}$. There are two important things to note. The first is that the downstream crystal is heating more strongly than the upstream one. This is the same as already observed and discussed for the $T_{c,\text{base}} = 300\,\text{K}$ case. The second observation to note are the very pronounced spikes in the downstream crystal temperature evolution, with their magnitude ΔT (compared to $T_{c,\text{base}}$) scaling inversely with the base temperature. It is evident that these sharp spikes cause the sudden decrease in pulse energy. The spikes all show the qualitatively same characteristics of a very steep gradient before and after the maximum, partially with exception of the $T_{c,\text{base}} = 120\,\text{K}$ base temperature, where these features are much less pronounced. It therefore appears sufficient to discuss their nature for one exemplary temperature, which is set as $T_{c,\text{base}} = 50\,\text{K}$.

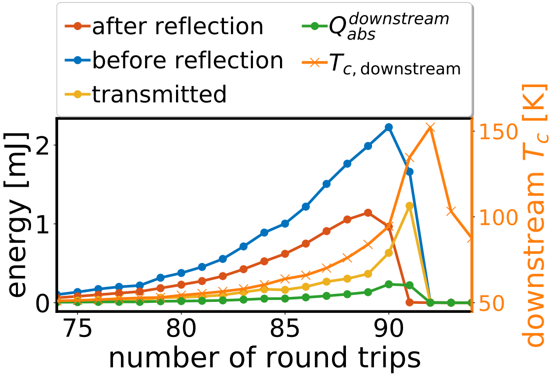

Figure 5.87: Pulse energy, heat load and downstream crystal temperature evolution for $T_{c,\text{base}} = 50\,\text{K}$ zoomed to the (first) round trip of maximum pulse energy.

Figure (5.87) displays the evolution of the pulse energy, the heat load and downstream crystal temperature for a base temperature of $T_{c,\text{base}} = 50\,\text{K}$ zoomed to the (first) round trip of maximum pulse energy. It shows that the maxima in pulse energy $Q_{\text{pulse}}^{\text{und.}}$ after the undulator and pulse energy $Q_{\text{pulse}}^{\text{seed}}$ of the seed are displaced by one round trip. This make perfectly sense, as the pulse energy $Q_{\text{pulse}}^{\text{und.}}$ after the undulator is affected by the strength of the seed of the prior round trip.

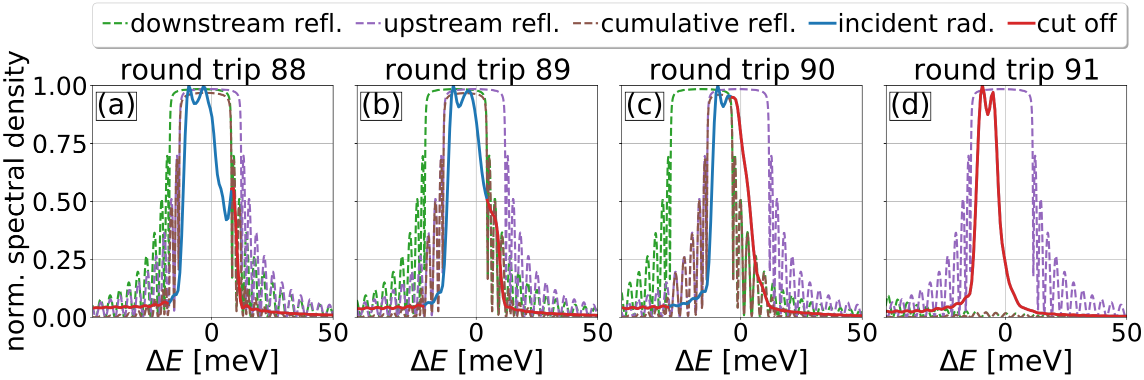

Figure 5.88: The spectrum after the undulator and before reflection (blue solid) together with the spectral reflection curves of the downstream (green dashed) and the upstream crystal (purple dashed) as well as the cumulative reflectivity (brown dashed), for different round trips around the maximum pulse energy (round trip 90). The red curve highlights the fraction of the incident radiation which gets cut off, or rather transmitted, at the downstream mirror and is, consequently, more strongly absorbed.

The pulse energy and temperature evolution as visible in Figure (5.87) relates to the change of the spectral reflectivity curves with the number of round trips, as displayed in Figure (5.88) for exemplary round trips around the pulse energy maximum. At round trip 88 the temperature difference $\Delta T_c^{\max}(\mathrm{rn} = 88) \approx 26\,\mathrm{K}$ does effect the downstream reflection curve only little and the overlap between the downstream and upstream curves remains very good. Hence, most of the incident energy gets reflected and the cavity losses and round trip gain remain stable. The high amount of absorbed heat $Q_{\mathrm{abs}}^{\mathrm{downstream}} = 107\,\mu\mathrm{J}$ at the intense incident pulse energy of $Q_{\mathrm{pulse}}^{\mathrm{und}} = 1.76\,\mathrm{mJ}$ leads to a further rise of the crystal temperature to $\Delta T_c^{\max}(\mathrm{rn} = 89) \approx 34\,\mathrm{K}$. Keeping in mind that the thermal expansion is strongly nonlinear and scales with roughly a power of three to the temperature (see equations (3.43) and (3.48)), this further shifts the downstream crystal reflection curve to lower photon energies. Still, at this point the spectral overlap of the downstream and upstream reflectivity curves remains high enough to sustain a positive round trip gain. Due to the increase in absorbed heat load to $Q_{\mathrm{abs}}^{\mathrm{downstream}}$ =133 µJ, the crystal temperature rises further to $\Delta T_c^{\max}(\mathrm{rn} = 90) \approx 44.5\,\mathrm{K}$. The temperature rise is, beside the higher heat load, additionally increased by the non-linearity of the thermal diffusion process, which slows down at elevated base temperatures as visible from Figure (5.84(c)). At this temperature the elevated spectral losses, induced by the poor overlap of downstream and upstream reflection curves, finally lead to a round trip gain smaller than one and, consequently, a drop in pulse energy from $Q_{\mathrm{pulse}}^{\mathrm{und}}(\mathrm{rn} = 90)$ =2.23 mJ to $Q_{\mathrm{pulse}}^{\mathrm{und}}(\mathrm{rn} = 91)$ =1.66 mJ. From the experience of the room temperature evolution one would now expect that the pulse energies begin to fluctuate around that point. However, the shift in the downstream reflectivity curve also forces a higher fraction of incident pulse energy being transmitted, as is also sketched by the red ‘cut off’ fraction of the incident spectral curve in Figure (5.88(c)) for round trip 90. As the transmitted fraction of the incident pulse is more strongly absorbed than the reflected fraction, due the reduced penetration depth of latter, the absorbed pulse energy is almost doubled to $Q_{\mathrm{abs}}^{\mathrm{downstream}}(\mathrm{rn} = 90)$ =233 µJ. In connection with the non-linearity of the thermal diffusion, the induced heating is accelerated and the remnant crystal temperature at arrival of the subsequent X-ray pulse elevates to $\Delta T_c^{\max}(\mathrm{rn} = 91) \approx 89\,\mathrm{K}$. At this temperature, the cumulative reflection becomes almost zero and the pulse energy evolution abruptly aborts. Additionally, the entire fraction of the still intense incident radiation is mainly transmitted through and partially absorbed by the crystal. This keeps the heat load at a high level of $Q_{\mathrm{abs}}^{\mathrm{downstream}}$ =222 µJ and farther rises the crystal temperature[87]. This leads to the situation that almost no radiation remains in the X-ray cavity and the entire seeding process needs to start anew.

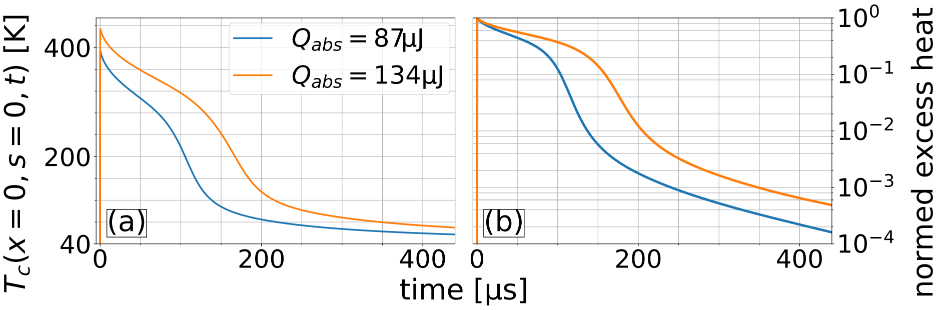

Figure 5.89: The surface temperature $T_c(\boldsymbol{x}_\perp = 0, s = 0, t)$ (a) and normed heat energy $Q_{\mathrm{heat}}(\boldsymbol{x}_\perp = 0, s = 0, t)/Q_{\mathrm{heat}}(\boldsymbol{x}_\perp = 0, s = 0, t = 0)$ (b) evolution after absorption of two different pulses with the same spatial distribution but different integrated heat load, starting at a common base temperature of $T_{c,\mathrm{base}}$ =50 K. The incident heat loads correspond to the round trips 87 and 88. Unlike the linear theory (5.4), which predicts a relative thermalization $Q_{\mathrm{heat}}(\boldsymbol{x}_\perp = 0, s = 0, t)/Q_{\mathrm{heat}}(\boldsymbol{x}_\perp = 0, s = 0, t = 0)$ independent of the initial heatload $Q_{\mathrm{heat}}(\boldsymbol{x}_\perp = 0, s = 0, t = 0)$, graph (b) shows a slowing of the heat diffusion with higher initial heat load. For the specific example, a 1.25 times higher initial heat load leads to a 1.5 times higher remnant excess heat at $t = t_{\mathrm{rep}}$ =444 ns.

There are two aspects which make behavior of the CBXFEL demonstrator at low temperatures and at room temperature different. The first is the strong non-linearity of the heat conduction process at low temperatures, also due to much higher incident pulse energies. With increasing heat load, the diffusion process actually slows down due to the strong decrease in the thermal diffusivity $\mathcal{D}_{th}$. This is emphasized by Figure (5.89(b)), which exhibits a notable decrease in the crystal thermalization efficiency caused by a 1.25 fold increase in incident heat load. The diffusion is additionally slowed by the remnant, spread out heat of the prior round trips, which decrease the local curvature $\boldsymbol{\nabla}^2 T$. The resulting decrease in thermalization efficiency causes an exponentially growing impact of the crystal heating on the lattice expansion and, hence, the diffraction process. This is very obvious from Figure (5.88), where a only ~50 % increase in incident pulse energy induces a shift from nearly complete spectral overlap to zero spectral overlap.

The second aspect to the different behavior is the impact of the non-homogeneous heat dis-

---

[87] It should be mentioned at this point that in Figure (5.87) there is a small difference between the energy entering the cavity and exiting it, be it by transmission, absorption or as seeding radiation. For one this is due to the transmission and absorption at the upstream crystal being omitted in the figure. The second reason is the reduced ‘propagation window’, as is described in Section **4.2** about the propagation routine. This window is centered around the reflection bandwidth of the crystal and ignores outliers far from it to speed up the calculation. Consequently, these outliers are neither apparent in the transmission nor the absorption. As they amount to only little pulse energy, they have, however, only very minor influence on the results discussed.

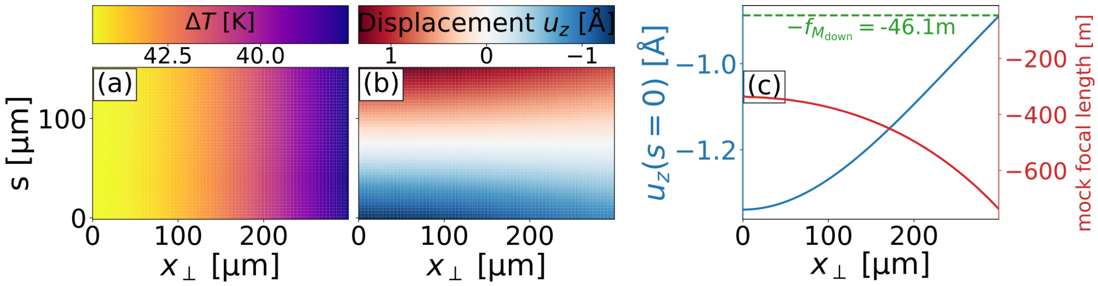

Figure 5.90: Temperature (a) and displacement (b) profiles at arrival of the 90th round trip X-ray pulse. The non-homogenous distribution of the temperature $T_c(x_\perp, s)$ also leads to a non-homogenous distribution of the displacement field $u_z(x_\perp, s)$. Unlike the room temperature case in Figure (5.81), the tranverse variation of the normal displacement is, however, very small compared to the (almost linear) in-depth variation. Correspondingly, the surface curvature (c, blue curve, Å units) and the resulting focussing is comparably little. This can be seen in (c) from comparison of a localized 'mock' focal length $f_{\text{mock}} = -\frac{x_\perp}{2\partial u_z(x_\perp, 0)/\partial x_\perp}$ in red with the dashed green line, representing the (negative) focal length of the Montel mirrors. It shows a minimum 'mock' focal length about five times bigger in magnitude than the focal length of the Montel mirrors (with the focussing strenght scaling inversely to the focal length).

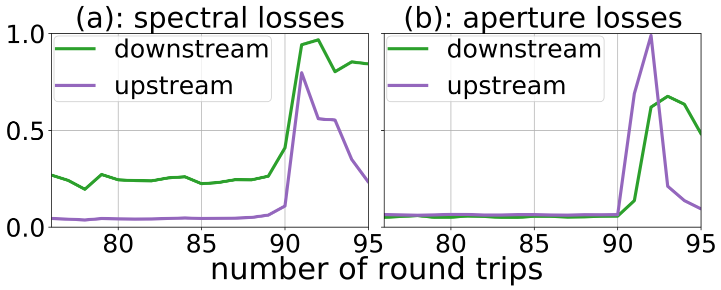

Figure 5.91: Evolution of the spectral (a) and aperture (b) cut-off losses. While the spectral losses are strongly increasing after round trip 88 due the strong crystal heating, the aperture losses remain stable up to round trip 91.

tribution, which causes a curvature of the mirror surface (see Figure (5.81)) and which was the driving force for the gain oscillations observed for the $T_c = 300\,\mathrm{K}$ case. For the $T_c = 50\,\mathrm{K}$ case, however, the effect is very small, as can be seen exemplarily for the round trip 90, where, according to Figure (5.88(c)) and Figure (5.91(a)), the heating already has significantly increased the spectral cut off losses. At the same time, as displayed in Figure (5.90), the inhomogeneity of the temperature has induced a rather small curvature on the crystal shape. According to Figure (5.91(b)), a corresponding increase in aperture losses is hardly apparent. This does change at round trip 91, where the significantly higher peak temperature is accompanied by a notable curvature and the upstream aperture losses are increased manifold. However, the spectral cut off losses amount to nearly 100 % at the same round trip, so the additional aperture losses have a negligible impact on the actual CBXFEL demonstrator performance[88].

It should be mentioned that a domination of the aperture losses would probably lead to a more stable CBXFEL demonstrator. This is due to the spectral losses being self enhancing. As a stronger spectral cut off comes with a risen fraction of absorbed energy, this also leads to an increase in the heating and, hence, to an increase in the spectral cut off losses. On the other hand the radiation lost due to the transverse cut off at the mirror apertures fully leaves the cavity and does not further accelerate the heating.

---

[88] The inhomogeneity of the temperature distribution will become important for the "passive cavity-switching" scheme discussed in Paragraph **5.2.3.6**.

To summarize, also cooling the crystal down to low temperatures, and, thereby, significantly enhancing the crystal cooling, does not permit a stable operation of the CBXFEL demonstrator. While the demonstrator reaches peak pulse energies in the millijoule range, which scale inversely with the crystal base temperature, the seeding process is sharply aborting directly after reaching the peak. Afterwards, the entire process starts anew, given the crystal time to cool down. The physical reasons for the sharp drop off, which differs strongly from the comparably smooth fluctuations observed at room temperature, are both the non-linearity of the thermal diffusion, slowing down with increasing heat load, and the self-increasing spectral cut off losses. These two effects combine to a steep growth of the impact of the crystal thermal response. It should be emphasized that this effect could only be resolved by using the fully coupled computationally framework developed in this thesis.

Even though none of the crystal base temperatures permit the CBXFEL demonstrator to actually reach a stable operational state, it is certain that stronger cooling does strongly enhance the thermal diffusion. As such, it is from a physical point of view definite that running the demonstrator at a temperature of $T_{c,\mathrm{base}} = 40\,\mathrm{K}$ is favorable to running it at higher temperatures. However, one has to consider that the actual cooling power of the pulse tube cooler is dropping with decreasing temperature [89]. This cooling power becomes important for transmitting the heat from the crystal to the cooler in the 100 ms in between the RF pulses, to return the crystal to its initial state at the beginning of the next pulse train. This is also one reason why the cryogenically cooled channel-cut is operated at $T_{c,\mathrm{base}}$=100 K, where the cooling power amounts to comparably high 40 W in comparison to 5 W at $T_{c,\mathrm{base}}$=40 K. As the thermal diffusion at $T_{c,\mathrm{base}}$ =100 K is much worse, a compromise between thermalization efficiency and cooling power can be found at $T_{c,\mathrm{base}}$ ≈77 K[89], where latter still amounts to 30 W [89]. Also, effects out of the scope of the diffusive Fourier's law, which are only partially accounted for in this work, become more important at lower temperatures due to the increase in (mode resolved) mean free path. Also accounting that the actual differences of the demonstrator characteristics between $T_{c,\mathrm{base}} = 77\,\mathrm{K}$ and $T_{c,\mathrm{base}} < 77\,\mathrm{K}$ are only in quantitative but not in qualitative nature, at this point, it appears tolerable to conduct the CBXFEL demonstrator experiment at this temperature. Therefore, in the following often a crystal temperature of $T_{c,\mathrm{base}} = 77\,\mathrm{K}$ is assumed for discussion. Principally, it should be noted that if using the above mentioned pulse tube cooler, this is not a fundamental choice, as both base temperatures of $T_{c,\mathrm{base}} = 77\,\mathrm{K}$ and $T_{c,\mathrm{base}} = 40\,\mathrm{K}$ can be experimentally tested.

Finally, it is noteworthy that at the time the seeding process aborts, nearly the entire fraction of incident pulse energy is transmitted. As such, the process behaves comparable to a cavity dumped pulsed laser source [52, ch. 9.5]. This will be discussed in Paragraph **5.2.3.6**.

5.2.3.3 Low Temperatures at t_c=250 µm crystal thickness One possible attempt to enable stable operation of the CBXFEL demonstrator, is to enhance the thermal diffusion efficiency.

---

[89] This temperature is also historically grown, as it corresponds to the boiling point of liquid nitrogen (`https://pubchem.ncbi.nlm.nih.gov/element/7`), which could also serve as a means to cool the diamonds.

One way to do so, would be, to increase the projected pulse width on the diamond crystals' surfaces. This would already reduce the remnant heat in the linear model (see (5.4)), but is especially helpful in the non-linear case, where a reduced peak thermal load corresponds to a strongly enhanced local thermal diffusivity. Unfortunately, for the demonstrator the pulse widths of the X-ray pulse are fixed to a narrow range by both the electron beam size and the stability criteria of the X-ray cavity. Hence, to increase the projected beam width, one has to vary the angle of the reflecting diamond crystals with respect to the undulator axis. Yet, for the simplistic backscattering geometry as planned for the CBXFEL demonstrator experiment, the angle of the reflecting planes is fixed with respect to the incident X-ray pulse. The only possibility to increase the projected pulse width is to use a so-called strongly asymmetric reflection, which means that the reflecting planes form an angle $\eta \neq 0$ with the crystal surface. These asymmetric reflection add a high degree of complexity to the system, both in the manufacturing of the diamonds, and as they add angular dispersion to the reflection process (see the end of Subsection **3.1.2** about two beam reflection). However, this increase in complexity contradicts the main principle of the demonstrator experiment, which is to keep the setup as simple as possible. Hence, this approach will not be pursued farther in the following.

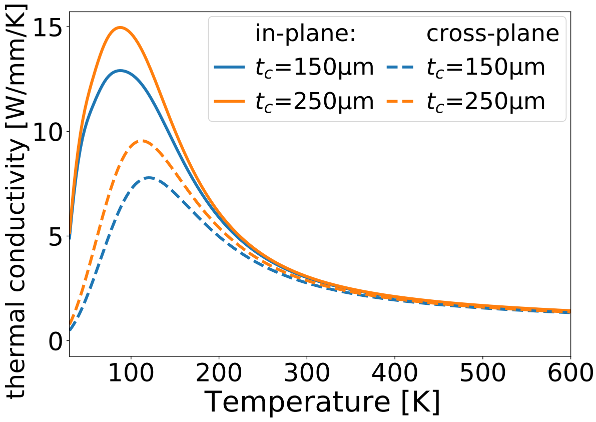

Figure 5.92: Effective in-plane (solid line) and cross-plane (dashed line) thermal conductivity of diamond crystals with t_c =150 µm (blue curves) and t_c =250 µm (orange curves) crystal thickness. The thicker crystal shows a slightly enhanced thermal conductivity.

Another, less effective, approach to enhance the thermal diffusion is to increase the thickness of the diamond crystals. For one, following the discussion of Paragraph **3.2.4.2** and equations (4.38) and (4.39), this leads to a decrease in boundary scattering and, therefore, to an increase in thermal conductivity. This is supported by Figure (5.92), which shows a (small) increase in thermal conductivity of a t_c=250 µm thick crystal compared to a t_c=150 µm thick one. Additionally, an increase in thickness also increases the local volume of the thermal reservoir where the heat can diffuse to. For the SASE case, where the heat load is approximately homogeneously distributed over the crystal thickness due to the millimeter scale absorption length, the increase in thermal volume gets fully compensated by the increase in total absorption. For the presented CBXFEL case, however, the absorbed heat load consists of a fraction determined by the absorption length and a usually stronger fraction determined by the reflection penetration depth, which is on the micrometer scale (see Figure (3.3)). While the prior fraction grows proportionally with the crystal thickness, as in the SASE case, the latter fraction remains constant. This causes the total amount of absorbed heat growing less than the thermal volume. Consequently, an increase in thickness t_c effectively enhances the thermal diffusion efficiency, even when neglecting the increase in thermal conductivity $\boldsymbol{\kappa}$.

For the following study the diamond thickness is set to t_c =250 µm for both diamond crystals. This value is chosen for two reasons. First, an increase in crystal thickness also limits the transmitted radiation in the outcoupling scheme planned for the experiment. t_c =250 µm poses a good comprise between enhancement in thermal diffusion and bearable reduction in transmission, with latter dropping from $T = 0.86$ at t_c =150 µm to $T = 0.77$ at t_c =250 µm for the spectral range outside the reflection bandwidth. The second reason is that a diamond thickness of t_c =250 µm represents roughly the limit of what can be conveniently grown in the superior X-ray optics quality required for the demonstrator setup.

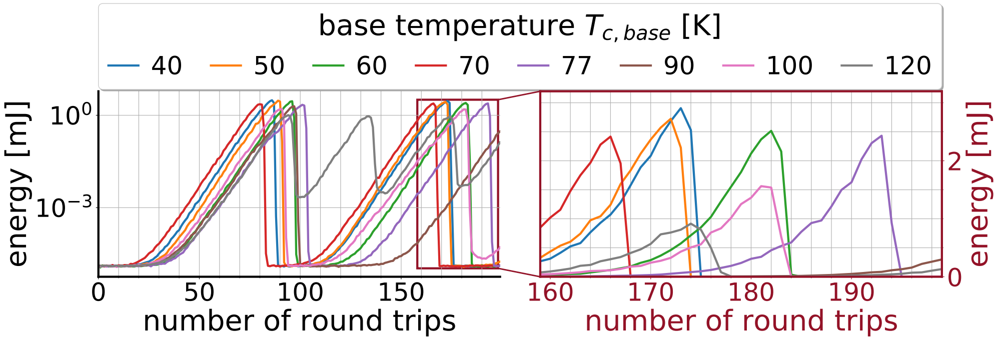

Figure 5.93: Pulse energy evolution under the influence of the crystals' thermal response for different crystal base temperatures $T_{c,\mathrm{base}}$ =40 K, 50 K, 60 K, 70 K, 77 K, 90 K, 100 K and 120 K at t_c =250 µm. The CBXFEL demonstrator clearly is not stable, but the pulse energy reach higher peak values than for the t_c =150 µm thickness case.

Table 10: The peak pulse energies $Q^{(\mathrm{und})}_{\mathrm{pulse,max}}$ for different crystal base temperatures $T_{c,\mathrm{base}}$ and crystal thicknesses t_c. The noted values are only rough estimates due to the lack of datapoints (only one to three per parameter) and, hence, statistics.

$Q^{(\mathrm{und})}_{\mathrm{pulse,max}}$ [mJ]		crystal base temperature $T_{c,\mathrm{base}}$ [K]							
		40	50	60	70	77	90	100	120
t_c [µm]	150	2.23(5)	2.21(2)	1.91(3)	1.81(5)	1.72(5)	1.4(2)	1.24(5)	0.83(2)
	250	3.0(1)	2.9(2)	2.7(2)	2.35(7)	2.3(2)	1.96([a])	1.57(1)	0.95(6)

[a] For this specific data point only one peak was inside the data range, so no statistics can be given. It does not mean that there will be no fluctuation in the peak energy.

From the pulse energy evolution plotted in Figure (5.93) it is evident that also the enhanced thermal diffusion efficiency at t_c =250 µm does not enable a stable operational state of the CBXFEL demonstrator. Actually, from first sight there hardly is any difference compared to the t_c =150 µm case displayed in Figure (5.85). However, comparing the peak pulse energies, which are visible in more detail in the zoomed, linear scale, plots in Figure (5.85) and Figure (5.93) and are additionally noted in Table 10, one can see that the increased thickness enables the CBXFEL demonstrator to reach about 1.3 to 1.4 times higher peak pulse energies. Taking into account the strong non-linearity of the thermal diffusion process, which exponentially slows down with rising heat load, as discussed in the last section, such an increase in pulse energy corresponds to a considerable enhancement in thermal diffusion efficiency.

To summarize, an increase of the diamond thickness from t_c =150 µm to t_c =250 µm enhances the thermal diffusion process and, therefore, increase the CBXFEL demonstrator tolerance towards incident heat load. Considering the only minor decrease in outcoupling efficiency caused by the increased absorption, planning the demonstrator with thicker diamond crystals certainly is favorable. However, also with the increased tolerance provided by the thicker crystals, the demonstrator does not reach a stable operational state, if planned with the parameters as provided by the Subsection **5.2.1** for the cases ignoring the thermal response. Enhancing the cooling efficiency by increasing the X-ray pulse width on the crystals, unfortunately, is not possible due to the constraints given by the simplistic backscattering geometry. Hence, to reach a stable operational state, the impinging heat load needs to be reduced. Two ways to achieve that will be discussed in the following two paragraphs.

5.2.3.4 Reduced FEL gain: In the simplistic setup as discussed in Section **2.4**, there is no possibility to only reduce the total amount of heat load while keeping the overall circulating pulse energy at a multiple millijoule level. Hence, to reduce the heat load one has to equally reduce the X-ray pulse energy incident on the diamond crystals. As was shown for the CBXFEL demonstrator at $E_c = 9.05\,\mathrm{keV}$, the newly generated pulse energy $Q_{\mathrm{pulse}}^{\mathrm{new}}$ in saturation amounts to about 3 mJ. This value, which is basically set by the electron beam properties and can be estimated by the approximation (2.77), is rather independent of the magnitude of both FEL gain and losses. This is evident from the results of the idealized case and the cases including combined error sources with four and three undulator sections (see Figures Figure (5.20), Figure (5.68) and Figure (5.73)), which all show $Q_{\mathrm{pulse,sat}}^{\mathrm{new}}$ ≈3 mJ. However, as was shown in the last paragraphs, the heat load corresponding to this value is too high for the CBXFEL demonstrator to remain in a stable operational state. Therefore, $Q_{\mathrm{pulse,sat}}^{\mathrm{new}}$ needs to be reduced to a lower value. As the FEL gain begins to decrease already much before reaching the maximal saturated value predetermined by the electron beam, it is possible by either significantly increasing the losses or by further reducing the FEL gain, to have both cancel each other at a lower amount of pulse energy in the system. Here, the second approach shall be studied. As was thoroughly discussed for the idealized CBXFEL demonstrator **5.2.1**, the losses are higher in the *startup regime*. So, the initial gain needs to be greater than what would be required for the *seeding regime*, which, consequently, sets a lower limit of $Q_{\mathrm{pulse,sat}}^{\mathrm{new}}$ ≈1 mJ to the newly produced radiation in saturation.

The most direct way to decrease the FEL gain is to detune the undulator parameter K_{und}. Here the undulator parameter is shifted by 6 × 10^{-4} from $K_{\mathrm{Und}} = 3.381$ to $K'_{\mathrm{Und}} = 3.383$.

In Figure (5.94) the pulse energy evolution is displayed for the CBXFEL demonstrator with three undulator sections and detuned undulator parameter K'_{und}. The simulations were further based

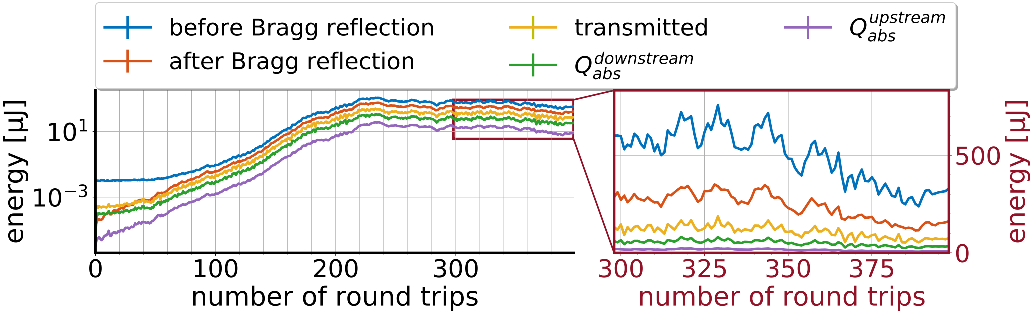

Figure 5.94: The evolution of the pulse energy and the integrated absorbed heat load at the downstream and upstream mirror of the three undulator sections CBXFEL demonstrator including the influence of heat load at a crystal base temperature of $T_{c,\text{base}} = 77\,\text{K}$ and t_c =250 µm with reduced FEL gain. While the stability is significantly improved compared to the 'high' gain case in Figure (5.93), one can see a slow decrease in conjunction with some weak oscillations of the pulse energy after the demonstrator reaches its peak.

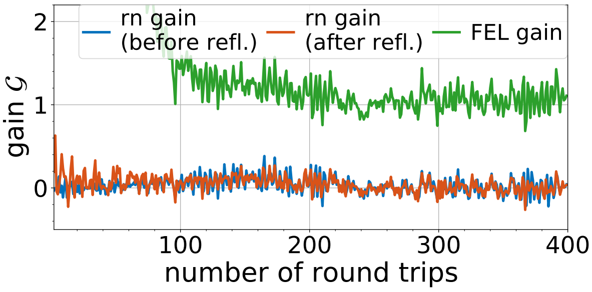

Figure 5.95: Round trip gain Eq. (5.1) directly after the undulator (blue curve), after traversing the cavity (red curve) and integrated FEL gain Eq. (5.2) for the reduced gain CBXFEL demonstrator including the crystals' thermal response at $T_{c,\text{base}}$=77 K.

on two t_c =250 µm diamond crystals at $T_{c,\text{base}}$ =77 K base temperature. The $T_{c,\text{base}}$ =77 K was chosen for posing a good compromise between thermal diffusion efficiency and technical constraints, as was discussed before. From Figure (5.94) one makes a couple of observations. The most evident is the much reduced round trip gain, which is both evident from Figure (5.95), displaying the gain evolution, and by the necessity of more than 200 round trips to reach millijoule pulse energies. The FEL gain, which is at around a value of 1.2 and reduced to about 1 close to saturation[90], did not change with respect to the 'high gain' three undulator CBXFEL demonstrator, as presented in Figure (5.73). However, the actual round trip gain is significantly reduced. This is due to the shift in undulator parameter amounting to an off-centering of the spectral gain curve, which causes increased spectral cut-off losses and, ultimately, a round trip gain very close to zero.

The more fundamental observation from Figure (5.94) is that, in comparison to the energy evolutions Figure (5.93) or Figure (5.85), the CBXFEL demonstrator indeed is much more stable, as the energy evolution is rather smooth and does not show any sudden drop offs. This is also evident in the, in average, almost constant round trip gain. Also, no fluctuations as for the $T_{c,\text{base}}$ =300 K case are apparent.

However, the pulse energies displayed in Figure (5.94) do not remain at a stable saturated value, but show a slow decrease after reaching the maximum. More precisely, the pulse energy reduces

---

[90] This has the side effect that the newly generated radiation always has about the same pulse energy as the seeding radiation

from its maximum $Q_{\mathrm{pulse}^{\max}} = Q^{\mathrm{und.}}_{\mathrm{pulse}}(rn = 234) = 1.1\,\mathrm{mJ}$ at round trip 234 to $Q^{\mathrm{und.}}_{\mathrm{pulse}}(rn = 399)$ =330 µJ at round trip 399, which is more than threefold. The pulse energy after reflection, the transmitted pulse energy, as well as the absorbed heat load, show a nearly perfectly linear correlation to the pulse energy after the undulator. This reflects that the crystals' thermal response impact on the cavity losses also behaves rather linearly, which gives the CBXFEL process time to adapt to the changed circumstances.

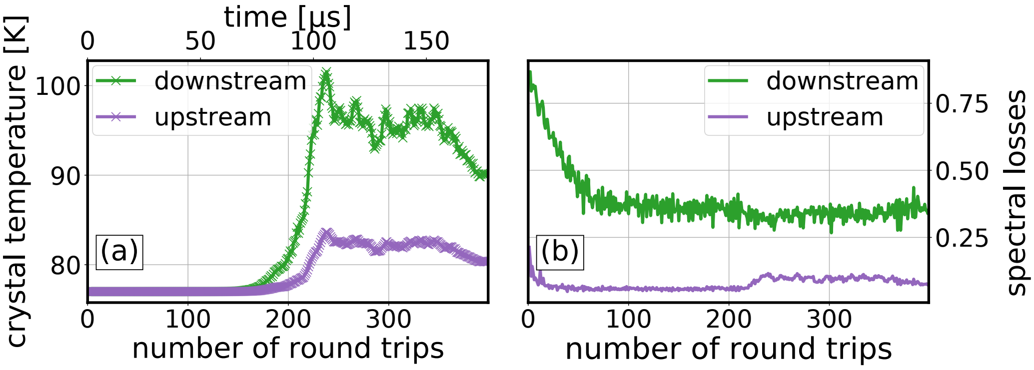

Figure 5.96: (a) shows the central temperature $T(r = 0, s = 0, t)$ evolution of the downstream (green) and upstream (purple) crystal in a fully coupled CBXFEL demonstrator run with $T_{c,\mathrm{base}} = 77\,\mathrm{K}$, t_c =250 µm and weak round trip gain, corresponding to the pulse energy evolution in Figure (5.94). Only the crystals' temperatures at the arrival time of the subsequent X-ray pulse are shown. After heating up to a maximum temperature of $T_{c,M1} \approx 100\,\mathrm{K}$, the crystal cools down again, correlating to the decrease in incident heat load in Figure (5.94). (b) displays the induced evolution of the spectral cutoff losses at the downstream and upstream mirrors.

In regard of the prior paragraphs, it naturally comes to mind that the decrease in pulse energy is caused by an increase in remnant heat in the crystal. However, as is evident from the temperature evolution in Figure (5.96(a)), the crystal temperatures decrease in correspondence to the decrease in heat load on the crystal. Hence, as is confirmed by the stable level of spectral losses in Figure (5.96(b)), the crystal heating cannot account as a sole reason for the decrease in pulse energy.

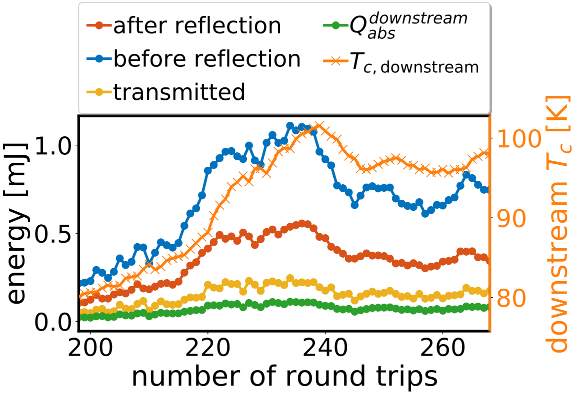

Figure 5.97: Pulse energy, heat load and downstream crystal temperature evolution for $T_{c,\mathrm{base}} = 77\,\mathrm{K}$ at reduced gain zoomed to the (first) round trip of maximum pulse energy.

Yet, near the point of maximum pulse energy the heating does lead to an drop of pulse energy. This can be seen in Figure (5.97), where the pulse energy and temperature evolution is zoomed to the round trips close to the point of maximum pulse energy. After reaching a $Q^{\mathrm{und.}}_{\mathrm{pulse}}$ ≈1 mJ pulse energy level around round trip 220, the CBXFEL demonstrator remains at this level for roughly twenty round trips. During this time the elevated level of impinging heat load, which amounts to $Q_{\mathrm{abs},M1} \approx 100\,\mu\mathrm{J}$, leads to a steady rise in the downstream crystal temperature. After the downstream crystal reaches a temperature of $T_c \approx 100\,\mathrm{K}$ at round trip 239, the induced shift of the reflection curve and the therefore increased spectral losses cause the round trip gain to drop below zero for some round trips. Unlike the drop offs discussed for the 'high' gain cases, the low gain and the, in consequence, approximately linear rise of the crystal temperature and the generally lower level of heat load enable a smooth transition to $\mathcal{G}_{rt} < 0$. With the drop of impinging pulse energy and, hence, heat load the crystal cools down by some degree, until the demonstrator reaches a semi-stable state at a pulse energy of $Q^{\mathrm{und}}_{\mathrm{pulse}}$=0.6(1) mJ and a downstream crystal temperature of $T_c = 96(2)\,\mathrm{K}$. This semi-stable state, which persists until around round trip 350, shows relatively strong fluctuations in the FEL gain, which imprint on the round trip gain (see Figure (5.95)) and, ultimately, on the pulse energies. These strong fluctuations are caused by the jittering of the electron beam properties, especially the electron energy jitter, as was discussed in Paragraph **5.2.2.1** and can be seen from Figure (5.98). In the presented case the impact is especially high for two reasons.

First, unlike the cases ignoring the crystals' thermal response, the round trip gain is, as requested, reaching zero at newly generated pulse energies of $Q^{\mathrm{new}}_{\mathrm{pulse,sat}}$=0.32(6) mJ much before the saturation limit of $Q^{\mathrm{new}}_{\mathrm{pulse,sat}} \approx 3$ mJ dictated by the electron beam properties (2.77). As was often pointed out in the discussion on the impact of the different error sources, after reaching this value, the actual amount of newly generated energy becomes quite robust towards errors. This is due to the gain reduced by the badly matched electron energy in those parts of the electron beam, which are not yet saturated, getting compensated by other fractions, which are being less subjected to oversaturation and, hence, show an increased gain. As this regime is not reached in the present case, the jittering of the longitudinally resolved gain length rather linearly influence the total gain.

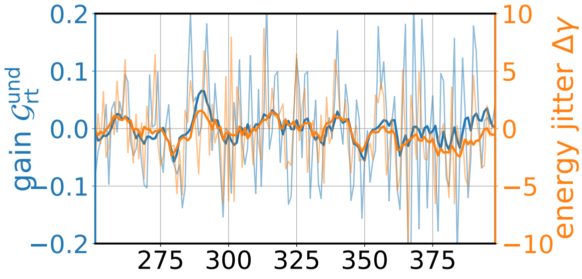

Figure 5.98: Evolution of the round trip gain $\mathcal{G}_{\mathrm{rt}}^{\mathrm{und}}$ after the undulator (blue) and pulse to pulse electron energy shift $\Delta\gamma$ (orange). The semi-transparent curves show the strongly fluctuating pulse to pulse resolved values and the opaque lines rolling averages, averaged over ten subsequent round trips, for better visualization. The curves, especially the rolling averages, clearly show a strong correlation.

The second reason for the stronger impact of the jitter is the deliberately shifted gain curve. For maximized gain, the gain curve in dependence of the energy shift $\Delta\Gamma$ is almost symmetric around $\Delta\Gamma = 0$ (see Figure (2.10)). By tuning the undulator parameter, the curve is shifted and $\Delta\Gamma = 0$ is now on the flank of the gain curve[91]. Therefore, the electron beam energy jitter

---

[91] This assumes that the gain characteristics are not changed by a small change in K_{und}. Then a change in K_{und} corresponds to moving in $\eta \propto K_{\mathrm{und}}^{-2}$.

corresponds to a jittering of the gain curve position. For the maximized gain case, both positive as well as negative shifts of the electron beam energy lead to a small reduction in gain. For the present case, positive energy shift leads to a stronger gain and negative energy shift to a reduced gain. This is apparent from Figure (5.98). Furthermore, it is expressed by a significant, positive *Pearson correlation coefficient* of $\rho_{\mathcal{G},\Delta\gamma} = \frac{\langle(\mathcal{G}-\langle\mathcal{G}\rangle)(\Delta\gamma-\langle\Delta\gamma\rangle)\rangle}{\sigma_{\mathcal{G}}\sigma_{\gamma}} = 0.48$ [92] of the FEL gain $\mathcal{G}_{\mathrm{FEL}}$ to the absolute, shot to shot electron beam energy shift $\Delta\gamma$ for the round trips >250.
After around round trip 350 the pulse energy begins to decrease again to pulse energies $Q^{\mathrm{und}}_{\mathrm{pulse}} \approx$ 300 µJ. It has already been discussed that this does not originate from the crystals' thermal response. In contrary, the drop of heat load causes a cooling of the crystal and, hence, a slight decrease in spectral cut off losses (see Figure (5.96)), which is opposing the decrease in round trip gain. Actually, the decrease in round trip gain also appears to be rooted in the electron beam energy jitter. As is visible in Figure (5.98), after round trip 350 the rolling average of the electron beam energy shift $\Delta\gamma$ is constantly below zero. Following above argumentation, this leads also to a reduction in FEL and round trip gain. While there is no immanent physical reason behind the decrease, it does, however, emphasize the instability of the system and its strong dependency on the electron beam jitter.

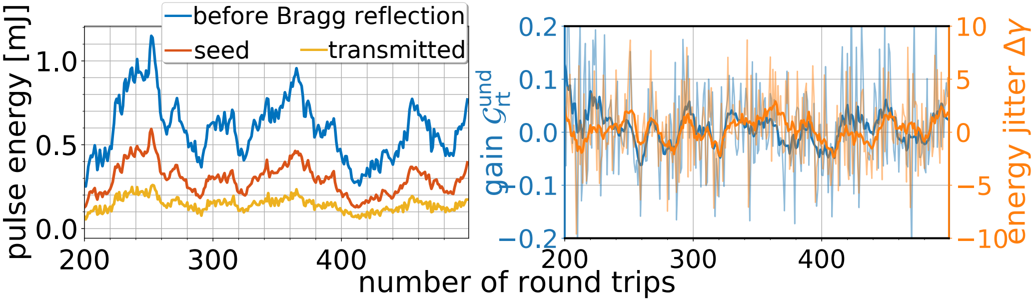

Figure 5.99: Evolution of the pulse energies evolution (left) and of the round trip gain $\mathcal{G}^{\mathrm{und}}_{\mathrm{rt}}$ after the undulator (right, blue) as well as the pulse to pulse electron energy shift $\Delta\gamma$ (right, orange). The semi-transparent curves show the strongly fluctuating pulse to pulse resolved values and the opaque lines rolling averages, averaged over ten subsequent round trips, for better visualization.

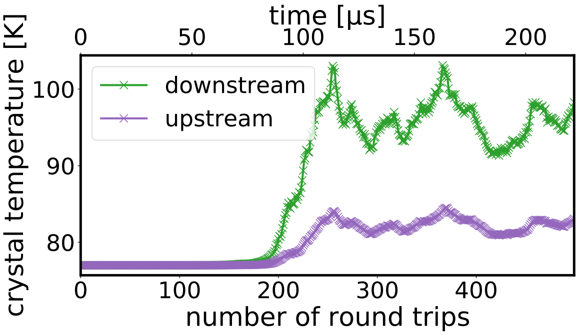

Figure 5.100: Evolution of the central temperature $T(r=0, s=0, t)$ of the downstream (green) and upstream (purple) crystal for a second fully coupled CBXFEL demonstrator run with $T_{c,\mathrm{base}} = 77\,\mathrm{K}$, t_c =250 µm and weak round trip gain. Only the crystals' temperatures at the arrival time of the subsequent X-ray pulse are shown. Especially the downstream crystal shows pronounced temperature maxima at round trips 255 and 367, correlating to maxima in the pulse energy in Figure (5.99(left)).

As displayed in Figure (5.99(left)), especially the strong fluctuations of the pulse energies can

---

[92] The Pearson correlation coefficient takes a value of 1 for a perfectly linear correlation, -1 for perfectly negative linear correlation and 0 for linear relationship. All other values signify partially linear correlation. Non-linear correlation cannot be interpreted by the Pearson correlation coefficient [175, ch. 14.5].

be seen, as confirmed by a second simulation run with the same base parameters, but, following the random nature of the electron beam energy jitter, different distribution of γ versus the round trip number. Following Figure (5.99(right)), for this simulation run one can see a strong correlation between pulse to pulse electron beam energy shift $\Delta\gamma$ and the round trip gain. However, one has to note that different from the prior run displayed in Figure (5.98), the correlation is clearly broken at around round trips 350 to 380, where the gain is dropping in contrast to the in average positive $\Delta\gamma$. Yet, this can be easily explained by the crystal temperature evolution, shown in Figure (5.100), which exhibits pronounced temperatures maxima both at round trips 255 and 367. The herewith related regimes of elevated temperature lead, as already discussed for the temperature peak in the prior run, to an increase in spectral cut off losses and, hence, to a decrease in round trip gain $\mathcal{G}_{\mathrm{rt}}^{\mathrm{und}}$.

Table 11: Main parameters of the X-ray pulses in saturation for a CBXFEL at $E_c = 9.05\,\mathrm{keV}$ including combined error sources and the crystals' thermal response for a deliberately shifted undulator parameter and, in consequence, reduced gain. The errors denote the standard deviation of the shot-to-shot fluctuation in the semi-stable operational state after round trip 250 for a single run. For comparison, the three undulator sections case ignoring the thermal response and without the shifted undulator parameter is shown.

Photon Energy E_{ph} [keV]	9.05			
undulator parameter K_{und}	3.383		3.381 (no heat)	
	before refl.	transmitted	before refl.	transmitted
Pulse Energy Q_{pulse} [mJ]	0.54(8)	0.14(3)	10.9(2)	0.862(34)
Bandwidth $\sigma_{E_{\mathrm{ph}}}{}^{a}$ [meV]	40(2)	66.7(7)	15.2(3)	63.6
Pulse Length $\sigma_t{}^{a}$ [fs]	65(3)	178(11)	128(2)	115(2)
Peak Brilliance $\mathcal{B}$ [^{b}]	$5(1) \times 10^{33}$	$1.2(3) \times 10^{33}$	$5.3(2) \times 10^{35}$	$6.8(6) \times 10^{34}$
coherence time τ [fs]	88(4)	24(1)	190(4)	26(1)
gaussian quality J	9.1(5)	2.1(1)	15.2(3)	2.18(6)

[a] The bandwidth/duration is computed using the mean absolut deviation $\mathcal{D}_{u,\mathrm{MAD}}$ (2.14), which is less sensitive to the wide tails in the spectral distribution. It is then transformed into the more common standard deviation $\sigma_u \approx \sqrt{\frac{\pi}{2}}\mathcal{D}_{E_{\mathrm{ph}},\mathrm{MAD}}$.

[b] #Phot/s/mm^2/mrad^2/0 1%BW

In Table 11, the figures of merit are displayed for the CBXFEL demonstrator including the crystals' thermal response and using a shifted undulator parameter to yield a low gain. The values are averages obtained from the round trips 250 to 399. The round trips 350 to 399 are not specifically accounted for, as the reduced pulse energies are most probably of statistical nature and can therefore enter into the means and standard deviations. Compared to the three undulator case, also shown in Table 11 for comparison, the figures of merit are drastically reduced. Especially for the pulse characteristics directly after the undulator, all values except for the gaussian quality factor J have worsened. This cumulates in a two orders of magnitude decrease in peak brilliance. For the transmitted pulse only the actual pulse energy and the time duration (and time bandwidth product) have worsened. Latter is dominantly due to the increased thickness t_c =250 µm of the crystal compared to the no thermal response case with $t_c = 150\,\mu\mathrm{m}$. The larger thickness causes a higher probability of multiple reflection events and, hence, a larger stretching of the pulse in the vicinity of the total reflection region. The peak brilliance $\mathcal{B}_p^{\mathrm{weak}\mathcal{G}}$ =1.2(3) × 10^{33} #Phot/s/mm^2/mrad^2/0 1% BW of the transmitted pulse is worse than that of a SASE with $\mathcal{B}_p^{\mathrm{SASE}}$ ≈5 × 10^{33} #Phot/s/mm^2/mrad^2/0 1% BW[48]. Furthermore, the shot to shot variations in pulse energy are on the twenty percent level and even higher for the brilliance.

To summarize, by shifting the undulator parameter the FEL gain can be reduced. With this reduced gain, the FEL oscillator saturation case, when the cavity losses and the FEL gain cancel each other, can be reached well before the saturation limit dictated by the electron beam with $Q_{\mathrm{pulse}}^{\mathrm{new}} \approx 3\,\mathrm{mJ}$. In consequence, the heat load does become manageable for the CBXFEL demonstrator and does neither cause the drastic drop off in pulse energy evolution as observed for the maximized gain, low temperature CBXFEL demonstrator nor the fluctuations observed for the room temperature demonstrator. On the other hand, the actual gain becomes very dependent on the electron beam energy jitter, which causes the demonstrator performance to strongly fluctuate in ‘saturation’, with the relative standard deviation of the transmitted beam pulse energy being as high as twenty percent. Besides, the actual peak brilliance of the transmitted beam becomes smaller than that of a SASE FEL. This is, anyhow, tolerable for a proof-of-principle demonstrator experiment as planned. It should be noted, too, that the peak spectral flux is still increased by one order of magnitude compared to SASE. But in comparison to self-seeding, which aims for the same pulse characteristics, it would be inferior.

5.2.3.5 Additional outcoupling: As was discussed in the beginning of the prior paragraph, another way to manipulate the maximum amount of newly generated pulse energy per round trip is to adjust the cavity losses instead of the FEL gain. Ideally, this would be done such that the losses are low for the first round trips, allowing for a fast increase of pulse energy and stability during the *start up regime* and initial *exponential gain regime*,but would be increased shortly before entering the *saturation regime*. Actually, this partially occurs already with the heating of the crystals and the therewith increasing cut off losses with increasing pulse energy. However, referring to the prior paragraphs this is not happening in a linear manner and does not lead to a stable CBXFEL demonstrator. Considering the short microsecond scale time durations required to reach saturation, alternative continuos adjustments of the cavity losses seem infeasible. This is especially true, when regarding the paradigma “*As simple as possible,...*”. Hence, only a static increase of the cavity losses will be considered here.

Ideally, these losses should be spectrally and transversely homogenous, at least in the transverse and spectral bandwidth of the X-ray pulses. The simplest device to acquire such an effect would be to add an (adjustable) number of absorbing layers before the downstream diamond mirror. This, however, has two downsides. First, the absorber material needs to be sufficiently thin to transmit the majority of the radiation, while having to withstand the high amount of heat load.

A possible choice would be diamond, which is tuned away from reflection and, therefore, only transmits and absorbs the impinging radiation. The second problem is that all the absorbed radiation in this scheme is effectively lost, which obviously would be a shame. A more satisfactory approach is to use transmissive gratings or crystal beam splitters as mentioned in Section **2.4** about outcoupling methods. Both are adjustable, to a certain degree, in their outcoupling coefficient and, consequently, loss fraction. Yet, the crystal beam splitters, also being based on thin diamonds and dynamic diffraction, are subject to the same heating problems as the diamond mirrors. But it does aid that they can be aligned at a higher grazing angle, reducing the impact of the heat load as was discussed before. Anyways, diamond gratings appear to be the better choice, as they are not based on the internal crystal structure and are, therefore, less sensible to lattice expansion. However, all three possibilities add complexity to the system with the absorbing layers being the simplest, but also the least desirable option.

In the following, only an idealized outcoupling device will be accounted for. This device is freely adjustable in the static outcoupling coefficient $\mathcal{L}_{out}$ and does not have any other impact on the radiation pulse but dividing it into an fraction staying in the cavity and an outcoupled fraction. The outcoupling coefficient is set such that the demonstrator saturates at a specified value of newly generated pulse energy $Q^{\text{new}}_{\text{pulse},s}$. In order to do so, one needs to know both the evolution of the round trip gain $\mathcal{G}_{rt}$ and either the cavity quality $\mathcal{Q}_{\text{cav}}$ (without additional outcoupling) or the FEL gain $\mathcal{G}_{FEL}$ (both can be deduced from the other in knowledge of $\mathcal{G}_{rt}$). By requesting that

$$\begin{aligned} \mathcal{G}'_{rt,s} &\doteq 0 \\ \leftrightarrow \mathcal{L}_{\text{out},s} &= \frac{\mathcal{G}_{\text{FEL},s}}{\mathcal{G}_{\text{FEL},s}+1}, \\ \text{for} \quad \mathcal{G}_{\text{FEL,s}} Q^{\text{seed}}_{\text{pulse},s} &= Q^{\text{new}}_{\text{pulse},s}, \end{aligned}$$

one can determine the necessary required outcoupling losses $\mathcal{L}_{\text{out}}$. In above equation, $\mathcal{G}'_{rt,s} = \mathcal{G}_{rt,s}\left(1-\mathcal{L}_{\text{out}}\right)-\mathcal{L}_{\text{out}}$ refers to the round trip gain with additional losses in saturation and $\mathcal{G}_{rt,s}$ to the corresponding round trip gain without additional losses at the same round trip. It has further been used that $\mathcal{Q}_{i+1} = \left(1-\mathcal{L}_{i+1}\right)\mathcal{Q}'_i$, where $\mathcal{Q}_{i+1}$ refers to the cavity quality with one additional element with loss factor $\mathcal{L}_{i+1}$ added.

For the following study the three undulator sections CBXFEL demonstrator with maximized gain and including the combined error sources, as discussed in Paragraph **5.2.2.9**, was adapted. The additional outcoupling losses were set as $\mathcal{L}_{\text{out}}$=15 %, which would yield an amount $Q^{\text{new}}_{\text{pulse},s} \approx$ 800 µJ of newly generated radiation in saturation, based on the cavity losses and FEL gain ignoring the crystals' thermal response as shown in Figure (5.73). This is also sketched in Figure (5.101). Taking latter into account, as will be seen below, leads to a further reduction of $Q^{\text{new}}_{\text{pulse},s}$ due to the increase in spectral cut off losses.

In Figure (5.102) the pulse energy evolution is displayed for the CBXFEL demonstrator with three undulator sections and additional outcoupling factor $\mathcal{L}_{\text{out}}$=15 %. The simulations were

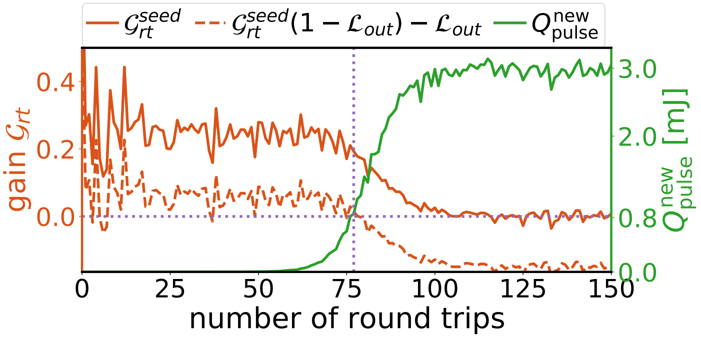

Figure 5.101: Round trip gain of one specific run of the three undulator sections case including error sources discussed in Paragraph **5.2.2.9** with additional losses of $\mathcal{L}_{\text{out}}$=15 % (red dashed) and without additional losses (red solid). The gain evolution with additional losses is simply calculated via $\mathcal{G}'_{rt} = \mathcal{G}_{rt}(1-\mathcal{L}_{out}) - \mathcal{L}_{\text{out}}$ from the gain $\mathcal{G}_{rt}$ without additional losses. Also the newly generated energy evolution for the case without additional losses is shown in green. The evolution of $\mathcal{G}'_{rt}$ is highly artificial, as it neglects that the pulse energy evolution is slower and, hence, the decrease of the gain in the *saturation regime* begins at a later round trip. The purple dashed vertical line shows where the (artifical) round trip gain with additional losses crosses zero. The value of $Q_{\text{pulse}}^{\text{new}} = 0.81\,\text{mJ}$ at this point is approximately equal to the saturated $Q_{\text{pulse},s}^{\text{new}}$ for the case including $\mathcal{L}_{out}$.

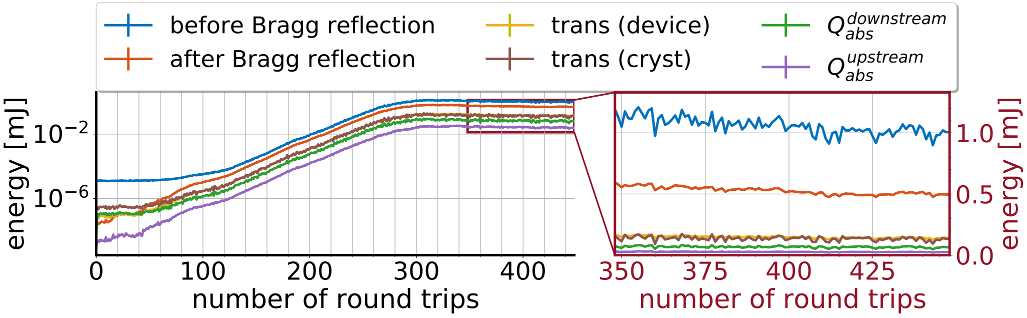

Figure 5.102: The evolution of the pulse energy and the integrated absorbed heat load at the downstream and upstream mirror of the three undulator sections CBXFEL demonstrator including the influence of heat load at a crystal base temperature of $T_{c,\text{base}} = 77\,\text{K}$ and t_c =250 µm with an additional ‘device’ outcoupling factor $\mathcal{L}_{\text{out}}$=15 % before the downstream mirror. It is assumed that the additional outcoupling can be used and is labeled as ‘trans (device)’ (orange curve) in the above plot. Also, the transmission through the crystal still exists and is named ‘trans (cryst)’ (brown curve). While the maximum pulse energy is strongly reduced and the time to saturation about doubled compared to the cases without additional outcoupling, the CBXFEL demonstrator remains stable over 450 round trips.

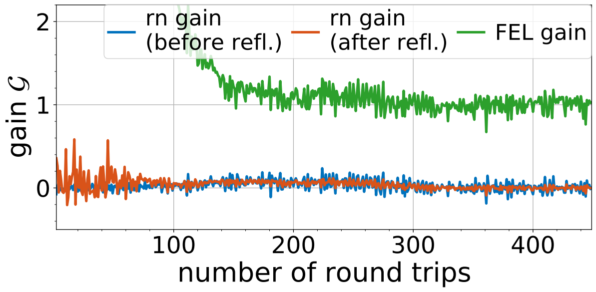

Figure 5.103: Round trip gain Eq. (5.1) directly after the undulator (blue curve), after traversing the cavity (red curve) and integrated FEL gain Eq. (5.2) for the CBXFEL demonstrator with additional outcoupling of $\mathcal{L}_{\text{out}}$=15 % before the downstream mirror, including the crystals’ thermal response at $T_{c,\text{base}}$=77 K.

further based on two t_c =250 µm diamond crystals at $T_{c,\text{base}}$ =77 K base temperature. As desired, the maximum pulse energy is strongly reduced compared to the $T_{c,\text{base}}$ =77 K case without additional outcoupling displayed in Figure (5.93). This is due to the deliberately reduced round trip gain, as shown in Figure (5.103), caused by the reduced cavity quality $\mathcal{Q}_{\text{cav}}$, whereas the integrated FEL gain $\mathcal{G}_{\text{FEL}}$ remains unchanged compared to the no-additional outcoupling case. Most importantly, the round trip gain and, hence, the pulse energies remain comparably stable. Also, in comparison to the weak gain case discussed in the last Paragraph **5.2.3.4**, the fluctuations in pulse energy are much less severe.

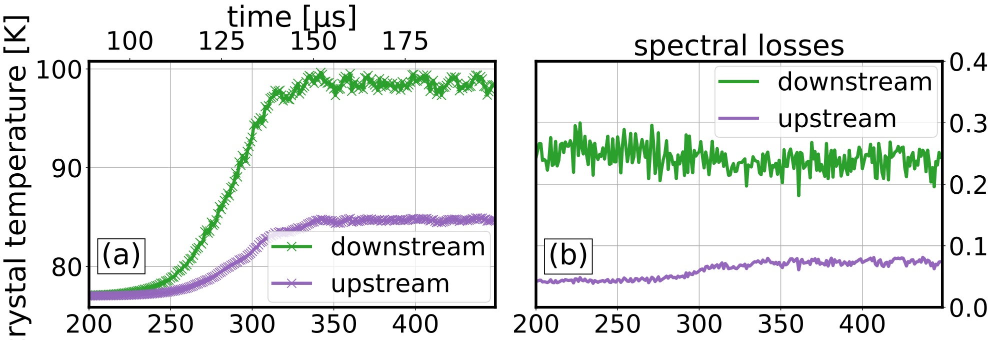

Figure 5.104: (a) shows the central temperature $T(r = 0, s = 0, t)$ evolution of the downstream (red) and upstream (green) crystal in a fully coupled CBXFEL demonstrator run with $T_{c,\text{base}} = 77\,\text{K}$, t_c =250 µm and with additional outcoupling $\mathcal{L}_{\text{out}}$=15 %, corresponding to the pulse energy evolution in Figure (5.102). Only the crystals' temperatures at the arrival time of the subsequent X-ray pulse are shown. (b) displays the induced evolution of the spectral cutoff losses at the downstream and upstream mirrors. The temperature and, hence, the crystal cut off losses remain stable after reaching a maximum of T_c ≈99 K.

As in the case of the weak gain, after reaching a maximum in pulse energy of $Q_{\text{pulse}}^{\text{max}}$ =1.35 mJ at round trip 313, the pulse energy decreases to a stable value of $Q_{\text{pulse},s}^{\text{und}}$ =1.05(6) mJ. This is due to the remnant temperature rise induced by the corresponding heat load, which further rises the temperature from $T_c = 97.2\,\text{K}$ at round trip 313 to $T_c = 99.6\,\text{K}$ at round trip 342. This is shown in Figure (5.104(a)). As this temperature rise also leads to an increase in the spectral cut-off losses, as displayed in Figure (5.104(b)), the round trip gain falls below 0 and the pulse energy decreases. As the decrease in pulse energy corresponds to a decrease in heat load, the temperature does not rise further and stabilizes at a value of $\bar{T}_{c,sat} = 98.5(5)\,\text{K}$. This stability in temperature also comes with a stabilization in round trip gain, aside the influence of the electron beam jitter, and, therefore, in pulse energy. At this stable state, the amount of newly generated radiation is $Q_{\text{pulse,s}}^{\text{new}}$ =0.52(5) mJ. This value is well below $Q_{\text{pulse},s}^{\text{new}}$ ≈800 µJ discussed above and shown in Figure (5.101) due to the increased spectral cut off losses.

As was discussed above, it is assumed that the radiation outcoupled through the artificial 'device', be it grating or crystal beam splitter, can be used as transmitted radiation for analysis (or potentially for experiments). At the same time, the radiation transmitted through the downstream crystal obviously also is present. It is further supposed that both radiation pulses can be separated and used individually. The longitudinal and transverse distributions of the saturated radiation pulse outcoupled through the device are displayed in Figure (5.105), and in Figure (5.106) that of the saturated pulse transmitted through the downstream crystal. Both pulses show strongly deviating distributions.

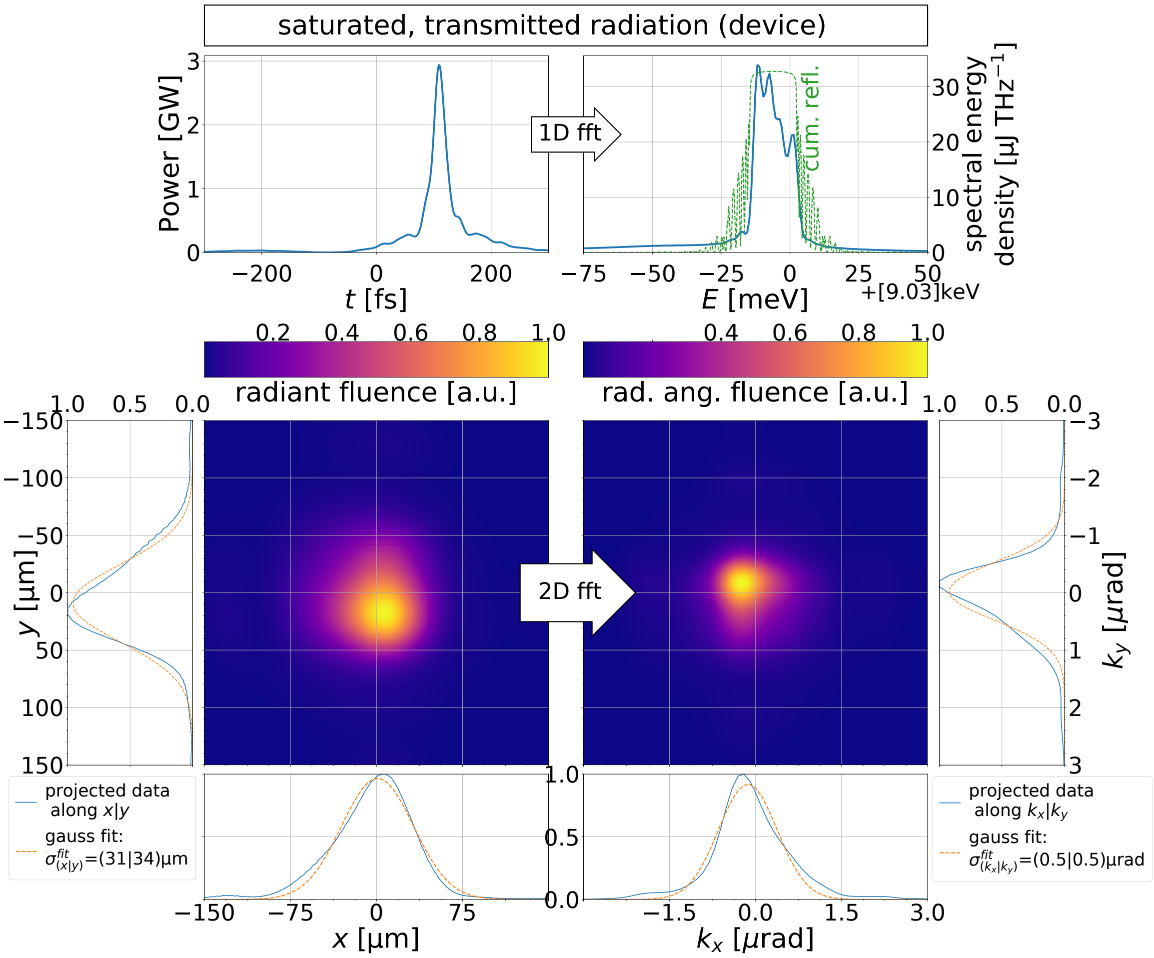

Figure 5.105: Longitudinal and transverse representations of the radiation pulse outcoupled through the artificial 'device' with $\mathcal{L}_{out}$ =15 % in saturation. The distributions were averaged over the round trips 360 to 450.

The pulse outcoupled through the 'device' is basically identical to that circulating in the cavity (before reflection), but with only 15 % of the intensity. As such it has a comparably low bandwidth of $\sigma_E^{(\mathrm{tr,dev})} = 30(2)\,\mathrm{meV}$, on the order of the reflection bandwidth. The bandwidth is nearly twice as big as that of the three undulator sections case ignoring the thermal response and without additional outcoupling, which amounts to $\sigma_E^{(3\ \mathrm{und.})} = 15.2(3)\,\mathrm{meV}$. This is due to the high fraction, about 50 %, of newly generated radiation, having a wider spectral distribution, contributing to the outcoupled pulse. Also, the spectral narrowing of the newly generated radiation, effectively caused by the oversaturation process, is not present here. On the other hand, the high fraction of newly generated radiation leads to a much reduced pulse duration of $\sigma_t^{(\mathrm{tr,dev})}$=67(2) fs compared to $\sigma_t^{(3\ \mathrm{und.})}$=128(2) fs. Time- and spectral domain combined have a rather good time-bandwidth product of $\sigma_f \sigma_t = 0.19(1)$, which is about trice the minimum value of $^1/_{4\pi}$. Likewise, the temporal coherence is with $\tau_{\mathrm{coh}}^{(\mathrm{tr,dev})}$ =120(7) fs quite good. However, the transverse distribution is heavily affected by the figure errors of the upstream and downstream mirror assemblies, as was discussed in Paragraph **5.2.2.6**. As such, the gaussian quality factor $J = 9.2(7)$ shows a strong deviation from an ideal gaussian. It is better than that of the three undulator sections case ignoring heat load and without additional outcoupling, which is, again,

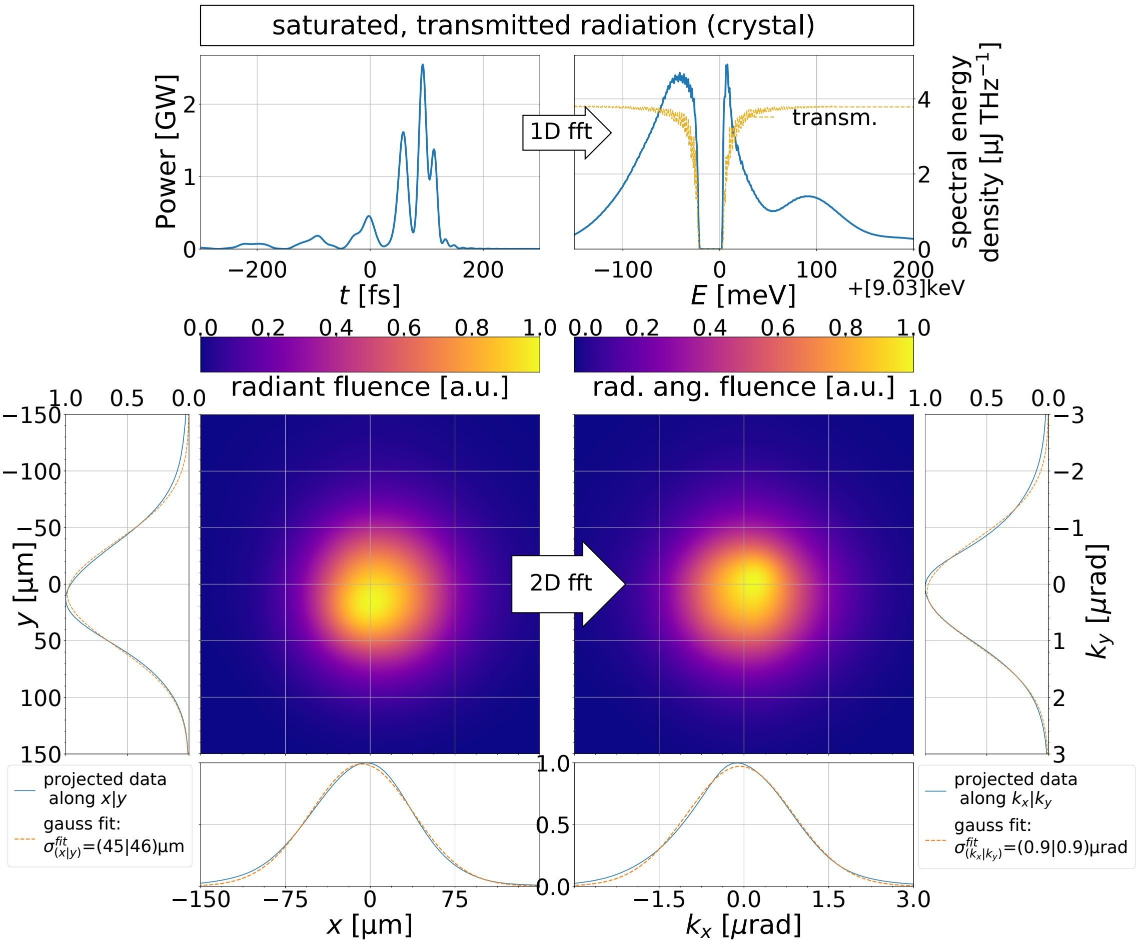

Figure 5.106: Longitudinal and transverse representations of the radiation pulse transmitted through the downstream crystal in saturation. The distributions were averaged over the round trips 360 to 450.

due to the high fraction of newly generated radiation. Latter is 'cleaned' by the FEL process and its gain guiding.

In contrast to the 'device' outcoupled radiation, the transverse distribution of the pulse transmitted through the crystal is rather close to a perfect gaussian, with a quality factor of $J = 1.94(15)$. This is due to it being fully based on the 'cleansed' newly generated radiation. But then, the longitudinal distribution is, as usually for this kind of outcoupling, much inferior. The spectral bandwidth is with $\sigma_E^{(\mathrm{tr,cryst})} = 83(2)\,\mathrm{meV}$ nearly trice as wide. Additionally, also the time duration is with $\sigma_t^{(\mathrm{tr,cryst})}$=162(10) fs much longer. Both together yield an increased time-bandwidth product of $\sigma_f\sigma_t = 3.3(1)$, which is also reflected in the poorer longitudinal coherence $\tau_{\mathrm{coh(tr,cryst)}}$ =25 fs.

The above discussed values are also listed in Table 12. In comparison, it is evident that the pulse outcoupled via the 'device' is much closer to the promise of a CBXFEL to provide longitudinally coherent radiation pulses. But, due to the wavefront distortions introduced by the mirrors' figure errors, the transverse properties are worse than a regular SASE FEL. This also the reason why the brilliance $\mathcal{B}_p^{\mathrm{tr,dev}}$ =1.9(2) × 10^{33} #Phot/s/mm^2/mrad^2/0 1% BW is only slightly better than $\mathcal{B}_p^{\text{tr,cryst}}$ =1.7(4) × 10^{33} #Phot/s/mm^2/mrad^2/0 1% BW of the radiation transmitted through the downstream crystal. It should be noted, however, that the brilliance of the pulse outcoupled through the 'device' can be further improved by cleansing the transverse distribution by propagation through the long X-ray beamline to the experiments, where the spoiled parts of the distribution are naturally separated by means of divergence. In comparison to the properties of the CBXFEL demonstrator with three undulator sections ignoring the crystals' thermal response and without additional outcoupling, which are also listed in Table 12, both means of transmission remain much inferior.

Table 12: Main parameters of the X-ray pulses in saturation for a CBXFEL at $E_c = 9.05\,\text{keV}$ including combined error sources and the crystals' thermal response with an additionally induced outcoupling factor $\mathcal{L}_{\text{out}}$ =15 %. The errors denote the standard deviation of the shot-to-shot fluctuation in the semi-stable operational state after round trip 360 for a single run. For comparison the three undulator sections case ignoring the thermal response and without the shifted undulator parameter is shown.

Ph. Energy E_{ph} [keV]	9.05				
	$\mathcal{L}_{\text{out}}$ =15 %			$\mathcal{L}_{\text{out}}$ =0 %, no heat	
	before refl.	trans (dev.)	trans (cryst)	before refl.	trans (cryst)
Pulse Energy Q_{pulse} [mJ]	1.05(6)	0.16(1)	0.15(2)	10.9(2)	0.862(34)
Bandwidth $\sigma_{E_{\text{ph}}}$[a] [meV]	30(2)	30(2)	83(2)	15.2(3)	63.6
Pulse Length σ_t[a] [fs]	67(2)	67(2)	162(10)	128(2)	115(2)
Peak Brilliance $\mathcal{B}$ [[b]]	1.2(2) × 10^{34}	1.9(2) × 10^{33}	1.7(4) × 10^{33}	5.3(2) × 10^{35}	6.8(6) × 10^{34}
coherence time τ [fs]	120(7)	120(7)	24.8(7)	190(4)	26(1)
gaussian quality J	9.2(6)	9.2(6)	1.9(2)	15.2(3)	2.18(6)

[a] The bandwidth/duration is computed using the mean absolut deviation $\mathcal{D}_{u,\text{MAD}}$ (2.14), which is less sensitive to the wide tails in the spectral distribution. It is then transformed into the more common standard deviation $\sigma_u \approx \sqrt{\frac{\pi}{2}}\mathcal{D}_{E_{\text{ph}},\text{MAD}}$.

[b] #Phot/s/mm^2/mrad^2/0 1%BW

In summary, it has been shown that the amount of pulse energy in saturation can be tuned by adding an additional loss factor. Setting it to $\mathcal{L}_{\text{add.}}$=15 %, the CBXFEL demonstrator using three undulator sections and at a base temperature of $T_{c,\text{base}} = 77\,\text{K}$, the demonstrator can be stabilized. Yet, the pulse energies in saturation are strongly reduced and it takes about trice the number of round trips to reach saturation. Hence, also the pulse transmitted through the downstream crystal shows inferior properties compared to the case without the additional loss factor and ignoring the crystals' thermal response. While the pulse still shows a better longitudinal coherence and peak spectral flux than a SASE, due to the strongly reduced pulse energies $\mathcal{Q}_{\text{pulse,s}}^{\text{tr,cryst}}$ =0.15(2) mJ the peak brilliance is inferior.

However, it would principally be possible to introduce the loss factor by means of a spectrally and transversely homogenous outcoupling device, for example a crystal beam splitter or a transmissive grating. Then, this outcoupled beam can also be used for analysis and, potentially, experiments. This obviously come with the cost of adding additional complexity to the cavity

X-ray optics, especially if this outcoupled beam shall be separated in space from the beam transmitted through the downstream crystal. This outcoupled beam carries the same characteristics as the radiation pulse in the cavity before reflection, but with only $\mathcal{L}_{\mathrm{out}} = \mathcal{L}_{\mathrm{add.}}$=15 % of the intensity. As such, it has a longitudinally very pure distribution with a high degree of coherence and is in that means clearly advantageous to a SASE. Also, the shot-to-shot fluctuations remain on the single percentage level for the intensity and about ten percent for the brilliance. While this is not outstanding, it is clearly better then what was shown for the reduced gain CBXFEL in the last paragraph and also much better than a monochromatized SASE pulse. But, as this outcoupled beam also carries the wavefront distortions introduced by the mirrors' figure errors, which are only partially cleaned by the FEL process, the tranverse distributions are significantly deviating from a perfect gaussian. This also causes a peak brilliance, which is still inferior to a SASE. In regard of the proof-of-principle nature of the CBXFEL demonstrator experiment, it has, nonetheless, the big advantage of following the identical transverse and longitudinal distributions as the radiation circulating in the cavity. Therefore, analyzing this outcoupled radiation gives direct access to information on the radiation inside the actual X-ray cavity, whereas the beam transmitted through the crystal is strongly affected by the spectral transmission curve. This promises to be useful for the analysis of the experiment. However, one has to note that the bandwidth of the circulating and outcoupled radiation is on the same order as the bandwidth of the single crystal monochromators at the European XFEL [220, 221] and well below the resolution of the HIREX spectrometer [56]. Hence, it will not be possible to fully assess the spectral information of the outcoupled radiation. On the other hand, it should be possible to analyze the transverse distributions using the FEL imagers [222].

In conclusion, adding an outcoupling device with an outcoupling coefficient $\mathcal{L}_{\mathrm{out}}$ on the ten percent level would enhance the CBXFEL demonstrator properties. Not only does it lead to stabilization, it also brings a lot of information directly from the X-ray cavity to the diagnostics (and potentially experiments) downstream. Nonetheless, the significant technical demands to realize this kind of outcoupling are only hardly in the scope of *As simple as possible, as complicated as necessary*. This is farther complicated by the need to match the outcoupling coefficient to the actual cavity losses and FEL gain, which are not known a priori. This demands either for the outcoupling factor to be tunable over some percentage, or for the outcoupling device to be added at a later stage of the experiment, when this data was already measured. It remains subject to further discussion, if the benefits of this additional outcoupling, which are mainly in the increased amount of information carried from the cavity to the already existing diagnostics, are worth the additional complexity.

5.2.3.6 Passively Cavity Dumped System: It has been shown in Paragraphs **5.2.3.2** and **5.2.3.3** that when the pulse energy abruptly drops off, a significant amount of pulse energy is transmitted. As visible from Figures (5.85) and (5.93), this outcoupling occurs at a, more or less, stable rate. As such, it resembles a classical cavity dumped laser oscillator, as frequently used for low repetition rate, high power optical lasers [52, ch. 9.5] and as shortly presented in

Section **2.4** in the framework of CBXFELs. The cavity dumping is often also termed as 'Q-switch' [77], due to it also being based on a rapid switch of the cavity quality factor. Yet, the term 'Q-switch' is usually reserved for a process in the field of optical laser physics, where an initially low cavity quality Q, which allows the laser medium to build up strong inversion, is suddenly increased, which causes an intense stimulated emission [52, ch. 9.5.1]. In the following, the term *cavity dumped* will be continued to be used for differentiation. A big difference to the usually actively controlled Q-switches or cavity dumps is that, in the presented case, the switch is passively driven by the strongly coupled system itself. As such, there is no control over the amount of stabilization occurring before the outcoupling. Here, the properties and reproducibility of these comparably intense, outcoupled pulses shall be studied. Unlike the prior cases, four instead of three undulator sections will be considered. This provides a much higher round trip gain and, hence, less number of pulses between the drop-offs, which in consequence yields a higher rate of 'cavity-dumped' pulses.

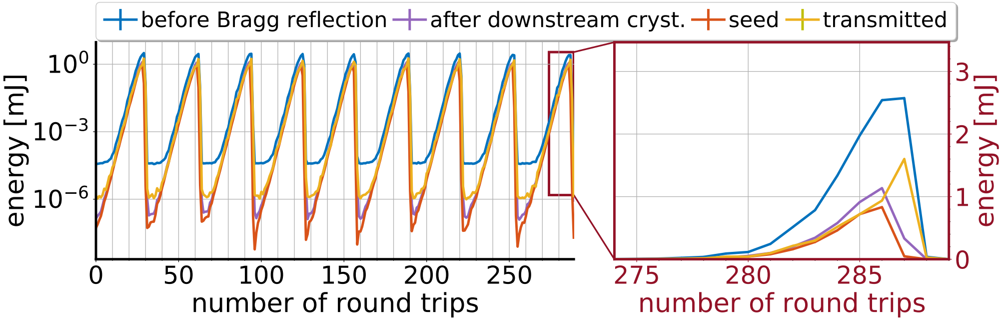

Figure 5.107: Pulse energy evolution for a CBXFEL demonstrator using four undulator sections under the influence of the crystals' thermal response for $T_{c,\text{base}}$ =40 K and t_c =250 µm. Besides the pulse energies $Q^{\text{und}}_{\text{pulse}}$ after the undulator, after traversing the cavity as seeding radiation $Q^{\text{seed}}_{\text{pulse}}$ and of the transmitted pulse $Q^{\text{tr}}_{\text{pulse}}$, also the pulse energy $Q^{\text{refl,M1}}_{\text{pulse}}$ after reflection at the downstream mirror is shown. As in the case of the three undulator sections, the pulse energies show a sharp drop-off after reaching the maximum. At these round trips, a considerable fraction of pulse energy is transmitted and only a smaller fraction is reflected. Due to the missing spectral overlap with the upstream crystal, this small reflected fraction is then completely transmitted. The periodicity of the drop-offs is rather stable, ranging from 30 to 34 round trips, with a mean of 32 round trips.

Figure (5.107) shows the pulse energy evolution for a low crystal base temperature of $T_c = 40\,\text{K}$ and crystal thickness t_c =250 µm. The curves strongly resemble that of the three undulator sections case displayed in Figure (5.93), but, as expected, with a smaller period between the individual peaks. At the round trip at which the reflected fraction falls to zero, the incoming radiation pulse is mostly divided into a transmitted and an absorbed fraction, with latter amounting to $\mathcal{A}_{\text{abs}}$ ≈25 %. Also, as shown with the purple curve, a, sometimes not so small, fraction of the pulse energy is still being reflected at the downstream mirror, limiting the total amount of transmitted pulse energy (and also having an influence on the spectrum of the transmitted pulse). Due to the missing spectral overlap with the upstream crystal reflection curve, this fraction is then completely transmitted through the upstream crystal. As this reflected fraction stores up to $Q^{\text{refl,M1}}_{\text{pulse}}$ =800 µJ, this need to be taken into account to prevent radiation damage to the upstream components. The periodicity of the peaks in the transmitted energy are rather stable, ranging from 31 to 34 round trips. The first peak is reached a little bit faster, after 30 round trips, as for the later peaks, the crystal needs one to two round trips after reaching the maximum to cool down to a temperature which allows effective seeding.

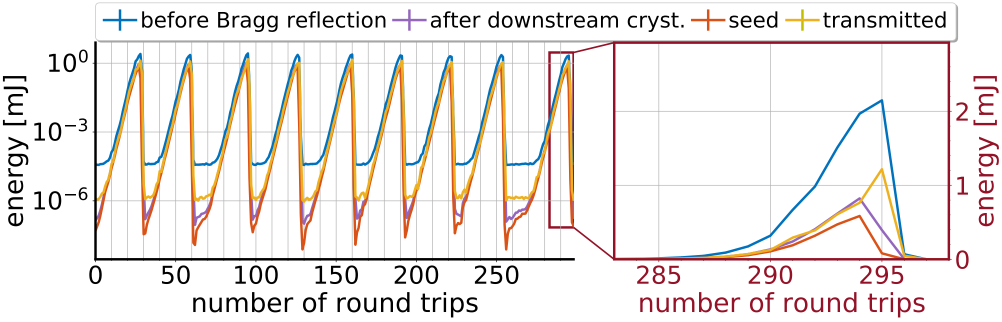

Figure 5.108: Pulse energy evolution for a CBXFEL demonstrator using four undulator sections under the influence of the crystals' thermal response for $T_{c,\text{base}}$ =77 K and t_c =250 µm. Besides the pulse energies $Q_{\text{pulse}}^{\text{und}}$ after the undulator, after traversing the cavity as seeding radiation $Q_{\text{pulse}}^{\text{seed}}$ and of the transmitted pulse $Q_{\text{pulse}}^{\text{tr}}$, also the pulse energy $Q_{\text{pulse}}^{\text{refl,M1}}$ after reflection at the downstream mirror is shown. As in the case of the three undulator sections, the pulse energies show a sharp drop-off after reaching the maximum. At these round trips a considerable fraction of pulse energy is transmitted and only a smaller fraction is reflected. Due to the missing spectral overlap with the upstream crystal, this small reflected fraction is then completely transmitted through the upstream crystal. The periodicity of the drop-offs is less stable than for the $T_{c,\text{base}}$ =40 K case shown in Figure (5.107), ranging from 29 to 41 round trips, with a mean of 33 round trips.

Figure (5.108) shows the energy evolution for a technically more feasible base temperature of $T_{c,\text{base}}$ =77 K. It strongly resembles that of the $T_{c,\text{base}}$ =40 K case in Figure (5.107), with the difference of slightly smaller pulse energies, caused by the poorer thermal diffusion efficiency, as was discussed in Paragraphs **5.2.3.2** and **5.2.3.3**. The difference is a little bit smaller compared to the three undulator sections case, due to the higher round trip gain, which leads to the cut off being reached at about the same number of round trips. Actually, the range of the peak periods is broader, reaching from 29 to 41 round trips, with a mean of 33 round trips. This is both due to the crystal needing more time to cool down after reaching the maximum, and due to statistical fluctuations independent of the base temperature.

In Figure (5.109) some peak resolved figures of merit for these 'cavity dumped' pulses are displayed. One sees that, indeed, the average transmitted pulse energy is with $Q_{\text{pulse}}^{\text{CD,40K}}$=1.6(3) mJ for the $T_{c,\text{base}}$ =40 K case roughly 1.3 times greater than $Q_{\text{pulse}}^{\text{CD,77K}}$=1.25(25) mJ for $T_{c,\text{base}}$ =77 K[93]. Both temperature cases show about a 20 % total fluctuation in the total pulse energy. This range of fluctuation certainly is not small, especially considering the promise of the CBXFEL to provide very stable output. Yet, it does appear tolerable for a proof of principle experiment. Also, the bandwidth of the transmitted 'cavity-switched' pulses shows strong fluctuation over about 40 %. However, these fluctuations are very small compared to that of the gaussian quality fac-

---

[93] Due to the lack of sufficient statistics, the maximum deviation of all peak values compared to the respective mean is taken as error.

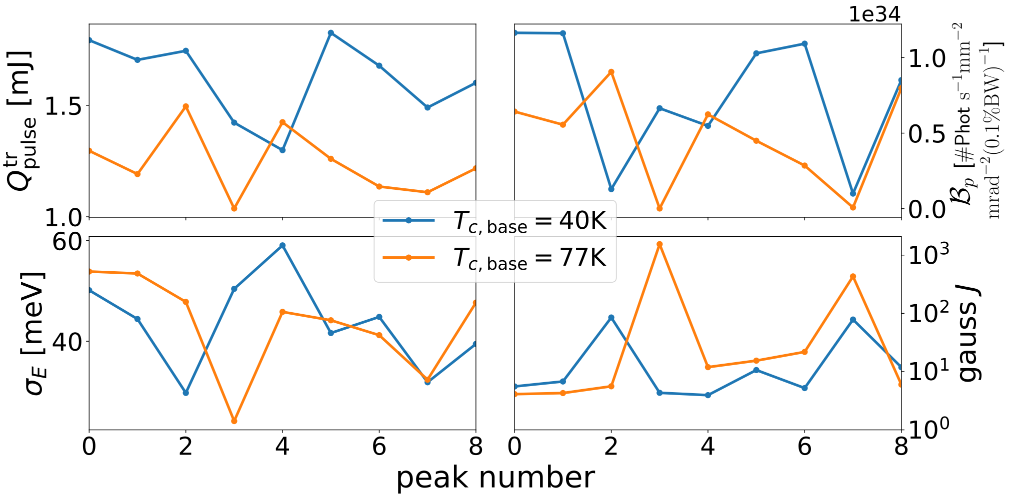

Figure 5.109: Peak resolved properties of the ‘cavity dumped’ radiation pulses for $T_{c,\mathrm{base}}$ =40 K and 77 K. The pulse energies $Q^{\mathrm{CD}}_{\mathrm{pulse}}$ (upper left), peak brilliance $\mathcal{B}^{\mathrm{CD}}_p$ (upper right), bandwidth σ^{CD}_E (lower left) and gaussian quality factor J^{CD} (lower right) are displayed, latter in logarithmic scale. While the pulse energies and the bandwidth only show moderate fluctuations, the brilliance and gaussian quality factor differ by orders of magnitude from peak to peak, especially for the $T_{c,\mathrm{base}}$ =77 K case.

tor J, which differs over multiple orders of magnitude, especially for the $T_{c,\mathrm{base}}$ =77 K case. In regard of the dependence of the peak brilliance $\mathcal{B}_p \tilde{\propto} J^{-1}$ on J, the brilliance fluctuates likewise. While the ‘good’ pulses have a gaussian quality as low as $J^{\mathrm{CD}} \approx 4$, which is caused by the cleansing of the seeding radiation by the strong gain, the ‘bad’ pulses reach up to $J^{\mathrm{CD,40K}} \approx 80$ for $T_{c,\mathrm{base}}$ =40 K or even $J^{\mathrm{CD,77K}} \approx 1500$ for $T_{c,\mathrm{base}}$ =77 K. These distortions are not caused by a bad seed, as is evident from the gaussian quality of the pulse before transmission having a rather constant $J^{\mathrm{und}} = 5.0(3)$. Hence, one can deduce that the distortions are caused by the transmission itself.

The Figures (5.110) and (5.111) display the longitudinal and transverse distributions of one exemplary ‘good’ and one exemplary ‘bad’ transmitted pulse, referring to the peaks zero and three at $T_{c,\mathrm{base}} = 77$ K from Figure (5.109). Both pulses strongly deviate from each other, both in longitudinal and transverse domain. For the ‘good’ pulse in Figure (5.110), which is at a crystal peak temperature of $T_{c,\mathrm{max}}$≈116 K, the reflectivity curve (or the hole in the transmissivity) is close to the spectral peak. For the ‘bad’ pulse in Figure (5.111), which is at a much higher crystal peak temperature of $T_{c,\mathrm{max}}$≈163 K due to a more strongly absorbed prior pulse, the center of the reflectivity curve is shifted quite far away from the spectral peak. Also, the transmission and reflection curves are dependent on the transverse position, which will be important in the later discussion. For the ‘good’ pulse, the vicinity to the edges of the reflection curve introduces fluctuations in the time-domain profile, which are also apparent in a comparably poor time-bandwidth product of $\sigma_f \sigma_t \approx 3.4$, and likewise reduced longitudinal coherence $\tau^{\mathrm{p0,77K}}_{\mathrm{coh}}$ ≈65 fs at $\sigma^{\mathrm{p0,77K}}_t \approx 189$ fs total duration. While these values are worse than the properties of the circulating pulse for the cases ignoring the crystals’ thermal response in Table 8, they are better than the ones of the (stabily) transmitted pulses. For the ‘bad’ pulse, the time-domain profile appears much smoother, but is also strongly stretched by the crystal transmission to $\sigma^{\mathrm{p3,77K}}_t \approx 500$ fs,

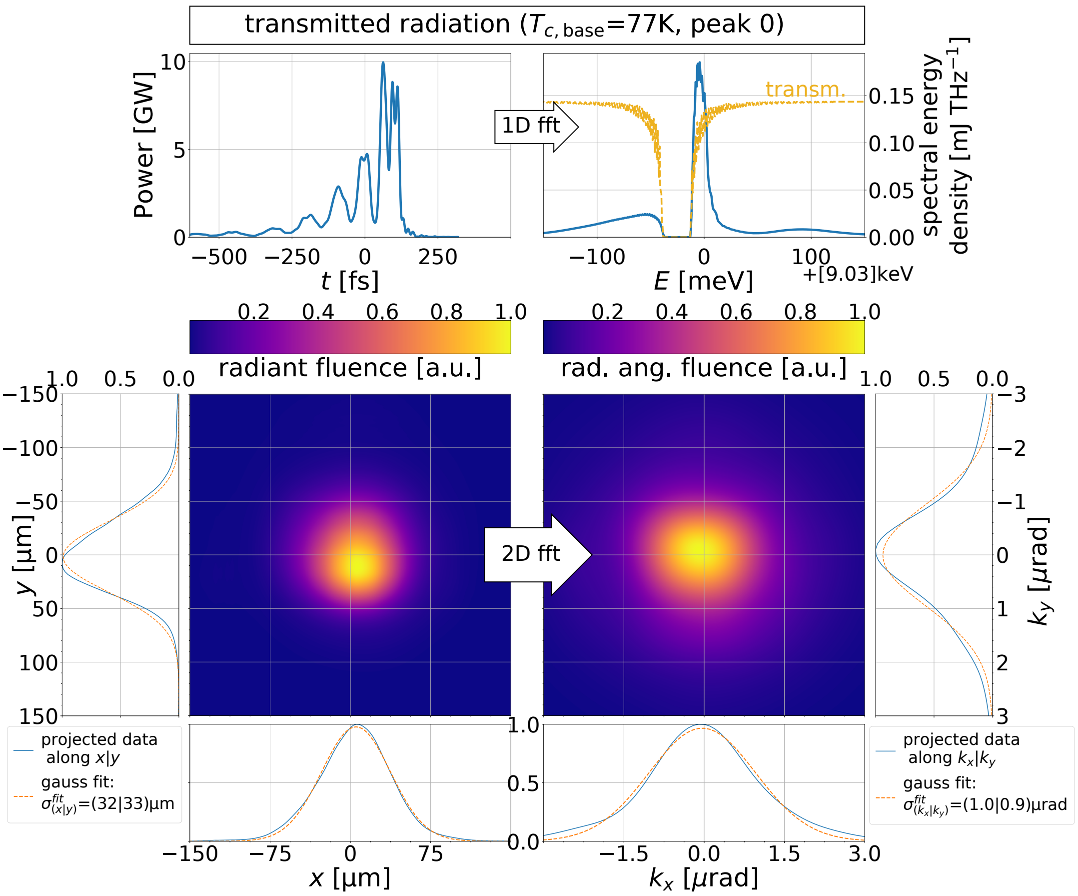

Figure 5.110: Longitudinal and transverse representations of a 'good' transmitted pulse, corresponding to peak 0 at $T_{c,\mathrm{base}}$ =77 K in Figure (5.109). Due to the thermally induced spectral shift of the transmission curve (orange), the transmitted spectrum still exhibits the main spectral peak of the incident radiation. Due to the vicinity to the reflection curve edge, the time-domain power profile shows the multi-peak structure as usually observed for the crystal transmission. The transverse distributions are approximately gaussian, corresponding to $J^{\mathrm{p0,77K}}$ ≈4.1.

resulting in an even poorer time-bandwith product of $\sigma_f \sigma_t \approx 7.5$ and an in relation to the pulse length worse temporal coherence of $\tau_{\mathrm{coh}}^{\mathrm{p0,77K}}$ ≈120 fs[94].

The most pronounced difference between the two pulses is in the angular-space representation. While the 'good' pulse exhibits a mostly gaussian distribution, the 'bad' pulse is strongly distorted and displays interference patterns[95]. It suggests itself that this specific form does not originate from physical reasons, but rather from the numerical treatment. Actually, it appears that the angular-space distribution in Figure (5.111) is strongly twisted by fourier transform aliasing effects (see Paragraph **4.2.3.1**), which occur due to a folding of k-space components outside the sampling bandwidth back into the computational domain, therefore leading to overlap and artificial interference of physically independent components. This is also hinted at by the huge

---

[94] It has to be noted, that the validity of the integrated measures and the assumption of a separable longitudinal and transverse coherence is highly questionable in the case of the 'bad' pulse.

[95] The circular shape of the pattern is related to the axial symmetric treatment of the crystal thermal response. Any distortions introduced by this response will, consequently, have an axial symmetric shape.

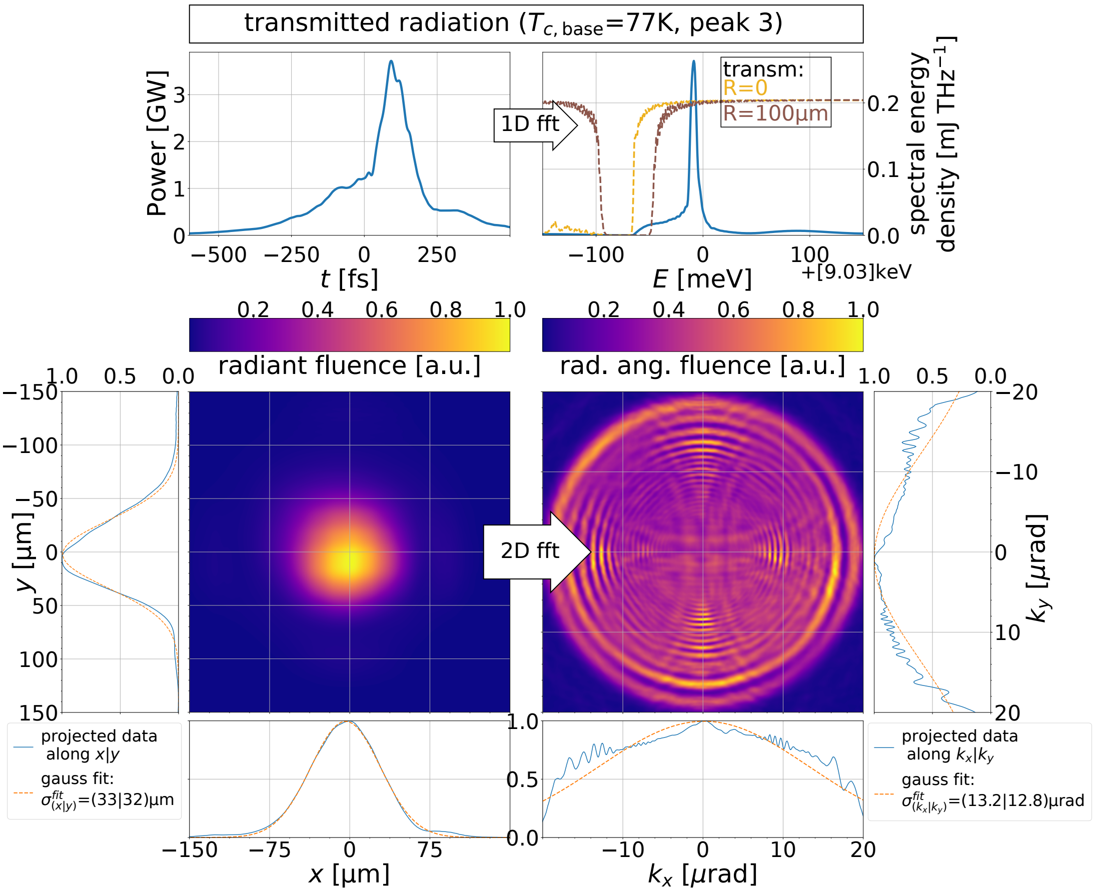

Figure 5.111: Longitudinal and transverse representations of a 'bad' transmitted pulse, corresponding to peak 3 at $T_{c,\text{base}}$ =77 K in Figure (5.109). Due to the thermally induced spectral shift of the transmission curve, which is stronger than for the 'good' pulse in Figure (5.110), the transmitted spectrum still exhibits the main spectral peak of the incident radiation. The time-domain power profile shows a rather smooth progression, but is significantly stretched. It is also important to note that the transmission curve is differing between the transverse position at $x_\perp = 0$ and $x_\perp$ =100 µm. While the spatial distribution is approximately gaussian, the angular distribution is strongly distorted, with a circular shape induced by the radial symmetric treatment of the crystals' thermal response. The severity of the distortions is probably caused by numeric artifacts of the discrete fourier transformation.

angular width of σ_k ≈13 µrad. The k-space representation and, hence, also the huge gaussian quality factor J cannot serve as quantitative basis for describing the pulse. Nonetheless, the question remains, where these high angular components come from, which cause the failure of the numeric treatment. The reason is already hinted at in the spectral representation in Figure (5.111), or more precisely, in the spatial dependence of the transmissivity. As was already mentioned before and also used for the analysis of the mirror figure errors, wavefront distortions are caused by a non-vanishing spatial gradient of the phase of the optical response function, in this case of the phase of the transmission.

Figure (5.112(a)) shows the spatial temperature distribution of the downstream crystal at arrival of the X-ray pulse, which corresponds to the 'bad' transmitted pulse in Figure (5.111). Besides the strong temperature rise of $T_{c,\max}$≈163 K already mentioned before, the distribution shows a considerable variation of the temperature with position (unlike the distribution for peak zero, which is rather homogenously distributed). This variation introduces a spatially varying trans-

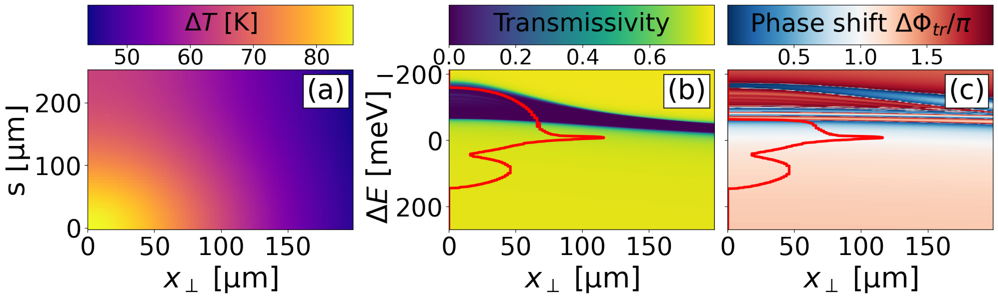

Figure 5.112: Spatial distribution of the difference of the downstream crystal temperature towards its base temperature $\Delta T = T_c - T_{c,\mathrm{base}}$ (a) at the arrival of the X-ray pulse at the 128th round trip, corresponding to the 'bad' third peak at base temperature T_c =77 K in Figure (5.109). This temperature distribution brings about a spatially varying transmissivity $T = |t_{00}|^2$ (b) and a spatially varying, transmission induced phase shift $\Delta\Phi_{tr} = \mathrm{phase}\,(t_{00})$ (c). In (b) also the 99 % contour (the coordinates after which the distribution falls below 1 % of its maximum) of the incoming pulse in photon energy and radial position is plotted in red. In (c) the 99 % contour of the transmitted pulse is plotted, visualizing which parts of it are subject to a spatially varying phase shift, which is consequently deforming the pulse wavefront.

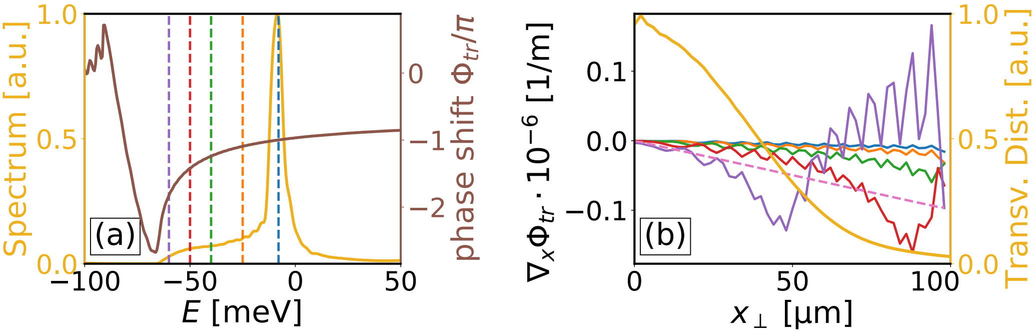

Figure 5.113: (a) shows the frequency distribution of the 'bad' pulse from Figure (5.111) (orange) together with the transmissive phase shift $\Delta\Phi_{tr} = \mathrm{phase}\,(t_{00})$ at the transverse position $\boldsymbol{x}_\perp = 0$ (brown). (b) displays the normed transverse distribution (orange) together with the spatially resolved phase gradients $\nabla_{x_\perp}\Delta\Phi_{tr} = \mathrm{phase}\,(t_{00})$ for exemplary photons energies. These are shown in (a) as dashed, vertical lines in matching colors. A stronger gradient corresponds to a stronger impact on the wavefront. To have an estimate on the relevance the dashed pink line also shows the gradient of the phase shift $\Delta\Phi_f = -\dfrac{k}{2f}\boldsymbol{x}_\perp^2$, which would be introduced by the downstream grazing incidence mirrors with f =46.1 m. It is evident that only the purple and the red line have a significant impact. These correspond to $\Delta E = E_{\mathrm{ph}} - E_c$ =−60 meV and ΔE =−50 meV, respectivey, and are rather well separated from the main spectral peak at ΔE =−8 meV.

missivity $T = |t_{00}|^2$ and, most importantly, a spatially varying transmission induced phase shift $\Delta\Phi_{tr} = \mathrm{phase}\,(t_{00})$, displayed in Figure (5.112(b) and (c)), respectively. While the strong variation of the phase in frequency, which introduce the distortions of the time-domain profile, were frequently discussed, the spatial variation of the phase additionally introduces distortions of the pulse wavefront, which ultimately lead to the numeric artifact in Figure (5.111). This is supported by Figure (5.113(b)), which shows the gradient of the transmissive phase for exemplary photon energies as measure for the impact on the wavefront. It shows that at photon energies close to the 'transmission gap' the transmission has a significant effect on the wavefront and, consequently, on the k-space distribution. On the other hand, it is also evident that in the direct vicinity of the main spectral peak there is hardly any spatial variation of $\Delta\Phi_{tr}$. Hence, one can expect that the components introducing the tremendous k-space distortion in Figure (5.111) are located on the flank of the spectral distribution. By further propagation of this transmitted X-ray pulse downstream the beamline, these components will naturally separate. This should leave behind a well distributed X-ray pulse, both in the longitudinal as in the transverse domain. Unfortunately, this cannot be tested by means of the *pXCP* program to date, due to the inherent incompatibility with the fourier propagation formalism. On the other hand, it poses a nice experimental problem to study with the CBXFEL demonstrator experiment.

In summary, from the quasi-static thermal considerations so far, it would be principally possible to use the inherent instability, caused by the crystals' thermal response, to couple out intense radiation pulses from the X-ray cavity. This is much in analogy to classic cavity dumped pulsed laser sources. However, unlike these cases, here the outcoupling is not actively controlled, but passively driven by the CBXFEL process itself. This causes strong fluctuations in the properties of the transmitted X-ray pulses, mainly due to variations in the downstream crystal's temperature distribution at the round trips of maximal transmission. Especially, some of the transmitted pulses show strongly distorted transverse distributions. These are caused by the inhomogeneity of the spatial temperature profile, which leads to spatial variation of the crystal transmission induced phase shift $\Delta\Phi_{\mathrm{tr}}\left(x_{\perp}, E_{\mathrm{ph}}\right)$. As the spatial gradient of the radiation phase determines the shape of the pulse's wavefront, these variations induce the transverse distortions observed. However, the strength of the effect appears exaggerated due to numerical problems, or more precisely due to shortcomings of the discrete fourier transformation to treat components out of the computational bandwidth (see Paragraph **4.2.3.1**). Furthermore, it seems that the source of these transverse distortions are localized on the flanks of the spectral distribution and do not affect the central spectral peak. As these distortions exhibit a strong angular deviation, they would naturally separate from the 'good' part of the X-ray pulse. Consequently, they could be accounted for by spectral filtering, leaving behind a comparably high brilliance X-ray pulse. However, due to the afore mentioned problems of the numeric treatment, this has to be checked by experiment. Finally, a big advantage of this "passive cavity dumping" scheme is that it would, by simulation, occur naturally and does not require any changes in the demonstrator setup. This is with exception of the need for strong radiation protection, which is necessary considering the high pulse energies and comparably high beam losses.

5.2.3.7 Thermoelastic response: As was discussed in the beginning of Chapter **3**, this thesis concentrates on the thermal diffusion subfraction of the crystals' thermal response. More specifically, in the prior studies the elastic expansion of the crystal was assumed to be a quasi-static process, which is entirely dictated by the temperature distribution and the following thermal expansion at each specific time. As such, the elastic equations by itself is assumed to be time-independent. However, this is a very rough approximation. In reality, also the elastic response is a dynamic process. The rapid expansion of the crystal lattice, caused by the strong crystal heating and the following thermal expansion, creates a thermal stress field $\boldsymbol{\sigma}\left(\boldsymbol{x}, t\right)$ varying with time, with $\boldsymbol{\sigma}$ being a second order tensor. This stress triggers an elastic response, which tries to compensate the stress and causes expansion/compression waves traveling through the crystal [85–87, 223, 224]. Under the assumption of continuum theory, local thermal quasi-equibilibria and infinitesimal strain theory, this process is governed by the *equations of thermoelasticity*, which become for the specific case of an isotropic material such as diamond [85, ch. 3.4][96]:

$$\rho \frac{\partial^2 \boldsymbol{u}}{\partial t^2} = \boldsymbol{\nabla} \cdot \boldsymbol{\sigma} + \boldsymbol{F} \approx E \boldsymbol{\nabla} \cdot \left[\boldsymbol{\epsilon} - \mathbb{1} \int_{T_{c,\text{base}}}^{T_c} \alpha_L(T') \mathrm{d}T' \right] , \tag{5.6}$$

where $\boldsymbol{u}$ is the vector displacement field from the reference position at $t = 0, T_c = T_{c,\text{base}}$, $\boldsymbol{\epsilon} = \frac{1}{2} \left(\text{grad}\,(\boldsymbol{u}) + [\text{grad}\,(\boldsymbol{u})]^T \right)$ is the (tensorial) strain field, α_L is the thermal expansion coefficient, $\mathbb{1}$ is the unity matrix and E =1125 GPa [85, p. 49ff.] is the Young's modulus, which has been approximated to be constant. For simplification it has also be assumed that the poisson ratio $\nu \approx 0$, which is a fairly accurate approximation for diamond (see [85])[97]. Above constituting equation obviously needs to be amended by appropriate boundary conditions.

The complicated thermoelastic response by CBXFEL like heat loads has been thoroughly studied in the Phd thesis of *I. Bahns* [85], both by experiment as by simulation. His results strongly indicate a high relevance to take into account these effects. Unfortunately, at the current state the simulations are computationally very expensive and need about one day of simulation time for one single round trip, using a radial symmetric approximation and reducing the crystal radius to only one millimeter. Hence, a fully coupled treatment covering at least one hundred round trips as for the thermal diffusion is not affordable. Due to the very involved nature of the thermoelastic response, with low temperature effects potentially also playing a role, and the dependence on the exact crystal geometry, the measured results and the simulations do not perfectly agree in the thesis by *I. Bahns*. Nonetheless, the agreement is surprisingly good and the qualitative features measured by *I. Bahns* remain the same as predicted by simulation. However, one has to note that the measurements by *I. Bahns* only assess the displacement at the backside and do not provide any direct information on the strain inside the crystal. So, principally, the internal strain distribution might also qualitatively vary between the simulations and reality. Yet, owing to the lack of a more appropriate theoretic and, foremost, simulative framework for the thermoelastic effects at the low-temperature scale [85], the use of Eq. (5.6), also in the axisymmetric approximation, appears a justifiable means to predict the influence of thermoelastic effects on the CBXFEL demonstrator.

Here, the impact of the elastic distortions, introduced by the thermoelastic response, on the wavefront propagation shall be sketched. For a full discussion on the physics and features of the thermoelastic response, the interested reader is referred to the thesis by *I. Bahns* [85]. The simulations for the following study are adapted from this work. Equally to the computational

---

[96] Principally, the elastic response also has an impact on the thermal diffusion process. However, this is usually very small and can be omitted [85, 87].

[97] It should be noted that a poisson ratio $\nu \neq 0$ does enter into the numerical solutions discussed below using *Comsol Multiphysics*™, but it makes Eq. (5.6) fairly more complicated.

treatment of the thermal diffusion in this thesis (see Subsection **4.3.1**), they are based on the commercial FEM software *Comsol Multiphysics™*. The axisymmetric computational domain also is similar to the one presented in Figure (4.8) and used in the prior studies, with the difference of the crystal being assumed to have a radius of only one millimeter, as already mentioned above, to keep the computational demands low. Further, due to the incompatibility with the elastic partial differential equation, the feature of *infinite elements* is omitted. For the elastic problem, the boundary conditions are assumed to be free (no constraints, no loads) on all boundaries except the outer radial edge, which is assumed to be rigidly fixed ($\boldsymbol{u} = 0$). For the thermal diffusion problem, all boundaries are assumed to be thermally insulating, which is very accurate for the duration between two X-ray pulses [85]. Initially, the entire crystal is assumed to be at the base temperature $T_{c,\text{base}}$ and in rest ${}^{\partial \boldsymbol{u}}\!/\!{}_{\partial t} = \boldsymbol{u} = 0$.

For this study, the thermoelastic response due to the absorption of one single, intense X-ray pulse will be simulated. This pulse is chosen from the CBXFEL demonstrator at $T_{c,\text{base}} = 77\,\text{K}$ including artificial outcoupling losses (see Paragraph **5.2.3.5**), which was exhibiting the most stable operation. The pulse used is from the round trip number 320, which has a particularly high pulse energy of $Q_{\text{pulse}}^{\text{und}}$ ≈1.15 mJ and correspondingly high heat load of $Q_{\text{abs}}^{\text{downstream}}$ ≈82 µJ for the downstream crystal and $Q_{\text{abs}}^{\text{upstream}}$ ≈33 µJ for the upstream crystal. The spatially resolved heat load distributions are shown in Figure (5.114).

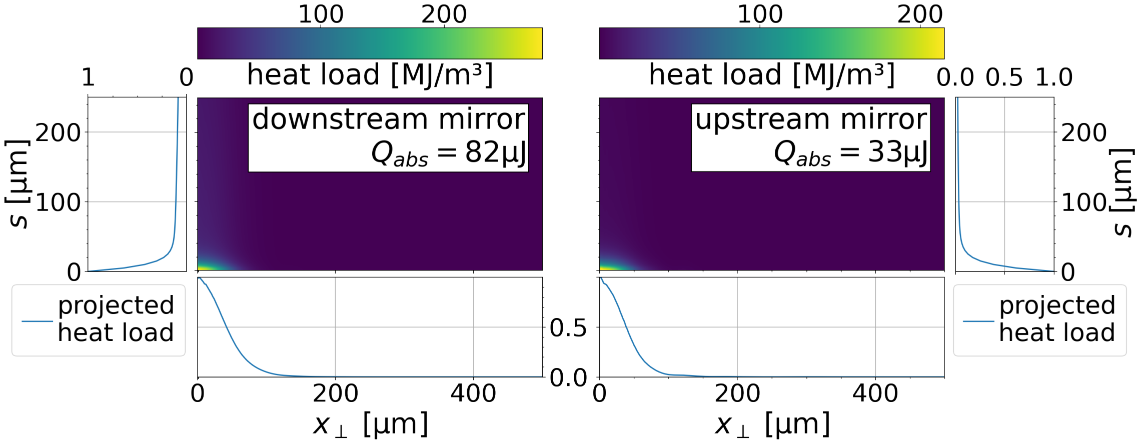

Figure 5.114: Heat load distributions at the downstream (a) and upstream mirror (b) as used for the thermoelasticity simulation. They correspond to the X-ray pulse at the 320th round trip of the CBXFEL demonstrator simulation at $T_{c,\text{base}} = 77\,\text{K}$, including artificial outcoupling losses (see Paragraph **5.2.3.5**). Both profiles follow, as usually (see equation (5.3)), a gaussian profile in the transverse direction and a superposition of one rapidly and one slowly exponential decaying curve progression in depth. The slowly decaying contribution is very low for the upstream mirror. Also, while the total amount of deposited heat energy is much higher for the downstream crystal, the maximum heat load density is comparable.

Figure (5.115) displays the spatially resolved crystal temperature $T_c\left(\boldsymbol{x}_\perp, s, t_{\text{rep}}\right)$ and normal strain $\eta_{ss}\left(\boldsymbol{x}_\perp, s, t_{\text{rep}}\right) = {}^{\partial(\boldsymbol{u}\hat{\boldsymbol{e}}_s)}\!/\!{}_{\partial s}\left(\boldsymbol{x}_\perp, s, t_{\text{rep}}\right)$ one round trip time t_{rep} =444 ns after absorption of the above heat load distributions. The crystal temperature in Figure (5.115(a) and (c)), which

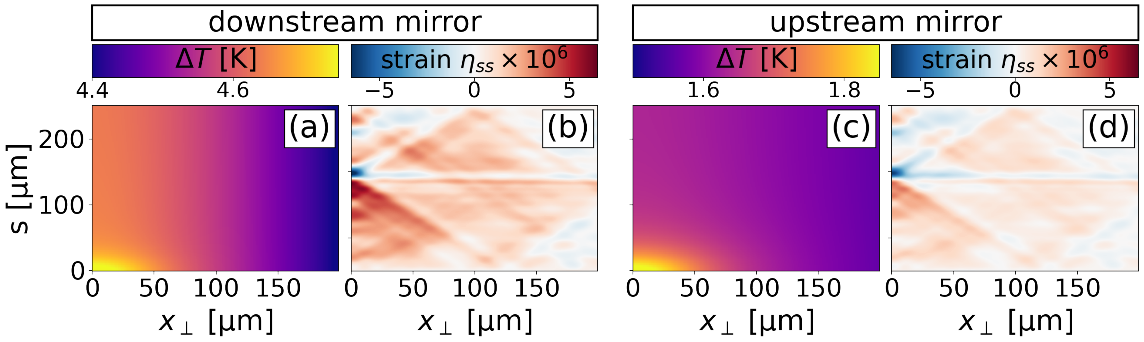

Figure 5.115: Temperature (a,c) and strain (b,d) distributions at the downstream (left) and upstream (right) crystal, t_{rep} =444 ns after absorption of $Q_{\mathrm{abs}}^{\mathrm{downstream}}$ ≈82 µJ for the downstream mirror and $Q_{\mathrm{abs}}^{\mathrm{upstream}}$ ≈33 µJ for the upstream mirror, including the crystals' thermoelastic response. While the temperature distributions are almost homogenous, the strain distributions show clear, stripe-like patterns with a total magnitude of $\Delta\eta_{ss}^{\max} = \eta_{ss}^{\max} - \eta_{ss}^{\min} \approx 1.3\times 10^{-5}$ for the downstream mirror and $\Delta\eta_{ss}^{\max} = \eta_{ss}^{\max} - \eta_{ss}^{\min} \approx 0.97\times 10^{-5}$ for the upstream one. Also, while the maximum remnant heat energy density differs from $Q_{\mathrm{heat}}^{\max,M1} \approx 0.156\,\mathrm{MJ/m^3}$ at the downstream mirror to between the $Q_{\mathrm{heat}}^{\max,M1} \approx 0.058\,\mathrm{MJ/m^3}$ at the upstream mirror by roughly a factor of three, the maximum strain variation only differs by a factor of 1.3.

is governed by the thermal diffusion, is rather homogenously distributed[98] with maximum temperature shifts $\Delta T_{c,\mathrm{M1}}^{\max} \approx 4.85\,\mathrm{K}$ and $\Delta T_{c,\mathrm{M1}}^{\max} \approx 1.87\,\mathrm{K}$, respectively, which are approximately irrelevant for the diffraction process. Also, as usual the maximum temperature shift is much bigger for the downstream crystal (a) than for the upstream one (c). In contrast, the strain distributions in Figure (5.115(b) and (d)) display strong spatial variations, which are following a complex stripe pattern[99]. In comparison with the temperature distributions, it is evident that these strain patterns are caused by the elastic response of the crystals. Furthermore, the maximum variation of the strain $\Delta\eta_{ss}^{\max} = \eta_{ss}^{\max} - \eta_{ss}^{\min} \approx 1.3\times 10^{-5} > 1\times 10^{-5}$ is slightly bigger than what was proposed as tolerance for the static clamping strain in Paragraph **5.2.2.7**. Additionally, it is notable that the maximum magnitude of the strain is comparable for the downstream and upstream mirror, in contrary to the temperature distributions. This is due to the elastic waves being driven by the maximum magnitude of initial strain after absorption of the X-ray pulse, which is comparable for both mirrors, as evident in Figure (5.114).

Figure (5.116) displays the spatially varying spectral reflectivity $R\left(\boldsymbol{x}_\perp, E_{\mathrm{ph}}\right)$((a) and (c)) and reflection induced phase shift $\Delta\Phi_R\left(\boldsymbol{x}_\perp, E_{\mathrm{ph}}\right)$[100] ((b) and (d)) for the downstream (left) and upstream mirror (right), corresponding to the strain distributions in Figure (5.115(b) and (d)). It is obvious that the reflectivity is strongly distorted by the thermoelastic response. For one the reflectivity is stretched to about twice the bandwidth, which would principally not be a problem. But second, the corresponding phase shift is strongly varying both spectrally and spatially in-

---

[98] The temperature distribution is less homogenous than for the prior simulations at comparable heat load. This is due to the reduced size of the crystal as assumed for the thermoelastic calculations.

[99] For details on this involved pattern, the reader is again referred to the thesis by *I. Bahns* [85]

[100] The phase shift $\Delta\Phi_R\left(\boldsymbol{x}_\perp, E_{\mathrm{ph}}\right)$ includes both a fraction introduced by traversing the crystal, as well as a fraction caused by the surface curvature and the consequent transversely varying optical path difference, following Eq. (4.22).

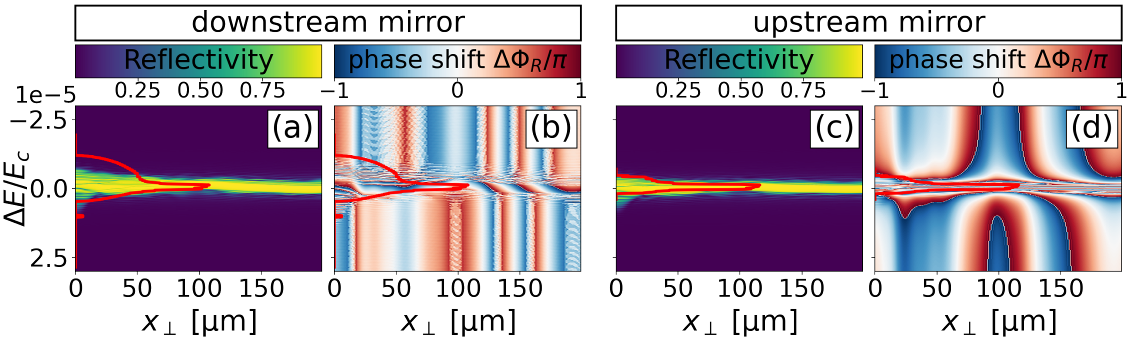

Figure 5.116: Spectral-spatial reflectivity $R\,(\boldsymbol{x}_\perp, E_\mathrm{ph})$ (a,c) and reflection induced phase shift $\Delta\Phi_R\,(\boldsymbol{x}_\perp, E_\mathrm{ph})$ distributions ((b) and (d)) at the downstream (left) and upstream (right) crystal, corresponding to the strain distributions displayed in Figure (5.115(b) and (c)). The distributions show strong spectral and spatial variations. The red lines sketch the 99 % contour of the incident X-ray pulses.

side the spectral and spatial bandwidth of the incoming radiation pulse, introducing distortions in the time-domain and angular-space pulse distributions, respectively (see Paragraphs **5.2.2.7** and **5.2.3.6**).

In Figure (5.117) the spectral-domain (first row), time-domain (second row), spatial-domain (third row) and angular-domain (last row) distributions are displayed for different position in the cavity. These are directly after the undulator (first column), after reflection at the downstream crystal (second column), after reflection at the upstream crystal (third column) and reentering the undulator as seed radiaton (last column). First, considering the spectral distribution, it is evident that reflections at the mirrors only have minor influence on the integrated spectral energy density. The impact is even lower than for the case neglecting thermoelasticity, which is due to the increased spectral width of reflection distribution in Figure (5.116(a) and (b)). For the unstrained crystal with a narrower bandwidth, the crystal reflection cuts out a smaller subfraction of the incident spectrum. The notable decrease from the first to the second column is caused by the outcoupling of $\mathcal{L}_\mathrm{out}$ =15 % of the radiation at the artificial outcoupling device, as the X-ray optical cavity of Paragraph **5.2.3.5** was adapted. The notable decrease in spectral energy density from the third to the fourth column neither is (directly) caused by the upstream crystal, but by the spatial cut off at the upstream montel assembly's effective aperture. In total, traversing the cavity amounts to a threefold decrease of pulse energy from $Q^\mathrm{und}_\mathrm{pulse}$ ≈1.1 mJ to $Q^\mathrm{seed}_\mathrm{pulse} \approx 0.37\,\mathrm{mJ}$. As this decrease is only slightly higher than for the case neglecting thermoelasticity (see Paragraph **5.2.3.5**), it could principally be compensated by a corresponding increase in FEL gain, which would be inside the margins of what is possible with the four undulator sections CBXFEL demonstrator as planned (see Figure (5.68)),

However, the actual effect on the seeding X-ray pulse is worse than a simple reduction in total pulse energy. As was already discussed for the case of the static clamping strain in Paragraph **5.2.2.7**, the strong spectral variation of the reflection induced phase shift, accounting for different penetration depths and back and forth reflections at different depths of the crystal, causes a stretching of the X-ray pulse in the time-domain. This is evident from the change of the time-domain power profile in Figure (5.117(second row)), taking into account the logarith-

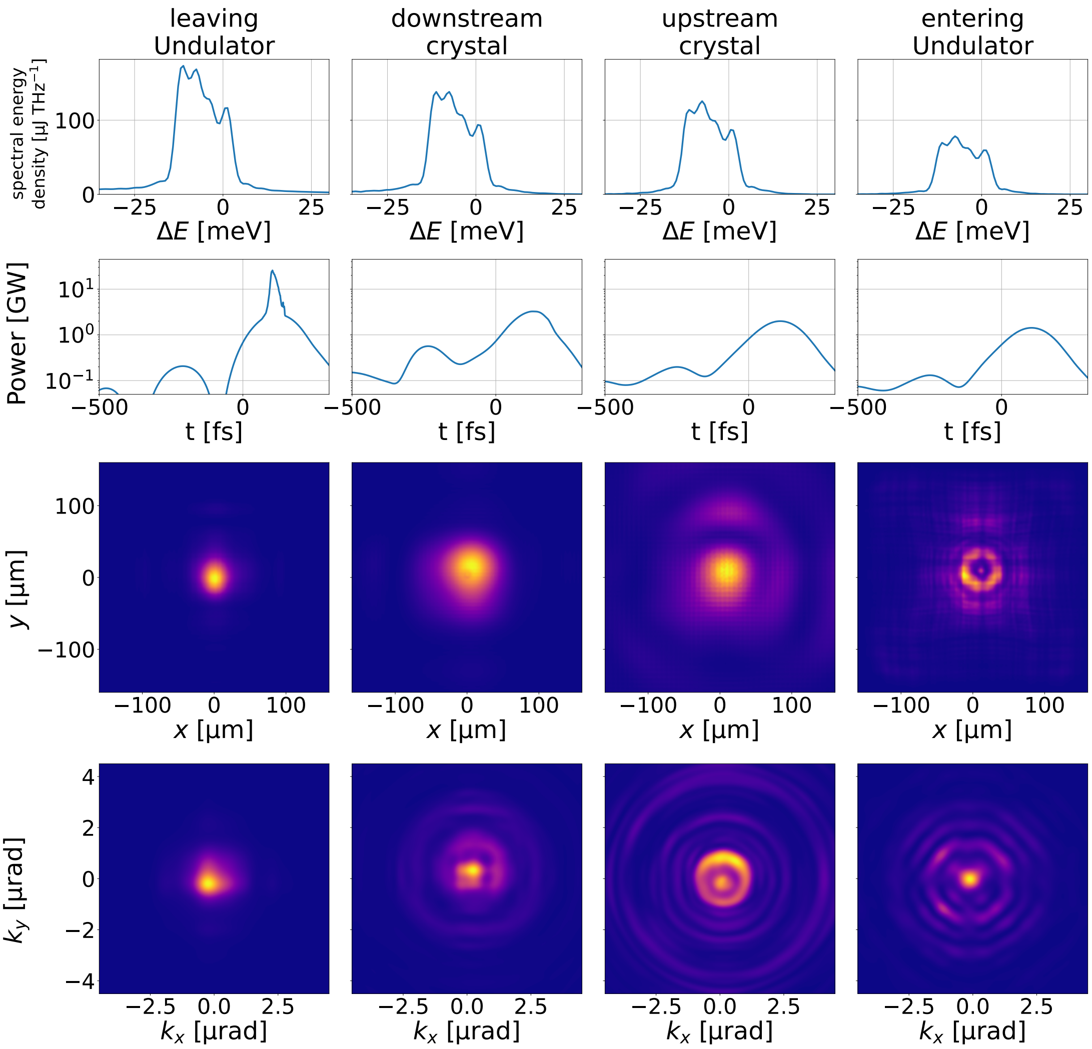

Figure 5.117: Spectral-domain (first row), time-domain (second row), spatial-domain (third row) and angular-domain (last row) distributions for different position in the cavity. These are directly after the undulator (first column), after reflection at the downstream crystal (second column), after reflection at the upstream mirror (third column) and reentering the undulator as seed radiaton (last column). While the spectral profile only shows comparably small variations, the time-domain and ,especially, both transverse domain distributions are strongly influenced by the reflection at the strained downstream and upstream crystals, with the reflectivity as displayed in Figure (5.116).

mic y-axis scale. After traversing the cavity, the peak power drops by more than one order of magnitude. For the short, 250 pC electron bunch usually employed at the European XFEL, the measure relevant for the FEL process is the power inside a narrow time window of $\Delta t_{\text{seed}} \approx 40\,\text{fs}$ (see Paragraph **5.2.2.7**) and not the totally integrated pulse energy. Hence, the FEL gain would need to be correspondingly higher.

Furthermore, the two last rows of Figure (5.117) additionally exhibit an significant impact of the crystal strain on the spatial and angular transverse distributions after reflection. Due to the spatially varying reflectivity $R\,(E_{\text{ph}}, x_{\perp})$, one can see a influence of the reflection on the spatial profile, apparent as spots of reduced energy densityaround $(x, y) = (0, 0)$ after reflection at the downstream mirror (second column). For the spatial profile in the third column one can additionally see the impact of the effective aperture, which introduces a comb pattern (see Paragraph **5.2.2.4** and/or [174, ch. 5.3]). More importantly, the impact of these spatial variations are amended, as was already discussed for the last Paragraph **5.2.3.6**, by the wavefront distortions introduced by the spatially varying phase shift $\Delta\Phi_R$. This leads to a heavily distorted seeding beam (last column) and to the strong aperture cut off at the upstream mirror assembly already mentioned in the discussion of the reduction of spectral energy density.

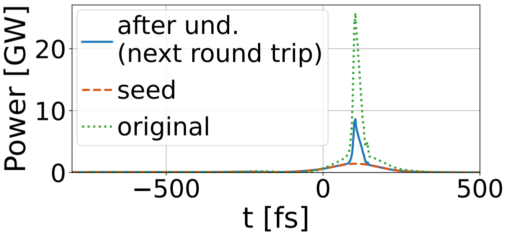

Figure 5.118: The time-domain profile after gaining power through the FEL process (blue curve) in the undulator, with the seeding radiation (red curve) from Figure (5.117(right column)). The green dotted line shows the original power profile from Figure (5.117(left column)), before being reflected at the distorted crystals.

Cumulating all these effects, it is obvious, that the CBXFEL demonstrator experiment could not run stably. Indeed, as displayed in Figure (5.118), while the FEL process still leads to a roughly factor of six gain in peak power of the distorted seeding pulse, it cannot restore the $P^{\text{und}}_{\text{max}}$ ≈25 GW peak power of the previous round trip.

Essentially, these distortions can be accounted for as effective beam losses, as a small fraction of the beam remains nicely distributed. This is for example apparent as the well collimated ‘core’ in the angular distribution of the seeding beam. As such, they could be compensated by increasing the FEL gain to, in this specific case, $\mathcal{G}_{\text{FEL}} \approx 18$ by about a factor of three. Yet, there are two problems with that. For one, it is a very ineffective way to treat the problem, as a lot of X-ray pulse energy is essentially wasted. Second, the significantly increased FEL gain leads to a increased fraction of newly generated X-ray power, which would become bigger than the power of the circulating radiation. This means that the output characteristics shift from a pulse which is averaged over multiple round trips and, consequently, partially stabilized, characteristic for an FEL oscillator, to that of an FEL amplifier, with the characteristics being strongly influenced by one single electron bunch. As such it would be very much similar to the self-seeding method. This is essentially what is proposed in different publications as high-gain X-ray regenerative amplifier (see Section **2.4** or for example [21, 31, 32, 216]).

A more sophisticated way to treat the above problem would be to suppress it in magnitude. A promising approach is, as for the thermal diffusion problem, to increase the extent of the X-ray pulse projected on the crystal mirrors. This would strongly decrease the local heat energy densities and, hence, the magnitude of initially generated strain, which is dominantly determining the amplitude of the expansion/compression waves of the elastic response. Unfortunately, as was already discussed for the thermal diffusion and quasi-static thermal expansion problem in Paragraph **5.2.3.4**, this is not compliant with the “As simple as possible, …” demonstrator concept.

To summarize, besides the ‘simple’ case of the elastic state of the crystal being statically determined by the temperature distribution at each time, as treated in the prior paragraphs, the rapid heating of the crystals after absorption of the X-ray pulse causes a dynamic elastic answer. This answer is governed by the theory of thermoelasticity and is thoroughly studied in the thesis by *I. Bahns* [85]. Using the computational approach developed in this thesis, it becomes apparent, that the crystals’ thermoelastic response has a significant influence on the pulse propagation through the CBXFEL demonstrator X-ray cavity. Using the heat load of a single X-ray pulse, taken from the before stable demonstrator case with additional outcoupling losses in Paragraph **5.2.3.5**, the crystals’ reflection, affected by the thermoelastic response, would significantly distort the X-ray pulse and lead to an order of magnitude decrease in seeding strength.

Two ways to treat this effect are to either increase the FEL gain by a factor of three or to widen the pulse projection on the crystals. The first approach might be possible, considering an ideal alignment of the four undulator sections. The more sophisticated, second approach is, unfortunately, not compatible with the CBXFEL demonstrator setup as planned. However, incorporating this into the setup would add a lot of complexity and is deviating from the principle “As simple as possible, …”. If the thermoelastic response would render the entire CBXFEL process impossible, this additional complexity would be justifiable by “…, as complicated as necessary”. Yet, just as the heat diffusion problem, the thermoelastic problem only becomes relevant when the X-ray pulse deposits a high amount of heat into the crystals, which requires that it has already undergone considerable seeding from the weak initial pulse. Consequently, the main purpose of the proof-of-principle CBXFEL demonstrator experiment, which is to proof that seeding indeed occurs, is neither impeded by the thermal nor the elastic response of the crystal.

Additionally, the magnitude of the thermoelastic response’s effect on the crystal reflection is not ascertained. Especially the actual crystal geometry, which will be used for the experiment, will certainly deviate from the axial symmetry assumed for the simulations, which is necessary to ease the huge computational demands. At present, it is unclear how this would affect the complex pattern of the elastic compression/expansion waves created by the thermoelastic response. Furthermore, unlike the strongly non-linear impact of the thermal diffusion related quasi-static strain, the thermoelastic response is approximately linear in the amount of absorbed heat load. As such, it seems plausible that it would lead to the cavity losses increasing linearly with the pulse energy. This would then lead to a saturation of the FEL process at a much lower pulse energy than the roughly millijoule pulse energies discussed for the thermal response. Finally, the thermoelastic response poses a very interesting study case for the CBXFEL demonstrator experiment. The (involved) means and necessary diagnostics to actually measure the thermoelastic response, and how to integrate them into the European XFEL beamline, are currently under discussion[101].

---

[101] The most direct way to assess the crystal thermoelastic response would be to use the interferometric measurement setup developed by *I. Bahns* [85] directly at the CBXFEL setup. This, however, would require major interventions into the photon and electron beamline at the position of the demonstrator setup and appears to be infeasible for the period of the project. Another, less invasive, approach is to use the regularly transmitted X-ray

5.2.3.8 Summary on the influence of the heat load induced crystal's response: In the prior Subsection **5.2.2**, it was shown that the CBXFEL demonstrator would remain stable under both reasonable errors of the (X-ray) optics and fluctuations of the electron bunch properties. Also, even under influence of these errors, the characteristics of the transmitted pulse would be superior to SASE FELs, especially in terms of the peak spectral flux. However, when taking account of the crystals' thermal response, **this is not the case anymore**, neither at room temperature nor with the crystals cooled to low temperatures in the range $T_{c,\text{base}}$ =40 K to 150 K to aid the efficiency of the thermal diffusion. It was shown that the crystals thermal response, neglecting the dynamic thermoelastic contribution, at room temperature and at the low temperatures leads to quite different influences on the CBXFEL demonstrator performance.

At room temperature, or rather $T_{c,\text{base}} = 300\,\text{K}$ (see Paragraph **5.2.3.1**), at which the heat equation (3.55) can be linearized in good approximation, one could observe a **strong reduction of the peak pulse energies by more than two orders of magnitude** to $Q^{\text{max}}_{\text{pulse}}$ ≈20 µJ, which were further showing fluctuations by a factor of three. Both effects could be retraced to the inhomogeneity of the temperature distribution at the arrival time of the subsequent pulses, leading to a defocussing of the X-ray pulse and, in consequence, increased cut-off losses. While the room temperature case was concluded to be a bad choice due to above observations, the linearity of the heat equation in this specific case allowed for comparably accurate analytic approximations (Equations Eqs. (5.3) to (5.5)). Comparison with the numeric modelling (see Subsection **4.3.1**) showed excellent agreement, **serving as a good benchmark for the numeric approach**.

It was discussed by theoretic considerations as well as shown by simulation that **for low temperatures in the range $T_{c,\text{base}}$ =40 K to 120 K the efficiency of thermal diffusion process can be significantly enhanced** (see Paragraph **5.2.3.2**). This allowed for reaching maximum pulse energies up to $Q_{\text{pulse}^{\text{max}}}$ ≈2.2 mJ at $T_{c,\text{base}} = 40\,\text{K}$, with **the maximally reached pulse energies scaling inversely to the crystal base temperature**. The thermal diffusion and, consequently, **the maximum pulse energies can further be increased by using thicker $t_c = 250\,\mu\text{m}$ crystals** (see Paragraph **5.2.3.3**), which have the sole drawback of slightly reduced transmission compared to the $t_c = 150\,$ţm crystals assumed before. However, **for all base temperatures and crystal thicknesses the CBXFEL process becomes very instable**, with order of magnitude breaking-offs of the pulse energies directly after reaching the maximum. The source of this severe discontinuity was determined to be the strong non-linearity of the crystals' thermal response, with $\Delta T \gg 100\,\text{K}$ after absorption of the X-ray pulses, as well as the non-linearity of the X-ray absorption at these low temperatures. **It has only been possible to study the effect of this non-linearity and their interplay by the fully coupled computational approach developed in Section 4**.

It has been proposed in Paragraph **5.2.3.6** to use the highly intense transmitted pulses at the moments of breaking-off, in the sense of a **passive 'cavity dumping' scheme**. Yet, while these pulses rather consistently carry **at least a millijoule of pulse energy for $T_{c,\text{base}} <$ 77 K, they**

---

pulse in combination with a knife-edge method, which also promises to give very accurate information on the X-ray pulse pointing and was also partially used in the thesis by *I. Bahns* [85] in the optical wavelength regime.

show strong fluctuations in the other pulse characteristics, predominantly in the transverse distributions, which are induced by the inhomogeneity of the temperature profile in the these round trips of maximum transmission. Nonetheless, as this scheme comes with no additional complexity and/or costs for the simplistic experimental setup discussed in Section **5.1**, **it should surely be applied at the proof-of-principle experiment**.

Besides the 'cavity dumping' scheme, which makes uses of the discontinuity of the CBXFEL process, two ways were discussed to stabilize the CBXFEL demonstrator, which only needs comparably minor, if any, modifications to the experimental setup. These are to decrease the FEL gain (see Paragraph **5.2.3.4**) or to increase the cavity losses (see Paragraph **5.2.3.5**). Both indeed show stabilization of the pulse energy evolution, but the decreased gain case exhibits notable variations in the transmitted pulse characteristics by more than 100 %. **The case of the increased losses proofs to be more stable and, hence, more useful, especially if realized by means of an additional X-ray outcoupling before the downstream mirror**. Yet, it also is more complicated, as it requires additional X-ray optical components in the cavity.

Also, the impact of the **thermoelastic response**, which is thoroughly treated by *I. Bahns* in his PhD thesis [85], was superficially studied in Paragraph **75**. Inclusion of this very involved physical mechanism, which was only examined on a single cavity round trip bases, showed that **even the previously stable case of increased cavity losses would not be a valid working condition**. The simulation definitely ascertained the importance of the thermoelastic response, but **the realistic, quantitative magnitude of the impact is not clear to-date**. This is mainly due to differences of the axisymmetric computational domain to the final geometry. Besides, it appears probable that even with the thermoelastic response the CBXFEL can reach a stable working point, but at a (much) reduced peak power. However, to ascertain this assumption a fully coupled, multiple round trips simulation would be necessary, which is not feasible at this point due to the very high computational demands.

Finally, it should be noted that both the thermal response problems by means of the thermal diffusion as the thermoelastic response could be eased by using a high grazing angle of the crystal with respect to the incoming radiation, which would increase the projected width of the X-ray pulse on the crystals. Unfortunately, this is not compatible with the experimental setup of the CBXFEL demonstrator (see Subsection **5.1**). While one could argue that it falls under the point of "*..., as complicated as necessary*", it is to be emphasized that **both effects do not impede the principle goal of the CBXFEL demonstrator proof-of-principle experiment**, which is to proof that seeding and exponential growth actually occurs in a CBXFEL scheme. However, the simulations in the present subsection strongly show a **demand to measure and resolve the described effects in the actual experiment**, in order to develop measures against them.

6 Conclusion

In this work a *Cavity Based X-ray Free-Electron Laser* (CBXFEL) demonstrator experiment for the SASE1 FEL line of the European XFEL facility was conceptually studied. The main goal of the CBXFEL demonstrator is to observe effective seeding of the fresh electron bunches and an exponential build up of the radiation field in the X-ray cavity. As a proof-of-principle experiment which is not meant for user operation, it follows the paradigma "As simple as possible, as complicated as necessary". Hence, the demonstrator is planned as a simple, $L_{\text{cav}} \approx 66.6\,\text{m}$ long two diamond crystal 'backscattering' cavity, with no other X-ray optical components but two additional total reflecting mirrors in montel geometry amended to each of the crystals. For outcoupling the regular transmission of t_c =250 µm thick diamond crystals is foreseen. By technical consideration as by simulation, the FEL photon energy was fixed to $E_c = 9.05\,\text{keV}$, which corresponds to diamond C (3 3 3) orientation.

For the study of the CBXFEL demonstrator a well benchmarked computational approach was developed, which couples the FEL generation, simulated by *Genesis-1.3*, with the self written *parallel X-ray Cavity Propagator* (pXCP) wavefront propagation code and the computation of the crystals' thermal response, based on finite element analysis. **This strongly coupled approach has proven to be absolutely necessary to gain sufficient understanding of the CBXFEL processes.**

Thorough simulations were carried out, based on a realistic phase space distribution of the regularly used 250 pC electron bunches and taking into account both intra RF-pulse electron bunch fluctuations as well as a multitude of X-ray optical errors. These simulations revealed that by demanding feasible tolerances to the X-ray optics, in detail 100 nrad mirror alignment tolerance, 1 µm longitudinal positioning tolerance and $\sigma_h \leq 1.5\,\text{nm}$ figure error (rms) of the total reflecting mirrors of $l_M = 9\,\text{cm}$ individual length, **the simple demonstrator geometry will indeed fulfill the main experimental goal to proof effective seeding**. This still upholds when reducing the planned number of standard EuXFEL undulator modules from four to three, to account for non-ideal undulator performance.

However, by considering the crystals' thermal response to the intense heat load, it becomes evident that **the second goal of the CBXFEL demonstrator experiment, to show stable, high brilliance X-ray pulses in saturation, will not be feasible**. Even when cooling down to crystal base temperatures as low as 40 K and increasing the crystal thickness from 150 µm to 250 µm for the price of transmission, the lasing process is very unstable. Only including the thermal diffusion subfraction of the thermal response, up to millijoule pulse energies can be reached, with a lower base temperature allowing higher energies. After reaching these energies, an abrupt drop off of the circulating pulse energy occurs and the seeding process starts anew. It was shown that at the moments of drop off, the majority of pulse energy actually gets transmitted, which could principally be used in a 'passive cavity dumping' scheme. This would provide strongly fluctuating, but high brilliance X-ray pulses with a reduced repetition rate. Also, by adding longitudinally and transversely homogeneous cavity losses before the downstream crystal, the

CBXFEL demonstrator would be stabilized at reduced intensities. This would ideally be realized by means of additional outcoupling, for example by using a transmissive diamond grating. Unlike the regular crystal transmission, which only transmits the newly generated radiation outside the reflection bandwidth, the grating outcoupling would have the additional benefit of giving direct informational access to the full radiation trapped inside the cavity. **However, both 'cavity dumping' as the additional losses scheme become infeasible when accounting for the thermoelastic subfraction of the crystals' thermal response.** A superficial treatment of this highly involved effect reveals that at millijoule pulse energy levels the crystal mirrors would be strongly distorted, which would lead to high effective cavity losses, beyond the limit of stable operation.

Both the impact of the thermal diffusion as the thermoelastic subfraction of the crystals' response could be principally eased by widening the projected X-ray pulse width on the crystals. In the fixed two crystal cavity configuration, this would only be realizable by means of an asymmetric reflection crystal geometry, which would both add complexity as dispersion to the demonstrator setup. The necessity of this additional complexity is questionable, as in general, **the crystals' thermal response, which only becomes relevant at high heat load and, consistently, high pulse energies, does not impede the principle goal of the CBXFEL demonstrator.** Nonetheless, it is of high importance, to plan for **sufficient diagnostics to be able to resolve the thermal response related effects in order to develop counter measures.**

6.1 Outlook

With the CBXFEL demonstrator project being funded and planned for operation by 2023 to 2024, very practical and technical issues need to be addressed. These include the fixation of the actual focussing strength. Also, the actual shape of the diamond crystal mirrors needs to be decided on. To this end, the 2D axisymmetric simulations carried out in this thesis need to be extended to also account for effects of the finite volume and, hence, total heat capacity of the crystals as well as their shape and the resulting boundary conditions. Besides, it needs to be decided if an additional transmissive diamond grating will also be installed. This also influences the very fundamental point of necessary diagnostics, which have to fulfill a couple of demands. First, one needs to be able to diagnose the actual seeding process, which means the pulse energy evolution and spectral evolution of the X-ray pulses with the number of round trips. Second, as was emphasized above, it is necessary to resolve the thermal response related effects. And third, they need to be sufficient to enable the very strict alignment on the $\Delta\Theta = 100\,\mathrm{nrad}$ angular and 1 µm positional level. The last point goes hand in hand with the very important development of an alignment procedure.

A Electron Beam Dynamics

While this thesis strongly focusses on the radiation side of the FEL physics, some definitions and parameters relating to the electron beam will be frequently used. They shall therefore be superficially presented in this paragraph.

To begin with, it shall be noted that for the FEL we always deal with ultrarelativistic electron dynamics, meaning that the electrons move with a speed $v_e \approx c$. In this regard, two common parameters will be introduced. First the Lorentz factor

$$\gamma = \frac{E_\mathrm{e}}{m_e c^2} \tag{A.1}$$

as the ratio between the electron energy E_e and the electron mass at rest m_e will be used as a measure of energy. Also, the scaled velocity $\boldsymbol{\beta} = {}^{v}\!/_{c}$ is used, which is related to γ via

$$|\boldsymbol{\beta}| = \beta = \sqrt{1 - {}^{1}\!/_{\gamma^2}}. \tag{A.2}$$

The electron dynamics are expressed in a six-dimensional phase space, consisting of the three position and three momenta degrees of freedom. Adapting a coordinate system where the motion of the electrons is primary directed along an axis $\hat{z}$, these phase space coordinates can be usually expressed as a function of the longitudinal position z in the accelerator. As, especially in a linear accelerator such as the European XFEL, the longitudinal and transverse degrees of freedom differ considerably, it is additionally convenient to divide the phase space into transverse degrees and longitudinal degrees of freedom. The transverse position will be noted as $\boldsymbol{x} = (x, y)$ and the transverse momentum will be expressed as angle $\boldsymbol{x}' = (x', y')$ to the longitudinal axis $\hat{z}$. The longitudinal position will be noted as s, which is the longitudinal distance to a reference particle, and the longitudinal momentum as $\Delta\gamma$, which is the difference in energy with respect to the energy of the same reference particle.

As we are usually not interested in an individual particle but in an electron bunches of typical charges of 1 pC to 1 nC and therefore N_e ~10×10^7 to 10×10^{10} particles, parameters relating to the full electron phase space distribution shall be used. As such the nth order moments $\langle i^n \rangle = \sum_j i^n / N_e$ of a parameter i averaged over the full distribution will usually be used. Choosing the reference trajectory such that the average motion of the electrons is along $\hat{z}$ the first momenents of the transverse position $\boldsymbol{x} = (x, y)$ and transverse slope $\boldsymbol{x}' = (x', y')$ with respect to the $\hat{z}$ axis will vanish:

$$\langle \boldsymbol{x} \rangle = \frac{1}{N_e} \sum_j \boldsymbol{x}_j = \langle \boldsymbol{x}' \rangle = \frac{1}{N_e} \sum_j \boldsymbol{x}'_j = 0$$

On the other hand, the root-mean-square (rms) moments

$$\sigma_x^2 = \langle \boldsymbol{x}^2 \rangle \neq 0, \quad \sigma_{x'}^2 = \langle \boldsymbol{x}'^2 \rangle \neq, \quad \langle \boldsymbol{x}\boldsymbol{x}' \rangle \neq 0 \tag{A.3}$$

persist. For a electron bunch under linear transport – meaning only elements are considered which a only linearly dependent on the phase-space coordinates are considered – it is meaningful to introduce the *geometric emittance*

$$\epsilon_{i=(x|y)} = \sqrt{\sigma_i^2 \sigma_{i'}^2 - \langle ii' \rangle^2}. \tag{A.4}$$

The emittance quantizes the phase space area occupied by an electron and is therefore, following Louisville's theorem, invariant under linear transport. As such it is evident, that for decreasing the beam size σ_x one has to increase the beam divergence $\sigma_{x'}$ and vice versa. Relating to the emittance $\epsilon_{x,y}$, it is convenient to express the so-called *Courant-Snyder* or *Twiss*-parameters[102]

$$\beta_x = \frac{\sigma_x^2}{\epsilon_x}, \quad \gamma_x = \frac{\sigma_{x'}^2}{\epsilon_x} \quad \text{and } \alpha_x = -\frac{\langle xx' \rangle}{\epsilon_x} = -\frac{1}{2}\frac{\partial \beta}{\partial z}. \tag{A.5}$$

While the emittance is an inherent property of the electron beam, the Twiss parameters can be considered properties of the magnetic lattice and are often adjusted to produce the desired beam size or divergence.

B The European XFEL

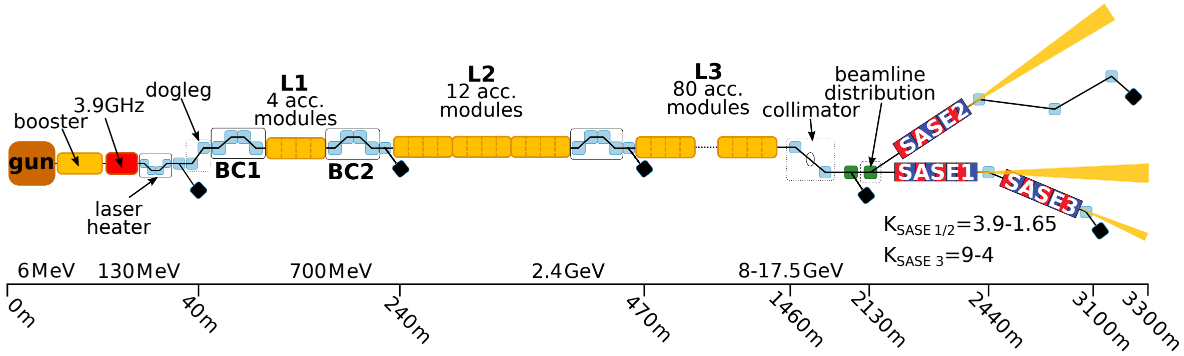

Figure B.1: Schematic layout of the European XFEL. The orange boxes indicate the 1.3 GHz accelerating modules, the red-blue boxes the undulators, blue boxes the main dipoles, the green box the beamline distribution kicker and the black boxes the beam dumps. Figure adapted from [225], under a Creative Commons licence (`https://creativecommons.org/licenses/by/3.0/`).

The *European X-ray Free-Electron Laser* (EuXFEL) is an X-ray free electron laser for soft and hard X-rays, covering photon energies in the range 0.25 keV to 25 keV [208]. The photons are generated in three (potentially five [226]) undulator beamlines (SASE1,SASE2 and SASE3) [208], which serve seven distinct experimental stations (see Figure (B.2)). The European XFEL is operated in pulsed mode, with up to 2700 electron bunches being accelerated with an up to 4.5 MHz repetition rate within one 600 µs long RF-pulse, which is repeated every 10 ms [208]. First lasing and first user operation in the SASE1 beamline was achieved in

---

[102] Unfortunately as well the β as the γ-parameter use the same symbol as the scaled electron velocity and the Lorentz-factor. But as this notation is the commonly used, it shall also be adapted in this thesis.

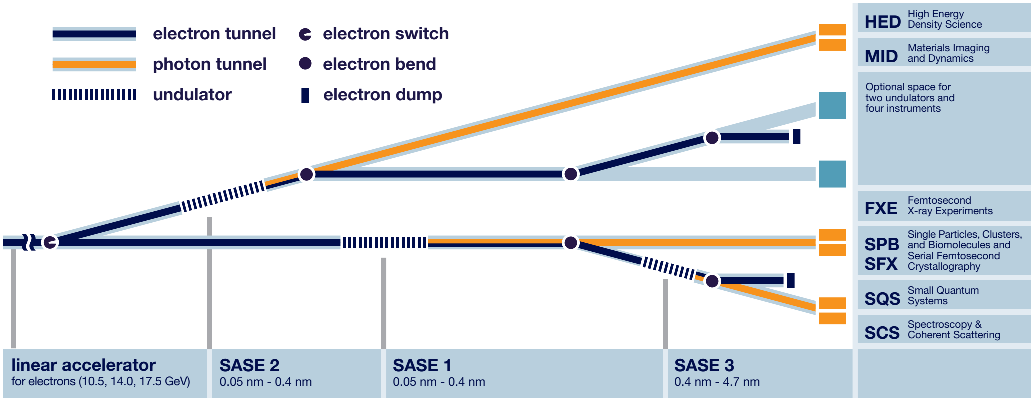

Figure B.2: Conceptual layout of the photon beamlines at the European XFEL with the (currently operational) experimental stations. Credit: European XFEL GmbH

2017 [208, 225]. Figure (B.1) shows a schematic overview of the accelerator and the photon beam systems, which have a total length of 3.3 km.

The photo-injector, as starting point of the 20 pC to 1000 pC electron bunches being accelerated, is a normal conducting 1.6 cell 1.3 GHz L-band cavity, with a Cs_2Te photo-cathode inserted at the back plane, which is illuminated by a 257 nm UV-laser pulses [208, 227]. It is of the same type as used for the *Free-Electron Laser in Hamburg* (Flash) facility [228]. It is followed by a TESLA-type superconducting 9-cell 1.3 GHz accelerating module [229], cooled to 2 K, which accelerates the electron bunches to $\sim$130 MeV [227] and a third harmonic 3.9 GHz module to manipulate the longitudinal phase space of the bunches and, mainly, to linearize the energy profile [208, 227]. The injector is completed by a laser heater, a diagnostics station and an electron dump [208].

The bunch compression is done in three tunable stages, with the final peak current being reaching up to several kiloampere, typically $I_p \approx 5\,\mathrm{kA}$ [205, 208]. The actually linac, which consists of a total 96 superconducting TESLA-type accelerating modules, is divided into three parts by the bunch compressors, called L1, L2 and L3. L1 consists of four modules, powered by a single 10 MW klystron, which accelerate the electrons by ΔE_1 =570 MeV to E_1 =700 MeV [205]. In L2, which is composed of 12 accelerating modules powered by 3 klystrons, the beam energy is further increased by ΔE_2=1700 MeV to E_2 =2400 MeV [205]. In the up to 80 accelerating modules of L3, powered by 20 10 MW klystrons, the electrons are accelerated to their final beam energy of E_{final}=8 GeV to 17.5 GeV [208]. After a linac, a collimator is used to protect the downstream hardware.

The distribution of the electron bunches to the two undulator beamlines displayed in Figure (B.1) is achieved using two fast-rise, high-precision kickers. One downstream to deliver the electron to the specific beamline, and one upstream to dump the bunches if required. Both together allow for a freely adjustable bunch pattern in the undulator beamlines, without demanding an adjustment of the linac parameters [208].

Both hard X-ray FEL systems, SASE 1 and SASE2, make use of multiple 5 m long, 40 mm period, variable gap undulator segments, which each are separated by 1.1 m sections filled with

quadrupole magnets for focussing, electron beam position monitors (BPMs), permanent magnet phase shifters and air coils [208, 230]. The variable undulator gap, which has an operational tunability of 10 mm to 20 mm, allows for adjust the undulator parameter in the range $K_{\mathrm{SASE1/2}}$ =1.65 to 3.9 with an accuracy better than $|\Delta K_{\mathrm{und}}|/K_{\mathrm{und}} < 2 \times 10^{-4}$, thereby setting the photon energy λ_l =0.5 Å to 4 Å (see equation (2.49)) [230]. The SASE1 beamline, which is also where the CBXFEL demonstrator experiment will be positioned (see Chapter **5**), consists of 35 of such segments, which have a total length of 213.5 m. It will serve the FXE and SPB/SFX instruments. The SASE2 FEL line, which produces photons for the HED and MID instruments, is conceptually identical to the SASE1 line, also consisting of 35 individual undulator segments. As of 2019, the SASE2 beamline also hosts a two-stage transmissive hard X-ray self-seeding setup (HXRSS) [19, 203], which promises to deliver longitudinal coherent, wavelength tunable hard X-ray radiation. It consists of two variable offset magnetic chicanes, each with a monochromator chamber in the center, which hosts two interchangeable diamond crystals, which can be varied in a wide angular range [204].
The SASE3 FEL beamline is delivering photons in the soft X-ray regime with λ_l $\in$0.4 nm to 4.7 nm to the SCS and SQS instruments. To do so, the undulators are slightly different in comparison to the SASE1/2 undulators, with a undulator period of λ_u =68 mm and gap tunable in the range 10 mm to 25 mm. However, the module configuration is unchanged, with 5 m length of the undulator segments and 1.1 m spacing in between. The SASE3 line consists of 21 of such modules [231]. As visible in Figure (B.1) and Figure (B.2), it is located downstream in the same electron beamline as SASE1. In order to keep the lasing quality high, a *betratron switching fresh bunch* scheme is applied, where the beam distribution kicker upstream of SASE1 is introducing betraton oscillations in the electron bunch at SASE1, thereby suppressing lasing, which is then corrected upstream of SASE3 [232].

C Mirror assembly

For the CBXFEL demonstrator only grazing incidence mirrors are foreseen beside the crystal 'Bragg' mirrors, which are thoroughly described in Section **3.1**. These are very common optical elements, which shall not be further described here. However, it is planned to assemble these mirrors in two uncommon ways, precisely in a retroreflecting (for the two grazing incidence and the crystal mirror per monochromator chamber) and a 'Montel' (for the two grazing incidence mirrors) arrangement. In the following, the basic notations and orientations of the mirror assembly shall be highlighted. Then the concept of retroreflectivity shall be explained in more detail and, at last, the Montel setup shall be further highlighted.

C.1 Geometry and notation

In Figure (C.1) the mirror assembly is sketched as planned for the CBXFEL demonstrator experiment. The two grazing incidence, total reflecting mirrors and the crystal mirror are each

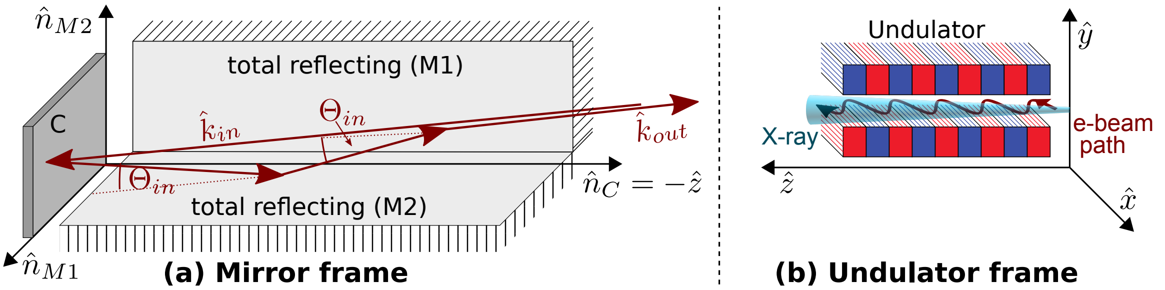

Figure C.1: Schematics of the mirror assembly as planned for the CBXFEL demonstrator experiment with its respective coordinate system, called *mirror frame* (a) as well as the coordinate system in the *undulator frame*. It consists of one crystal mirror (C) and two grazing incidence, total reflecting mirrors (M1 and M2) in Montel geometry (see below **C.3**). The individual mirrors are oriented perpendicular to each other, forming a retroreflector (see below **C.2**). The orientation of the assembly is such, that both M1 and M2 form an grazing angle of Θ_{in} with respect to the nominal ray $\boldsymbol{k}_{in} = \boldsymbol{k}_0$. Latter is set as being parallel to the undulator axis ($\hat{\boldsymbol{z}}$ in the undulator frame).

oriented perpendicular to each other, forming a retroreflector (see below **C.2**). The mirrors are assumed as perfectly flat, neglecting the deliberately introduced surface curvature to archive focussing. This is well justified, as the radius of curvature are on the multiple kilometer scale (see Section **5.1**) and are therefore very big in relation to the size of the assembly on the centimeter scale.

For the discussion of this assembly, it is useful to define two different coordinate systems. One is the *mirror frame*, sketched in Figure (C.1(a)), and the other is the *undulator frame* sketched in Figure (C.1(b)), in which the $\hat{z}$-axis is equal to the undulator axis. Before the first reflection, the undulator frame coordinate system is equal to the photon pulse internal coordinate system. The orientation of the mirror normals in the mirror frame (m) is defined as

$$\hat{\boldsymbol{n}}_{M1}^{(m)} = \begin{pmatrix} \cos(\alpha) \\ \sin(\alpha) \\ 0 \end{pmatrix}, \qquad \hat{\boldsymbol{n}}_{M2}^{(m)} = \begin{pmatrix} -\sin(\alpha) \\ \cos(\alpha) \\ 0 \end{pmatrix}, \qquad \hat{\boldsymbol{n}}_{C}^{(m)} = \begin{pmatrix} 0 \\ 0 \\ -1 \end{pmatrix}, \tag{C.1}$$

where $M1$ and $M2$ refer to the total reflecting mirrors and C to the crystal mirror. α is an angle noting the orientation of the total reflecting mirrors with respect to the crystal mirror. It will have some importance in defining the mirror aperture as done for the Montel geometry.

The reflection operation $\mathcal{S}_i$ carried out by the individual mirrors be expressed in matrix notation $\mathcal{S} : \boldsymbol{k}_{in} = \mathbb{S}\boldsymbol{k}_{in} = \boldsymbol{k}_{out}$ with the hermetian, unitary reflection matrix $\mathbb{S} = \mathbb{1} - 2\hat{\boldsymbol{n}}\hat{\boldsymbol{n}}^T$. $\mathbb{1}$ is the 3×3 unity matrix and $\hat{\boldsymbol{n}}$ is the mirror normal. For the mirror normals, expressed in equation (C.1), this becomes

$$\mathbb{S}_{M1} = \begin{pmatrix} \cos(2\alpha) & -\sin(2\alpha) & 0 \\ -\sin(2\alpha) & \cos(2\alpha) & 0 \\ 0 & 0 & 1 \end{pmatrix}, \tag{C.2a}$$

$$\mathbb{S}_{M2} = \begin{pmatrix} \cos(2\alpha) & \sin(2\alpha) & 0 \\ \sin(2\alpha) & -\cos(2\alpha) & 0 \\ 0 & 0 & 1 \end{pmatrix}, \tag{C.2b}$$

$$\mathbb{S}_{C} = \begin{pmatrix} 1 & 0 & 0 \\ 0 & 1 & 0 \\ 0 & 0 & -1 \end{pmatrix}. \tag{C.2c}$$

Noting that the undulator orientation is fixed, the relation of the mirror frame with respect to the undulator frame is specified by the rotation of the mirror assembly with respect to the undulators. This reflection is defined here in terms of the *pitch-roll-yaw convention* as shown in Figure (C.2). Currently, it is foreseen to keep the *yaw* angle fixed. So it will be set dropped in the following. The rotation $\mathbb{R}_{MU}$, transforming from the mirror frame (m) into the undulator frame (u) $\boldsymbol{r}^(u) = \mathbb{R}_{MU}\boldsymbol{r}^(m)$ is then defined as

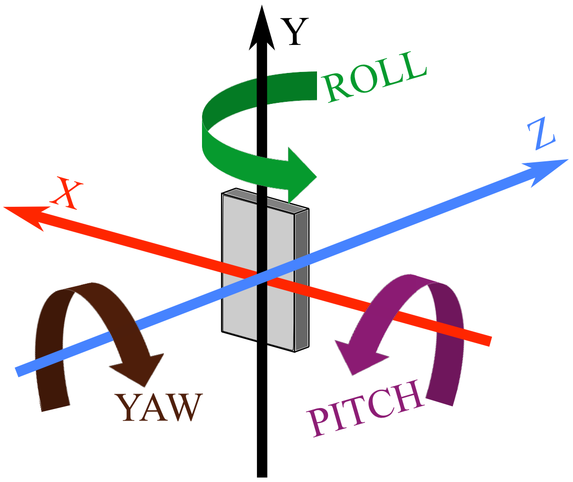

Figure C.2: The pitch-roll-yaw convention used for setting up the crystal with respect to the photon pulse. The coordinate system at zero rotation coincides with the undulator frame coordinate systems and, hence, with the photon pulse' internal coordinate system. It is important to note, that a pitch angle of $P = 90°$ refers to zero rotation and a positive ΔP means a counter-clockwise rotation. This is done in order to ensure consistency with the Bragg angle

$$\mathbb{R}_{MU} = \begin{pmatrix} \cos(R) & 0 & \sin(R) \\ \sin(R)\cos(P) & \sin(P) & -\cos(P)\cos(R) \\ -\sin(P)\sin(R) & \cos(P) & \sin(P)\cos(R) \end{pmatrix}, \tag{C.3}$$

where P is the pitch and R is the roll angle. The inverse transformation $\boldsymbol{r}^(m) = \mathbb{R}_{UM}\boldsymbol{r}^(u)$ from the undulator (u) into the mirror frame (m) is set by the matrix

$$\mathbb{R}_{UM} = \mathbb{R}_{MU}^{T} = \begin{pmatrix} \cos(R) & \sin(P)\cos(R) & -\sin(P)\sin(R) \\ 0 & \sin(P) & \cos(P) \\ \sin(R) & -\cos(P)\cos(R) & \sin(P)\cos(R) \end{pmatrix}. \tag{C.4}$$

The angles P and R are fully set by requesting that the beam $\boldsymbol{k}_0^{(u)} = (0,0,1)$ forms an angle of Θ_{in} with both total reflecting mirrors M1 and M2 after reflection at the crystal C. By applying the transformation (C.4) and the reflection (C.2c), the beam $\boldsymbol{k}_0$ becomes

$$\boldsymbol{k}_{0,R}^{(m)} = \mathbb{S}_C \mathbb{R}_{UM} \begin{pmatrix} 0 \\ 0 \\ 1 \end{pmatrix} = \mathbb{S}_C \begin{pmatrix} -\sin(P)\sin(R) \\ \cos(P) \\ \sin(P)\cos(R) \end{pmatrix} = \begin{pmatrix} -\sin(P)\sin(R) \\ \cos(P) \\ -\sin(P)\cos(R) \end{pmatrix}. \tag{C.5}$$

By requesting that the reflected $\boldsymbol{k}_{0,R}^{(m)}$ forms the same grazing angle Θ_{in} with both mirrors M1 and M2 ($\boldsymbol{k}_{0,R} \cdot \hat{\boldsymbol{n}}_{M1} \doteq \boldsymbol{k}_{0,R} \cdot \hat{\boldsymbol{n}}_{M2} \doteq -\sin(\Theta_{in})$), one yields for the pitch and roll angles[103]

$$P = \cos^{-1}\left(-\sqrt{2}\sin\left(\Theta_{in}\right)\sin\left(\alpha + \frac{\pi}{4}\right)\right) \tag{C.6}$$

$$\begin{aligned} \text{and} \quad R &= \sin^{-1}\left(\frac{\sqrt{2}\sin\left(\Theta_{in}\right)\cos(\alpha + \frac{\pi}{4})}{\sqrt{1 - 2\sin^2\left(\Theta_{in}\right)\sin^2(\alpha + \frac{\pi}{4})}}\right) \\ &\approx \sin^{-1}\left(\sqrt{2}\sin\left(\Theta_{in}\right)\cos(\alpha + \frac{\pi}{4})\right), \end{aligned} \tag{C.7}$$

where for the last step it was approximated that $\Theta_{in}^3 \approx 0$.

To clarify the question, how the finite size of the mirrors enact on the photon pulse, one must understand how latter projects on the mirror. To do so, it will be approximated that the photon pulse is completely described by a single wavevector $\boldsymbol{k}_{in} = \boldsymbol{k}_0 = (0,0,1)_u$. This is well justified, considering that the distances between the individual mirrors will be small and the X-ray pulse divergence is on the single microradian scale. Neglecting the longitudinal length of the pulses, the X-ray field incident on the crystal mirrors can then be represented by the collection of rays $\boldsymbol{r}$ following the parametrization

$$\boldsymbol{r}^{(u)}(t) = \begin{pmatrix} x_B \\ y_B \\ 0 \end{pmatrix} + t \cdot \underbrace{\begin{pmatrix} 0 \\ 0 \\ 1 \end{pmatrix}}_{\boldsymbol{k}_0^{(u)}},$$

where x_B and y_B are the pulse's internal $\hat{\boldsymbol{x}}$ and $\hat{\boldsymbol{y}}$ coordinates and t is an arbitrary real number denoting the length of the vector. After reflection at the crystal mirror, this becomes in the mirror

---

[103] The step by step solution is rather lengthy without providing much physical insight. Therefore, it will be omitted here.

frame

$$\begin{aligned}\boldsymbol{r}_C^{(m)}(t) =&\boldsymbol{r}^{(u)}(t'=0) + t\cdot\mathbb{S}_C\boldsymbol{k}_0^{(m)}\\ =&\begin{pmatrix} x_B\\ y_B\\ 0\end{pmatrix} + t\cdot\underbrace{\begin{pmatrix} -\sqrt{(2)}\sin(\Theta_{in})\cos\left(\alpha+\frac{\pi}{4}\right)\\ -\sqrt{(2)}\sin(\Theta_{in})\sin\left(\alpha+\frac{\pi}{4}\right)\\ \sin^2(\Theta_{in})-1\end{pmatrix}}_{\mathbb{S}_C\boldsymbol{k}_0^{(m)}}.\end{aligned}$$

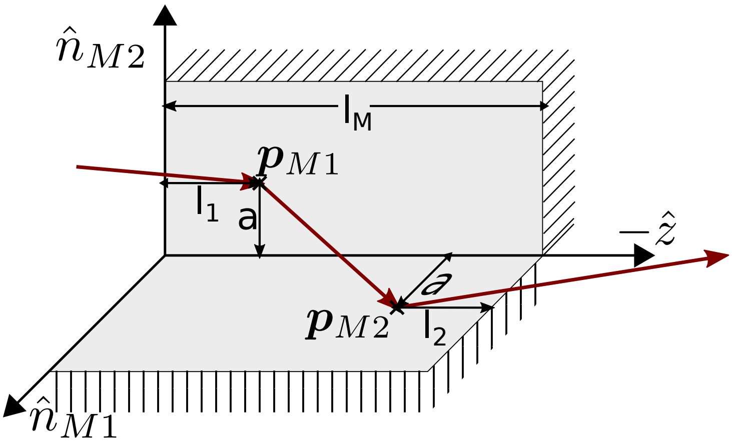

Figure C.3: Sketch of scales of the mirror assembly in relation to the incoming X-ray beam.

In order to relate the mirrors to the beam, the respective position needs to be fixed. It will, without loss of generality, be assumed that the central ray with $x_B = y_B = 0$ coincides with the first mirror at the position

$$\boldsymbol{p}_{M1}^{(m)} = a\hat{\boldsymbol{n}}_{M2} + l_1\hat{\boldsymbol{n}}_C^{(m)}, \tag{C.8}$$

as sketched in Figure (C.3). Knowing that the X-ray pulse makes per definition an grazing angle of Θ_{in} with both total reflecting mirrors, and defining that both mirrors intersect on the $\hat{\boldsymbol{z}}^{(m)}$ axis, one can easily derive for the intersection with the second mirror

$$\boldsymbol{p}_{M2}^{(m)} = a\hat{\boldsymbol{n}}_{M1} + \left(a\frac{\cos^2(\Theta_{in})}{\sin(\Theta_{in})} + l_1\right)\hat{\boldsymbol{n}}_C^{(m)}. \tag{C.9}$$

For the projections of the rays $\boldsymbol{r}_C^{(m)}(t)$ with the mirrors, one can employ the vector-plane intersection formula $\boldsymbol{r}_C^{(m)}(t')\hat{\boldsymbol{n}}_{Mi}^{(m)} = 0$ in the normal form, where it is assumed for now that the mirrors extent to infinity. Also, the central intersection points $\boldsymbol{p}_{Mi}$ can added be by means of a simple translation, as $\boldsymbol{p}_{Mi}\hat{\boldsymbol{n}}_{Mi} = 0$. This leads to

$$\boldsymbol{r}_{onM1}\left(x_B, y_B\right) = \begin{array}{l} \left[a - x_B\sqrt{2}\sin\left(\alpha + \frac{\pi}{4}\right) + \sqrt{2}y_B\cos\left(\alpha + \frac{\pi}{4}\right)\right]\boldsymbol{n}_{M2} \\ + \left[l_1 + \dfrac{x_B\cos(\alpha) + y_B\sin(\alpha)}{\sin(\Theta_{in})}\right]\hat{\boldsymbol{n}}_C \end{array} \tag{C.10}$$

$$\boldsymbol{r}_{onM2}\left(x_B, y_B\right) = \begin{array}{l} \left[a - x_B\sqrt{2}\sin\left(\alpha + \frac{\pi}{4}\right) + \sqrt{2}y_B\cos\left(\alpha + \frac{\pi}{4}\right)\right]\boldsymbol{n}_{M1} \\ + \left[l_1 + \dfrac{a\cos(\Theta^2) - x_B\sin(\alpha) + y_B\cos(\alpha)}{\sin(\Theta_{in})}\right]\hat{\boldsymbol{n}}_C. \end{array} \tag{C.11}$$

For the projection on the second mirror M2, it was used that the beam was once reflected on M1, which leads to a factor -1 in the term parallel to $\hat{\boldsymbol{n}}_{M1}$. Anyhow, due to the mirror symmetry of the system, such a factor -1 is principally negtlable. Defining the entire length of the mirror assembly as l_M in accordance with Figure (C.3), one can express the $\hat{\boldsymbol{z}}$ projection on the mirror in the form of an rectangular aperture (4.11):

$$f_{M1M2} = f_{rect}\left(\begin{array}{l} x' = \boldsymbol{x}_\perp\hat{\boldsymbol{n}}_{M1}, y' = \boldsymbol{x}_\perp\hat{\boldsymbol{n}}_{M2}, x'_0 = -l_1\sin(\Theta), \\ y'_0 = -l_1\sin(\Theta_{in}) + a\cos^2(\Theta_{in}), w_x = w_y = l_M\sin(\Theta_{in}) \end{array}\right), \tag{C.12}$$

$$\text{with} \qquad f_{rect}(x', y', x'_0, y'_0, w_x, w_y) = \operatorname{rect}\left(\frac{x' - x'_0}{w_x}\right)\operatorname{rect}\left(\frac{y' - y'_0}{w_y}\right),$$

where $\boldsymbol{x}_\perp = (x_B, y_B, 0)$ was introduced. From above equation it directly follows that the center of the aperture shifts with the intersection point $\boldsymbol{p}_{M1}^{(m)} = a\hat{\boldsymbol{n}}_{M2} + l_1\hat{\boldsymbol{n}}_C^{(m)}$. Assuming that the X-ray pulse is approximately circular symmetric around $\boldsymbol{x}_\perp = 0$, it is obvious that the aperture is having the least influence, if $l1 = l_m/2$ and $a = 0$. As this also means that the center of the pulse is directly incident on the axis where the both mirrors intersect, this also comes with a downside. This shall be further discussed in the Section about the Montel geometry **C.3**.

C.2 Retroreflector

In Figure (C.4) a retroreflecting setup is sketched, which consists of two total reflecting, grazing incidence mirrors and one crystal mirror. By aligning these mirrors perfectly perpendicular to each other, the rays reflected by this setup will always be perfectly antiparallel to the incoming ones[104]. This can be easily proven by vector analysis. Using the general form of the reflection matrix $\mathbb{S}_i = \mathbb{1} - 2\hat{\boldsymbol{n}}_i\hat{\boldsymbol{n}}_i^T$ and noting that $\hat{\boldsymbol{n}}_i\hat{\boldsymbol{n}}_{j\neq i} = 0$ for three perpendicular mirrors i, j, then $\mathbb{S}_{\text{ass.}} = \mathbb{S}_3\mathbb{S}_2\mathbb{S}_1 = -\mathbb{1}$. It directly follows, that any incoming ray with wavevector $\boldsymbol{k}_{in}$ will be transformed to $\boldsymbol{k}_{out} = \mathbb{S}_{\text{ass.}}\boldsymbol{k}_{in} = -\boldsymbol{k}_{in}$. Hence, as noted above, the reflected ray will always be antiparallel to the incoming one, no matter the initial orientation. The same also

---

[104] This property is obviously restricted by the finite angular acceptance of the incoming rays. This finite acceptance is, anyhow, on the milliradian scale and, hence, much less demanding than the $\Delta\Theta \approx$100 nrad required by the X-ray optical cavity (see Subsection **5.2.2.2**)

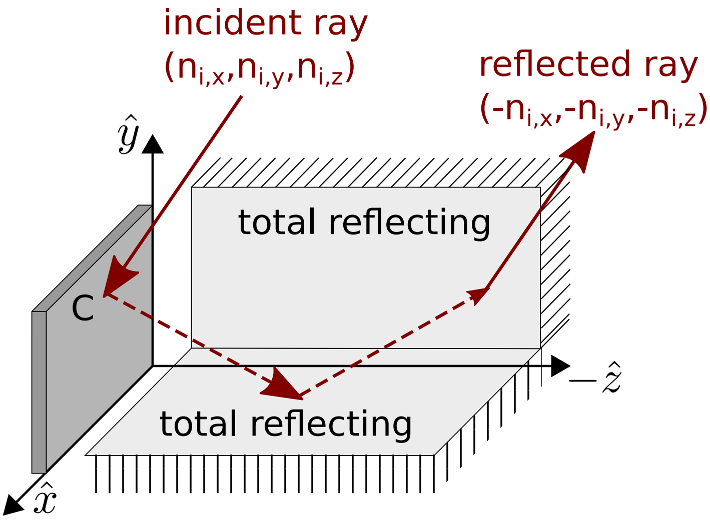

Figure C.4: Schematics of a 3D retroreflector, where three mirrors (two grazing incidence, total reflecting ones and one crystal (C) mirror) are assembled perpendicular to each other. In this way, the reflected ray will always be antiparallel to the incoming one, given it remains in the angular acceptance of the individual mirrors. The sketched angles are strongly exaggerated compared to the real case for better visual representation.

holds for the three perpendicular mirror orientations of the demonstrator setup as written down in equation (C.1). The use of these orientations can therefore decouple the entire setup from outer vibrations, meaning variations in the incoming wavevector $\boldsymbol{k}_{in} = \boldsymbol{k}_0 + \Delta\Theta \boldsymbol{n}_\perp$, with $\boldsymbol{k}_0$ being a nominal orientation, which is reflected back to itself, and $\boldsymbol{n}_\perp \perp \boldsymbol{k}_0$. This is unlike the action of a single mirror, for which the reflected ray $\boldsymbol{k}_{out} = \mathbb{S}_{\text{single}}\boldsymbol{k}_{in}$ will form an angle $\measuredangle(\boldsymbol{k}_{in}, \boldsymbol{k}_{out}) \approx \pi - 2\Delta\Theta$ with the incoming one. However, it should be emphasized, that it does not decouple against the motions of a single mirror inside the setup, as this breaks the perpendicularity of the system.

Obviously, above assumption about perfectly perpendicular mirror orientations are idealistic. It will be shown, however, that also under influence of a *dyadic error* $\Delta\alpha$, meaning an angular shift away from the perpendicular orientation, the tolerance towards angular variation of $\boldsymbol{k}_{in}$ can be significantly enhanced.

For the planned setup, the orientation between the total reflecting mirrors will be fixed, whereas the orientation of the crystal with respect to them will be tunable to a certain degree. Therefore, it will be assumed, without loss of generality, that the dyadic error will be present in the orientation of the second total reflecting mirror

$$\boldsymbol{n}'_{M2} = \begin{pmatrix} \sin(\alpha+\Delta\alpha) \\ -\cos(\alpha+\Delta\alpha) \\ 0 \end{pmatrix} \approx \begin{pmatrix} \sin(\alpha) \\ -\cos(\alpha) \\ 0 \end{pmatrix} + \Delta\alpha \begin{pmatrix} \cos(\alpha) \\ \sin(\alpha) \\ 0 \end{pmatrix} = \boldsymbol{n}_{M2} + \Delta\alpha \boldsymbol{n}_{M1},$$

which gives a reflection matrix of

$$\mathbb{S}'_{M2} =\approx \mathbb{S}_{M2} + 2\Delta\alpha \begin{pmatrix} \sin(2\alpha) & \cos(2\alpha) & 0 \\ \cos(2\alpha) & \sin(2\alpha) & 0 \\ 0 & 0 & 0 \end{pmatrix}.$$

For above equations, it has been approximated that $\Delta\alpha^2 \approx 0$[105]. It can be generally shown, that the product of any three reflection matrices $\mathbb{S}_{\text{ass.}}$, no matter how oriented they may be, has one specific eigenvalue of $A = -1$ [41, ch.2.10.1][106]. This means, that the corresponding eigenvector $\boldsymbol{k}_0$ will return antiparellel to itself after reflection. For the present set of reflection matrices $\mathbb{S}_{\text{ass.}} = \mathbb{S}'_{M2}\mathbb{S}_{M1}\mathbb{S}_C$, $\boldsymbol{k}_0 = (0, 0, 1)$. However, the actual $\boldsymbol{k}_0$, corresponding to an eigenvalue of -1, can be set by appropriately adjusting the orientation of the crystal mirror. The actual rotation for doing so is rather complicatedly dependent on $\alpha, \Delta\alpha$ and the desired $\boldsymbol{k}_0$. It will usually be numerically set such that $\boldsymbol{k}_0$ becomes equal to the undulator axis, as was already discussed in more detail in the last section about the mirror geometry.
Now assuming an incoming vector

$$\boldsymbol{k}_{in} = \boldsymbol{k}_0 + \Delta\Theta\hat{x},$$

which is the same as assuming a tilt of the mirror in the roll angle by $\Delta R = \Delta\Theta$, this becomes

$$\boldsymbol{k}_{out} = \mathbb{S}'_{\textbf{ass.}}\boldsymbol{k}_{in} \approx -\boldsymbol{k}_{in} - \begin{pmatrix} 0 \\ 2\Delta\alpha\Delta\Theta \\ 0 \end{pmatrix}.$$

For the angular 'error' after reflection, which is defined as the angle between the actual reflected ray and the ideally reflected ray $\Delta\Theta_{out} = \measuredangle\left(-\boldsymbol{k}_{in}, \boldsymbol{k}_{out}\right)$, one then calculates

$$\Delta\Theta_{out} = \cos^{-1}\left(\frac{-\boldsymbol{k}_{in}\cdot\boldsymbol{k}_{out}}{|\boldsymbol{k}_{in}||\boldsymbol{k}_{out}|}\right) \approx \cos^{-1}\left(\frac{1}{\sqrt{1+(2\Delta\alpha\Delta\Theta)^2}}\right) \approx 2\Delta\Theta\Delta\alpha, \tag{C.13}$$

where again it was approximated that $\Delta\alpha^2 \approx 0$. This means that a variation of the incoming radiation beam with respect to the mirror assembly can be compensated by roughly a factor $2\Delta\alpha$. Assuming a feasibility of the the dyadic error on the order $\Delta\alpha \tilde{<} 2\,\text{mrad}$, as told by commercial manufacturers, a $\tilde{<} 4E-3$ reduction in angular error can be achieved. In Figure (C.5) the angular error $\Delta\Theta_{out}$ is plotted in dependence of the angular variation $\Delta\Theta_{in}$ with respect to the eigenvector $\boldsymbol{k}_0$. The solid lines correspond to numerical vector analysis of a more general mirror orientation and the dashed lines to the equation (C.13). Both curves agree very well, showing the reliability of approximation (C.13).

C.3 Montel Mirror

For the CBXFEL demonstrator experiment it is planned to assemble the grazing incidence total reflecting mirrors in a nested *Montel* geometry (see **5.1**). As sketched in Figure (C.6(a)), in this

---

[105] It should be noted, that with this small angle approximation the reflection matrix is not unitary any more. This is fine, as long as the vectors are appropriately normed after reflection

[106] For the perfect retroreflector all three eigenvalues A, B and C become -1 and, hence, all vectors, being a linear combination of the corresponding set of eigenvectors, return antiparallel to themselves.

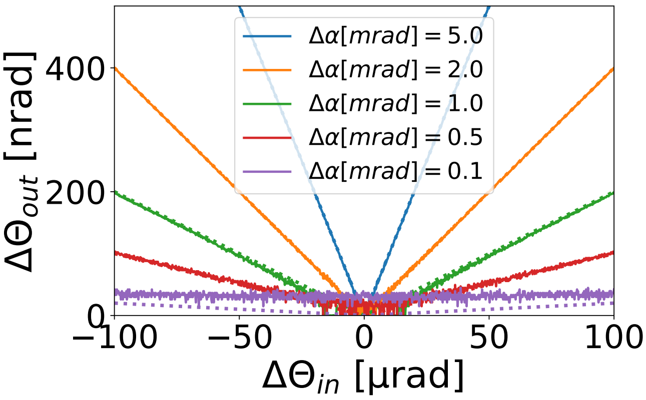

Figure C.5: Influence of the diadic error on the retroreflector compensation. The solid lines correspond to numerical vector analysis, where the orientation of the crystal mirror was tuned such that the beam $\boldsymbol{k}_0$ coinciding with the undulator axis gets reflected back to itself after total reflection and would make an angle of $\Theta_i = 3.1\,\mathrm{mrad}$ with both total reflecting mirrors after reflection at the crystal for the case of $\Delta\alpha = 0$. The dashed lines correspond to the approximation (C.13). The agreement is surprisingly good, except for $\Delta\alpha$ =0.1 mrad, where the numeric results becomes very noisy due to rounding errors.

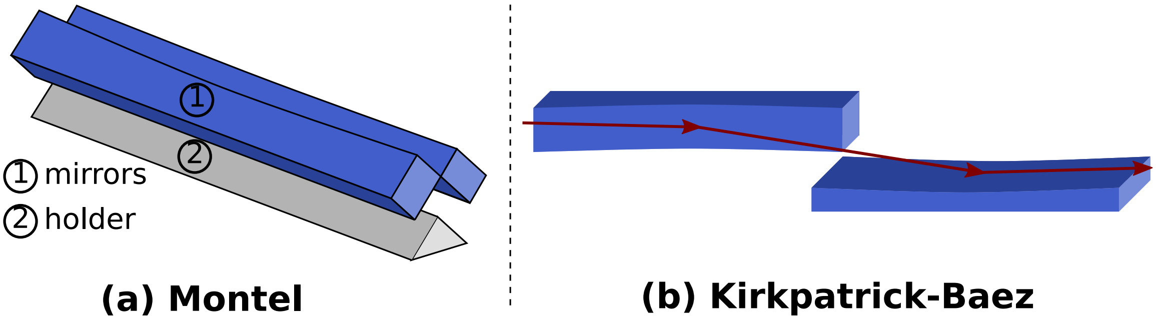

Figure C.6: Sketch of a nested *Montel* geometry (a), where two mirrors are mounted perpendicular to each other on a common holder, as well as of a common *Kirkpatrick-Baez* geometry (b), where both mirrors are independent.

geometry two total reflecting mirrors are mounted on a common holder at a (nominally) right angle with respect to each other. This is in contrast to the Kirkpatrick-Baez (KB) assembly, where two (focussing) grazing incidence mirrors are individually mounted at tunable. The Montel geometry has some advantages compared to the KB one. For one, by mounting both mirrors on a common holder at right angles, hence fulfilling the retroreflector requirement, the complexity of the system is significantly reduced compared to the KB geometry. Im the latter, both mirrors need to be aligned individually, which obviously adds many degrees of freedom and therefore complexity to the alignment procedure. On the other hand, this theoretically allows to position them truly perpendicular to each other, whereas in the Montel geometry the angle between the two mirrors and, hence, also any dyadic error $\Delta\alpha$ is fixed after mounting. However, as was discussed in the prior section, keeping $\Delta\alpha$ reasonably small with $\Delta\alpha \tilde{<} 2\,\mathrm{mrad}$, the impact on the retroreflecting properties are very small.

Another advantage of the Montel geometry is that it is much less bulky than the KB one. For one it only needs one holder instead of two. And second, by centering the photon beam on the intersection between the two mirrors and on their longitudinal middle, half the length of the assembly can achieve the same aperture size as for the KB geometry. This was already discussed with respect to the aperture function (C.12). However, centering the photon pulse on the intersection comes with a severe downside. Depending on the mounting procedure, both a physical gap as well as an area of elevated roughness of width $w_{\text{gap}} \gtrsim 5$ µm can be found at the intersection [199]. The beam incident on this area is effectively lost. Hence, this can be regarded as an absorbing stripe introducing the aperture function

$$\begin{aligned} f_{gap} &= 1 - f_{\text{stripe}}\left(x_B, y_B, c = -\frac{w_{gap}/2 + a}{\sqrt{2}}, \Theta = \alpha + \frac{\pi}{4}, \frac{w_{gap}}{\sqrt{2}}\right) \qquad \text{(C.14)} \\ \text{with} \qquad f_{stripe}(x, y, c, \Theta, l) &= \text{rect}\left(\frac{-x \sin\Theta + y \cos\Theta - c}{l}\right). \end{aligned}$$

a is the shortest distance from the intersection to the point where the center of the X-ray beam ($\boldsymbol{x}_\perp = (0, 0)$) intersects with the first mirror. In Figure (C.7) the slit function is plotted together with the aperture function (C.12) for different positions $\boldsymbol{p}_{M1} = a\hat{\boldsymbol{n}}_{M1} + l_1\hat{\boldsymbol{n}}_C$ of the X-ray beam center on the mirrors. The left and middle plot are the 'extreme' cases where either the maximum size of the mirrors is used for the cost of having the Montel gap in the center of the beam (left) or moving the gap the furthest out of the beam for the cost of reducing the effective mirror length by a factor of two[107]. The right plot is an example for an compromise, where the effective mirror size is less reduced, but also the gap has some (reduced) impact on the photon pulse.

Simulations in Section **5.2.2.5** show that the Montel gap as a very strong, negative impact on the properties of the CBXFEL demonstrator. Hence, the middle case principally is the most preferable, if it is possible to achieve a sufficiently long total mirror length l_m. If this happens to pose a problem, a compromise as shown in the right plot could still be used.

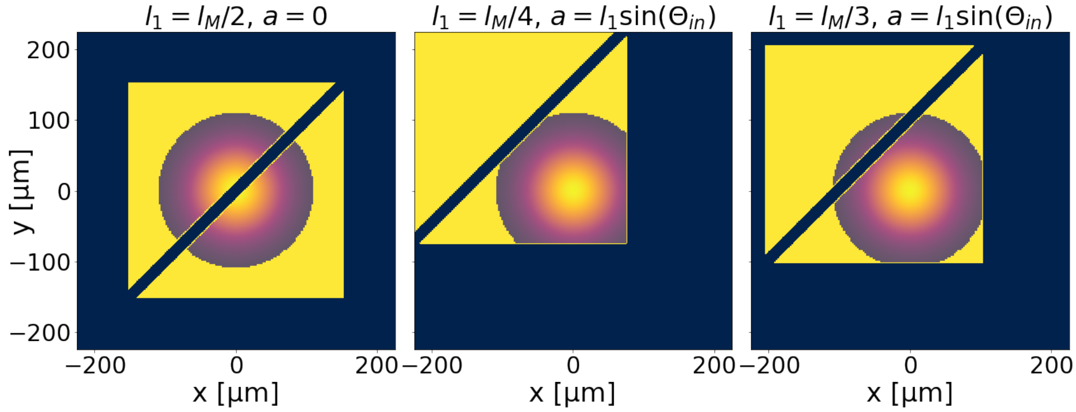

Figure C.7: A mapping of the Montel aperture (C.12) together with the Montel slit (C.14) for different position for the center of the X-ray beam on the first mirror $\boldsymbol{p}_{M1} = a\hat{\boldsymbol{n}}_{M1} + l_1\hat{\boldsymbol{n}}_C$. The yellow shading signifies reflection at the mirrors and the blue signifies cut off. As a reference a gaussian beam profile with σ_r =40 µm multiplied by the respective aperture is also shown. The orientation of the mirrors is $\alpha = 0$.

---

[107] One should note that by shifting the intersection position $\boldsymbol{p}_{M1} = a\hat{\boldsymbol{n}}_{M1} + l_1\hat{\boldsymbol{n}}_C$ away from $a = 0, l_1 = l_M/2$, the aperture is not symmetric around $\boldsymbol{x}_\perp = (0, 0)$ anymore.

D Gaussian Beams and Optical Cavities

Gaussian beam modes are often use to describe the characteristics of laser radiation. They owe their popularity to the fact that they pose fundamental (and comparably simple) solutions to a variety of resonant laser cavities [41, ch. 6.9]. Also for FELs, the fundamental (TEM00) gaussian mode typically shows the largest gain and therefore describes the output characteristic of FEL radiation rather well [39, ch. 5.5, 37, ch. 7.2.2]. In this section, the properties of gaussian beams shall be sketched and how they behave under propagation through a system of linear optical elements. These properties shall be used to analyze the stability criteria of optical cavities and what these dictate for the transverse characteristics of the trapped radiation. The very fundamentals of gaussian optics, what makes them fundamental solutions or how they can be extended to higher modes to cover an even wider field of problems, will not be described here. The interested reader is referred to the wide variety of literature on the topic, for example [41, ch. 6, 52, p. 40, ff. 233, ch. 3].

Gaussian beams are one possible solution to the Helmholtz-equation (4.4) in the (monochromatic) paraxial approximation [233, ch. 2.2C]

$$\begin{aligned} \nabla_\perp^2 E(\boldsymbol{x}_\perp, z) + 2ik\frac{\partial E(\boldsymbol{x}_\perp, z)}{\partial z} &\approx 0, \\ \text{where} \quad \left|\frac{\partial^2 E}{\partial z^2}\right| &\ll kE(\boldsymbol{x}_\perp, z), \end{aligned}$$

with the complex electric field E amplitude and the wave-number $k = {}^{2\pi}/_{\lambda}$. The fundamental gaussian mode, in the assumption of circular symmetry in the transverse directions, is defined as [233, ch. 3.1]

$$E_G\left(\boldsymbol{x}_\perp, z'\right) = E_0 \frac{w_0}{w(z')} e^{-\dfrac{x_\perp^2}{w^2\left(z'\right)}} e^{-ik\dfrac{x_\perp}{2R}} e^{-ikz'} e^{i(\Phi_G(z')-\Phi_0)}, \tag{D.1}$$

where $w\left(z\right)$ denotes the spot size radius

$$w(z) = w_0\sqrt{1 + \left(\frac{z}{z_R}\right)^2}, \tag{D.2}$$

$R\left(z\right)$ the wavefront curvature

$$R(z) = z\left(1 + \left(\frac{z}{z_R}\right)^2\right), \tag{D.3}$$

$\Phi_G\left(z\right)$ the *Gouy*-phase

$$\Phi_G\left(z\right) = \arctan\left(\frac{z}{zR}\right) \tag{D.4}$$

and Φ_0 is an arbitrary initial phase. In above equations the longitudinal coordinate z is defined as the distance to the *beam waist*, which is the position at which the beam radius assumes its minimum value ${w_0}^{108}$ and the wavefront curvature diverges, hence, become identical to that of a plane wave. Above equations make use of an additional parameter, the *rayleigh*-length

$$z_R = \frac{\pi w_0^2}{\lambda}. \tag{D.5}$$

At $|z| \leq z_R$ the beam radius stays within a factor $\sqrt{2}$ of its minium value w_0, which makes the rayleigh length a measure for the depth of focus. From the evolution of the beam radius $w(z)$, it is evident that for $z \gg z_R$ the gaussian beam width evolves linearly with

$$w\left(z\right) \approx w_0 \frac{z}{z_R} = \Theta_0 z \qquad \text{for} \quad z \gg z_R,$$

where the gaussian beam divergence

$$\Theta_0 = \frac{\lambda}{\pi w_0} \tag{D.6}$$

was introduced. It is evident from above relation (D.6) that a strong focus and, consequently, small waist radius w_0 causes a strong divergence and vice versa. The ratio of the beam divergence to the beam radius also serves as measure of a quality of a gaussian beam, with

$$M^2 = \frac{w_0 \Theta_0}{\pi \lambda} \geq 1,$$

where the equality only holds for a perfect gaussian [233, ch. 3.1C]. Consequently, any difference $M^2 > 1$ serves as a measure for the deviation of the distribution from an ideal gaussian beam.

Above parameters can be summarized in the complex q-parameter [233, ch. 3.1A]

$$q\left(z\right) = i z_R + z = q_0 + z = \left[\frac{1}{R} + i \frac{\lambda}{\pi w\left(z\right)}\right]^{-1}, \tag{D.7}$$

which allows to rewrite the complex field amplitude $E_G\left(x_\perp, z\right)$ from equation(D.1) as

$$E_G\left(\boldsymbol{x}_\perp, z\right) = E_0 \frac{q_0}{q_0 + z} e^{ik \frac{x_\perp^2}{2\left(q_0 + z\right)}} e^{ikz'}. \tag{D.8}$$

A fundamental property of a gaussian beam is that it remains a gaussian beam under propagation through a system of linear, optical elements with axial symmetric [41, ch. 6.5.6]. In detail one

---

[108] The waist radius w_0 is two times the rms width (2.12) σ_r of the intensity distribution, as commonly used in Section **5**

can use the $\mathcal{ABCD}$ matrix approach of ray optics, which relate [41, ch. 2.7]

$$\begin{pmatrix} x_\perp \\ \varsigma \end{pmatrix} = \begin{pmatrix} A & B \\ C & D \end{pmatrix} \begin{pmatrix} x_{\perp 0} \\ \varsigma_0 \end{pmatrix}, \tag{D.9}$$

where $x_\perp$ denotes the transverse distance to the optical propagation axis $\hat{z}$ and ς the angle of the ray with respect to that axis, the paramters A, B, C, D are specific to the actual circular symmetric, linear optical element and $x_{\perp,0}$ and ς_0 are the coordinates before transformation by the optical element. For translation by a distance d through vacuum, $A = 1, B = d, C = 0$ and $D = 1$, For focussing by an ideal lense, $A = 1, B = 0, C = -1/f$ and $D = 1$. Likewise, for reflection by an spherical mirror of radius R_m, $A = 1, B = 0, C = -2/R_m$ and $D = 1$. For gaussian beams, one can define the effect of an optical element describable by the $ABCD$ matrix as transform of the $q-$parameter [233, ch. 3.2D]

$$q_{\text{out}} = \frac{Aq_{\text{in}} + B}{Cq_{\text{in}} + D}, \tag{D.10}$$

where q_{in} is the q-parameter before the optical element and q_{out} behind it. Equation (D.10) is the *ABCD*-law of gaussian beam optics. For propagation by a distance d through vacuum this becomes $q_d = q_0 + d = iz_R + d$, which was already apparent from the very definition (D.7). For transformation by a lense of focal length f [41, ch. 6.5.1]

$$\frac{1}{q_{\text{out},f}} = \frac{1}{q_{\text{in}}} - \frac{1}{f}$$

These transformation can be used to study how an gaussian beam behaves in a (closed) optical cavity. Only the simplest case of an linear optical cavity, consisting of two spherical mirrors of radius $R_i = 2f_i$ and infinite transverse extent at a distance of L_{cav} to each other, will be considered. Also, only the spatial dimension will be accounted for, neglecting the spectral and spatiotemporal resonances dictated by the cavity. Defining the upstream mirror as both plane of departure and arrival, one can construct the $ABCD$ matrix for propagating once through the cavity as [41, ch. 6.9.1]

$$\begin{aligned}
\begin{pmatrix} A & B \\ C & D \end{pmatrix} &= \begin{pmatrix} 1 & 0 \\ -1/R_1 & 1 \end{pmatrix} \begin{pmatrix} 1 & L_{\text{cav}} \\ 0 & 1 \end{pmatrix} \begin{pmatrix} 1 & 0 \\ -1/R_2 & 1 \end{pmatrix} \begin{pmatrix} 1 & 0 \\ -1/R_2 & 1 \end{pmatrix} \begin{pmatrix} 1 & L_{\text{cav}} \\ 0 & 1 \end{pmatrix} \begin{pmatrix} 1 & 0 \\ -1/R_1 & 1 \end{pmatrix} \\
&= \begin{pmatrix} g_2 & L_{\text{cav}} \\ \frac{1}{L_{\text{cav}}} (g_1 g_2 - 1) & g_1, \end{pmatrix} \begin{pmatrix} g_1 & L_{\text{cav}} \\ \frac{1}{L_{\text{cav}}} (g_1 g_2 - 1) & g_2, \end{pmatrix} \\
&= \begin{pmatrix} 2g_1 g_2 - 1 & 2L_{\text{cav}} g_2 \\ -\frac{2}{L_{\text{cav}}} (g_1 g_2 - 1) \, g_1 & 2g_2 g_1 - 1, \end{pmatrix}
\end{aligned}$$

with

$$g_{1,2} = 1 - \frac{L_{\text{cav}}}{R_{1,2}} = 1 - \frac{L_{\text{cav}}}{2f}, \tag{D.11}$$

where for the last equality it was assumed that the spherical mirrors would be replaced by combinations of a plane mirrors and an ideal lense of focal length f. Requesting 'self-reproduction' of the field, $q = q_{out} = q_{\text{in}}$, to assure stability even after an infinite number of round trips, leads to [41, ch. 6.9.1]

$$\frac{1}{q} = \frac{1}{R} + i\frac{\lambda}{\pi w^2} = \pm\frac{1}{L_{\text{cav}}}\sqrt{\frac{g_1}{g_2}\left(g_1 g_2 - 1\right)}.$$

From above relation, it is evident that a gaussian beam only is a solution for the self-reproducing field in the cavity, if [41, ch. 6.9.1]

$$0 \leq g_1 g_2 \leq 1. \tag{D.12}$$

A cavity fulfilling above relation is said to be *stable*, where as cavities not fulfilling it are named *unstable*. Usually, a cavity is constructed such that is well within the region of stability, as small deviations in the parameters R_1, R_2 and L_{cav} are less critical.
From the propagation properties of the gaussian beam, one can directly determine the beam waist and the position $z_{1,2}$ of the waist plane with respect to the mirrors from the cavity parameters R_1, R_2 and L_{cav} [41, ch. 6.9.1]:

$$\begin{aligned} w_0^2 &= \frac{\lambda}{\pi}\frac{\sqrt{L_{\text{cav}}\left(R_1 - L_{\text{cav}}\right)\left(R_2 - L_{\text{cav}}\right)\left(R_1 + R_2 - L_{\text{cav}}\right)}}{\left(R_1 + R_2 - 2L_{\text{cav}}\right)}, \\ z_1 &= -L\frac{R_2 - L_{\text{cav}}}{R_1 + R_2 - 2L_{\text{cav}}} \quad \text{and} \quad z_2 = L\frac{R_1 - L_{\text{cav}}}{R_1 + R_2 - 2L_{\text{cav}}}. \end{aligned} \tag{D.13}$$

The other gaussian beam parameters at arbitrary position z in the cavity can be directly deduced using the equations Eqs. (D.2) to (D.6).

References

[1] H.-J. Kull, *Laserphysik*. de Gruyter Oldenbourg, 2015, ISBN: 3486779052.

[2] A. Halavanau, A. Benediktovitch, A. A. Lutman, *et al.*, “Population inversion x-ray laser oscillator”, *Proceedings of the National Academy of Sciences*, vol. 117, no. 27, pp. 15 511–15 516, 2020. DOI: `10.1073/pnas.2005360117`.

[3] W. C. Röntgen, “Über eine neue art von strahlen (on a new kind of rays)”, *Vorläufige Mittheilung. Aus den Sitzungsberichten der Würzburger Physik.-medic. Gesellschaft.*, pp. 137–147, 1895.

[4] P. Willmott, *An Introduction to Synchrotron Radiation*. John Wiley & Sons, 2019, 504 pp., ISBN: 9781119280378.

[5] Lightsources.org. (2020), [Online]. Available: `https://lightsources.org/history/`.

[6] D. H. Bilderback, P. Elleaume, and E. Weckert, “Review of third and next generation synchrotron light sources”, *Journal of Physics B: Atomic, Molecular and Optical Physics*, vol. 38, no. 9, pp. 773–797, 2005. DOI: `10.1088/0953-4075/38/9/022`.

[7] Z. Huang and K.-J. Kim, “Review of x-ray free-electron laser theory”, *Physical Review Special Topics - Accelerators and Beams*, vol. 10, no. 3, 2007. DOI: `10.1103/physrevstab.10.034801`.

[8] T. Inada, T. Yamaji, S. Adachi, *et al.*, “Search for photon–photon elastic scattering in the x-ray region”, *Physics Letters B*, vol. 732, pp. 356–359, 2014. DOI: `10.1016/j.physletb.2014.03.054`.

[9] K. Tamasaku, E. Shigemasa, Y. Inubushi, *et al.*, “X-ray two-photon absorption competing against single and sequential multiphoton processes”, *Nature Photonics*, vol. 8, no. 4, pp. 313–316, 2014. DOI: `10.1038/nphoton.2014.10`.

[10] S. Reiche, “Overview of seedings methods for FELs”, in *IPAC2013 Proceedings, Shanghai, China*, vol. 4, 2013.

[11] G. Paraskaki, S. Ackermann, B. Faatz, *et al.*, “Study of a seeded oscillator-amplifier fel”, en, *Proceedings of the 39th Free Electron Laser Conference*, vol. FEL2019, Germany, 2019. DOI: `10.18429/JACOW-FEL2019-TUP077`.

[12] G. Paraskaki, V. Grattoni, T. Lang, J. Zemella, B. Faatz, and W. Hillert, “Optimization and stability of a high-gain harmonic generation seeded oscillator amplifier”, *Physical Review Accelerators and Beams*, vol. 24, no. 3, p. 034 801, 2021. DOI: `10.1103/physrevaccelbeams.24.034801`.

[13] G. Geloni, V. Kocharyan, and E. Saldin, “A novel self-seeding scheme for hard x-ray FELs”, *Journal of Modern Optics*, vol. 58, no. 16, pp. 1391–1403, 2011. DOI: `10.1080/09500340.2011.586473`.

[14] J. Amann, W. Berg, V. Blank, *et al.*, “Demonstration of self-seeding in a hard-x-ray free-electron laser”, *Nature Photonics*, vol. 6, no. 10, pp. 693–698, 2012. DOI: `10.1038/nphoton.2012.180`.

[15] C.-K. Min, I. Nam, H. Yang, *et al.*, “Hard x-ray self-seeding commissioning at PAL-XFEL”, *Journal of Synchrotron Radiation*, vol. 26, no. 4, pp. 1101–1109, 2019. DOI: `10.1107/s1600577519005460`.

[16] I. Inoue, T. Osaka, T. Hara, *et al.*, “Generation of narrow-band x-ray free-electron laser via reflection self-seeding”, *Nature Photonics*, vol. 13, no. 5, pp. 319–322, 2019. DOI: `10.1038/s41566-019-0365-y`.

[17] W. Decking, L. Froehlich, N. Golubeva, *et al.* (2020). First results of the hard x-ray self-seeding commissioning at the european xfel, [Online]. Available: `https://www.ipac20.org/shan-liu-desy/`.

[18] G. Geloni, V. Kocharyan, and E. Saldin, “Cascade self-seeding scheme with wake monochromator for narrow-bandwidth x-ray fels”, 2010.

[19] S. Liu, W. Decking, V. Kocharyan, *et al.*, “Preparing for high-repetition rate hard x-ray self-seeding at the european x-ray free electron laser: Challenges and opportunities”, *Physical Review Accelerators and Beams*, vol. 22, no. 6, 2019. DOI: `10.1103/physrevaccelbeams.22.060704`.

[20] K.-J. Kim, Y. Shvyd’ko, and S. Reiche, “A proposal for an x-ray free-electron laser oscillator with an energy-recovery linac”, *Physical Review Letters*, vol. 100, no. 24, 2008. DOI: `10.1103/physrevlett.100.244802`.

[21] Z. Huang and R. D. Ruth, “Fully coherent x-ray pulses from a regenerative-amplifier free-electron laser”, *Physical Review Letters*, vol. 96, no. 14, p. 144 801, 2006. DOI: `10.1103/physrevlett.96.144801`.

[22] K.-J. Kim and Y. V. Shvyd’ko, “Tunable optical cavity for an x-ray free-electron-laser oscillator”, *Physical Review Special Topics - Accelerators and Beams*, vol. 12, no. 3, 2009. DOI: `10.1103/physrevstab.12.030703`.

[23] R. R. Lindberg, K.-J. Kim, Y. Shvyd’ko, and W. M. Fawley, “Performance of the x-ray free-electron laser oscillator with crystal cavity”, *Physical Review Special Topics - Accelerators and Beams*, vol. 14, no. 1, 2011. DOI: `10.1103/physrevstab.14.010701`.

[24] R. R. Lindberg, K.-J. Kim, Y. Cai, Y. Ding, and Z. Huang, “Transverse gradient undulator for a storage ring x-ray fel oscillator”, in *Proceeding of FEL2013, New York, NY, USA*, 2013, pp. 740–748, ISBN: 978-3-95450-126-7.

[25] T. J. Maxwell, J. Arthur, Y. Ding, *et al.*, “Feasibility study for an x-ray fel oscillator at the lcls-ii”, in *Proceedings of IPAC2015*, 2015, pp. 1897–1900, ISBN: 978-3-95450-168-7.

[26] J. Zemella, J. Rossbach, C. Maag, M. Tolkiehn, and H. Sinn, “Numerical simulations of an XFELO for the European XFEL driven by a spent beam”, in *Proc. of FEL2012, Nara, Japan*, paper WEPD29, 2012, pp. 429–433, ISBN: ISBN 978-3-95450-123-6.

[27] P. Rauer, I. Bahns, W. Decking, W. Hillert, J. Rossbach, and H. Sinn, “Integration of an xfelo at the european xfel facility”, en-us, *Proceedings of the 39th Free Electron Laser Conf.*, vol. FEL2019, Germany–, 2019. DOI: `10.18429/JACOW-FEL2019-TUP009`.

[28] K. Li and H. Deng, “Systematic design and three-dimensional simulation of x-ray FEL oscillator for shanghai coherent light facility”, *Nuclear Instruments and Methods in Physics Research Section A: Accelerators, Spectrometers, Detectors and Associated Equipment*, vol. 895, pp. 40–47, 2018. DOI: `10.1016/j.nima.2018.03.072`.

[29] B. W. Adams and K.-J. Kim, “X-ray comb generation from nuclear-resonance-stabilized x-ray free-electron laser oscillator for fundamental physics and precision metrology”, *Physical Review Special Topics - Accelerators and Beams*, vol. 18, no. 3, 2015. DOI: `10.1103/physrevstab.18.030711`.

[30] W. Qin, K.-J. Kim, R. R. Lindberg, and J. Wu, “X-ray FEL Oscillator Seeded Harmonic Amplifier for High Energy Photons”, in *Proc. of International Free Electron Laser Conference (FEL’17), Santa Fe, NM, USA, August 20-25, 2017*, (Santa Fe, NM, USA), ser. International Free Electron Laser Conference, Geneva, Switzerland: JACoW, 2018, pp. 196–199, ISBN: 978-3-95450-179-3. DOI: `10.18429/JACoW-FEL2017-MOP062`.

[31] H. P. Freund, P. J. M. van der Slot, and Y. Shvyd’ko, “An x-ray regenerative amplifier free-electron laser using diamond pinhole mirrors”, *New Journal of Physics*, vol. 21, no. 9, p. 093 028, 2019. DOI: `10.1088/1367-2630/ab3f72`.

[32] G. Marcus, A. Halavanau, Z. Huang, *et al.*, “Refractive guide switching a regenerative amplifier free-electron laser for high peak and average power hard x rays”, *Physical Review Letters*, vol. 125, no. 25, p. 254 801, 2020. DOI: `10.1103/physrevlett.125.254801`.

[33] R. Margraf, Z. Huang, J. MacArthur, and G. Marcus, “Microbunch rotation as an outcoupling mechanism for cavity-based x-ray free electron lasers”, en, *Proceedings of the 11th International Particle Accelerator Conference*, vol. IPAC2020, France, 2020. DOI: `10.18429/JACOW-IPAC2020-WEVIR03`.

[34] European XFEL GmbH. (). Facts and Figures, [Online]. Available: `http://www.xfel.eu/overview/facts_and_figures/`.

[35] S. Stoupin, F. Lenkszus, R. Laird, K. Goetze, K.-J. Kim, and Y. Shvyd'ko, "Nanoradian angular stabilization of x-ray optical components", *Review of Scientific Instruments*, vol. 81, no. 5, p. 055 108, 2010. DOI: `10.1063/1.3428722`.

[36] C. Maag, J. Zemella, and G. J. Rossbach, "Numerical studies of the influence of the electron bunch arrival time jitter on the gain process of an xfel-oscillator for the european xfel", in *Proc. of FEL2015, Daejon, Korea*, paper TUP032, 2015, pp. 436–438. DOI: `10.18429/JACoW-FEL2015-TUP032`.

[37] P. Schmüser, M. Dohlus, J. Rossbach, and C. Behrens, *Free-Electron Lasers in the Ultraviolet and X-Ray Regime*, 3rd ed. Springer International Publishing, 2014, 248 pp., ISBN: 978-3-319-37446-8. DOI: `10.1007/978-3-319-04081-3`.

[38] E. L. Saldin, E. A. Schneidmiller, and M. V. Yurkov, *The Physics of Free Electron Lasers*. Springer Berlin Heidelberg, 2000. DOI: `10.1007/978-3-662-04066-9`.

[39] K.-J. Kim, Z. Huang, and R. Lindberg, *Synchrotron Radiation and Free-Electron Lasers*. Cambridge University Press, 2017. DOI: `10.1017/9781316677377`.

[40] E. Jaeschke, *Synchrotron light sources and free-electron lasers : accelerator physics, instrumentation and science applications*. Switzerland: Springer Reference, 2016, ISBN: `9783319143941`.

[41] G. Giusfredi, *Physical Optics*. Springer, Berlin, 2019, 933 pp., ISBN: 3030252787.

[42] B. N. T. Peter J. Mohr David B. Newell and E. Tiesinga. (2020). The 2018 CODATA Recommended Values of the Fundamental Physical Constants (Web Version 8.1). Database developed by J. Baker, M. Douma, and S. Kotochigova., [Online]. Available: `http://physics.nist.gov/constants`.

[43] J. Alda, "Laser and gaussian beam propagation and transformation", in *Encyclopedia of Optical and Photonic Engineering, Second Edition*, CRC Press, 2015, pp. 1–15. DOI: `10.1081/e-eoe2-120009751`.

[44] V. K. Rohatgi and A. K. M. E. Saleh, *An Introduction to Probability and Statistics*. John Wiley & Sons, Inc, 2015. DOI: `10.1002/9781118799635`.

[45] J. Bahrdt, "Shaping photon beams with undulators and wigglers", in *Synchrotron Light Sources and Free-Electron Lasers*, Springer International Publishing, 2016, pp. 751–819. DOI: `10.1007/978-3-319-14394-1_16`.

[46] I. A. Vartanyants and A. Singer, "Coherence properties of third-generation synchrotron sources and free-electron lasers", in *Synchrotron Light Sources and Free-Electron Lasers*, Springer International Publishing, 2016, pp. 821–863. DOI: `10.1007/978-3-319-14394-1_23`.

[47] E. L. Saldin, E. A. Schneidmiller, and M. V. Yurkov, "Coherence properties of the radiation from x-ray free electron laser", *Optics Communications*, vol. 281, no. 5, pp. 1179–1188, 2008. DOI: `10.1016/j.optcom.2007.10.044`.

[48] G. Geloni, E. Saldin, L. Samoylova, *et al.*, “Coherence properties of the European XFEL”, *New Journal of Physics*, vol. 12, no. 3, p. 035 021, 2010. DOI: `10.1088/1367-2630/12/3/035021`.

[49] S. Serkez, O. Gorobtsov, D. E. Rivas, *et al.*, “Wigner distribution of self-amplified spontaneous emission free-electron laser pulses and extracting its autocorrelation”, *Journal of Synchrotron Radiation*, vol. 28, no. 1, pp. 3–17, 2021. DOI: `10.1107/s160057752001382x`.

[50] K. Zhukovsky, “Undulators for short pulse x-ray self-amplified spontaneous emission-free electron lasers”, in *High Energy and Short Pulse Lasers*, R. Viskup, Ed. BoD–Books on Demand, 2016.

[51] J. D. Jackson, *Klassische Elektrodynamik*. DE GRUYTER, 2013. DOI: `10.1515/9783110334470`.

[52] D. Meschede, *Optics, Light and Lasers*. Wiley-VCH, 2017, 528 pp., ISBN: 9783527685516.

[53] J. M. J. Madey, “Relationship between mean radiated energy, mean squared radiated energy and spontaneous power spectrum in a power series expansion of the equations of motion in a free-electron laser”, *Il Nuovo Cimento B Series 11*, vol. 50, no. 1, pp. 64–88, 1979. DOI: `10.1007/bf02737622`.

[54] R. Bonifacio, C. Pellegrini, and L. Narducci, “Collective instabilities and high-gain regime in a free electron laser”, *Optics Communications*, vol. 50, no. 6, pp. 373–378, 1984. DOI: `10.1016/0030-4018(84)90105-6`.

[55] E. L. Saldin, E. A. Schneidmiller, and M. V. Yurkov, “Coherence properties of the radiation from SASE FEL”, *Nuclear Instruments and Methods in Physics Research Section A: Accelerators, Spectrometers, Detectors and Associated Equipment*, vol. 507, no. 1-2, pp. 106–109, 2003. DOI: `10.1016/s0168-9002(03)00848-9`.

[56] N. Kujala, W. Freund, J. Liu, *et al.*, “Hard x-ray single-shot spectrometer at the european x-ray free-electron laser”, *Review of Scientific Instruments*, vol. 91, no. 10, p. 103 101, 2020. DOI: `10.1063/5.0019935`.

[57] R. Ischebeck, J. Feldhaus, C. Gerth, *et al.*, “Study of the transverse coherence at the TTF free electron laser”, *Nuclear Instruments and Methods in Physics Research Section A: Accelerators, Spectrometers, Detectors and Associated Equipment*, vol. 507, no. 1-2, pp. 175–180, 2003. DOI: `10.1016/s0168-9002(03)00866-0`.

[58] M. Xie, “Exact and variational solutions of 3d eigenmodes in high gain FELs”, *Nuclear Instruments and Methods in Physics Research Section A: Accelerators, Spectrometers, Detectors and Associated Equipment*, vol. 445, no. 1-3, pp. 59–66, 2000. DOI: `10.1016/s0168-9002(00)00114-5`.

[59] K.-J. Kim and M. Xie, “Self-amplified spontaneous emission for short wavelength coherent radiation”, *Nuclear Instruments and Methods in Physics Research Section A: Accelerators, Spectrometers, Detectors and Associated Equipment*, vol. 331, no. 1-3, pp. 359–364, 1993. DOI: `10.1016/0168-9002(93)90072-p`.

[60] N. Kroll, P. Morton, and M. Rosenbluth, “Free-electron lasers with variable parameter wigglers”, *IEEE Journal of Quantum Electronics*, vol. 17, no. 8, pp. 1436–1468, 1981. DOI: `10.1109/jqe.1981.1071285`.

[61] Y. V. Shvyd’ko, S. Stoupin, A. Cunsolo, A. H. Said, and X. Huang, “High-reflectivity high-resolution x-ray crystal optics with diamonds”, *Nature Physics*, vol. 6, no. 3, pp. 196–199, 2010. DOI: `10.1038/nphys1506`.

[62] J. Zemella, D. Novikov, M. Tolkiehn, J. Rossbach, and H. Sinn, “Study of a silicon based xfelo for the european xfel”, in *Proc. of FEL2011, Shanghai, China*, paper TUPA07, 2011, pp. 202–205, ISBN: 978-3-95450-117-5.

[63] R. Hajima, N. Nishimori, N. Sei, M. Shimada, and N. Nakamura, “Simulations of xfelo for the kek erl”, *Proceedings of FEL12*, pp. 433–437, 2012.

[64] H.-X. Deng and Z.-M. Dai, “Harmonic lasing of x-ray free electron laser: On the way to smaller and cheaper”, *Chinese Physics C*, vol. 37, no. 10, p. 102 001, 2013. DOI: `10.1088/1674-1137/37/10/102001`.

[65] K. Li, J. Yan, C. Feng, M. Zhang, and H. Deng, “High brightness fully coherent x-ray amplifier seeded by a free-electron laser oscillator”, *Physical Review Accelerators and Beams*, vol. 21, no. 4, 2018. DOI: `10.1103/physrevaccelbeams.21.040702`.

[66] K.-J. Kim, V. Blank, Y. Ding, *et al.*, “An oscillator configuration for full realization of hard x-ray free electron laser”, in *7th International Particle Accelerator Conference (IPAC’16), Busan, Korea, May 8-13, 2016*, JACOW, Geneva, Switzerland, 2016, pp. 801–804.

[67] K. Li and H. Deng, “Gain-guided x-ray free-electron laser oscillator”, *Applied Physics Letters*, vol. 113, no. 6, p. 061 106, 2018. DOI: `10.1063/1.5037180`.

[68] R. L. Sheffield, D. C. Nguyen, J. C. Goldstein, N. A. Ebrahim, C. M. Fortgang, and J. M. Kinross-Wright, “Compact 1-kW infrared regenerative amplifier FEL”, in *Free-Electron Laser Challenges*, P. G. O’Shea and H. E. Bennett, Eds., SPIE, 1997. DOI: `10.1117/12.274394`.

[69] D. C. Nguyen, R. L. Sheffield, C. M. Fortgang, J. C. Goldstein, J. M. Kinross-Wright, and N. A. Ebrahim, “First lasing of the regenerative amplifier FEL”, *Nuclear Instruments and Methods in Physics Research Section A: Accelerators, Spectrometers, Detectors and Associated Equipment*, vol. 429, no. 1-3, pp. 125–130, 1999. DOI: `10.1016/s0168-9002(99)00090-x`.

[70] H. P. Freund, D. C. Nguyen, P. A. Sprangle, and P. J. M. van der Slot, “Three-dimensional, time-dependent simulation of a regenerative amplifier free-electron laser”, *Physical Review Special Topics - Accelerators and Beams*, vol. 16, no. 1, p. 010 707, 2013. DOI: `10.1103/physrevstab.16.010707`.

[71] Y. Feng, D. Zhu, A. Robert, *et al.*, “Ultra-thin bragg crystals for LCLS beam-sharing operation”, in *X-Ray Free-Electron Lasers: Beam Diagnostics, Beamline Instrumentation, and Applications*, S. P. Moeller, M. Yabashi, and S. P. Hau-Riege, Eds., SPIE, 2012. DOI: `10.1117/12.930944`.

[72] T. Kolodziej, P. Vodnala, S. Terentyev, V. Blank, and Y. Shvyd’ko, “Diamond drumhead crystals for x-ray optics applications”, *Journal of Applied Crystallography*, vol. 49, no. 4, pp. 1240–1244, 2016. DOI: `10.1107/s1600576716009171`.

[73] Y. Shvyd’ko, “Output coupling from x-ray free-electron laser cavities with intracavity beam splitters”, *Physical Review Accelerators and Beams*, vol. 22, no. 10, p. 100 703, 2019. DOI: `10.1103/physrevaccelbeams.22.100703`.

[74] M. Makita, P. Karvinen, D. Zhu, *et al.*, “High-resolution single-shot spectral monitoring of hard x-ray free-electron laser radiation”, *Optica*, vol. 2, no. 10, p. 912, 2015. DOI: `10.1364/optica.2.000912`.

[75] K. Li, Y. Liu, M. Seaberg, M. Chollet, T. M. Weiss, and A. Sakdinawat, “Wavefront preserving and high efficiency diamond grating beam splitter for x-ray free electron laser”, *Optics Express*, vol. 28, no. 8, p. 10 939, 2020. DOI: `10.1364/oe.380534`.

[76] M. Sander, R. Bauer, V. Kabanova, *et al.*, “Demonstration of a picosecond bragg switch for hard x-rays in a synchrotron-based pump–probe experiment”, *Journal of Synchrotron Radiation*, vol. 26, no. 4, pp. 1253–1259, 2019. DOI: `10.1107/s1600577519005356`.

[77] J. Krzywiński, Y. Feng, A. Halavanau, *et al.*, “Q-switching of x-ray optical cavities by using boron doped buried layer under a surface of a diamond crystal”, en, *Proceedings of the 39th Free Electron Laser Conference*, vol. FEL2019, Germany, 2019. DOI: `10.18429/JACOW-FEL2019-TUP033`.

[78] J. P. MacArthur, A. A. Lutman, J. Krzywinski, and Z. Huang, “Microbunch rotation and coherent undulator radiation from a kicked electron beam”, *Physical Review X*, vol. 8, no. 4, p. 041 036, 2018. DOI: `10.1103/physrevx.8.041036`.

[79] B. Beckhoff, N. Langhoff, B. Kanngießer, R. Wedell, and H. Wolff, Eds., *Handbook of Practical X-Ray Fluorescence Analysis*. Springer-Verlag GmbH, 2006, ISBN: 3540286039.

[80] S. P. Hau-Riege and T. Pardini, “Effect of high-intensity x-ray radiation on bragg diffraction in silicon and diamond”, *Journal of Applied Physics*, vol. 112, no. 11, p. 114 904, 2012. DOI: `10.1063/1.4765719`.

[81] B. Ziaja, N. Medvedev, V. Tkachenko, T. Maltezopoulos, and W. Wurth, “Time-resolved observation of band-gap shrinking and electron-lattice thermalization within x-ray excited gallium arsenide”, *Scientific Reports*, vol. 5, no. 1, 2015. DOI: `10.1038/srep18068`.

[82] N. Gerasimova, R. Treusch, S. Dziarzhytski, and H. Sinn, “The photon beam loss monitors as a part of equipment protection system at European XFEL”, in *36th International Free Electron Laser Conference*, European XFEL, 2014.

[83] A. V. Osadchy, I. I. Vlasov, O. S. Kudryavtsev, *et al.*, “Luminescent diamond window of the sandwich type for x-ray visualization”, *Applied Physics A*, vol. 124, no. 12, 2018. DOI: `10.1007/s00339-018-2230-0`.

[84] N. Medvedev, H. O. Jeschke, and B. Ziaja, “Nonthermal graphitization of diamond induced by a femtosecond x-ray laser pulse”, *Physical Review B*, vol. 88, no. 22, pp. 224–304, 2013. DOI: `10.1103/physrevb.88.224304`.

[85] I. Bahns, “Nondestructive interaction of powerful electromagnetic waves with Bragg reflectors”, PhD thesis, Hamburg, Univ., 2021.

[86] C. Thomsen, H. T. Grahn, H. J. Maris, and J. Tauc, “Surface generation and detection of phonons by picosecond light pulses”, *Physical Review B*, vol. 34, no. 6, pp. 4129–4138, 1986. DOI: `10.1103/physrevb.34.4129`.

[87] B. Yang, S. Wang, and J. Wu, “Transient thermal stress wave and vibrational analyses of a thin diamond crystal for x-ray free-electron lasers under high-repetition-rate operation”, *Journal of Synchrotron Radiation*, vol. 25, no. 1, pp. 166–176, 2018. DOI: `10.1107/s1600577517015466`.

[88] V. A. Bushuev, “Influence of thermal self-action on the diffraction of high-power x-ray pulses”, *Journal of Surface Investigation. X-ray, Synchrotron and Neutron Techniques*, vol. 10, no. 6, pp. 1179–1186, 2016. DOI: `10.1134/s1027451016050487`.

[89] X. Dong, D. Shu, and H. Sinn, “Design of a cryo-cooled artificial channel-cut crystal monochromator for the european XFEL”, *AIP Conference Proceedings*, vol. 1741, p. 040 027, 2016. DOI: `10.1063/1.4952899`.

[90] C. Maag, I. Bahns, J. Rossbach, and P. Thiessen, “An experimental setup for probing the thermal properties of diamond regardings its use in an XFELO”, in *Proc. of FEL2017, Santa Fe, USA*, paper MOP064, 2017, pp. 200–203. DOI: `10.18429/JACoW-FEL2017-MOP064`.

[91] W. Friedrich, P. Knipping, and M. Laue, “Interferenzerscheinungen bei röntgenstrahlen”, *Annalen der Physik*, vol. 346, no. 10, pp. 971–988, 1913. DOI: `10.1002/andp.19133461004`.

[92] W. H. B. W. L. Bragg, “The reflection of x-rays by crystals”, *Proceedings of the Royal Society of London. Series A*, vol. 88, no. 605, pp. 428–438, 1913. DOI: `10.1098/rspa.1913.0040`.

[93] A. M. Rudolf Gross, *Festkörperphysik*. Gruyter, Walter de GmbH, 2018, ISBN: 311055822X.

[94] Y. Shvyd'ko, *X-Ray Optics*. Springer Berlin Heidelberg, 2004, 424 pp., ISBN: 3540214844.

[95] A. Authier, *Dynamical theory of x-ray diffraction*. Oxford: Oxford University Press, 2001, ISBN: 0198559607.

[96] T. Schoonjans, A. Brunetti, B. Golosio, *et al.*, "The xraylib library for x-ray–matter interactions. recent developments", *Spectrochimica Acta Part B: Atomic Spectroscopy*, vol. 66, no. 11-12, pp. 776–784, 2011. DOI: `10.1016/j.sab.2011.09.011`.

[97] V. G. Kohn, "A theory of multiple bragg diffraction ofx rays in multilayer crystal systems", *J. Moscow Phys. Soc*, vol. 1, pp. 425–434, 1991.

[98] S. Stepanov, "Method of transfer matrices and dynamical thick-crystal approximation in surface x-ray diffraction by multilayer structures", *CryRp*, vol. 39, no. 2, pp. 182–187, 1994.

[99] S. A. Stepanov, U. Pietsch, and G. T. Baumbach, "A matrix approach to grazing-incidence x-ray diffraction in multilayers", vol. 96, pp. 341–347, 1995, ISSN: 0722-3277. DOI: `10.1007/bf01313056`.

[100] S. A. Stepanov, E. A. Kondrashkina, R. Köhler, D. V. Novikov, G. Materlik, and S. M. Durbin, "Dynamical x-ray diffraction of multilayers and superlattices: Recursion matrix extension to grazing angles", *Physical Review B*, vol. 57, no. 8, p. 4829, 1998. DOI: `10.1103/PhysRevB.57.4829`.

[101] A. Souvorov, T. Ishikawa, A. Y. Nikulin, Y. P. Stetsko, S.-L. Chang, and P. Zaumseil, "X-ray multiple diffraction from crystalline multilayers: Application to a 90° bragg reflection", *Physical Review B*, vol. 70, no. 22, p. 224 109, 2004. DOI: `10.1103/physrevb.70.224109`.

[102] S. Takagi, "A dynamical theory of diffraction for a distorted crystal", *Journal of the Physical Society of Japan*, vol. 26, no. 5, pp. 1239–1253, 1969. DOI: `10.1143/jpsj.26.1239`.

[103] D. Taupin, "Théorie dynamique de la diffraction des rayons x par les cristaux déformés", *Bulletin de la Société française de Minéralogie et de Cristallographie*, vol. 87, no. 4, pp. 469–511, 1964. DOI: `10.3406/bulmi.1964.5769`.

[104] J. Gronkowski, "Propagation of x-rays in distorted crystals under dynamical diffraction", *Physics Reports*, vol. 206, no. 1, pp. 1–41, 1991. DOI: `10.1016/0370-1573(91)90086-2`.

[105] A.-P. Honkanen, C. Ferrero, J.-P. Guigay, and V. Mocella, "A finite-element approach to dynamical diffraction problems in reflection geometry", *Journal of Applied Crystallography*, vol. 51, no. 2, pp. 514–525, 2018. DOI: `10.1107/s1600576718001930`.

[106] A. G. Shabalin, O. M. Yefanov, V. L. Nosik, V. A. Bushuev, and I. A. Vartanyants, "Dynamical effects in Bragg coherent x-ray diffraction imaging of finite crystals", *Physical Review B*, vol. 96, no. 6, p. 064 111, 2017. DOI: `10.1103/physrevb.96.064111`.

[107] R. Peierls, "Zur kinetischen theorie der wärmeleitung in kristallen", *Annalen der Physik*, vol. 395, no. 8, pp. 1055–1101, 1929. DOI: `10.1002/andp.19293950803`.

[108] A. J. H. McGaughey, A. Jain, and H.-Y. Kim, "Phonon properties and thermal conductivity from first principles, lattice dynamics, and the boltzmann transport equation", *Journal of Applied Physics*, vol. 125, no. 1, p. 20, 2019. DOI: `10.1063/1.5064602`.

[109] S. Hunklinger, *Festkörperphysik*. Munich, Germany: Oldenbourg Verlag, 2011, ISBN: 9783486705478.

[110] L. Lindsay, "First principles peierls-boltzmann phonon thermal transport: A topical review", *Nanoscale and Microscale Thermophysical Engineering*, vol. 20, no. 2, pp. 67–84, 2016. DOI: `10.1080/15567265.2016.1218576`.

[111] A. Gulans, S. Kontur, C. Meisenbichler, *et al.*, "Exciting: A full-potential all-electron package implementing density-functional theory and many-body perturbation theory", *Journal of Physics: Condensed Matter*, vol. 26, no. 36, p. 363 202, 2014. DOI: `10.1088/0953-8984/26/36/363202`.

[112] J. Carrete, B. Vermeersch, A. Katre, *et al.*, "almaBTE : A solver of the space–time dependent boltzmann transport equation for phonons in structured materials", *Computer Physics Communications*, vol. 220, pp. 351–362, 2017. DOI: `10.1016/j.cpc.2017.06.023`.

[113] W. DeSorbo, "Specific heat of diamond at low temperatures", *The Journal of Chemical Physics*, vol. 21, no. 5, pp. 876–880, 1953. DOI: `10.1063/1.1699050`.

[114] R. R. Reeber and K. Wang, "Thermal expansion, molar volume and specific heat of diamond from 0 to 3000k", *Journal of Electronic Materials*, vol. 25, no. 1, pp. 63–67, 1996. DOI: `10.1007/bf02666175`.

[115] J. E. Desnoyehs and J. A. Morrison, "The heat capacity of diamond between 12.8° and 277°k", *Philosophical Magazine*, vol. 3, no. 25, pp. 42–48, 1958. DOI: `10.1080/14786435808243223`.

[116] C. Hua, L. Lindsay, X. Chen, and A. J. Minnich, "Generalized fourier's law for nondiffusive thermal transport: Theory and experiment", *Physical Review B*, vol. 100, no. 8, 2019. DOI: `10.1103/physrevb.100.085203`.

[117] J.-P. M. Peraud, C. D. Landon, and N. G. Hadjiconstantinou, "MONTE CARLO METHODS FOR SOLVING THE BOLTZMANN TRANSPORT EQUATION", *Annual Review of Heat Transfer*, vol. 17, pp. 205–265, 2014. DOI: `10.1615/annualrevheattransfer.2014007381`.

[118] Q. Hao, G. Chen, and M.-S. Jeng, “Frequency-dependent monte carlo simulations of phonon transport in two-dimensional porous silicon with aligned pores”, *Journal of Applied Physics*, vol. 106, no. 11, p. 114 321, 2009. DOI: `10.1063/1.3266169`.

[119] D. G. Cahill, P. V. Braun, G. Chen, *et al.*, “Nanoscale thermal transport. II. 2003–2012”, *Applied Physics Reviews*, vol. 1, no. 1, p. 011 305, 2014. DOI: `10.1063/1.4832615`.

[120] W. Li, J. Carrete, N. A. Katcho, and N. Mingo, “ShengBTE: A solver of the boltzmann transport equation for phonons”, *Computer Physics Communications*, vol. 185, no. 6, pp. 1747–1758, 2014. DOI: `10.1016/j.cpc.2014.02.015`.

[121] A. Ward, D. A. Broido, D. A. Stewart, and G. Deinzer, “Ab initiotheory of the lattice thermal conductivity in diamond”, *Physical Review B*, vol. 80, no. 12, 2009. DOI: `10.1103/physrevb.80.125203`.

[122] J. A. Pascual-Gutiérrez, J. Y. Murthy, and R. Viskanta, “Thermal conductivity and phonon transport properties of silicon using perturbation theory and the environment-dependent interatomic potential”, *Journal of Applied Physics*, vol. 106, no. 6, p. 063 532, 2009. DOI: `10.1063/1.3195080`.

[123] D. A. Broido, M. Malorny, G. Birner, N. Mingo, and D. A. Stewart, “Intrinsic lattice thermal conductivity of semiconductors from first principles”, *Applied Physics Letters*, vol. 91, no. 23, p. 231 922, 2007. DOI: `10.1063/1.2822891`.

[124] L. Wei, P. K. Kuo, R. L. Thomas, T. R. Anthony, and W. F. Banholzer, “Thermal conductivity of isotopically modified single crystal diamond”, *Physical Review Letters*, vol. 70, no. 24, pp. 3764–3767, 1993. DOI: `10.1103/physrevlett.70.3764`.

[125] J. R. Olson, R. O. Pohl, J. W. Vandersande, A. Zoltan, T. R. Anthony, and W. F. Banholzer, “Thermal conductivity of diamond between 170 and 1200 k and the isotope effect”, *Physical Review B*, vol. 47, no. 22, pp. 14 850–14 856, 1993. DOI: `10.1103/physrevb.47.14850`.

[126] A. Ward and D. A. Broido, “Intrinsic phonon relaxation times from first-principles studies of the thermal conductivities of si and ge”, *Physical Review B*, vol. 81, no. 8, 2010. DOI: `10.1103/physrevb.81.085205`.

[127] J. Callaway, “Model for lattice thermal conductivity at low temperatures”, *Physical Review*, vol. 113, no. 4, pp. 1046–1051, 1959. DOI: `10.1103/physrev.113.1046`.

[128] O. Y. Gorobtsov, G. Mercurio, F. Capotondi, *et al.*, “Seeded x-ray free-electron laser generating radiation with laser statistical properties”, *Nature Communications*, vol. 9, no. 1, 2018. DOI: `10.1038/s41467-018-06743-8`.

[129] A. Togo, L. Chaput, and I. Tanaka, “Distributions of phonon lifetimes in brillouin zones”, *Physical Review B*, vol. 91, no. 9, 2015. DOI: `10.1103/physrevb.91.094306`.

[130] K. Esfarjani, G. Chen, and H. T. Stokes, “Heat transport in silicon from first-principles calculations”, *Physical Review B*, vol. 84, no. 8, 2011. DOI: `10.1103/physrevb.84.085204`.

[131] J.-P. M. Péraud and N. G. Hadjiconstantinou, “Extending the range of validity of fourier’s law into the kinetic transport regime via asymptotic solution of the phonon boltzmann transport equation”, *Physical Review B*, vol. 93, no. 4, 2016. DOI: `10.1103/physrevb.93.045424`.

[132] G. H. Tang, C. Bi, and B. Fu, “Thermal conduction in nano-porous silicon thin film”, *Journal of Applied Physics*, vol. 114, no. 18, p. 184 302, 2013. DOI: `10.1063/1.4829913`.

[133] S. Hamian, T. Yamada, M. Faghri, and K. Park, “Finite element analysis of transient ballistic–diffusive phonon heat transport in two-dimensional domains”, *International Journal of Heat and Mass Transfer*, vol. 80, pp. 781–788, 2015. DOI: `10.1016/j.ijheatmasstransfer.2014.09.073`.

[134] A. A. Joshi and A. Majumdar, “Transient ballistic and diffusive phonon heat transport in thin films”, *Journal of Applied Physics*, vol. 74, no. 1, pp. 31–39, 1993. DOI: `10.1063/1.354111`.

[135] A. Majumdar, “Microscale heat conduction in dielectric thin films”, *Journal of Heat Transfer*, vol. 115, no. 1, p. 7, 1993. DOI: `10.1115/1.2910673`.

[136] J. Maassen and M. Lundstrom, “A simple boltzmann transport equation for ballistic to diffusive transient heat transport”, *Journal of Applied Physics*, vol. 117, no. 13, p. 135 102, 2015. DOI: `10.1063/1.4916245`.

[137] ——, “Steady-state heat transport: Ballistic-to-diffusive with fourier’s law”, *Journal of Applied Physics*, vol. 117, no. 3, p. 035 104, 2015. DOI: `10.1063/1.4905590`.

[138] ——, “Modeling ballistic effects in frequency-dependent transient thermal transport using diffusion equations”, *Journal of Applied Physics*, vol. 119, no. 9, p. 095 102, 2016. DOI: `10.1063/1.4942836`.

[139] J. Kaiser, T. Feng, J. Maassen, X. Wang, X. Ruan, and M. Lundstrom, “Thermal transport at the nanoscale: A fourier’s law vs. phonon boltzmann equation study”, *Journal of Applied Physics*, vol. 121, no. 4, p. 044 302, 2017. DOI: `10.1063/1.4974872`.

[140] M. Asheghi, Y. K. Leung, S. S. Wong, and K. E. Goodson, “Phonon-boundary scattering in thin silicon layers”, *Applied Physics Letters*, vol. 71, no. 13, pp. 1798–1800, 1997. DOI: `10.1063/1.119402`.

[141] A. Jain, Y.-J. Yu, and A. J. H. McGaughey, “Phonon transport in periodic silicon nanoporous films with feature sizes greater than 100 nm”, *Physical Review B*, vol. 87, no. 19, 2013. DOI: `10.1103/physrevb.87.195301`.

[142] J. Cuffe, J. K. Eliason, A. A. Maznev, *et al.*, "Reconstructing phonon mean-free-path contributions to thermal conductivity using nanoscale membranes", *Physical Review B*, vol. 91, no. 24, 2015. DOI: `10.1103/physrevb.91.245423`.

[143] A. J. H. McGaughey, E. S. Landry, D. P. Sellan, and C. H. Amon, "Size-dependent model for thin film and nanowire thermal conductivity", *Applied Physics Letters*, vol. 99, no. 13, p. 131 904, 2011. DOI: `10.1063/1.3644163`.

[144] A. J. H. McGaughey and A. Jain, "Nanostructure thermal conductivity prediction by monte carlo sampling of phonon free paths", *Applied Physics Letters*, vol. 100, no. 6, p. 061 911, 2012. DOI: `10.1063/1.3683539`.

[145] K. D. Parrish, J. R. Abel, A. Jain, J. A. Malen, and A. J. H. McGaughey, "Phonon-boundary scattering in nanoporous silicon films: Comparison of monte carlo techniques", *Journal of Applied Physics*, vol. 122, no. 12, p. 125 101, 2017. DOI: `10.1063/1.4993601`.

[146] D. P. Sellan, J. E. Turney, A. J. H. McGaughey, and C. H. Amon, "Cross-plane phonon transport in thin films", *Journal of Applied Physics*, vol. 108, no. 11, p. 113 524, 2010. DOI: `10.1063/1.3517158`.

[147] J. E. Turney, A. J. H. McGaughey, and C. H. Amon, "In-plane phonon transport in thin films", *Journal of Applied Physics*, vol. 107, no. 2, p. 024 317, 2010. DOI: `10.1063/1.3296394`.

[148] B. Vermeersch, J. Carrete, and N. Mingo, "Cross-plane heat conduction in thin films with ab-initio phonon dispersions and scattering rates", *Applied Physics Letters*, vol. 108, no. 19, p. 193 104, 2016. DOI: `10.1063/1.4948968`.

[149] B. Fu, K. D. Parrish, H.-Y. Kim, G. Tang, and A. J. H. McGaughey, "Phonon confinement and transport in ultrathin films", *Physical Review B*, vol. 101, no. 4, 2020. DOI: `10.1103/physrevb.101.045417`.

[150] B. Vermeersch and N. Mingo, "Quasiballistic heat removal from small sources studied from first principles", *Physical Review B*, vol. 97, no. 4, 2018. DOI: `10.1103/physrevb.97.045205`.

[151] M. E. Siemens, Q. Li, R. Yang, *et al.*, "Quasi-ballistic thermal transport from nanoscale interfaces observed using ultrafast coherent soft x-ray beams", *Nature Materials*, vol. 9, no. 1, pp. 26–30, 2009. DOI: `10.1038/nmat2568`.

[152] J. A. Johnson, A. A. Maznev, J. Cuffe, *et al.*, "Direct measurement of room-temperature nondiffusive thermal transport over micron distances in a silicon membrane", *Physical Review Letters*, vol. 110, no. 2, p. 025 901, 2013. DOI: `10.1103/physrevlett.110.025901`.

[153] D. Ding, X. Chen, and A. J. Minnich, “Radial quasiballistic transport in time-domain thermoreflectance studied using monte carlo simulations”, *Applied Physics Letters*, vol. 104, no. 14, p. 143 104, 2014. DOI: `10.1063/1.4870811`.

[154] A. J. Minnich, J. A. Johnson, A. J. Schmidt, *et al.*, “Thermal conductivity spectroscopy technique to measure phonon mean free paths”, *Physical Review Letters*, vol. 107, no. 9, p. 095 901, 2011. DOI: `10.1103/physrevlett.107.095901`.

[155] A. J. Minnich, “Determining phonon mean free paths from observations of quasiballistic thermal transport”, *Physical Review Letters*, vol. 109, no. 20, p. 205 901, 2012. DOI: `10.1103/physrevlett.109.205901`.

[156] L. Zeng, K. C. Collins, Y. Hu, *et al.*, “Measuring phonon mean free path distributions by probing quasiballistic phonon transport in grating nanostructures”, *Scientific Reports*, vol. 5, no. 1, 2015. DOI: `10.1038/srep17131`.

[157] J. C. Maxwell, “Iv. on the dynamical theory of gases”, *Philosophical transactions of the Royal Society of London*, no. 157, pp. 49–88, 1867.

[158] C. Cattaneo, “Sur une forme de l’equation de la chaleur eliminant la paradoxe d’une prop- agation instantantee”, *Comptes Rendus*, vol. 247, pp. 431–433, 1958.

[159] P. Vernotte, “The true heat equation”, *Comptes Rendus*, vol. 247, p. 2103, 1958.

[160] D. D. Joseph and L. Preziosi, “Heat waves”, *Rev. Mod. Phys.*, vol. 61, pp. 41–73, 1 1989. DOI: `10.1103/RevModPhys.61.41`.

[161] Z. Qu, “Photo-thermo-mechanical analysis and control for high-brightness and high-repetition-rate x-ray optics”, PhD thesis, UC Merced, 2020.

[162] S. Reiche, “GENESIS 1.3: a fully 3D time-dependent FEL simulation code”, *Nuclear Instruments and Methods in Physics Research Section A: Accelerators, Spectrometers, Detectors and Associated Equipment*, vol. 429, no. 1, pp. 243–248, 1999, ISSN: 0168-9002. DOI: `https://doi.org/10.1016/S0168-9002(99)00114-X`.

[163] S. Reiche, “Numerical studies for a single pass high gain free-electron laser”, PhD thesis, Universität Hamburg, 1999.

[164] ——, (). Genesis 1.3, [Online]. Available: `http://genesis.web.psi.ch/`.

[165] J. Zemella, “Untersuchungen zu einem Freie-Elektronen-Laser-Oszillator im Röntgen-Wellenlängenbereich für den European XFEL”, PhD thesis, Hamburg, Univ., 2013.

[166] The HDF5 Group. (1997-NNNN). Hierarchical Data Format, version 5, [Online]. Available: `https://www.hdfgroup.org/HDF5/`.

[167] A. Kostenbauder, “Ray-pulse matrices: A rational treatment for dispersive optical systems”, *IEEE Journal of Quantum Electronics*, vol. 26, no. 6, pp. 1148–1157, 1990. DOI: `10.1109/3.108113`.

[168] J. G. Karssenberg, P. J. M. van der Slot, I. V. Volokhine, J. W. J. Verschuur, and K.-J. Boller, “Modeling paraxial wave propagation in free-electron laser oscillators”, *Journal of Applied Physics*, vol. 100, no. 9, p. 093 106, 2006. DOI: `10.1063/1.2363253`.

[169] P. J. M. van der Slot and K.-J. Boller, “Recent Updates to the Optical Propagation Code OPC”, English, in *Proceedings of the FEL2014, Basel, Switzerland*, 36th International Free Electron Laser Conference, FEL 2014, FEL ; Conference date: 25-08-2014 Through 29-08-2014, 2014, pp. 412–415.

[170] The MPI Forum, “MPI: A Message Passing Interface”, in *Proceedings of the 1993 ACM/IEEE conference on Supercomputing - Supercomputing ’93*, ACM Press, 1993. DOI: `10.1145/169627.169855`.

[171] J. Goodman, *Introduction to Fourier optics*. New York: McGraw-Hill, 1996, ISBN: 0070242542.

[172] O. Chubar, M.-E. Couprie, M. Labat, G. Lambert, F. Polack, and O. Tcherbakoff, “Time-dependent FEL wavefront propagation calculations: Fourier optics approach”, *Nuclear Instruments and Methods in Physics Research Section A: Accelerators, Spectrometers, Detectors and Associated Equipment*, vol. 593, no. 1-2, pp. 30–34, 2008. DOI: `10.1016/j.nima.2008.04.058`.

[173] J. Schmidt, *Numerical simulation of optical wave propagation with examples in MATLAB*, ser. SPIE Press Monograph. Bellingham, Wash: SPIE, 2010, vol. Vol. PM199, ISBN: 9780819483263.

[174] D. Voelz, *Computational fourier optics : a MATLAB tutorial*. Bellingham, Wash: SPIE Press, 2011, ISBN: 9780819482051.

[175] W. H. Press, S. A. Teukolsky, W. T. Vetterling, and B. P. Flannery, *Numerical recipes : the art of scientific computing*, 3rd ed. Cambridge University Press, 2007, 1256 pp., ISBN: 9780511335556.

[176] W. Q. Hua, F. G. Bian, Y. M. He, *et al.*, “Using the power spectral density method to characterize and evaluate the x-ray mirrors surfaces”, in *Proceedings of 4th International Particle Accelerator Conference, IPAC 2013, May 13-17, 2013, Shanghai, China*, 2013.

[177] K. Yamauchi, H. Mimura, S. Matsuyama, *et al.*, “Focusing mirror for coherent hard x-rays”, in *Synchrotron Light Sources and Free-Electron Lasers: Accelerator Physics, Instrumentation and Science Applications*, E. Jaeschke, S. Khan, J. R. Schneider, and J. B. Hastings, Eds. Springer International Publishing, 2016, pp. 927–956, ISBN: 978-3-319-04507-8. DOI: `10.1007/978-3-319-04507-8_54-1`.

[178] V. A. Bushuev, “Effect of the thermal heating of a crystal on the diffraction of pulses of a free-electron x-ray laser”, *Bulletin of the Russian Academy of Sciences: Physics*, vol. 77, no. 1, pp. 15–20, 2013. DOI: `10.3103/s1062873813010061`.

[179] Z. Qu, Y. Ma, G. Zhou, and J. Wu, “Analytical model for monochromator performance characterizations under thermal load”, *Optics Express*, vol. 28, no. 20, p. 30 075, 2020. DOI: `10.1364/oe.394958`.

[180] The Open MPI Project. (2021). Open MPI v4.1.0 documentation, [Online]. Available: `https://www.open-mpi.org/doc/v4.1/`.

[181] The HDF5 Group. (2012-NNNN). Parallel HDF5, [Online]. Available: `https://portal.hdfgroup.org/display/HDF5/Introduction%20to%20Parallel%20HDF5`.

[182] I. Agapov, G. Geloni, S. Tomin, and I. Zagorodnov, “OCELOT: A software framework for synchrotron light source and FEL studies”, *Nuclear Instruments and Methods in Physics Research Section A: Accelerators, Spectrometers, Detectors and Associated Equipment*, vol. 768, pp. 151–156, 2014. DOI: `10.1016/j.nima.2014.09.057`.

[183] M. Frigo and S. G. Johnson, “The design and implementation of FFTW3”, *Proceedings of the IEEE*, vol. 93, no. 2, pp. 216–231, 2005. DOI: `10.1109/jproc.2004.840301`.

[184] V. G. Kohn, “Program for calculating the scattering parameters used in the x-ray standing wave method”, *Crystallography Reports*, vol. 51, no. 6, pp. 936–940, 2006. DOI: `10.1134/s1063774506060034`.

[185] H. X. Gao and L.-M. Peng, “Parameterization of the temperature dependence of the debye–waller factors”, *Acta Crystallographica Section A Foundations of Crystallography*, vol. 55, no. 5, pp. 926–932, 1999. DOI: `10.1107/s0108767399005176`.

[186] P. Jacobson and S. Stoupin, “Thermal expansion coefficient of diamond in a wide temperature range”, *Diamond and Related Materials*, vol. 97, p. 107 469, 2019. DOI: `10.1016/j.diamond.2019.107469`.

[187] S. Stoupin and Y. V. Shvyd’ko, “Ultraprecise studies of the thermal expansion coefficient of diamond using backscattering x-ray diffraction”, *Phys. Rev. B*, vol. 83, p. 104 102, 10 2011. DOI: `10.1103/PhysRevB.83.104102`.

[188] Y. Hu, T. Feng, X. Gu, *et al.*, “Unification of nonequilibrium molecular dynamics and the mode-resolved phonon boltzmann equation for thermal transport simulations”, *Physical Review B*, vol. 101, no. 15, 2020. DOI: `10.1103/physrevb.101.155308`.

[189] B. Vermeersch, “Compact stochastic models for multidimensional quasiballistic thermal transport”, *Journal of Applied Physics*, vol. 120, no. 17, p. 175 102, 2016. DOI: `10.1063/1.4965866`.

[190] Y.-C. Hua and B.-Y. Cao, “The effective thermal conductivity of ballistic–diffusive heat conduction in nanostructures with internal heat source”, *International Journal of Heat and Mass Transfer*, vol. 92, pp. 995–1003, 2016. DOI: `10.1016/j.ijheatmasstransfer.2015.09.068`.

[191] A. Christensen and S. Graham, “Multiscale lattice boltzmann modeling of phonon transport in crystalline semiconductor materials”, *Numerical Heat Transfer, Part B: Fundamentals*, vol. 57, no. 2, pp. 89–109, 2010. DOI: `10.1080/10407790903582942`.

[192] J.-P. M. Péraud and N. G. Hadjiconstantinou, “Deviational phonons and thermal transport at the nanoscale”, in *Volume 7: Fluids and Heat Transfer, Parts A, B, C, and D*, American Society of Mechanical Engineers, 2012. DOI: `10.1115/imece2012-87547`.

[193] G. A. Radtke, J.-P. M. Péraud, and N. G. Hadjiconstantinou, “On efficient simulations of multiscale kinetic transport”, *Philosophical Transactions of the Royal Society A: Mathematical, Physical and Engineering Sciences*, vol. 371, no. 1982, p. 20 120 182, 2013. DOI: `10.1098/rsta.2012.0182`.

[194] M. Maldovan, “Specular reflection leads to maximum reduction in cross-plane thermal conductivity”, *Journal of Applied Physics*, vol. 125, no. 22, p. 224 301, 2019. DOI: `10.1063/1.5092341`.

[195] H. P. Langtangen and K.-A. Mardal, *Introduction to Numerical Methods for Variational Problems*. Springer International Publishing, 2019. DOI: `10.1007/978-3-030-23788-2`.

[196] H. Sinn, “Heat load estimates for the xfel beamline optics”, HASYLAB, annual report, 2007.

[197] A. Logg, K.-A. Mardal, and G. Wells, Eds., *Automated Solution of Differential Equations by the Finite Element Method*. Springer Berlin Heidelberg, 2012. DOI: `10.1007/978-3-642-23099-8`.

[198] S.-W. Hung, S. Hu, and J. Shiomi, “Spectral control of thermal boundary conductance between copper and carbon crystals by self-assembled monolayers”, *ACS Applied Electronic Materials*, vol. 1, no. 12, pp. 2594–2601, 2019. DOI: `10.1021/acsaelm.9b00587`.

[199] W. Liu, G. E. Ice, L. Assoufid, *et al.*, “Achromatic nested kirkpatrick–baez mirror optics for hard x-ray nanofocusing”, *Journal of Synchrotron Radiation*, vol. 18, no. 4, pp. 575–579, 2011. DOI: `10.1107/s0909049511010995`.

[200] Y. Shvyd’ko, S. Stoupin, V. Blank, and S. Terentyev, “Near-100% bragg reflectivity of x-rays”, *Nature Photonics*, vol. 5, no. 9, pp. 539–542, 2011. DOI: `10.1038/nphoton.2011.197`.

[201] Y. Shvyd’ko, V. Blank, and S. Terentyev, “Diamond x-ray optics: Transparent, resilient, high-resolution, and wavefront preserving”, *MRS Bulletin*, vol. 42, no. 06, pp. 437–444, 2017. DOI: `10.1557/mrs.2017.119`.

[202] T. Kolodziej, Y. Shvyd’ko, D. Shu, *et al.*, “High bragg reflectivity of diamond crystals exposed to multi-kW mm-2 x-ray beams”, *Journal of Synchrotron Radiation*, vol. 25, no. 4, pp. 1022–1029, 2018. DOI: `10.1107/s1600577518007695`.

[203] G. Geloni, J. Anton, V. Blank, *et al.*, "Status of the hard x-ray self-seeding setup at the european xfel", en, *Proceedings of the 39th Free Electron Laser Conference*, vol. FEL2019, Germany, 2019. DOI: `10.18429/JACOW-FEL2019-TUP079`.

[204] L. Samoylova, D. Shu, X. Dong, *et al.*, "Design of hard x-ray self-seeding monochromator for european XFEL", Author(s), 2019. DOI: `10.1063/1.5084579`.

[205] I. Zagorodnov, M. Dohlus, and S. Tomin, "Accelerator beam dynamics at the european x-ray free electron laser", *Physical Review Accelerators and Beams*, vol. 22, no. 2, 2019. DOI: `10.1103/physrevaccelbeams.22.024401`.

[206] C. Pellegrini, A. Marinelli, and S. Reiche, "The physics of x-ray free-electron lasers", *Reviews of Modern Physics*, vol. 88, no. 1, p. 015 006, 2016. DOI: `10.1103/revmodphys.88.015006`.

[207] MXL - Operation of the XFEL Accelerator. (2020). Performance - Pulse Energies vs. Photon Energies Overview, [Online]. Available: `https://xfel.desy.de/operation/performance/`.

[208] W. Decking, S. Abeghyan, P. Abramian, *et al.*, "A MHz-repetition-rate hard x-ray free-electron laser driven by a superconducting linear accelerator", *Nature Photonics*, vol. 14, no. 6, pp. 391–397, 2020. DOI: `10.1038/s41566-020-0607-z`.

[209] S. Schulz, M. Czwalinna, M. Felber, *et al.*, "Few-femtosecond facility-wide synchronization of the european xfel", *Proceedings of the 39th Free Electron Laser Conference*, vol. FEL2019, Germany, 2019. DOI: `10.18429/JACOW-FEL2019-WEB04`.

[210] J. Liu, F. Dietrich, and J. Grünert, "Technical design report: Photon arrival time monitor (pam) at the european xfel", no. REPORT. XFEL.EU TR-2017-002, 2017. DOI: `10.22003/XFEL.EU-TR-2017-002`.

[211] "Metrology report mr2020-008: Sample 17-0140-sts-3,short substrate(ibf- polished, uncoated)", Metrology Report MR2020-008, European XFEL GmbH, Tech. Rep., 2020, Metrology Report MR2020-008.

[212] P. Pradhan, M. Wojcik, X. Huang, *et al.*, "Small bragg-plane slope errors revealed in synthetic diamond crystals", *Journal of Synchrotron Radiation*, vol. 27, no. 6, pp. 1553–1563, 2020. DOI: `10.1107/s1600577520012746`.

[213] J. Dai, H. Deng, and Z. Dai, "Proposal for an x-ray free electron laser oscillator with intermediate energy electron beam", *Physical Review Letters*, vol. 108, no. 3, 2012. DOI: `10.1103/physrevlett.108.034802`.

[214] K. Li, M. Song, and H. Deng, "Simplified model for fast optimization of a free-electron laser oscillator", *Physical Review Accelerators and Beams*, vol. 20, no. 3, 2017. DOI: `10.1103/physrevaccelbeams.20.030702`.

[215] K.-J. Kim, L. Assoufid, F.-J. Decker, *et al.*, “Test of an x-ray cavity using double-bunches from the lcls cu-linac”, en, *Proceedings of the 10th Int. Particle Accelerator Conf.*, vol. IPAC2019, Australia, 2019. DOI: `10.18429/JACOW-IPAC2019-TUPRB096`.

[216] G. Marcus, J. Anton, L. Assoufid, *et al.*, “Cavity-based free-electron laser research and development: A joint argonne national laboratory and slac national laboratory collaboration”, en, *Proceedings of the 39th Free Electron Laser Conference*, vol. FEL2019, Germany, 2019. DOI: `10.18429/JACOW-FEL2019-TUD04`.

[217] I. Petrov, J. Anton, U. Boesenberg, *et al.*, “Effect of heat load on cryo-cooled monochromators at the european x-ray free-electron laser: Simulations and first experimental observations”, en, *Proceedings of the 39th Free Electron Laser Conference*, vol. FEL2019, Germany, 2019. DOI: `10.18429/JACOW-FEL2019-WEP079`.

[218] H. S. Carslaw and J. C. Jaeger, *Conduction of heat in solids*. Oxford: Clarendon Press, 1959, ISBN: 9780198533689.

[219] M.-Q. Song, Q.-M. Zhang, Y.-H. Guo, K. Li, and H.-X. Deng, “Numerical modeling of thermal loading of diamond crystal in x-ray FEL oscillators”, *Chinese Physics C*, vol. 40, no. 4, p. 048 101, 2016. DOI: `10.1088/1674-1137/40/4/048101`.

[220] T. Tschentscher, C. Bressler, J. Grünert, *et al.*, “Photon beam transport and scientific instruments at the european XFEL”, *Applied Sciences*, vol. 7, no. 6, p. 592, 2017. DOI: `10.3390/app7060592`.

[221] W. Freund, L. Fröhlich, S. Karabekyan, *et al.*, “First measurements with the k-monochromator at the european XFEL”, *Journal of Synchrotron Radiation*, vol. 26, no. 4, pp. 1037–1044, 2019. DOI: `10.1107/s1600577519005307`.

[222] J. Grünert, M. P. Carbonell, F. Dietrich, *et al.*, “X-ray photon diagnostics at the european XFEL”, *Journal of Synchrotron Radiation*, vol. 26, no. 5, pp. 1422–1431, 2019. DOI: `10.1107/s1600577519006611`.

[223] I. Bahns, C. Maag, J. Rossbach, V. Sleziona, H. Sinn, and P. Thiessen, “Thermal and mechanical stability of bragg reflectors under pulsed xfel radiation”, in *Proc. of FEL2017, Santa Fe, USA*, Paper TUC02, 2017.

[224] I. Bahns, W. Hillert, P. Rauer, J. Rossbach, and H. Sinn, “Interaction of powerful electromagnetic fields with bragg reflectors”, en-us, *Proceedings of the 39th Free Electron Laser Conf.*, vol. FEL2019, Germany–, 2019. DOI: `10.18429/JACOW-FEL2019-THP041`.

[225] W. Decking and H. Weise, “Commissioning of the european xfel accelerator”, en, *Proceedings of the 8th Int. Particle Accelerator Conf.*, vol. IPAC2017, Denmark, 2017. DOI: `10.18429/JACOW-IPAC2017-MOXAA1`.

[226] M. Altarelli, *XFEL : the European X-ray free-electron laser : technical design report*. Hamburg: DESY XFEL Project Group, 2006, ISBN: 9783935702171.

[227] F. Brinker, “Commissioning of the european xfel injector”, en, *Proceedings of the 7th Int. Particle Accelerator Conf.*, vol. IPAC2016, Korea, 2016. DOI: `10.18429/JACOW-IPAC2016-TUOCA03`.

[228] S. Schreiber, S. Lederer, P. Michelato, L. Monaco, and D. Sertore, “Update on the lifetime of cs2te photocathodes operated at flash”, en, *Proceedings of the 38th Int. Free Electron Laser Conf.*, vol. FEL2017, USA, 2018. DOI: `10.18429/JACOW-FEL2017-WEP003`.

[229] B. Aune, R. Bandelmann, D. Bloess, *et al.*, “Superconducting TESLA cavities”, *Physical Review Special Topics - Accelerators and Beams*, vol. 3, no. 9, p. 092 001, 2000. DOI: `10.1103/physrevstab.3.092001`.

[230] S. Abeghyan, M. Bagha-Shanjani, G. Chen, *et al.*, “First operation of the SASE1 undulator system of the european x-ray free-electron laser”, *Journal of Synchrotron Radiation*, vol. 26, no. 2, pp. 302–310, 2019. DOI: `10.1107/s1600577518017125`.

[231] E. Schneidmiller and M. Yurkov, “Baseline parameters of the european xfel”, en, *Proceedings of the 38th Int. Free Electron Laser Conf.*, vol. FEL2017, USA, 2018. DOI: `10.18429/JACOW-FEL2017-MOP033`.

[232] S. Liu, R. Boll, F. Brinker, *et al.*, “Parallel operation of sase1 and sase3 at the european xfel”, en, *Proceedings of the 39th Free Electron Laser Conference*, vol. FEL2019, Germany, 2019. DOI: `10.18429/JACOW-FEL2019-TUA01`.

[233] B. Saleh, *Fundamentals of photonics*. Hoboken, NJ: Wiley, 2019, ISBN: 9781119702115.

Acknowledgments

I would like to thank my supervisors Prof. em. Dr. Jörg Roßbach and Dr. Winfried Decking for their support, advice and effort during my work on this thesis. Without their knowledge and guidance, this thesis would not have been possible. Thank you for always having an open door and open ears for my concerns! Jörg, thank you for helping me out even during your free time and vacations!

Many thanks go to Dr. Harald Sinn for providing lots of insights and discussion on the topic of X-ray optics, as well as for actively integrating me into the XFELO/CBXFEL project at the European XFEL.

For always keeping his office door open for issues on the ‘electron side’ of the CBXFEL, I would also like to thank Prof. Dr. Wolfgang Hillert.

I am grateful to Maurizio Vannoni as my direct supervisor at the European XFEL for introducing me to the X-ray optics group and who kindly dealt with any questions I confronted him with.

For making me feel as a full and acknowledged member, I am very grateful to the members of X-ray optics group.

A special thanks goes to my co-worker Immo Bahns, whose PhD thesis was closely related to mine, and with whom I spent many hours of fruitful conversation over our respective issues, especially with regard to the impact of the crystals’ thermal response on the CBXFEL performance.

I want to thank my ‘predecessors’ Dr. Christoph Maag and Dr. Johann Zemella for introducing me to the involved physics of the X-ray free-electron laser oscillators.

For letting me participate in the Hard X-ray Self-Seeding (HXRSS) commissioning and thereby acquainting me with the do’s and don’ts of the complicated European XFEL machine, I am thankful to Dr. Gianluca Geloni and the entire HXRSS project team.

I am very grateful to Daniele La Civita for many sessions of examining the mechanic constraints of a simplified XFELO experiment at the HXRSS setup and for the dedicated CBXFEL demonstrator.

I would also like to thank Dr. Liubov Samoylova and Vivien Sleziona for their time talking about X-ray dynamic diffraction theory.

I acknowledge the support from DESY (Hamburg, Germany), a member of the Helmholtz Association HGF, as well as the European XFEL GmbH (Schenefeld, Germany).

I also recognize the support through the Maxwell computational resources operated at Deutsches Elektronen- Synchrotron (DESY), Hamburg, Germany.

I am grateful to the BMBF for partially funding this research in the framework of the project ”*LoKoFEL: Longitudinale Kohärenz am Freie-Elektronen-Laser - Kontrolle, Analyse und Anwendungen*” (FKZ 05K16GU4).

A big thanks goes to Philipp Amstutz, Dr. Florian Christie, Christian Henkel, Max Kellermeier, Dr. Willi Kuropka and Dr. Thorsten Hellert for the many coffees, debates and laughs shared in the renowned office 365/30b on the DESY campus.

I would like to thank my parents Jens Thiessen and Deborah Denino-Thiessen, for providing me helping hands.

Last but not least, I want to give a big thanks to my beloved family. I thank my wonderful wife Elisa Rauer, whose radiating positiveness, for her continuous support, backing me up at home in times of intensified work and always cheering me up. Finally, I thank my toddler Nathan for being an active source of joyful distraction.

Eidesstattliche Versicherung

Ich erkläre hiermit an Eides statt, die vorliegende Dissertationsschrift selbst verfasst und keine anderen als die angegebenen Hilfsmittel und Quellen benutzt zu haben; die aus fremden Quellen direkt oder indirekt übernommenen Gedanken sind als solche kenntlich gemacht.
Die eingereichte schriftliche Fassung entspricht der auf dem elektronischem Speichermedium.
Die Dissertation wurde bisher in gleicher oder ähnlicher Form in keiner anderen Prüfungsbehörde vorgelegt und auch noch nicht veröffentlicht.

Hamburg, den May 31, 2022

____

Patrick Rauer